issn 0424-7116
An open-access journal by the German Quaternary Association
Editor-in-chief: Christopher Lüthgens

E&G

Quaternary Science Journal

Eiszeitalter und Gegenwart

Volume 71
No. 1 & 2
2022

An open-access journal of the German Quaternary Association

Copernicus Publications
The Innovative Open Access Publisher

E&G Quaternary Science Journal

An open-access journal of the German Quaternary Association

E&G Quaternary Science Journal (EGQSJ) is an interdisciplinary open-access journal, which publishes peer-reviewed articles and express reports, and retrospectives, as well as thesis abstracts related to Quaternary geology, paleo-environments, paleo-ecology, soil science, paleo-climatology, geomorphology, geochronology, archaeology, geoarchaeology, and now also encompassing methodological advances and aspects of the societal relevance of Quaternary research. EGQSJ is a non-profit, community-based effort: It is run by Quaternary scientists, financed by Quaternary scientists, and supporting Quaternary scientists, because any revenue generated is only used to support publications in the journal.

Copernicus Publications
The Innovative Open Access Publisher

Copernicus Publications
Bahnhofsallee 1e
37081 Göttingen
Germany

Phone: +49 551 90 03 39 0
Fax: +49 551 90 03 39 70

publications@copernicus.org
https://publications.copernicus.org

Printed in Germany.
Schaltungsdienst Lange o.H.G.

ISSN 0424-7116

Published by Copernicus GmbH (Copernicus Publications) on behalf of the German Quaternary Association (DEUQUA).

Image credit:
Caption: Aerial view of the lagoons between the islands Rügen and Hiddensee, part of the national park "Vorpommersche Boddenlandschaft" by Reinhard Lampe (2007)

E&G Quaternary Science Journal
An open-access journal of the German Quaternary Association
https://www.eg-quaternary-science-journal.net/

E&G Quaternary Science Journal
An open-access journal of the German Quaternary Association
https://www.eg-quaternary-science-journal.net/

E&G Quaternary Science Journal
An open-access journal of the German Quaternary Association
https://www.eg-quaternary-science-journal.net/

Advisory board

Copernicus Publications
The Innovative Open Access Publisher

Editorial Support

Natascha Töpfer
editorial@copernicus.org

Publication Production

Sarah Schneemann
production@copernicus.org

E&G Quaternary Sci. J., 71, 1–22, 2022
https://doi.org/10.5194/egqsj-71-1-2022

Open Access E&G Quaternary Science Journal

Research article

Late Quaternary landform evolution and sedimentary successions in the Miaoli Tableland, northwestern Taiwan

Shih-Hung Liu, Robert Hebenstreit, and Margot Böse

Institute of Geographical Sciences, Department of Earth Sciences, Freie Universität Berlin, 12249 Berlin, Germany

Correspondence: Shih-Hung Liu (liushihhung@zedat.fu-berlin.de)

Relevant dates: Received: 28 April 2021 – Revised: 24 September 2021 – Accepted: 6 December 2021 – Published: 18 January 2022

How to cite: Liu, S.-H., Hebenstreit, R., and Böse, M.: Late Quaternary landform evolution and sedimentary successions in the Miaoli Tableland, northwestern Taiwan, E&G Quaternary Sci. J., 71, 1–22, https://doi.org/10.5194/egqsj-71-1-2022, 2022.

Abstract: Elevated Quaternary sedimentary complexes in the western foreland of the central mountain ranges of Taiwan are called tablelands. Their mostly flat surfaces are deeply incised by fluvial processes. The landforms and the fluvial systems in the Miaoli Tableland are investigated by high-resolution terrain analyses based on different datasets. Sediments are described in 51 outcrops and characterized by grain size composition. The outcrops revealed complete or incomplete sequences of the general scheme from bottom to top: sandy tidal–coastal units overlain by gravel- and cobble-rich fluvial deposits always with a fine-grained silt-rich top cover layer influenced by aeolian deposits. All layers are unconsolidated sediments. Three subtypes of this sequence were identified, with respect to the occurrence of the fluvial deposits. The relation of tectonic and erosional processes including the rework of gravels is discussed. The results reveal a tableland surface much more disaggregated than previously mapped, suggesting that individual tableland segments represent remnants of an inferred palaeotopography. The tableland surfaces have been separated into Sedimentary Highlands (SH-I and SH-II) and Sedimentary Terraces (ST) by geometrical properties. The Alluvial and Coastal Plains (AL) represent broad valley bottoms ("box-shaped valleys") in the dendritic drainage systems below 150 m and the coastal plains. The landforms and predominantly the sediment sequences are discussed in the context of the existing stratigraphical schemes of the Toukoshan Formation and the so far rarely used Lungkang Formation. The latter is recommended as the stratigraphical term for the refined subdivision of the uppermost part of late Quaternary sediments in the Miaoli Tableland.

1 Introduction

Sedimentary terraces are landforms which are formed by deposition, base level change, and subsequent erosion. They provide stratigraphic records and represent archives for changes in sedimentary and erosional processes (Charlton, 2008). The process-inducing environmental factors are climate change, sea-level change, and local tectonism, which have been studied in various regions worldwide for interpreting the landscape evolution of sedimentary terraces (e.g. Bridgland and Westaway, 2008; Robustelli et al., 2014; Pickering et al., 2014; Mather et al., 2017).

Huge sedimentary complexes are distributed in the western foreland of the Taiwanese mountain ranges (Yu and Chou, 2001; Yang et al., 2006) (Fig. 1a). They are dissected by fluvial incision, thus forming terraces, which are called

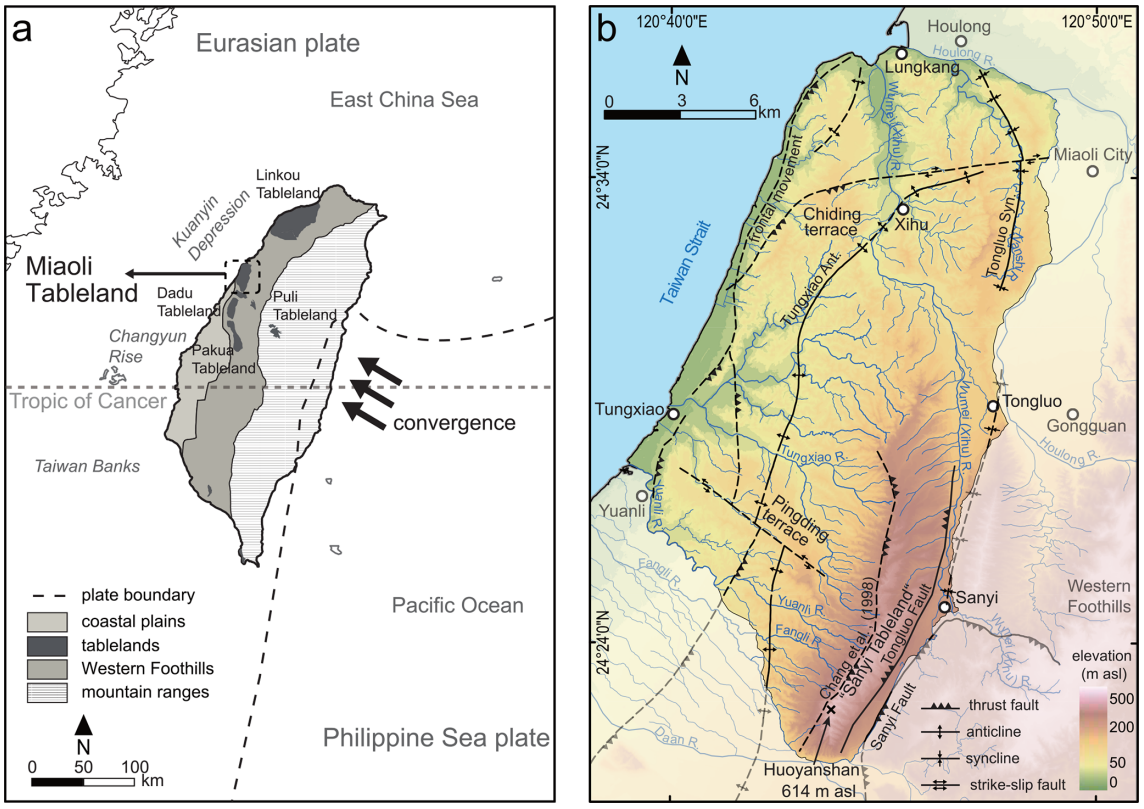

Figure 1. Location of the Miaoli Tableland and other tablelands in Taiwan. Generalized tectonic context after Angelier et al. (1986) and Suppe (1984); geological divisions modified after Ho (1988). **(b)** Detail map of the study area. Elevation extracted from an open-access digital elevation model (DEM) with 20 m resolution (Satellite Survey Center, 2018); tectonic features adapted from geological maps (Central Geological Survey, 2017); locations of the Tongluo Fault and name of "Sanyi Tableland" by Ota et al. (2006).

"tablelands" by local scientists (Lin, 1957; Teng, 1979; Lin and Chou, 1978; Tomita, 1954; Chang et al., 1998; Tsai et al., 2006, 2010). Landforms similar to the tablelands have been described in the western Pacific area, such as in Japan (Matsu'ura et al., 2014) and Korea (Choi et al., 2009).

However, until now, the detailed formation history of these sedimentary terraces has been widely unclear, even though detailed studies focused on different aspects of the tableland morphology such as the local tectonism (Shyu et al., 2005; Yang et al., 2006; Shih and Yang, 1985), the long-term sedimentation since the Neogene (Teng, 1996b; Teng et al., 2001), or weathering degrees and their corresponding relative chronology of the surface materials (Ota et al., 2002; Shih and Yang, 1985; Tsai et al., 2006). The majority of these studies follow the interpretations that, according to the continuous tectonic uplift since the Pliocene, the age of the tablelands' sedimentary units ranges from the Pliocene to early Pleistocene (Chang, 1953). Only a few studies included or focused on the late Quaternary sedimentation and surface morphology of the tablelands (Ota et al., 2006; Tseng et al., 2013; Horng, 2014; Chang et al., 1998; Teng et al., 2001; Siame et al., 2012).

The sedimentary sequences represent potentially valuable archives of the Quaternary landscape history of western Taiwan. As the mountainous island is located in a unique position at the Tropic of Cancer between the Asian continent and the western Pacific, these archives may even have implications for the entire region in terms of palaeoclimate and sea-level change. Thus, more detailed morphological studies are required in order to understand the complicated nature of these terraces on the basis of a reconstruction of the process history. This study presents – as a first step – an approach for interpreting morphological processes by the combination of a concise 3D terrain analysis and sedimentological studies by field observation and particle size characterization in a defined research area in northwestern Taiwan, the Miaoli Tableland. A detailed chronology of the sediment sequence is not in the scope of this morphological study.

2 Regional setting

2.1 Tectonic background and erosion rates of the Taiwanese mountain ranges and their foreland

The orogeny of the Taiwanese mountain ranges is caused by the arc-continent collision at the convergence zone of the Eurasian plate and the Philippine Sea plate in the western Pacific (Fig. 1a), which has been active since the Plio-Pleistocene (Suppe, 1984; Angelier et al., 1986; Teng, 1990; Willemin and Knuepfer, 1994; Teng, 1992; Yu and Song, 2000). Today, the mountain ranges of central Taiwan reach an elevation of 3952 m a.s.l. and are composed of Tertiary sedimentary rocks and low-grade metamorphic rocks at the western limb. Their westernmost part, a 10–20 km wide frontal belt has been called the "Western Foothills" (WF) (Fig. 1a) (Ho, 1988; Pelletier and Stephan, 1986) and has a general height below 2500 m a.s.l. The western foreland of the mountain ranges is a Neogene basin (Yang et al., 2006). The basin depositions have been interpreted as a succession of Tertiary sedimentary rocks overlain by Quaternary sediments yielded from the mountain ranges (Fig. 1a) (Simoes and Avouac, 2006; Yu and Chou, 2001; Lin and Watts, 2002; Lin et al., 2003; Chen et al., 2001; Ho, 1994; Covey, 1986). However, their precise chronology is not available yet (Ota et al., 2006; Chang et al., 1998; Teng, 1996b; Lin, 1963; Ho, 1994). Parts of these Quaternary sediments have been uplifted to present altitudes with a maximum height of ca. 1000 m a.s.l. Due to the complexity of the tectonism, the long-term uplift rates of the WF and the Neogene basin are still unclear (Deffontaines et al., 1997; Shyu et al., 2005; Yang et al., 2016; Teng, 1996a; Ching et al., 2011).

The strong uplift of the island and the subtropical monsoon climate including frequent typhoon events induce erosion rates with an average of 3–6 mm a^{-1} (Dadson et al., 2003). The precipitation is mainly concentrated during the summer and autumn; on average about two to three typhoons strike Taiwan annually (average 1949–2019) (Central Weather Bureau, 2019). Typhoons often cause extreme precipitation events and floods.

2.2 Quaternary sea-level change in Southeast Asia

The post-Last Glacial Maximum (LGM) sea-level curve of the Taiwan Strait has been established by radiocarbon dating of marine sediments (Liu et al., 2008; Chen and Liu, 1996). However, a pre-LGM sea-level curve is not yet established. The combination with global and regional models that reach back further, especially from the Sunda Shelf (Hanebuth et al., 2011; Shackleton, 2000), shows that the sea level was much lower than today after the end of the Eemian sea-level high stand, with a minimum during the LGM (−120 to −140 m). As the depth of the Taiwan Strait west of the Miaoli Tableland is less than 60 m, it was dry land during most of the Late Pleistocene (Horng and Huh, 2011; Huh et al., 2011), and the palaeoflow directions of the northwestern Taiwanese rivers were north to northeast toward the Kuanyin Depression (Huh et al., 2011) (Fig. 1a). After the general Holocene sea-level rise, a short-term high stand during the Mid-Holocene reached +5 m (Liu et al., 2004; Chen and Liu, 1996).

2.3 The tablelands in Taiwan

The uplift, sea-level changes, and the subsequent erosional processes have dissected the foreland sediments. These sedimentary terraces are called "-Ding/-頂" in the local language, i.e. terraces (Chen et al., 2004; Tomita, 1954) or tablelands (Tsai et al., 2010, 2006; Lin, 1957; Teng, 1979; Teng et al., 2001; Shih and Yang, 1985; Lin and Chou, 1978) according to different concepts of the landform evolution, respectively.

Tablelands are mainly distributed in a ca. 5–20 km wide area along the western margin of the WF (Fig. 1a), as well as in mountain basins. In the past, the tableland surfaces were differentiated morphologically and sedimentologically by the following criteria: (1) the lithification degree of the sediments, (2) the driving force of current morphology (fluvial incision/tectonic displacement), (3) the weathering characteristics of the cover sediments (relatively old and intensively weathered substrate/relatively young alluvial deposits), and (4) the elevation of surfaces as a relative chronological index of different morphological stages (Lin, 1957; Tomita, 1953, 1951, 1954). The resulting categories of the tableland surfaces were named "Laterite Highlands" for the higher-elevated quasi-flat surfaces that are covered by reddish, highly weathered sediments; "Laterite Terraces" for the lower-elevated quasi-flat surfaces that are covered by brownish/reddish highly weathered sediments; and "Fluvial Terraces" for the modern fluvial terraces/plains in the immediate vicinity of fluvial paths (Lin, 1957).

In recent decades there have been more detailed studies on the origin and development of the tablelands, e.g. studies on tectonism at the Dadu Tableland and Pakua Tableland (Delcaillau, 2001; Shih and Yang, 1985), the soil development and relative chronology at the Dadu Tableland (Tsai et al., 2010) and Pakua Tableland (Tsai et al., 2006), and the morphology and sediment chronology of the Puli Tableland (Tseng et al., 2013). The depositional environments and biostratigraphy of the sedimentary sequence as well as the morphology corresponding to active tectonism were studied in the Linkou Tableland (Horng, 2014; Teng et al., 2001) as well as the relative and absolute chronology, erosion, and tectonism of smaller terraces in other regions (Chen et al., 2004; Ota et al., 2009, 2002, 2005; Chen et al., 2003). All these studies gave a frame for an understanding of the tableland formation; however, neither an overall morphological model nor a detailed chronology of the tableland development has been established so far.

In past publications the terms "laterite/lateritic" have been used according to the local context, which describes the reddish/brownish, fine-grained soils on the surfaces. However, the usage of this term has recently been challenged by soil

studies (Tsai et al., 2010). According to the latest review of the soil taxonomy in Taiwan, these so-called laterite cover sediments on the tablelands have been revised as "Ultisols" or "Oxisols" by their chemical composition, respectively (Chen et al., 2015). To avoid over-interpretation of soil development characteristics and because the pedological factors of the sediments are not the subjects of this study, the following geomorphological descriptive terms are used in this text: "Sedimentary Highlands" (SH) for Laterite Highlands, "Sedimentary Terraces" (ST) for Laterite Terraces, and "Alluvial and Coastal Plains" (AL) for Fluvial Terraces.

2.4 Study area: the Miaoli Tableland

The sedimentary complexes in the Miaoli region are called the Miaoli Tableland (Teng, 1979) or Miaoli Hills (Chang et al., 1998). We prefer the former term because the geological and morphological settings of the area are consistent with the other tablelands in northwestern Taiwan (Lin and Chou, 1978; Teng, 1979). The Miaoli Tableland is located on the northwestern coast of Taiwan between the Houlong River and the Daan River (120°38′10″ to 120°48′57″ E, 24°36′51″ to 24°21′32″ N). Both rivers have their source area in the mountain belt and therefore a different hydrological regime than the other rivers in the study area. The Miaoli Tableland covers an area of ca. 283 km^2. Its topographical surface is characterized by terraces with different elevation levels. The highest elevation is located at the southernmost part at about 614 m a.s.l. This point is called "Huoyanshan/火炎山", also known as "Fire Mountain" (Fig. 1b). A narrow coastal plain forms a 30 km long stretch between the Wumei (Xihu) River and Yuanli River (Fig. 1b). It is composed of alluvial sediments that are carried by the longshore current (Jan et al., 2002; Wang et al., 2003); according to climate statistics from 2003 to 2020, the tidal difference in the shore area of Miaoli is 4–6 m (Central Weather Bureau, 2020).

The study area is mainly drained by the Tungxiao River and the Wumei (Xihu) River as well as other small local catchments (Fig. 1b). However, many of the fluvial paths in the area are artificially constrained by levees for defending from flooding. For example, the flooding which affected the Miaoli region on 7 August 1959 ("八七水災") was the most severe flooding in the 20th century in Taiwan (The Taiwan Provincial Weather Institution, 1959; Central Weather Bureau, 2019).

The geological maps and the studies of tectonic features exhibit one inferred syncline, two inferred anticlines with low dip angles, and four inferred thrust faults with steep dip angles in the study area (Fig. 1b). These features are almost parallel aligned, striking mainly northeast to southwest (Chang, 1990, 1994; Ho, 1994; Yu et al., 2013; Lin and Watts, 2002; Yu and Chou, 2001; Yang et al., 2016). The coastal area is affected by the tentatively called "frontal movement", which is assumed to be the youngest thrust movement in the Miaoli area (Shyu et al., 2005). Two active thrust faults have been identified at the eastern margin of the Miaoli Tableland (Ota et al., 2006), and an inferred thrust fault at the western fringe of the highlands has been proposed by Chang et al. (1998) (Fig. 1b). There are no direct studies on Quaternary uplift rates in the Miaoli area. Results from the southerly Pakua Tableland, based on radiocarbon dating of different heights of the terrace surfaces, show that it can be assumed to be around 1 mm a^{-1} (Ota et al., 2002, 2006).

The general formation of the Miaoli Tableland has been explained by two hypotheses. Chang et al. (1998) assumed that the present Sedimentary Highlands and the southwest of the Sedimentary Terraces area (the Pingding terrace, Fig. 1b) represent jointed alluvial fans. The gravels and cobbles, which build up the fans, were yielded from the Houlong, Wumei (Xihu), and Daan (palaeo-)rivers. The rest of the area (the Tungxiao River catchment) was interpreted as a palaeobay, which was subsequently filled with sediments (Appendix A). Following the traditional classification of Lin (1957), Chang et al. (1998) assumed that differentiated uplift and erosion during the late Quaternary have dissected the palaeotopography into terraces. They subdivided the surfaces of the Miaoli Tableland into the three surface elevation levels as Laterite Highlands, Laterite Terraces, and Fluvial Terraces (see Sect. 2.2).

In contrast, Ota et al. (2006) focused on differentiated tectonism in the Miaoli region. They assumed that folding along the Tungxiao Anticline (Fig. 1b) caused uplift in the present ST area. This induced the erosion of the overlying sediments, resulting in a topographic inversion along the anticline. The thrust of the Tongluo Fault (Fig. 1b) caused the uplift of the southern SH (tentatively named the "Sanyi Tableland"). This resulted in the separation of the ST and SH along a distinct topographic escarpment, which subsequently was rapidly eroded eastward causing the beheading of the valleys in the southern SH. Colluvial depositions of gravels and cobbles on the western slope foot of the escarpment exhibit the ongoing erosion (Chen, 1983).

The southeastern SH (former Laterite Highlands) is the most detailed studied part of the Miaoli Tableland. Ota et al. (2006) mapped massive, deeply dissected, and tectonically deformed fluvial terraces here. The strata are inclined $> 30°$ to the east in the Fire Mountain area (Chang, 1994). The inclination is assumed to be affected by the westward thrust of the Sanyi Fault (Yang et al., 2007) (Fig. 1b).

2.5 Former stratigraphical interpretations of the Miaoli Tableland

The stratigraphical interpretations of the sedimentary layers in the study area were proposed in the 1930s and redefined in the latter half of the 20th century. The sedimentary layers in the study area were described in different terms as follows.

2.5.1 Toukoshan Formation (Tk Formation)

The Tk Formation is the common term for the Pliocene–Quaternary strata that are exposed along the mountain front of the WF in northern and central Taiwan (Chang, 1990, 1994; Ho, 1994; Lee, 2000; Chen et al., 2001; Chang, 1953). However, information on the dimension and composition of the Tk Formation vary in the available publications. The composition is described as fine-grained sediments in the lower and coarse-grained fluvial sediments in the uppermost sections with a total thickness up to more than 1000 m in central Taiwan (Chang, 1948, 1955; Torii, 1935; Chen et al., 2001). The well-rounded shape of the fluvial gravels and cobbles shows that they might be reworked and transported over certain distances (Teng, 1996b). Some authors described the lower units as already consolidated (Chang, 1955; Ho, 1988; Chang, 1990). Biostratigraphical studies on planktonic foraminifera indicated that the deposition of the Tk Formation started after the end of Olduvai event (Huang, 1984), and a time span of 1.24–0.46 Ma was given by the comparison between the abundance of species and the biozones (Lee et al., 2002).

2.5.2 Tûsyô/Tungxiao/Lungkang Formation (Ts/Lk Formation)

Beside the broadly used term Tk Formation, an older definition of the sediment strata specifically in the Miaoli Tableland is called the Tûsyô Formation (as Ts Formation, according to pronunciations of Japanese of the local name "*通霄*"). It was proposed by Makiyama (1934, 1937) and renamed in Chinese as the Tungxiao Formation by Chang (1948) to describe the loose, poorly cemented sedimentary layers in the Miaoli Tableland with a sequence from bottom to top of intercalated marine sediments, tidal–coastal layers, gravel and cobble beds, and a surface layer with ocher-coloured soils. In 1963, Lin proposed the term Lungkang Formation (as Lk Formation) for the uppermost 10–15 m of the same succession in the coastal area of the Miaoli Tableland. The only difference between these two definitions is that the cover layer of the Lungkang Formation was interpreted as dune sand (Lin, 1963). The absolute chronology of these strata is uncertain. Makiyama (1934) assumed a late Tertiary deposition according to the composition of fossils by the palaeontological concept at that time. Radiocarbon dating on molluscs gave an early Holocene time span (Lin, 1969). The Ts/Lk Formation has been rarely mentioned by other authors after the 1960s.

2.5.3 "Alluvium Deposits", "Terrace Deposits", and "Lateritic Terrace Deposits"

These are different terms for the description of non-cemented deposits on various geographical surfaces (i.e. tablelands, valley floors, flood plains, coastal plains, and estuaries) in the geological maps of the study area (Ota et al., 2006; Chang et al., 1998; Chang, 1990, 1994; Ho, 1994; Chen et al., 2004). They are composed of gravel, aeolian sands, and a mixture of dusty fine sediments. No direct dating has been proceeded yet. A late Quaternary age was assumed based on the loose, poorly consolidated consistency of the deposits. The thickness of them varies depending to the palaeotopography; it reaches a maximum of about 20 m (Chang, 1990; Ho, 1994).

3 Material and methods

3.1 Terrain analyses

Systematic terrain analyses were undertaken by the combination and integration of 3D and 2D datasets: (1) open-access digital elevation models from the Ministry of the Interior of Taiwan (resolution 20 m) and the Shuttle Radar Topography Mission (SRTM, resolution 1 arcsec, ca. 80 m) (Satellite Survey Center, 2018; NASA JPL, 2013), (2) aerial photos and satellite imagery from the open-access Web Map Tile Service in a geographical information system (GIS) (Center for GIS RCHSS Academia Sinica, 2017; National Land Surveying and Mapping Center, 2016), (3) published topographic maps at a 1 : 25 000 scale accessible online (National Land Surveying and Mapping Center, 2016), and (4) geological maps of Taiwan (1 : 50 000) accessible online (Central Geological Survey, 2017).

For the identification and classification of different topographical landforms, we merged the information of absolute and relative elevation with the terrain steepness by applying automatic functions of the GIS software and manual mapping. The aim is to distinguish between the present fluvial paths, tableland surfaces, modern fluvial plains, and coastal plains as well as the slopes in between (Fig. 2).

Four terrain categories were defined:

- The category "fluvial paths" was derived from a calculation using the "Arc Hydro Tools" function in the GIS programme compared with the topographic maps and the aerial photos. The fluvial paths were mapped as line features, whilst other categories were mapped as surface features (polygons).

- The category "tableland" was defined as a quasi-flat surface with the following criteria: (1) the steepness is lower than 10°; (2) it is larger than 400 m^2 (1 pixel in the DEM); and (3) the flat surface is not in the direct vicinity of a flow path (Fig. 2). The steepness threshold was adapted from the study of Saito and Oguchi (2005), in which they proceeded the terrain analysis of 690 alluvial fans in Japan, Taiwan, and the Philippines. All fans show a terrain steepness lower than 7°; the majority of them have one less than 5°, including all 71 studied alluvial fans in this context in Taiwan (Saito and Oguchi, 2005). The edges of the tableland segments were determined by hand mapping. Comparing the direct raster to polygon conversion, it has concisely performed the noise reduction and the edge-smoothing pro-

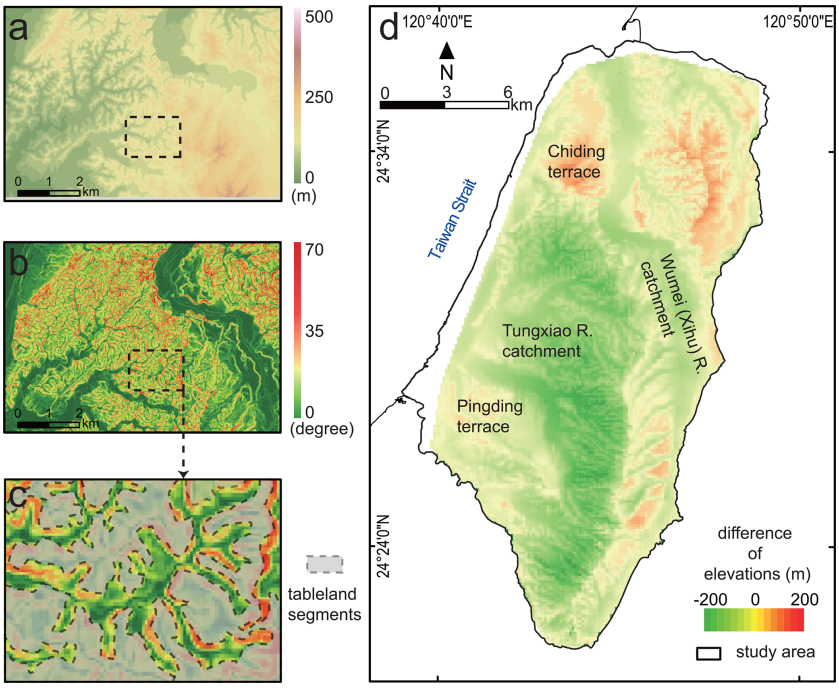

Figure 2. Mapping of the tableland segments. **(a)** The original digital elevation models (Satellite Survey Center, 2018). **(b)** Surface steepness was subsequently calculated by an ArcGIS function (slope). **(c)** An example of hand mapping of the tableland segments in GIS. The tableland segments were recognized by the gentle terrace surfaces. **(d)** Results of the calculation of relative surface elevations: negative values represent DEM elevations lower than the theoretical linear surface and vice versa. The spatial distribution of negative and positive values shows a clear separation at the divide of the Wumei (Xihu) River and the Tungxiao River catchments and at the southern margin of the Chiding terrace.

cedures. For a normalization of the general surface inclination of the Miaoli Tableland from the southeast to northwest, we calculated a theoretical linear-trend surface from the highest point of the terrain to the distal edge of the tableland surfaces, adapting the method of Volker et al. (2007), by using a triangulated irregular network (TIN) interpolation into a raster. Tableland areas above and below this theoretical linear-trend surface were defined as Sedimentary Highlands (SH) and Sedimentary Terraces (ST), respectively (Fig. 2d).

- Quasi-flat surfaces (less than 5°) in the immediate vicinity of the fluvial paths (e.g. valley floors) were defined as "modern fluvial plains". The "coastal plains" were defined as the plains which have a steepness less than 5° and an elevation lower than 30 m a.s.l. along the coast of the Taiwan Strait. The boundary of the plain was marked by the slope foot of the edge of the distal-tableland segments. The modern fluvial plains and the coastal plains were combined and defined as Alluvial and Coastal Plains (AL).

- The category "slopes" was defined for the rest of the surfaces which are steeper than 5°.

3.2 Field observations and sampling

The internal sedimentological composition of the tableland segments was studied to characterize and identify typical layer sequences throughout the study area; 51 field sites were chosen for a detailed description by the following criteria: the sites are (1) easily accessible and provide a good overview of the sedimentary layers, (2) evenly distributed across the study area, and (3) contain more than two visible sedimentary layers for a representative sampling and comparison with other outcrops.

The elevations of the sites were extracted from the DEMs and compared with a handhold GPS receiver in the field. The sedimentary layers in the outcrops were recorded by standard characteristics: shape of boundaries, thickness, sedimentary structures, texture, particle size, and visible fossil content (Miall, 2014; Vail et al., 1991). The sediment colour was only described in a general way to identify individual layers in the field. A specific determination of soil parameters as well as a detailed facies analysis of individual layers are not in the scope of this study. The sedimentary layers were identified in each field site independently, and then the records were compared to find identical layers and sequences throughout the study area. At 12 selected sites, 41 samples were taken for particle size analyses including 2 samples from modern beach (dune) sand for comparison.

3.3 Particle size measurements

The particle size analyses were conducted with a Beckman Coulter™ LS-13320 laser diffractometer at Section 3: Geochronology of the Leibniz Institute for Applied Geophysics, Hanover, Germany. This technique is well adapted for high-precision measurements of fine-grained particles smaller than 2 mm (Konert and Vandenberghe, 1997; Eshel et al., 2004; Beuselinck et al., 1998). None of the samples contained particles > 2 mm, even including the matrix of the gravel and cobble beds.

The sample preparations and measurements were proceeded as follows: for each sample, ca. 20–50 mg of the sediments was filled into the test tubes and treated with 1 % ammonium hydroxide (NH_4OH) solution, in order to disperse the aggregates of sediments for the subsequent particle size analyses. The test tubes were rotated for 24 h at 30 rpm to mix the solution and sediments. Organic matter was not removed. The particle size was measured five times for each sample to reduce the random error. The results were accepted when the value of polarization intensity differential scattering (> 80 %) and obscuration (< 10 %) passed both criteria. The statistical index of the coefficient of variance mean (< 5 %) and coefficient of variance standard variation (< 5 %) were chosen to evaluate the reproducibility of the results (Konert and Vandenberghe, 1997). The particle size fractions and the texture classifications (Jahn et al., 2006) were correlated for the characterization of sedimentary records.

4 Results

4.1 Terrain analyses – topography of the Miaoli Tableland

The topographical analyses reveal the proportion of different morphological categories in the study area: the tablelands (SH + ST) represent 24.2 % (ca. 68.7 km^2); the slopes and gullies represent 44.8 % (ca. 127.2 km^2); the fluvial plains represent 24.2 % (ca. 68.9 km^2); and coastal plains represent 6.6 % (ca. 18.7 km^2) (Fig. 3).

The tableland surfaces are unevenly spread throughout the study area. Their sizes vary from only a few hundred square metres to several square kilometres. The larger tableland segments with widths ranging from ca. 100–1500 m, such as Pingding (ca. 7.0 km^2), Chiding (ca. 4.3 km^2), and other parts (from 2.0 to 0.5 km^2) represent ca. 14 % of the total terrain. However, the high-resolution mapping revealed that the overall spatial pattern of the tableland surface is made up of numerous smaller segments, which are only ca. 40–200 m wide (Fig. 3). They generally represent the water divides between the fluvial paths and are broadly distributed in the study area. Their distribution and shape depend also on different fluvial drainage patterns in the study area.

Figure 3. Results of the terrain analyses and the classification of tableland segments. The Sedimentary Highlands (SH) represent the fluvial terraces, located in the southeastern (SH-I) and northern part (SH-II) divided by the Wumei (Xihu) River. The Sedimentary Terraces (ST) are mainly located in the Tungxiao River catchment. The Alluvial and Coastal Plains (AL) represent the flat surfaces beside the fluvial channels. Detailed mapping of drainage patterns and the elevation profiles of the fluvial valleys is presented in Fig. 4.

The differentiation between the SH and ST can be clearly inferred from the relative height between the true elevations and the theoretical linear-trend surface (Fig. 2d). Furthermore, both show different directions of their inclination in general. The SH is composed of tablelands with ca. 2° northwest-inclining surfaces, while the ST tableland surfaces incline ca. 1° to the west (Fig. 3).

The topographical divide between the ST and the SH is represented by a continuous, west-facing escarpment bending from the southeast to the northwest. The steepness of the slope is about 30° and more. Its relative height is ca. 130–200 m in the south, decreasing northwestward to about 30 m.

4.1.1 The Sedimentary Highlands (SH)

The Sedimentary Highlands (SH) are located in the east and the north of the study area. They were divided into two subgroups by their surface elevation and their location with respect to the Wumei (Xihu) River. The area south of the Wumei (Xihu) River with elevations of about 250 to 614 m a.s.l. is named SH-I. These tableland surfaces are dissected to a minor degree and incline quasi-continuously northward to the left bank of the Wumei (Xihu) River (Fig. 3). The fluvial paths incised in the SH-I segments flow to the northeast. They are tributaries of the Wumei (Xihu) River and show a parallel pattern. The tableland in the northern and the northwestern part of the study area with elevations between 30 and 250 m a.s.l. is classified as SH-II (Fig. 3). The tableland segments are separated by the Wumei (Xihu) River into a western and an eastern part. The western part has larger coherent tableland surfaces, i.e. the tableland segment in Chiding, which is here the topographical divide between the Wumei (Xihu) River and the Taiwan Strait. The eastern SH-II is well dissected, and the remaining tableland segments are the interfluves between the tributaries of the Wumei (Xihu) River, the Nanshi River, and the Houlong River (Fig. 3). The fluvial paths between the SH-II segments are mainly below 150 m a.s.l. and have formed dendritic drainage patterns. All these streams flow in a western or northwestern direction to join the Wumei (Xihu) River and Houlong River or directly to the coast, respectively.

4.1.2 The Sedimentary Terraces (ST)

The Sedimentary Terraces (ST) are located to the west of the SH-I. They are distributed over the whole Tungxiao River catchment and extend further south to other smaller catchments. The majority of ST is lower than 250 m (the highest point is 445 m a.s.l., located at the boundary to the SH-I) and dropping to ca. 30 m at the distal edge close to the coast (Fig. 3 and Appendix A). The larger tableland segments (i.e. Pingding) are located south of the main stream of the Tungxiao River. The smaller tableland segments make up the bulk of the ST surfaces and can be connected tentatively by a quasi-flat inferred surface through the whole ST area (Fig. 3). Their topographic height is ca. 30 m in the east and decreases westward to ca. 5 m at the distal-tableland segments.

The drainage patterns in the ST are differentiated by the elevation. Streams above 150 m a.s.l. form a parallel drainage pattern similar to the SH-I (Fig. 3). Most of them begin near the topographic escarpment (i.e. western slope of the SH-I), and their flow path gradients vary from 1.0 to 14.0° (Fig. 3). The streams below 150 m a.s.l. in the central and western part of the ST have formed dendritic drainage patterns. The fluvial pattern in the SH-II shows also a dendritic system.

4.1.3 Slopes

The gradient of the slopes ranges from 10 to 66° with a majority of 10 to 26°. The spatial distribution of the gradients clearly shows a pattern in different scales. At an overall scale, the slopes in the north and west are gentler than the slops in the south and east, while the differences between individual slopes are not so distinct. In the areas of the dendritic drainage patterns, the vertical shape of the slopes tends to be concave; i.e. the upper part of the slope is steeper than its foot. Reversely, in the areas of the parallel drainage patterns, the vertical shape of the slope is more convex (Fig. 4). Thus, the sections of the upper valleys above 150 m are typically V-shaped.

4.1.4 The Alluvial and Coastal Plains (AL)

The Alluvial and Coastal Plains (AL) reach elevations up to 150 m a.s.l. and represent the wide valley floors and the coastal area (Fig. 3). The main streams' flow paths have gradients from 0.1 to 0.2°, whereas the tributaries' flow paths are steeper (up to 8.0°). The majority of them are braided rivers, except the meandering Nanshi River, a tributary to the Houlong River (Fig. 3). The valley width is not consistent. It is up to kilometres in the main streams and ca. 20–100 m in most of the tributaries. Therefore, the AL represents the active fluvial plains as well as the terraces adjacent to the fluvial paths with one or two levels. The relative height of these terraces is < 10 m. Their sizes are constrained by their location and the stream order. The larger ones ($> 1\,km^2$) in the vicinity of main streams are up to 2100 m wide; the smaller ones ($< 1\,km^2$) in the tributaries are ca. 20–40 m wide (Fig. 3). The AL occurs only in those areas of the SH-II and ST with a dendritic drainage pattern. The valleys are ca. 150–1300 m wide and ca. 20–50 m deep and show relatively narrow flow paths (< 10 m mostly) (Figs. 3 and 4 and Appendix A). In combination with the steep slopes, valley cross sections show a quasi-rectangular transverse profile for which we introduce the term "box-shaped valley".

The coastal plain has a consistent width of around 500–1000 m, but it widens up to 1500 m in the area of the estuaries. The topographic boundary between the coastal plain and distal-tableland segments can be clearly identified by the slope foot of the tableland segments (Fig. 3).

4.2 Sediment descriptions

The 51 studied outcrops in the Miaoli Tableland are located at the edges of the tableland segments (Fig. 5, Table 1) and provide therefore a vertical insight into their internal composition.

Their height ranges from about 3 to 50 m, and they are characterized by up to six relevant unconsolidated sediment layers (Figs. 5 and 6). However, only two of the outcrops show all layers of the succession (i.e. 001_HLPT and 010_EFB). Only a limited number of layers is exposed in

Table 1. List of studied outcrops.

No.	Name	Latitude	Longitude	Location	Height (m)	Elevation (m a.s.l.)
1	HLPT (Hou-Long Petroleum)	24°35′45.30″ N	120°48′24.01″ E	SH-II	49	37
2	BTL (Ban-Tian-Liao)	24°35′47.02″ N	120°43′38.77″ E	SH-II	6	73
3	CSW (Chiuan-Shuei-Wo)	24°35′6.78″ N	120°48′28.61″ E	SH-II	7	97
5	RSK (Rong-Shu-Keng)	24°34′37.68″ N	120°44′23.69″ E	SH-II	4	74
6	NBK (Nan-Bei-Keng)	24°34′21.97″ N	120°44′6.16″ E	SH-II	8	105
7	NCT (Nan-Ching Temple)	24°34′19.24″ N	120°43′32.91″ E	SH-II	3	71
8	MYK (Ma-Yuan-Keng)	24°34′2.42″ N	120°46′48.54″ E	SH-II	6	165
9	LG (Long-Gang)	24°34′1.12″ N	120°48′21.08″ E	SH-II	4	116
10	EFB (Er-Fu Bridge)	24°33′50.55″ N	120°44′48.17″ E	SH-II	11	28
11	FTK (Fu-Tou-Keng)	24°33′37.89″ N	120°44′21.63″ E	SH-II	10	107
12	ZW (Zhang-Wo)	24°32′50.93″ N	120°46′36.74″ E	SH-II	7	68
13	TKD (Tu-Kan-Ding)	24°32′23.29″ N	120°42′27.86″ E	ST	3	148
15	XP (Xin-Pu)	24°32′8.56″ N	120°41′41.95″ E	ST	3	10
17	BW (Bei-Wo)	24°31′12.20″ N	120°43′3.51″ E	ST	6	26
18	DBD (Da-Bi-Dou)	24°30′54.09″ N	120°43′14.00″ E	ST	8	46
20	GCW (Gu-Cuo-Wo)	24°29′48.64″ N	120°44′55.34″ E	ST	5	94
22	ZG (Zhu-Gang)	24°28′55.02″ N	120°42′8.09″ E	ST	20	21
23	XNPW (Xiao-Nan Power Substation)	24°28′17.69″ N	120°40′12.99″ E	ST	2	29
24	YZS (Yuan-Zih-Shan)	24°27′45.38″ N	120°43′15.15″ E	ST	6	67
25	JJC (Jin-Ji Company)	24°27′31.52″ N	120°39′48.64″ E	ST	7	16
26	SLK (Shiau-Lan-Keng)	24°25′45.22″ N	120°44′37.25″ E	ST	7	227
27	TZK (Tian-Zih-Keng)	24°25′58.22″ N	120°41′24.60″ E	ST	5	47
28	HDK (Hu-Dong-Kou)	24°34′49.79″ N	120°45′48.85″ E	SH-II	4	50
29	GJW (Gong-Jiao-Wan)	24°31′14.41″ N	120°47′29.54″ E	SH-II	7	179
30	TYGC (Tiao-Yan-Gu-Chi)	24°26′51.29″ N	120°45′13.33″ E	SH-I	5	335
31	XNPWH (Xiao-Nan Power Substation Heights)	24°28′15.05″ N	120°40′17.79″ E	ST	2	38
32	THST (Dong-He Steelworks)	24°34′13.42″ N	120°44′27.13″ E	SH-II	3	75
33	SZZ (San-Zuo-Wu)	24°22′14.62″ N	120°42′41.03″ E	ST	11	177
34	ZNQ (Zhong-Nan Quarry)	24°30′19.62″ N	120°41′23.91″ E	ST	5	25
35	YCZ (Yu-Cuo-Zhuang)	24°23′59.15″ N	120°42′17.68″ E	ST	10	118
36	KNS (Keng-Nei South)	24°35′12.39″ N	120°46′34.24″ E	SH-II	6	50
37	PD (Ping-Ding)	24°28′2.00″ N	120°41′0.36″ E	ST	7	64
38	JJW (Jie-Jih-Wo)	24°29′6.06″ N	120°43′44.16″ E	ST	5	70
39	JSS (Jin-Shan South)	24°24′58.39″ N	120°41′43.93″ E	ST	27	117
40	RGK (Lei-Gong-Keng)	24°32′32.61″ N	120°46′53.79″ E	SH-II	7	96
41	CHL (Chung-He-Li)	24°35′38.90″ N	120°44′16.56″ E	SH-II	10	55
42	GGF (Guo-Gang Fossils)	24°36′17.61″ N	120°43′49.20″ E	SH-II	4	18
43	SLP (Shuei-Liou-Po)	24°25′59.15″ N	120°41′42.66″ E	ST	10	60
44	NZ (Nan-Zhuang)	24°28′28.28″ N	120°43′21.62″ E	ST	7	63
45	SFK (Shuang-Fong-Kou)	24°28′43.12″ N	120°47′50.39″ E	SH-II	6	192
46	SFB (Shuang-Fu Bridge)	24°30′50.62″ N	120°42′48.73″ E	ST	10	28
47	XBW (Xia-Bei-Wo)	24°31′27.81″ N	120°44′4.72″ E	ST	10	55
48	CTC (Chih-Tu-Ci)	24°35′3.58″ N	120°43′36.15″ E	SH-II	4	69
49	HBK (Hong-Beng-Kan)	24°25′49.87″ N	120°42′33.61″ E	ST	4	121
50	LD (Long-Dong)	24°32′38.91″ N	120°46′29.13″ E	SH-II	2.5	79
51	LK (Long-Kang)	24°36′37.61″ N	120°44′52.69″ E	SH-II	9	3
52	NWII (Nan-Wo II)	24°30′5.68″ N	120°43′53.50″ E	ST	7	57
53	CLK (Che-Lun-Keng)	24°25′51.17”N	120°43′32.89”E	ST	2	157
54	JW (Jiang-Wo)	24°33′3.55″ N	120°45′54.91”E	SH-II	10	34
56	IFF (Yi-Fang Farm)	24°32′29.53″ N	120°46′52.54″ E	SH-II	6	86
57	CTK (Chang-Tan-Keng)	24°26′12.68″ N	120°46′19.75″ E	SH-I	30	301

Note: 57 outcrops were documented initially, but 6 of them were excluded because of visible disturbances.

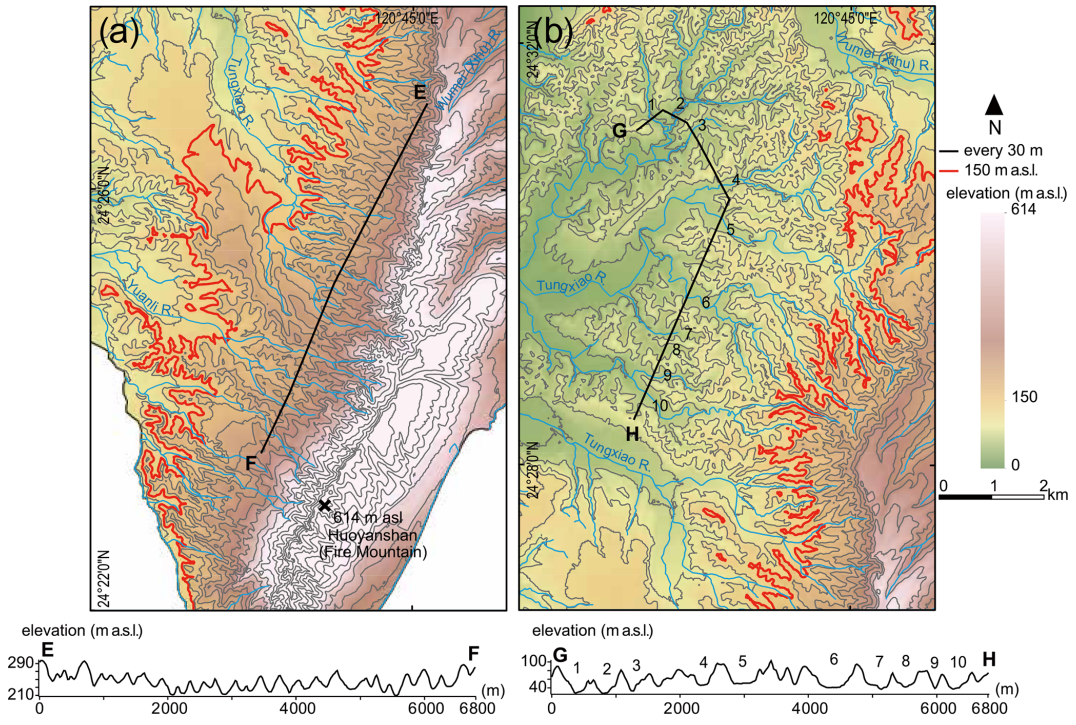

Figure 4. Detail maps of different fluvial drainage patterns in the Sedimentary Terraces (ST) with the respective elevation profiles of the valley cross sections. **(a)** Parallel patterns near the west-facing topographic escarpment between the SH-I (southeast) and ST (northwest) with valley bottoms mostly higher than 150 m a.s.l. Profile E–F shows the typical V-shaped valley cross sections. **(b)** Dendritic patterns in the northern ST area, especially with valley bottoms lower than 150 m a.s.l. Profile G–H shows wider and mainly box-shaped valley cross sections.

the rest of the outcrops – in general the upper part of the sequence. The layers were named according to their grain size composition applying the classification of the FAO (Food and Agriculture Organization of the United Nations; Jahn et al., 2006). They are from bottom to top (1) greyish loam (L), (2) loamy sand (LS), (3) alternations between greyish and yellowish silt loam (SiC), (4) sandy loam (SL), (5) gravel and cobble bed (CSB), and (6) silty loamy cover layer (SiL). The results of their respective grain size properties are listed in Table 2 and summarized in Fig. 7.

4.2.1 Greyish loam layer (L)

This layer is exposed only in three outcrops (01_HLPT, 10_EFB, and 025_JJC; Figs. 5 and 6 and Appendix C). They are located in the north of the SH-II and in the west of the ST. The upper 7 m of the layer are visible, but its total thickness is unclear, as the lower boundary is not exposed (Fig. 6). The upper boundary of this layer is even, continuous, and very distinct. Its internal structure is simple and massive; i.e. no bedding or laminae are visible. The sediment is poorly consolidated. However, it is quite sticky and difficult to excavate with hand tools. The grain size proportions range from 39 % to 52 % sand, 37 % to 48 % silt, and 11 % to 15 % clay, based on three samples (Fig. 7). This layer contains abundant mollusc detritus, which is poorly oriented and mixed with the sediments without layering for identifying the palaeoflow direction.

4.2.2 Loamy sand layer (LS)

This layer is exposed in outcrops of the tablelands ST and SH-II ($n = 16$) (Fig. 6 and Appendix C). It is ca. 5–20 m thick. The internal structure of this layer is simple and massive. At some outcrops, thin layers (less than 1 cm) with iron coating are recorded at the upper 50 cm. The sediment is very poorly consolidated and easily to scratch by hand tools. The dominating grain size in the five samples is sand (62 %–88 %). Two of them show a slightly higher content of silt. The clay content is less than 10 % in all samples. The texture is in the range of sand to sandy loam (Fig. 7). This layer's biological content is too low to be distinguished macroscopically.

4.2.3 Alternation of greyish silt loam and yellowish silt loam layers (SiC)

These sediments are exposed in outcrops ($n = 27$; see Fig. 6 and Appendix C) at the tablelands of the ST and SH-II. Their thickness is ca. 10–15 m. The layer is also visible on the tidal flat in outcrop 051_LK during the neap tide. The internal

Table 2. Results of grain size analyses.

Sample ID	Layer	Sand (%)	Silt (%)	Clay (%)	Sediment texture (Jahn et al., 2006)
LK 0-4 sand dune 0-1	Modern beach sand	97.0	1.8	1.2	Sand
LK 0-4 sand dune 0-2	Modern beach sand	97.0	1.9	1.2	Sand
HLPT 0-7	SiL	45.3	43.1	11.6	Loam
NCT0-3	SiL	51.0	37.9	11.1	Loam
XNPW0-2	SiL	46.1	42.7	11.1	Loam
HDK0-4	SiL	34.8	50.2	14.9	Silt loam
TYGC-2	SiL	22.6	57.1	20.3	Silt loam
XP-1	SiL	44.2	39.7	16.2	Loam
XNPWH-2	SiL	43.0	42.2	14.7	Loam
TKD-3	SiL	50.9	36.7	12.4	Loam
JJC-2	SiL	38.8	44.0	17.1	Loam
HLPT 0-6	CSB	37.7	42.3	20.0	Loam
TKD-2	CSB	48.7	34.9	16.4	Loam
HLPT 0-5	SL-b	39.4	41.9	18.7	Loam
NCT0-2	SL-b	44.7	40.0	15.3	Loam
XNPW0-1	SL-b	25.3	53.6	21.1	Silt loam
DBD0-1	SL-b	50.3	42.4	7.3	Loam
XNPWH-1	SL-b	44.3	40.1	15.6	Loam
GJW-2	SL-b	32.8	47.3	19.9	Loam
TKD-1	SL-b	41.6	43.5	14.9	Loam
JJC-1	SL-b	42.3	40.9	16.9	Loam
NCT0-1	SL-y	60.4	29.8	9.8	Sandy loam
HDK0-1	SL-y	79.0	15.9	5.1	Loamy sand
HDK0-2	SL-y	71.3	21.4	7.3	Sandy loam
HDK0-3	SL-y	66.3	23.9	9.8	Sandy loam
LK 0-1	SL-y	89.3	7.7	3.0	Sand
LK 0-2	SL-y	89.9	7.2	2.9	Sand
LK 0-3	SL-y	73.0	19.8	7.2	Sandy loam
THST-1	SL-y	84.0	11.2	4.7	Loamy sand
THST-2	SL-y	56.3	32.4	11.4	Sandy loam
TYGC-1	SL-y	70.8	21.8	7.5	Sandy loam
LK 0-5 yellowish loam	SiC	22.9	68.0	9.2	Silt loam
LK 0-5 greyish silt loam	SiC	8.3	79.7	12.0	Silt loam/silt
HLPT 0-2 001	LS	86.7	10.3	3.0	Sand
HLPT 0-3 001	LS	70.4	25.0	4.7	Sandy loam
HLPT 0-4 upper	LS	85.6	11.4	2.9	Sand
LK 0-6	LS	88.2	8.4	3.4	Sand
LK 0-7	LS	62.4	31.6	6.0	Sandy loam
HLPT 0-1 middle	L	40.5	44.3	15.2	Loam
JJC-A-1	L	39.2	48.0	12.8	Loam
JJC-A-2	L	51.6	37.7	10.7	Loam

structure shows thin beds of (I) the yellowish sandy sediments and (II) greyish clayey and silty sediments (10–100 layers with ca. 5–10 cm thickness of each layer) (Fig. 6). Iron precipitation can be distinguished on the contacts between these thin beds. The sediments are generally poorly consolidated; the greyish sediments are stickier than the yellowish sediments. Silt is the dominating grain size in both sublayers (68 %–80 %), of which the yellowish one has a certain sand content (23 %, Fig. 7). No molluscs or other biological remains are distinguishable in this layer.

4.2.4 Sandy loam layer (SL)

This ca. 10–30 m thick layer is exposed in outcrops across the entire study area ($n = 43$) (Fig. 6 and Appendix C). The upper contact to the overlying gravel and cobble bed (CSB) is continuous and very distinct. However, the contact is difficult to distinguish when the CSB is missing, and this layer is overlain directly by the silty loamy cover layer (SiL) (Fig. 6 and Appendix A). The sedimentary texture of this layer shows significant vertical variations among the outcrops and is therefore subdivided into three categories. (I) The light

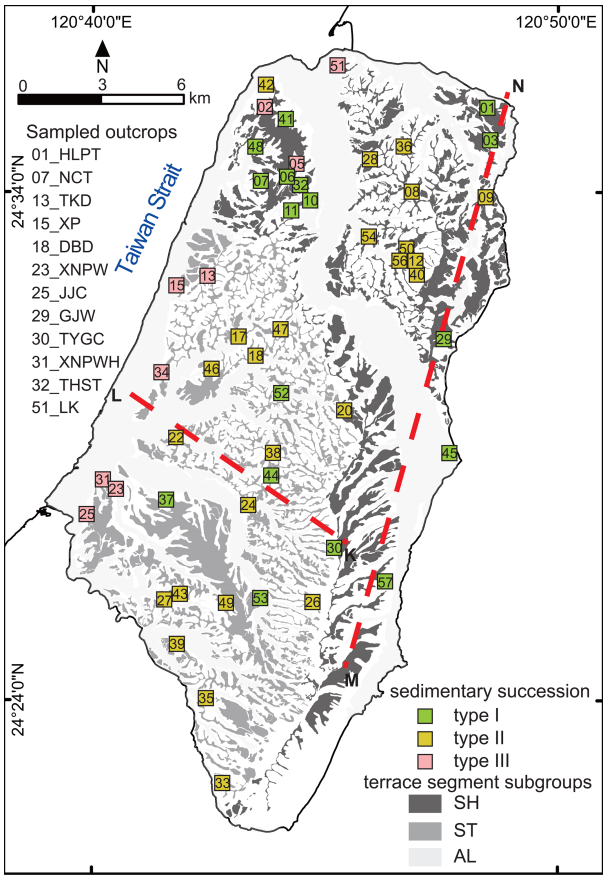

Figure 5. Location of the 51 studied outcrops (see Table 1); 26 outcrops are located in the SH, and 25 outcrops are in the ST. The 12 sampled outcrops for the grain size analyses are listed (see Table 2 for results). For profiles K–L and M–N and sedimentary subtype description, see Fig. 8.

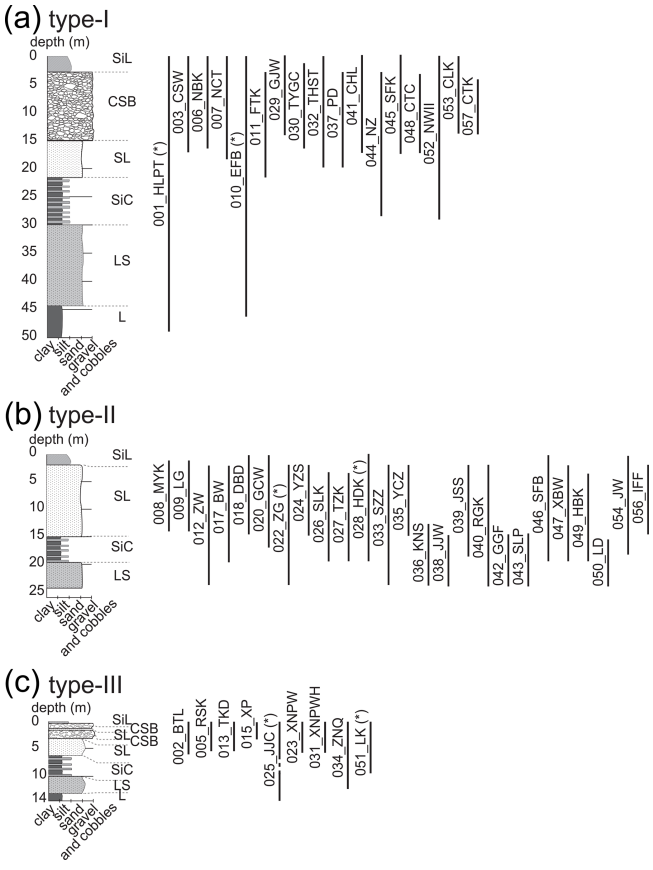

Figure 6. Schematic profiles of different sedimentary successions in the SH-II and ST with the respective outcrop numbers. **(a)** Type I: complete succession, located mainly in the larger tableland segments. **(b)** Type II: incomplete succession with the missing gravel and cobble bed ("remnants"), located mainly in the smaller tableland segments. **(c)** Type III: the succession with one or more thin gravel and cobble bed(s), located in the distal-tableland segments near the coast. Sediment layers are named after the FAO classification (Jahn et al., 2006): L – greyish loam, LS – loamy sand, SiC – alternations of greyish silt loam and yellowish silt loam, SL – sandy loam, CSB – coarse sand with stones and boulders (gravels and cobbles), and SiL – silty loam (cover layer). (*) Vertical lines indicate the relative depth of the outcrops with the respective sediment layers, which are visible in the field. The metrical depth scales are taken from the representative outcrops for each succession type.

greyish sandy material is in the lower metres (SL-g, not sampled). (II) The yellowish sandy material is in the middle part (ca. 5–10 m), which contains more than 50 % and – in two samples – nearly 90 % sand (SL-y) (Fig. 7). The upper ca. 1 m consists of brownish sandy loamy substrate (SL-b) with more than 40 % silt. The sediments in all three subtypes are very poorly consolidated; only the brownish sediments are stickier. The overall internal structure of SL-g and SL-b is massive. In the SL-y, iron coating in thin beds is visible. Debris of molluscs can be found in this layer; especially outcrop 035_YZS contains abundant detritus of molluscs.

4.2.5 The gravel and cobble bed (CSB)

Gravel and cobble beds are widely distributed in the Miaoli Tableland and exposed in 26 outcrops (Figs. 6 and 7 and Appendix C). Their thickness is varying according to the location: ca. 5–20 m in the SH-II, < 10 m in the ST, and < 2 m in the distal edge of the tableland. The sedimentary structure of the layer is mostly clast-supported but is matrix-supported in some outcrops at the distal edge of the tableland. Therefore the layer is classified as "coarse sand, with stones and boulders" (CSB) according to Jahn et al. (2006). In the clast-supported outcrops, the gravels are horizontally aligned with the long axes. The imbrication is poor; therefore, a precise analysis of flow directions is not possible. The gravels and cobbles consist of quartzite. Their sizes range from ca. 10 to 40 cm in the SH-II and from < 10 to ca. 30 cm in the ST. The gravels are well-rounded; their sphericity is moderate to platy.

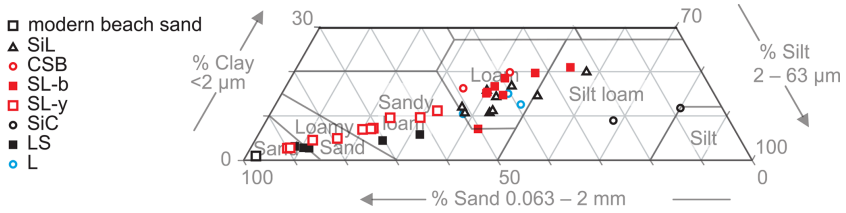

Figure 7. Grain size compositions presented in a combined ternary diagram; the samples were grouped for the respective sediment layers. The sandy loam layer (SL) is subdivided into the lower SL-y and the upper SL-b. The clay content in the samples is relatively constant, while sand and silt change significantly. Sediment nomenclature after Jahn et al. (2006). For detailed grain size distribution curves, see Appendix B.

The matrix material in the two samples taken from outcrops in the distal-tableland area is loamy; it consists of ca. 80 % sand and silt. The CSB in the distal tableland contains biological remains such as roots and wood debris.

The situation in the SH-I is different. Here the gravel and cobble bed is more than 20 m thick, and its elevation above the sea level is higher than in the SH-II and the ST. Its lower boundary is rarely visible. In the southernmost part of the SH-I (i.e. Fire Mountain), the gravel and cobble layer is inclined (estimated to be ca. 30°) to the east, which is in accordance with the records from the geological maps. Unfortunately, they are accessible only in few locations. The two studied outcrops show well-rounded quartz gravels and cobbles from 10–40 cm with poor imbrication.

4.2.6 Silty loamy cover layer (SiL)

The dusty cover layer can be found across the entire study area ($n = 25$) with a thickness from tens of centimetres up to 1.5 m (Fig. 6 and Appendix C). Its lower boundary, especially to the CSB, is very distinct. Its internal structure is simple and massive. It consists of a yellowish to reddish mixture of sand (35 %–51 %) and silt (30 %–44 %); clay occurs at 12 %–20 %. Only two of the nine samples have a silt content higher than 50 % (Fig. 7). The sediment is very loose and contains abundant fresh roots of the modern vegetation.

4.3 Subtypes of the sedimentary succession

The described sedimentary succession is unevenly exposed in the study area. Most outcrops show only a limited number of the layers. However, layers in neighboured outcrops can be recognized and linked over most of the study area. Nevertheless, small variations in the sedimentary succession have been recognized. Three subtypes of the layer assemblage were observed (Figs. 5, 6, and 8 and Appendices A and C): (I) the complete succession, (II) the quasi-complete succession with a missing gravel and cobble layer, and (III) the presence of a thin gravel and cobble bed(s) on the surface (0–3 m).

Type I is widely distributed in larger tableland segments of the SH-II and the ST (Figs. 5 and 8). The outcrops comprise identical sedimentary successions, and the gravel bed (CSB) is getting thinner toward the coast. The complete succession is exposed with all layers only at two locations (001_HLPT and 010_EFB). However, also the smaller outcrops show an order of the layers, which is in accordance with the complete succession (Figs. 6 and 8).

The sedimentary succession in the SH-I is still unclear. The two studied outcrops contain a very thick gravel and cobble layer (> 20 m mainly). Subjacent sandy substrate is only exposed in outcrop 030_TYGC. Therefore, the sedimentary succession of the SH-I is named "quasi-type I", because the sedimentary succession below the gravel unit is virtually unknown (Fig. 8).

Type II is found at the smaller tableland segments of the ST and the SH-II (Figs. 5 and 8). The outcrops include all the fine-grained sedimentary layers, but the overlying gravel and cobble layer is missing. In most outcrops in the SH-II, a sequence of LS–SiC–SL–SiL is exposed (Figs. 6 and 8). In contrast, the outcrops in the ST show a relatively thick layer of SL (ca. 20 m or more), while the L, LS, and SiC layers are rarely exposed.

Type III occurs in the ST and the SH-II along the fringe of the distal-tableland segments and at the coast (Figs. 5 and 8) at elevations below 50 m a.s.l. It includes SL, SiC, SiL, and L at the lower part and one or two thin (< 2 m) gravel and cobble bed(s) intercalated with sandy (SL) layers on the upper part to the surface (Figs. 6 and 8). The gravel bed(s) is getting thinner coastward.

Beside the gravel and cobble beds in the tableland segments, gravels and cobbles occur in the AL as well. For example, abundant gravels and cobbles are deposited in most of the fluvial paths especially in tributaries of the Tungxiao River within areas with dendritic drainage patterns (Appendix A). According to the field observations, these gravels and cobbles are composed of quartzite, their shapes are round, but the components are poorly sorted.

5 Discussion

The general topography of the Miaoli Tableland inclines from the highland in the southeast towards the coast in the north and in the west. A clear spatial separation of three main areas can be distinguished: the Sedimentary Highlands in the southeastern part (SH-I) and in the northern part (SH-II) as

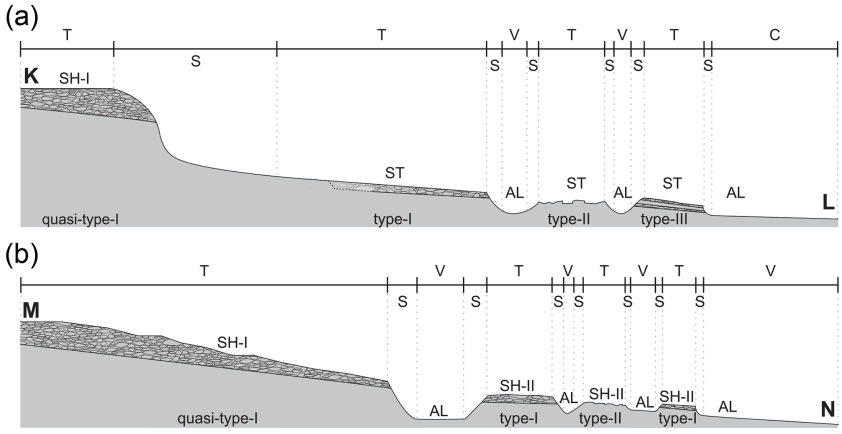

Figure 8. Schematic surface elevation profiles from **(a)** the highlands to the coastal plain through the SH-I and the ST (K–L) and **(b)** the highest point (i.e. Fire Mountain) to the Houlong River through the SH-I and the SH-II (M–N). The terrain categories and the corresponding subtypes of the sedimentary succession are marked (T: tableland segment, V: valley floor, C: coastal plain, and S: slope).

well as the Sedimentary Terraces (ST) in the western part. Especially the cliff-like topographic divide between the SH-I and the ST is a distinctive topographic landscape element in the Miaoli Tableland. This elevation-data-based topographical classification agrees in general with previous findings (Chang et al., 1998; Ota et al., 2006). However, the high resolution of the DEMs reveals that the topography of the tableland is much more disaggregated into larger and smaller segments than previously mapped. These segments cover most of the area of the Miaoli Tableland, and their surfaces can be tentatively connected or geometrically interpolated to an inferred palaeotopography in the respective areas (Figs. 2d and 3).

The internal sedimentary succession of the tableland segments is consistent in the SH-II and the ST areas but different in the SH-I. The individual strata of the SH-II and ST appear in the same order. The lower to middle part of the studied sedimentary sequence (L–LS–SiC–SL) represents an intertidal to supratidal deposition sequence, which has been reported by case studies in various locations globally (Goodbred and Saito, 2011; Dalrymple and Choi, 2007; Chen et al., 2014; Olariu et al., 2012; Buatois et al., 2012). This general tidal-dominant environment setting is consistent with the interpretation of the study of molluscs and foraminifera taken from this succession previously (Lee et al., 2002; Lin, 1969), although their stratigraphical context is not clear in detail. It is possibly due to sea-level changes (Shackleton, 2000) and long-term uplift of the Miaoli area (Ota et al., 2006; Yang et al., 2016). The distinct boundaries of each sedimentary layer may result from the interruption of sedimentation or the subsequent erosion, especially during the aforementioned regression periods (Davis, 2012).

Depending on the location, the studied sequence is topped by units of fluvial gravels and cobbles with different thickness. Previously, tablelands were identified by their flat surface and the occurrence of gravels and cobbles on their surface (Chang et al., 1998; Lin and Chou, 1978; Teng, 1979). We found that this is mainly the case for the larger and also some smaller segments, which represent sedimentation type I (Figs. 5 and 8 and Appendix A). On most of the small segments, the gravels and cobbles are missing (type II, Figs. 5 and 8 and Appendix A). However, the inferred palaeotopography implies a formerly continuously distributed gravel and cobble layer in the ST and the SH-II, where the smaller segments represent remnants, from which the gravels and cobbles were eroded. The fact that gravels and cobbles are also accumulated in the channels between segments with missing a gravel and cobble layer supports the idea that they were reworked from higher positions on the ST and the SH-II into the AL. This is new in comparison with Chang et al. (1998) and Ota et al. (2006), who did not assume a continuous gravel and cobble layer in the ST and SH-II area. In the distal segments near the coast, the gravels and cobbles tend to be smaller and occur in several thin layers (type III, Figs. 5 and 8 and Appendix A); thus we assume that the gravels and cobbles are reworked from the nearby sources (i.e. the proximal segments and remnants in the SH-II and ST).

The clast-supported structure and the moderate sorting of the fluvial deposits indicate that the deposition occurred rapidly, assumably during high-precipitation and discharge events. These characteristics are similar to the gravel and cobble beds in the other tablelands in northern Taiwan (Teng, 1996b). Although Chang et al. (1998) measured the cobble imbrication at several locations, we were not able to confirm their results due to the poor conservation of the sampling sites in recent decades. Moreover, the sphericity of the gravels and cobbles in our outcrops hinders the reconstruction of individual transport directions.

Regardless of the occurrence of gravels and cobbles, the whole area is covered by a layer of fine-grained material (SiL), which has been interpreted as the in situ lateritic soil formation before (Chang et al., 1998; Ho, 1988; Chang,

1955). However, the grain size data yielded a high content of fine silt rather than clay in this layer (Fig. 7). The fine silt is typical for aeolian transport (Pye and Zhou, 1989). Therefore, this study follows the assumption of a significant aeolian dust input (Chen et al., 2013; Tsai et al., 2008; Hebenstreit and Böse, 2015) besides the local weathering. Dust transport may also explain the silt enrichment in the upper part of the SL layer.

The whole sedimentary sequence in the SH-II and the ST is in agreement with the descriptions in early sedimentary studies of the Miaoli Tableland, where it has been named the Lungkang (Lk) Formation (Lin, 1963, 1969) or Tûsyô/Tungxiao (Ts) Formation (Chang, 1948; Makiyama, 1934, 1937). This study refers to those definitions because they are based on the descriptions of the uppermost 50–100 m of the succession directly in the study area, although the former studies tended to use the term Toukoshan (Tk) Formation (Chang, 1955), which includes however the whole Plio-Quaternary strata in western Taiwan (Chen et al., 2001; Ota et al., 2006; Lee et al., 2002; Huang, 1984; Tsai et al., 2006; Yang et al., 2016).

Early studies assumed that all fine-grained sediments of the succession are the result of in situ weathered bedrock (Chang, 1955; Ho, 1988). That interpretation might be due to a different usage of the term "bedrock", which describes in general the underlying beds in the Taiwanese literature. Although the top sediment layers in the Miaoli Tableland are intensively weathered, the loose and not lithified lower sediment units appear unweathered, and the entire sedimentary succession comprises unconsolidated sediments.

The tableland segments are separated by ongoing fluvial incision and backward erosion. Their special layout and morphology follow the fluvial pattern of the respective river catchments, which is dendritic in the SH-II and ST and more parallel in the SH-I. The cross sections of the fluvial channels between the segments are V-shaped above and box-shaped below 150 m a.s.l., respectively. This altitude marks at present the point in the longitudinal river profile where the fluvial morphodynamic changes from linear incision to lateral erosion with gravel accumulation (Charlton, 2008) representing the alluvial plains (AL). The box-shaped valleys are developed in the catchments with the dendritic drainage pattern. The formation of this pattern is supported by the fact that the lithology is basically consistent within the whole study area; thus the flow paths have developed freely, and they are not constrained by the geological or tectonic factors (e.g. the Tungxiao Anticline).

Integrating the results of this study into previous concepts (Chang et al., 1998; Ota et al., 2006), the landscape evolution of the Miaoli Tableland can be summarized as follows:

- Tidal and coastal sediments were deposited in the mountain foreland during periods of different but generally high sea levels in the Taiwan Strait. They are visible as the fine-grained sediments in the present ST and SH-II areas. These sediments represent the bay sediments in the interpretation of Chang et al. (1998). Whether they were also deposited in the present SH-I area is unknown.

- Subsequently, gravels and cobbles were deposited in the foreland basin in the form of one or several alluvial fans, which made up the present SH-I. Chang et al. (1998) suggested that they covered parts of the coastal sediments in the SH-II area. If they were transported by a single event or by multiple independent events by the Daan River, Wumei (Xihu) River, and Houlong River is also unknown. The terrain of the SH-I was subsequently uplifted along the Tongluo Fault (Ota et al., 2006), and thus the alluvial fans were prevented from further gravel and cobble accumulation.

- The ongoing uplift and the simultaneous incision of the SH-I induced the remobilization of the gravels and cobbles which were transported into the western and northern foreland of the SH-I, where they are accumulated as the present gravel and cobble layers of the SH-II and the ST. Further uplift of the SH-I along the present escarpment between the SH-I and the ST, which was assumed to be an inferred thrust fault (Chang et al., 1998), separated both terrains, stopped the gravel and cobble transport into the ST, and beheaded the valleys of the SH-I. The sediments in the ST area were slightly folded along the Tungxiao Anticline (Ota et al., 2006) during this terrain uplift. The folding may have enhanced the subsequent incision of the ST, where backward erosion is continuing in the upper and steeper channel sections. In this way, the gravels and cobbles are reworked again – from the ST surface into the AL channels and the (coastal) distal-tableland surfaces.

- The result of the rework is a cascade of gravel and cobble transportation in the Miaoli Tableland: previously from the mountains to the Sedimentary Highlands, then to the Sedimentary Terraces, and recently to the Alluvial and the Coastal Plains.

6 Conclusion

This study gives new detailed insights into the surface morphology and the sedimentary sequences of the Miaoli Tableland. The new high-resolution mapping enables the reconstruction of the palaeotopography of the region. The presented classification of tableland segments is thereby inferred from a mathematical calculation and widely independent from a subjective interpretation.

From the newly reconstructed palaeosurfaces in the western and northern part of the tableland we concluded that a quasi-continuous gravel and cobble cover existed not only in the Sedimentary Highlands but also in the Sedimentary Terraces, which is new in comparison with previous interpreta-

tions (Chang et al., 1998; Ota et al., 2006). This means that the Sedimentary Terraces (ST) and the northern Sedimentary Highlands (SH-II) covered originally a wider area than previously mapped (Chang et al., 1998). Our interpretation of cascade-like gravel and cobble rework implies that the main mass of gravels and cobbles was deposited originally in the southern Sedimentary Highlands (SH-I) and was reworked from there to the northern Sedimentary Highlands (SH-II) and the Sedimentary Terraces (ST).

Our sedimentological results suggest that the concept of the Lungkang Formation (Lin, 1963) or the Tûsyô/Tungxiao Formation (Chang, 1948; Makiyama, 1934, 1937) may be considered adequate stratigraphic terms to describe the tidal–fluvial–aeolian sediment succession of the uppermost 50–100 m in the northern and western part (SH-II and ST) of the Miaoli Tableland. Although absolute dating results are not available at this stage of research, the succession may represent one sedimentation cycle, which can be tentatively correlated with the last glacial cycle. Subsequent uplift brought the terrestrial sediments into a position above the Holocene sea-level high stand, provoking incision. The overall tableland morphology exhibits a stepwise sequence of sedimentation, uplift, and erosion in the area.

Fluvial incision created a characteristic drainage network with different patterns, depending on topographical parameters like the altitude and the location in the respective tableland areas but widely independent from the lithology in the Miaoli Tableland. The loose and easily erodible sediments enabled the formation of wide valley cross sections in the alluvial plains, which we tentatively named box-shaped valleys.

This study of terrace landforms in the frontal part of the mountain foreland in Taiwan has highlighted the possibility that a systematical terrain and sediment analysis can reveal new insights into the differentiated landform evolution in the Taiwanese foothills in the future.

Appendix A: Field photos of the Miaoli Tableland

Figure A1. Overview on the Tungxiao River catchment (the ST area) seen from the SH-I terrace (location: 24°26′57.92″ N, 120°45′15.42″ E; facing northwest, 24 October 2018). The tableland segments are dissected by channels of the dendritic fluvial network, visible in the centre of the photo.

Figure A2. Example of type I succession in outcrop 001_HLPT (location: 24°35′45.30″ N, 120°48′24.01″ E; facing west, 3 April 2015). The outcrop is about 49 m high and located on the left bank of the Houlong River. It shows fine-grained coastal sediments in the lower and central part and fluvial gravels and cobbles in the upper part.

Figure A3. Example of type II succession in outcrop 022_ZG (location: 24°28′55.02″ N, 120°42′8.09″ E; facing west, 8 January 2017). The outcrop is about 20 m high and located in the Tungxiao River catchment. It is excavated by a small creak, which is located between the outcrop and the road in the foreground. It represents the remnant of a tableland segment with fine-grained coastal sediments (greyish sand in the lower part and brownish sand in the upper part). The succession is covered by the silty cover layer (SiL) directly. This cover layer is barely visible between the vegetation in the upper central part of the picture.

Figure A4. Panorama photo of an example of type III succession in outcrop 051_LK (location: 24°36′37.61″ N, 120°44′52.69″ E; facing southeast, 23 October 2018). The outcrop is about 9 m high and located at the coast between the estuaries of the Houlong River and the Wumei (Xihu) River. It represents the sedimentary succession of the distal-tableland segments as part of the SH-II. The outcrop shows fine-grained sandy sediments covered by gravels and cobbles and modern aeolian sand. The gravels and cobbles appear as a channel infill in the centre of the picture.

Figure A5. A modernized channel in the box-shaped valley in the Tungxiao River catchment (location: 24°27′20.90″ N, 120°44′6.72″ E; facing west, 25 December 2014). The tableland segments in the background of this photo are classified as the ST. The valley floor is classified as AL; the fluvial channel is constrained by the artificial levees and covered by abundant gravel and cobble depositions.

Appendix B: Grain size distribution curves of all the studied samples

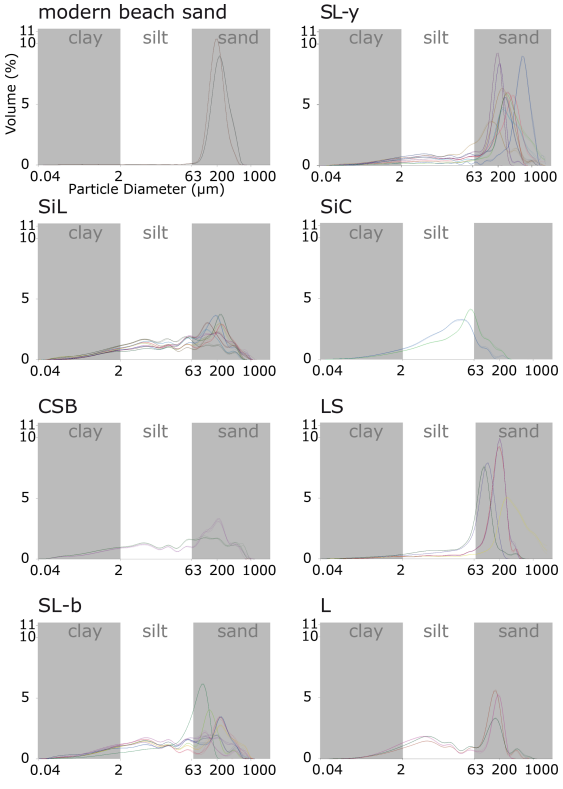

Figure B1. Samples are subgrouped by the corresponding sedimentary layers. Two samples are taken from the modern beach (dune) sand for comparison with the sandy materials in other layers. The grain size fractions are after the Wentworth scale.

Appendix C: Columnar sections and pictures of the outcrops in the Miaoli Tableland

See supplementary data of file 001-HLPT to 057-CTK at https://doi.org/10.17169/refubium-31813 (Liu et al., 2021).

Data availability. All relevant data used in this study are cited and presented in the text. Supplementary data of file 001-HLPT to 057-CTK are available at https://doi.org/10.17169/refubium-31813 (Liu et al., 2021).

Author contributions. All authors, SHL, RH, and MB, carried out the conceptualization, methodology, and investigation of this study together. SHL completed the fieldwork and the software and formal analyses, which are in the context of a PhD study programme supervised by MB. SHL and RH carried out the data visualization. This paper was drafted by SHL and revised by RH and MB.

Competing interests. Margot Böse is currently a member of the advisory board of *E&G Quaternary Science Journal*.

Disclaimer. Publisher's note: Copernicus Publications remains neutral with regard to jurisdictional claims in published maps and institutional affiliations.

Acknowledgements. The authors thank Jiun-Chuan Lin, Chia-Han Tseng, and Chia-Hung Jen for their friendly support of the fieldwork and Manfred Frechen for providing the access to the sediment lab. Moreover, we would like to thank Yu-Jia Chiu for the technical support of the base maps in Taiwan. Thanks go to Yan Li and Dirk Wenske for the discussion on the relevant topics and Christopher Lüthgens for the comments during the field observations. Thanks go to Shyh-Jeng Chyi and Lih-Der Ho for the comments during the INQUA Congress 2019. Thanks go to the Jing-Ji company and Chang Chun Petrochemical Co., Ltd Miaoli factory for the assessment of the outcrops. Finally, special thanks go to Li-Chun Xiao for managing the legal issues of open-access data usage for this study and Chu-Pan Lin for supporting the fieldwork.

Financial support. We acknowledge support from the Open Access Publication Initiative of Freie Universität Berlin.

Review statement. This paper was edited by Tony Reimann and reviewed by Toru Tamura and one anonymous referee.

References

Angelier, J., Barrier, E., and Chu, H. T.: Plate collision and paleostress trajectories in a fold-thrust belt: The foothills of Taiwan, Tectonophysics, 125, 161–178, https://doi.org/10.1016/0040-1951(86)90012-0, 1986.

Beuselinck, L., Govers, G., Poesen, J., Degraer, G., and Froyen, L.: Grain-size analysis by laser diffractometry: comparison with the sieve-pipette method, Catena, 32, 193–208, https://doi.org/10.1016/S0341-8162(98)00051-4, 1998.

Bridgland, D. and Westaway, R.: Climatically controlled river terrace staircases: A worldwide Quaternary phenomenon, Geomorphology, 98, 285–315, https://doi.org/10.1016/j.geomorph.2006.12.032, 2008.

Buatois, L. A., Santiago, N., Herrera, M., Plink-Björklund, P., Steel, R. O. N., Espin, M., and Parra, K.: Sedimentological and ichnological signatures of changes in wave, river and tidal influence along a Neogene tropical deltaic shoreline, Sedimentology, 59, 1568–1612, https://doi.org/10.1111/j.1365-3091.2011.01317.x, 2012.

Center for GIS RCHSS Academia Sinica: Taiwan Historical Atlas Web Map Tile Service [data set], available at: http://gis.sinica.edu.tw/tileserver/wmts (last access: 14 January 2022), 2017.

Central Geological Survey: National Geological Data Warehouse [data set], available at: https://gis3.moeacgs.gov.tw/gwh/gsb97-1/sys8/t3/index1.cfm (last access: 14 January 2022), 2017.

Central Weather Bureau: Typhoon Data Base [data set], available at: https://rdc28.cwb.gov.tw/TDB/ (last access: 14 January 2022), 2019.

Central Weather Bureau: Tidal level statistics [data set], available at: https://www.cwb.gov.tw/V8/C/C/MMC_STAT/sta_tide.html (last access: 14 January 2022), 2020.

Chang, H.-C.: Baishatun, Central Geological Survey, Geological Map of Taiwan scale 1 : 50 000, Taipei, Taiwan, available at: https://twgeoref.moeacgs.gov.tw/GipOpenWeb/wSite/ct?xItem=118492&ctNode=1303&mp=6 (last access: 14 January 2022), 1990.

Chang, H.-C.: Dajia, Central Geological Survey, Geological Map of Taiwan scale 1 : 50 000, Taipei, Taiwan, available at: https://twgeoref.moeacgs.gov.tw/GipOpenWeb/wSite/ct?xItem=118453&ctNode=333&mp=106 (last access: 14 January 2022), 1994.

Chang, J.-C., Teng, K.-H., and Liu, M.-C.: A Geomorphological Study on River Terraces in Miaoli Hills, Geogr. Res., 29, 97–112, https://doi.org/10.6234/JGR, 1998.

Chang, L.-S.: The revision of stratigraphy categories of Taiwan (continued), Geological Review, 13, 291–310, 1948.

Chang, L.-S.: Geologic map of Taiwan, Geological Survey of Taiwan, Taipei, Taiwan, available at: https://twgeoref.moeacgs.gov.tw/GipOpenWeb/wSite/ct?xItem=111421&ctNode=217&mp=6 (last access: 14 January 2022), 1953.

Chang, L.-S.: The strata of Taiwan, Quarterly Journal of the Taiwan Bank, 7, 26–49, 1955.

Charlton, R.: Fundamentals of fluvial geomorphology, Routledge, New York, USA, https://doi.org/10.4324/9780203371084, 2008.

Chen, C.-G.: Miaoli County, The soil investigation report of the slopes, Mountain Agricultural Resources Development Bureau,

Nantou, Taiwan, available at: https://tssurgo.tari.gov.tw/Tssurgo (last access: 14 January 2022), 1983.

Chen, H.-F., Yeh, P.-Y., Song, S.-R., Hsu, S.-C., Yang, T.-N., Wang, Y., Chi, Z., Lee, T.-Q., Chen, M.-T., Cheng, C.-L., Zou, J., and Chang, Y.-P.: The Ti/Al molar ratio as a new proxy for tracing sediment transportation processes and its application in aeolian events and sea level change in East Asia, J. Asian Earth Sci., 73, 31–38, https://doi.org/10.1016/j.jseaes.2013.04.017, 2013.

Chen, S., Steel, R. J., Dixon, J. F., and Osman, A.: Facies and architecture of a tide-dominated segment of the Late Pliocene Orinoco Delta (Morne L'Enfer Formation) SW Trinidad, Mar. Petrol. Geol., 57, 208–232, https://doi.org/10.1016/j.marpetgeo.2014.05.014, 2014.

Chen, W.-S., Ridgway, K. D., Horng, C.-S., Chen, Y.-G., Shea, K.-S., and Yeh, M.-G.: Stratigraphic architecture, magnetostratigraphy, and incised-valley systems of the Pliocene-Pleistocene collisional marine foreland basin of Taiwan, GSA Bulletin, 113, 1249–1271, https://doi.org/10.1130/0016-7606(2001)113<1249:SAMAIV>2.0.CO;2, 2001.

Chen, W.-S., Chen, Y.-G., Shih, R.-C., Liu, T.-K., Huang, N.-W., Lin, C.-C., Sung, S.-H., and Lee, K.-J.: Thrust-related river terrace development in relation to the 1999 Chi-Chi earthquake rupture, Western Foothills, central Taiwan, J. Asian Earth Sci., 21, 473–480, https://doi.org/10.1016/S1367-9120(02)00072-X, 2003.

Chen, Y.-G. and Liu, T.-K.: Sea Level Changes in the Last Several Thousand Years, Penghu Islands, Taiwan Strait, Quaternary Res., 45, 254–262, https://doi.org/10.1006/qres.1996.0026, 1996.

Chen, Y.-G., Shyu, J. B. H., Ota, Y., Chen, W.-S., Hu, J.-C., Tsai, B.-W., and Wang, Y.: Active structures as deduced from geomorphic features: a case in Hsinchu Area, northwestern Taiwan, Quaternary Int., 115–116, 189-199, https://doi.org/10.1016/s1040-6182(03)00107-1, 2004.

Chen, Z.-S., Hseu, Z.-Y., and Tsai, C.-C.: The soils of Taiwan, World soils book series, Springer, Dordrecht, https://doi.org/10.1007/978-94-017-9726-9, 2015.

Ching, K.-E., Hsieh, M.-L., Johnson, K. M., Chen, K.-H., Rau, R.-J., and Yang, M.: Modern vertical deformation rates and mountain building in Taiwan from precise leveling and continuous GPS observations, 2000–2008, J. Geophys. Res., 116, B08406, https://doi.org/10.1029/2011jb008242, 2011.

Choi, J. H., Kim, J. W., Murray, A. S., Hong, D. G., Chang, H. W., and Cheong, C.-S.: OSL dating of marine terrace sediments on the southeastern coast of Korea with implications for Quaternary tectonics, Quatern. Int., 199, 3–14, https://doi.org/10.1016/j.quaint.2008.07.009, 2009.

Covey, M.: The Evolution of Foreland Basins to Steady State: Evidence from the Western Taiwan Foreland Basin, in: Foreland Basins, Blackwell Publishing Ltd., 77–90, https://doi.org/10.1002/9781444303810.ch4, 1986.

Dadson, S. J., Hovius, N., Chen, H., Dade, W. B., Hsieh, M.-L., Willett, S. D., Hu, J.-C., Horng, M.-J., Chen, M.-C., Stark, C. P., Lague, D., and Lin, J.-C.: Links between erosion, runoff variability and seismicity in the Taiwan orogen, Nature, 426, 648–651, https://doi.org/10.1038/nature02150, 2003.

Dalrymple, R. W. and Choi, K.: Morphologic and facies trends through the fluvial–marine transition in tide-dominated depositional systems: A schematic framework for environmental and sequence-stratigraphic interpretation, Earth-Sci. Rev., 81, 135–174, https://doi.org/10.1016/j.earscirev.2006.10.002, 2007.

Davis, R. A.: Tidal Signatures and Their Preservation Potential in Stratigraphic Sequences, in: Principles of tidal sedimentology, edited by: Davis, R. A. and Dalrymple, R. W., Springer, Dordrecht, 35–55, https://doi.org/10.1007/978-94-007-0123-6_3, 2012.

Deffontaines, B., Lacombe, O., Angelier, J., Chu, H. T., Mouthereau, F., Lee, C. T., Deramond, J., Lee, J. F., Yu, M. S., and Liew, P. M.: Quaternary transfer faulting in the Taiwan Foothills: evidence from a multisource approach, Tectonophysics, 274, 61–82, https://doi.org/10.1016/S0040-1951(96)00298-3, 1997.

Delcaillau, B.: Geomorphic response to growing fault-related folds: example from the foothills of central Taiwan, Geodin. Acta, 14, 265–287, https://doi.org/10.1016/S0985-3111(01)01071-3, 2001.

Eshel, G., Levy, G. J., Mingelgrin, U., and Singer, M. J.: Critical Evaluation of the Use of Laser Diffraction for Particle-Size Distribution Analysis, Soil Sci. Soc. Am. J., 68, 736–743, https://doi.org/10.2136/sssaj2004.7360, 2004.

Goodbred, S. and Saito, Y.: Tide-Dominated Deltas, in: Principles of tidal sedimentology, edited by: Davis, R. A. and Dalrymple, R. W., Springer, Dordrecht, 129–149, https://doi.org/10.1007/978-94-007-0123-6_7, 2011.

Hanebuth, T. J. J., Voris, H. K., Yokoyama, Y., Saito, Y., and Okuno, J. I.: Formation and fate of sedimentary depocentres on Southeast Asia's Sunda Shelf over the past sea-level cycle and biogeographic implications, Earth-Sci. Rev., 104, 92–110, https://doi.org/10.1016/j.earscirev.2010.09.006, 2011.

Hebenstreit, R. and Böse, M.: Quaternary mineral aeolian dust deposits in Taiwan and their potentials as a new archive, XIX INQUA Congress, 27 July–2 August 2015, Nagoya, Japan, available at: https://www.inqua-seqs.org/files/INQUA2015_program_web.pdf (last access: 14 January 2022), 2015.

Ho, C.-S.: An introduction to the geology of Taiwan: explanatory text of the geologic map of Taiwan, Central Geological Survey, Taipei, Taiwan, available at: https://twgeoref.moeacgs.gov.tw/GipOpenWeb/wSite/ct?xItem=109139&ctNode=1303&mp=6 (last access: 14 January 2022), 1988.

Ho, H.-C.: Miaoli, Central Geological Survey, Geological Map of Taiwan scale 1 : 50 000, Taipei, Taiwan, available at: https://twgeoref.moeacgs.gov.tw/GipOpenWeb/wSite/ct?xItem=118489&ctNode=1303&mp=6 (last access: 14 January 2022), 1994.

Horng, C.-S.: Age of the Tananwan Formation in Northern Taiwan: A Reexamination of the Magnetostratigraphy and Calcareous Nannofossil Biostratigraphy, Terr. Atmos. Ocean. Sci., 25, 137–147, https://doi.org/10.3319/tao.2013.11.05.01(tt), 2014.

Horng, C.-S. and Huh, C.-A.: Magnetic properties as tracers for source-to-sink dispersal of sediments: A case study in the Taiwan Strait, Earth Planet. Sc. Lett., 309, 141–152, https://doi.org/10.1016/j.epsl.2011.07.002, 2011.

Huang, T.: Planktic foraminiferal biostratigraphy and datum planes in the Neogene sedimentary sequence in Taiwan, Palaeogeogr. Palaeocl., 46, 97–106, https://doi.org/10.1016/0031-0182(84)90028-2, 1984.

Huh, C.-A., Chen, W., Hsu, F.-H., Su, C.-C., Chiu, J.-K., Lin, S., Liu, C.-S., and Huang, B.-J.: Modern (< 100 years) sedimentation in the Taiwan Strait: Rates and source-to-sink pathways elucidated from radionuclides and particle size distribution, Cont. Shelf Res., 31, 47–63, https://doi.org/10.1016/j.csr.2010.11.002, 2011.

Jahn, R., Blume, H. P., Asio, V. B., Spaargaren, O., and Schad, P.: Guidelines for soil description, 4th edn., Food and Agriculture Organization of the United Nations, Rome, ISBN 9251055211, 2006.

Jan, S., Wang, J., Chern, C.-S., and Chao, S.-Y.: Seasonal variation of the circulation in the Taiwan Strait, J. Marine Syst., 35, 249–268, https://doi.org/10.1016/S0924-7963(02)00130-6, 2002.

Konert, M. and Vandenberghe, J.: Comparison of laser grain size analysis with pipette and sieve analysis: a solution for the underestimation of the clay fraction, Sedimentology, 44, 523–535, https://doi.org/10.1046/j.1365-3091.1997.d01-38.x, 1997.

Lee, C.-L., Huang, T., Shieh, K.-S., and Chen, Z.-H.: The chronostratigraphy and sedimentary environments of the Toukoshan Fm. in Beishatun area, Miaoli, Annual Report of Central Geological Survey, MOEA, 1999–2000, 17–20, available at: https://twgeoref.moeacgs.gov.tw/GipOpenWeb/wSite/ct?xItem=111058&ctNode=1303&mp=6 (last access: 14 January 2022), 2002.

Lee, J.-F.: Dongshi, Central Geological Survey, Geological Map of Taiwan scale 1 : 50 000, Taipei, Taiwan, available at: https://twgeoref.moeacgs.gov.tw/GipOpenWeb/wSite/ct?xItem=118454&ctNode=1303&mp=6 (last access: 14 January 2022), 2000.

Lin, A. T. and Watts, A. B.: Origin of the West Taiwan basin by orogenic loading and flexure of a rifted continental margin, J. Geophys. Res.-Sol. Ea., 107, ETG 2-1–ETG 2-19, https://doi.org/10.1029/2001jb000669, 2002.

Lin, A. T., Watts, A. B., and Hesselbo, S. P.: Cenozoic stratigraphy and subsidence history of the South China Sea margin in the Taiwan region, Basin Res., 15, 453–478, https://doi.org/10.1046/j.1365-2117.2003.00215.x, 2003.

Lin, C. C.: Geomorphology of Taiwan, The Historical Research Commission of Taiwan Province, Taipei, Taiwan, 1957.

Lin, C. C.: The Lungkang Formation, lower marine terrace deposits near Miaoli, Petroleum Geology of Taiwan, 2, 87–105, 1963.

Lin, C. C.: Holocene Geology of Taiwan, Acta Geologica Taiwanica, 13, 83–126, 1969.

Lin, C. C. and Chou, J. T.: Geology of Taiwan, Maw Chang Book Co., Ltd., Taipei, Taiwan, 1978.

Liu, J. P., Milliman, J. D., Gao, S., and Cheng, P.: Holocene development of the Yellow River's subaqueous delta, North Yellow Sea, Mar. Geol., 209, 45–67, https://doi.org/10.1016/j.margeo.2004.06.009, 2004.

Liu, J. P., Liu, C. S., Xu, K. H., Milliman, J. D., Chiu, J. K., Kao, S. J., and Lin, S. W.: Flux and fate of small mountainous rivers derived sediments into the Taiwan Strait, Mar. Geol., 256, 65–76, https://doi.org/10.1016/j.margeo.2008.09.007, 2008.

Liu, S.-H., Böse, M., and Hebenstreit, R.: The columnar sections and pictures of the outcrops in Miaoli Tableland, Refubium – Freie Universität Berlin Repository [data set], https://doi.org/10.17169/refubium-31813, 2021.

Makiyama, T.: Hakusyaton Sheet, Bureau of Productive Industries, Government-General of Taiwan, Explanatory text of the geological map of Taiwan (1 : 50 000), Tokyo, Japan, available at: https://twgeoref.moeacgs.gov.tw/GipOpenWeb/wSite/ct?xItem=119130&ctNode=217&mp=6 (last access: 14 January 2022), 1934.

Makiyama, T.: The topographic and geological map of Tûsyô petroleum field, Bureau of Productive Industries, Government-General of Taiwan, Tokyo, Japan, available at: https://twgeoref.moeacgs.gov.tw/GipOpenWeb/wSite/ct?xItem=108126&ctNode=1304&mp=104 (last access: 14 January 2022), 1937.

Mather, A. E., Stokes, M., and Whitfield, E.: River terraces and alluvial fans: The case for an integrated Quaternary fluvial archive, Quaternary Sci. Rev., 166, 74–90, https://doi.org/10.1016/j.quascirev.2016.09.022, 2017.

Matsu'ura, T., Kimura, H., Komatsubara, J., Goto, N., Yanagida, N., Ichikawa, K., and Furusawa, A.: Late Quaternary uplift rate inferred from marine terraces, Shimoka Peninsula, northeastern Japan: A preliminary investigation of the buried shoreline angle, Geomorphology, 209, 1–17, https://doi.org/10.1016/j.geomorph.2013.11.013, 2014.

Miall, A. D.: Fluvial Depositional Systems, Springer Geology, Springer International Publishing, Switzerland, 316 pp., https://doi.org/10.1007/978-3-319-24304-7, 2014.

NASA JPL: 1 Arc Second scene N24 E120 [data set], https://doi.org/10.5067/MEaSUREs/SRTM/SRTMGL1.003, 2013.

National Land Surveying and Mapping Center: Taiwan Map Service [data set], available at: https://wmts.nlsc.gov.tw/wmts (last access: 14 January 2022), 2016.

Olariu, C., Steel, R. J., Dalrymple, R. W., and Gingras, M. K.: Tidal dunes versus tidal bars: The sedimentological and architectural characteristics of compound dunes in a tidal seaway, the lower Baronia Sandstone (Lower Eocene), Ager Basin, Spain, Sediment. Geol., 279, 134–155, https://doi.org/10.1016/j.sedgeo.2012.07.018, 2012.

Ota, Y., Shyu, J. B., Chen, Y.-G., and Hsieh, M.-L.: Deformation and age of fluvial terraces south of the Choushui River, central Taiwan, and their tectonic implications, Western Pacific Earth Sciences, 2, 251–260, 2002.

Ota, Y., Chen, Y.-G., and Chen, W.-S.: Review of paleoseismological and active fault studies in Taiwan in the light of the Chichi earthquake of September 21, 1999, Tectonophysics, 408, 63–77, https://doi.org/10.1016/j.tecto.2005.05.040, 2005.

Ota, Y., Lin, Y.-N. N., Chen, Y.-G., Chang, H.-C., and Hung, J.-H.: Newly found Tunglo Active Fault System in the fold and thrust belt in northwestern Taiwan deduced from deformed terraces and its tectonic significance, Tectonophysics, 417, 305–323, https://doi.org/10.1016/j.tecto.2006.02.001, 2006.

Ota, Y., Lin, Y.-N. N., Chen, Y.-G., Matsuta, N., Watanuki, T., and Chen, Y.-W.: Touhuanping Fault, an active wrench fault within fold-and-thrust belt in northwestern Taiwan, documented by spatial analysis of fluvial terraces, Tectonophysics, 474, 559–570, https://doi.org/10.1016/j.tecto.2009.04.034, 2009.

Pelletier, B. and Stephan, J. F.: Middle miocene deduction and late miocene beginning of collision registered in the hengchun peninsula: Geodynamic implications for the evolution of Taiwan, Tectonophysics, 125, 133–160, https://doi.org/10.1016/0040-1951(86)90011-9, 1986.

Pickering, J. L., Goodbred, S. L., Reitz, M. D., Hartzog, T. R., Mondal, D. R., and Hossain, M. S.: Late Quaternary sedimentary record and Holocene channel avulsions of the Jamuna and Old Brahmaputra River valleys in the upper Bengal delta plain, Geomorphology, 227, 123–136, https://doi.org/10.1016/j.geomorph.2013.09.021, 2014.

Pye, K. and Zhou, L.-P.: Late Pleistocene and Holocene aeolian dust deposition in North China and the Northwest Pacific Ocean, Palaeogeogr. Palaeocl., 73, 11–23, https://doi.org/10.1016/0031-0182(89)90041-2, 1989.

Robustelli, G., Ermolli, E. R., Petrosino, P., Jicha, B., Sardella, R., and Donato, P.: Tectonic and climatic control on geomorphological and sedimentary evolution of the Mercure basin, southern Apennines, Italy, Geomorphology, 214, 423–435, https://doi.org/10.1016/j.geomorph.2014.02.026, 2014.

Saito, K. and Oguchi, T.: Slope of alluvial fans in humid regions of Japan, Taiwan and the Philippines, Geomorphology, 70, 147–162, https://doi.org/10.1016/j.geomorph.2005.04.006, 2005.

Satellite Survey Center: Ministry of the Interior 20 m raster digital elevation model [data set], available at: https://data.gov.tw/dataset/35430 (last access: 14 January 2022), 2018.

Shackleton, N. J.: The 100,000-Year Ice-Age Cycle Identified and Found to Lag Temperature, Carbon Dioxide, and Orbital Eccentricity, Science, 289, 1897–1902, https://doi.org/10.1126/science.289.5486.1897, 2000.

Shih, T.-T. and Yang, G.-S.: The Active Faults and Geomorphic Surfaces of Pakua Tableland in Taiwan, Geogr. Res., 11, 173–186, 1985.

Shyu, J. B. H., Sieh, K., Chen, Y.-G., and Liu, C.-S.: Neotectonic architecture of Taiwan and its implications for future large earthquakes, J. Geophys. Res., 110, B08402, https://doi.org/10.1029/2004jb003251, 2005.

Siame, L. L., Chen, R.-F., Derrieux, F., Lee, J.-C., Chang, K.-J., Bourlès, D. L., Braucher, R., Léanni, L., Kang, C.-C., Chang, C.-P., and Chu, H.-T.: Pleistocene alluvial deposits dating along frontal thrust of Changhua Fault in western Taiwan: The cosmic ray exposure point of view, J. Asian Earth Sci., 51, 1–20, https://doi.org/10.1016/j.jseaes.2012.02.002, 2012.

Simoes, M. and Avouac, J. P.: Investigating the kinematics of mountain building in Taiwan from the spatiotemporal evolution of the foreland basin and western foothills, J. Geophys. Res., 111, B10401, https://doi.org/10.1029/2005jb004209, 2006.

Suppe, J.: Kinematics of arc-continent collision, flipping of subduction, and back-arc spreading near Taiwan, Memoir of the Geological Society of China, 6, 131–146, 1984.

Teng, K.-H.: A Quantitative Study on the Landforms of Lateritic Gravel Tablelands in Northwestern Taiwan, The College of Chinese Culture Institute of Geography Science Reports, 3, 113–186, 1979.

Teng, L. S.: Geotectonic evolution of late Cenozoic arc-continent collision in Taiwan, Tectonophysics, 183, 57–76, https://doi.org/10.1016/0040-1951(90)90188-E, 1990.

Teng, L.-S.: Geotectonic evolution of Tertiary continental margin basins of Taiwan, Petroleum Geology of Taiwan, 27, 1–19, 1992.

Teng, L. S.: Extensional collapse of the northern Taiwan mountain belt, Geology, 24, 949–952, 1996a.

Teng, L. S.: Geological background of the gravel formations of Taiwan, Sine-Geotechnics, 55, 5–24, https://doi.org/10.30140/SG.199606.0001, 1996b.

Teng, L. S., Lee, C., Peng, C.-H., Chen, W.-F., and Chu, C.-J.: Origin and geological evolution of the Taipei basin, northern Taiwan, Western Pacific Earth Sciences, 1, 115–142, 2001.

The Taiwan Provincial Weather Institution: Report on Floods of 7th August, 1959, The Taiwan Provincial Weather Institution, Taipei, Taiwan, available at: https://photino.cwb.gov.tw/rdcweb/lib/cd/cd02tyrp/typ/1959/6.pdf (last access: 14 January 2022), 1959.

Tomita, Y.: On the geomorphological classification of fans in Taiwan (Formosa), Journal of Geography (Chigaku Zasshi), 60, 2–9, 1951.

Tomita, Y.: The classification of fluvial terraces, Annals of The Tohoku Geographycal Asocciation, 6, 1–6, https://doi.org/10.5190/tga1948.6.1, 1953.

Tomita, Y.: Surface Geology and Correlation of River Terraces, Annals of The Tohoku Geographycal Asocciation, 6, 51–58, https://doi.org/10.5190/tga1948.6.4_51, 1954.

Torii, K.: Tosei Sheet, Bureau of Productive Industries, Government-General of Taiwan, Explanatory text of the geological map of Taiwan (1 : 50 000), Tokyo, available at: https://twgeoref.moeacgs.gov.tw/GipOpenWeb/wSite/ct?xItem=104094&ctNode=217&mp=6 (last access: 14 January 2022), 1935.

Tsai, H., Huang, W.-S., Hseu, Z.-Y., and Chen, Z.-S.: A River Terrace Soil Chronosequence of the Pakua Tableland in Central Taiwan, Soil Science, 171, 167–179, https://doi.org/10.1097/01.ss.0000187376.76767.21, 2006.

Tsai, H., Maejima, Y., and Hseu, Z.-Y.: Meteoric 10Be dating of highly weathered soils from fluvial terraces in Taiwan, Quaternary Int., 188, 185–196, https://doi.org/10.1016/j.quaint.2007.06.007, 2008.

Tsai, H., Hseu, Z.-Y., Huang, S.-T., Huang, W.-S., and Chen, Z.-S.: Pedogenic properties of surface deposits used as evidence for the type of landform formation of the Tadu tableland in central Taiwan, Geomorphology, 114, 590–600, https://doi.org/10.1016/j.geomorph.2009.09.020, 2010.

Tseng, C.-H., Wenske, D., Böse, M., Reimann, T., Lüthgens, C., and Frechen, M.: Sedimentary features and ages of fluvial terraces and their implications for geomorphic evolution of the Taomi River catchment: A case study in the Puli Basin, central Taiwan, J. Asian Earth Sci., 62, 759–768, https://doi.org/10.1016/j.jseaes.2012.11.028, 2013.

Vail, P. R., Audemade, F., Bowman, S. A., Eisner, P. N., and Perez-Cruz, C.: The stratigraphic signatures of tectonics, eustacy and sedimentology – an overview, in: Cycles and Events in Stratigraphy, edited by: Einsele, G., Ricken, W., and Seilacher, A., Springer-Verlag, Berlin, 617–659, ISBN 3540527842, 1991.

Volker, H. X., Wasklewicz, T. A., and Ellis, M. A.: A topographic fingerprint to distinguish alluvial fan formative processes, Geomorphology, 88, 34–45, https://doi.org/10.1016/j.geomorph.2006.10.008, 2007.

Wang, Y. H., Jan, S., and Wang, D. P.: Transports and tidal current estimates in the Taiwan Strait from shipboard ADCP observations (1999–2001), Estuar., Coast. Shelf Sci., 57, 193–199, https://doi.org/10.1016/S0272-7714(02)00344-X, 2003.

Willemin, J. H. and Knuepfer, P. L. K.: Kinematics of arc-continent collision in the eastern Central Range of Taiwan inferred from geomorphic analysis, J. Geophys. Res.-Sol. Ea., 99, 20267–20280, https://doi.org/10.1029/94JB00731, 1994.

Yang, K.-M., Huang, S.-T., Wu, J.-C., Ting, H.-H., and Mei, W.-W.: Review and New Insights on Foreland Tectonics in Western Taiwan, Int. Geol. Rev., 48, 910–941, https://doi.org/10.2747/0020-6814.48.10.910, 2006.

Yang, K.-M., Huang, S.-T., Jong-Chang, W., Ting, H.-H., Wen-Wei, M., Lee, M., Hsu, H.-H., and Lee, C.-J.: 3D geometry of the Chelungpu thrust system in central Taiwan: Its implications for active tectonics, Terr. Atmos. Ocean. Sci., 18, 143, https://doi.org/10.3319/TAO.2007.18.2.143(TCDP), 2007.

Yang, K.-M., Rau, R.-J., Chang, H.-Y., Hsieh, C.-Y., Ting, H.-H., Huang, S.-T., Wu, J.-C., and Tang, Y.-J.: The role of basement-involved normal faults in the recent tectonics of western Taiwan, Geol. Mag., 153, 1166–1191, https://doi.org/10.1017/S0016756816000637, 2016.

Yu, H.-S. and Chou, Y.-W.: Characteristics and development of the flexural forebulge and basal unconformity of Western Taiwan Foreland Basin, Tectonophysics, 333, 277–291, https://doi.org/10.1016/S0040-1951(00)00279-1, 2001.

Yu, H.-S. and Song, G. S.: Submarine physiographic features in Taiwan region and their geological significance, Journal of the Geological Society of China, 43, 267–286, 2000.

Yu, N.-T., Teng, L. S., Chen, W.-S., Yue, L.-F., and Chen, M.-M.: Early post-rift sequence stratigraphy of a Mid-Tertiary rift basin in Taiwan: Insights into a siliciclastic fill-up wedge, Sediment. Geol., 286–287, 39–57, https://doi.org/10.1016/j.sedgeo.2012.12.009, 2013.

E&G Quaternary Sci. J., 71, 23–43, 2022
https://doi.org/10.5194/egqsj-71-23-2022

Open Access E&G Quaternary Science Journal

Research article

Evaluation of geochemical proxies and radiocarbon data from a loess record of the Upper Palaeolithic site Kammern-Grubgraben, Lower Austria

Lilian Reiss[1], Christian Stüwe[1], Thomas Einwögerer[2], Marc Händel[2], Andreas Maier[3], Stefan Meng[4], Kerstin Pasda[5], Ulrich Simon[2], Bernd Zolitschka[6], and Christoph Mayr[1,7,8]

[1]Institute of Geography, Friedrich-Alexander-Universität Erlangen-Nürnberg, Wetterkreuz 15, 91058 Erlangen, Germany
[2]Austrian Archaeological Institute, Austrian Academy of Sciences, Hollandstrasse 11–13, 1020 Vienna, Austria
[3]Institute of Prehistoric Archaeology, University of Cologne, Bernhard-Feilchenfeld-Strasse 11, 50969 Cologne, Germany
[4]Institute for Geography and Geology, University of Greifswald, Friedrich-Ludwig-Jahnstraße 16/17a, 17489 Greifswald, Germany
[5]Institute of Pre- and Protohistoric Archaeology, Friedrich-Alexander-Universität Erlangen-Nürnberg, Kochstrasse 4/18, 91054 Erlangen, Germany
[6]Institute of Geography, University of Bremen, Celsiusstrasse 2, 28359 Bremen, Germany
[7]Department Earth and Environmental Sciences, Ludwig-Maximilians-Universität München, Richard-Wagner-Strasse 10, 80333 Munich, Germany
[8]GeoBio-Center, Ludwig-Maximilians-Universität München, Richard-Wagner-Strasse 10, 80333 Munich, Germany

Correspondence: Lilian Reiss (lilian.reiss@fau.de)

Relevant dates: Received: 28 July 2021 – Revised: 21 December 2021 – Accepted: 14 January 2022 – Published: 14 February 2022

How to cite: Reiss, L., Stüwe, C., Einwögerer, T., Händel, M., Maier, A., Meng, S., Pasda, K., Simon, U., Zolitschka, B., and Mayr, C.: Evaluation of geochemical proxies and radiocarbon data from a loess record of the Upper Palaeolithic site Kammern-Grubgraben, Lower Austria, E&G Quaternary Sci. J., 71, 23–43, https://doi.org/10.5194/egqsj-71-23-2022, 2022.

Abstract: Two loess sections from the Upper Palaeolithic site of Kammern-Grubgraben (Lower Austria) were analysed to test geochemical proxies, as well as radiocarbon data of different components, for their reliability and consistency in an archaeological context. Only a reliable basal age (28.9–27.8 ka cal BP) was obtained from charcoal fragments derived from a tundra gley underlying the archaeological horizons and assigned to Greenland Interstadials 3 or 4. Grain size, organic and inorganic geochemistry, and stable isotopes of the fine organic fraction ($\delta^{13}C_{org}$) and of rhizoconcretions ($\delta^{13}C$, $\delta^{18}O$) were analysed to provide information on palaeoenvironmental conditions. Low-resolution geochemical and sedimentological analyses document a humidity-related variability, while $\delta^{13}C_{org}$ values indicate predominant C_3 vegetation. High-resolution elemental variations derived from X-ray fluorescence scanning exhibit increasing Ca and decreasing Fe and Ti values, indicating drier conditions towards the top. Secondary pedogenic carbonate concretions provide post-sedimentary (Holocene) ages and are not suitable for assessing climate and environmental changes for the Palaeolithic.

Kurzfassung: Ziel dieser Studie ist es, geochemische Proxies sowie verschiedene Materialien für die Radiokohlenstoff-Datierung auf ihre Zuverlässigkeit und Konsistenz an zwei Lößprofilen aus der

paläolithischen Fundstelle Kammern-Grubgraben in Niederösterreich im archäologischen Kontext zu testen. Nur vereinzelte Holzkohlestückchen lieferten hierfür ein zuverlässiges Alter (28,9–27,8 ka cal BP). Es stammt aus einem Tundra-Gley von der Basis des Profils, unterhalb der archäologischen Horizonte und wird dem Grönland-Interstadial 3 oder 4 zugeordnet. Korngrößen, organische und anorganische geochemische Analysen, sowie Analysen der stabilen Isotope an der organischen Feinfraktion ($\delta^{13}C_{org}$) und an Wurzelkonkretionen ($\delta^{13}C$, $\delta^{18}O$) wurden vorgenommen, um Informationen über Paläoumweltbedingungen zu erhalten. Die geochemischen Proxies ($CaCO_3$, TOC-Gehalte und C / N-Verhältnisse) weisen auf Variationen der Feuchtigkeit hin, während die $\delta^{13}C_{org}$-Werte eine vorherrschende C_3-Vegetation anzeigen. Hochauflösende Elementvariationen, abgeleitet aus Röntgenfluoreszenz-Analysen, deuten zunehmende Ca- bzw. abnehmende Fe- und Ti-Verläufe mit abnehmendem Alter und somit zunehmende Trockenheit an. Die sekundären pedogenen Karbonatkonkretionen besitzen postsedimentäre (holozäne) Alter und sind nicht geeignet, um Klima- und Umweltveränderungen in den untersuchten Profilen zu beurteilen.

1 Introduction

During the last glacial, extensive loess deposits accumulated in central Europe between the Fennoscandian Ice Shield and Alpine glaciers (Smalley et al., 2011; Sprafke, 2016; Lehmkuhl et al., 2021). Predominantly, loess sediments are deposited in valleys, in sedimentary basins of low mountain ranges, and along large rivers. Thus, both the distance to the source area of aeolian dust and the local geomorphology have influenced the thickness of loess deposits (Lehmkuhl et al., 2016). A key area of loess research in the Alpine realm is located in Lower Austria at the western edge of the middle Danube basin, where loess landscapes are widespread (Smalley et al., 2009; Sprafke, 2016; Terhorst et al., 2011). Prevailing westerly winds together with dry and cold katabatic winds from the Alps and Fennoscandian ice sheets favoured the transport of mineral dust from glacial forelands and river floodplains (Renssen et al., 2007; Lowe and Walker, 2015). However, heavy-mineral studies on loess suggest that local dust sources initially mobilised by fluvial transport dominate over far-distance sources in the Lower Austrian study area (Újvári and Klötzli, 2015). Fine silty material was transported farther than coarser grains, and loess predominantly accumulated on slopes exposed to the east, i.e. in lee-side positions (Lowe and Walker, 2015; Sprafke, 2016). Loess deposits formed under (peri)glacial conditions (Frechen et al., 2003; Fitzsimmons et al., 2012), while soils developed during milder interglacials or interstadials (Terhorst et al., 2011; Buggle et al., 2009; Bronger, 2003). Therefore, the resulting loess palaeosol sequences (LPSs) reflect Quaternary climate variability with its glacial–interglacial and stadial–interstadial periods (Bronger, 1999; Frechen et al., 2003; Antoine et al., 2009; Buggle et al., 2009; Sprafke, 2016) and represent prominent natural archives for climate and environmental reconstructions (Porter, 2001; Marković et al., 2015; Lehmkuhl et al., 2016). Different sedimentological or pedological proxies are used for reconstructions of dust accumulation rates, soil formation, weathering, wind intensity, and palaeovegetation (Zech et al., 2007; Gocke et al., 2014).

Moreover, LPSs provide occasional evidence of human activities. The regional Palaeolithic record includes open-air sites such as at Dolní Věstonice (Tomášová, 1995; Antoine et al., 2013; Svoboda et al., 2015) and Pavlov (Svoboda, 1994; Adovasio et al., 1996; Fewlass et al., 2019), both in the Czech Republic, as well as the Lower Austrian sites of Willendorf (Nigst et al., 2008; Teyssandier and Zilhão, 2018; Zeeden and Hambach, 2021), Krems-Wachtberg (Händel et al., 2009, 2014; Terhorst et al., 2014), and Kammern-Grubgraben (Haesaerts and Damblon, 2016; Neugebauer-Maresch et al., 2016; Händel et al., 2021).

Pleistocene sediment sequences were investigated in these areas predominantly with the aim of palaeoclimatic reconstructions but frequently independent of the archaeological background (Fink, 1954, 1962, 1976–1978; Terhorst et al., 2011, 2014; Meyer-Heintze et al., 2018; Sprafke et al., 2020). Studies using geochemical approaches have rarely been applied to archaeological sites, which makes comparisons with well-studied LPSs devoid of archaeological layers difficult. In many cases, this is also due to imprecise and/or contradictory age models. As a result of periglacial environmental conditions, palaeoclimatological and palaeoenvironmental records of the Last Glacial Maximum (LGM) from eastern and central Europe are frequently fragmentary and restricted regarding the choice of proxies (Kovács et al., 2012; Maier et al., 2021; Stojakowits et al., 2021). The LGM is defined here as the period with maximum global ice extent and therefore the lowest global sea levels. Consequently, we use the LGM definition sensu Lambeck et al. (2014) with 30–16.5 ka cal BP, being aware that other definitions exist (e.g. 23–19 ka cal BP, Mix et al., 2001; 26.5–19 ka cal BP, Clark et al., 2009; 27.5–23.3 ka cal BP, Hughes and Gibbard, 2015), and maximum glaciation varied geographically.

Sampling of sediment sequences with embedded archaeological context is a prerequisite for linking environmental variability to human occupation. Especially for the Upper

Palaeolithic (Epigravettian) site of Kammern-Grubgraben, such combined studies are scarce (Haesaerts et al., 2016; Haesaerts and Damblon, 2016). Therefore, in this study we aim at (a) testing organic matter for radiocarbon dating, (b) evaluating proxies regarding their reliability for palaeoclimate research at archaeological sites, (c) shedding new light on palaeoclimate variability and palaeoenvironmental conditions during the LGM, and finally (d) placing the archaeological findings in an environmental context. From a longer perspective, this study helps in developing methodologies for linking local human activity with more comprehensive regional environmental records from adjacent LPSs using their geochemical and sedimentological signatures.

2 Site description

The Upper Palaeolithic open-air site of Kammern-Grubgraben (48.48° N, 15.72° E; Fig. 1) is located in the municipality of Hadersdorf. The surrounding area is characterised by the partly loess-capped hills of the Bohemian Massif. Terracing was carried out in historical times for agri- and viniculture (Neugebauer-Maresch et al., 2016). The excavation site Kammern-Grubgraben is located in a trough-shaped valley sloping gently to the south between the hills of Heiligenstein in the west and Geißberg in the east (Fig. 1b). The area drains to the river Kamp, a tributary of the Danube. This setting seems to have been an attractive campsite for hunter-gatherers in an overall probably rather inhospitable environment.

Systematic archaeological and stratigraphic studies at Kammern-Grubgraben have been carried out since the 1980s (Urbanek, 1990; Brandtner, 1996; Montet-White, 1990; Haesaerts and Damblon, 2016; Haesaerts et al., 2016; Neugebauer-Maresch et al., 2016; Händel et al., 2021). These previous excavations (1985–1994) documented five succeeding archaeological layers (AL 1–5) attributed to at least five separate phases of occupation (Haesaerts et al., 2016; Neugebauer-Maresch et al., 2016). Humic horizons in the sedimentary context of AL 2–4 are reported by Haesaerts and Damblon (2016). Fieldwork was interrupted for about 20 years but recommenced in 2015. Preliminary results of recent investigations, however, suggest that only two main occupations are manifested in the archaeological horizons (AHs) AH 1 and AH 2 (Händel et al., 2021). AH 2 is characterised by complex structures made of stone slabs and densely accumulated artefacts, while the faint upper AH 1 contains fewer finds (Montet-White, 1990; Händel et al., 2021). AH 2 is further described as a horizon representing a range of settlement activities including synoccupational reorganisation/restructuring as well as post-occupational disintegration processes (Händel et al., 2021). While AH 1 corresponds to the previous AL 1, AH 2 represents the former AL 2–4. Humic horizons in the context of AH 2 have not been traced in the new profiles. AL 5 has hitherto only been

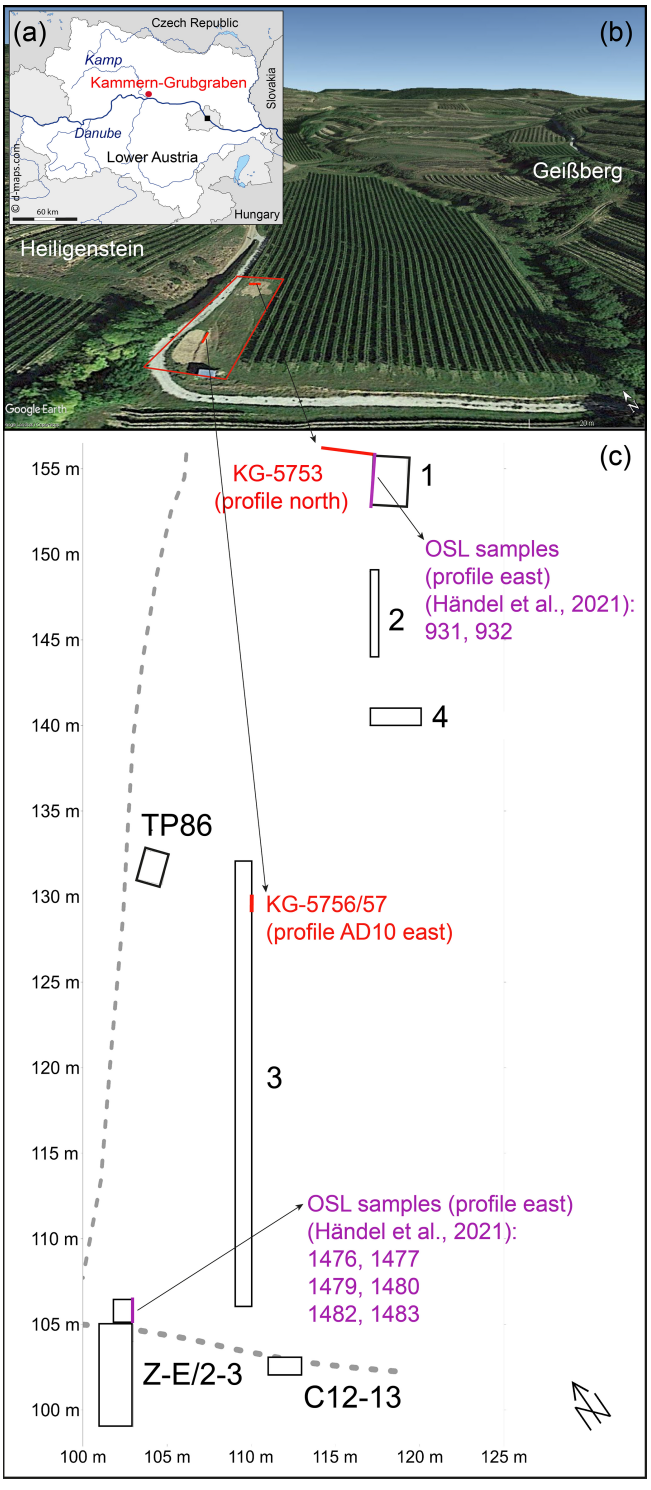

Figure 1. Overview of the study site Kammern-Grubgraben. **(a)** Map of Lower Austria with the study site Kammern-Grubgraben (map source: d-maps, 2021). **(b)** Aerial view (© Google Earth 2020) of the study site. The red polygon represents the excavation site, and the red lines show the locations of extracted loess sections. **(c)** Ground plan of the study site with exact locations (red lines) of the loess sections sampled in 2018 (local excavation grid) and the profiles with OSL samples (purple lines) published in Händel et al. (2021).

found in a small area and can therefore not yet be contextualised from an archaeological perspective. The ^{14}C ages of mammal remains (bones and teeth) obtained from AH 1 and 2 (AL 1–4) point at human activity between approximately 23–20 ka cal BP (Haesaerts et al., 2016; Händel et al., 2021), a time interval including Greenland Interstadials (GIs) GI-2.1 and GI-2.2 (Rasmussen et al., 2014). Besides the mammal fauna (Logan, 1990; West, 1997), the gastropods of previous excavations were studied (Haesaerts, 1990; Frank and Rabeder, 1996, 1997; Frank, 2006).

Goals of the ongoing excavations are, among others, establishing the limits of the previous excavations, reassessment of the archaeological stratigraphy, and determining the site limits. The first results of these new investigations have recently been published (Händel et al., 2021). Of major importance for the study we present here is the stratigraphic connection between the area of previous excavations around trenches 1 and 2 and TP86 and the trenches in the southwest (Z-E/2-3 and C12-13), which document a far greater extent of the site than previously known (Fig. 1c). A stratigraphic connection was established by excavation of trench 3, in which the main archaeological horizon AH 2, with its pronounced stone structures, could be traced, while analyses of the lithic material confirmed cultural coherency of the artefact inventories, and chronometric results suggest contemporaneity (Händel et al., 2021). This forms the basis for the correlations of the profiles presented here (Fig. 2).

3 Material and methods

3.1 Field sampling of loess profiles

Two sections were sampled at the Upper Palaeolithic excavation site Kammern-Grubgraben (Fig. 1a, b) in 2018. The first section (KG-5753) is 91.3 cm long and was taken from the north profile in trench 1. The other two overlapping sections KG-5756 and KG-5757 are 91.3 and 85.5 cm long, respectively, and come from profile AD10 east in trench 3 (Fig. 1c). Whereas AH 1 was only present in one section, AH 2 is documented in both analysed profiles (Fig. 2a, b).

The sediment sections were sampled in the field with the help of sheet steel profiles (28 × 27 mm, 0.6 mm thick, Knauf, Germany) with U-shaped cross-sections. Loess section KG-5753 starts 50 cm below the surface, and the 0–10 cm sampling depth contains the lower part of the modern soil, hereafter referred to as Anthrosol (Fig. 2a).

Loess sections KG-5757 and KG-5756 do not include the modern Anthrosol and were sampled with an overlap of 21.5 cm (Fig. 2b). Both sections were merged into a composite 155 cm long profile based on macroscopic and field observations as well as on geochemical records. The positions of loess sections within the excavation grid as well as absolute elevations (m a.s.l.) of their surface were determined by an electronic tachymeter.

3.2 XRF core scanning and subsampling of loess sections

With few exceptions (Liang et al., 2012; Sun et al., 2016), it has been common practice to carry out X-ray fluorescence (XRF) analyses of loess samples on discrete samples (Profe et al., 2018a; Profe and Ohlendorf, 2019) or to use a handheld scanner (Ward et al., 2018; Goff et al., 2020). In this study, sediment sections were analysed continuously in their sheet steel profiles. Prior to scanning, the sediment surfaces were thoroughly smoothened with a utility knife.

Sediment sections were photographically documented and analysed with an XRF core scanner (Itrax, Cox Analytical Systems, Sweden). Polarised light and a resolution of 500 dpi were used for imaging. The recording resolution of XRF spectra was 1 mm and counting time 5 s. A Cr tube was used at 30 kV and 50 mA. Repeated analyses on the same loess section revealed that only the most frequent elements Si, K, Ca, Ti, and Fe provide reproducible results. The element counts were standardised using the centred log-ratio (clr) transformation (Aitchison, 1982; Martin-Puertas et al., 2017). This transformation accounts for matrix effects caused by, for example, variations in grain size or water and organic matter contents and approximates true element concentrations (Weltje et al., 2015).

After scanning, the sections were continuously subsampled at a 1 cm resolution. This resulted in a total of 92 (KG-5753, KG-5756) and 85 (KG-5757) samples. Each sample represented a volume of ca. 7 cm^3, which is equivalent to about 10 g. Samples were suspended in deionised water and thereafter lyophilised for further analytical procedures. This treatment allowed dispersion of the dried sediment without mechanical force, preventing the destruction of microfossils. After drying, each sample was subdivided into three fractions for grain-size analyses (0.5 g), isotope-geochemical analyses (0.65 g), and sieving for microfossils (5–8 g).

3.3 Grain-size analyses

Grain-size distribution was determined for every fifth centimetre, using a laser particle analyser (LS 200, Beckman Coulter). Samples were sieved to ≤ 2 mm. For each of the selected samples, 0.5 g was weighed into centrifuge tubes and left overnight with 1 mL of 30 % H_2O_2 to destroy organic matter. Afterwards, the tubes were placed in a drying cabinet at 105 °C for 2 h. To dissolve secondary carbonates, 2.4 mL of 10 % HCl was added to each sample, which was placed in a drying cabinet at 85 °C for 4 min. Afterwards, the samples were washed with deionised water and centrifuged until a pH of 4.5 was reached. Subsequently, 24 mL of 2 M NaOH was added to each tube and left in a drying cabinet at 85 °C for 5 min. Samples were washed with deionised water and centrifuged until a pH of 8 was reached. Then, to lower the pH to 7, a drop of 5 % HCl was added, and samples were washed and centrifuged again. Subsequently, samples were

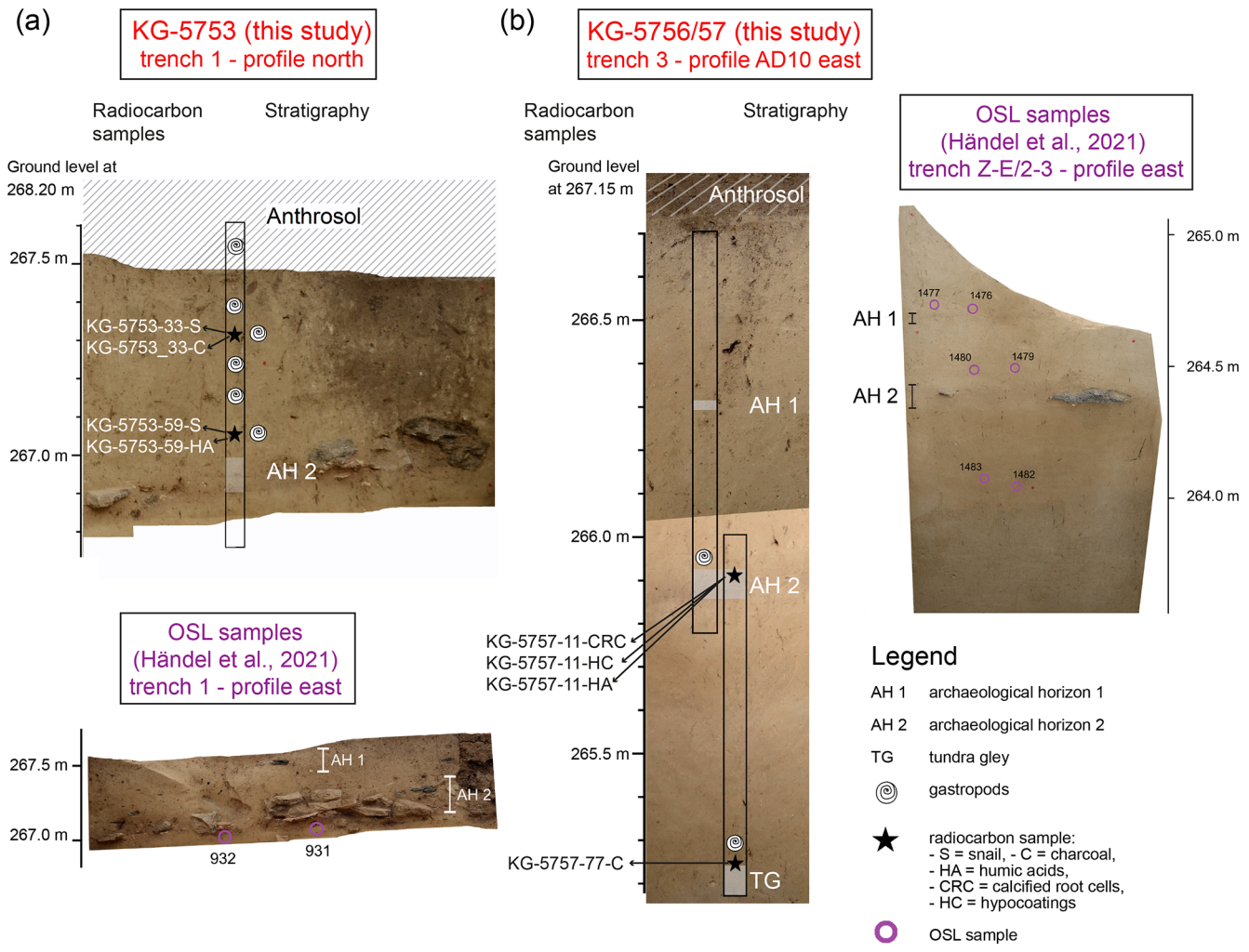

Figure 2. Orthophotographs of excavation profiles with projected positions of **(a)** loess profile KG-5753 – profile north in trench 1 and OSL samples (932, 931) taken from profile east in trench 1 (Händel et al., 2021), **(b)** KG-5756 (upper part) and KG-5757 (lower part) from profile AD10 east in trench 3, and **(c)** OSL samples (1482, 1483, 1479, 1480, 1476, and 1477) taken from profile east in trench Z-E/2-3 (Händel et al., 2021). Hatched areas represent the modern Anthrosol. Archaeological horizons (AH 1 and AH 2) as well as the underlying tundra gley (TG) in KG-5757 are shaded. Stratigraphic positions of gastropods are given for both loess profiles.

mixed with $(NaPO_3)_n$ and $NaCO_3$ and left on a rotator for 8 h for dispersion.

Each sample was analysed in at least three runs to eliminate possible outliers and to check for reproducibility. The first run was taken as a test run. Results were calculated from runs two and three. Results of laser particle analyses were processed with GRADISTAT (Blott and Pye, 2001). Only for the median grain size were the raw data used. Grain sizes were classified according to standard size classes: coarse sand (cS, 630–2000 µm), middle sand (mS, 200–630 µm), fine sand (fS, 63–200 µm), coarse silt (cSi, 20–63 µm), middle silt (mSi, 6.3–20 µm), fine silt (fSi, 2–6.3 µm), and clay (cl, < 2 µm). Grain-size indices (20–50 µm / < 20 µm) and U ratios (16–44 µm / 5.5–16 µm) were determined using the size fractions according to Rousseau et al. (2002) and Vanderberghe et al. (1997), respectively.

3.4 Geochemical analyses

Carbon (C) and nitrogen (N) contents were analysed for every centimetre with a CN analyser (vario EL cube, Elementar Analysensysteme GmbH, Germany). For each lyophilised sample, 500 mg was homogenised with a mortar and a pestle. Macroscopic remains were removed prior to homogenisation. For determination of total carbon (TC) and total nitrogen (TN), 20 mg was weighed in tin capsules and analysed in the CN analyser. The samples were measured twice to check reproducibility. To estimate total inorganic carbon (TIC), another fraction of each sample was dried at 105 °C overnight. Thereafter, 400 mg of each sample was weighed in porcelain crucibles and put in a muffle furnace at 550 °C for 4 h to remove total organic carbon (TOC) (Heiri et al., 2001). After this high-temperature heating, samples were weighed

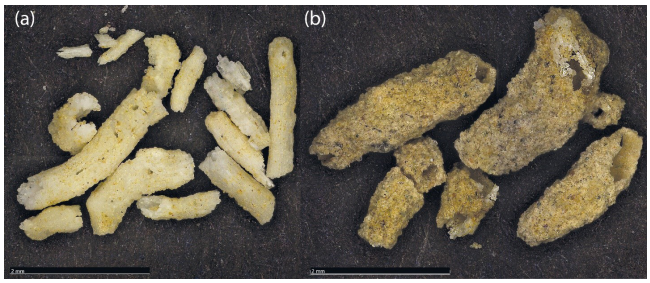

Figure 3. Photographs of examples of **(a)** CRC (KG-5756, 30 cm depth) and **(b)** HC (KG-5756, 60 cm). The scales are 2 mm each.

again for the CN analyser to analyse TIC. TOC was calculated as the difference between TC and TIC, corrected for the weight loss from loss on ignition (LOI). Assuming that TIC is present as $CaCO_3$, the carbonate content of the samples was calculated from TIC using a stoichiometric factor of 8.33. All data are given in per cent (%) of dry mass.

3.5 Pedogenic carbonates

Remaining after previous analyses, 5–8 g of the lyophilised bulk sediment was sieved with a 500 µm mesh to separate coarse particles and secondary (pedogenic) carbonates from every centimetre sample. The coarse particles were screened under a microscope, and microscale secondary carbonates were characterised following the criteria of Barta (2011). They generally comprise calcified root cells (CRC), hypocoatings (HC), carbonate coatings (CC), earthworm biospheroids (EBS), and needle-fibre calcites (NFC). CRC are identifiable by elongated calcite crystals that form tubes of up to 1 cm in length and are of bright whitish to light brownish colour, the latter representing the decalcified margin (Becze-Deák et al., 1997; Barta, 2011). HC on the other hand are pore walls of the soil matrix impregnated with $CaCO_3$ (Barta, 2011). They consist of micritic or small calcite tubes mixed with other minerals such as mica (Becze-Deák et al., 1997; Barta, 2011, 2014). Their cylindrical and branched shape is of 1–6 mm length and 3–4 mm width on average (Barta, 2014). In this study, only CRC and HC were present in the sediment (up to 66 mg HC per gram of sediment in 46–47 cm depth in KG-5753). They were handpicked, separated, and documented using the extended-depth-of-field option of a digital reflected-light microscope (Smartzoom 5, Carl Zeiss Microscopy GmbH, Germany) (Fig. 3).

3.6 Stable isotope analyses

Secondary carbonate concretions were not evenly distributed in the sediment cores. In total, 56, 74, and 26 (88, 92, and 75) samples of the KG-5753, KG-5756, and KG-5757 sections, respectively, contained sufficient CRC (HC) for isotope analyses. CRC (70–150 µg) and HC (150–200 µg) were crushed with a pestle and weighed into borosilicate-glass septum vials using a microbalance (Sartorius, ME36S, Germany). Carbonates reacted with concentrated, water-free phosphoric acid in the previously helium-flushed septum vial. After at least 3 h of equilibration at constantly 70 °C in a heating block, the evolved CO_2 gas was transferred via a GasBench II (Thermo Fisher, USA) coupled to an isotope-ratio mass spectrometer (IRMS) (Delta V Advantage, Thermo Fisher, USA) for carbon ($\delta^{13}C$) and oxygen ($\delta^{18}O$) stable isotope analyses.

For the measurement of $\delta^{13}C_{org}$, bulk sediment samples were decalcified following the method of Pötter et al. (2020). Of each sample, 150 mg was weighed into centrifuge tubes, treated with 25 mL of hydrochloric acid (HCl, 5 %), and kept in a water bath at 50 °C for 4 h. Subsequently, samples were washed with deionised water by repeated centrifugation. After the removal of HCl, samples were lyophilised. For stable isotope analysis, a sample amount equivalent to 50–300 µg of organic carbon (2–40 mg dry matter) was weighed into tin capsules. Samples were combusted at 1080 °C in an elemental analyser (EA) (NC 2500, Carlo Erba, Italy) coupled to an isotope-ratio mass spectrometer (IRMS) (DeltaPlus, Thermo Finnigan, Germany) used for isotope analyses.

All results are expressed as delta (δ) values in per mil (‰) relative to international standards.

The δ notation is defined as

$$\delta = \left(R_{\text{Sample}} / R_{\text{Standard}} - 1\right), \quad (1)$$

where R is the mass ratio of the heavier isotope to the lighter isotope (e.g. $^{13}C / ^{12}C$ or $^{18}O / ^{16}O$) of the sample and an international standard (Vienna Pee Dee Belemnite (VPDB) for carbon, Vienna Standard Mean Ocean Water (VSMOW) for oxygen). The international standards NBS 18 and NBS 19 (Brand et al., 2014) and a laboratory standard consisting of pure Solnhofen limestone ("Pfeil"; Oehlerich et al., 2013) were used to calibrate the stable isotope analyses of secondary carbonates. For stable isotope analyses of bulk organic carbon, the international standards IAEA-CH-7 and USGS41 (Brand et al., 2014) and a laboratory standard ("Peptone"; Mayr et al., 2017a) were used.

3.7 Radiocarbon dating

Loess sequences are commonly dated with luminescence (Thiel et al., 2011a; Veres et al., 2018) or radiocarbon techniques (Újvári et al., 2014; Haesaerts et al., 2016). At the studied site of Kammern-Grubgraben, published radiocarbon measurements are only available for bone material from the archaeological layers and reveal ages around 23–22 ka cal BP (Haesaerts et al., 2016; Händel et al., 2021). Thus, additional ^{14}C measurements were carried out in order to place the loess sections into a more precise timeframe. However, suitable materials (charcoal, bones) are barely available outside of the well-dated archaeological horizons. Therefore, radiocarbon age determination was tested on gastropods, humic acid fractions, and secondary pedogenic carbonates. The weights

of the respective samples are listed in Table 1. Gastropods (mainly the species *Vallonia costata*) were handpicked after sieving with a 500 µm mesh to separate coarse particles from bulk sediment. Almost all gastropods were fragmented and allowed identification only to the genus level, except for a few specimens which had a well-preserved aperture allowing species identification. Only two gastropods provided a sufficient mass (1.6 mg each) for radiocarbon dating.

All these materials have been previously tested at other loess sites with some success (e.g. Pustovoytov and Terhorst, 2004; Gocke et al., 2011; Xu et al., 2011; Wang et al., 2014; Újvári et al., 2016a). If possible, different sample pairs (Fig. 2) from the same depths were handpicked under a binocular microscope, thoroughly cleaned with distilled water, dried, and then sent to the Poznan Radiocarbon Laboratory (Poland) for radiocarbon accelerator mass spectrometry (AMS) measurements. Gastropod shell samples were rinsed with HCl and H_2O_2 prior to radiocarbon measurement. However, due to the small sample size, there was no control on the amount of material removed during these steps. The residues of these samples were then leached using H_3PO_4, resulting in very small portions of available carbon. The IntCal20 curve (Reimer et al., 2020) and CALIB 8.2 (Stuiver et al., 2020) were used for calibration of radiocarbon ages. Note that for reasons of comparability with the new radiocarbon ages presented here, all ages are given as calibrated kiloyears (ka cal BP) although other dating methods were partly used.

4 Results

4.1 Sediment description and grain-size distribution

Based on sedimentary features like colour, amount of carbonate concretions, rooting, and aggregate texture, the sections were subdivided into different units separated by archaeological horizons and the basal tundra gley. These units are overlain by an Anthrosol in both sections, which was sampled only in KG-5753 (Fig. 2a). This Anthrosol is a disturbed and machine-worked vineyard soil, which shows characteristic soil features such as roots and an aggregate texture. It further appears much darker than the rest of the section. The next unit consists of lighter-coloured loess sediment, which contains some root remains. High amounts of secondary carbonates are present from 11 to 24 cm depth and again from 40 to 45 cm depth and around AH 2. With increasing depth, the sediment becomes slightly darker. Rock fragments of 1–5 mm diameter are present around AH 2, corresponding to the lateral presence of up to decimetre-sized boulders in AH 2 (Fig. 2a). Profile KG-5756–KG-5757 (hereafter KG-5756/57) starts immediately below the modern Anthrosol (Fig. 2b). The upper part contains carbonate concretions and is equivalent to the loess above AH 2 in KG-5753. The position of AH 1 was estimated from adjacent sections, as the sediment is hardly distinguishable from the surrounding substrate in KG-5756. AH 2 contains rock fragments and artefacts in KG-5756/57 and serves as the tie point for merging both sub-profiles with an overlap of about 21 cm. AH 2 contains the highest amount of secondary carbonates (CRC and HC) in KG-5756/57. The unit below AH 2 consists of more homogenous loess almost without CRC but with occasional root traces. Field observations suggest that the slightly bleached horizon at the base of KG-5757 (in the lowermost 15 cm) represents a tundra-gley soil. In the present study, terrestrial gastropods (*Vallonia costata* and *Pupilla* sp.) were found only in very small numbers and often only as shell fragments (Fig. 2a, b).

The grain-size analyses of KG-5753 and KG-5756/57 show a dominance of silt in all measured samples, while cS is practically absent in all profiles (Fig. 4). The profile KG-5753 contains between 7.9 % and 8.8 % cl. fSi has a similar distribution to mSi, although an overall lower content is evident. MSi increases slowly from 15 % at 90 cm depth to 20.0 % at 10 cm. cSi varies between 49 % and 41 % from 75 to 10 cm depth. The fS content decreases from 34.5 % at 90 cm depth to 24.4 % at the top. The mS content reaches up to 5.0 % at the bottom of the profile and shows the highest content of 9.5 % at the top, i.e. the Anthrosol. The grain-size index and *U* ratio show a decreasing trend from bottom to top with a slight decrease in AH 2.

In KG-5756/57, the clay content slightly decreases from the bottom of the profile to 100 cm depth and then shows a small but steady increase from 100 cm depth to the top (Fig. 4b). The sand fraction slightly decreases from bottom to top. The fS fraction is most prominent at 101 cm depth, and then again between 70 and 50 cm depth. An increase in mS is present between 110 and 90 cm depth and again from 65 to 50 cm depth. Thus, the mS fraction is dominant below and above the archaeological layer located between 88 and 78 cm depth. Both fS and mS are highest at 100 cm depth. The *U* ratio ranges from 2.0 to 2.7 and the grain-size index from 1.0 to 1.4. Low values occur in the tundra gley and at the top of the profile; maximum values are between 110–95 cm. In the archaeological horizons (AH 2, AH 1) local minima of the *U* ratio as well as the grain-size index are visible.

4.2 Geochemistry

4.2.1 Organic geochemistry

The TOC content of profile KG-5753 is < 1 % except in the upper 12 cm, in which TOC increases from 1.3 % to 3.4 %, reflecting the Anthrosol (Fig. 5a). The $\delta^{13}C_{org}$ values range from −28.4 ‰ to −23.7 ‰. The TOC content of the merged profile KG-5756/57 ranges from 0.2 % to 0.6 %, showing minima between 107 and 105 cm depth, at 91, 86, 67, 37, and 16–13 cm depth (Fig. 5b). Maxima are recognisable at 151 and at 119 cm depth. The lowest $\delta^{13}C_{org}$ value is −28.3 ‰ (in KG-5757, 90 cm depth) and the highest −23.9 ‰ (in KG-5756, 92 cm depth).

Although the C / N ratios of both profiles must be considered with caution since TN contents are close to the detection

Table 1. Radiocarbon ages of different materials. Stratigraphically consistent ages are indicated in bold.

Sample ID	Lab no.	Sampling depth (cm)	Uncalibrated radiocarbon date (BP ± analytical error)	Calibrated age range (cal BP and probabilities (2σ))	Material	Weight (mg)
KG-5753-33-S	Poz-128063	33	**12 390 ± 170**	**15 160–14 020** (0.999)	Terrestrial gastropod	1.6
				13 900 (0.001)	(*Vallonia costata*)	
KG-5753-33-C	Poz-128202	33	117.23 ± 1.33 pMC	Younger than 1950 CE	Recent root	2.77
KG-5753-59-S	Poz-128064	59	9960 ± 100	11 760–11 210 (0.983)	Terrestrial gastropod	1.6
				11 810–11 790 (0.017)	(*Vallonia costata*)	
KG-5753-59-HA	Poz-128200	59	5060 ± 80	5940–5600 (0.997)	Humic acids	2998.6
				5980 (0.003)		
KG-5757-11-CRC	Poz-128065	79	2305 ± 30	2360–2300 (0.778)	Rhizoconcretions	14.2
				2230–2180 (0.222)	(CRC)	
KG-5757-11-HC	Poz-128067	79	5000 ± 40	5860–5810 (0.291)	Rhizoconcretions	12.8
				5790 (0.009)	(HC)	
				5770–5650 (0.608)		
				5640–5600 (0.092)		
KG-5757-11-HA	Poz-128201	79	2860 ± 40	3080–2860 (0.961)	Humic acids	3086.7
				3110–3100 (0.017)		
				3140–3130 (0.021)		
KG-5757-77-C	Poz-128204	145	**24 240 ± 240**	**28 930–27 830**	Charcoal	1.0

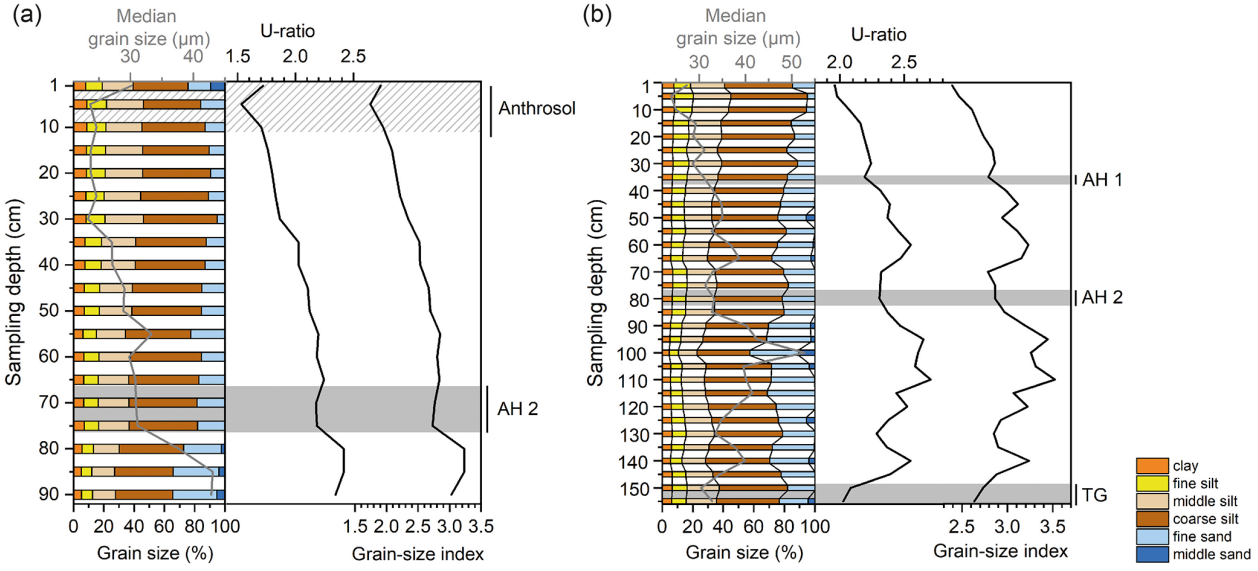

Figure 4. Grain-size distribution, median grain size, *U* ratio (16–44 µm / 5.5–16 µm), and grain-size index (20–50 µm / < 20 µm) of **(a)** KG-5753 and **(b)** KG-5756/57. Grain sizes are classified according to standard size classes with coarse sand (cS, 630–2000 µm), medium sand (mS, 200–630 µm), fine sand (fS, 63–200 µm), coarse silt (cSi, 20–63 µm), medium silt (mSi, 6.3–20 µm), fine silt (fSi, 2–6.3 µm), and clay (cl, < 2 µm). The hatched area in **(a)** represents the base of the sampled Anthrosol; shaded areas represent the archaeological horizons (AH 1 and AH 2) and the tundra gley (TG).

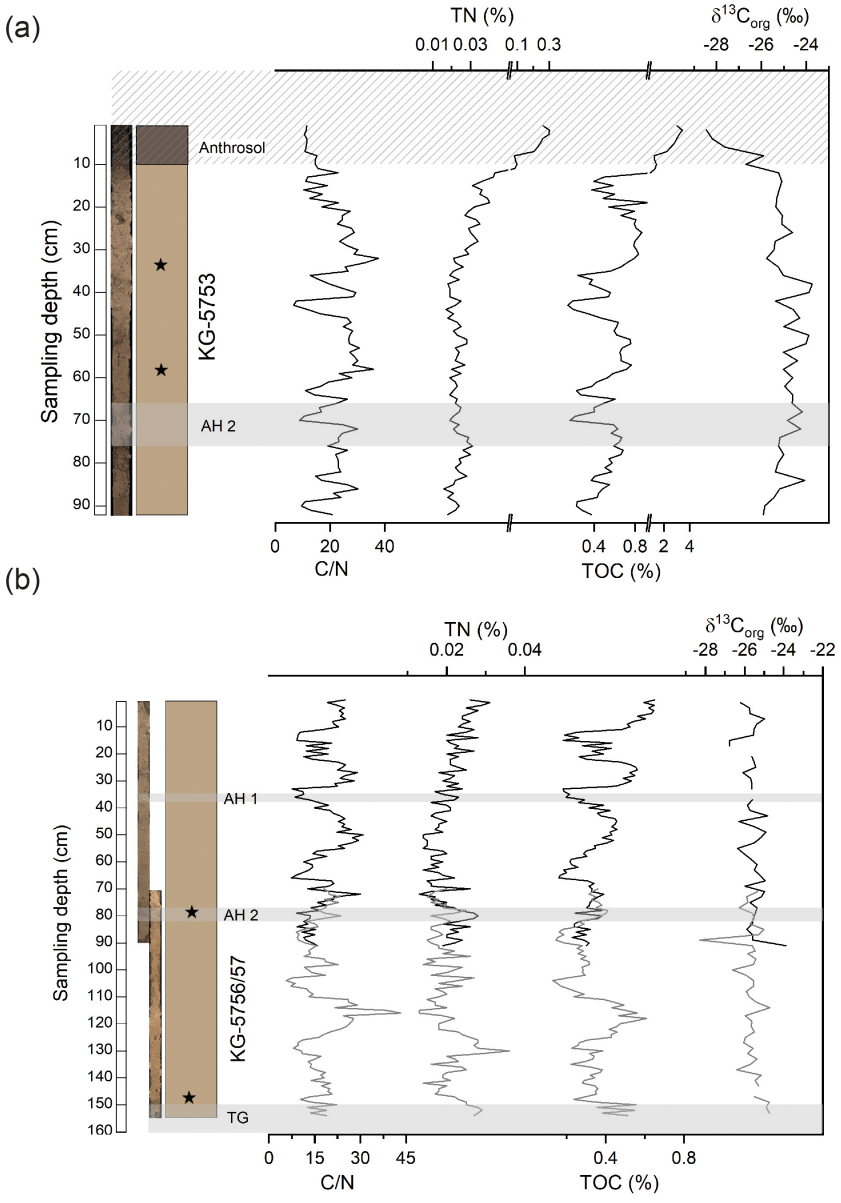

Figure 5. Organic geochemistry including C / N (carbon-to-nitrogen ratio), TN (total nitrogen), TOC (total organic carbon), and $\delta^{13}C_{org}$ (organic carbon isotope ratio) of **(a)** KG-5753 and **(b)** KG-5756/57. The hatched area in **(a)** represents the base of the sampled Anthrosol; shaded areas represent the archaeological horizons (AH 1 and AH 2) and the tundra gley (TG). Black stars symbolise the positions of radiocarbon samples. Missing values are indicated by gaps. Note axis breaks and scale changes in **(a)** for TN and TOC.

limit for all profiles (maximum values of 0.3 % and 0.03 % in KG-5753 and KG-5756/57, respectively), they show a comparable range and similar variations, pointing to environmental control of C / N variations.

4.2.2 Inorganic geochemistry

The $CaCO_3$ content in KG-5753 shows an increase from the bottom to 45 cm depth and a decrease from 37 % to 25 % between 15 and 10 cm depth (Fig. 6a). As an overall pattern the $CaCO_3$ content of KG-5756/57 slightly increases from bottom to top with values ranging from 23.1 % at 147 cm depth to 32.7 % at 129 cm depth. A minimum of 22.6 % is evident at 101 cm depth, followed by a further increase to 41.2 % at 13 cm depth (Fig. 6b).

XRF-core-scanning analyses provided results for the elements Cr, K, Mn, Zn, Sr, Ca, Si, Ti, Fe, and Rb. However, only Ca, K, Si, Ti, and Fe exhibited high signal-to-noise ratios and are therefore considered for further discussion.

The influence of the topsoil explains the higher variability in analysed elements above a depth of 13 cm in KG-5753 (Fig. 6a). Aside from that, the variations in Fe and Ti are in-

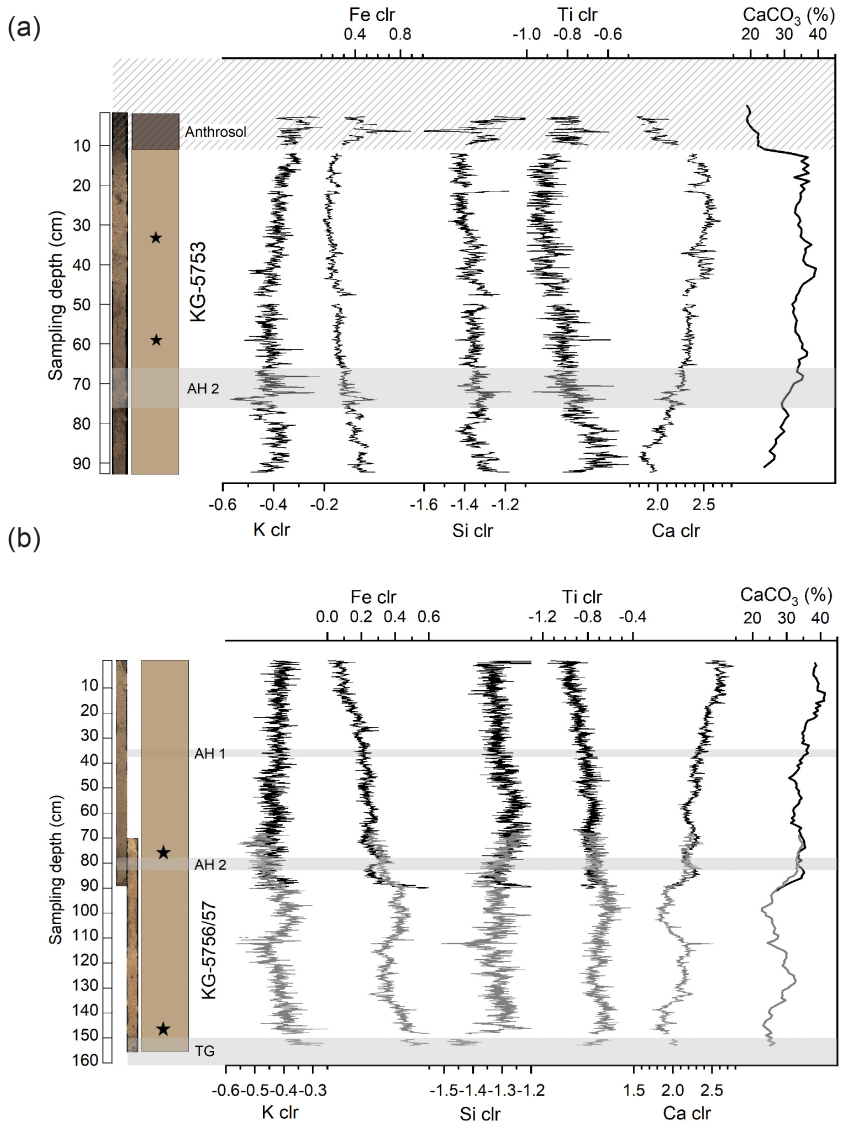

Figure 6. Element and $CaCO_3$ contents of **(a)** KG-5753 and **(b)** KG-5756/57. Hatched area in **(a)** represents the base of the sampled Anthrosol, shaded areas the archaeological horizons (AH 1 and AH 2) and the tundra gley (TG). Black stars symbolise the positions of radiocarbon samples. Missing values are indicated by gaps. For element contents derived from XRF-scanning analyses, clr-transformation was applied to account for matrix effects.

versely correlated to Ca (R^2 is 0.83 and 0.67, respectively, in KG-5753, and R^2 is 0.89 and 0.80, respectively, in KG-5756/57), the element with the highest counts of the records. The comparison with $CaCO_3$ analyses shows that Ca is predominantly bound to carbonates (Fig. 6a, b). Thus, Fe and Ti variations are presumably the result of dilution caused by varying carbonate amounts. In contrast to Fe and Ti, the overall trends in K and Si are not antagonistic to Ca, but the variability in these elements is rather low.

The distribution of Ca, however, shows a different pattern, as there is an increasing trend from bottom to top. Within this increase, Ca shows minima at 145 cm depth and between 115 and 95 cm depth (Fig. 6b). The Ca distribution derived from XRF scans is significantly correlated with the $CaCO_3$ content for both profiles (KG-5753 $R^2 = 0.55$ and KG-5756/57 $R^2 = 0.84$). For this correlation, XRF Ca clr values are averaged in 10 mm steps to account for the lower resolution of $CaCO_3$ analyses.

4.3 Radiocarbon dating

Radiocarbon dating of different materials shows high variabilities (Table 1).

Only sample KG-5757-77-C reveals an expected age range of 28 930–27 830 cal BP. This piece of charcoal derives from the upper part of the tundra gley. Terrestrial gastropods from

the upper part of the loess section KG-5753 reveal ^{14}C ages between approximately 11 and 15 ka cal BP. In some cases, however, the results show age inversions. Humic acids as well as rhizoconcretions (CRC and HC) reveal a Holocene formation. Sample KG-5753-33-C was most likely a recent root, which explains the postmodern age, i.e. younger than 1950 CE.

4.4 Stable isotopes of carbonate concretions

In KG-5753, 43 samples contain sufficient CRC for isotope analyses. The $\delta^{18}O_{CRC}$ values range from −13.8 ‰ to −7.2 ‰. The $\delta^{13}C_{CRC}$ range is exceptionally high with values ranging from −30.9 ‰ to −6.7 ‰ (Fig. 7a). At about 45 cm depth, an increase is detectable for the $\delta^{18}O_{CRC}$ and $\delta^{13}C_{CRC}$ records of both profiles. Furthermore, $\delta^{18}O_{CRC}$ and $\delta^{13}C_{CRC}$ are significantly correlated ($R^2 = 0.70$). HC were found in 70 samples in KG-5753. The $\delta^{18}O_{HC}$ values range from −11.7 ‰ to −4.8 ‰ and $\delta^{13}C_{HC}$ from −8.9 ‰ to −1.9 ‰.

In KG-5756/57, isotope analyses of CRC were limited to 73 samples with sufficient amount. The $\delta^{18}O_{CRC}$ values range from −14.2 ‰ to −5.7 ‰. The lowest $\delta^{13}C_{CRC}$ value is −29.9 ‰ and the highest −3.9 ‰ (Fig. 7b). $\delta^{18}O_{CRC}$ and $\delta^{13}C_{CRC}$ records are significantly correlated ($R^2 = 0.68$). HC were found in 114 samples in KG-5756/57. The $\delta^{18}O_{HC}$ values range from −6.8 ‰ to −4.2 ‰ and the $\delta^{13}C_{HC}$ values from −8.0 ‰ to −1.2 ‰ (Fig. 7b). $\delta^{18}O_{HC}$ and $\delta^{13}C_{HC}$ records are significantly correlated ($R^2 = 0.89$).

5 Discussion

5.1 Age determination and stratigraphy

Previous ^{14}C measurements of bones and teeth obtained from archaeological layers revealed ages between 23.7 and 22.1 ka cal BP (Haesaerts et al., 2016; Händel et al., 2021). Optically stimulated luminescence (OSL) ages provide additional age control for over- and underlying strata (Händel et al., 2021). These samples stem from different profiles but from the same stratigraphic positions (Figs. 1 and 2) and are listed with published radiocarbon measurements from the archaeological horizons in Table 2.

In our study, we also tested radiocarbon age determinations on various materials regarding reliability and consistency. Only two samples, namely a piece of charcoal (KG-5757-77-C) and a terrestrial snail (KG-5753-33-S), revealed results in the expected age range to be considered reliable (Table 1). However, the ^{14}C age of the analysed gastropod should be considered with caution since a second terrestrial snail (KG-5753-59-S) with a younger age was found about 20 cm deeper (Table 1). This uncertainty could be related to the small quantity of the snail samples (< 1.7 mg) or to possible relocation caused by bioturbation. In general, the ingestion of dead carbon can also influence radiocarbon ages of terrestrial snails. This effect was observed in 22 % of modern snails dated in the course of a comprehensive study in North America (Pigati et al., 2010). However, this effect cannot explain the age of KG-5753-59-S, which appears too young and can thus not serve as an explanation for this case. We rather assume that this particular sample possibly contained carbonate contamination of more recent age; i.e. the sample shows an open-system behaviour. Ages of gastropods were compared with charcoal ages in a study of the Dunaszekcső loess record (Újvári et al., 2016a). In that study, 7 out of 11 mollusc shells revealed a similar age to charcoal samples from the same stratigraphic levels, suggesting a predominantly closed-system behaviour for radiocarbon of loess snails, while at least one of these samples also clearly showed an open-system behaviour, similarly to our study.

At least the formation of CRC has frequently been described as synsedimentary (Becze-Deák et al., 1997; Wang and Greenberg, 2007; Barta, 2011, 2014; Koeniger et al., 2014). Radiocarbon ages of HC and CRC in our study do not support this assumption. Generally, the formation of CRC is linked to $CaCO_3$ in the soil matrix, which is dissolved by H^+–HCO_3^- exchange. Ca^{2+} then becomes available for the plant and is subsequently absorbed by roots and accumulates in the vacuole where it precipitates as $CaCO_3$. While the cells calcify, the outer part of the cells, namely the parenchyma cells of the roots, mineralise during plasmolysis (Becze-Deák et al., 1997; Barta, 2011). For the formation of HC, two main hypotheses exist (Becze-Deák et al., 1997; Barta, 2011). The origin of the HCs either can be attributed to the evaporation of Ca-rich solutions from the soil matrix or may be due to carbonate precipitation from the soil solution into the soil matrix or along the pores (Barta, 2011). The other hypothesis is related to the metabolism of the roots. The release of CO_2 leads to the crystallisation of dissolved calcium from the soil solution, resulting in the formation of micrite crystals. Cemented together, they enclose the root remnants or rather the pores formed by the roots within the soil matrix (Becze-Deák et al., 1997; Barta, 2011).

To conclude, the ^{14}C results of secondary carbonate concretions further corroborate previous findings that they cannot be used for dating purposes of loess deposits of Late Pleistocene age (Gocke et al., 2011; Újvári et al., 2014). With regard to their young ages, they cannot be linked to soil processes during loess build-up. In our study, humic acids also provided Holocene ages and thus were too young to be used for age inferences of the loess sections. This is in contradiction to previous studies in which humic acid fractions were considered reliable (Runge et al., 1973; Wang et al., 2014).

In summary, the most reliable age determination from the loess section in our study derives from a singular sample with charcoal particles. Such particles, however, are very scarce at Kammern-Grubgraben. As an alternative for future dating approaches, the more abundant terrestrial snails could provide an option for layers where neither charcoal nor hard tissue vertebrate remains are available. However, more studies

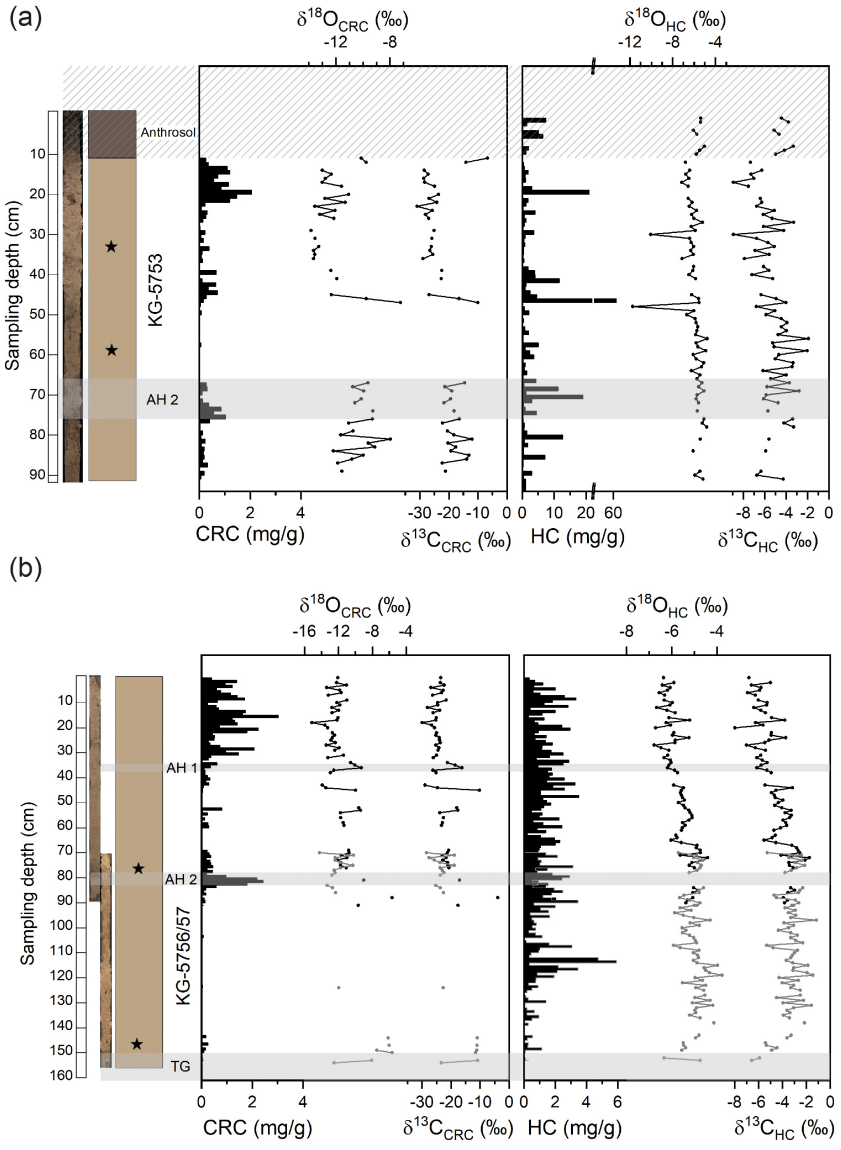

Figure 7. Stable isotope data of secondary carbonates (CRC and HC) and their concentration (mg g^{-1}) along the profile in **(a)** KG-5753 and **(b)** KG-5756/57. The hatched area in **(a)** represents the base of the sampled Anthrosol; shaded areas represent the archaeological horizons (AH 1 and AH 2) and the tundra gley (TG). Black stars symbolise the positions of radiocarbon samples. Missing values are due to the absence of secondary carbonates at their respective positions and are indicated by gaps. Note the axis break and scale change in **(a)** for the concentration of HC.

are needed with larger amounts of gastropod material. Such a larger amount of snail carbonate would also allow a controlled mild acid pretreatment to remove shell contaminations prior to dating as proposed by Újvári et al. (2016a), which was not reliably carried out in our study.

5.2 Critical evaluation of secondary pedogenic carbonate isotopes

The isotopic composition of secondary pedogenic carbonates has been frequently studied (e.g. Cerling, 1984; Dworkin et al., 2005; Gocke et al., 2011; Koeniger et al., 2014). The variable concentration of microscale secondary carbonates in loess sequences is thought to be a sensitive indicator of environmental changes, such as alternating dust accumulation or changes in moisture regime (Barta, 2014; Koeniger et al., 2014). The formation of secondary carbonates is mostly accompanied by relocation (vertical, horizontal) of primary carbonates in the sediment (Barta, 2011, 2014; Koeniger et al., 2014). Vertical relocation is linked either to infiltration of meteoric water, which leads to leaching and thus to dissolution and re-precipitation of carbonates, or to pore- and groundwater rising through evaporation, which results in upward dislocation (Monger, 2002; Barta, 2014). In situ-

Table 2. OSL and radiocarbon ages from Händel et al. (2021). Note that radiocarbon dates were re-calibrated with IntCal20 (Reimer et al., 2020). For OSL dating, quartz in the fraction of 63–90 µm was used.

Lab no.	Type of sample	Material and species	Approximate depth (cm) and archaeological layer	Age (BP) $\pm 1\sigma$	Calibrated age range (cal BP) and probabilities (2σ)	OSL age (ka) $\pm 1\sigma$
MAMS-32966	^{14}C	reindeer tooth	35 (AH 1)	18 590 ± 60	22 750–22 710 (0.012)	
					22 690–22 340 (0.988)	
MAMS-26430	^{14}C	horse/reindeer bone	81–76 (AH 102, corr. to AH 2)	18 300 ± 70	22 400–22 090 (1.000)	
MAMS-30165	^{14}C	horse/reindeer bone	81–76 (AH 2)	19 250 ± 70	23 690–23 600 (0.063)	
					23 360–22 970 (0.937)	
MAMS-40115	r^{14}C	horse/reindeer bone	81-76 (AH 2)	18 860 ± 60	22 970–22 560 (1.000)	
MAMS-40116	^{14}C	horse/reindeer bone	81–76 (AH 2)	19 230 ± 60	23 670–23 630 (0.021)	
					23 330–22 960 (0.979)	
KG-1476	OSL	quartz	18–27			26.8 ± 2.1
KG-1477	OSL	quartz	18–27			19.8 ± 1.6
KG-1479	OSL	quartz	48–70			19.5 ± 1.6
KG-1480	OSL	quartz	48–70			21.6 ± 1.8
KG-931	OSL	quartz	93–103			26.2 ± 2.1
KG-932	OSL	quartz	93–103			25.3 ± 1.9
KG-1482	OSL	quartz	93–103			25.6 ± 2.0
KG-1483	OSL	quartz	93–103			25.5 ± 2.0

formed secondary carbonates are associated with chemical weathering of the surrounding substrate (Pécsi, 1990; Monger, 2002; Barta, 2014). The precipitation of carbonates is associated with solution of weathered Ca^{2+}, which results from root and microbial respiration (Becze-Deák et al., 1997; Monger, 2002; Barta, 2014).

In our study, the distribution of CRC and HC in the profiles is not congruent. CRC accumulated at the top of the loess profile and in AH 2 but are largely absent in the Anthrosol below AH 2 and around 65 cm sampling depths. In contrast, HC are more evenly distributed and also occur in the Anthrosol (Fig. 7). This may indicate different time periods of formation, as also suggested by the radiocarbon ages of HC that are ca. 3400 years older compared to CRC at 11 cm depth of KG 5757, corresponding to AH 2 (Table 1). Both ages are far too young for AH 2, which was deposited between 23.7 and 22.1 ka cal BP (Händel et al., 2021). Interestingly, the δ^{13}C values of CRC and HC also differ largely (average −22 ‰ and −4 ‰, respectively). Similar differences are also reported by Koeniger et al. (2014) and Luo et al. (2020). The lower δ^{13}C values of CRC suggest a formation from respiratory CO_2, which typically has δ^{13}C values close to leaf biomass (Bowling et al., 2008). However, various admixtures of atmospheric CO_2 can increase δ^{13}C values substantially (Cerling, 1984), which is probably the reason for the much more ^{13}C-enriched values of HC. Thus, it seems that two different sources, respiratory CO_2 and atmospheric CO_2, predominated during the Holocene formation of CRC and HC, respectively.

In contrast, Koeniger et al. (2014) suggest that stable isotope variability is linked to palaeoclimatic variations and assume that the formation of CRC and HC is associated with the time of dust accumulation. They further propose that stable isotope records of secondary carbonates in loess records are reliable palaeoenvironmental proxies for moisture and soil formation processes (Koeniger et al., 2014). Our results, however, show that this is not necessarily the case as the rhizoconcretions (CRC and HC) were considerably younger than the surrounding loess. In several other studies, rhizoconcretions in loess also reveal a Holocene formation and thus confirm a post-sedimentary origin (e.g. Pustovoytov and Terhorst, 2004; Gocke et al., 2011; Újvári et al., 2014). Such overprinting of loess profiles with Holocene material or invading of post-sedimentary deep roots may bias the results of loess-based palaeoenvironmental studies (Gocke, 2011). Under laboratory and field conditions, the importance of vegeta-

tion for the formation and re-crystallisation of pedogenic carbonates was shown by Gocke (2011). Roots and microorganisms had a direct influence on these processes, while climatic factors exerted indirect influence. A correct interpretation of the isotopic composition of secondary carbonates thus also requires considering the evolution of carbonates in the soil (Koeniger et al., 2014), i.e. an exchange of carbon from primary loess carbonates with carbon from the air (CO_2) during the formation of rhizoliths by respiration of roots and microorganisms (Gocke et al., 2011).

Due to their Holocene formation, the isotope results of secondary carbonates can also not be used for tracing glacial palaeoenvironmental conditions. Therefore, our results have implications for other stable isotope studies on rhizoconcretions, and we recommend testing post-sedimentary formation via radiocarbon dating prior to using them for palaeoenvironmental reconstructions.

5.3 Environmental implications from other geochemical proxies and grain size

The $\delta^{13}C_{org}$ variations in both profiles show a range typical of C_3 vegetation (O'Leary 1981; Rounick and Winterbourn, 1986; Hatté et al., 1998), which can be considered prevalent during the Late Pleistocene in this area (Arppe et al., 2011; Schatz et al., 2011; Kovács et al., 2012). During the period of human occupation (at the time of AH 1 and AH 2; ca. 23 ka cal BP), the presence of a steppe-like open grassland can be assumed (Stojakowits et al., 2021). However, clusters of woody vegetation (*Pinus cembra* and *Juniperus* sp.) were also present as inferred from pollen data of the archaeological site (Montet-White et al., 1990; Haesaerts and Damblon, 2016).

This type of ecosystem can also be reconstructed based on the distribution of gastropods. In our study, the distribution of gastropods shows no differences between horizons. Almost exclusively *Vallonia costata* occurs except for one single sample of *Pupilla* sp., which derives from the underlying tundra gley of profile KG-5756/57. Frank and Rabeder (1996, 1997) found 18 terrestrial gastropod taxa in the Kammern-Grubgraben profile, but their stratigraphic context is unclear. The Kammern-Grubgraben mollusc fauna indicates a herb-rich meadow steppe, partly with shrubs and isolated groups of trees. Among others, *Vallonia costata* and *V. pulchella* are especially common in milder cold-period sections (Ložek, 1964, 1982; Mania, 1973; Fűköh, 1993; Krolopp and Sümegi, 1995; Frank, 2006). In contrast, *Vallonia tenuilabris*, the indicator species of colder periods that is widespread in central Europe, has so far been absent from Kammern-Grubgraben. With *Columella columella*, however, at least one element of a cold tundra was recorded.

Although $\delta^{13}C_{org}$ values range between $-24\,‰$ and $-28\,‰$ in both sections, their variability does not show a clear palaeoclimatic trend. The slight increase at the base of profile KG-5756/57 may indicate a shift from drier conditions for older sediments to more humid conditions upwards considering the fact that water loss through evapotranspiration is limited by stomatal constriction of the plants. This physiological reaction is accompanied by a reduced carbon isotope fractionation resulting in higher $\delta^{13}C$ values (Hatté et al., 1998). Water availability may be inferred based on the $\delta^{13}C$ values of organic matter. It seems, however, that the results are not in accordance with the TOC and $CaCO_3$ contents. Apart from the upper part of profile KG-5753, which is influenced by the overlying modern Anthrosol, explaining its high TOC content (0–13 cm depth, Fig. 5a), values vary between 0.2 % and 0.4 % (min value 0.1 % and max value 0.9 % in KG-5753; Fig. 5) for both profiles. Typical glacial loess deposits in northwestern Europe show organic carbon contents of less than 0.1 % (Antoine et al., 2013; Mayr et al., 2017b). However, increased TOC contents, as recorded at the base of KG-5756/57, might be a result of accumulation or preservation of organic carbon due to warmer and/or wetter climate conditions (Zech et al., 2013; Mayr et al., 2017b), but any environmental inferences from our TOC record are hampered by unknown dust accumulation rates.

Implications about moisture can also be derived from the calcium contents, since the moisture regime of the soil influences the $CaCO_3$ content and the Ca distribution (Monger, 2002; Barta, 2014). Under more humid conditions, Ca is sensitive to leaching (Buggle et al., 2011; Barta, 2014; Profe et al., 2018b), which may explain the decreasing trend of Ca and $CaCO_3$ towards the bottom in both profiles (Fig. 6). XRF scanning from Chinese LPSs revealed that Ca and Si decrease in palaeosol layers relative to the surrounding loess sediments (Sun et al., 2016). This is also evident from an LPS from Süttő, Hungary, where Ca / Ti ratios derived from high-resolution XRF scanning of discrete samples are used as a proxy for weathering intensity, and, consequently, low Ca / Ti values are explained by decalcification (Profe et al., 2018b). Thus, our observations could suggest a climatic shift from more humid–warmer conditions during the formation of the older sediments towards drier–colder conditions during the main occupation period, which was also reported by Haesaerts and Damblon (2016). Whether such climatic changes are related to the postulated shift of storm tracks in the Alpine area during the LGM (Luetscher et al., 2015) remains to be investigated in more detail in future studies using longer LPSs. Additionally, dust sources may have changed, as glaciers progressively advanced into the Alpine foreland between 30 and 25 ka cal BP and retreated again before 22 ka cal BP (Stojakowits et al., 2021). In contrast, geochemical provenancing and U–Pb isotope dating of detrital zircons in loess from the Krems area suggest a predominant source from nearby Bohemian Massif sources (< 10 km). This implies an initial fluvial transport and a subsequent aeolian re-deposition in the study area rather than changes in palaeowind directions (Újvári and Klötzli, 2015). However, such provenance data would have to be extended to also infer the temporal changes in dust sources.

Ti is frequently a component of weathering-resistant minerals such as titanium oxides and ilmenite (Profe et al., 2018b; Mayr et al., 2019). The elements Fe and Ti behave very similarly and show a negative covariance with Ca in our records (Fig. 6a, b). Ti and Fe are likely considered to be of detrital origin and mainly influenced by varying concentrations of carbonates. In contrast, K and Si also show negative correlations with Ca below AH 2 but do not exhibit a decreasing trend from bottom to top as Fe and Ti do (Fig. 6a, b). K is frequently bound to mica, feldspars, and clay minerals (Mayr et al., 2019). The rather evenly distributed clay contents in the profiles (Fig. 4a, b) may explain the small variations in the K record. The slight increase in K below AH 2 (Fig. 6b), however, cannot be explained with clay content alone but rather by increased sand input (Profe et al., 2018b). K-feldspars are a common constituent of the sand-sized fraction in loess sequences of Lower Austria (Thiel et al., 2011b), possibly explaining the increase in that stratigraphic level. In the long >100 kyr loess record from Süttő, Si / K and Ca / Ti ratios are correlated with grain size and carbonate content, respectively (Profe et al., 2018b). In our records, these element ratios do not provide additional information to the clr-transformed element records (Fig. S1 in the Supplement), and their variability in the short time period covered by our LGM record is expected to be small (Profe et al., 2018b).

The climate conditions at the Marine Isotope Stage (MIS) 3–2 transition are characterised by climatic deterioration. However, two short interstadials (GI-4 and GI-3) were recorded and placed at 28.8 and 27.7 ka (Rasmussen et al., 2014). The lower part of KG-5756/57 corresponds to the late phase of MIS 3 or the MIS 3–MIS 2 transition (Stojakowits et al., 2021), as inferred from the radiocarbon age of a charcoal fragment (ca. 28.9–27.8 ka cal BP, Table 1) deriving from the basal tundra gley. Gleyic features from this period are also reported from other LPSs in the Alpine realm (Buch and Zöller, 1990; Moine et al., 2017; Mayr et al., 2017b) and related to a warming event, possibly related to GI-4 with milder climate conditions (Mayr et al., 2017b; Stojakowits et al., 2021). This timeframe is also supported by luminescence data for the loess unit between tundra gley and the main archaeological horizon AH 2 (KG-931, KG-932 and KG-1482, KG-1483; Fig. 2a, c; Table 2). A connection of the deposition of this sediment to Greenland Stadial 3 (GS-3) has been proposed by Händel et al. (2021).

For the loess build-up, palaeowind intensity plays an important role (Buggle et al., 2008; Ludwig et al., 2021). In general, grain-size distribution in loess is mainly linked to wind intensity and thus may provide information about the distance as well as the main source of the sediment (Gavrilov et al., 2018) in combination with single-grain geochemical provenancing (Újvári and Klötzli, 2015). Colder periods are associated with high wind intensity, resulting in an accumulation of coarser grains, whereas the distribution of finer grains is related to weaker or constant winds in warmer periods (Novothny et al., 2011). However, this simplified relation is weakened if the distance to the source changes in time and valid only if several other factors like topography play a minor role (Újvari et al., 2016b). Grain-size parameters such as the U ratio combined with clay content (Vanderberghe et al., 1997; Vanderberghe, 2013) or the grain-size index (Rousseau et al., 2002) are often used to reconstruct wind dynamics. In KG-5756/57, the clay content is slightly higher in the basal tundra gley, while the U ratio and the grain-size index show lower values. This is in accordance with previous findings, e.g. in the Nussloch section in Germany, where higher grain-size indices were found in coarser grain-sized loess while the lowest values corresponded to tundra-gley units (Rousseau et al., 2002). Higher grain-size indices were further correlated with higher $\delta^{13}C$ values, which was explained by stronger wind dynamics accompanied by drier environmental conditions and decreased vegetation cover. This pattern, however, is not clearly evident in our study, where a significant trend is absent in the $\delta^{13}C_{org}$ record and the dominant grain-size fraction is cSi (Fig. 4). This is also reflected by the geochemical composition; silicon (Si) in aeolian sediments is preferentially linked to grain-size fractions like coarse silt and sand (Muhs and Bettis, 2000; Buggle et al., 2008), which explains the constantly high amounts of Si in both analysed profiles (Fig. 6). However, the overall percentage of coarse sand is rather low, pointing to reduced wind intensities and continuous dust accumulation. According to Novothny et al. (2011), a coarse sand content of $<0.5\,\%$ refers to lower palaeowind intensities, indicating rather low wind energy during loess deposition, which is documented for both analysed profiles (KG-5753 and KG-5756/57). It is noticeable, though, that the sand fraction is more prevalent shortly above and below the main archaeological layer (AH 2) in both profiles (Fig. 4). This could point to an increase in wind intensity during these specific periods. Physical weathering of the stone slabs, introduced by hunter-gatherer occupants into the archaeological layer from nearby rock sources, can largely be excluded as a source for the sand fraction due to its short exposure to the atmosphere. Examinations of the profiles in the field, however, also revealed the presence of undulating sandy bands of a few centimetres' thickness. As the site is located between two erosion channels with gradients to the north, south, and east, this is more likely a result of slope processes (e.g. solifluction or surficial creep) and thus attributable to the overall topography rather than to aeolian processes.

To summarise, based on the proxies we evaluated, we could not find indications for a period of ameliorated climate during the AH 2 phase, as previously postulated by Haesaerts and Damblon (2016). Our data suggest rather constant environmental conditions before, during, and after the formation of AH 2. Only the tundra gley exposed at the base of KG-5756/57 points at more favourable conditions.

6 Conclusions

We applied a multi-proxy approach to two profiles exposed by recent excavations at the Upper Palaeolithic site of Kammern-Grubgraben, including analyses of grain size, organic geochemistry (TOC, TN, C / N, $\delta^{13}C_{org}$), inorganic geochemistry (XRF-based elemental counts, $CaCO_3$), and stable isotope analyses ($\delta^{13}C$, $\delta^{18}O$) of secondary carbonates (HC, CRC). In addition, we radiocarbon-dated different material from the same stratigraphic layers and compared these to previously obtained ages (AH 2). Our analyses showed that secondary carbonates and humic acids were formed during the Holocene as manifested by their radiocarbon ages. Therefore, loess profiles in the excavation area are overprinted by Holocene deep-rooting vegetation. In our study, we were able to extract, for the first time, a sufficiently large charcoal sample for obtaining a radiocarbon age of 28 930–27 830 cal BP from the tundra gley underneath AH 2, which could be related to interstadial conditions during GI-4 or GI-3. Terrestrial gastropods provided another source for radiocarbon ages, albeit the low sample amounts probably affected dating quality.

XRF core scanning provided high-resolution element distributions, which were calibrated using centred log-ratio transformation. Ca represents the most pronounced element record and is in agreement with the independently analysed $CaCO_3$ record. To our knowledge, we provide the first continuous XRF-scanning record on a European loess sequence and demonstrate that this technique provides reliable results for the most abundant elements.

In order to provide more detailed information about palaeoenvironmental and climatic conditions, extractions of longer, undisturbed LPSs are essential for future studies, as the studied sections were rather short and close to the modern surface. In addition, material suitable for radiocarbon age determination is scarce outside of archaeological horizons, causing difficulties for obtaining chronological control. Such prerequisites make it worthwhile to examine LPSs from sites as close by as possible to the archaeological site to obtain more datable material. XRF scanning could be extremely useful to synchronise these LPSs with the archaeological trench sections.

Data availability. Original data will be made available via the database PANGAEA after publication.

Supplement. The supplement related to this article is available online at: https://doi.org/10.5194/egqsj-71-23-2022-supplement.

Author contributions. CM designed the sedimentological investigations with contributions of TE, AM, KP, US, and MH. Fieldwork was carried out by CM, TE, US, and MH. CS and LR carried out most of the laboratory work with contributions of CM. SM identified terrestrial gastropods. LR wrote the original draft with contributions of CM, MH, BZ, and CS. All co-authors reviewed and approved the manuscript.

Competing interests. The contact author has declared that neither they nor their co-authors have any competing interests.

Disclaimer. Publisher's note: Copernicus Publications remains neutral with regard to jurisdictional claims in published maps and institutional affiliations.

Acknowledgements. We acknowledge the German Research Foundation (DFG) for financial support; Rafael Stiens for technical assistance with grain-size analyses and evaluation; Christian Ohlendorf for help with XRF scanning; Ute Schmidt for assistance with elemental analyses; and Nadja Schlieder, Roswitha Höfner-Stich, and Philipp Bartmann for assistance in the isotope laboratory. We thank the two anonymous reviewers for their comments to improve a previous version of the manuscript and the editor and editorial team for their thorough editorial handling.

Financial support. This research has been supported by the Deutsche Forschungsgemeinschaft (grant no. MA 4235/12-1, project no. 424736737).

Review statement. This paper was edited by Christopher Lüthgens and reviewed by two anonymous referees.

References

Adovasio, J. M., Soffer, O., and Klíma, B.: Upper Palaeolithic fibre technology: interlaced woven finds from Pavlov I, Czech Republic, c. 26,000 years ago, Antiquity, 70, 526–534, https://doi.org/10.1017/S0003598X0008368X, 1996.

Aitchison, J.: The statistical analysis of compositional data, J. Roy. Stat. Soc. B, 44, 139–177, 1982.

Antoine, P., Rousseau, D.-D., Moine, O., Kunesch, S., Hatté, C., Lang, A., Tissoux, H., and Zöller, L.: Rapid and cyclic aeolian deposition during the Last Glacial in European loess: a high-resolution record from Nussloch, Germany, Quaternary Sci. Rev., 28, 2955–2973, 2009.

Antoine, P., Rousseau, D.-D., Degeai, J.-P., Moine, O., Lagroix, F., Kreutzer, S., Fuchs, M., Hatté, C., Gauthier, C., Svoboda, J., and Lisá, L: High-resolution record of the environment response to climatic variations during the Last Interglacial-Glacial cycle in Central Europe: the loess paleosol sequence of Dolní Věstonice (Czech Republic), Quaternary Sci. Rev., 67, 17–38, 2013.

Arppe, L., Aaris-Sørensen, K., Daugnora, L., Lõugas, L., Wojtal, P., and Zupiòš, I.: The palaeoenvironmental $\delta^{13}C$ record in European woolly mammoth tooth enamel, Quatern. Int., 245, 2885–290, 2011.

Barta, G.: Secondary carbonates in loess-paleosoil sequences: a general review, Cent. Eur. J. Geosci., 3, 129–146, 2011.

Barta, G.: Paleoenvironmental reconstruction based on the morphology and distribution of secondary carbonates of the loess-paleosol sequence at Süttő, Hungary, Quatern. Int., 319, 64–75, 2014.

Becze-Deák, J., Langohr, R., and Verrecchia, E. P.: Small scale secondary $CaCO_3$ accumulations in selected sections of the European loess belt. Morphological forms and potential for paleoenvironmental reconstructions, Geoderma, 76, 221–252., 1997.

Blott, S. J. and Pye, K: GRADISTAT: A grain size distribution and statistic package for the analysis of unconsolidated sediments, Earth Surf. Proc. Land., 26, 1237–1248, 2001.

Bowling, D. R., Pataki, D. E., and Randerson, J. T.: Carbon isotopes in terrestrial ecosystem pools and CO_2 fluxes, New Phytol., 178, 24–40, https://doi.org/10.1111/j.1469-8137.2007.02342.x, 2008.

Brand, W. A., Coplen, T. B., Vogl, J., Rosner, M., and Prohaska, T: Assessment of international reference materials for isotope-ratio analysis (IUPAC Technical Report), Pure Appl. Chem., 86, 425–467, 2014.

Brandtner, F.: Zur geostratigraphischen und kulturellen Zuordnung der Paläolithstation Grubgraben bei Kammern, NÖ, in: Paleolithic in the Middle Danube Region, edited by: Svoboda, J., Festschrift for B. Klíma, Dolní Věstonice Studies 4, Brno, 121–146, 1996.

Bronger, A.: Löß-Paläoboden-Sequenzen Zentralasiens als Indikatoren einer globalen Kimageschichte des Quartärs?, E&G Quaternary Sci. J., 49, 35–54, https://doi.org/10.3285/eg.49.1.03, 1999.

Bronger, A.: Correlation of loess-paleosol sequences in East and Central Asia with SE Central Europe: towards a continental Quaternary pedostratigraphy and paleoclimatic history, Quatern. Int., 106–107, 11–31, 2003.

Buch, M. W. and Zöller, L.: Gliederung und Thermolumineszenz-Chronologie der Würmlösse im Raum Regensburg, E&G Quaternary Sci. J., 40, 63–84, https://doi.org/10.3285/eg.40.1.05, 1990.

Buggle, B., Glaser, B., Zöller, L., Hambach, U., Marković, S., Glaser, I., and Gerasimenko, N.: Geochemical characterization and origin of Southeastern and Eastern European loesses (Serbia, Romania, Ukraine), Quaternary Sci. Rev., 27, 1058–1075, 2008.

Buggle, B., Hambach, U., Glaser, B., Gerasimenko, N., Marković, S., Glaser, I., and Zöller, L.: Stratigraphy, and spatial and temporal paleoclimatic trends in Southeastern/Eastern European loess-paleosol sequences, Quatern. Int., 196, 86–106, 2009.

Buggle, B., Glaser, B., Hambach, U., Gerasimenko, N., and Marković, S.: An evaluation of geochemical weathering indices in loess-paleosol studies, Quatern. Int., 240, 12–21, 2011.

Cerling, T. E.: The stable isotopic composition of modern soil carbonate and its relationship to climate, Earth Planet. Sc. Lett., 71, 229–240, 1984.

Clark, P. U., Dyke, A. S., Shakun, J. D., Carlson, A. E., Clark, J., Wohlfarth, B., Mitrovica, J. X., Hostetler, S. W., and McCabe, A. M.: The last glacial maximum, Science 325, 710–714, https://doi.org/10.1126/science.1172873, 2009.

d-maps: Landkarte Niederösterreich (Österreich), d-maps, https://d-maps.com/carte.php?num_car=33842&lang=de, last access: 28 April 2021.

Dworkin, S. I., Nordt, L., and Atchley, S.: Determining terrestrial paleotemperatures using the oxygen isotopic composition of pedogenic carbonate, Earth Planet. Sc. Lett., 237, 56–68, 2005.

Fewlass, H., Talamo, S., Kromer, B., Bard, E., Tuna, T., Fagault, Y., Sponheimer, M., Ryder, C., Hublin, J.-J., Perri, A., Sázelová, S., and Svoboda, J.: Direct radiocarbon dates of mid Upper Palaeolithic human remains from Dolní Věstonice II and Pavlov I, Czech Republic, J. Archaeol. Sci.: Reports, 27, 102000, https://doi.org/10.1016/j.jasrep.2019.102000, 2019.

Fink, J.: Die fossilen Böden im österreichischen Löss, Quartär, 6, 85–108, 1954.

Fink, J.: Studien zur absoluten und relativen Chronologie der fossilen Böden in Österreich. II. Wetzleinsdorf und Stillfried, Archaeologia Austriaca, 31, 1–18, 1962.

Fink, J.: Exkursion durch den österreichischen Teil des Alpenvorlandes und den Donauraum zwischen Krems und Wiener Pforte, Mitteilungen der Quartärkommission der Österreichischen Akademie der Wissenschaften, Vienna, 1, 1–113, 1976–1978.

Fitzsimmons, K. E., Marković, S. B., and Hambach, U.: Pleistocene environmental dynamics recorded in the loess of the middle and lower Danube basin, Quaternary Sci. Rev., 41, 104–118, 2012.

Frank, C.: Plio-pleistozäne und holozäne Mollusken Österreichs, Mitteilungen der Prähistorischen Kommission, 62, 860 pp., ISBN 978-3-7001-3674-3, 2006.

Frank, C. and Rabeder, G.: Neue malakologische Befunde aus dem jüngstpleistozänen Lößprofil vom Grubgraben bei Kammern (Niederösterreich), Beiträge zur Paläontologie, 21, 21–31, 1996.

Frank, C. and Rabeder, G.: Grubgraben bei Kammern, in: Pliozäne und pleistozäne Faunen Österreichs, edited by: Döppes, D. und Rabeder, G., Mitteilungen der Kommission für Quartärforschung, Österreichische Akademie der Wissenschaften, 10, 16–20, 1997.

Frechen, M., Oches, E. A., and Kohfeld, K. E.: Loess in Europe – mass accumulation rates during the Last Glacial Period, Quaternary Sci. Rev., 22, 1835–1857, 2003.

Fűköh, L.: Holocene malacology in Hungary, Scripta Geologica, Special Issue 2, 121–125, 1993.

Gavrilov, M. B., Marković, S. B., Schaetzl, R. J., Tošić, I., Zeeden, C., Obreht, I., Sipos, G., Ruman, A., Putniković, S., Emunds, K., Perić, Z., Hambach, U., and Lehmkuhl, F.: Prevailing surface winds in Northern Serbia in the recent and past time periods; modern- and past dust deposition, Aeolian Res., 31, 117–129, https://doi.org/10.1016/j.aeolia.2017.07.008, 2018.

Gocke, M.: Pedogenic carbonates in loess formation rates, formation conditions and source apportionment assessed by isotopes and molecular proxies, Dissertation, Bayreuth, 1–179, https://epub.uni-bayreuth.de/id/eprint/360 (last access: 18 June 2021), 2011.

Gocke, M., Pustovoytov, K., Kühn, P., Wiesenberg, G. L. B., Löscher, M., and Kuzyakov, Y.: Carbonate rhizoliths in loess and their implications for paleoenvironmental reconstruction – revealed by isotopic composition: $\delta^{13}C$, ^{14}C, Chem. Geol., 283, 251–260, 2011.

Gocke, M., Hambach, U., Eckmeier, E., Schwark, L., Zöller, L., Fuchs, M., Löscher, M., and Wiesenberg, G. L. B.: Introducing an improved multi-proxy approach for paleoenvironmental reconstruction of loess-paleosol archives applied on the Late Pleis-

tocene Nussloch sequence (SW Germany), Paleogeogr. Paleocl., 410, 300–315, 2014.

Goff, K., Schaetzl, R. J., Chakraborty, S., Weindorf, D. C., Kasmerchak, C., and Bettis III, E. A.: Impact of sample preparation methods for characterizing the geochemistry of soils and sediments by portable X-ray fluorescence, Soil Sci. Soc. Am. J., 84, 131–143, https://doi.org/10.1002/saj2.20004, 2020.

Haesaerts, P.: Stratigraphy of the Grubgraben Loess Sequence, in: The epigravettian site of Grubgraben, Lower Austria: The 1986 and 1987 excavations, edited by: Montet-White, A., Eraul, 40, 15–35, OCLC-number 24578227, 1990.

Haesaerts, P. and Damblon, F.: The Late Palaeolithic Site of Kammern-Grubgraben (Lower Austria). Additional Data on Loess Stratigraphy and Palaeoenvironment, Archaeologia Austriaca, 100, 255–269, 2016.

Haesaerts, P., Damblon, F., Neugebauer-Maresch, C., and Einwögerer, T.: Radiocarbon Chronology of the Late Palaeolithic Loess Site of Kammern-Grubgraben (Lower Austria), Archaeologia Austriaca, 100, 271–277, 2016.

Händel, M., Simon, U., Einwögerer, T., and Neugebauer-Maresch, C.: Loess deposits and the conservation of the archaeological record – The Krems-Wachtberg example, Quatern. Int., 198, 46–50, 2009.

Händel, M., Einwögerer, T., Simon, U., and Neugebauer-Maresch, C.: Krems-Wachtberg excavations 2005-12: Main profiles, sampling, stratigraphy, and site formation, Quatern. Int., 351, 38–49, 2014.

Händel, M., Simon, U., Maier, A., Brandl, M., Groza-Săcaciu, S. M., Timar-Gabor, A., and Einwögerer, T.: Kammern-Grubgraben revisited – First results from renewed investigations at a well-known LGM site in east Austria, Quatern. Int., 587–588, 137–157, https://doi.org/10.1016/j.quaint.2020.06.012, 2021.

Hatté, C., Fotugne, M., Rousseau, D.-D., Antoine, P., Zöller, L., Tisnérat-Laborde, N., and Bentaleb, I: δ^{13}C variations of loess organic matter as a record of the vegetation response to climatic changes during Weichselian, Geology, 26, 583–586, 1998.

Heiri, O., Lotter, A. F., and Lemcke, G.: Loss on ignition as a method for estimating organic and carbonate content in sediments: reproducibility and comparability of results, J. Paleolimnol., 25, 101–110, 2001.

Hughes, P. D. and Gibbard, P. L.: A stratigraphical basis for the Last Glacial Maximum (LGM), Quatern. Int., 383, 174–185, https://doi.org/10.1016/j.quaint.2014.06.006, 2015.

Koeniger, P., Barta, G., Thiel, C., Bajnóczi, B., Novothny, Á., Horváth, E., Techmer, A., and Frechen, M.: Stable isotope composition of bulk and secondary carbonates from the Quaternary loess-paleosol sequence in Süttő, Hungary, Quatern. Int., 319, 38–49, 2014.

Kovács, J., Moravcová, M., Újvári, G., and Pintér, A. G.: Reconstructing the paleoenvironment of East Central Europe in the Late Pleistocene using oxygen and carbon isotopic signal of tooth in large mammal remains, Quatern. Int., 276–277, 145–154, 2012.

Krolopp, E. and Sümegi, P.: Palaeoecological reconstruction of the late Pleistocene, based on loess malacofauna in Hungary, GeoJournal, 36, 213–222, 1995.

Lambeck, K., Rouby, H., Purcell, A., Sun, Y., and Sambridge, M.: Sea level and global ice volumes from the Last Glacial Maximum to the Holocene, P. Natl. Acad. Sci. USA, 111, 15296–15303, https://doi.org/10.1073/pnas.1411762111, 2014.

Lehmkuhl, F., Zens, J., Krauß, L., Schulte, P., and Kels, H.: Loess-paleosol sequences at the northern European loess belt in Germany: Distribution, geomorphology and stratigraphy, Quaternary Sci. Rev., 153, 11–30, 2016.

Lehmkuhl, F., Nett, J. J., Pötter, S., Schulte, P., Sprafke, T., Jary, Z., Antoine, P., Wacha, L., Wolf, D., Zerboni, A., Hošek, J., Marković, S. B., Obreht, I., Sümegi, P., Veres, D., Zeeden, C., Boemke, B.. Schaubert, V., Viehweger, J., and Hambach, U.: Loess landscapes of Europe – Mapping, geomorphology, and zonal differentiation, Earth-Sci. Rev., 215, 103496, https://doi.org/10.1016/j.earscirev.2020.103496, 2021.

Liang, L., Sun, Y., Yao, Z., Liu, Y., and Wu, F.: Evaluation of high-resolution elemental analyses of Chinese loess deposits measured by X-ray fluorescence core scanner, CATENA, 92, 75–82, 2012.

Logan, B.: The hunted of Grubgraben: an analysis of faunal remains, in: The Epigravettian Site of Grubgraben, Lower Austria: The 1986 and 1987 Excavations, edited by: Montet-White, A., ERAUL – Études et Recherche Archéologiques de l'Université de Liège 40, Liège 1990, 65–91, OCLC-number 24578227, 1990.

Lowe, J. and Walker, M.: Reconstructing Quaternary Environments, 3rd edition, Routledge, London, New York, https://doi.org/10.4324/9781315797496, 2015.

Ložek, V.: Die Quartärmollusken der Tschechoslowakei, Rozpravy ústředního ústavo geologického, 31, 374 pp., ark:/13960/t2996v274, 1964.

Ložek, V.: Faunengeschichtliche Grundlinien zur spät- und nacheiszeitlichen Entwicklung der Molluskenbestände in Mitteleuropa. Rozpravy Československ, Akad. Věd, Řada Mat. Přírod. Věd., 92, 106 pp., 1982.

Ludwig, P., Gavrilov, M. B., Marković, S. B., Újvári, G., and Lehmkuhl, F.: Simulated regional dust cycle in the Carpathian Basin and the Adriatic Sea region during the Last Glacial Maximum, Quatern. Int., 581–582, 114–127, 2021.

Luetscher, M., Boch, R., Sodemann, H., Spötl, C., Cheng, H., Edwards, R. L., Frisia, S., Hof, F., and Müller, W.: North Altlantic storm track changes during the Last Glacial Maximum recorded by Alpine speleothems, Nat. Commun., 6, 1–6, https://doi.org/10.1038/ncomms7344, 2015.

Luo, X., Wang, H., An, Z., Zhang, Z., and Liu, W.: Carbon and oxygen isotopes of calcified root cells, carbonate nodules and total inorganic carbon in the Chinese loess–paleosol sequence: The application of paleoenvironmental studies, J. Asian Earth Sci., 201, 104515, https://doi.org/10.1016/j.jseaes.2020.104515, 2020.

Maier, A., Stojakowits, P., Mayr, C., Pfeifer, S., Preusser, F., Zolitschka, B., Anghelinu, M., Bobak, D., Duprat-Oualid, F., Einwögerer, T., Hambach, U., Händel, M., Kaminská, L., Kämpf, L., Łanczont, M., Lehmkuhl, F., Ludwig, P., Magyari, E., Mroczek, P., Nemergut, A., Nerudová, Z., Niţă, L., Polanská, M., Połtowicz-Bobak, M., Rius, D., Römer, W., Simon, U., Škrdla, P., Újvári, G., and Veres, D.: Cultural evolution and environmental change in Central Europe between 40 and 15 ka, Quatern. Int., 581–582, 225–240, 2021.

Mania, D.: Paläoökologie, Faunenentwicklung und Stratigraphie des Eiszeitalters im mittleren Elbe-Saalegebiet auf Grund von Molluskengesellschaften, Geologie, 21, 1–175, 1973.

Marković, S. B., Stevens, T., Kukla, G. J., Hambach, U., Fitzsimmons, K. E., Gibbard, P., Buggle B., Zech, M., Guo, Z., Hao, Q., Wu, H., O'Hara Dhand, K., Smalley, I. J., Újvári, G., Sümegi, P., Timar-Gabor, A., Veres, F. Sirocko, D., Vasiljević, D. A., Jary, Z., Svensson, A., Jović, V., Lehmkuhl, F., Kovács, J., and Svirčev, Z.: Danube loess stratigraphy – Towards a pan-European loess stratigraphic model, Earth-Sci. Rev., 148, 228–258, 2015.

Martin-Puertas, C., Tjallingii, R., Bloemsma, M., and Brauer, A.: Varved sediment responses to early Holocene climate and environmental changes in Lake Meerfelder Maar (Germany) obtained from multivariate analyses of micro X-ray fluorescence core scanning data, J. Quaternary Sci., 32, 427–436, 2017.

Mayr, C., Brandlmeier, B., Diersche, V., Stojakowits, P., Kirscher, U., Matzke-Karasz, R., Bachtadse V., Eigler M., Haas U., Lempe B., Reimer P., and Spötl, C.: Nesseltalgraben, a new reference section of the last glacial period in southern Germany, J. Paleolimnol., 58, 213–229, 2017a.

Mayr, C., Matzke-Karasz, R., Stojakowits, P., Lowick, S. E., Zolitschka, B., Heigl, T., Mollath, R., Theuerkauf, M., Weckend, M.-O., Bäumler, R., and Gregor, H.-J.: Palaeoenvironments during MIS 3 and MIS 2 inferred from lacustrine intercalations in the loess–palaeosol sequence at Bobingen (southern Germany), E&G Quaternary Sci. J., 66, 73–89, https://doi.org/10.5194/egqsj-66-73-2017, 2017b.

Mayr, C., Stojakowits, P., Lempe, B., Blaauw, M., Diersche, V., Grohganz, M., López Correa, M., Ohlendorf, C., Reimer, P., and Zolitschka, B.: High-resolution geochemical record of environmental changes during MIS 3 from the northern Alps (Nesseltalgraben, Germany), Quaternary Sci. Rev., 218, 122–136, https://doi.org/10.1016/j.quascirev.2019.06.013, 2019.

Meyer-Heintze, S., Sprafke, T., Schulte, P., Terhorst, B., Lomax, J., Fuchs, M., Lehmkuhl, F., Neugebauer-Maresch, C., Einwögerer, T., Händel, M., Simon, U., and Castillo, B. S.: The MIS 3/2 transition in a new loess profile at Krems-Wachtberg East – A multimethodological approach, Quatern. Int., 464, 370–385, 2018.

Mix, A. C., Bard, E., and Schneider, R.: Environmental processes of the ice age: land, oceans, glaciers (EPILOG), Quaternary Sci. Rev., 20, 627–657, https://doi.org/10.1016/S0277-3791(00)00145-1, 2001.

Moine, O., Antoine, P., Hatté, C., Landais, A., Mathieu, J., Prud'homme, C., and Rousseau, D.-D.: The impact of Last Glacial climate variability in wet-European loess revealed by radiocarbon dating of fossil earthworm granules, P. Natl. Acad. Sci. USA, 114, 6209–6214, https://doi.org/10.1073/pnas.1614751114, 2017.

Monger, C. H.: Pedogenic carbonate: links between biotic and abiotic $CaCO_3$, in: Proc. 17th World Congress of Soil Science, 14–21 August 2002, Bangkok, Thailand, 897, 1–9, OCLC-number: 796897124, 2002.

Montet-White, A. (Ed.): The Epigravettian Site of Grubgraben, Lower Austria: The 1986 and 1987 Excavations, ERAUL – Études et Recherche Archéologiques de l'Université de Liège 40, Liège 1990, 159–162, OCLC-number 24578227, 1990.

Montet-White, A., Haesaerts, P., and Logan, B.: The Epigravettian of Grubgraben: an overview of the 1986/87 excavations, in: The Epigravettian Site of Grubgraben, Lower Austria: The 1986 and 1987 Excavations, edited by: Montet-White, A., ERAUL – Études et Recherche Archéologiques de l'Université de Liège 40, Liège 1990, 159–162, OCLC-number 24578227, 1990.

Muhs, D. R. and Bettis III, E. A.: Geochemical variations in Peoria loess of Western Iowa indicate paleowinds of midcontinental North America during last glaciation, Quaternary Res., 53, 49–61, 2000.

Neugebauer-Maresch, C., Einwögerer, T., Richter, J., Maier, A., and Hussain, S. T.: Kammern-Grubgraben. Neue Erkenntnisse zu den Grabungen 1989–1994, Archaeologia Austriaca, 100, 225–254, https://doi.org/10.1553/archaeologia100s225, 2016.

Nigst, P. R., Viola, T. B., Haesaerts, P., Blockley, S., Damblon, F., Frank, C., Fuchs, M., Götzinger, M., Hambach, U., Mallol, C., Moreau, L., Niven, L., Richards, M., Richter, D., Zöller, L., Trnka, G., and Hublin, J.-J.: New research on the Aurignacian of Central Europe: A first note on the 2006 fieldwork at Willendorf II, Quartär, 55, 9–15, 2008.

Novothny, Á., Frechen, M., Horváth, E., Wacha, L., and Rolf, C.: Investigating the penultimate and last glacial cycles of the Süttő loess section (Hungary) using luminescence dating, high-resolution grain size, and magnetic susceptibility data, Quatern. Int., 234, 75–85, 2011.

Oehlerich, M., Baumer, M., Lücke, A., and Mayr, C.: Effects of organic matter on carbonate stable isotope ratios ($\delta^{13}C$, $\delta^{18}O$ values) – implications for analyses of bulk sediments, Rapid Commun. Mass Sp., 27, 707–712, 2013.

O'Leary, M. H.: Carbon isotope fractionation in plants, Phytochemistry, 20, 553–567, 1981.

Pécsi, M.: Loess is not just the accumulation of dust, Quatern. Int., 7–8, 1–21, 1990.

Pigati, J. S., Rech, J. A., and Nekola, J. C.: Radiocarbon dating of small terrestrial gastropod shells in North America, Quat. Geochronol., 5, 519–532, 2010.

Porter, S.: Chinese loess record of monsoon climate during the last glacial–interglacial cycle, Earth-Sci. Rev., 54, 115–128, 2001.

Pötter, S., Schmitz, A., Lücke, A., Schulte, P., Obreht, I., Zech, M., Wissel, H., Marković, S. B., and Lehmkuhl, F.: Middle to Late Pleistocene environments based on stable organic carbon and nitrogen isotopes of loess-palaeosol sequences from the Carpathian Basin, Boreas, 50, 184–204, https://doi.org/10.1111/bor.12470, 2020.

Profe, J. and Ohlendorf, C.: X-ray fluorescence scanning of discrete samples – An economical perspective, Quatern. Int., 514, 68–75, 2019.

Profe, J., Wacha, L., Frechen, M., Ohlendorf, C., and Zolitschka, B.: XRF scanning of discrete samples – A chemostratigraphic approach exemplified for loess-paleosol sequences from the Island of Susak, Croatia, Quatern. Int., 494, 34–51, 2018a.

Profe, J., Neumann, L., Novothny, Á., Barta, G., Rolf, C., Frechen, M., Ohlendorf, C., and Zolitschka, B.: Paleoenvironmental conditions and sedimentation dynamics in Central Europe inferred from geochemical data of the loess-paleosol sequence at Süttő (Hungary), Quaternary Sci. Rev., 196, 1–17, https://doi.org/10.1016/j.quascirev.2018.07.034, 2018b.

Pustovoytov, K. and Terhorst, B.: An isotope study of a late Quaternary loess-paleosol sequence in SW Germany, Rev. Mex. Cienc. Geol., 21, 88–93, 2004.

Rasmussen, S. O., Bigler, M., Blockley, S. P., Blunier, T., Buchardt, S. L., Clausen, H. B., Cvijanovic, I., Dahl-Jensen, D., Johnsen,

S. J., Fischer, H., Gkinis, V., Guillevic, M., Hoek, W. Z., Lowe, J. J., Pedro, J B., Popp, T., Seierstadt, I. K., Steffensen, J. P., Svensson, A. M., Vallelonga, P., Vinther, B. M., Walker, M. J. C., Wheatley, J. J., and Winstrup, M.: A stratigraphic framework for abrupt climatic changes during the Last Glacial period based on three synchronized Greenland ice-core records: refining and extending the INTIMATE event stratigraphy, Quaternary Sci. Rev., 106, 14–28, 2014.

Reimer, P. J., Austin, W. E. N., Bard, E., Bayliss, A., Blackwell, P. G., Bronk Ramsey, C., Butzin, M., Cheng, H., Edwards, R. L., Friedrich, M., Grootes, P. M., Guilderson, T. P., Hajdas, I., Heaton, T. J., Hogg, A. G., Hughen, K. A., Kromer, B., Manning, S. W., Muscheler, R., Palmer, J. G., Pearson, C., van der Plicht, J., Reimer, R. W., Richards, D. A., Scott, E. M., Southon, J. R., Turney, C. S. M., Wacker, L., Adolphi, F., Büntgen, U., Capano, M., Fahrni, S. M., Fogtmann-Schulz, A., Friedrich, R., Köhler, P., Kudsk, S., Miyake, F., Olsen, J., Reinig, F., Sakamoto, M., Sookdeo, A., and Talamo, S.: The IntCal20 Northern Hemisphere Radiocarbon Age Calibration Curve (0–55 cal kBP), Radiocarbon, 62, 725–757, 2020.

Renssen, H., Kasse, C., Vandenberghe, J., and Lorenz, S. J.: Weichselian Late Pleniglacial surface winds over northwest and central Europe: a model-data comparison, J. Quaternary Sci., 22, 281–293, 2007.

Rounick, J. S. and Winterbourn, M. J.: Stable carbon isotopes and carbon flow in ecosystems, BioScience, 36, 171–177, 1986.

Rousseau, D. D., Antoine, P., Hatté, C., Lang, A., Zöller, L., Fontugne, M., Othman, D. B., Luck, J. M., Moine, O., Labonne, M., Bentaleb, I., and Jolly, D.: Abrupt millennial climatic changes from Nussloch (Germany) Upper Weichselian eolian records during the Last Glaciation, Quaternary Sci. Rev., 21, 1577–1582, 2002.

Runge, E. C. A., Goh, K. M., and Rafter, T. A.: Radiocarbon Chronology and Problems in Its Interpretation for Quaternary Loess Deposits-South Canterbury, New Zealand, Soil Sci. Soc. Am. Pro., 37, 742–746, 1973.

Schatz, A. K., Zech, M., Buggle, B., Gulyás, S., Hambach, U., Marković, S. B., Sümegi, P., and Scholten, T.: The late Quaternary loess record of Tokaj, Hungary: Reconstructing palaeoenvironment, vegetation and climate using stable C and N isotopes and biomarkers, Quatern. Int., 240, 52–61, 2011.

Smalley, I., O'Hara-Dhand, K., Wint, J., Machalett, B., Jary, Z., and Jefferson, I.: Rivers and loess: The significance of long river transportation in the complex event-sequence approach to loess deposit formation, Quatern. Int., 198, 7–18, 2009.

Smalley, I., Marković, S. B., and Svirčev, Z.: Loess is [almost totally formed by] the accumulation of dust, Quatern. Int., 240, 4–11, 2011.

Sprafke, T.: Löss in Niederösterreich: Archiv quartärer Klima- und Landschaftsveränderungen, Dissertation, Würzburg University Press, Würzburg, 1–272, https://doi.org/10.25972/WUP-978-3-95826-039-9, 2016.

Sprafke, T., Schulte, P., Meyer-Heintze, S., Händel, M., Einwögerer, T., Simon, U., Peticzka, R., Schäfer, C., Lehmkuhl, F., and Terhorst, B.: Paleoenvironments from robust loess stratigraphy using high-resolution color and grain-size data of the last glacial Krems-Wachtberg record (NE Austria), Quaternary Sci. Rev., 248, 106602, https://doi.org/10.1016/j.quascirev.2020.106602, 2020.

Stojakowits, P., Mayr, C., Ivy-Ochs, S., Preusser, F., Reitner, J. M., and Spötl, C.: Environments at the MIS 3/2 transition in the northern Alps and their foreland, Quatern. Int., 581–582, 99–113, 2021.

Stuiver, M., Reimer, P. J., and Reimer, R. W: CALIB 8.2., http://calib.org/calib/, last access: 21 October 2020.

Sun, Y., Liang, L., Bloemendal, J., Li, Y., Wu, F., Yao, Z., and Liu, Y.: High-resolution scanning XRF investigation of Chinese loess and its implications for millennial-scale monsoon variability, J. Quaternary Sci., 31, 191–202, 2016.

Svoboda, J.: The Pavlov Site, Czech Republic: Lithic Evidence from the Upper Palaelithic, J. Field Archaeol., 21, 69–81, https://doi.org/10.1179/jfa.1994.21.1.69, 1994.

Svoboda, J., Hladilová, Š., Horáček, I., Kaiser, J., Králík, M., Novák, J., Novák, M., Pokorný, P., Sázelová, S., Smolíková, L., and Zikmund, T.: Dolní Věstonice IIa: Gravettian microstratigraphy, environment, and the origin of baked clay production in Moravia, Quatern. Int., 359–360, 195–210, 2015.

Terhorst, B., Tiehl, C., Peticzka, R., Sprafke, T., Frechen, M., Fladerer, F. A., Roetzel, R., and Neugebauer-Maresch, C.: Casting new light on the chronology of the loess/paleosol sequences in Lower Austria, Quaternary Sci. J., 60, 270–277, https://doi.org/10.3285/eg.60.2-3.04, 2011.

Terhorst, B., Kühn, P., Damm, B., Hambach, U., Meyer-Heintze, S., and Sedov, S.: Palaeoenvironmental fluctuations as recorded in the loess-paleosol sequence of the Upper Paleolithic site Krems-Wachtberg, Quatern. Int., 351, 67–82, 2014.

Teyssandier, N. and Zilhão, J.: On the Entity and Antiquity of the Aurignacian at Willendorf (Austria): Implications for Modern Human Emergence in Europe, Journal of Paleolithic Archaeology, 1, 107–138, 2018.

Thiel, C., Buylaert, J.-P., Murray, A., Terhorst, B., Hofer, I., Tsukamoto, S., and Frechen, M.: Luminescence dating of the Stratzing loess profile (Austria) – Testing the potential of an elevated temperature post-IR IRSL protocol, Quatern. Int., 234, 23–31, 2011a.

Thiel, C., Terhorst, B., Jaburová, I., Buylaert, J.-P., Murray, A. S., Fladerer, F. A., Damm, B., Frechen, M., and Ottner, F.: Sedimentation and erosion processes in Middle to Late Pleistocene sequencesexposed in the brickyard of Langenlois/Lower Austria, Geomorphology, 135, 295–307, https://doi.org/10.1016/j.geomorph.2011.02.011, 2011b.

Tomášová, S.: A site in history: archaeology at Dolní Věstonice/Unterwisternitz, Antiquity, 69, 301–316, 1995.

Újvári, G. and Klötzli, U.: U–Pb ages and Hf isotopic composition of zircons in Austrian last glacial loess: constraints on heavy mineral sources and sediment transport pathways, Int. J. Earth Sci., 104, 1365–1385, https://doi.org/10.1007/s00531-014-1139-x, 2015.

Újvári, G., Molnár, M., Novothny, Á., Páll-Gergely, B., Kovács, J., and Várhegyi, A.: AMS ^{14}C and OSL/IRSL dating of the Dunaszekcső loess sequence (Hungary): chronology for 20 to 150 ka and implications for establishing reliable age-depth models for the last 40 ka, Quaternary Sci. Rev., 106, 140–154, 2014.

Újvári, G., Molnár, M., and Páll-Gergely, B.: Charcoal and mollusc shell ^{14}C-dating of the Dunaszekcső loess record, Hungary, Quat. Geochronol., 35, 43–53, 2016a.

Újvári, G., Kok, J. F., Varga, G., and Kovács, J.: The physics of wind-blown loess: implications for grain size proxy inter-

pretations in Quaternary paleoclimate studies, Earth-Sci. Rev., 154, 247–278, https://doi.org/10.1016/j.earscirev.2016.01.006, 2016b.

Urbanek, M.: A review of archaeological research at Grubgraben prior to 1980, in: The Epigravettian Site of Grubgraben, Lower Austria: The 1986 and 1987 Excavations, edited by: Montet-White, A., ERAUL – Études et Recherche Archéologiques de l'Université de Liège 40, Liège 1990, 7–13, OCLC-number 24578227, 1990.

Vanderberghe, J.: Grain size of fine-grained windblown sediment : A powerful proxy for process identification, Earth-Sci. Rev., 121, 18–30, https://doi.org/10.1016/j.earscirev.2013.03.001, 2013.

Vanderberghe, J., Zhisheng, A., Nugteren, G., Huayu, L., and Van Huissteden, K.: New absolute time scale for the Quaternary climate in Chinese loess region by grain size analysis, Geology, 25, 35–38, 1997.

Veres, D., Tecsa, V., Gerasimenko, N., Zeeden, C., Hambach, U., and Timar-Gabor, A.: Short-term soil formation events in last glacial east European loess, evidence from multi-method luminescence dating, Quaternary Sci. Rev., 200, 34–51, 2018.

Wang, H. and Greenberg, S. E.: Reconstructing the response of C_3 and C_4 plants to decadal-scale climate change during the late Pleistocene in southern Illinois using isotope analyses of calcified rootlets, Quaternary Res., 67, 136–142, 2007.

Wang, Z., Zhao, H., Dong, G., Zhou, A., Liu, J., and Zhang, D.: Reliability of radiocarbon dating on various fractions of loess-soil sequence for Dadiwan section in the western Chinese Loess Plateau, Front. Earth Sci., 8, 540–546, https://doi.org/10.1007/s11707-014-0431-1, 2014.

Ward, C. R., Kelloway, S. J., Vohra, J., French, D., Cohen, D. R., Marjo, C. E., and Wainwright, I. E.: In-situ inorganic analysis of coal seams using a hand-held field-portable XRF Analyser, Int. J. Coal Geol., 191, 172–188, 2018.

Weltje, G., Bloemsma, M., Tjallingii, R., Heslop, D., Röhl, U., Croudace, I.: Prediction of Geochemical Composition from XRF Core Scanner Data: A New Multivariate Approach Including Automatic Selection of Calibration Samples and Quantification of Uncertainties, in: Micro-XRF Studies of Sediment Cores, edited by: Croudace, I. and Rothwell, R., Springer, Dordrecht, 507–534, https://doi.org/10.1007/978-94-017-9849-5_21, 2015.

West, D.: Hunting strategies in Central Europe during the last glacial maximum, British Archaeological Reports International Series 672, Hadrian Books, Oxford, 1–153, ISBN 9780860549123, 1997.

Xu, B., Gu, Z., Han, J., Hao, Q., Lu, Y., Wang, L., Wu, N., and Peng, Y.: Radiocarbon age anomalies of land snail shells in the Chinese Loess Plateau, Quat. Geochronol., 6, 383–389, 2011.

Zech, M., Zech, R., and Glaser, B.: A 240,000-year stable carbon and nitrogen isotope record from a loess-like palaeosol sequence in the Tumara Valley, Northeast Siberia, Chem. Geol., 242, 307–318, 2007.

Zech, R., Zech, M., Marković, S., Hambach, U., and Huang, Y.: Humid glacials, arid interglacials? Critical thoughts on pedogenesis and paleoclimate based on multi-proxy analyses of the loess-paleosol sequence Crvenka, Northern Serbia, Palaeogeogr. Palaeocl., 387, 165–175, 2013.

Zeeden, C. and Hambach, U.: Magnetic Susceptibility Properties of Loess from the Willendorf Archaeological Site: Implications for the Syn/Post-Depositional Interpretation of Magnetic Fabric, Front. Earth Sci., 8, 1–11, https://doi.org/10.3389/feart.2020.599491, 2021.

E&G Quaternary Sci. J., 71, 45–58, 2022
https://doi.org/10.5194/egqsj-71-45-2022

Open Access E&G Quaternary Science Journal

Research article

Timing and intensity of humid interglacial and interstadial periods from the Eemian in the southwestern Mediterranean region: new chronological and stable isotope data from Aït Said ou Idder (Middle Atlas) and comparison with other regional tufa deposits (Morocco and southern Spain)

Julie Dabkowski[1], Quentin Wackenheim[1,2], Christophe Falguères[3], Denis Fiorillo[4], Olivier Tombret[3], Nicole Limondin-Lozouet[1], Larbi Boudad[5], and Jean-François Berger[6]

[1]Laboratoire de Géographie Physique: environnements quaternaires et actuels (UMR 8591), CNRS – Université Paris 1 Panthéon-Sorbonne – Université Paris-Est Créteil, Meudon, France
[2]Trajectoires (UMR 8215), CNRS – Université Paris 1 Panthéon-Sorbonne, Paris, France
[3]Histoire Naturelle de l'Homme Préhistorique (UMR 7194), CNRS – MNHN, Paris, France
[4]Archéozoologie – Archéobotanique. Sociétés, pratiques et environnements (UMR 7209), CNRS – MNHN, Paris, France
[5]Département de Géologie, Université Mohammed V de Rabat, Rabat, Morocco
[6]Environnement, Ville, Société (UMR 5600, IRG), CNRS – Université de Lyon, Lyon, France

Correspondence: Julie Dabkowski (julie.dabkowski@lgp.cnrs.fr)

Relevant dates: Received: 22 July 2021 – Revised: 3 December 2021 – Accepted: 14 January 2022 – Published: 14 March 2022

How to cite: Dabkowski, J., Wackenheim, Q., Falguères, C., Fiorillo, D., Tombret, O., Limondin-Lozouet, N., Boudad, L., and Berger, J.-F.: Timing and intensity of humid interglacial and interstadial periods from the Eemian in the southwestern Mediterranean region: new chronological and stable isotope data from Aït Said ou Idder (Middle Atlas) and comparison with other regional tufa deposits (Morocco and southern Spain), E&G Quaternary Sci. J., 71, 45–58, https://doi.org/10.5194/egqsj-71-45-2022, 2022.

Abstract: In the last few decades, multidisciplinary research on calcareous tufas as palaeoenvironmental and palaeoclimatic records has intensively grown, which has provided an increasing number of well-documented sites. Consequently, inter-site comparisons and regional- to continental-scale reviews have developed, discussing the link between tufa distribution and climate or providing diachronic comparisons of climatic and environmental conditions prevailing during Quaternary interglacials (and interstadials). This paper proposes such a review for the southeastern Mediterranean area, including new dating and isotopic data from Aït Said ou Idder (northern Morocco) to be compared with available regional data, in order to discuss the intensity of some humid periods of the last 125 kyr.

According to several radiocarbon and U–Th dates, three chronological phases are indeed identified at Aït Said ou Idder: the Holocene, the Dansgaard–Oeschger (D–O) interstadial 8 and the Marine Isotopic Stage (MIS) 5e. Similarly, other tufa deposits from both Morocco and southern Spain (mostly Andalusia) appear to have preferentially developed during interglacial or interstadial periods, marked by maximal developments of the Mediterranean forest as reported in the palynological records from

regional marine cores. Furthermore, isotopic data (δ^{18}O and δ^{13}C) from Aït Said ou Idder (and from other southeastern Mediterranean tufa deposits where available) suggest no significant difference in terms of temperature or air mass circulation between the Holocene, D–O 8 and MIS 5e. In terms of humidity conditions, no evidence of strong aridity is recorded even if D–O 8 appears drier than both interglacials. Conditions seems slightly wetter during the Holocene than during MIS 5e, but δ^{13}C values at Aït Said ou Idder could also reflect strong differences in the seasonality of these interglacials. We demonstrate that calcareous tufa deposits have promising potential for discussing, in both space and time, the climate variability in the southeastern Mediterranean area, but new investigations, including dating and stable isotopes, are required to accurately feed such discussions.

Kurzfassung:

In den letzten Jahrzehnten ist die multidisziplinäre Forschung zur Rolle von Kalktuffen (Tufa) als Paläoumwelt- und Paläoklima-Archiv intensiv ausgebaut worden, wodurch nun eine weiterhin wachsende Zahl gut dokumentierter Standorte vorliegt. Infolgedessen war es im Rahmen von Vergleichen zwischen verschiedenen Standorten und auf der Grundlage vergleichender Bewertungen auf regionalem bis hin zu kontinentalem Maßstab einerseits möglich, den Zusammenhang zwischen der Verteilung von Kalktuffen und Klima zu diskutieren, sowie andererseits diachrone Vergleiche von klimatischen Bedingungen und Umweltbedingungen während der Interglaziale (und Interstadiale) im Quartär durchzuführen. Diese Studie stellt eine solche vergleichende Bewertung für den südöstlichen Mittelmeerraum bereit und präsentiert darüber hinaus neue Datierungen und Isotopen-Daten aus Aït Said ou Idder (nördliches Marokko), die mit vorliegenden regionalen Daten verglichen werden, um somit eine Einschätzung der Intensität ausgewählter humider Abschnitte der letzten 125 kyr vornehmen zu können.

Basierend auf mehreren Radiokohlenstoff- und U–Th-Datierungen können in Aït Said ou Idder drei chronologische Phasen ausgewiesen werden: das Holozän, das Dansgaard/Oeschger Interstadial 8 und das MIS 5e. In ähnlicher Weise scheinen sich andere Kalktuffablagerungen sowohl aus Marokko als auch aus Südspanien (hauptsächlich Andalusien) bevorzugt während solcher Interglazial- oder Interstadialperioden entwickelt zu haben, die basierend auf der palynologischen Auswertung regionaler mariner Bohrkernarchive durch eine maximale Entwicklung mediterraner Wälder gekennzeichnet sind. Darüber hinaus deuten Isotopendaten (δ^{18}O and δ^{13}C) aus Aït Said ou Idder (und aus anderen Kalktuffen des südöstlichen Mittelmeerraumes, sofern verfügbar) darauf hin, dass es keine signifikanten Unterschiede in Bezug auf Temperatur oder Luftmassenzirkulation zwischen dem Holozän, dem D/O 8 und dem MIS 5e gab. Im Hinblick auf die Feuchtigkeitsbedingungen finden sich keine Hinweise starker Aridität, auch wenn das D/O 8 relativ trockener erscheint als beide Interglaziale. Die Bedingungen scheinen während des Holozäns etwas feuchter gewesen zu sein als während des MIS 5e, aber die δ^{13}C-Werte in Aït Said ou Idder könnten auch starke Unterschiede in der Saisonalität dieser Interglaziale widerspiegeln. Unsere Studie zeigt, dass Kalktuffablagerungen ein vielversprechendes Potenzial haben, um die Klimavariabilität im südöstlichen Mittelmeerraum sowohl räumlich als auch zeitlich zu diskutieren, aber neue Untersuchungen, einschließlich Datierungen und Untersuchungen an stabilen Isotopen, sind erforderlich, um diese Diskussion sorgfältig und genau zu untermauern. (*Abstract was translated by Christopher Luethgens.*)

1 Introduction

In the last few decades, multidisciplinary research on calcareous tufas has intensively grown regarding their potential for palaeoenvironmental and palaeoclimatic studies: they are one of the few continental archives to simultaneously provide records of past environments (including fauna and flora) and independent proxies for climatic variations (from calcite stable isotopes) which can also be precisely and objectively dated (Andrews, 2006; Capezzuoli et al., 2014; Dabkowski, 2014). In parallel, as the number of well-documented sites has increased, inter-site comparisons and regional- to continental-scale reviews have developed, either discussing the link between tufa chronological distribution and climate and/or anthropogenisation (e.g. Dabkowski, 2020; Goudie et al., 1993; Ollivier et al., 2006; Pentecost, 1995; Vaudour, 1994; Weisrock, 1986) or providing diachronic comparisons of climatic and environmental conditions prevailing during Quaternary interglacials (Limondin-Lozouet, 2011; Limondin-Lozouet and Preece,

2014; Dabkowski and Limondin-Lozouet, 2021). However, investigations have mostly focused on European tufas so far. In Morocco, reviews on the ages of tufa deposits have been initiated on the basis of U–Th dating (Falguères et al., 2016; Rousseau et al., 2017; Weisrock et al., 2008), but they concerned indurated, well-crystallised deposits (so-called "travertines"), from which palaeoenvironmental and palaeoclimatic data are more difficult to retrieve (Capezzuoli et al., 2014; Dabkowski, 2014). The tufa sequence of Aït Said ou Idder in the Middle Atlas is the first to have recently provided palaeoenvironmental reconstructions based on malacological data (Wackenheim et al., 2020).

This paper proposes to review the climatic significance of tufa deposits in the southeastern Mediterranean area based on their chronological distribution and isotopic signal. It will first present new U–Th dating and isotopic data from Aït Said ou Idder to be compared with available regional data from Morocco and Andalusia in order to discuss the intensity of some humid periods of the last 125 kyr.

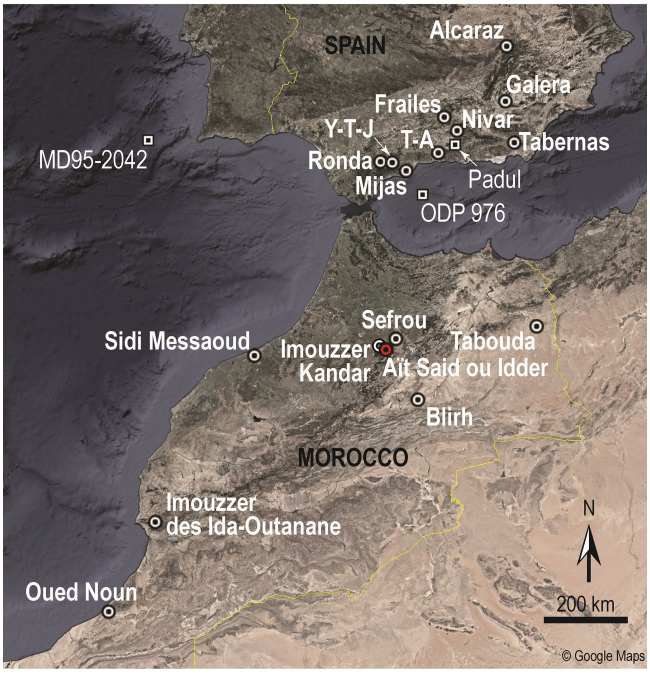

Figure 1. Localisation map of Aït Said ou Idder (red spot) and other tufa deposits discussed in this paper (circles). T–A: Tejeda–Almijara; Y–T–J: Yunquera–Tolox–Jorox. Squares show other palaeoenvironmental or palaeoclimatic records mentioned in the text (background map from © Google Maps, modified by Julie Dabkowski).

2 Studied site and material

The Aït Said ou Idder (ASI) tufa is located in the Middle Atlas, northeast Morocco, about 40 km south of Fez in the vicinity of the Dayet Aoua (33°38′49.50″ N, 4°59′38.33″ E; Fig. 1). The studied profile, ca. 45 m long and 3 to 4 m high, was previously described in detail by Wackenheim et al. (2020). Two main phases of tufa deposition have been observed on the field (Fig. 2). The lower stratigraphical units 10 to 7 are sub-horizontal and characterised by fluvio-paludal facies (Pedley, 1990; Pedley et al., 2003) including large oncoliths and indurated phytoherms (units 10 and 9), silty to sandy stratified levels (unit 8), and a fine mudstone-like whitish unit at the top (unit 7; Fig. 2). No major discontinuity is clearly observed within these lower units in the eastern part of the profile where they are better exposed. However, in the central part, a stepped-shape incision at the top of unit 8 is locally observed, which may correspond to a hiatus between units 8 and 7 (Fig. 2, red line).

The upper part of the unit 7 is then clearly affected by erosive processes, and indurated angular fragments of it are preserved within the base of the overlying unit 6. The following units 6 to 1 show an east-to-west inclination and facies that are typical of slope tufa (Pedley, 1990), namely silty to granular tufa comprising fragments of encrusted vegetation alternating with silty to sandy tufa (Fig. 2). The lowermost unit 6 especially provides burned tufa fragments and millimetric charcoals evidencing a local fire event. These charcoals were large enough to be dated with confidence (see below). The whole ASI sequence, except unit 9 which was too indurated, was sampled for malacology and geochemistry (Fig. 2). The malacological investigations provide detailed palaeoenvironmental reconstructions and allow selecting shells of suitable species to be dated (Wackenheim et al., 2020). The resulting chronological data are summarised in the following section.

3 Chronological data

3.1 Former radiocarbon dating

All the previous dates obtained at ASI were through radiocarbon dating and are summarised in Table 1. Dated material includes three millimetric individual charcoals from unit 6, a bunch of microcharcoals from unit 5, and five bunches of mollusc shells from units 1, 3, 4 and 7 (Table 1 and Fig. 2; Wackenheim et al., 2020). While charcoals from unit 6 were handpicked on the field, the bunch of microcharcoal from unit 5 was subsampled within sedimentological samples under a binocular microscope. Dated shells were carefully selected within the malacological assemblages according to their abundance to have enough material to be dated from a single sample. In order to avoid the reservoir effect by old carbonate ingestion, the selection of tiny humidity-demanding species (*Vertigo antivertigo*, *Pupilla muscorum*, *Cochlicopa lubrica*) has been favoured (Table 1) (Pigati et al., 2013; Forman et al., 2021; Granai and Wackenheim, 2022). Radiocarbon date of the xerothermic *Cochlicella barbara* shell is consistent with the chronological framework (Wackenheim et al., 2020).

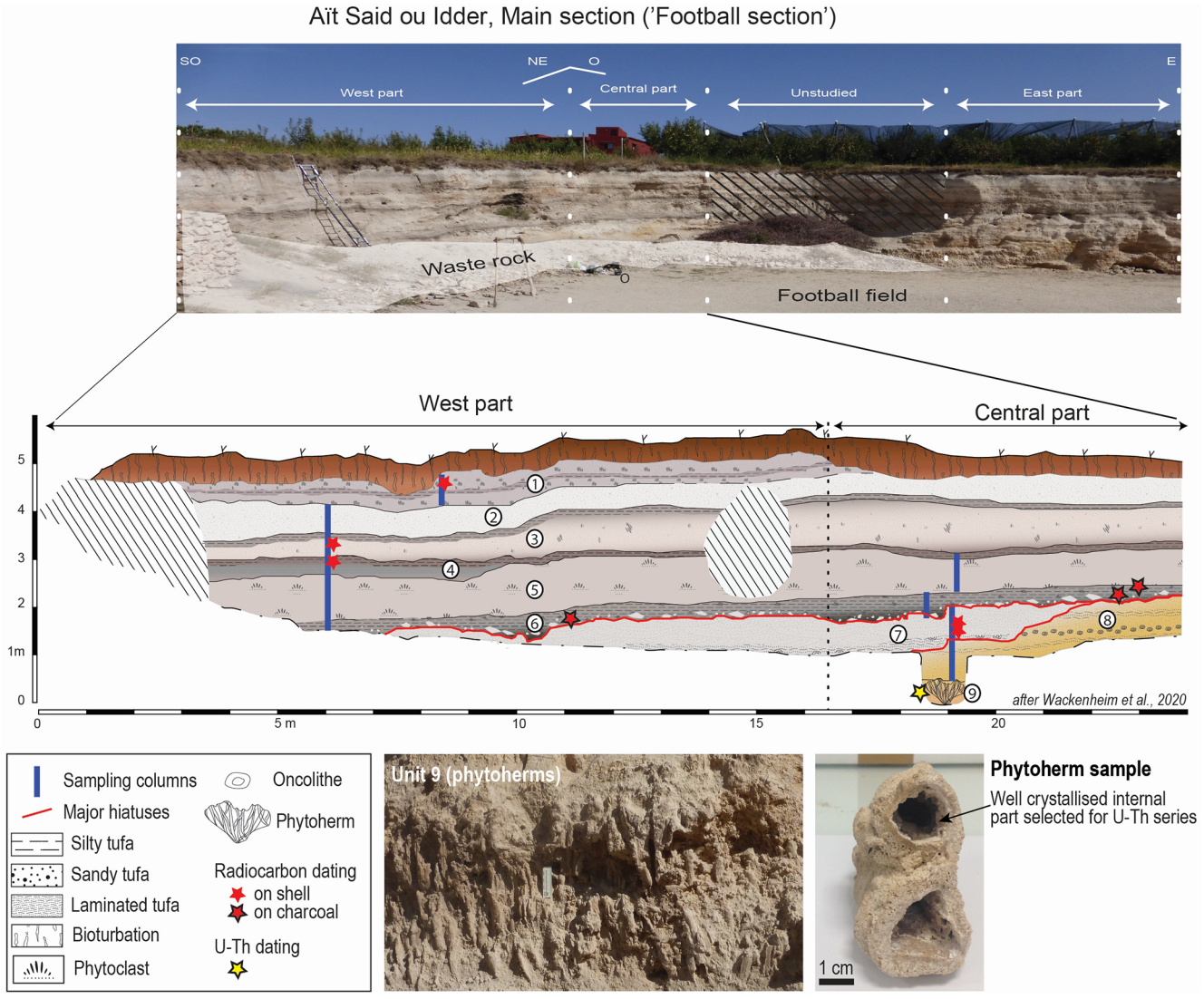

Figure 2. Main section of the Aït Said ou Idder tufa and detailed stratigraphy of the west and central parts where geochemical samples were collected, parallel to malacological samples (modified after Wackenheim et al., 2020). On the bottom right, the picture shows a detailed view of the phytoherm facies from unit 9, which was sampled for the U–Th dating.

Table 1. Details of radiocarbon ages obtained on the Aït Said ou Idder tufa sequence.

Laboratory code	Sample name	Stratigraphic level	Material	^{14}C BP	cal BP 2σ	cal BCE 2σ
Poz-83678	Asi16-Ch	Lower part of grey level D	Charcoal	5830 ± 40	6740–6508	4790–4558
Beta-477595	Asi17-Ch3	Lower part of grey level D	Charcoal	690 ± 30	6553–6405	4604–4456
Beta-477596	Asi17-Ch4	Upper part of grey level D	Charcoal	5470 ± 30	6310–6209	4361–4260
Poz-115941	Asi17-G9	Base unit 5	Charcoal	4730 ± 370	6292–4452	4342–2502
SacA-54562	Asi17-M30	Grey level A	*Vertigo antivertigo*	4375 ± 30	5039–4859	3089–2909
SacA-54563	Asi17-M21	Grey level B	*Cochlicella barbara*	5085 ± 30	5911–5747	3961–3797
SacA-54564	Asi17-M16	Grey level C	*Vertigo antivertigo*	5375 ± 30	6280–6019	4330–4096
DeA-17402	I/1889/1	Unit 7	*Pupilla muscorum*	35 920 ± 530	41 590–39 380	39 640–37 430
DeA-17403	I/1889/2	Unit 7	*Cochlicopa lubrica*	36 720 ± 570	42 170–40 150	40 220–38 200

Radiocarbon dates assigned the upper part of the ASI tufa to the Middle Holocene (from ca. 6800 and 4800 cal BP) while unit 7 from the lower part is dated from the Upper Pleistocene by two coherent dates on land shells (around 37–40 ka cal BP; Table 1 and Fig. 3). To strengthen this chronological framework, we sought an additional date at the base of the tufa deposit. While no suitable organic material or shell was found in units 9 or 10, well-crystallised calcite deposits such as the strongly indurated phytoherms from unit 9 are suitable material for U–Th series analyses (Fig. 2).

3.2 Additional U–Th dating

The U–Th dating method requires well-crystallised calcite samples that are not easily retrieved from tufa deposits dominated by crumbly silty to sandy facies such as those at ASI (Fig. 2); only phytoherms from unit 9 are suitable here for such analyses. One sample selected from unit 9 (Fig. 2) was thus analysed by U series using ICP-Q-MS at the Muséum national d'Histoire naturelle (France). This method relies on the difference in solubility between uranium and thorium. The amount of radiogenic ^{230}Th formed in ratio to its parent ^{234}U yields the age of formation of the calcite (Bourdon et al., 2003; Ivanovich and Harmon, 1992).

The sample was selected in the well-crystallised internal part of the phytoherm cylinder (Fig. 2), cleaned by removing clay and sand adhering on calcite, then cut using a mini rotary tool (Dremel™-like) with a diamond disc, and finally washed with distilled water in an ultrasonic bath. The carbonate (about 0.5 g) was dissolved in HNO_3 acid, and a ^{233}U–^{236}U–^{229}Th mixed spike was added. U and Th chemical extractions and purifications on UTEVA resins were performed according to the protocol detailed by Douville et al. (2010). Each fraction was then dried and dissolved in 2 % $HNHO_3$ before dilution for isotopic analyses by ICP-Q-MS. The measurements were performed on a Thermo iCAP RQ ICP-Q-MS coupled with a Teledyne CETAC Aridus 3 desolvator device. Pre-screening analysis was first performed in order to optimise the final dilutions of each fraction. Then they were combined to be analysed together.

The interface was configured for high sensitivity, and the signal was optimised (tuning) for ^{238}U and ^{235}U on the desolvator and mass spectrometer. The signal intensities of the isotopes ^{229}Th, ^{230}Th, ^{233}U, ^{234}U, ^{235}U and ^{236}U were measured on an electron multiplier (SEM) in pulse-counting mode, and those of ^{232}Th were measured in analogue mode. The helium mode (CCTS) of the collision/reaction cell was used to increase the signal by optimising the ions' focusing. The mass fractionation was corrected by comparing the measured ^{233}U/^{236}U spike ratio with its true known value. The ^{234}U/^{238}U ratio is obtained via the ^{234}U/^{235}U measurement according to the universal natural ^{238}U/^{235}U ratio (Hiess et al., 2012). An analytical standard (without chemistry) of uraninite (HU-1) with a spike, in secular radioactive equilibrium, was analysed along the sequence for machine deviation control. The calculated activity ratios obtained should correspond to the true ratios.

Ages were calculated using half-lives of 75.584 and 245.620 ka for ^{230}Th and ^{234}U, respectively (Cheng et al., 2013). The age uncertainty was estimated taking into account all sources of analytical uncertainty. The U content, isotopic ratios and U-series age of the ASI phytoherm sample are shown in Table 2. The U content is 57 ppb. The ^{234}U/^{238}U is high (more than 3.4) as usually observed in continental carbonates from Morocco (see Ghaleb et al., 2019). An age of 129 ± 4 ka was obtained without correction, but the measured ^{230}Th/^{232}Th ratio of 14 indicates that correction of the age from detritic Th is mandatory. The corrected age, taking into account the average value of the ^{232}Th/^{238}U atomic ratio of the Earth's crust (3.8 ± 2; Ludwig and Paces, 2002), is 123 ± 4 ka and demonstrates the contemporaneity of the bottom of the ASI sequence with Marine Isotopic Stage (MIS) 5e (Fig. 3).

4 Stable isotopes

4.1 Methods

The whole tufa sequence at ASI was sampled continuously every 5 cm (ca. 20 g of tufa was collected for each sample), with local adjustment to stratigraphy when required and excepting the lowermost units 9 and 10, which were too indurated. Each sample was ground when needed and then sifted to < 200 µm to obtain 2 to 5 g of fine material. Stable isotope analyses were performed on CO_2 derived from 40 ± 10 µg of sifted sample, individually reacted with three drops of orthophosphoric acid (H_3PO_4) at 70 °C. Isotope ratios were measured at the Service de Spectrométrie de Masse Isotopique (SSMIM) of the Muséum national d'Histoire naturelle in Paris (France) on a Thermo DELTA V Advantage spectrometer interfaced to a Thermo KIEL IV Carbonate automatic preparation device.

4.2 Results

A summary of ASI isotopic data is given in Table 3, and both δ^{18}O and δ^{13}C are shown in stratigraphic order in Fig. 3. Replicate analyses of the home-made laboratory standard ($n = 29$) gave 2σ precision of 0.1 ‰ for δ^{18}O and 0.08 ‰ for the δ^{13}C. Maximal values, for both δ^{18}O and δ^{13}C, are recorded in samples G81 (−5.3 ‰ and −5.67 ‰, respectively) and G82 (−5.3 ‰ and −6.15 ‰) at the very top of unit 7, below the important sedimentary hiatus with unit 6. These singular values (Fig. 3) are likely to reflect strong diagenetic effects (due to surface alteration and the fire event) and were excluded from the following discussion.

For the remaining samples ($n = 103$), the δ^{18}O values range between −7.8 ‰ and −6.9 ‰ (mean value -7.3 ± 0.1 ‰), whereas δ^{13}C values range between −9.74 ‰ and −7.56 ‰ (mean value -9.25 ± 0.08 ‰; Table 3). Correla-

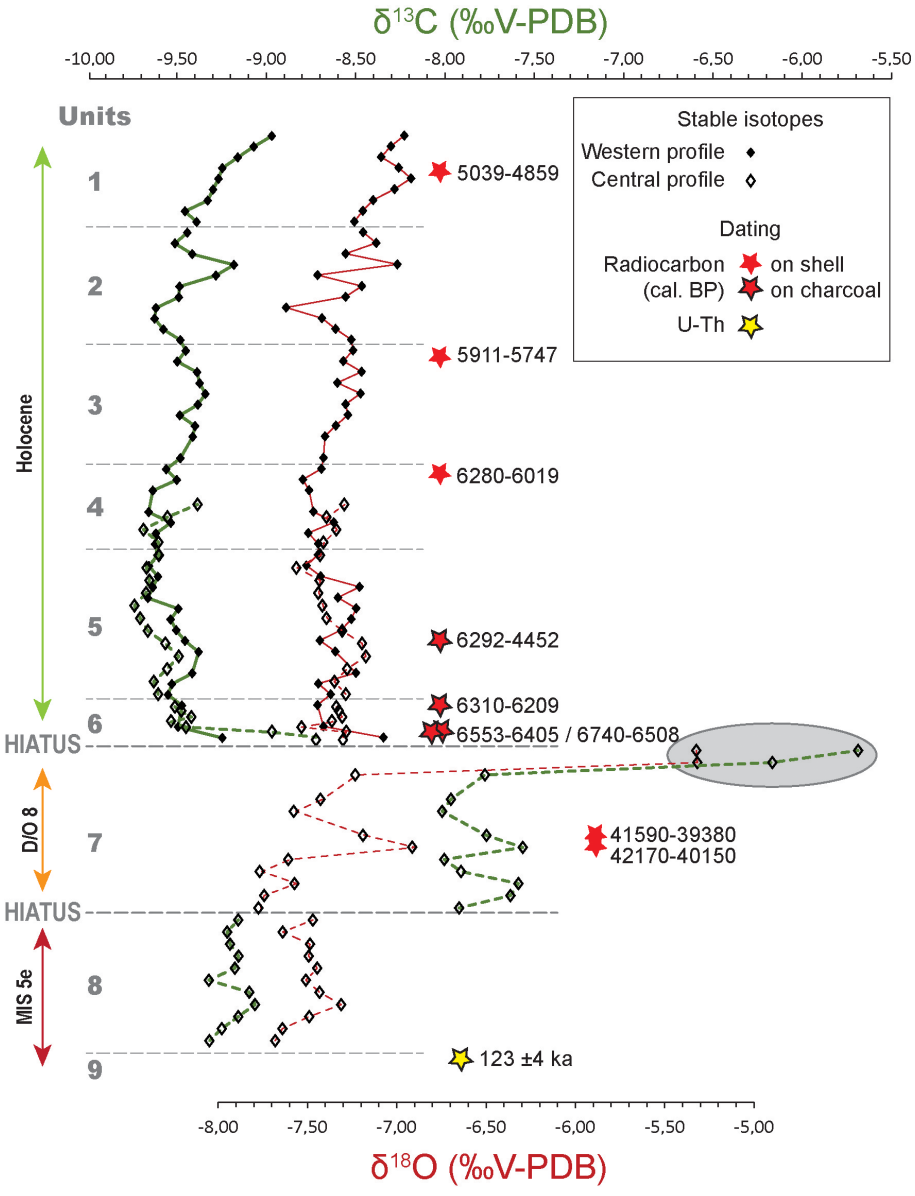

Figure 3. Carbon and oxygen stable isotopes from Aït Said ou Idder tufa calcite shown in stratigraphical order according to tufa units (with no respect to sample depth). The stratigraphical positions of radiocarbon and U–Th ages are also reported.

Table 2. Detailed data from the U series using ICP-Q-MS analyses and resulting age of the phytoherm sample from unit 9 at Aït Said ou Idder.

^{232}Th ppb	± ($k = 2$)	^{234}U/^{238}U	± ($k = 2$)	^{230}Th/^{234}U	± ($k = 2$)	^{230}Th/^{238}U	± ($k = 2$)	^{230}Th/^{232}Th	± ($k = 2$)	Calculated age (ka)	Pos. err.	Neg. err.	Age corr.
29.177	0.488	3.048	0.051	0.771	0.014	2.350	0.042	13.920	0.126	129	4	4	123

Table 3. Summary of stable isotope data from the whole ASI tufa sequence and for the three main phases separated by hiatuses (see text for details).

	$\delta^{18}O$ (‰ V-PDB)	$\delta^{13}C$ (‰ V-PDB)
Conf. int.	0.1	0.08
All, $n = 103$		
Range	−7.8 to −6.9	−9.74 to −7.56
Mean	−7.3	−9.25
SD	0.2	0.57
Upper part, $n = 80$		
Range	−7.6 to −6.9	−9.74 to −8.72
Mean	−7.3	−8.72
SD	0.1	0.18
Unit 7, $n = 12$		
Range	−7.8 to −6.9	−8.01 to −7.56
Mean	−7.4	−7.78
SD	0.3	0.17
Unit 8, $n = 11$		
Range	−7.7 to −7.3	−9.31 to −9.06
Mean	−7.5	−9.18
SD	0.1	0.08

Conf. int.: confidence interval. SD: standard deviation.

tion between $\delta^{18}O$ and $\delta^{13}C$ is not significant ($r = -0.09$; $p = 0.37$; $n = 103$).

At ASI, three phases can be defined, based on sharp variations in the $\delta^{13}C$ at the units 8–7 and then units 7–6 boundaries (Fig. 3 and Table 3): the mean $\delta^{13}C$ value is -9.18 ± 0.08 ‰ ($n = 11$) in the lowermost unit 8, then increases to −7.78 in unit 7 ($n = 12$), and finally decreases suddenly to −9.18 in the rest of the sequence (units 6 to 1; $n = 80$). Boundaries between these three phases are correlated to main hiatuses observed in the stratigraphic sequence of ASI (Fig. 2). Conversely, the $\delta^{18}O$ remains stable from part to part (−7.5 ‰, −7.4 ‰ and -7.3 ± 0.1 ‰, respectively; Table 3). Within each phase, variations in both $\delta^{13}C$ and $\delta^{18}O$ are low (standard variations equal or close to confidence intervals; Table 3). According to stratigraphy and dating, these phases correspond to three distinct periods of time separated by hiatuses: from bottom to top, units 9 and 8 are assigned to the early MIS 5e, unit 7 is dated to around 37–40 ka cal BP (during MIS 3), and units 6 to 1 record part of the Middle Holocene (Fig. 3).

5 Discussion

5.1 ASI tufa chronology compared to other regional tufas and its climatic significance

In Morocco, Late Pleistocene tufa deposits are reported during both odd and even Marine Isotopic Stages (MISs) (Rousseau et al., 2017; Weisrock et al., 2008), i.e. during interglacial and glacial periods (Fig. 4). Over the last 130 kyr, at the northern border of the Moroccan Sahara, Weisrock et al. (2008) showed (based on U–Th dating) that most tufas were deposited during MIS 5, then between 50–30 and 24–11 ka (Figs. 1 and 4). In detail, at least two main phases of deposition occurred during MIS 5, at 120–130 ka (i.e. during MIS 5e) and 90–74 ka (Fig. 4; Boudad et al., 2003; Falguères et al., 2016; Weisrock et al., 2008). Few Holocene tufas have been reported in Morocco so far, except in the Ksabi basin (e.g. at Blirh and Aït Blal; Lefèvre, 1989; Limondin-Lozouet et al., 2013; Vaudour, 1986) and the Aïn Beni Mathar basin (Depreux et al., 2021; Wengler and Vernet, 1992), in the Moulouya catchment, where they are dated from the Early Holocene (Figs. 1 and 4). Later tufa deposits were recently dated from the last 5000 years at Imouzzer Kandar (Azennoud et al., 2022), only a few kilometres from ASI (Figs. 1 and 4).

On the other side of the Strait of Gibraltar, Spanish tufa deposits have been more extensively studied for decades and regional synthesis are available (see González Martín and González Amuchastegui, 2014). Many tufa or travertine deposits have thus been reported in Andalusia, mostly supporting geomorphological and sedimentological investigations (Durán, 1996; García-García et al., 2014; Martìn-Algarra et al., 2003; Pla-Pueyo et al., 2017; Prado-Pérez et al., 2013). From a climatic point of view, northeastern Morocco and Andalusia nowadays present strong similarities as they both experience Mediterranean conditions with hot summers and low-pressure westerlies bringing air masses from the Atlantic which result in mean annual precipitation in excess of 100 to 250 mm yr^{-1} during winters and springs (Larrasoaña et al., 2013; Lionello, 2012; New et al., 2000). It thus seems relevant in order to expand the corpus of comparison sites to include data from Andalusia where five phases of maximal tufa deposition have been identified since 130 ka (Delgado Castilla, 2007; Durán, 1996; Martìn-Algarra et al., 2003), including both MIS 1 and MIS 5 interglacials but also the MIS 2–MIS 1 transition and two phases during the Last Glacial Period at around 20–25 ka (MIS 2) and around 40 ka (MIS 3; Fig. 4).

Pleistocene deposits observed at ASI during the early MIS 5e, then around 37–40 ka cal BP, are thus contemporaneous with phases of maximal tufa deposition observed in both Spain and Morocco (Fig. 4). The youngest phase of maximal tufa deposition at ASI has only been faintly observed in Morocco, where only a few well-dated Holocene tufa deposits

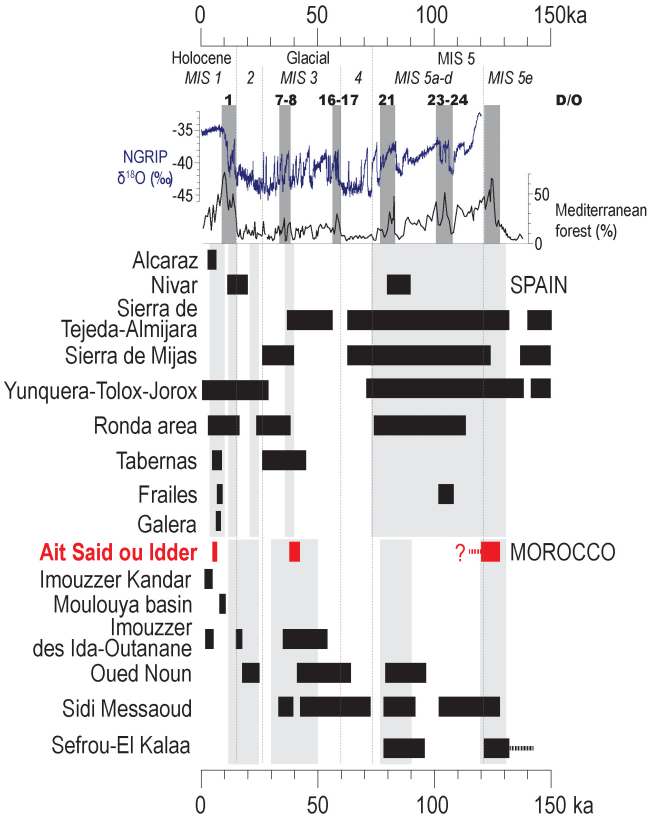

Figure 4. Chronological distribution of tufa deposits from southern Spain (Andrews et al., 2000; Delannoy et al., 1993; Delgado Castilla, 2009; Durán, 1996; García-García et al., 2014; Martìn-Algarra et al., 2003; Wolf et al., 2021) and from Morocco (Azennoud et al., 2022; Boudad et al., 2003; Depreux et al., 2021; Falguères et al., 2016; Lefèvre, 1989; Mercier et al., 2009; Rousseau et al., 2006; Weisrock et al., 2008) including ASI (this study, in red) compared to the evolution of Greenland δ^{18}O (North Greenland Ice Core Project members, 2004) and Mediterranean forest at the SW Iberian margin (MD95-2042; Sánchez Goñi et al., 2008) during the last climatic cycle. MIS: Marine Isotopic Stage. D/O: Dansgaard–Oeschger events (in bold). Darker grey bars highlight the main developments of the Mediterranean forest (associated with precession minima and high atmospheric methane concentrations, after Sánchez Goñi et al., 2008). Lighter grey bars highlight maxima in tufa depositions in Spain (Durán, 1996) and in northern Morocco (Rousseau et al., 2006; Weisrock et al., 2008). Localisation of sites is shown in Fig. 1.

have been reported (in the Moulouya basin), but has been well identified in Spain (Fig. 4).

Under European mid-latitudes, tufa deposits are usually associated with interglacial conditions (Pentecost, 1993, 1995), but some examples show that they can rapidly develop as soon as climatic conditions improve and before the establishment of trees in the deglaciated landscape. Less is known about tufas in sub-tropical areas (Ford and Pedley, 1996), but they are usually considered records of humid (pluvial) phases (Butzer et al., 1978; Delgado Castilla, 2009; Hamdan and Brook, 2015; Nicod, 2000).

As recorded by maxima of the Mediterranean forest in marine cores from the SW Iberian margin and the Alboran Sea, the Mediterranean climate (characterised by warm and dry summers and especially humid winters) appears well expressed during interglacials (MIS 1 and MIS 5e); MIS 5 interstadials; and D–O interstadials 16–17, 8 and 7 (Combourieu-Nebout et al., 2002; Fletcher and Sánchez Goñi, 2008; Sánchez Goñi et al., 2008, 2000). Specifically, D–O event 8 corresponds to one of the longest and wettest interstadials recorded in the western Mediterranean during the glacial period (Combourieu-Nebout et al., 2002; Margari et al., 2010; Sánchez Goñi et al., 2008).

Phases of maximal tufa deposition observed in Morocco and southern Spain thus appear contemporaneous with these periods of maximal development of the Mediterranean forest, which confirms that their chronological distribution is mainly driven by climatic parameters (Delgado Castilla, 2007; Rousseau et al., 2006; Weisrock et al., 2008). At ASI, tufa deposits are reported during periods when Mediterranean climatic conditions, especially winter humidity, were particularly marked, i.e. during the Holocene, the Eemian, and D–O interglacial 8 (Sánchez Goñi et al., 2008; Shackleton et al., 2004; Zielhofer et al., 2017; Fig. 4).

5.2 Comparison of intensities of the Holocene and Eemian interglacials and D–O interstadial 8 at Aït Said ou Idder

Climatic parameters influencing stable isotopes in modern and Quaternary tufa deposits have been well identified (Andrews, 2006; Andrews et al., 1997; Dabkowski et al., 2011). Tufa calcite δ^{18}O is directly linked to local air mass composition, which mainly depends on their source, rainout effects due to "continentality", altitude or processes such as the amount effect, and changes in the atmospheric temperature. On the other hand, tufa calcite δ^{13}C is influenced by biomass type and abundance and rainfall amount (i.e. moisture availability).

The three chronological phases identified at ASI are characterised by different isotopic signatures: regarding the δ^{13}C, sedimentary hiatuses between those phases correspond to shifts in the carbon isotope composition of tufa, while the δ^{18}O shows smaller variations (Fig. 3). This remarkable homogeneity of δ^{18}O values (Table 3) suggests no significant difference in terms of temperature or air mass circulation between the Holocene, D–O interstadial 8 and MIS 5e. Regarding carbon isotopes, D–O 8 records values close to -8 ‰ (Table 3), significantly higher than during the interglacials, which reflect a lesser development of soil and vegetation under relatively "drier" conditions during this MIS 3 interstadials (Fig. 5). On the other hand, both interglacials present δ^{13}C values typical of a strong influence from C_3 plant-/soil-zone CO_2 in δ^{13}C (Andrews, 2006; Fig. 5), suggesting rela-

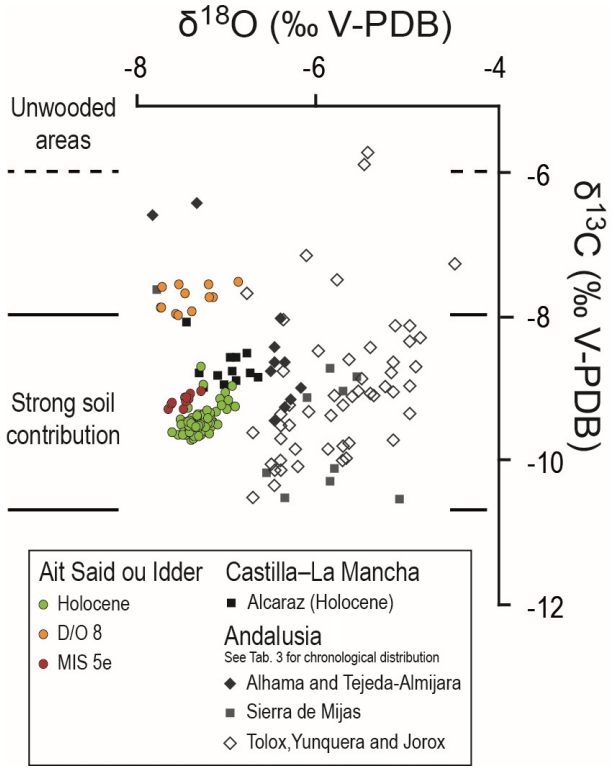

Figure 5. Combined δ^{18}O and δ^{13}C plot for Aït Said ou Idder compared to isotopic data available from some southern Spain tufa deposits. The three phases of tufa depositions are shown for ASI data, but detailed chronological attribution is not available for Andalusian tufa deposits (Table 4): at Frailes, two phases of tufa deposits are dated from the Holocene and from MIS 5, respectively (see Fig. 4), and seven unassigned samples were analysed for isotopes (García-García et al., 2014; Pla-Pueyo et al., 2017); other Andalusian tufa deposits are dated from the Late and Middle Pleistocene with only two samples assigned to the Holocene at Jorox (Durán, 1996). All Alcaraz data (Castilla–La Mancha) are from the Holocene (Andrews et al., 2000). Ranges of carbon isotopic values related to sites where soils are well developed or, conversely, unwooded areas are according to Andrews (2006) and Andrews et al. (1997).

tively wet conditions. The narrower range of carbon isotope variations recorded during MIS 5e at ASI may result from a lower number of samples for the period ($n = 11$) compared to the Holocene ($n = 80$; Table 3); however, considering means and standard deviations, MIS 5e seems to record higher δ^{13}C values, suggesting slightly reduced moisture with regard to the Holocene (Table 3).

These observations are consistent with the environmental reconstructions provided by malacological investigations on the very same profile at ASI (Wackenheim et al., 2020): mollusc assemblages assigned to D–O 8 (i.e. from unit 7) suggest a more open environment under drier conditions than during the Holocene (from units 6 to 1). In the units assigned to MIS 5e, shells are fewer but may suggest wet conditions, similar to those observed during the Holocene.

Palaeoclimatic reconstructions obtained from a transfer function technique on fossil pollen assemblages from marine cores from west and east Iberia (MD95-2042 and ODP 976; Fig. 1) suggest that temperature conditions during MIS 3 interstadials were similar to present-day (Holocene) values (Sánchez Goñi et al., 2002) as also suggested by the ASI δ^{18}O record. Estimated annual rainfall is less reliable due to methodological limits. Nevertheless, the transfer function reconstructs annual precipitation that is similar during D–O 8 and MIS 1 on both sides of Iberia (Sánchez Goñi et al., 2002). However, MIS 3 interstadials, including D–O 8, are millennial-scale events during which the development of temperate and Mediterranean forests remained reduced with respect to the MIS 1 and MIS 5e interglacials (Camuera et al., 2019; Combourieu-Nebout et al., 2002; Sánchez Goñi et al., 2000; Fig. 4). As the moisture signal recorded by tufa δ^{13}C partly depends on the biomass abundance, the higher carbon isotopic values observed at ASI during D–O 8 could reflect the lesser development of the forest cover while the rainfall amount and other moisture factors are consistent with those from interglacial periods.

Comparing the Holocene and MIS 5e interglacials, a compilation of continental and marine palaeoenvironmental records from North Africa and the surrounding areas suggests that mean annual precipitation in Mediterranean Africa, including northern Morocco, was higher than in the present day at both 6–10 and 122–128 ka cal BP (up to 1000 mm yr^{-1}, while present-day mean annual precipitation is $\leq$ 500 mm yr^{-1}) (Larrasoaña et al., 2013). At the regional scale, the palynological data from a long core from the Padul wetland (Andalusia) suggest warmer and/or wetter conditions during the last interglacial compared to the Holocene (Camuera et al., 2019), as in other pollen records from the Mediterranean regions (e.g. Djamali et al., 2008; Litt et al., 2014; Tzedakis and Bennett, 1995). In detail, these different climates may result from strong differences in seasonality: explicitly more marked summer droughts but higher winter precipitation during the last interglacial (Camuera et al., 2019).

The growth of tufa deposits is by nature linked to water availability (Pentecost, 2005); tufa deposition is thus likely to be reduced during dry summers but favoured by autumn/winter rainfall. However, δ^{13}C data from ASI are not consistent with those observations as they rather suggest no difference or even slightly drier conditions during MIS 5e compared to the Holocene. We notice that such strong MIS 5e seasonality may also affect the δ^{18}O signal through the "amount effect" (concentration of precipitation during the wet/cool season) and the seasonal growth of tufa deposition, both of which would lead to the selective record of winter (cool) temperature conditions. In this case, the record of warmer (summer) MIS 5e conditions (as observed in the Padul record) in ASI δ^{18}O would be dampened.

5.3 Comparison with Spanish data

Isotopic data are also available from some tufa deposits from southern Spain (Figs. 1 and 5). The Alcaraz tufa deposits in Castilla–La Mancha have been clearly assigned to the Middle Holocene based on pollen and mollusc data and on two radiocarbon dates (Andrews et al., 2000). At least part of the Alcaraz deposits is contemporaneous with those from ASI (Fig. 4).

Unfortunately, the chronological attribution of the isotopic data available in Andalusia is less precise: the authors provide a chronology based on U–Th dating of several phases of tufa development in the area (Fig. 4) but have not clearly discriminated the geochemical samples according to those phases (Durán, 1996; García-García et al., 2014); i.e. each sample cannot be specifically assigned to a period. Data from Andalusian tufas shown in Fig. 5 are dated from the Late and Middle Pleistocene (Table 4), mostly from MIS 5 except in the Tolox–Yunquera–Jorox area, where more than half of the samples are older than 300 ka (Table 4). Only two samples, at Jorox, are assigned to the Holocene (Durán, 1996). At Frailes, tufa developed during MIS 5 (around 100–110 ka) and then during the Early Holocene, but the specific chronological attribution of the seven samples analysed at this site is not given (García-García et al., 2014; Pla-Pueyo et al., 2017).

As at ASI, most $\delta^{13}C$ values from southern Spain range between ca. $-10\,‰$ and $-8\,‰$, whatever their age, which demonstrates a strong influence from C_3 plant-/soil-zone CO_2 (Andrews, 2006; Fig. 5) and suggests relatively wet conditions. Carbon isotope values from Frailes are higher (up to $-6.35\,‰$; Pla-Pueyo et al., 2017) but remain close to those prevailing at ASI during D–O 8, never reaching values typical of unwooded areas (Fig. 5). On both sides of the western Mediterranean, there is thus no evidence of strong aridity that would have led to evaporation processes and less negative $\delta^{13}C$ values in tufa (Andrews, 2006). This is strongly consistent with the prior assumption that, in pluvial and subtropical areas, tufa deposits are observed during humid (interglacial or interstadial) phases (Butzer et al., 1978; Delgado Castilla, 2009; Depreux et al., 2021; Hamdan and Brook, 2015; Nicod, 2000).

Regarding $\delta^{18}O$ values, larger variations are observed. Alcaraz (Holocene) oxygen data are roughly similar to those from ASI (typically between $-7.5\,‰$ and $-6.7\,‰$; Andrews et al., 2000). At Frailes, $\delta^{18}O$ values remain close to those from ASI (ranging from $-6.70\,‰$ to $-5.67\,‰$; Pla-Pueyo et al., 2017), but those from Pleistocene Andalusian tufa deposits studied by Durán (1996) are significantly higher, whatever their age (Fig. 5). In the Tolox–Yunquera–Jorox area, where a majority of analysed samples are older than 300 ka (Table 4), $\delta^{18}O$ values are the highest and reach up to $-4.2\,‰$ (Fig. 5; Durán, 1996).

Using the Online Isotopes in Precipitation Calculator (OIPC; Bowen, 2022; Bowen and Revenaugh, 2003; IAEA/WMO, 2015), extrapolations of the mean annual $\delta^{18}O$ for modern precipitation are $-7.8 \pm 0.2\,‰$ at ASI, $-8.1 \pm 0.3\,‰$ at Alcaraz and $-7.2 \pm 0.3\,‰$ at Frailes, and they range between ca. $-6\,‰$ and $-5.5\,‰$ at other Andalusian sites. The rainfall water $\delta^{18}O$ values are thus similar at ASI, Frailes and Alcaraz but are up to $3\,‰$ higher at Andalusian sites studied by Durán (1996), the same amplitudes as observed in tufa $\delta^{18}O$ (Fig. 5).

ASI, Frailes and Alcaraz are all at relatively high altitude (> 975 m a.s.l.), while the other tufa deposits studied in Andalusia are below 500 m a.s.l. Tufa $\delta^{18}O$ values decreasing with altitude have been similarly observed at Alpine sites; the combined effects of the progressive rainout of air mass and condensation of water at high altitude result in lower rainfall $\delta^{18}O$ (Andrews et al., 1997). Consequently, the lower $\delta^{18}O$ values observed at ASI, Frailes and Alcaraz are likely to reflect orogenic effects. Furthermore, with the lack of precise chronological attribution of $\delta^{18}O$ data from Andalusia, whether or not Pleistocene interglacials were warmer compared to the Holocene in Spain cannot be solved, in contrast with Morocco where a remarkable consistency is recorded at ASI between MIS 5, D–O 8 and the Holocene.

6 Conclusion and further remarks

Tufa chronological distribution in the southwestern Mediterranean area is mainly driven by climatic parameters: tufas are characteristic of humid (interglacial or interstadial) phases. At Aït Said ou Idder and more generally in both Morocco and southern Spain, phases of maximal tufa deposition appear indeed contemporaneously with periods of maximal development of the Mediterranean forest. Additionally, ASI $\delta^{13}C$ values show no evidence of evaporation processes that may result from strong aridity, which is similarly observed in tufa deposits from Andalusia. However, we may notice that no tufa deposit is reported during D–O 16–17, neither in Morocco nor in southern Spain, while one of the strongest developments of the Mediterranean forest is recorded during this event (Fig. 4). This questions the relationship between tufa deposits and both the duration and the seasonality of humid periods: some humid events might be too short to allow the onset of tufa deposition, and/or contrasting seasons are not favourable to it.

No significant difference in terms of temperature or air mass circulation is observed in the Middle Atlas between the Holocene, D–O interstadial 8 and MIS 5e, according to ASI oxygen stable isotopes. Regarding moisture conditions, D–O 8 is marked by a lesser development of soil and vegetation as conditions were drier than during MIS 1 and MIS 5e. During both these interglacials, wet conditions are recorded according to ASI $\delta^{13}C$, but MIS 5e could be slightly less wet than the Holocene. However, comparisons with regional (marine and continental) climatic records suggest that this observation might actually reflect stronger seasonality during MIS 5e. Such diachronic comparison cannot be extended

Table 4. Number of samples analysed for stable isotopes in Andalusia and their chronological distribution according to Durán (1996), García-García et al. (2014) and Pla-Pueyo et al. (2017).

	> 300 ka	MIS 7	MIS 5	MIS 3	MIS 2	MIS 1	Total samples
Alhama and Tejeda–Almijara		5	6	2			13
Sierra des Mijas	1	4	5		2		12
Tolox, Yunquera and Jorox	32		18		1	2	53
Frailes			?			?	7
Total	33	9	≥ 29	2	3	≥ 2	85

to Morocco and southern Spain yet, nor can comparison between both sides of the Strait of Gibraltar be made because of the lack of well-dated isotopic data from tufa deposits in the area.

Our preliminary investigations thus demonstrate that calcareous tufa deposits have strong potential to feed discussions on climate variability, at different scales of space and time, in the southeastern Mediterranean area where they appear to be well represented. However, new dates and new isotopic data are required from both already known sites and newly investigated sequences.

Data availability. Full data are available on request to Julie Dabkowski (julie.dabkowski@lgp.cnrs.fr).

Sample availability. Tufa samples are available on request to Julie Dabkowski (julie.dabkowski@lgp.cnrs.fr).

Author contributions. JD, QW, NLL and LB conducted the fieldwork, with contributions from JFB. QW performed the malacological analyses under the supervision of NLL and provided selected material for radiocarbon dating on shells. CF and OT performed the U–Th series analyses on calcite. DF ran the isotopic analyses at the SSMIM (MNHN, Paris) and provided support to JD in terms of data discussion. The manuscript was written by JD with contributions from all the co-authors.

Competing interests. The contact author has declared that neither they nor their co-authors have any competing interests.

Disclaimer. Publisher's note: Copernicus Publications remains neutral with regard to jurisdictional claims in published maps and institutional affiliations.

Acknowledgements. The authors thank both reviewers for their kind and constructive comments on the manuscript.

Financial support. Fieldwork and analyses at Aït Said ou Idder were mostly funded by the PALEOMEX (INSU–INEE) Transect Maghreb research programme (Jean-François Berger). Radiocarbon ages have been supported by the LMC14 (CEA, Gif-sur-Yvette) Artemis programme and by the Czech Science Foundation (grant no. P504/17-05696S).

Review statement. This paper was edited by Becky Briant and reviewed by Jonathan Holmes and Philip Hopley.

References

Andrews, J. E.: Palaeoclimatic records from stable isotopes in riverine tufas: Synthesis and review, Earth-Sci. Rev., 75, 85–104, https://doi.org/10.1016/j.earscirev.2005.08.002, 2006.

Andrews, J. E., Riding, R., and Dennis, P. F.: The stable isotope record of environmental and climatic signals in modern terrestrial microbial carbonates from Europe, Palaeogeogr. Palaeocl., 129, 171–189, https://doi.org/10.1016/S0031-0182(96)00120-4, 1997.

Andrews, J. E., Pedley, M., and Dennis, P. F.: Palaeoenvironmental records in Holocene Spanish tufas: a stable isotope approach in search of reliable climatic archives, Sedimentology, 47, 961–978, 2000.

Azennoud, K., Baali, A., Ait Brahim, Y., Ahouach, Y., and Hakam, O.: Climate controls on tufa deposition over the last 5000 years: A case study from Northwest Africa, Palaeogeogr. Palaeocl., 586, 110767, https://doi.org/10.1016/j.palaeo.2021.110767, 2022.

Boudad, L., Kabiri, L., Farkh, S., Falguères, C., Rousseau, L., Beauchamp, J., Nicot, É., and Cairanne, G.: Datation par la méthode U/Th d'un travertin quaternaire du Sud-Est marocain: implications paléoclimatiques pendant le Pléistocène moyen et supérieur, C. R. Geosci., 335, 469–478, https://doi.org/10.1016/S1631-0713(03)00081-6, 2003 (in French with abridged English version).

Bourdon, B., Henderson, G. M., Lundstrom, C. C., and Turner, S.: U-series geochemistry, Rev. Mineral. Geochem., 52, 1–656, 2003.

Bowen, G. J.: The Online Isotopes in Precipitation Calculator, version 3.1, https://wateriso.utah.edu/waterisotopes/pages/data_access/oipc_citation.html, last access: 22 February 2022.

Bowen, G. J. and Revenaugh, J.: Interpolating the isotopic composition of modern meteoric precipitation: isotopic composi-

tion of modern precipitation, Water Resour. Res., 39, 1299, https://doi.org/10.1029/2003WR002086, 2003.

Butzer, K. W., Stuckenrath, R., Bruzewicz, A. J., and Helgren, D. M.: Late Cenozoic Paleoclimates of the Gaap Escarpment, Kalahari margin, South Africa, Quaternaty Res., 10, 310–339, https://doi.org/10.1016/0033-5894(78)90025-X, 1978.

Camuera, J., Jiménez-Moreno, G., Ramos-Román, M. J., García-Alix, A., Toney, J. L., Anderson, R. S., Jiménez-Espejo, F., Bright, J., Webster, C., Yanes, Y., and Carrión, J. S.: Vegetation and climate changes during the last two glacial-interglacial cycles in the western Mediterranean: A new long pollen record from Padul (southern Iberian Peninsula), Quaternary Sci. Rev., 205, 86–105, https://doi.org/10.1016/j.quascirev.2018.12.013, 2019.

Capezzuoli, E., Gandin, A., and Pedley, M.: Decoding tufa and travertin (fresh water carbonates) in the sedimentary record: The state of the art, Sedimentology, 61, 1–21, https://doi.org/10.1111/sed.12075, 2014.

Cheng, H., Edward, R. L., Shen, C.-C., Polyak, V. J., Asmerom, Y., Woodhead, J. , Hellstrom, J., Wang, Y., Kong, X. , Spötl, C., Wang X., and Alexander Jr., E. C.: Improvements in 230Th dating, ^{230}Th and ^{234}U half-life values, and U–Th isotopic measurements by multi-collector inductively coupled plasma mass spectrometry, Earth Planet. Sc. Lett., 371–372, 82–91, https://doi.org/10.1016/j.epsl.2013.04.006, 2013.

Combourieu-Nebout, N. C., Turon, J. L., Zahn, R., Capotondi, L., Londeix, L., and Pahnke, K.: Enhanced aridity and atmospheric high-pressure stability over the western Mediterranean during the North Atlantic cold events of the past 50 k.y., Geology, 30, 863–866, https://doi.org/10.1130/0091-7613(2002)030<0863:EAAAHP>2.0.CO;2, 2002.

Dabkowski, J.: High potential of calcareous tufas for integrative multidisciplinary studies and prospects for archaeology in Europe, J. Archaeol. Sci., 52, 72–83, https://doi.org/10.1016/j.jas.2014.07.013, 2014.

Dabkowski, J.: The late-Holocene tufa decline in Europe: Myth or reality?, Quaternary Sci. Rev., 230, 106141, https://doi.org/10.1016/j.quascirev.2019.106141, 2020.

Dabkowski, J. and Limondin-Lozouet, N.: Intensities (temperature and humidity) of MIS 11 and MIS 5e interglacials compared to the Holocene using stable isotopes from Northern France (Paris Basin) tufa deposits, Quaternary Res., 1–2, https://doi.org/10.1017/qua.2021.66, 2021.

Dabkowski, J., Limondin-Lozouet, N., Antoine, P., Marca-Bell, A., and Andrews, J.: Enregistrement des variations climatiques au cours des interglaciaires d'après l'étude des isotopes stables de la calcite de tufs calcaires pléistocénes du nord de la France : exemple des séquences de Caours (SIM 5e ; Somme) et de La Celle-sur-Seine (SIM 11; Seine-et-Marne), Quaternaire, 22, 275–283, https://doi.org/10.4000/quaternaire.6010, 2011 (in French).

Delannoy, J.-J., Guendon, J.-L., Quinif, Y., and Roiron, P.: Formaciones travertínicas del piedemonte mediterráneo de la Serranía de Ronda (Málaga), Cuadernos de geografía, 54, 189–222, 1993 (in Spanish).

Delgado Castilla, L.: Edades U/Th de los travertinos del cuaternario reciente de la cuenca de Tabernas, Almeria (SE de España) y sus implicaciones en la evolucion geodinámica y paleoambiental de esta, in: Contribuciones al Estudio del Periodo Cuaternario – Resúmenes XII Reunión Nacional de Cuaternario, edited by: Lario, J. and Silva, P. G., Aequa, Ávila, Spain, 45–46, 2007 (in Spanish).

Delgado Castilla, L.: Edades U/Th de los travertinos del cuaternario reciente de la cuenca de Tabernas, Almería: implicaciones en su evolución geodinámica y paleoambiental, Revista Cuaternario y Geomorfología, 23, 65–76, 2009 (in Spanish).

Depreux, B., Lefèvre, D., Berger, J.-F., Segaoui, F., Boudad, L., El Harradji, A., Degeai, J.-P., and Limondon-Lozouet, N.: Alluvial records of the African Humid Period from the NW African highlands (Moulouya basin, NE Morocco), Quaternary Sci. Rev., 255, 106807, https://doi.org/10.1016/j.quascirev.2021.106807, 2021.

Djamali, M., de Beaulieu, J.-L., Shah-hosseini, M., Andrieu-Ponel, V., Ponel, P., Amini, A., Akhani, H., Leroy, S. A. G., Stevens, L., Lahijani, H., and Brewer, S.: A late Pleistocene long pollen record from Lake Urmia, NW Iran, Quaternary Res., 69, 413–420, https://doi.org/10.1016/j.yqres.2008.03.004, 2008.

Douville, E., Sallé, E., Frank, N., Eisele, M., Pons-Branchu, E., and Ayrault, S.: Rapid and accurate U–Th dating of ancient carbonates using inductively coupled plasma-quadrupole mass spectrometry, Chem. Geol., 272, 1–11, https://doi.org/10.1016/j.chemgeo.2010.01.007, 2010.

Durán, J. J.: Los sistemas kársticos de la provincia de Málaga y su evolución: Contribución al conocimiento paleoclimático del Cuaternario en el Mediterráneo occidental, PhD thesis, Complutense University of Madrid, Spain, 409 pp., 1996 (in Spanish).

Falguères, C., Weisrock, A., Ghaleb, B., Haddad, M., Janati-Idrissi, N., Bejjit, L., Gourari, L., Rousseau, L., Boudad, L., Taous, A., Beauchamp, J., and Pozzi, J.-P.: Datations par les series de l'uranium et par ESR des travertins du Pleistocene superieur (MIS5) de Sefrou-El Kalaa (Maroc) et leurs implications paleoenvironnementales, in: Actes de la Septième Rencontre des Quaternaristes Marocains (RQM7), Quaternaire du Nord-Ouest de l'Afrique, Agadir, Maroc, 273–281, ISBN: 978-9954-0-5399-7, 2016 (in French).

Fletcher, W. J. and Sánchez Goñi, M. F.: Orbital- and sub-orbital-scale climate impacts on vegetation of the western Mediterranean basin over the last 48,000 yr, Quaternary Res., 70, 451–464, https://doi.org/10.1016/j.yqres.2008.07.002, 2008.

Ford, T. D. and Pedley, H. M.: A review of tufa and travertine deposits of the world, Earth-Sci. Rev., 41, 117–175, https://doi.org/10.1016/S0012-8252(96)00030-X, 1996.

Forman, S. L., Hockaday, W., Liang, P., and Ramsey, A.: Radiocarbon age offsets, ontogenetic effects, and potential old carbon contributions from soil organic matter for pre-bomb and modern detritivorous gastropods from central Texas, USA, Palaeogeogr. Palaeocl., 583, 110671, https://doi.org/10.1016/j.palaeo.2021.110671, 2021.

García-García, F., Pla-Pueyo, S., Nieto, L. M., and Viseras, C.: Sedimentology of geomorphologically controlled Quaternary tufas in a valley in southern Spain, Facies, 60, 53–72, https://doi.org/10.1007/s10347-013-0361-5, 2014.

Ghaleb, B., Falguères, C., Carlut, J., Pozzi, J. P., Mahieux, G., Boudad, L., and Rousseau, L.: Timing of the Brunhes-Matuyama transition constrained by U-series disequilibrium, Sci. Rep.-UK, 9, 6039, https://doi.org/10.1038/s41598-019-42567-2, 2019.

González Martín, J. A. and González Amuchastegui, M. J. (Eds.): Las Tobas en España, SEG, Badajoz, ISBN: 978-84-697-1469-0, 2014 (in Spanish).

Goudie, A. S., Viles, H. A., and Pentecost, A.: The late-Holocene tufa decline in Europe, The Holocene, 3, 181–186, 1993.

Granai, S. and Wackenheim, Q.: La datation radiocarbone sur coquilles de mollusques continentaux: quelles limites et quels usages?, in: Mesurer le temps de l'âge du Bronze, Actes de la journée thématique de l'APRAB, Saint-Germain-en-Laye, France, 21–33, 2022 (in French).

Hamdan, M. A. and Brook, G. A.: Timing and characteristics of Late Pleistocene and Holocene wetter periods in the Eastern Desert and Sinai of Egypt, based on ^{14}C dating and stable isotope analysis of spring tufa deposits, Quaternary Sci. Rev., 130, 168–188, https://doi.org/10.1016/j.quascirev.2015.09.011, 2015.

Hiess, J., Condon, D., McLean, N., and Noble, S. R.: $^{238}U/^{235}U$ systematics in terrestrial uranium-bearing minerals, Science, 335, 1610–1614, https://doi.org/10.1126/science.1215507, 2012.

Ivanovich, M. and Harmon, R. S.: Uranium-series Disequilibrium: Applications to Earth, Marine and Environmental Sciences, 2nd edn., Clarendon Press, Oxford, ISBN 978-1-4020-4496-0, 1992.

Larrasoaña, J. C., Roberts, A. P., and Rohling, E. J.: Dynamics of Green Sahara Periods and Their Role in Hominin Evolution, PLoS ONE, 8, e76514, https://doi.org/10.1371/journal.pone.0076514, 2013.

Lefèvre, D.: Formations continentales pléistocenes et paléoenvironnements sédimentaires dans le bassin de Ksabi (Moyenne Moulouya, Maroc), Bulletin de l'Association française pour l'étude du quaternaire, 26, 101–113, https://doi.org/10.3406/quate.1989.1897, 1989 (in French).

Limondin-Lozouet, N.: Successions malacologiques à la charnière Glaciaire/Interglaciaire: du modèle Tardiglaciaire-Holocène aux transitions du Pleistocène, Quaternaire, 22, 211–220, 2011 (in French).

Limondin-Lozouet, N. and Preece, R. C.: Quaternary perspectives on the diversity of land snail assemblages from northwestern Europe, J. Molluscan Stud., 80, 224–237, https://doi.org/10.1093/mollus/eyu047, 2014.

Limondin-Lozouet, N., Haddoumi, H., Lefèvre, D., Ghamizi, M., Aouraghe, H., and Salel, T.: Holocene molluscan succession from NE Morocco: Palaeoenvironmental reconstruction and biogeographical implications, Quatern. Int., 302, 61–76, https://doi.org/10.1016/j.quaint.2012.11.036, 2013.

Lionello, P. (Ed.): The climate of the Mediterranean region: from the past to the future, 1st edn., Elsevier, London; Waltham, MA, 502 pp., ISBN: 978-0-12-416042-2, 2012.

Litt, T., Pickarski, N., Heumann, G., Stockhecke, M., and Tzedakis, P. C.: A 600,000 year long continental pollen record from Lake Van, eastern Anatolia (Turkey), Quaternary Sci. Rev., 104, 30–41, https://doi.org/10.1016/j.quascirev.2014.03.017, 2014.

Ludwig, K. R. and Paces, J. B.: Uranium-series dating of pedogenic silica and carbonate, Cratere Flat, Nevada, Geochim. Geochosmochim. Ac., 66, 487–506, 2002.

Margari, V., Skinner, L. C., Tzedakis, P. C., Ganopolski, A., Vautravers, M., and Shackleton, N. J.: The nature of millennial-scale climate variability during the past two glacial periods, Nat. Geosci., 3, 127–131, https://doi.org/10.1038/ngeo740, 2010.

Martìn-Algarra, A., Martìn-Martìn, M., Andreo, B., Julià, R., and González-Gómez, C.: Sedimentary patterns in perched spring travertines near Granada (Spain) as indicators of the paleohydrological and paleoclimatological evolution of a karst massif, Sediment. Geol., 161, 217–228, https://doi.org/10.1016/S0037-0738(03)00115-5, 2003.

Mercier, N., Hatté, C., Fontugne, M., Reyss, J.-L., Valladas, H., Wengler, L., Brugal, J.-P., Ouammou, A., and Weisrock, A.: Chronology of Upper Pleistocene sequences at Sidi Messaoud (wadi Noun, southwestern Morocco) based on ^{14}C, optical and U-series dating, Quat. Geochronol., 4, 326–334, https://doi.org/10.1016/j.quageo.2009.02.019, 2009.

New, M., Hulme, M., and Jones, P.: Representing Twentieth-Century Space–Time Climate Variability. Part II: Development of 1901–96 Monthly Grids of Terrestrial Surface Climate, J. Climate, 13, 2217–2238, https://doi.org/10.1175/1520-0442(2000)013<2217:RTCSTC>2.0.CO;2, 2000.

Nicod, J.: Sources et hydrosystèmes karstiques des régions arides et semi-arides. Essai géographique, Karstologia, 35, 47–58, https://doi.org/10.3406/karst.2000.2458, 2000 (in French).

North Greenland Ice Core Project members: High-resolution record of Northern Hemisphere climate extending into the last interglacial period, Nature, 431, 147–151, https://doi.org/10.1038/nature02805, 2004.

Ollivier, V., Guendon, J.-L., Ali, A., Roiron, P., and Ambert, P.: Evolution postglaciaire des environnements travertineux provençaus et alpins: nouveau cadre chronologique, faciès et dynamiques morphosédimentaires, Quaternaire, 17, 51–67, 2006 (in French).

Pedley, H. M.: Classification and environmental models of cool freshwater tufas, Sediment. Geol., 68, 143–154, https://doi.org/10.1016/0037-0738(90)90124-C, 1990.

Pedley, M., Martín, J. A. G., Delgado, S. O., and García Del Cura, M. Á.: Sedimentology of Quaternary perched springline and paludal tufas: criteria for recognition, with examples from Guadalajara Province, Spain, Sedimentology, 50, 23–44, https://doi.org/https://doi-org.inee.bib.cnrs.fr/10.1046/j.1365-3091.2003.00502.x, 2003.

Pentecost, A.: British travertines: a review, P. Geologist. Assoc., 104, 23–39, https://doi.org/10.1016/S0016-7878(08)80152-6, 1993.

Pentecost, A.: The quaternary travertine deposits of Europe and Asia Minor, Quaternary Sci. Rev., 14, 1005–1028, https://doi.org/10.1016/0277-3791(95)00101-8, 1995.

Pentecost, A.: Travertine, Springer-Verlag, Berlin Heidelberg, 445 pp., https://doi.org/10.1007/1-4020-3606-X, 2005.

Pigati, J. S., McGeehin, J. P., Muhs, D. R., and Bettis, E. A.: Radiocarbon dating late Quaternary loess deposits using small terrestrial gastropod shells, Quaternary Sci. Rev., 76, 114–128, https://doi.org/10.1016/j.quascirev.2013.05.013, 2013.

Pla-Pueyo, S., Viseras, C., Henares, S., Yeste, L. M., and Candy, I.: Facies architecture, geochemistry and palaeoenvironmental reconstruction of a barrage tufa reservoir analog (Betic Cordillera, S. Spain), Non-Mar. Carbonates Multidiscip. Approach, 437, 15–36, https://doi.org/10.1016/j.quaint.2016.05.022, 2017.

Prado-Pérez, A. J., Huertas, A. D., Crespo, M. T., Sánchez, A. M., and Pérez Del Villar, L.: Late Pleistocene and Holocene mid-latitude palaeoclimatic and palaeoenvironmental reconstruction: an approach based on the isotopic record from a travertine formation in the Guadix-Baza basin, Spain, Geol. Mag., 150, 602–625, https://doi.org/10.1017/S0016756812000726, 2013.

Rousseau, L., Beauchamp, J., Bahain, J.-J., Boudad, L., Deschamps, P., Falguères, C., Ghaleb, B., Lartigot, A.-S., and Pozzi, J.-P.: Premiers résultats d'une étude pluridisciplinaire sur des

travertins quaternaires du Maroc, Quaternaire, 17, 343–350, https://doi.org/10.4000/quaternaire.913, 2006 (in French).

Rousseau, L., Falguères, C., Pozzi, J.-P., Weisrock, A., Ghaleb, B., Mahieux, G., Beauchamp, J., Ouammou, A., Haddad, M., Bejjit, L., Charif, A., and Lauriol, B.: Chronologie et enregistrements climatiques dans les dépôts travertineux du Maroc, L'Anthropologie, 121, 82–89, https://doi.org/10.1016/j.anthro.2017.03.009, 2017 (in French).

Sánchez Goñi, M., Cacho, I., Turon, J., Guiot, J., Sierro, F., Peypouquet, J., Grimalt, J., and Shackleton, N.: Synchroneity between marine and terrestrial responses to millennial scale climatic variability during the last glacial period in the Mediterranean region, Clim. Dyamn., 19, 95–105, https://doi.org/10.1007/s00382-001-0212-x, 2002.

Sánchez Goñi, M. F., Turon, J.-L., Eynaud, F., and Gendreau, S.: European Climatic Response to Millennial-Scale Changes in the Atmosphere–Ocean System during the Last Glacial Period, Quaternary Res., 54, 394–403, https://doi.org/10.1006/qres.2000.2176, 2000.

Sánchez Goñi, M. F., Landais, A., Fletcher, W. J., Naughton, F., Desprat, S., and Duprat, J.: Contrasting impacts of Dansgaard–Oeschger events over a western European latitudinal transect modulated by orbital parameters, Quaternary Sci. Rev., 27, 1136–1151, https://doi.org/10.1016/j.quascirev.2008.03.003, 2008.

Shackleton, N. J., Fairbanks, R. G., Chiu, T., and Parrenin, F.: Absolute calibration of the Greenland time scale: implications for Antarctic time scales and for $\Delta^{14}C$, Quaternary Sci. Rev., 23, 1513–1522, https://doi.org/10.1016/j.quascirev.2004.03.006, 2004.

Tzedakis, P. C. and Bennett, K. D.: Interglacial vegetation succession: A view from southern Europe, Quaternary Sci. Rev., 14, 967–982, https://doi.org/10.1016/0277-3791(95)00042-9, 1995.

Vaudour, J.: Introduction à l'étude des édifices travertineux holocènes, Méditerranée, 57, 3–10, https://doi.org/10.3406/medit.1986.2356, 1986 (in French).

Vaudour, J.: Évolution holocène des travertins de vallée dans le Midi méditéranéen français, Geogr. Phys. Quatern., 48, 315–326, 1994 (in French).

Wackenheim, Q., Limondin-Lozouet, N., Dabkowski, J., Boudad, L., and Berger, J.-F.: Reconstructing mid-Holocene palaeoenvironmental dynamic in the Middle Atlas (Morocco) inferred from non-marine molluscs succession of the Aït said ou Idder tufa sequence, Quaternaire, 31, 145–164, https://doi.org/10.4000/quaternaire.13783, 2020.

Weisrock, A.: Variations climatiques et périodes de sédimentation carbonatée à l'holocène, L'âge des dépôts, Méditerranée, 57, 165–167, https://doi.org/10.3406/medit.1986.2388, 1986 (in French).

Weisrock, A., Rousseau, L., Reyss, J.-L., Falguères, C., Ghaleb, B., Bahain, J.-J., Beauchamp, J., Boudad, L., Mercier, N., Mahieux, G., Pozzi, J.-P., and Abderrahmane Ouammou, N. J.-I.: Travertins de la bordure nord du Sahara marocain: dispositifs morphologiques, datations U/Th et indications paléoclimatiques, Géomorphologie, 14, 153–167, https://doi.org/10.4000/geomorphologie.6793, 2008 (in French).

Wengler, L. and Vernet, J.-L.: Vegetation, sedimentary deposits and climates during the Late Pleistocene and Holocene in eastern Morocco, Palaeogeogr. Palaeocl., 94, 141–167, https://doi.org/10.1016/0031-0182(92)90117-N, 1992.

Wolf, D., García-Tortosa, F. J., Richter, C., Dabkowski, J., Roettig, C. B., and Faust, D.: Holocene landscape evolution in the Baza Basin (SE-Spain) as indicated by fluvial dynamics of the Galera River, Quaternary Science Advances, 4, 100030, https://doi.org/10.1016/j.qsa.2021.100030, 2021.

Zielhofer, C., Fletcher, W. J., Mischke, S., De Batist, M., Campbell, J. F. E., Joannin, S., Tjallingii, R., El Hamouti, N., Junginger, A., Stele, A., Bussmann, J., Schneider, B., Lauer, T., Spitzer, K., Strupler, M., Brachert, T., and Mikdad, A.: Atlantic forcing of Western Mediterranean winter rain minima during the last 12,000 years, Quaternary Sci. Rev., 157, 29–51, https://doi.org/10.1016/j.quascirev.2016.11.037, 2017.

E&G Quaternary Sci. J., 71, 59–81, 2022
https://doi.org/10.5194/egqsj-71-59-2022

Open Access E&G Quaternary Science Journal

Research article

Chronostratigraphic and geomorphologic challenges of last glacial loess in Poland in the light of new luminescence ages

Ludwig Zöller[1,2], Manfred Fischer[1], Zdzisław Jary[3], Pierre Antoine[4], and Marcin Krawczyk[3]

[1]Geomorphology Chair, University of Bayreuth, 95440 Bayreuth, Germany
[2]BayCEER, University of Bayreuth, 95440 Bayreuth, Germany
[3]Institute of Geography and Regional Development, Faculty of Earth Sciences and Environmental Management, University of Wrocław, ul. Cybulskiego 34 (2nd floor), 50-205 Wrocław, Poland
[4]Laboratoire de Géographie Physique, Environnements Quaternaires et Actuels, CNRS, 1 Pl. A. Briand, 92195 Meudon CEDEX, France

Correspondence: Ludwig Zöller (ludwig.zoeller@uni-bayreuth.de)

Relevant dates: Received: 16 February 2021 – Revised: 29 January 2022 – Accepted: 23 February 2022 – Published: 1 April 2022

How to cite: Zöller, L., Fischer, M., Jary, Z., Antoine, P., and Krawczyk, M.: Chronostratigraphic and geomorphologic challenges of last glacial loess in Poland in the light of new luminescence ages, E&G Quaternary Sci. J., 71, 59–81, https://doi.org/10.5194/egqsj-71-59-2022, 2022.

Abstract: The aim of this study is to check the validity of luminescence ages obtained from last glacial–interglacial Polish loess palaeosol sequences (LPSs) by several established current protocols, with respect to sound geomorphological and chronostratigraphic interpretations. We report 38 new optically stimulated luminescence (OSL) ages from fine-grained (4–11 µm) quartz separates extracted from four loess palaeosol sequences in Poland, measured in the Bayreuth Luminescence Laboratory, Germany. The investigated sections are situated in Lower Silesia in the southwest (Zaprężyn, Trzebnica Hills, and Biały Kościół, Strzelin Hills), the Sandomierz Upland (Złota) in central Poland, and the Volhynian Upland (Tyszowce) in the east, allowing for regional comparison. From one Silesian section (Biały Kościół) 12 new post-infrared infrared stimulated luminescence (pIRIR) ages are presented in addition to the quartz ages of identical sample material. The obtained ages are compared to already published independently elaborated middle-grain (45–63 µm) and coarse-grain (90–125 µm) quartz ages and pIRIR ages from fine grains produced in the Gliwice Luminescence Laboratory (Poland). This comparison shows that in many cases the middle- and coarse-grain quartz ages underestimate the fine-grain quartz ages, but a general rule has not been able to be established so far, likely due to different geological origin of the quartz grains. Even fine-grain quartz ages $\geq\sim 50$ ka may be underestimated with respect to lithostratigraphic expectations. For pIRIR ages, however, no evidence for age underestimates has been found in the studied sections, but they are more easily prone to age overestimates due to unknown residual doses at deposition in a periglacial environment.

Basic agreement between the luminescence-based chronologies elaborated in the two involved laboratories can be stated for the first time in contrast to other previous studies. The observed age differences are, however, critical for the accurate time bracketing of geomorphologic and pedostratigraphic features such as ice wedging, thermokarst erosion events, and interstadial soil formations and for their attribution to marine isotope stages. Alternative interpretations are discussed including possible periglacial mirroring of pre-LGM ice advances (Ristinge and Klintholm advances) in the southwestern

Baltic Sea area. The uncertainty in luminescence ages from pre-Holocene loess due to fossil ice during permafrost conditions is the major systematic error source which will be addressed but at present is far from an unambiguous solution. The present study focuses on a complex of interstadial soils now labelled L1SS1 and on harsh periglacial climate afterwards and before, yielding some unexpected results for the timing of ice wedging and thermokarst processes. In order not to leave the users alone with the decision about the most credible dating, the suggested way forwards is to simultaneously apply various luminescence dating protocols including different quartz grain sizes and pIRIR from fine polymineral grains, as an honest approach to reliable time bracketing of geomorphological processes and stratigraphic events under debate. A refinement of this approach remains challenging as far as the sole reliable dating protocol is not ensured.

Kurzfassung:

Das Ziel dieser Studie ist die Überprüfung der Aussagekraft von Lumineszenzaltern aus Löss-Paläoboden-Sequenzen (LPS) des letzten Glazial-Interglazialzyklus in Polen, welche durch verschiedene etablierte aktuelle Protokolle erzielt wurden, unter Berücksichtigung gut fundierter geomorphologischer und chronostratigraphischer Interpretationen. Wir präsentieren 38 neue OSL-Alter von feinkörnigen (4–11 µm) Quarz-Separaten aus vier LPS in Polen, die im Lumineszenzlabor in Bayreuth (Deutschland) gemessen wurden. Die untersuchten Profile liegen in Niederschlesien (Zaprężyn, Trzebnica Hügelland und Biały Kościół, Strzelin Hügelland), im Sandomierz Oberland (Złota), und im Wolhynischen Oberland (Tyszowce) im Osten, wodurch auch regionale Vergleiche ermöglicht werden. Von einem schlesischen Profil (Biały Kościół) werden zusätzlich zu den Quarz-Altern 12 neue pIRIR-Alter vom identischen Probenmaterial mitgeteilt. Die erzielten neuen Alter werden mit bereits publizierten unabhängig erarbeiteten Quarz-Mittelkorn- (45–63 µm) und Quarz-Grobkorn- (90–125 µm) Altern aus dem Lumineszenz-Labor in Gliwice (Polen) verglichen. Dieser Vergleich zeigt, dass in vielen Fällen die Mittelkorn- und Grobkorn-Quarzalter die Feinkorn-Quarzalter unterschätzen. Aber eine generelle Regel kann noch nicht erstellt werden, vermutlich aufgrund unterschiedlicher geologischer Herkunft der Quarzkörner. Selbst Quarz-Feinkornalter $\geq\sim 50$ ka können in Bezug auf lithostratigraphische Erwartungen unterschätzt sein. Für pIRIR-Alter wurden jedoch in den untersuchten Profilen keine Hinweise auf Unterschätzung gefunden, sie sind hingegen eher anfällig für Altersüberschätzungen aufgrund unbekannter Residual-Dosen (Restalter) bei Ablagerung in einem periglazialen Milieu.

Grundsätzliche Übereinstimmung zwischen den Lumineszenz-basierten Chronologien aus den beiden involvierten Laboratorien kann erstmals – im Gegensatz zu früheren anderen Studien – festgestellt werden. Die beobachteten Altersunterschiede erweisen sich jedoch als kritisch für eine exakte zeitliche Eingrenzung geomorphologischer und pedostratigraphischer Merkmale wie Eiskeilbildungen, Thermokarst-Erosionsereignisse und interstadiale Bodenbildungen sowie deren Zuordnung zu Marinen Isotopen-Stadien. Alternative Interpretationen werden diskutiert einschließlich periglazialer Spiegelung von Prä-LGM-Eisvorstößen (Ristinge und Klintholm-Vorstöße) im Gebiet der südwestlichen Ostsee. Die Unsicherheit von Lumineszenz-Altern aus prä-Holozänem Löss aufgrund fossilen Bodeneises während periglazialer Verhältnisse stellt die bedeutendste systematische Fehlerquelle dar, die näher angesprochen wird aber noch weit von einer unzweideutigen Lösung entfernt ist. Die vorliegende Studie fokussiert auf einen Komplex von Interstadialböden, der jetzt als L1SS1 bezeichnet wird, sowie auf harsche periglaziale Klimabedingungen davor und danach, und führt zu einigen unerwarteten Ergebnissen für die Zeitstellung von Eiskeilbildungen und Thermokarst-Prozessen. Um die Anwender nicht alleine zu lassen mit der Entscheidung über die glaubwürdigste Datierung wird für den Weg vorwärts vorgeschlagen, simultan verschiedene Lumineszenzdatierungs-Protokolle anzuwenden einschließlich unterschiedlicher Quarz-Korngrößen und pIRIR an der polymineralischen Feinkornfraktion. Dieser Weg stellt den aufrichtigen Versuch dar, eine verlässliche zeitliche Eingrenzung in Frage stehender geomorphologischer Prozesse und stratigraphischer Ereignisse vorzunehmen. Eine Verfeinerung dieses Ansatzes bleibt eine Herausforderung solange ein einzig verlässliches Datierungsprotokoll nicht abgesichert ist.

1 Introduction

The European loess belt, extending from northern France to the Caspian Lowland (Haase et al., 2007; Antoine, 2013), is split into a northern and a southern branch by the Central European Uplands and the Carpathian Mountains. Whereas a largely conclusive and elaborate chronostratigraphy of loess palaeosol sequences (LPSs) for the last interglacial–glacial cycle was already available for the southern branch and the western part of the northern branch (Antoine et al., 2015; Fuchs et al., 2013; Moine et al., 2017; Rousseau et al., 2017), gaps of knowledge concerning the chronology persisted for the rest of the northern branch, in particular for areas east of the Rhine. The international workshop "Closing the gap – North Carpathian loess traverse in the Eurasian loess belt" held in Wrocław, Poland, in 2011 (Jary, 2011) brought together loess experts from many European countries and from the USA. It aimed at addressing pending problems in European loess chronostratigraphy. Due to the proximity to the maximum extent of the last glacial Scandinavian Ice Sheet (SIS), the northern branch is expected to be best suited for investigating the impact of temporal SIS dynamics on lithostratigraphic and pedostratigraphic characteristic features of LPSs off the ice margin. Considering the differentiation between the global LGM and regional LGM (Hughes et al., 2013) as well as the ice dynamics in the SW sector of the SIS (Lüthgens et al., 2020), a premature correlation with marine isotope stages (MISs) should be set aside to avoid jumping to conclusions.

Last glacial loess in southwestern Poland (Silesia) was deposited closer to the maximum ice advance of the Scandinavian Ice Sheet (SIS) than in the eastern part of Poland. The Odra ice lobe in particular reached quite far south in the German state of Brandenburg (Brandenburg stage) and in western Poland (Leszno stage; see Marks, 2005, 2011). Even if there is now luminescence dating evidence that the regional last glacial maximum (R-LGM; cf. Hughes et al., 2013) predates the global LGM by several thousand years (Lüthgens and Böse, 2011; Hardt et al., 2016), it can be expected that witnesses of harsh periglacial climate such as ice wedge networks are more probably found in ice-proximal than in distal loess. This instance is of special interest and advantageous for geomorphology, palaeoclimatology and loess stratigraphy. A disadvantage, however, is the fact that brutal collapse of ice wedge networks linked to permafrost decay (Murton, 2001) induces intense thermokarst erosion events in loess sequences (Antoine, 2013; Antoine et al., 2014). Such processes, already evidenced for the northern loess belt branch in western European LPSs (Antoine et al., 2015), lead to major erosional unconformities and, thus, to stratigraphic gaps, easily causing misinterpretations of the timing of those processes. Similar periglacial features are to be expected in Polish loess and will be one focus of this contribution.

Thermoluminescence (TL) and optically stimulated luminescence (OSL) dating have been widely applied to loess in Poland since the work by Butrym and Maruszczak (1983). At the end of the last century TL loess chronostratigraphy in Poland was well correlated with the marine record (Maruszczak, 1991, 2001), but these results have often been inconsistent with OSL ages (see review by Moska and Bluszcz, 2013). Luminescence dating methods applied to sediments are based on the accumulation of ionizing radiation damage in mineral grains after the last resetting of the latent (inherent) signal. In sediments resetting occurs by exposure to daylight (e.g. Preusser et al., 2008). Sources of error in luminescence dating are manifold, but before they can – perhaps – be eliminated, they must be detected and addressed. The main systematical error sources for sediments include incomplete resetting at deposition and the approximation of a representative past water content since burial.

Furthermore, redeposition of loess beds by gelifluction lobes (and also hillwash processes) in periglacial environments poses a major problem for luminescence dating, as geliflucted material consists of a mixture of optically reset (bleached) and unbleached components or even completely unbleached older loess-like sediments (Zöller, 1989). In narrow sections, the unconformities of such beds are often hard to detect and easily cause misinterpretations. Radiocarbon dating of buried organic material may also suffer from such problems, besides other complications affecting radiocarbon dating of loess beds, for example, post-burial C-isotope exchange (e.g. Gocke et al., 2010; Scheidt et al., 2021). In this contribution we present new optical dating results from important loess sections in Poland.

For stratigraphic orientation we use the system recently proposed for last glacial Polish loess by Jary and Ciszek (2013) and later modified by Marković et al. (2015), discriminating between four major units within the last interglacial–glacial cycle (from bottom to top, with S for soil, L for loess, and L1SS1 denoting the interstadial soil complex): S1, L1LL2, L1SS1, and L1LL1. Most of the sections worked on here have already been dated by Piotr Moska (Gliwice) in the past few years. Some problems were, however, found, among them an apparent grain size dependency of ages obtained from quartz grains (coarse silt and sand fractions). In the Bayreuth Luminescence Laboratory, only the fine-grain fraction (4–11 µm) was used for dating, following experiences by Kreutzer et al. (2012). The dating results will be compared, and divergences beyond 1σ errors will be discussed in view of the ages expected from lithostratigraphy.

We present optical dating results (OSL from quartz grains, post-infrared infrared stimulated luminescence (pIRIR) from fine polymineral grains) originating from LPSs in Silesia (Biały Kościół in the Strzelin Hills south of Wrocław, Zaprężyn, in the Trzebnica Hills north of Wrocław), Złota near Sandomierz and the river Vistula (Wisła), and Tyszowce in the Volhynian Upland southeast of Lublin (Fig. 1). The spatial context of the investigated sites and the ice advances of the last glacial (Vistulian) SIS can be seen in Fig. 2. With the exception of the Zaprężyn site, luminescence dating results ob-

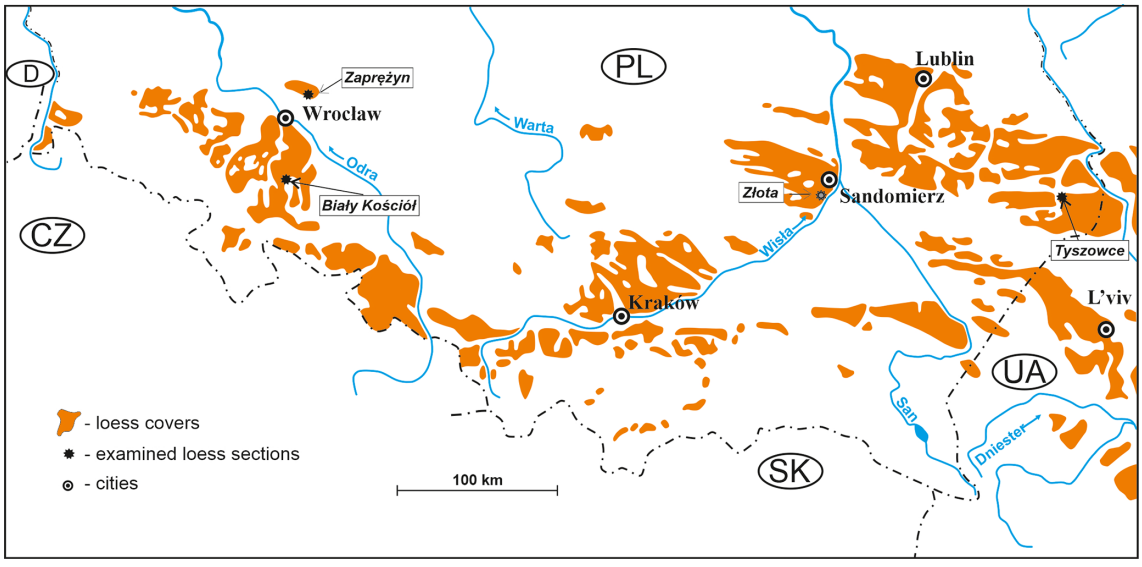

Figure 1. Loess map of Poland, with locations of investigated sites framed by black rectangles (from Jary et al., 2011, modified).

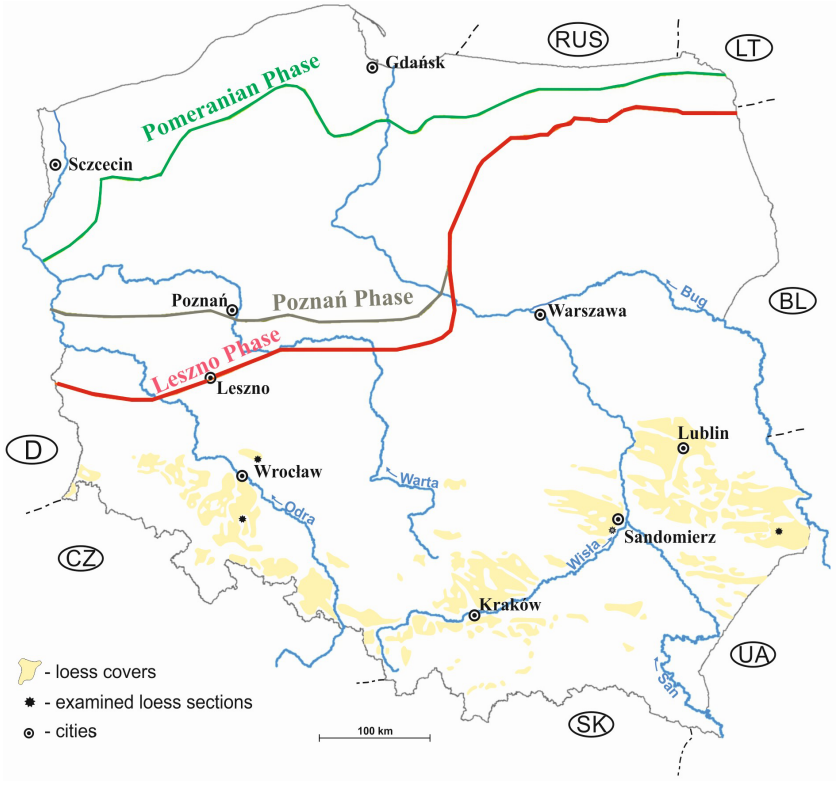

Figure 2. Limits of the major glacial phases during the Late Vistulian in Poland and spatial context of the loess belt.

tained in Gliwice have been published in recent years (Moska et al., 2011, 2012, 2015, 2017, 2018, 2019) including detailed site descriptions, whereas the ages obtained in Bayreuth have not been published so far. It should be noted that the two luminescence laboratories did not work on identical shared sample material, but with the exception of the lower part of the Tyszowce site, the sampling points could be correlated well, based on the lithostratigraphic subdivisions. Nevertheless, the present study offers a good opportunity to jointly compare and discuss luminescence dating results obtained in different laboratories.

2 Material and methods – luminescence dating

This contribution deals with chronostratigraphic problems and palaeoclimate-triggered geomorphological site formation of the investigated sites with loess exposures. Numerous other investigations have been carried out into lithostratigraphy, grain size variations, periglacial features, and geochemistry, which can be mentioned only briefly here with the relevant literature. Some radiocarbon ages are also mentioned but without further going into details of their reliability and specific problems.

Instead, this study deals mainly with the application of various established luminescence dating techniques. First of all, OSL dating of quartz is presented because feldspars are often affected by so-called anomalous fading of their luminescence signal, resulting in age underestimation (Preusser et al., 2008). Whereas the Gliwice laboratory has executed OSL dating mainly of middle-grain (45–63 µm) but also coarse-grain (90–125 µm) quartz separates, the Bayreuth laboratory contributes OSL fine-grain quartz ages, both laboratories using the single-aliquot regeneration (SAR) method (Murray and Wintle, 2000). The rather low natural dose saturation level of quartz OSL, however, limits the dating range of loess to ca. 100 ka or less. It was demonstrated that the post-infrared infrared stimulated luminescence (pIRIR) method can reduce anomalous fading significantly and, thus, extend the age range of IRSL dating far beyond the saturation limit of quartz (Thiel et al., 2011; Murray et al., 2013). Therefore, testing this method on the fine-grain feldspar-bearing fraction of Polish loess is recommendable.

2.1 Sampling and sample processing

Both involved laboratories use a very similar sampling procedure for unconsolidated rocks such as loess. A steel tube with an inner diameter of 40 mm (Gliwice) or more (50 to 60 mm, Bayreuth) is hammered horizontally into a well-cleaned vertical part of the exposure. After pulling or digging out the filled cylinder under shadow, both ends are immediately sealed with light-tight caps and taped. Additional material is taken from the hole for dosimetry and moisture measurements and sealed in airtight plastic bags. Some samples of more condensed layers for the Bayreuth laboratory were, however, cut as blocks with ca. 10 cm length edges and wrapped to be light-tight.

In the dark laboratory under subdued red light (in the Bayreuth laboratory 640 ± 42 nm; no wavelengths are given for the Gliwice laboratory) the cylinders and the blocks were opened and the outer 1 to 2 cm thick rims which may have seen some light during sampling were removed. It was thus assured that only material completely unexposed to daylight during sampling was processed for luminescence measurements. In the Bayreuth laboratory the removed sediment was later used for thick-source alpha counting (TSAC, for U and Th contents) and for ICP-OES (for K content) because it was situated closest to the further-processed sample material.

Further sample processing (sieving, chemical pretreatment, grain size separation, mineral separation) was handled slightly different in both laboratories, which did not affect, however, the aim to receive well-defined grain size classes and mineral separates. The procedures executed in the Gliwice laboratory are mentioned in the cited publications, for example, in Moska et al. (2015); those applied in the Bayreuth laboratory are described, for example, in Fuchs et al. (2013) or in Zöller et al. (2014). In Bayreuth unlike in Gliwice the fine-grain quartz fraction (4–11 µm) was measured by OSL and much attention had to be given to obtain pure quartz in this fraction by etching it for a minimum of 7 d in hydrofluoric acid (H_2SiF_6). The purity of the quartz enrichment was checked by IRSL measurements.

2.2 Luminescence measurements and data processing in the Bayreuth laboratory

OSL measurements to determine the equivalent dose (D_e) of fine-grain quartz separates were carried out on two Risø TL/OSL DA-15 readers, equipped with blue LEDs (470 ± 30 nm) for stimulation; a Thorn EMI 9235 QA photomultiplier combined with a Hoya U340 7.5 mm filter (290–370 nm) for detection; and a $^{90}Sr/^{90}Y$ β source (0.75 and 1.48 GBq, respectively) for irradiation, delivering a dose rate of 2.72 Gy min^{-1} to fine grains on aluminium discs for the Risø reader with the 0.75 GBq β source and 9.14 Gy min^{-1} for the Risø reader with the 1.48 GBq β source (reference date August 2010; cf. Fuchs et al., 2013, recalculated for the respective date of irradiation using the decay constant of ^{90}Sr). OSL decay curves were measured for 40 s at elevated temperatures (125 °C), using a cut heat for the test dose of 220 °C (same as preheat). Based on dose recovery and preheat plateau tests, a preheat temperature of 220 °C was chosen for the natural and regenerated OSL signals. For further processing OSL signals were integrated from the first 0.6 s of the decay curve minus a background averaged from the last 7.5 s.

For IRSL measurements the same readers were used but with infrared LEDs (850 nm – main peak) for stimulation and a 3 mm Chroma Technology D410/30× interference filter, restricting the detection window to the blue-violet wavelength band. For the fine-grain polymineral fraction of 12 samples from the new profile at Biały Kościół (2018), we used the $pIRIR_{290}$ protocol adopted from Murray et al. (2013; see Table 1). The first 0.6 s (first six channels) of the shine-down curves was evaluated for D_e determinations, and the segments from 150 to 200 s were used as background. Differently from Moska et al. (2019) no subtraction of an experimentally approximated residual background dose was executed (cf. Murray et al., 2013). The sequences are summarized in Table 1.

Table 1. Sequence of $pIRIR_{290}$ (left) and OSL (right) measurements.

pIRIR			Quartz OSL		
Step	Treatment	Observed	Step	Treatment	Observed
1	Dose		1	Dose	
2	Preheat, 60 s at 320 °C		2	Preheat, 10 s at 220 °C	
3	IR stimulation, 200 s at 50 °C	Lx	3	OSL, 40 s at 125 °C	Lx
4	IR stimulation, 200 s at 290 °C	Lx	4	Test dose	
5	Test dose		5	Cut heat to 220 °C	
6	Preheat, 60 s at 320 °C		6	OSL, 40 s at 125 °C	Tx
7	IR stimulation, 200 s at 50 °C	Tx	7	Return to step 1	
8	IR stimulation, 200 s at 290 °C	Tx			
9	Return to step 1				

The program Analyst version 4.31.9 (Duller, 2015) was used for processing and evaluation of OSL and IRSL data. Regenerated growth curves were fitted to a single exponential saturation function. Plots of OSL decay curves and regenerated growth curves for three samples (fine quartz grains) from the Biały Kościół section (BT 1672, BT 1673, and BT 1675) are shown in Fig. S4 in the Supplement, and a plot with preheat plateau test and recuperation for BT 1675 is shown in Fig. S5.

2.3 Dosimetry

U and Th concentrations were calculated from thick-source alpha counting (TSAC) after powdering following Zöller and Pernicka (1989) and after sealing the sample holders for a minimum of 3 weeks. A Littlemore TSAC system 7287 with three photomultiplier heads standing in a dark quasi-thermoconstant cellar room was used. Total counts reached a minimum of ca. 4000 events including slow and fast pair counts, allowing for ca. 10 % accuracy of calculated U and Th concentrations. Secular equilibrium of the U and Th decay chains was assumed for the samples consisting of loess or loess-derived sediments. The TONY standard (Zöller and Pernicka, 1989) was counted regularly in all three photomultiplier heads and was always found to be within ±3 % of the default count rate.

K concentrations were measured by ICP-OES in the BayCEER central laboratory at the University of Bayreuth. In the Gliwice laboratory high-resolution gamma spectrometry (HPGe detector) was used for determining activities of U and Th decay chains and ^{40}K, and conversion factors to the dose rate were by Guérin et al. (2011). Due to the large dry sample mass of 800 g (Marinelli beaker geometry), gamma emissions at very low energies are not resolved with an accuracy necessary to detect radioactive disequilibrium.

2.4 Age calculation

Luminescence ages were calculated using the program ADELE v2015 021a beta which was a test version of the recently released ADELE v2017 (Degering and Degering, 2020). It includes calculation of cosmic dose rates and dose conversion rates updated by Guérin et al. (2011). The determination of the alpha-efficiency factor (a value) for fine grains is unjustifiably consuming machine time. Therefore, a values for larger sets of Pleistocene samples are increasingly adopted from the literature with rather wide error bars. An a value of 0.035 ± 0.005 was taken for the OSL of fine-grain quartz samples (Lai et al., 2008) and 0.1 ± 0.01 for the $pIRIR_{290}$ of fine-grain samples (cf. Kreutzer et al., 2014, for $pIRIR_{225}$), but $pIRIR_{290}$ ages were also calculated with 0.085 ± 0.01 (cf. Schmidt et al., 2018). We decide, however, in favour of the a value of 0.1 ± 0.01 for the time being over the suggestion of Schmidt et al. (2018) (see below in Sect. 3, Results).

Moisture contents ranging between 11 % and 23 % were taken from measurements of bags sealed in the field as far as the wet unit weight could be dug up; otherwise 15 ± 5 % was inserted. Moisture contents used for age calculation are also listed in Table S1 in the Supplement. Higher soil moisture absorbs more of the energy of ionizing irradiation than low soil moisture, which is strongest for alpha particles, less for beta radiation, and even less for gamma radiation (Aitken, 1998). A lower moisture content used in the age equation will therefore yield a lower apparent age and vice versa. The problem of representative past moisture content needs a critical evaluation for two reasons. Pleistocene loess was deposited under climatic and environmental conditions quite different from Holocene ones. The climate during loess formation in central Europe was most of the time dryer and cooler than at present with an impact on mean annual to centennial soil moisture. Overall lower precipitation may, however, at least partially been counterbalanced by lower evapotranspiration. Furthermore, the last glacial–interglacial cycle experienced a number of climatic fluctuations at a periodicity comparable to Dansgaard–Oeschger cycles or even faster (Rousseau et al., 2017; Moine et al., 2017). The greatest problem concerning past soil moisture is posed by occurrence of permafrost, which can produce ice lensing and, thus, water and/or ice

oversaturation at a micro-scale to local scale for tens to several thousands of years in the research area (probably longer in higher latitudes). With respect to the diameter of the sampling tubes, ice lensing on a millimetre scale is not as severe as the formation of tabular ice many centimetres to decimetres thick, and most problematic are thick ice wedges. Even if the persistence of ice lenses and wedges may have lasted only a few per cent to 10 % of the total time span covering the last glacial cycle, the impact on water/ice content of the ground due to oversaturation may not be negligible. But the effect on the dose rate and, thus, on the luminescence age cannot be quantified; it can only be estimated to the best of one's knowledge. For this reason it is honest to assume higher-than-usual error limits for moisture content in the error calculation of a luminescence age. Soil scientists and palaeopedologists can give helpful advice to set limits for minimum and maximum water saturation of loess soils in the field. Systematic OSL dating studies in loess areas with actual permafrost, for example, Alaska or Siberia, may be a propellant to a better understanding of the problem.

3 Results

For all of the four LPS sections the new luminescence ages from the Bayreuth laboratory will be presented first. Analytical data and ages are given in Table S1. Obtained ages are then compared with already-available ages from the Gliwice laboratory, except for the Zaprężyn section (OSL ages not yet published).

3.1 The Silesian key section – Biały Kościół

The loess section is located near the village of Biały Kościół, on the western slope of the Oława valley (50°43′38.73″ N, 17°01′ 29.57″ E) at about 180 m a.s.l. Already in 2014 three test samples for the Bayreuth laboratory (BT 1482, BT 1483, and BT 1484 – violet in Fig. 3) were taken by Ludwig Zöller and Zdzisław Jary at a depth between ca. 4.4 and 5.7 m from the older exploratory excavation (2009), from which the samples for the Gliwice laboratory had also been taken some years before, but those three samples will not be further discussed. As this dig was severely endangered by collapses, a new dig was created by Zdzisław Jary and his team in 2017 and 2018, 6 m aside from the older one. Lithostratigraphic units could be followed from the older to the new dig; the "upper younger loess" L1LL1 is, however, a few decimetres thicker in the new dig. For optical dating between 3.7 and 9.5 m depth of the new section, 12 samples were extracted in June 2018.

Litho- and pedostratigraphic units are described in detail in Moska et al. (2019) together with physical and chemical soil properties. Dating results from fine quartz grains (OSL) and from fine polymineral grains ($pIRIR_{290}$) obtained in Bayreuth are shown in Fig. 3 (with an age–depth plot; see also Fig. S3); those obtained in Gliwice are shown in Fig. 4. Analytical results for the samples dated in Bayreuth are given in Table S1.

Quartz ages (4–11 µm) from Bayreuth are in stratigraphic order within their 1σ uncertainties. An arrangement in groups is obvious: (i) from L1LL1 (BT 1679) to the upper part of L1SS1 ranging from ca. 25 to ca. 35 ka, (ii) the L1SS1 lower brownish part and L1LL2 around ca. 60 ka, (iii) the upper part of the S1 complex at ca. 75 ka, and (iv) the lower part of the S1 complex at 112 ± 8.6 ka (Figs. 3 and S3 left).

Fine-grain polymineral ages ($pIRIR_{290}$) obtained in Bayreuth (PM) were calculated with an a value of 0.1 ± 0.01 since evidence for a positive correlation between the IRSL stimulation temperature and height of the a value was observed (Kreutzer et al., 2014). The complex of problems when using a common a value was, however, outlined by Schmidt et al. (2018). Following their suggestion the $pIRIR_{290}$ ages were recalculated using 0.085 ± 0.01, resulting in 4 % to 5 % higher ages, but so far there has been no proof of the trueness of this value, and the a-value determinations of Kreutzer et al. (2014) predominantly originate from Saxonian loess in the proximity of Lower Silesia. Therefore, in Fig. 3 only the $pIRIR_{290}$ ages for $a = 0.1$ are plotted. But for both a values, calculated ages are listed in Table S1. The $pIRIR_{290}$ ages are in stratigraphic order within their 1σ uncertainties, and for samples extracted from the L1LL1 loess (BT 1677 to BT 1679), they agree within error bars with the quartz ages. But from samples taken within the L1SS1 palaeosol or deeper $pIRIR_{290}$ ages are significantly older than the quartz ages. For sample BT 1676 the significant overestimate of the $pIRIR_{290}$ age (40.2 ± 3.4 ka) referred to the quartz age (28.0 ± 1.8 ka) is most likely due to incomplete bleaching of $pIRIR_{290}$ because this sample originates from reworked L1SS1 material, as is visualized in Fig. 3. An arrangement in groups is obvious (Figs. 3b and S3 right): (i) L1LL1 to L1SS1 from ca. 27 to ca. 45 ka, (ii) the L1SS1 lower brownish part and L1LL2 at ca. 70 ka, (iii) the upper part of the S1 complex at ca. 100 ka, and (iv) the lower part of the S1 complex at > 300 ka. Although the apparent $pIRIR_{290}$ age of the lowermost sample BT 1668 needs to be verified (because of dose saturation, only 4 of 15 aliquots were suitable, and also due to possible dose overestimation described by Avram et al., 2020), it points to a very long hiatus within the S1 complex. IRSL decay curves and a dose–response curve of a suitable aliquot are shown in Fig. S6. Another but not so long-lasting hiatus is apparent within the grey and the brownish part of L1SS1 from both fine-grain quartz and fine-grain polymineral ages. L1SS1 as characterized in Moska et al. (2019) appears therefore as a pedocomplex or a complex like in Saxonian loess (cf. Meszner et al., 2013). This ca. 25 kyr long hiatus within L1SS1 is also apparent from the $pIRIR_{290}$ ages.

Ages obtained by the $pIRIR_{290}$ protocol become significantly older than quartz ages from sample BT 1676 (top of L1SS1) downwards. This systematic behaviour of ages can hardly be explained by assuming a sudden increase in resid-

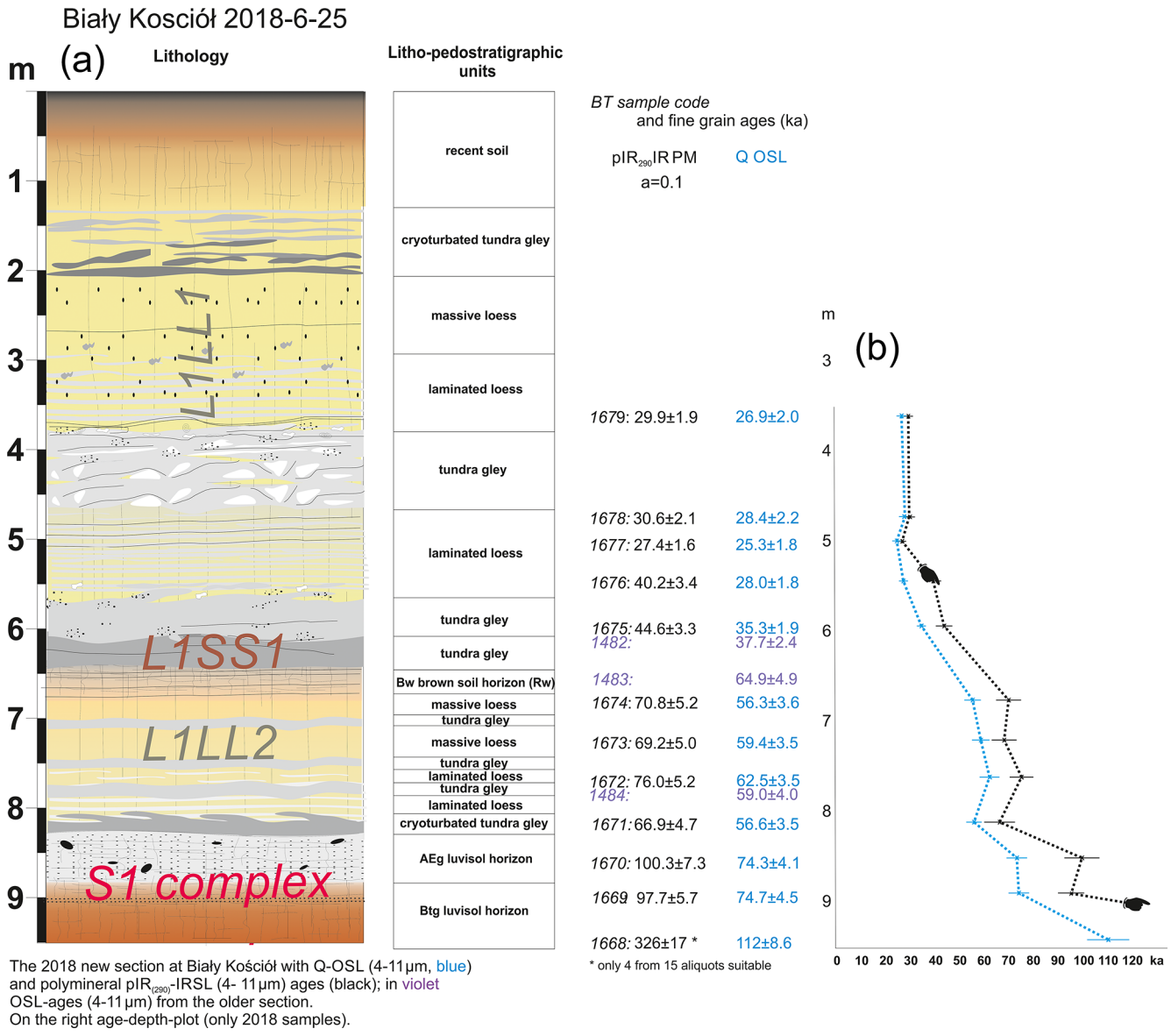

The 2018 new section at Biały Kościół with Q-OSL (4-11 µm, blue) and polymineral pIR$_{(290)}$-IRSL (4- 11 µm) ages (black); in violet OSL-ages (4-11 µm) from the older section.
On the right age-depth-plot (only 2018 samples).

Figure 3. **(a)** OSL ages from fine quartz grains and pIRIR$_{290}$ ages from fine polymineral grains obtained from the Biały Kościół section (2018) in the Bayreuth laboratory. Litho-pedostratigraphic units (legend) are by Marcin Krawczyk. **(b)** Age–depth plot of fine-grain quartz ages (blue) and pIRIR$_{290}$ ages from fine polymineral grains (black) obtained from the Biały Kościół section (2018) in the Bayreuth laboratory. Only samples from the 2018 section are regarded. The unconfident apparent pIRIR$_{290}$ age of BT 1688 is off the scale (hand to the right). Note the bulge of the pIRIR$_{290}$ plot below ca. 5.5 m depth (hand downwards) and sample BT 1671 at ca. 8.2 m. The quartz plot betokens this bulk less distinctly.

ual doses at deposition, even if the slightly higher pIRIR$_{290}$ ages referred to the quartz ages in the higher part of the section may be a sign of a residual dose in the range of some 10 to 15 Gy.

Dating results published by Moska et al. (2019) are presented from the coarse-grain quartz fraction (90–125 µm), the middle-grain quartz fraction (45–63 µm), and the fine-grain polymineral fraction (4–11 µm). Ages from the coarse-grain fraction show some stratigraphic inconsistencies (samples BK18, BK13, and BK8) which is not the case for the finer fractions within uncertainties. This cannot be attributed to changes in dose rates over burial time as these would have affected all dated fractions in the same direction. The age–depth plot (Fig. 4 right) visualizes that in the lower part (below L1LL2, samples BK1 to BK5) coarse-grain quartz ages systematically underestimate middle-grain quartz ages, which themselves underestimate the pIRIR$_{290}$ ages. These results argue for a longer-lasting hiatus within or at the base of the L1SS1 palaeosol (see above) and a very long hiatus within the S1 pedocomplex. The pIRIR$_{290}$ age of BK2

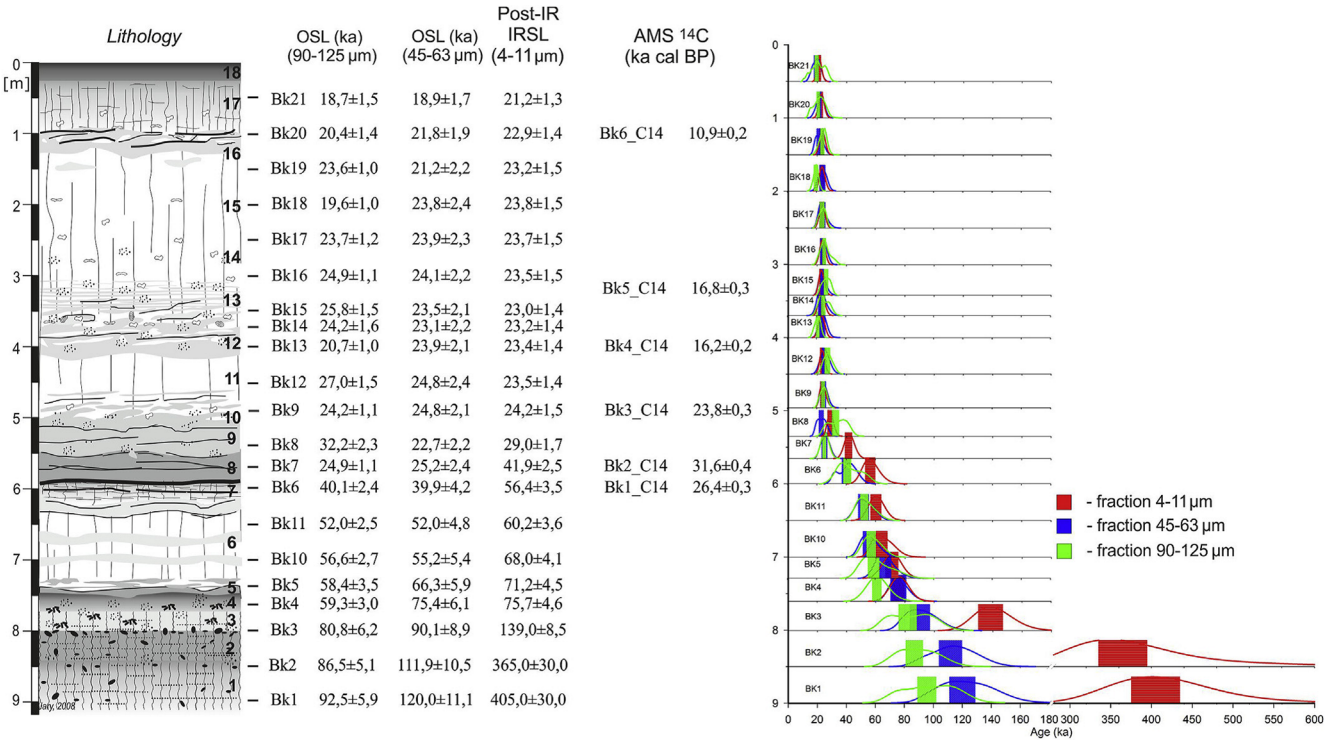

Figure 4. OSL ages from middle and coarse quartz grains and $pIRIR_{290}$ ages from fine polymineral grains obtained from the Biały Kościół (2009) section in the Gliwice laboratory (from Moska et al., 2019).

(365 ± 30 ka) agrees with the $pIRIR_{290}$ age of BT 1668 (343 ± 18 ka, with $a = 0.085$, which is similar to the value used for BK2). Despite some differences between the ages obtained in Gliwice and in Bayreuth, which will be discussed later, the comparison of the dataset from both laboratories evidences amazing accordance.

3.2 The surprise – Zaprężyn

The exposure near the village of Zaprężyn is situated at 51°14′43.7″ N, 17°11′51.8″ E at ca. 164 m a.s.l. in hilly ground at the southern end of the terminal moraine belt of the Wartanian stage (Saalian glaciation; Krzyszkowski, 1993). At the city of Trzebnica the terminal moraine (Winna Góra) is suggested to correlate to the Odranian stage (Jary and Krzyszkowski, 1994). It is supposed that the LPS rests on top of a Wartanian outwash cone; the hilly country in the surroundings may, however, also reflect a number of relatively small gredas (elongate loess ridge) (Różycki, 1967; Léger, 1990). Two horizons with ice wedge pseudomorphs were reported from the Zaprężyn section (Jary, 2009; Jary et al., 2011; Jary and Ciszek, 2013), but during sampling for OSL dating in September 2015, the lower one was no longer visible due to collapse and overgrowth of this part of the exposure. For sampling in 2015, we widened the excavation to the left where the upper ice wedge pseudomorphs' horizon was seen best (Fig. 5, at the spade). An erosional unconformity rising from the left to the right could then be followed over the whole length of the wall. It manifests itself as a tiny bed of fine sand some millimetres thick and will have an important role for the interpretation of the OSL ages. Loess and sandy loess above the unconformity are attributed to L1LL1 and loess below it to L1LL2 with a not yet clearly defined lower boundary with S1 supposed to lie between 5.3 and 6.0 m depth.

An exposed section of the ice wedge cast network and thermokarst features is shown in Fig. 6. At its top gelifluction tongues dipping slightly to the left are a result of permafrost decay. These elongated tongues are overlain by more or less parallel bedded sandy loess.

Based on previous ^{14}C AMS ages mentioned by Jary (2007, their Table 7, Poz-7998 and Poz-7649), the ice wedge pseudomorphs were supposed to originate from the LGM. This would fit well for the upper ice wedge pseudomorphs. Our within-error-bar stratigraphically consistent OSL quartz ages, however, contradict this opinion for the ice wedge pseudomorphs shown in Figs. 5 and 6. The OSL quartz ages are plotted in Fig. 7, together with the ^{14}C AMS ages. The OSL ages from Bayreuth suggest that the ice wedge formed earlier than 52.5 ± 3.7 ka (sample 12) and 56.8 ± 4.7 ka (sample 11) and later than 68.2 ± 5.6 ka (sample 10) and 64.7 ± 4.7 ka (sample 9), respectively. The oldest ^{14}C AMS age (> 50 ka BP, Poz-6939) from a humic layer OSL-dated to 95.7 ± 6.6 ka (sample 3) does not conflict with

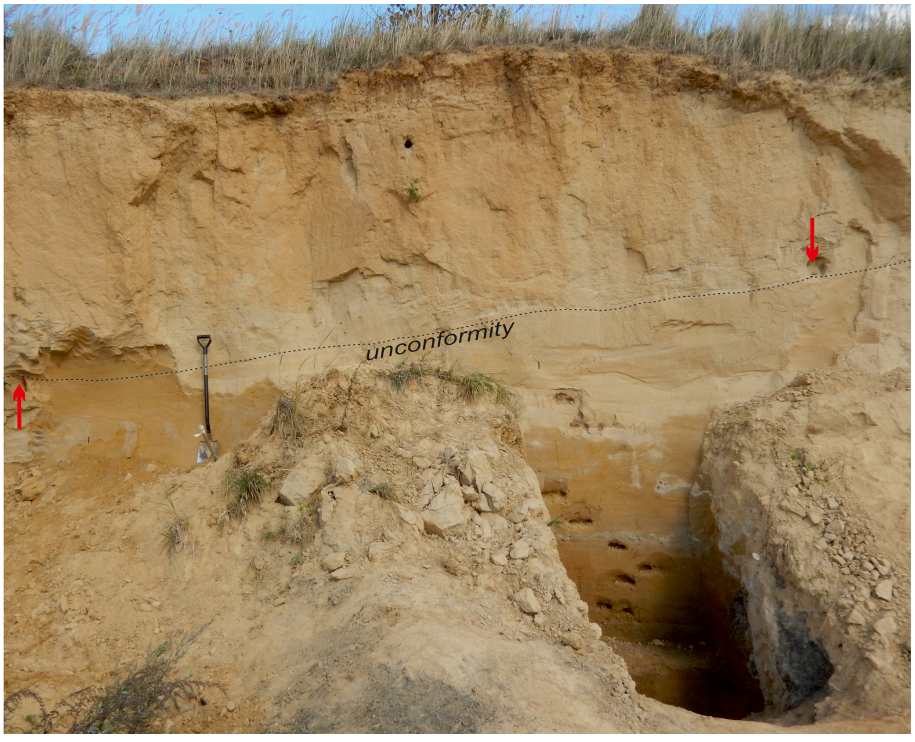

Figure 5. The Zaprężyn exploratory excavation in September 2015. The unconformity is visualized by the dotted line. Sample ZAPR12 (Bayreuth) was taken immediately below the unconformity at the left margin of the photo at the red pocket knife (red arrow upwards) and sample 13 immediately above the unconformity at the right (red arrow downwards). All other Bayreuth samples were extracted at the trench.

Figure 6. Detail of the Zaprężyn exposure in September 2015. Ice wedge pseudomorphs are visible to the left of the scraper (red tool) and its handle. Gelifluction tongues traced by greyish gleyed loess bend to the left and are overlain by striped brownish sandy loess. The position of OSL sample 12 is marked on top of the spade. Some of the gelifluction lobes are traced by dotted black lines.

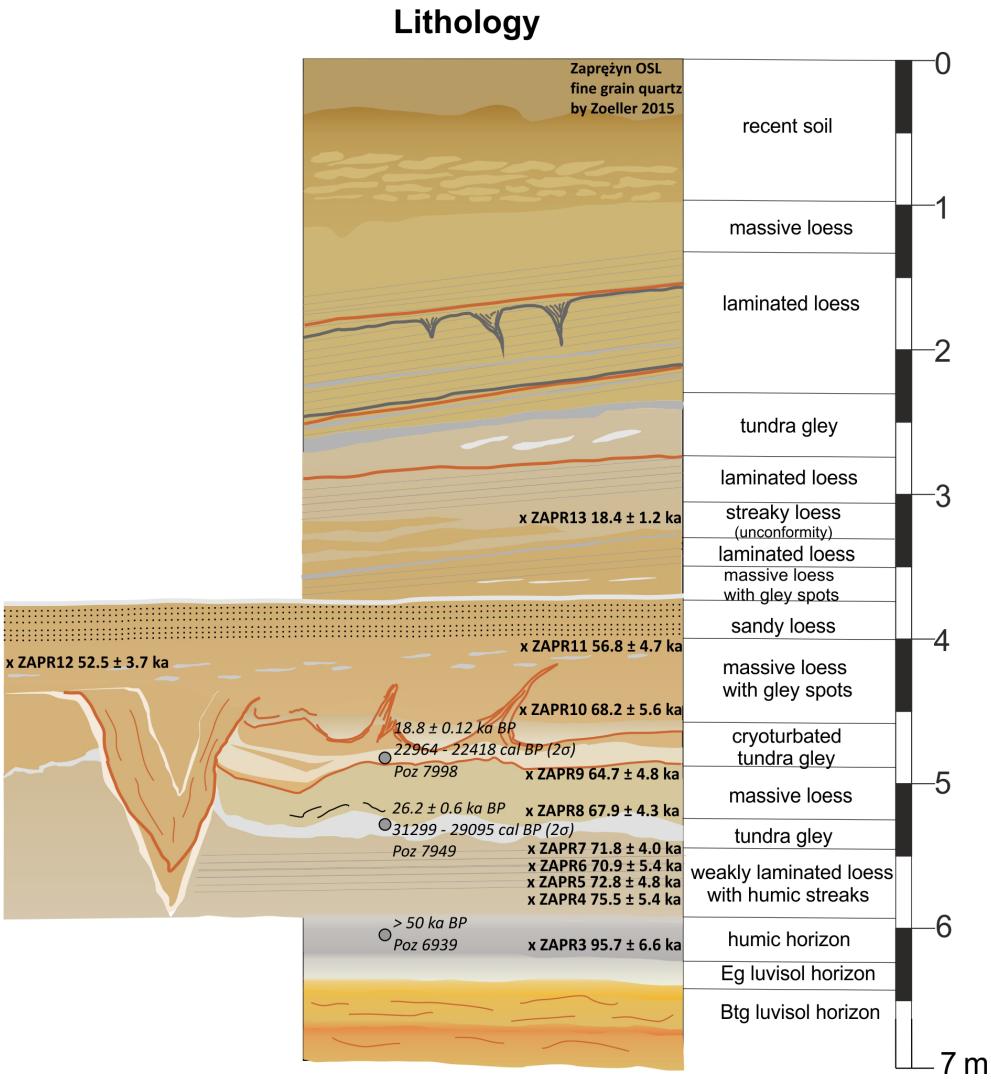

Figure 7. The Zaprężyn section with OSL ages (fine quartz grains) obtained in the Bayreuth laboratory and former ^{14}C AMS ages (Jary, 2007, grey circles).

the OSL ages. Despite some evidence for age underestimation also from quartz OSL ages, which will be discussed further below, the mentioned unconformity appears to represent a time span of ca. 29 to 39 ka in which the L1SS1 is to be expected but is denuded here. Formation of sandy loess above the unconformity starts at 18.4 ± 1.2 ka (sample 13), and gley horizons below the unconformity appear too old for L1SS1.

OSL ages from the 45–63 µm quartz fraction which were taken for the Gliwice laboratory will be published and discussed elsewhere. Marcin Krawczyk plotted the sampling positions (2015) for the Bayreuth laboratory in an informative design reflecting the soil colour, periglacial features and spatial distribution of the samples along the exposure (Fig. 7). Fine-grain quartz OSL ages obtained in Bayreuth are shown together with earlier published (Jary, 2007) ^{14}C AMS ages. In Fig. S1 the results are plotted in an older diagram which was used during sampling. Grain size composition of the profile is presented in Fig. S7.

3.3 The Sandomierz Upland key section – Złota

The sampled wall of the Złota section is situated at the southern margin of the Sandomierz Upland at 50°39′11″ N, 21°39′53″ E close to the Vistula. The exposed LPS including the entire last glacial–interglacial cycle is 13 m thick and reaches up to ca. 170 m a.s.l. The neighbouring but no-longer-accessible former loess exposure Polanów Samborzecki (Jary, 2007), which was studied for many years, is only some 200 m away. Previous research is outlined in Moska et al. (2015, 2018).

The L1SS1 pedocomplex is described to be up to 2 m thick and, thus, offers a good opportunity to study this interstadial soil complex and to contextualize it on the timescale.

As a detailed luminescence chronology of the whole section was already supplied by Moska et al. (2018, 2015) using middle quartz grains and fine polymineral grains, our sampling for the Bayreuth laboratory in September 2015 focused on the L1SS1 pedocomplex. Six samples were extracted between 6.0 and 7.75 m depth. The exploratory excavation from which the Gliwice samples were taken in 2012 had to be cleaned again and some decimetres of material removed. Thus, sample material for Gliwice and Bayreuth was not identical, but the Bayreuth samples could be unambiguously identified in the lithological profile of Moska et al. (2015).

Figure 8 shows on the right the whole profile at Złota, exhibiting the 25 pedo-sedimentary units distinguished during October 2013 fieldwork, with the zoomed-in part around L1SS1 with OSL ages of samples ZL-1 to ZL-6 from the Bayreuth laboratory on the left (field design by Pierre Antoine). The ages are stratigraphically consistent with mean ages of 26.5 to 27.6 ka (ZL-4, tundra gley, to ZL-6, all from L1LL1) above the L1SS1 palaeosol. The ages of ZL-3 (31.9 ± 1.9 ka, upper part of L1SS1, doubled tundra gley) and ZL-2 (38.6 ± 3.6 ka, lower part of L1SS1, brown soil) argue for a pedocomplex developed under different environmental conditions. Sample ZL-1 (50.0 ± 5.4 ka) originates from the unweathered loess L1LL2. If the L1SS1 pedocomplex is perceived as comprising units 13, 14, and 15a and unit 12 is taken out as a discrete palaeosol (tundra gley), the formation of L1SS1 at Złota can be narrowed down to between ca. 30 and ca. 40 ka.

Dating results obtained in the Gliwice laboratory are presented in Fig. 9 (from Moska et al., 2018, cut out from their Fig. 3). Note that the older lithostratigraphic nomenclature (L1L1, L1S1, L1L2) was used in this figure. For the L1LL1 and the top of L1SS1 (sample Złota9), loess quartz OSL ages (45–63 µm) and $pIRIR_{290}$ ages (fine polymineral grains) agree well, with the exception of the quartz age of sample Złota10 (inversion). For all stratigraphically older samples (Złota1 to Złota8), the quartz ages significantly underestimate the $pIRIR_{290}$ ages, which are stratigraphically consistent and correspond to geologically expected ages. It is worthwhile noting that even for the oldest samples from loess below S1 (142 ± 9 and 150 ± 12 ka, respectively), there is no indication of age underestimation. Comparing the Gliwice ages with those from Bayreuth (Fig. 8a), agreement of quartz ages is found despite the different grain sizes, with the exception of Złota10. As the quartz ages of samples Złota7 and Złota6 underestimate their $pIRIR_{290}$ ages, this must also be considered for the sample ZL-1 from Bayreuth (50.0 ± 5.4 ka). For the other quartz ages (4–11 µm) from Bayreuth, agreement with the $pIRIR_{290}$ ages is observed.

3.4 Ice wedges and thermokarst features in Upper Plenivistulian loess L1LL1 – Tyszowce

The village of Tyszowce is situated ca. 110 km southeast of the city of Lublin in the very east of Poland (Volhynian Upland) close to the Ukrainian border. The profile with exposed loess cover of 19 m (14 m thick L1LL1 above L1SS1!) was studied by Moska et al. (2017); samples for luminescence dating in Gliwice were taken in 2012 a few metres to the right of our trench visible in Figs. 10a and 11a.

This section was, however, no longer fully accessible, and for our own sampling in September 2015, a new 16 m deep trench had to be created by a shovel excavator followed by cleaning by hand. The coordinates were measured by GPS, yielding 50°36′29.1″ N, 23°42′38.6″ E and the top of the section at ca. 220 m a.s.l. In this new trench the L1SS1 was – in contrast to the former profile – more or less eroded as a result of periglacial dynamics (Fig. 10) and only some geliflucted or cryoturbated lumps evidenced the former existence of the pedocomplex (Fig. 10b). Thus, the ages published by Moska et al. (2017) cannot always smoothly be transferred to the new profile. Our sampling focused on the supposed remnants of L1SS1 and the onset of L1LL1.

OSL samples TYS 1 to TYS 4 (Figs. 10a and 11a) are closely spaced at intervals of 20 to 35 cm at depths of 11.0 m (TYS 1), 11.2 m (TYS 2), 11.45 m (TYS 3), and 11.8 m (TYS 4) on the right-hand side of the ice wedge pseudomorph which begins between TYS 3 and TYS 4. Samples TYS 5 to TYS 7 were extracted to the left of the ice wedge pseudomorph at 14 m (TYS 5) and ca. 16 m depth (TYS 6 and TYS 7, Fig. 11b). The position of all OSL samples in the entire profile is shown in Fig. 11a, with OSL ages of the fine-grain quartz fraction.

The ice wedge pseudomorph begins between samples TYS 4 (pre-dating the ice wedging) and TYS 3 (post-dating it as well as TYS 2 and TYS 1, horizontal bedding; Figs. 10a and 12). The ice wedging can thus be bracketed anywhere between ca. 30 and 25 ka, younger than L1SS1, which at Tyszowce is dated at around 40 ± 3 ka (Moska et al., 2017). The OSL age of TYS 7 (43.3 ± 3.0 ka, gley lump in a deeper position of the thermokarst, Fig. 11b) is identical within uncertainties and argues for affiliation of this gley remnant to L1SS1. The OSL age of TYS 6 (brown clayey loess, 67.9 ± 7.0 ka), however, attributes this material rather to L1LL2 or even to S1 (cf. Moska et al., 2017). The stratigraphic and geological storage conditions of this lump or bed appearing like a foreign body could, unfortunately, not be dug up further.

Comparing ages given by Moska et al. (2017) with our own ages (Fig. 11b) is not always straightforward because we did not use identical sample material and, in particular, due to the strong periglacial destruction observed in the 2015 excavation. For the entire set of luminescence ages from the Gliwice laboratory for the Tyszowce section, see Fig. 12, in which L1LL2 is only ca. 1.5 m thick (15.5 to 17 m depth) above S1. Some pIRIR ages from the Gliwice laboratory are projected onto the 2015 profile. For the horizontally bedded layers above the ice wedge cast (TYS 1, TYS 2, TYS 3), a comparison should be justified and the fine-grain quartz ages turn out to be older than the middle-grain quartz ages

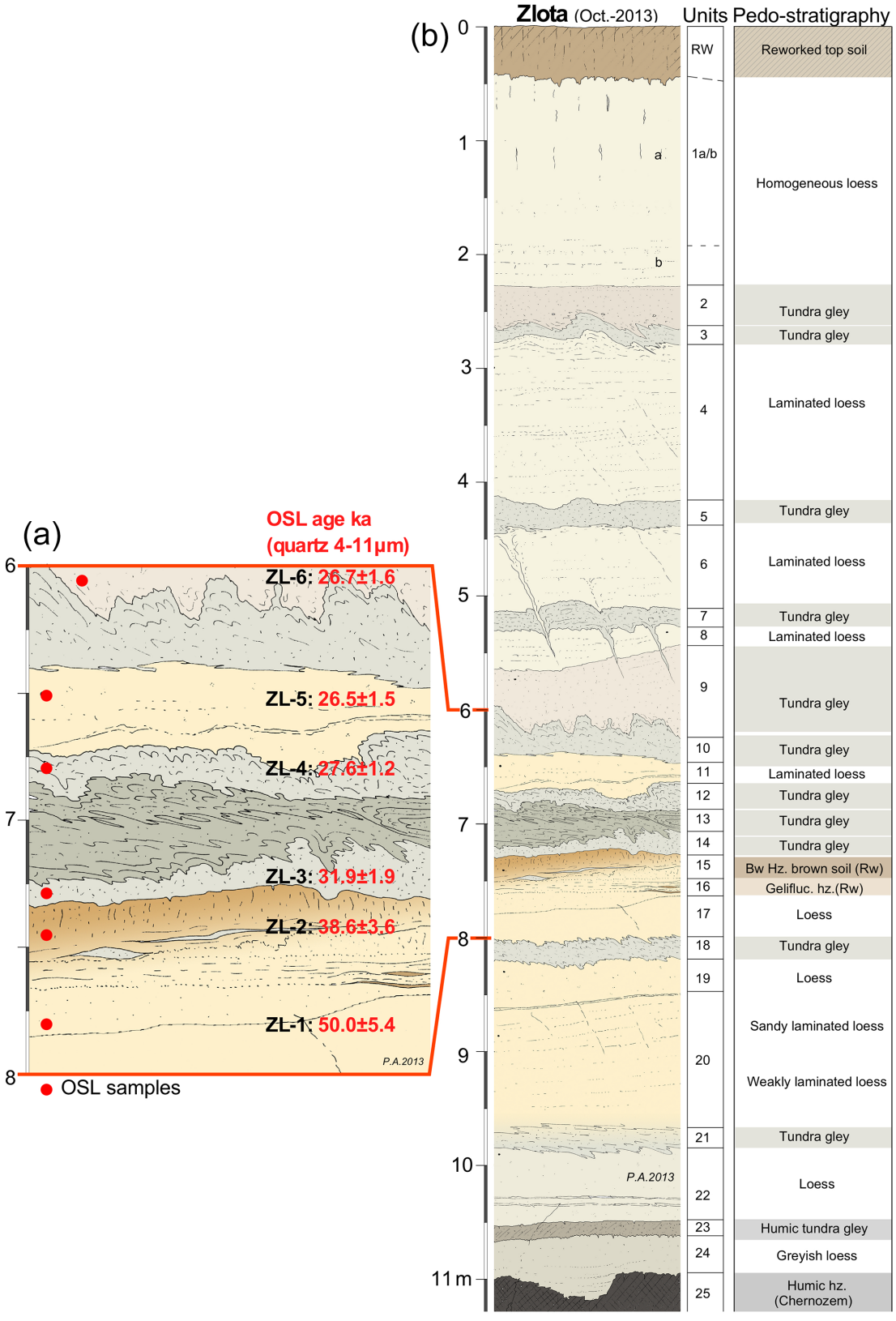

Figure 8. The profile at Złota (October 2013) **(b)** and the zoomed-in part around L1SS1 with OSL ages of samples ZL-1 to ZL-6 from the Bayreuth laboratory **(a)** (Pierre Antoine).

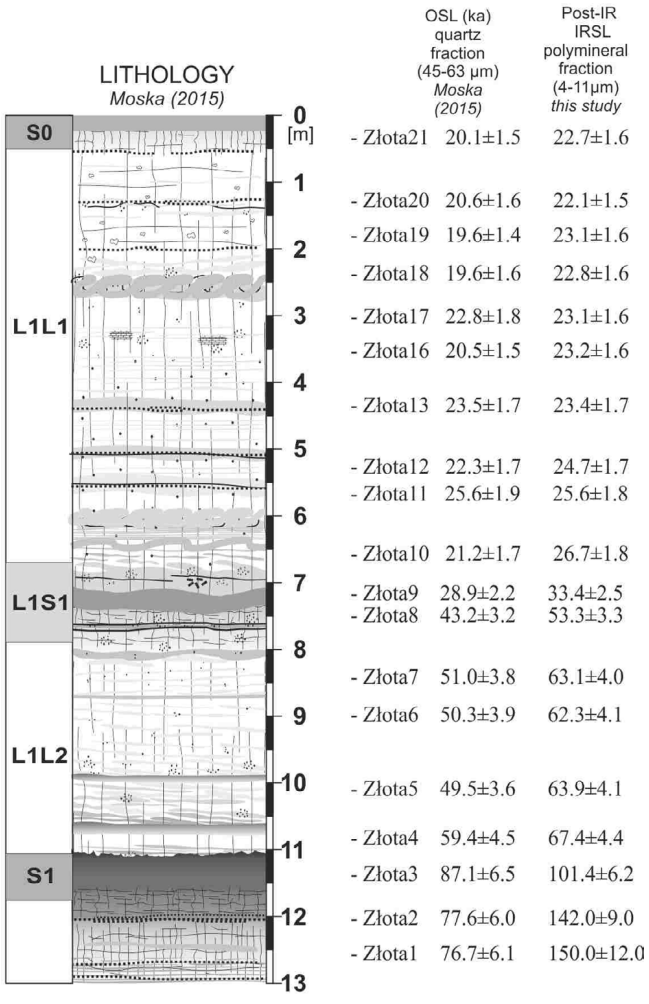

Figure 9. Luminescence ages from the Złota section obtained in the Gliwice laboratory (from Moska et al., 2018, cut out of Fig. 3).

(TYSZ_11, TYSZ_10; see also TYSZ_9 and TYSZ_8 in Fig. 12). The pIRIR ages of Moska et al. (2017) in the section shown in Fig. 11b, however, confirm their quartz ages with the exception of TYSZ_5 (55.5 ± 3.2 ka).

4 Discussion

The results presented above will be discussed from two aspects: (i) results for the individual profiles and (ii) general discussion focusing on the implications of different luminescence dating protocols.

4.1 Individual profiles

The fine-grain quartz ages from the Biały Kościół profile (2018, Fig. 3) are in stratigraphic order within uncertainties and do not conflict with the age conceptions of Jary and Ciszek (2013), with the exception of the oldest sample BT 1688, the quartz age of which is regarded as underestimated with respect to its deposition prior to S1 pedogenesis. It appears strange however that samples BT 1671 to BT 1674 from the L1LL2 loess yield a mean age value of 58.7 ka without any noticeable increase with depth. These samples under debate have equivalent doses of around 200 Gy (Table S1), which are considerably beyond the threshold value of ca. 100 Gy suggested for reliable OSL dating by Timar-Gabor et al. (2017) without rigorously ruling out higher doses as suggested by Avram et al. (2020), who estimate ∼ 150 to ∼ 250 Gy as a threshold value. Complete trust in these ages would imply that this up to 2 m thick loess including some weak tundra gleys was deposited very rapidly at the transition from MIS 4 to MIS 3. This is not impossible but sounds challenging. Therefore some age underestimation of these quartz ages must be taken into account (see also general discussion below). This assumption is supported by the pIRIR ages, which, however, may be somewhat overestimated due to a residual dose at deposition (in particular sample 1672, which may be derived from a bed mixed up with geliflucted material; see the bulge of the age–depth plot in Fig. 3 above BT 1671 for both pIRIR and OSL ages). In the Bayreuth laboratory it was not attempted to find a residual dose beyond the background subtraction as explained above. There is no proof at all that a subtraction of an experimentally approximated residual background dose would meet a natural residual at deposition better (cf. Avram et al., 2020). The close parallel courses of the age–depth plots (Fig. 3) between samples BT 1679 and BT 1677 can in fact be interpreted as an offset due to uncorrected residual doses of the pIRIR ages. Apart from BT 1672 the pIRIR ages are in agreement with the attribution of L1LL2 to MIS 4. A similar behaviour of fine-grain quartz and polymineral ages is seen in the data given by Moska et al. (2019). Their pIRIR ages in particular also argue for a MIS 4 age of the L1LL2, whereas quartz ages from this loess are also ambiguous and are prone to underestimation.

With respect to the stimulating publication by Lüthgens et al. (2020), another solution imposes on the discussion. The local LGM of the Ristinge (and probably Ellund–Warnow) ice advance (50 to 55 kyr old) affected mainly the southwestern part of the Baltic Sea and adjacent areas, most probably surrounded by a belt of harsh periglacial conditions. If the fine-grain quartz ages around 55 to 60 ka (±5 % to 7 %) are correct, the L1LL2 or at least its upper part including periglacial features may be attributed to this ice advance mirroring its periglacial surroundings. This interpretation would imply age overestimates of corresponding pIRIR ages.

Quartz ages (middle and coarse grains) from the L1LL1 obtained in Gliwice tend to be lower than those obtained in Bayreuth (fine grains), but this cannot be confirmed for the stratigraphically older samples. Our findings in the Gliwice and Bayreuth laboratories appear opposed to those of Avram et al. (2020) and Timar-Gabor et al. (2017) and may complicate the problem further. But a general rule relating to a grain size dependence of quartz ages cannot be supported

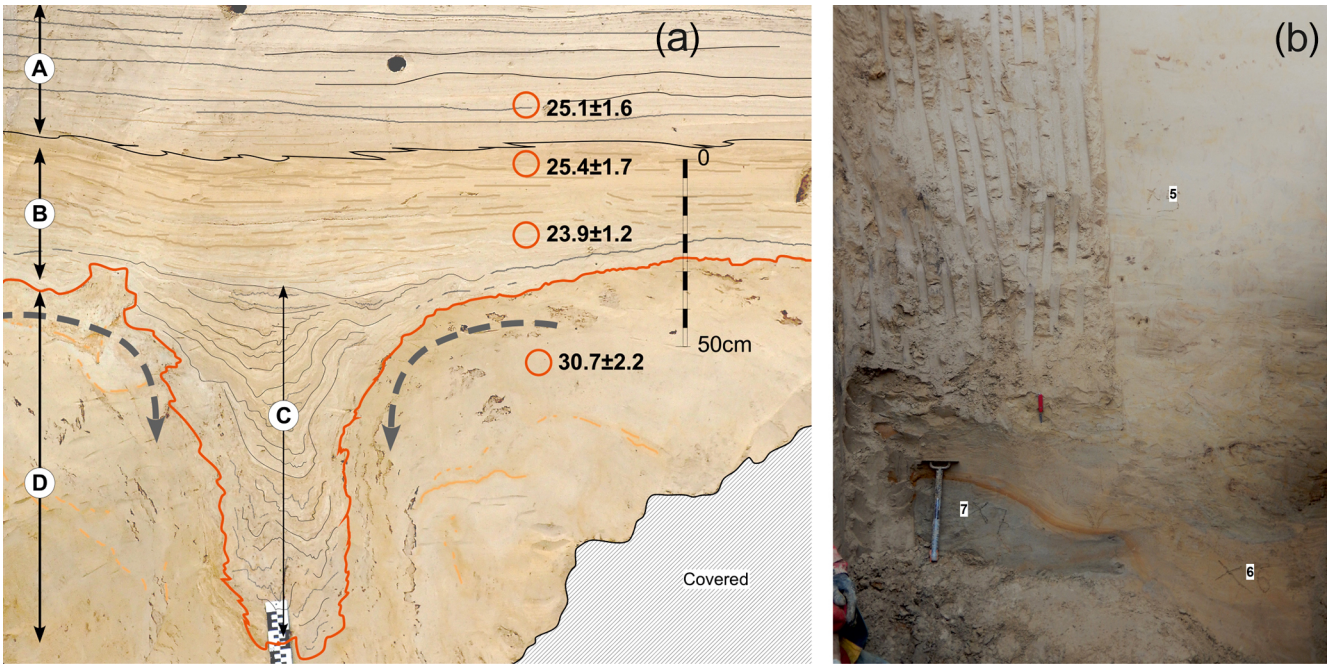

Figure 10. Tyszowce section. **(a)** Ice wedge pseudomorph (lower left corner) and brownish and greyish cryoturbated remnants of an interstadial soil. Explanatory drawing of the situation after a photo (Pierre Antoine). OSL ages (ka) of samples 1 to 4. A: very finely laminated (≤ 5 mm thick) light yellowish grey calcareous loess with sub-continuous undulated black lines of manganese oxide (cryptogamic crust remnants?). B: laminated calcareous loess with light brown to orange oxidation bands and hillwash stratifications (partly translocated by hillwash processes/small cross laminations). C: irregular hydromorphic loessic infilling of a former large ice wedge pseudomorph (> 100 cm $\times$ 60 cm) resulting from the collapse by gelifluction of the permafrost active layer (hydromorphic loess/greyish patches). D: homogeneous and dense pale yellowish calcareous loess with some orange oxidation lines and abundant black manganese oxide patches and lines (upper horizon of a former permafrost). **(b)** Thermokarst gelifluction lobe (grey, sample 7 lower left) from a clayey palaeosol (tundra gley, L1SS1?) beside the ice wedge pseudomorph, kneaded with older brownish and clayey loess (sample 6). Sample 5 (upper right) is from greyish brown reworked loess with streaks of a tundra gley, less compacted than samples 6 and 7.

by the data from the Biały Kościół section. It is supposable that such dependence exists but is concealed by different source areas of the lithological units. For Biały Kościół two major source areas must be considered: the northern glaciogenic area such as the Odra Pradolina (glacial valley, "Great Odra Valley"; Badura et al., 2013; Waroszewski et al., 2021) and the southern mountainous area dominated by Palaeozoic rocks of the Sudetes Mountains. In a periglacial environment with frequently changing wind directions, a frequent change of these main source areas is conceivably delivering quartz grains of different geological histories and different luminescence characteristics. The aeolian transport distance of different grain sizes superimposes this effect. So far, however, it can only be speculated about whether the unsteady behaviour of quartz luminescence at Biały Kościół can be explained. As a consequence, some geochronological questions at the Biały Kościół section such as the exact timing of the L1SS1 at this site can hardly be decided based on the quartz ages alone.

The $pIRIR_{290}$ ages from both luminescence laboratories are more consistent, but they are prone to age overestimates due to incomplete bleaching, independent of the question of whether a residual dose estimated by laboratory experiments is subtracted or not. In the case of the Biały Kościół section this subtraction as executed by Moska et al. (2019) appears to be justified. Nevertheless, the exact time bracketing of the L1SS1 remains challenging. If it is accepted that the quartz ages within and below L1SS1 are underestimated but the $pIRIR_{290}$ ages are perhaps overestimated, the true ages should lie in between. The evidence for a hiatus lasting many thousands of years within the L1SS1 suggests that at Biały Kościół the L1SS1 is not a pedocomplex but a complex (of soil remnants separated by erosion events and sediments) and, thus, a parallel to the Gleina Complex (Meszner et al., 2013) in Saxonian loess, eastern Germany. Consequently, the L1SS1 at the Biały Kościół section may not represent its complete and typical development as described elsewhere, for example, at Złota (see below). The unexpectedly high pIRIR ages (> 300 ka) of the lowermost samples (BT 1668 and Bk 2 and 1) may be affected by the $pIRIR_{290}$ dose overestimation recently described by Avram et al. (2020) and should be interpreted very cautiously, as they found that beyond ca. 400 Gy the natural $pIRIR_{290}$ signals overestimate the laboratory signals, implying age overestimates.

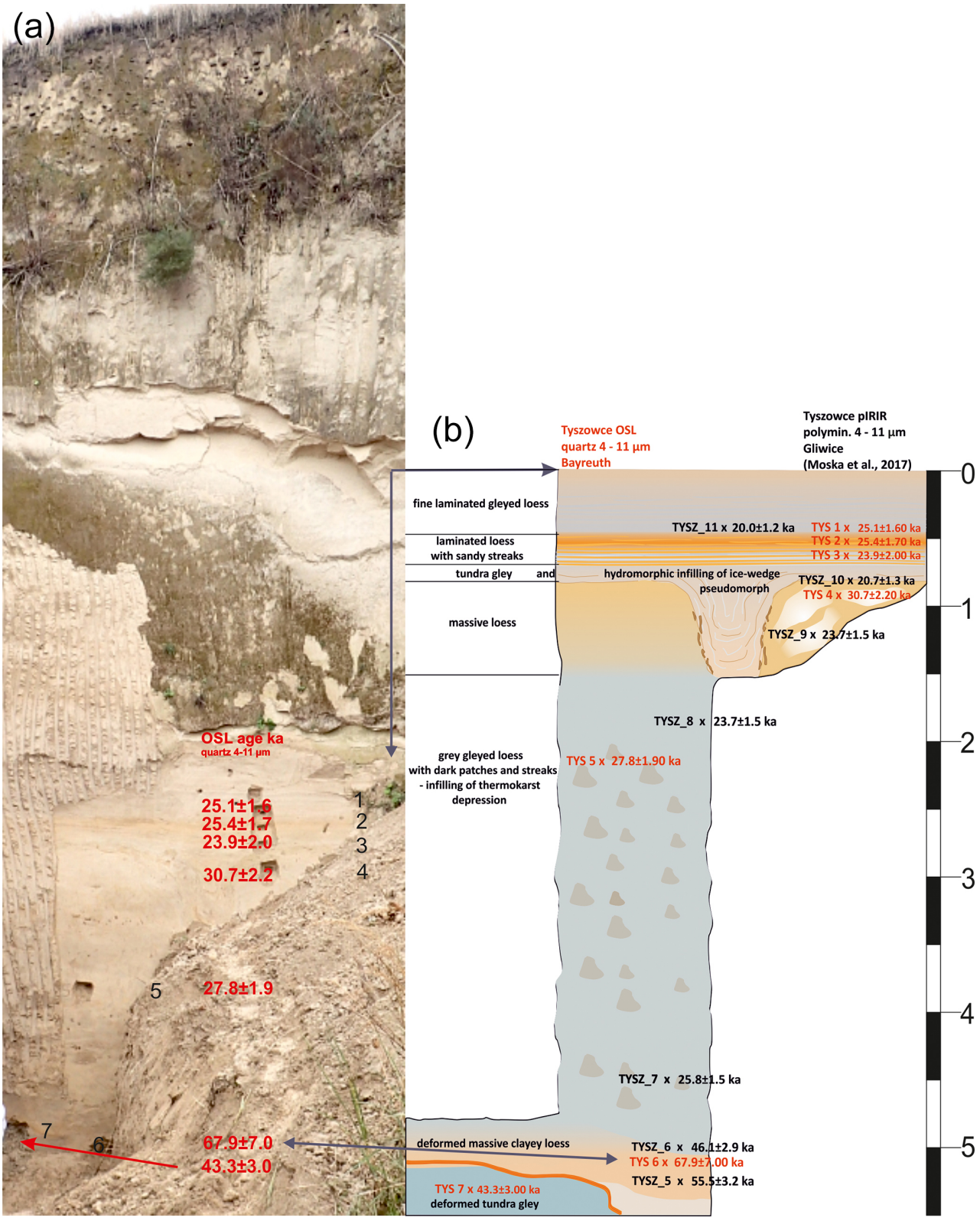

Figure 11. **(a)** The Tyszowce trench (16 m) from September 2015 with all OSL samples for the Bayreuth laboratory and their OSL ages (red). **(b)** Attempt to compile quartz OSL and polymineral pIRIR ages for the two trenches (2012 and 2015) of the Tyszowce section in a schematic plot (Marcin Krawczyk). Red characters: fine-grain quartz ages obtained in the Bayreuth laboratory. Black characters: selection of fine-grain polymineral pIRIR ages obtained in the Gliwice laboratory (from Moska et al., 2017) which are relevant for comparison with ages from the Bayreuth laboratory. Please note the different notation of Bayreuth samples (e.g. TYS 6) and Gliwice samples (TYSZ_6).

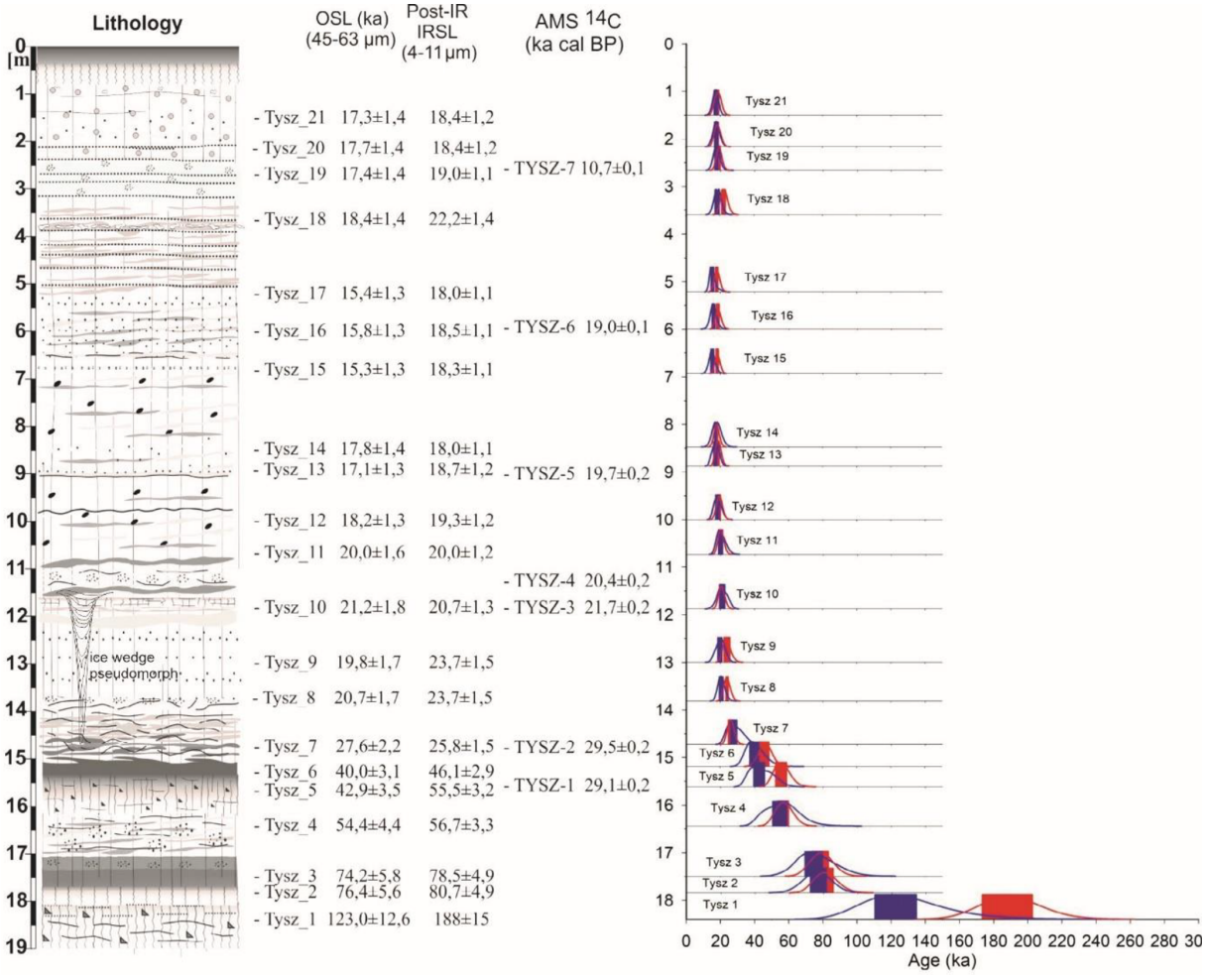

Figure 12. Lithology, OSL and pIRIR ages, radiocarbon ages, and relative probability plots for ages obtained for all samples versus depth at Tyszowce according to Moska et al. (2017). The ice wedge pseudomorph position is now marked.

At the Zaprężyn section the fine-grain quartz OSL ages from the Bayreuth laboratory (Figs. 7 and S1) indicate that the L1SS1 is completely missing. According to the fine-grain quartz ages (ZAPR8, ZAPR9, and ZAPR10), the loess deposited prior to the ice wedging can be attributed to MIS 4 and the age of ZAPR11 (sandy loess, 56.8 ± 4.7 ka) cannot clearly be allocated to MIS 4 or MIS 3, whereas ZAPR12 (lamellar sandy loess, 52.5 ± 3.7 ka) deposited after the melt out of the thermokarst argues for MIS 3. The lithology of the flashy loess with sand lamellas, however, supports cold windy climate conditions rather than a more temperate interstadial. Thus, this sandy loess (samples ZAPR11 and ZAPR12) may also mirror periglacial conditions caused by the Ristinge ice advance (see above).

From the profiles investigated in this study, Złota is best suited to bracketing the duration of soil formation of the L1SS1 pedocomplex between ca. 30 and 40 ka (see above). It comprises a lower brown (cambic) soil and an upper tundra gley soil with signs of gelifluction and cryoturbation. The L1SS1 at the Złota section is comparable to but not identical with the "Lohne Soil" in southern Germany (cf. Rousseau et al., 2017; Moine et al., 2017). Before or during the formation of the tundra gley, deposition of fresh loess started, as evidenced by the OSL age of ZL-3 (31.9 ± 1.9 ka) being significantly younger than ZL-2 (38.6 ± 3.6 ka) from the brown loess. ZL-3 gives evidence for the presence of ca. 32 kyr old loess, which had not been identified so far in the previous sections from Silesia. The age of the first great loess accumulation phase of what is called the Upper Pleniglacial in northern France, Belgium, and western Germany is also 31–32 ka (Antoine et al., 2015). OSL characteristics of fine-grained quartz confirm the change of parent material between ZL-2 and ZL-3: ZL-1 and ZL-2 are characterized by unusually low OSL sensitivity, in contrast to ZL-3 and samples positioned farther upwards. The tundra gley on top of L1SS1 (ZL-4, 27.6 ± 2.0 ka, unit 12) is regarded as a separate soil not included in L1SS1 but belonging to L1LL1. We attribute the relative complete stratigraphy of this part of the profile to

both the more continental climate referred to Silesia and to the proximity of the main source of the loess (Vistula valley). No inversions of fine-grain quartz ages were observed.

The reliability of the fine-grain quartz age of ZL-1 (50.0 ± 5.4 ka) from the L1LL2 loess (unit 17), however, can hardly be judged due to the lack of further fine-grain quartz samples from the L1LL2. Złota lies some 330 km south-southeast of Zaprężyn, and it appears very questionable whether the periglacial impact of the regional Ristinge ice advance could reach up to Złota. The consistent pIRIR ages by Moska et al. (2018) from the L1LL2 loess at Złota (ca. 62 to 67 ka) argue for attribution to MIS 4 and for a severe age underestimate of all the quartz ages from L1LL2. The obvious presence of ca. 32 ka loess (ZL-3) may, however, be connected with the extended Odra ice lobe of the Klintholm ice advance 30–34 kyr ago (Lüthgens et al., 2020; Figs. 4 and 5). Despite its potentially speculative character, this possibility deserves further discussion and attention, thereby considering that the ice-induced trigger of the climatic deterioration 30–34 kyr ago was superimposed by Heinrich Event 3 (H3), clearly reflected in LPSs of western central Europe (Antoine et al., 2015; Moine et al., 2017) and southwestern Europe (Wolf et al., 2018).

At the Tyszowce section two questions deserve discussion: the timing of the ice wedging and of the thermokarst processes and the age differences between the Gliwice and the Bayreuth laboratories for samples from L1LL1. As mentioned above, the two laboratories could not execute their dating using identical sample material. Moska et al. (2017) did not mention the ice wedge pseudomorph and the thermokarst, but strong periglacial reworking is evident from their Fig. 4 above L1SS1 between ca. 13.5 and ca. 15 m depth, connected with a considerable jump in luminescence ages (middle quartz grains and fine pIRIR grains). In Fig. 12 all luminescence ages obtained in Gliwice are plotted together with some AMS ^{14}C ages and the position of the ice wedge pseudomorph. The timing of the ice wedging cannot be directly derived from their ages but indirectly between ca. 29.5 ka cal BP (AMS ^{14}C, GdA-3133 TYSZ_1) and ca. 20 ka (TYSZ_11 and TYSZ_4). According to the OSL ages from Bayreuth, the ice wedging and subsequent thermokarst is bracketed between ca. 30 and ca. 25 ka, at the beginning of MIS 2 but posterior to the Klintholm ice advance. It is interesting to note that ice wedging in loess of northern France also occurred in the same time span at about 27–28 ka (levels F2–F3), whereas the main level F4 at ±32–31 ka (Antoine et al., 2014) was in time with the Klintholm advance. The ice wedging at Tyszowce, however, apparently pre-dates the Pomeranian ice advance triggered by a slight interstadial warming (Lüthgens et al., 2020) and rather witnesses a very cold and continental climate phase starving a major ice advance. Because of the limited depth and width of the 2015 dredge hole, it cannot clearly be decided if the thermokarst features in the lowermost part of the dredge hole are genetically related to this ice wedging or if they are older (MIS 3 or MIS 4; see Zaprężyn above).

The Bayreuth sample TYS 1 and the Gliwice sample TYSZ_11 originate from the same loess bed (for sample positions see Figs. 11b and 10a, unit "A"). Although non-identical sample material was dated, these two quartz OSL ages are particularly suitable for direct comparison. For sample TYSZ_11 (19.1 ± 1.4 ka for quartz 45–63 µm, differently from Fig. 4 in Moska et al., 2017, reproduced here as Fig. 12), exemplarily the age is calculated by the ADELE program using dosimetric and D_e values given in Moska et al. (2017, their Table 2) and yields 19.9 ± 1.0 ka. The ratio of effective dose rates $\dot{D}_{\mathrm{Moska}}/\dot{D}_{\mathrm{Adele}}$ for sample TYSZ_11 is 1.04 (2.73 and 2.62 Gy ka^{-1}). This demonstrates that the dose rates calculated by different age calculation programs cannot account for the observed discrepancy of ages. If from the mean D_e obtained from fine quartz grains in Bayreuth (76.8 Gy) the $\dot{D}\alpha$ (0.374 mGy a^{-1}) acquired over 25 kyr (9.35 Gy) is subtracted, 67.45 Gy remains as an approach for the D_e of the 45–63 µm quartz fraction. Moska et al. (2017, Table 2) find only 52.2 Gy, however. This crystallizes that determination of D_e for different grain sizes of quartz is the reason for the age discrepancies rather than dosimetry. How far laboratory illumination, being more critical for the fast OSL component from quartz than for IRSL from feldspars, may have influenced the D_e values for quartz grains cannot be currently assessed but should be a matter of further discussions. Different procedures for calibration of radioactive sources should also be borne in mind.

4.2 General discussion

The preceding exemplary discussion of samples TYS 1 and TYSZ_11 leads to a more general problem regarding grain size dependence of quartz OSL ages. The question has been addressed for several years (e.g. Lowick and Preusser, 2011; Chapot et al., 2012; Kreutzer et al., 2012; Timar-Gabor and Wintle, 2013; Timar-Gabor et al., 2015, 2017; Moska et al., 2015, 2019; Avram et al., 2020; Schmidt et al., 2021). A general rule cannot be proposed so far, however, because observed grain size dependencies of quartz ages point in opposite directions. In contrast to the results from Polish loess as well as from Saxonian loess (Kreutzer et al., 2012), observations from Romanian loess, for example, yield lower ages for fine quartz grains than for coarse quartz grains. It is furthermore astonishing that mean quartz OSL ages mentioned in this paper often "jump" in the stratigraphic order or even show age inversions, whereas quoted mean pIRIR ages by Moska et al. (2017, 2018, 2019) from identical samples stay "well-behaved" in stratigraphic order. It can, however, also be seen from the above-discussed sections that some samples whose pIRIR ages appear overestimated with respect to neighbouring samples also show a higher (mean) quartz age referred to underlying samples (cf. BT 1672 and BT 1678 from Biały Kościół). This probably indicates in-

complete bleaching due to periglacial reworking, and such samples are in general impeded for exact luminescence dating independent from the dated mineral fraction and should be thoroughly checked sedimentologically and geomorphologically.

Since the overall successful adaption of the quartz OSL-SAR protocol to dating of loess from the last glacial cycle, it has been favoured over IRSL or pIRSL because of higher sensitivity to daylight and the absence of anomalous fading. The results presented and discussed here, however, cast some doubts on the reliability of the quartz OSL ages unless the mentioned problems are better understood and apparent age underestimates due to reasons other than anomalous fading can be ruled out. Uncorrected OSL sensitivity change and different growth curve shapes for natural and laboratory-regenerated signal growth with doses are debated (e.g. Schmidt et al., 2021). Even if the present database is not yet sufficient, it is very likely that the quartz problems arise from the origin and geological history of quartz grains and mainly affect loess samples older than L1SS1. With respect to feldspars, quartz appears to be a relatively simple mineral, but the crystallization of quartz grains is very variable between magmatic, metamorphic, diagenetic or hydrothermal origin. Furthermore, (optical) zeroing and dosing cycles differentiate the luminescence characteristics of quartz. Due to the high chemical and mechanical resistance of quartz, the grains are often frequently recycled and eventually carry a history of several hundred million years around with them. As far as distinct source areas of quartz grains in certain sediment can be identified, quite similar OSL characteristics may be expected, but aeolian sediments such as loess often consist of quartz grains from very different source areas due to frequent changes in wind directions and due to various transport distances (and transport processes such as fluvial-induced mixing). The latter are reflected in the mean grain size, and coarser-grained quartz may originate from other more local sources than far-travelled fine quartz grains. It is hypothesized that these considerations are, besides diverging natural and laboratory growth curves, a further key to understanding the above-discussed problems with quartz OSL ages, in particular the grain size dependence owing to various source areas in a geologically manifold landscape with parent rocks from the Precambrian to the Neozoic in the source areas, as is the case for Polish loess areas.

The $pIRIR_{290}$ lends itself as an alternative but implies a higher risk for age overestimation due to incomplete bleaching compared to OSL from quartz. Given the fact that no $pIRIR_{290}$ age underestimates have been evidenced from the Polish loess sections discussed above, the problem of anomalous fading has apparently been erased. In view of the pending question of whether a dose residual should be subtracted from the D_e values and, if so, how to reliably estimate the residual dose, $pIRIR_{290}$ ages are prone to overestimation.

What should be done? "As you like it" is not passable. From this point of view we can suggest utilizing a two- or threefold strategy including $pIRIR_{290}$ and quartz OSL ages, reasoning that the true age lies anywhere between. As a priori it is unknown in which direction a possible grain size dependence of quartz points, fine-grain quartz fractions and middle- or coarse-grain quartz fractions should be dated and the higher quartz age compared to the $pIRIR_{290}$ age. Even if this approach requires considerably more human resources and machine time and the "bracketed true age range" may often not be precise enough to decide the geoscientific question involved (e.g. MIS 4 or MIS 3), it recommends itself as the most honest way to interact with users from geosciences. A well-dated marker horizon, ideally a volcanic tephra layer such as the Campanian Ignimbrite tephra, would be most helpful in this context but unfortunately is not known from the sections studied here, other than in Romania (Fitzsimmons and Hambach, 2013; Scheidt et al., 2021).

Such missing reliable age control in particular for loess > 30 ka also hampers the discussion about loess equivalents of the Ristinge and the Klintholm ice advances, which can so far only be assumed based on the fine-grain quartz ages. With respect to the $pIRIR_{290}$ ages, fine-grain quartz ages from L1LL2 ≥ 50 ka also appear to be underestimated in some profiles, whereas in other ones there is no proof. Underestimation of representative past water content cannot account for the observed amount of quartz age underestimates with $D_e > \sim 150$ Gy if referred to $pIRIR_{290}$ ages. The debate remains open at this stage and, thus, a too close backing of MISs to loess chronostratigraphy not taking into account other steering mechanisms in continental areas may be premature.

Despite the discussed pending problems, we can state that for the first time basic agreement was found in an inter-laboratory luminescence dating comparison of loess in Poland. The Bayreuth and Gliwice laboratories have worked completely independently with Zdzisław Jary acting as the only link. The achieved progress with regard to previous attempts is respectable. The advantage of independent dating work implied, however, the unavoidable disadvantage of not working with identical sample material. This gap is going to be closed, as Piotr Moska kindly supplied remains of his samples from Złota (< 45 µm) to the Bayreuth laboratory. These samples are in progress in Bayreuth, and the results will be published together elsewhere.

5 Conclusions

In the Bayreuth Luminescence Laboratory (Germany), self-consistent chronologies for four loess palaeosol sequences (LPSs) were achieved using OSL dating of fine-grained quartz (4–11 µm). From one section (Biały Kościół) fine-grain $pIRIR_{290}$ dating yielded significantly higher ages for samples older than ca. 30 ka. In comparison with quartz (middle and coarse grains) OSL ages and fine-grain $pIRIR_{290}$ ages obtained in the Gliwice laboratory (Poland), agree-

ment to a large extent was found, unlike in previous interlaboratory comparison of Polish luminescence laboratories. A meaningful agreement is the bracketing down of the L1SS1 pedocomplex, a most important stratigraphic level in Visutlian LPSs, to ca. 30 to 40 ka. Nevertheless some age differences between the Bayreuth and the Gliwice data call for further discussion.

An indication of grain size dependence from quartz ages is observed but in a reverse direction to those reported from, for example, loess in Romania (Avram et al., 2020, with further references therein), and, with respect to our observations, no general rule concerning the quartz grain diameter and OSL age underestimate can be established. For our samples, quartz OSL ages of fine grains are higher than (or at least equal to) those of middle and/or coarse grains. Age underestimation may, however, also affect fine quartz grains still far away from dose saturation (e.g. Złota, ZL-1), and assuming permanent water saturation (25 ± 5 % instead of 15 ± 5 %) for this sample would increase the age by 10 % only (55.0 ± 5.9 ka; see discussion above in Sect. 2 on luminescence dating). Since such a general rule for grain size dependence of quartz OSL ages cannot be derived from the data discussed in this contribution, we suggest that the strange behaviour of quartz ages from different grain sizes is rather caused by various sources (ranging from Paleozoic crystalline rocks to Quaternary glacial drift) with very different geological and thermal histories and, consequently, different OSL characteristics of quartz grains. Local and remote sources contribute to varying extents to individual sedimentary beds of LPSs, thereby being sorted by very variable transport mechanisms (wind strength and wind direction). Thus, fine grains and coarser grains from an individual sample may be derived from diverse sources.

From $pIRIR_{290}$ ages mentioned here, we found, however, no indication of age underestimates but some probability of overestimates caused by residual doses which cannot be estimated accurately, in particular for samples reworked under periglacial conditions. Determining $pIRIR_{290}$ ages complementing quartz ages is therefore advised for verification of quartz ages.

In the Zaprężyn section (Lower Silesia) ice wedging and subsequent thermokarst erosion more than 50 kyr old can be proved in loess below a long-lasting but hardly visible discordance, which completely removed the L1SS1 pedocomplex. In combination with the Tyszowce section (Volyn Hills, eastern Poland) where ice wedging is bracketed between ca. 30 and ca. 25 ka, two intervals of very harsh periglacial climate are identified in the studied sections. Whereas the latter coincides with the lower MIS 2 (beginning of the Upper Pleniglacial), the ice wedging at Zaprężyn most probably occurred during MIS 4. This corresponds to the presumably oldest ice wedge network and associated permafrost evidence for the last glacial in Poland but also in western central Europe (see Nussloch TK 2 before the lowest Gräselberg soil; Antoine et al., 2015). The overlying loess below the discordance in the Zaprężyn section with periglacial habitus (but without ice wedging) yields quartz ages around 50 to 57 ka, which argue for lower MIS 3. We hypothesize that this periglacial loess reflects the Ristinge ice advance (50–55 ka) in the southwestern Baltic Sea area. But attribution of luminescence ages to certain MISs is not yet always unambiguous. An analogue control by the Klintholm ice advance (30–34 ka) may be discussed for the loess of the upper L1SS1 pedocomplex at the Złota section (ZL-3, ca. 32 ka). The actual database is, however, too sparse to prove these hypotheses, and the discussed problems of optical dating need more clearness.

In spite of the addressed uncertainties, we can so far for honesty reasons recommend aiming at age bracketing as narrowly as possible, using OSL from different quartz fractions and pIRIR from fine polymineral grains. In the case of the L1SS1 pedocomplex, for example, age bracketing between ca. 30 and 40 ka demonstrates the helpfulness of this approach. Exact dating remains challenging, in particular for a periglacial environment with strong heterogeneity of the dated material (Fig. S2).

Data availability. Relevant data are given in the Supplement, in particular in Table S1 “Analytical data and ages”.

Supplement. The supplement related to this article is available online at: https://doi.org/10.5194/egqsj-71-59-2022-supplement.

Author contributions. LZ drafted the manuscript, conducted fieldwork and sampling, designed several figures, completed the check of luminescence dating results, and calculated final ages. MF undertook laboratory work including evaluation of luminescence measurements and the first calculation of ages. ZJ conducted fieldwork and sampling, designed several figures, was involved in continual discussions with all authors, and made fundamental contributions to the manuscript. PA conducted fieldwork and sampling at two sites, designed Figs. 8 and 10a, and contributed to the manuscript. MK conducted fieldwork and sampling, designed and finalized several figures, and gave a detailed description of profiles.

Competing interests. The contact author has declared that neither they nor their co-authors have any competing interests.

Disclaimer. Publisher’s note: Copernicus Publications remains neutral with regard to jurisdictional claims in published maps and institutional affiliations.

Acknowledgements. The research results were sponsored by the German Science Foundation DFG, project number ZO51/39-1, “Harsh periglacial climate at MIS 3/MIS 2 transition reflected in Central European Loess-Paleosol Sequences”, and by the National

Science Centre, Poland, project no. 2017/27/B/ST10/01854 entitled "Sudden COLD events of the Last Glacial in the central part of the European LOESS Belt – in Poland and in the western part of Ukraine (COLD LOESS)".

The authors thank the two anonymous reviewers for helpful remarks to improve the manuscript.

Financial support. This research has been supported by the Deutsche Forschungsgemeinschaft (grant no. ZO51/39-1) and the National Science Centre, Poland (grant no. 2017/27/B/ST10/01854).

This open-access publication was funded by the University of Bayreuth.

Review statement. This paper was edited by Tony Reimann and reviewed by two anonymous referees.

References

Aitken, M. J.: An introduction to optical dating, 267 pp., University Press, Oxford, ISBN 0198540922 (Hbk), 1998.

Antoine, P.: Thermokarst processes and features from west-European loess series: new evidences for rapid climatic warming events during the Last Glacial, Quatern. Int., 21, 279–280, https://doi.org/10.1016/j.quaint.2012.07.088, 2013.

Antoine, P., Goval, E., Jamet, G., Coutard, S., Moine, O., Herisson, D., Auguste, P., Guerin, G., Lagroix, F., Schmidt, E., Robert, V., Debenham, N., Meszner, S., and Bahain, J.-J.: Les séquences loessiques pléistocène supérieur d'Havrincourt (Pas-de-Calais, France): stratigraphie, paléoenvironnement, géochronologie et occupations paléolithiques, Quaternaire, 25, 321–368, https://doi.org/10.4000/quaternaire.7278, 2014.

Antoine, P., Coutard, S., Guerin, G., Deschodt, L., Goval, E., and Locht, J.-L.: Upper Pleistocene loess-palaeosol records from northern France in the European context: environmental background and dating of the Middle Palaeolithic, Quatern. Int., 411, 4–24, https://doi.org/10.1016/j.quaint.2015.11.036, 2015.

Avram, A., Constantin, D., Veres, D., Kelemen, S., Obreht, I., Hambach, U., Markovic, S. B., and Timar-Gabor, A.: Testing polymineral post-IR IRSL and quartz SAR-OSL protocols on Middle to Late Pleistocene loess at Batajnica, Serbia, Boreas, 49, 615–633, https://doi.org/10.1111/bor.12442, 2020.

Badura, J., Jary, Z., and Smalley, I.: Sources of loess material for deposits in Poland and parts of Central Europe: the lost big river, Quatern. Int., 296, 15–22, https://doi.org/10.1016/j.quaint.2012.06.019, 2013.

Butrym, J. and Maruszczak, H.: Thermoluminescence chronology of loesses at Nieledew profile, Scientific Research Report of Committee of Quaternary Research of the Polish Academy of Science 3, 1983 (in Polish).

Chapot, M. S., Roberts, H. M., Duller, G. A. T., and Lai, Z. P.: A comparison of natural- and laboratory-generated dose response curves for quartz optically stimulated luminescence signals from Chinese Loess, Radiat. Meas., 47, 1045–1052, 2012.

Degering, D. and Degering, A: Change is the only constant – time-dependent dose rates in luminescence dating, Quat. Geochronol., 58, 101074, https://doi.org/10.1016/j.quageo.2020.101074, 2020.

Duller, G. A. T.: The Analyst software package for luminescence data: overview and recent improvements, Ancient TL, 33, 35–42, 2015.

Fitzsimmons, K. E. and Hambach, U.: Loess accumulation during the last glacial maximum: Evidence from Urluia, southeastern Romania, Quatern. Int., 334–335, 74–85, https://doi.org/10.1016/j.quaint.2013.08.005, 2013.

Fuchs, M., Kreutzer, S., Rousseau, D. D., Antoine, P., Hatté, C., Lagroix, F., Moine, O., Gauthier, C., Svoboda, J., and Lisá, L.: The loess sequence of Dolní Věstonice, Czech Republic: A new OSL-based chronology of the Last Climatic Cycle, Boreas, 42, 664–677, https://doi.org/10.1111/j.1502-3885.2012.00299.x, 2013.

Gocke, M., Kuzyakov, Y., and Wiesenberg, G. L. B.: Rhizoliths in loess – evidence for post-sedimentary incorporation of root-derived organic matter in terrestrial sediments as assessed from molecular proxieset, Org. Geochem., 41, 1198–1206, https://doi.org/10.1016/j.orggeochem.2010.08.001, 2010.

Guérin, G., Mercier, N., and Adamiec, G.: Dose-rate conversion factors: update, Ancient TL, 29, 5–8, 2011.

Haase, D., Fink, J., Haase, G., Ruske, R., Pécsi, M., Richter, H., Altermann, M., and Jäger, K.-D.: Loess in Europe – its spatial distribution based on a European loess map, scale 1 : 2 500 000, Quaternary Sci. Rev. 26, 1301–1312, https://doi.org/10.1016/j.quascirev.2007.02.003, 2007.

Hardt, J., Lüthgens, C., Hebenstreit, R., and Böse, M.: Geochronological (OSL) and geomorphological investigations at the presumed Frankfurt ice marginal position in northeast Germany, Quaternary Sci. Rev., 154, 85–99, https://doi.org/10.1016/j.quascirev.2016.10.015, 2016.

Hughes, P. D., Gibbard, P. L., and Ehlers, J.: Timing of glaciation during the last glacial cycle: evaluating the concept of a global "Last Glacial Maximum" (LGM), Earth-Sci. Rev., 125, 171–198, https://doi.org/10.1016/j.earscirev.2013.07.003, 2013.

Jary, Z.: Record of climate changes in Upper Pleistocene loess-soil sequences in Poland and western part of Ukraine, Rozprawy Naukowe Instytutu Geografii i Rozwoju Regionalnego Uniwersytetu Wrocławskiego 1, 136 pp., Wrocław, ISBN 83-921524-5-X, 2007 (in Polish, with English abstract).

Jary, Z.: Periglacial markers within the Late Pleistocene loess-palaeosol sequences in Poland and western Ukraine, Quatern. Int., 198, 124–135, https://doi.org/10.1016/j.quaint.2008.01.008, 2009.

Jary, Z. (Ed.): Closing the gap – North Carpathian loess travers in the Eurasian loess belt, International Workshop, 6th Loess Seminar in Wrocław, Poland, 16–21 May 2011, Abstract and field guide book, Institute of Geography and Regional Development, University of Wrocław, ISBN 978-83-62673-06-3, 2011.

Jary, Z. and Ciszek, D.: Late Pleistocene loess-palaeosol sequences in Poland and western Ukraine, Quatern. Int., 296, 37–50, https://doi.org/10.1016/j.quaint.2012.07.009, 2013.

Jary, Z. and Krzyszkowski, D.: Stratigraphy, properties and origin of loess in Trzebnica Brickyard, southwestern Poland, Acta Universitatis Wratislaviensis No. 1702, Prace Instytutu Geograficznego, Seria A, Geografia Fizyczna VII, 63–83, ISBN 83-229-1228-5, 1994.

Jary, Z., Ciszek, D., Kida, J., Karamański, P., and Raczyk, J: Late Pleistocene loess-soil sequence in Zaprężyn, edited by: Jary, Z., Closing the gap – North Carpathian loess traverse in the Eurasian loess belt, International Workshop, 6th Loess Seminar, Wrocław, Poland, 16–21 May 2011, Abstract and field guide book, Institute of Geography and Regional Development, University of Wrocław, 51–52, ISBN 978-83-62673-06-3, 2011.

Kreutzer, S., Fuchs, M., Meszner, S., and Faust, D.: OSL chronostratigraphy of a loess-palaeosol sequence in Saxony/Germany using quartz of different grain sizes, Quat. Geochronol. 10, 102–109, https://doi.org/10.1016/j.quageo.2012.01.004, 2012.

Kreutzer, S., Schmidt, C., DeWitt, R., and Fuchs, M., The a-value of polymineral fine grain samples measured with the post-IR IRSL protocol, Radiat. Meas., 69, 18–29, 2014.

Krzyszkowski, D.: The Wartanian Siedlec Sandur (Zedlitzer Sandur) southwards the Trzebnica Hills, Silesian Lowland; Southwestern Poland: re-examination after fifty years, E&G Quaternary Sci. J., 43, 53–66, https://doi.org/10.3285/eg.43.1.05, 1993.

Lai, Z. P., Zöller, L., Fuchs, M., and Brückner, H.: Alpha efficiency determination for OSL of quartz extracted from Chinese loess, Radiat. Meas., 43, 767–770, https://doi.org/10.1016/j.radmeas.2008.01.022, 2008.

Léger, M.: Loess landforms, Quatern. Int., 7/8, 53–61, 1990.

Lowick, S. E. and Preusser, F.: Investigating age underestimation in the high dose region of optically stimulated luminescence using fine grain quartz, Quat. Geochronol., 6, 33–41, 2011.

Lüthgens, C. and Böse, M.: Chronology of Weichselian main ice marginal positions in north-eastern Germany, E&G Quaternary Sci. J., 60, 17, https://doi.org/10.3285/eg.60.2-3.02, 2011.

Lüthgens, C., Hardt, J., and Böse, M.: Proposing a new conceptual model for the reconstruction of ice dynamics in the SW sector of the Scandinavian Ice Sheet (SIS) based on the reinterpretation of published data and new evidence from optically stimulated luminescence (OSL) dating, E&G Quaternary Sci. J., 69, 201–223, https://doi.org/10.5194/egqsj-69-201-2020, 2020.

Marković, S. B., Stevens, T., Kukla, G. J., Hambach, U., Fitzsimmons, K. E., Gibbard, P., Buggle, B., Zech, M., Guo, Z., Hao, Q., Wu, H., O'Hara-Dhand, K., Smalley, I. J., Ujvari, G., Sumegi, P., Timar-Gabor, A., Veres, D., Sirocko, F., Vasiljević, D. A., Jary, Z., Svensson, A., Jović, V., Lehmkuhl, F., Kovacs, J., and Svircev, Z.: Danube loess stratigraphy – Towards a pan-European loess stratigraphic model, Earth Sci. Rev., 148, 228–258, https://doi.org/10.1016/j.earscirev.2015.06.005, 2015.

Marks, L.: Pleistocene glacial limits in the territory of Poland, Przegląd Geologiczny, 53, 988–993, 2005.

Marks, L.: Quaternary Glaciations in Poland, in: Developments in Quaternary Science, edited by: Ehlers, J., Gibbard, P. L., and Hughes, P. D., Amsterdam, the Netherlands, vol. 15, 299–303, ISBN 9780444534477, 2011.

Maruszczak, H.: Zróżnicowanie stratygraficzne lessów polskich (Stratigraphical differentiation of Polish loesses), 1991, in: Podstawowe profile lessów w Polsce (Main section of loesses in Poland), edited by: Maruszczak, H., Wyd. UMCS, Lublin, A, 13–35, ISBN 83-227-0388-0, 1991.

Maruszczak, H.: Schemat stratygrafii lessów i gleb śródlessowych w Polsce (Stratigraphic scheme of loesses and paleosols in Poland), in: Podstawowe profile lessów w Polsce II (Main section of loesses in Poland II), edited by: Maruszczak, H., Wyd. UMCS, Lublin, 17–29, ISBN 83-227-1723-7, 2001.

Meszner, S., Kreutzer, S., Fuchs, M., and Faust, D.: Late Pleistocene landscape dynamics in Saxony, Germany: Paleoenvironmental reconstruction using loess-paleosol sequences, Quatern. Int. 296, 94–107, https://doi.org/10.1016/j.quaint.2012.12.040, 2013.

Moine, O., Antoine, P., Hatté, C., Landais, A., Mathieu, J., Prud'homme, C., and Rousseau, D.-D.: The impact of Last Glacial climate variability in west-European loess revealed by radiocarbon dating of fossil earthworm granules, P. Natl. Acad. Sci. USA, 114, 6209–6214, https://doi.org/10.1073/pnas.1614751114, 2017.

Moska, P. and Bluszcz, A.: Luminescence dating of loess profiles in Poland, Quatern. Int., 296, 51–60, https://doi.org/10.1016/j.quaint.2012.09.004, 2013.

Moska, P., Adamiec, G., and Jary, Z.: OSL dating and lithological characteristics of loess deposits from Biały Kościół, Geochronometria, 38, 162–171, https://doi.org/10.2478/s13386-011-0013-x, 2011.

Moska, P., Adamiec, G., and Jary, Z.: High resolution dating of loess profile from Biały Kościół, southwest Poland, Quat. Geochronol., 10, 87–93, https://doi.org/10.1016/j.quageo.2012.04.003, 2012.

Moska, P., Jary, Z., Adamiec, G., and Bluszcz, A.: OSL chronostratigraphy of a loess-paleosol sequence in Złota using quartz and polymineral fine grains, Radiat. Meas., 81, 23–31, https://doi.org/10.1016/j.radmeas.2015.04.012, 2015.

Moska, P., Adamiec, G., Jary, Z., and Bluszcz, A.: OSL chronostratigraphy for loess deposits from Tyszowce – Poland, Geochronometria, 44, 307–318, https://doi.org/10.1515/geochr-2015-0074, 2017.

Moska, P., Adamiec Jary, Z. G., Bluszcz, A., Poręba, G., Piotrowska, N., Krawczyk, M., and Skurzyński, J.: Luminescence chronostratigraphy for the loess deposits in Złota, Poland, Geochronometria, 45, 44–55, 2018.

Moska, P., Jary, Z., Adamiec, G., and Bluszcz, A.: Chronostratigraphy of a loess-palaeosol sequence in Biały Kościół, Poland using OSL and radiocarbon dating, Quatern. Int., 502, 4–17, https://doi.org/10.1016/j.quaint.2018.05.024, 2019.

Murray, A. S. and Wintle, A. G.: Luminescence dating of quartz using an improved single aliquot regenerative-dose protocol, Radiat. Meas., 32, 57–73, 2000.

Murray, A. S., Schmidt, E. D., Stevens, T. Buylaert, J.-P., Marković, S. B., Tsukamoto, S., and Frechen, M.: Dating Middle Pleistocene loess from Stari Slankamen (Vojvodina, Serbia) – Limitations imposed by the saturation behaviour of an elevated temperature IRSL signal, Catena, 117, 34–42, https://doi.org/10.1016/j.catena.2013.06.029, 2013.

Murton, J. B.: Thermokarst sediments and sedimentary structures, Tuktoyaktuk Coastlands, western Arctic Canada, Global Planet. Change, 28, 175–192, 2001.

Preusser, F., Degering, D., Fuchs, M., Hilgers, A., Kadereit, A., Klasen, N., Krbetschek, M., Richter, D., and Spencer, J. Q. G.: Luminescence dating: basics, methods and applications, E&G Quaternary Sci. J., 57, 95–149, https://doi.org/10.3285/eg.57.1-2.5, 2008.

Rousseau, D.-D., Boers, N., Sima, A., Svensson, A., Bigler, M., Lagroix, F., Taylor, S., and Antoine, P.: (MIS3 & 2) millennial oscillations in Greenland dust and Eurasian aeolian records – A paleosol perspective, Quaternary Sci. Rev., 169, 99–113, https://doi.org/10.1016/j.quascirev.2017.05.020, 2017.

Różycki, S. Z.: Le sens des vents portant la poussiere de loess a la lumiere de l'analyse des formes d'accumulation du loess en Bulgarie et en Europe Centrale, Revue de geomorphologie dynamique, 1, 1–9, 1967.

Scheidt, S., Berg, S., Hambach, U., Klasen, N., Pötter, S., Stolz, A., Veres, D., Zeeden, C., Brill, D., Brückner, H., Kusch, S., Laag, C., Lehmkuhl, F., Melles, M., Monnens, F., Oppermann, L., Rethemeyer, J., and Nett, J. J.: Chronological assessment of the Balta Alba Kurgan loess-paleosol section (Romania) – a comparative study on different dating methods for a robust and precise age model, Front. Earth Sci., 8, 598448, https://doi.org/10.3389/feart.2020.598448, 2021.

Schmidt, C., Bösken, J., and Kolb, T.: Is there a common alpha-efficiency in polymineral samples measured by various infrared stimulated luminescence protocols?, Geochronometria, 45, 160–172, 2018.

Schmidt, C., Zeeden, C., Krauß, L., Lehmkuhl, F., and Zöller, L.: A chronological and palaeoenvironmental re-evaluation of two loess-palaeosol records in the northern Harz foreland (Germany) based on innovative modelling tools, Boreas, 50, 746–763, https://doi.org/10.1111/bor.12510, 2021.

Thiel, C., Buylaert, J.-P., Murray, A. S., Terhorst, B., Tsukamoto, S., Frechen, M., and Sprafke, T.: Investigating the chronostratigraphy of prominent palaeosols in Lower Austria using post-IR IRSL dating, E&G Quaternary Sci. J., 60, 11, https://doi.org/10.3285/eg.60.1.10, 2011.

Timar-Gabor, A. and Wintle, A. G.: On natural and laboratory generated dose response curves for quartz of different grain sizes from Romanian loess, Quat. Geochronol., 18, 34–40, 2013.

Timar-Gabor, A., Constantin, D., Buylaert, J. P., Jain, M., Murray, A. S., and Wintle, A. G.: Fundamental investigations of natural and laboratory generated SAR dose response curves for quartz OSL in the high dose range, Radiat. Meas., 81, 150–156, 2015.

Timar-Gabor, A., Buylaert, J.-P., Guralnik, B., Trandafir-Antohi, O., Constantin, D., Anachitei-Deacu, V., Jain, M., Murray, A. S., Porat, N., Hao, Q., and Wintle, A. G.: On the importance of grain size in luminescence dating using quartz, Radiat. Meas., 106, 464–471, https://doi.org/10.1016/j.radmeas.2017.01.009, 2017.

Waroszewski, J., Pietranik, A., Sprafke, T., Kabała, C., Frechen, M., Jary, Z., Kot, A., Tsukamoto, S., Meyer-Heintze, S., Krawczyk, M., Łabaz, B., Schultz, B., and Erban Kochergina, Y. V.: Provenance and paleoenvironmental context of the Late Pleistocene thin aeolian silt mantles in southwestern Poland. A widespread parent material for soils, Catena, 204, 105377, https://doi.org/10.1016/j.catena.2021.105377, 2021.

Wolf, D., Kolb, T., Alcaraz-Castaño, M., Heinrich, S., Baumgart, P., Calvo, R., Sánchez, J., Ryborz, K., Schäfer, I., Bliedtner, M., Zech, R., Zöller, L., and Faust, D.: Climate deteriorations and Neanderthal demise in interior Iberia, Sci. Rep., 8, 7048, https://doi.org/10.1038/s41598-018-25343-6, 2018.

Zöller, L.: Geomorphologische und geologische Interpretation von Thermolumineszenz-Daten, Bayreuther Geowissenschaftliche Arbeiten, 14, 103–112, 1989.

Zöller, L. and Pernicka, E.: A note on overcounting in alpha-counters and its elimination, Ancient TL, 7, 11–14, 1989.

Zöller, L., Richter, D., Blanchard, H., Einwögerer, T., Händel, M., and Neugebauer-Maresch, C.: Our oldest children: Age constraints for the Krems-Wachtberg site obtained from various thermoluminescence dating approaches, Quatern. Int., 351, 83–87, https://doi.org/10.1016/j.quaint.2013.05.003, 2014.

E&G Quaternary Sci. J., 71, 83–90, 2022
https://doi.org/10.5194/egqsj-71-83-2022

Open Access E&G Quaternary Science Journal

Research article

^{18}O analyses of bulk lipids as novel paleoclimate tool in loess research – a pilot study

Jakob Labahn[1], Lucas Bittner[1], Philip Hirschmann[1], Christopher-Bastian Roettig[1], Diana Burghardt[2], Bruno Glaser[3], Slobodan B. Marković[4], and Michael Zech[1]

[1]Heisenberg Chair of Physical Geography with Focus on Paleoenvironmental Research, Technische Universität Dresden, Helmholtzstraße 10, 01069 Dresden, Germany
[2]Institute of Groundwater Management, Department of Hydro Sciences, Technische Universität Dresden, Bergstraße 66, 01069 Dresden, Germany
[3]Soil Biogeochemistry, Institute of Agronomy and Nutritional Sciences, Martin Luther University Halle-Wittenberg, Von-Seckendorff-Platz 3, 06120 Halle (Saale), Germany
[4]Chair of Physical Geography, Faculty of Sciences, University of Novi Sad, Trg D. Obradovića 3, 21000 Novi Sad, Serbia

Correspondence: Jakob Labahn (jakob.labahn@tu-dresden.de) and Michael Zech (michael.zech@tu-dresden.de)

Relevant dates: Received: 2 November 2021 – Revised: 25 February 2022 – Accepted: 28 February 2022 – Published: 13 April 2022

How to cite: Labahn, J., Bittner, L., Hirschmann, P., Roettig, C.-B., Burghardt, D., Glaser, B., Marković, S. B., and Zech, M.: ^{18}O analyses of bulk lipids as novel paleoclimate tool in loess research – a pilot study, E&G Quaternary Sci. J., 71, 83–90, https://doi.org/10.5194/egqsj-71-83-2022, 2022.

Abstract: The analysis of the stable oxygen isotopes ^{18}O and ^{16}O has revolutionized paleoclimate research since the middle of the last century. Particularly, $\delta^{18}O$ of ice cores from Greenland and Antarctica is used as a paleotemperature proxy, and $\delta^{18}O$ of deep-sea sediments is used as a proxy for global ice volume. Important terrestrial archives to which $\delta^{18}O$ as a paleoclimate proxy is successfully applied are speleothems, lake sediments, or tree rings. By contrast, $\delta^{18}O$ applications to loess–paleosol sequences (LPSs) are scarce. Here we present a first continuous $\delta^{18}O$ record ($n = 50$) for the LPS Crvenka in Serbia, southeastern Europe, spanning the last glacial–interglacial cycle (since 145 ka). From a methodological point of view, we took advantage of a recently proposed paleoclimate/paleohydrological proxy based on bulk $\delta^{18}O$ analyses of plant-derived lipids. The Crvenka $\delta^{18}O_{\text{bulk lipid}}$ values range between $-10.2‰$ and $+23.0‰$ and are systematically more positive in the interglacial and interstadial (paleo-)soils corresponding to marine oxygen-isotope stage (MIS) 1, 3, and 5, compared to the loess layers (MIS 2, 4, and 6). Our Crvenka $\delta^{18}O_{\text{bulk lipid}}$ record provides no evidence for the occurrence of interstadials and stadials comparable to the Dansgaard–Oeschger events known from the Greenland $\delta^{18}O_{\text{ice core}}$ records. Concerning the interpretation of our Crvenka $\delta^{18}O_{\text{bulk lipid}}$ record, plant-derived lipids such as fatty acids and alcohols are certainly strongly influenced by climatic factors such as temperature (via $\delta^{18}O_{\text{precipitation}}$) and relative air humidity (via ^{18}O enrichment of leaf water due to evapotranspiration). However, pool effects in the form of non-water-correlated lipids such as sterols or the input of root-derived lipids need to be considered, too. Similarly, the input of soil-microbial lipids and oxygen exchange reactions represent uncertainties challenging quantitative paleoclimate/paleohydrological reconstructions based on $\delta^{18}O_{\text{bulk lipid}}$ analyses from LPSs.

Published by Copernicus Publications on behalf of the Deutsche Quartärvereinigung (DEUQUA) e.V.

Kurzfassung:

Die Analyse der stabilen Sauerstoffisotope ^{18}O und ^{16}O hat die Paläoklimaforschung seit Mitte des letzten Jahrhunderts revolutioniert. Insbesondere wird $\delta^{18}O$ von Eisbohrkernen aus Grönland und der Antarktis als Paläo-Temperaturproxy sowie $\delta^{18}O$ von Tiefseesedimenten als Proxy für das globale Eisvolumen verwendet. Wenngleich sich in terrestrischen Archiven, wie Speläothemen, Seesedimenten oder Baumringen, paläoklimatische Rekonstruktionen unter der Anwendung von $\delta^{18}O$ als Proxy bewährt haben, wurden solche Analysen bislang in Löß-Paläobodensequenzen (LPS) selten durchgeführt. In dieser Studie präsentieren wir einen ersten kontinuierlichen $\delta^{18}O$ Datensatz ($n = 50$) für die LPS Crvenka in Serbien, der den letzten Glazial-Interglazial-Zyklus (~ 145 ka) abdeckt. Die $\delta^{18}O$-Werte basieren auf der Analyse von pflanzlichen Lipiden, deren Anwendung als paläoklimatischer/hydrologischer Proxy vor Kurzem vorgeschlagen wurde.

Die $\delta^{18}O_{bulk-lipid}$-Werte von Crvenka liegen zwischen -10.2 ‰ und $+23.0$ ‰ und sind in den interglazialen und interstadialen (Paläo-)Böden, die den marinen Sauerstoff-Isotopenstufen (MIS) 1, 3 und 5 entsprechen, systematisch positiver als in den Lößlagen (MIS 2, 4 und 6). Sie liefern keine Hinweise für das Auftreten von Interstadialen und Stadialen, die mit den aus den grönländischen $\delta^{18}O_{ice-core}$ bekannten Dansgaard-Oeschger-Ereignissen vergleichbar wären. In Bezug auf die Interpretation der $\delta^{18}O_{bulk-lipid}$-Werte gilt es zu berücksichtigen, dass die Isotopie pflanzlicher Lipide, wie z.B. von Fettsäuren und Alkoholen, stark durch die Klimafaktoren Temperatur (über $\delta^{18}O$-Niederschlag) und relativer Luftfeuchtigkeit (über die ^{18}O-Anreicherung des Blattwassers aufgrund von Evapotranspiration) beeinflusst werden. Weiter zu beachtende Faktoren stellen Einträge von Sterolen sowie von generell wurzel-bürtigen Lipiden dar (Pool-Effekte). In ähnlicher Weise bergen der Einfluss von bodenmikrobiellen Lipiden und Sauerstoffaustauschreaktionen Unsicherheiten, die quantitative paläoklimatische/hydrologische Rekonstruktionen auf der Grundlage von $\delta^{18}O_{bulk-lipid}$-Analysen aus LPS erschweren können.

1 Introduction

The analysis of the stable oxygen isotopes ^{18}O and ^{16}O has revolutionized paleoclimate research since the middle of the last century. Particularly, the oxygen isotopic composition $\delta^{18}O$ of ice cores from Greenland and Antarctica is used as a paleotemperature proxy (e.g., NGRIP members, 2004), and $\delta^{18}O$ of deep-sea sediments is used as a proxy for global ice volume (e.g., Lisiecki and Raymo, 2005). Important terrestrial archives to which $\delta^{18}O$ as a paleoclimate proxy is currently successfully applied are speleothems (e.g., Spötl et al., 2006), lake sediments (e.g., Bittner et al., 2021), or tree rings (e.g., Roden et al., 2000). In all these archives, the $\delta^{18}O$ signal of paleoprecipitation ($\delta^{18}O_{precipitation}$) plays a major role, for which four effects can be highlighted. (1) The "temperature effect" describes that the colder the temperature is, the more negative $\delta^{18}O_{precipitation}$ becomes. (2) The "amount effect" describes that $\delta^{18}O_{precipitation}$ becomes more negative with increasing precipitation amount. (3) The "altitude effect" describes that $\delta^{18}O_{precipitation}$ becomes more negative with increasing altitude. (4) The "source effect" explains that air masses derived from different moisture sources can have distinct and variable $\delta^{18}O_{precipitation}$ values (e.g., Dansgaard, 1964; Lachniet, 2009; Lemma et al., 2021).

In contrast to the aforementioned terrestrial archives, $\delta^{18}O$ applications to loess–paleosol sequences (LPSs) are still scarce, although these represent unique and widespread occurring paleoenvironmental archives. For instance, Pustovoytov and Terhorst (2004) examined calcified root cells in an LPS using $\delta^{13}C$ and $\delta^{18}O$ analyses to determine climatic conditions based on the signal obtained during post-sedimentary Holocene soil formation, and Prud'homme et al. (2016) used $\delta^{18}O$ of earthworm calcite granules from an LPS to reconstruct paleotemperatures. Other approaches with respect to isotope analyses in loess archives have lately focused on the study of biomarkers (e.g., R. Zech et al., 2013; Schäfer et al., 2016; Häggi et al., 2019). These biomarkers are primarily compounds derived from plants, such as lipids or sugars (monosaccharides). For example, M. Zech et al. (2013) applied compound-specific $\delta^{18}O$ analysis of plant-derived sugar biomarkers to a permafrost LPS from Siberia. Similar to compound-specific $\delta^{2}H$ analyses of leaf-wax-derived *n*-alkane biomarkers (R. Zech et al., 2013), $\delta^{18}O$ of sugar biomarkers has a great potential to serve as a paleoclimate proxy in sedimentary archives (Zech et al., 2014). However, this latter approach could not be adopted so far due to the considerable carbonate amounts in classical LPSs. To sum up, no continuous $\delta^{18}O$ records could be established for classical LPSs up to now.

Recently, Silva et al. (2015) and Maxwell et al. (2018) proposed $\delta^{18}O$ of plant-derived bulk lipids ($\delta^{18}O_{bulk\,lipids}$) as a proxy for reconstructing ecosystem water balances. Lipids are important constituents of cuticular waxes and comprise, e.g., non-oxygen-bearing long-chain *n* alkanes as well as oxygen-bearing molecules such as long-chain alkanols and

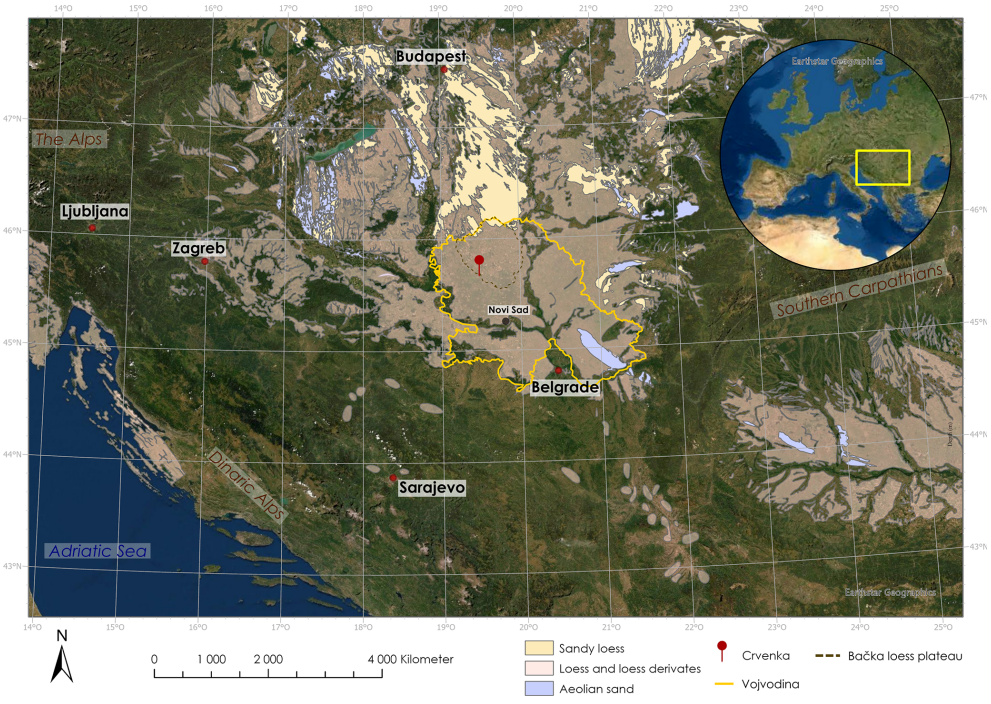

Figure 1. Map of the Carpathian basin with loess deposits according to Lehmkuhl et al. (2021) and location of the Crvenka study area (created with ArcGIS Pro).

alkanoic acids. From an analytical point of view, total lipid extraction from plants, soils, or sediments for yielding bulk lipids is relatively simple and can be achieved, e.g., by Soxhlet, ultrasonic, or microwave extraction. Lipids are generally hydrophobic and thus not specifically prone to translocation by percolating water in soils. Moreover, they are relatively persistent against biodegradation and can thus be studied even over geological timescales in paleosols and sediments. According to our knowledge, $\delta^{18}O_{bulk\ lipid}$ analyses have hitherto not been applied to paleoenvironmental archives such as LPSs.

The aim of our pilot study presented here was therefore to test the applicability of $\delta^{18}O_{bulk\ lipid}$ analyses to LPSs. Given that abundant research, including numerical dating, has already been conducted there, we chose the late Middle Pleistocene–Holocene LPS Crvenka in Serbia (Marković et al., 2015; Stevens et al., 2011; R. Zech et al., 2013) and followed the following specific research questions and objectives:

- How high are the bulk lipid contents in the LPS Crvenka, and are the extractable amounts sufficient for $\delta^{18}O_{bulk\ lipid}$ analyses?
- In the case that a $\delta^{18}O_{bulk\ lipid}$ record can be established for the LPS Crvenka, does it show variations coinciding with the marine oxygen-isotope stage (MIS) or with interstadials known from Greenland $\delta^{18}O_{ice\ core}$ records?
- Which factors need to be considered when interpreting $\delta^{18}O_{bulk\ lipid}$ records?

2 Material and methods

2.1 Study site and sampling

The LPS Crvenka (45°39.750′ N, 19°28.774′ E; 108 m a.s.l.) is located in the center of the Carpathian basin, southeastern Europe, in a brickyard exposure on the southwestern edge of the Bačka loess plateau in the Vojvodina region (see Fig. 1). According to the effective classification of Köppen, the current climate in the Carpathian basin is mainly classified as Cfb (i.e., C – temperate, f – without dry season, b – warm summers), but the regional climate can vary greatly due to its location in the border area between the Atlantic, continental, and Mediterranean climate zones. In January the average temperature is −0.1 °C, and in July it is 21.9 °C, while mean annual precipitation is 612 mm with a maximum in spring (Peel et al., 2007). We chose the LPS Crvenka (spanning about the last 145 kyr) for our $\delta^{18}O_{bulk\ lipid}$ pilot study due to previous detailed stratigraphic and pedologic descriptions, geochemical analyses, and numerical dating (Marković et al., 2015; Stevens et al., 2011; R. Zech et al., 2013). The chronostratigraphy can be summarized as follows: vertically, the profile extends over a depth of approximately 10 m (Fig. 2).

The oldest pale-yellow loess unit ("L2") of the Crvenka LPS consists mainly of penultimate glacial silts and extends only over the lowest 100 cm of the profile. The over-

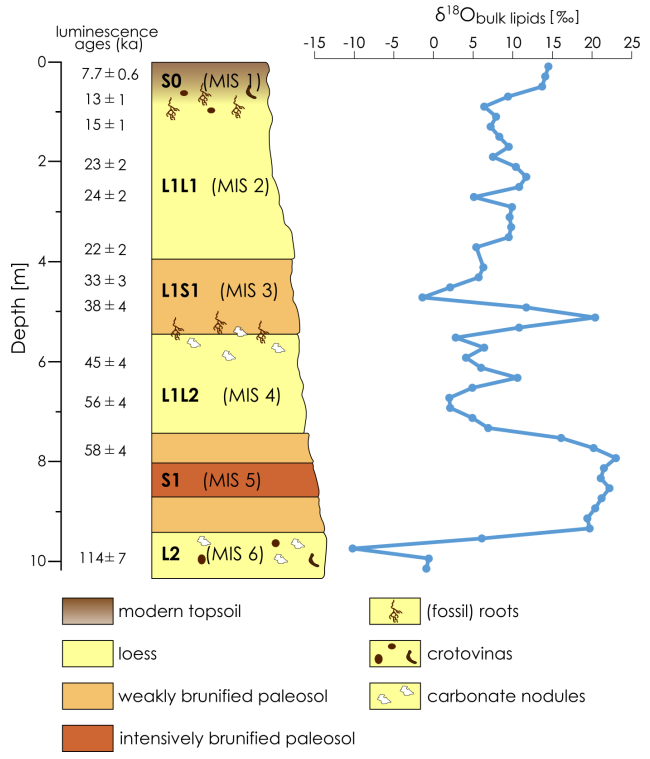

Figure 2. Stratigraphy of the LPS Crvenka after R. Zech et al. (2013) and the $\delta^{18}O_{bulk\,lipid}$ record. Note that the luminescence ages of Stevens et al. (2011) are "preferred" ages and that a numerical age model could only be constructed for the last 50 to 60 kyr. Lower luminescence ages than expected for older sediments probably indicate post-depositional effects on the luminescence signal (Stevens et al., 2011).

lying reddish-brown, clay-rich, and strongly brunified paleosol complex, with a thickness between 215–235 cm ("S1"), is correlated with MIS 5 and thus formed during the last interglacial. Above there is a loess package (L1) up to 8 m thick, which was deposited over the last glacial period. It is composed of two loess layers L1L1 (top) and L1L2 (bottom) separated by a weakly developed paleosol complex ("L1S1"). The lower light-yellow-grey L1L2 layer correlates with MIS 4 and is coarser-grained than the very porous L1L1 loess layer assigned to MIS 2. The interstadial, weakly developed paleosol complex ("L1S1") corresponds roughly to MIS 3. The uppermost part of the profile consists of a black-to-reddish-brown Holocene soil ("S0") that ranges in thickness from 50 to 80 cm and can be associated with MIS 1.

For our $\delta^{18}O_{bulk\,lipid}$ pilot study, we used 50 loess and paleosol samples that were taken by continuous sampling in ~ 20 cm intervals by Zech et al. (2013) in 2009.

2.2 Total lipid extraction and $\delta^{18}O_{bulk\,lipid}$ measurement

Total lipid extraction from about 20 g of sample material was performed using an ultrasonic bath for 15 min and 30 mL of DCM : MeOH (9 : 1) as a solvent. In preceding tests, we found that bulk lipid yields from loess–paleosol samples are much lower when, e.g., hexane is used as a solvent instead of DCM : MeOH (9 : 1) and that the $\delta^{18}O_{bulk\,lipid}$ results are less reproducible. The total lipid extracts were centrifuged at 2000 rpm for 15 min and were subsequently passed over pipette columns filled with glass fiber. The extraction and purification procedures were repeated two more times with 20 mL of solvent for each sample. After solvent reduction using rotary evaporation, the total lipid extracts were transferred into silver capsules with DCM. Bulk lipid yields were quantified by weighing the silver capsules before and after the transfer and solvent evaporation. The bulk $\delta^{18}O$ measurements of the lipids were performed at the Institute of Groundwater Management of the Technische Universität (TU) Dresden using an EA IsoLink elemental analyzer coupled to a Delta V Plus IRMS (isotope ratio mass spectrometer; Thermo Fisher Scientific GmbH, Bremen, Germany). For calibration, the reference materials NBS 127, GISP, VSMOW2 (Vienna Standard Mean Ocean Water), CH_3, and CH_6 (all from the International Atomic Energy Agency, IAEA) were used. The standard deviation for replication measurements of these reference materials was on average 0.5 ‰ and never exceeded 1.2 ‰. All results are reported in the usual δ notation versus the Vienna Standard Mean Ocean Water (VSMOW).

3 Results and discussion

3.1 Bulk lipid contents and comparison of the Crvenka $\delta^{18}O_{bulk\,lipid}$ record with marine oxygen-isotope stages and Greenland $\delta^{18}O$ records

The bulk lipid contents of the LPS Crvenka range from 0.023 to 0.140 mg g^{-1}, and the absolute amounts range between 0.5 and 2.9 mg. These amounts allowed us to perform $\delta^{18}O_{bulk\,lipid}$ measurements for all samples: the $\delta^{18}O_{bulk\,lipid}$ values range between −10.2 ‰ and +23.0 ‰ and are systematically more positive in the interglacial (paleo-)soils compared to the loess layers (see Figs. 2 and 3). The modern Holocene soil, roughly corresponding with MIS 1, is characterized by $\delta^{18}O_{bulk\,lipid}$ values around +14 ‰, and the intensively brunified last interglacial paleosol complex V S1 coinciding with MIS 5 is characterized by $\delta^{18}O_{bulk\,lipid}$ values > +20 ‰. MIS 5 substages a–e are generally not differentiated by pedogenetic or analytical features in the Serbian LPSs (Marković et al., 2015; R. Zech et al., 2013). It is therefore not surprising that our $\delta^{18}O_{bulk\,lipid}$ record does not indicate these substages either. The weakly developed interstadial paleosol complex L1S1, coinciding with MIS 3, shows a striking large fluctuation with a minimum $\delta^{18}O_{bulk\,lipid}$ value of −1.4 ‰ in the middle and a maximum $\delta^{18}O_{bulk\,lipid}$ value of +20.4 ‰ in the lower part. The $\delta^{18}O_{bulk\,lipid}$ values of the last glacial loess layers L1L1 and L1L2 (coinciding with MIS 2 and 4, respectively) range between +2.0 ‰

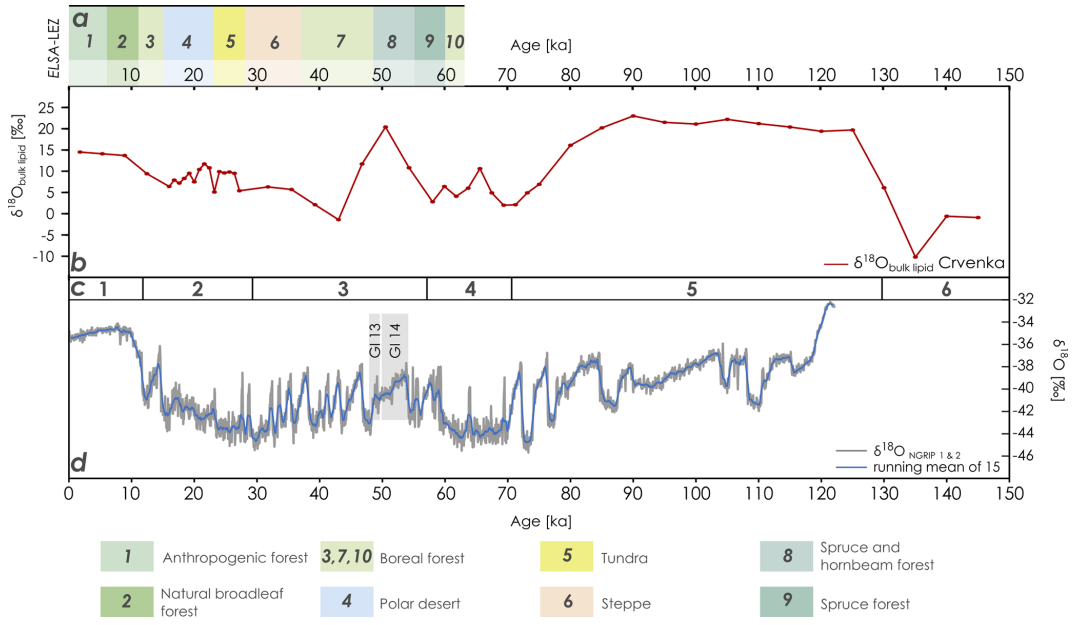

Figure 3. Comparison of **(a)** the landscape evolution zones after Sirocko et al. (2016), **(b)** the Crvenka $\delta^{18}O_{bulk\ lipid}$ record (based on the MIS-based age–depth model of R. Zech et al., 2013), **(c)** the marine isotope stages after Lisiecki and Raymo (2005), and **(d)** the Greenland $\delta^{18}O$ records (based on data of NGRIP members, 2004). GI 13 and 14 represent Greenland Interstadial 13 and 14, respectively. ELSA-LEZ: landscape evolution zones (LEZs) reconstructed from the Eifel Laminated Sediment Archive (ELSA). NGRIP: North Greenland Ice Core Project.

and +11.7 ‰. Loess layer L2, representing the penultimate glacial and coinciding with MIS 6, is characterized by the most negative $\delta^{18}O_{bulk\ lipid}$ values of up to −10.2 ‰.

In order to enable the comparison of our Crvenka $\delta^{18}O_{bulk\ lipid}$ record with Greenland $\delta^{18}O_{ice\ core}$ records, we adopted the MIS-scale age–depth model of R. Zech et al. (2013). Although the LPS Crvenka is one of the best luminescence-dated LPSs in the Carpathian basin (Stevens et al., 2011), we refrain from applying a luminescence-based age–depth model (see Fig. 2 for preferred ages according to Stevens et al., 2011) due to likely age underestimations. Figure 3 shows that the Crvenka $\delta^{18}O_{bulk\ lipid}$ record only partly resembles the Greenland $\delta^{18}O_{NGRIP}$ record. Particularly the Holocene and the time period from around 80 to 130 ka, including the Eemian interglacial, are characterized by more positive $\delta^{18}O_{bulk\ lipid}$ values. While one striking $\delta^{18}O_{bulk\ lipid}$ maximum occurs around 50 ka, our Crvenka $\delta^{18}O_{bulk\ lipid}$ record does not reflect the succession of stadials and interstadials known from the Greenland ice core records, i.e., the famous Dansgaard–Oeschger events. When comparing our southeastern European $\delta^{18}O_{bulk\ lipid}$ record with the mid-European landscape evolution zones (LEZs) identified by Sirocko et al. (2016) based on pollen and total carbon analyses from laminated Eifel maar sediments, LEZ 8 ranging from 49 to 55 ka is characterized by the unexpected dominance of thermophilous tree taxa (see Fig. 3a). This suggests that Greenland Interstadial 13 and 14 (see Fig. 3d; the latter is often referred to as the Glinde interstadial) were the warmest periods of MIS 3. However, the chronological resolution of MIS 3 in the LPS Crvenka is quite limited. Thus, similar to unresolved MIS 5 substages a–e, the absence of stadial–interstadial successions in our $\delta^{18}O_{bulk\ lipid}$ record in the LPS Crvenka does not necessarily mean that these climate variations did not occur in southeastern Europe. However, interestingly around this period very high $\delta^{18}O_{bulk\ lipid}$ values are found in our LPS as well.

The last glacial maximum (around 25 to 20 ka) is not characterized, as one might expect, by particularly negative $\delta^{18}O_{bulk\ lipid}$ values. Last but not least, the amplitude of the Crvenka $\delta^{18}O_{bulk\ lipid}$ values cover around double the amplitude compared to the $\delta^{18}O_{NGRIP}$ amplitude (Fig. 3). Possible explanations for these two findings, as well as all factors needing consideration when interpreting $\delta^{18}O_{bulk\ lipid}$ records from LPSs, are discussed in the following section.

3.2 Paleoclimatic interpretation of the Crvenka $\delta^{18}O_{bulk\ lipid}$ record

$\delta^{18}O$ analyses of cellulose are a widely applied tool in paleoclimate research. Yet, its application to classical LPSs is still hampered by analytical challenges mainly associated with low cellulose and high carbonate contents, hindering the acid-hydrolytic extraction of (hemi-)cellulose-derived sugar biomarkers. In their groundbreaking study "Beyond the cellulose: Oxygen isotope composition of plant lipids as a proxy for terrestrial water balance", Silva et al. (2015) ob-

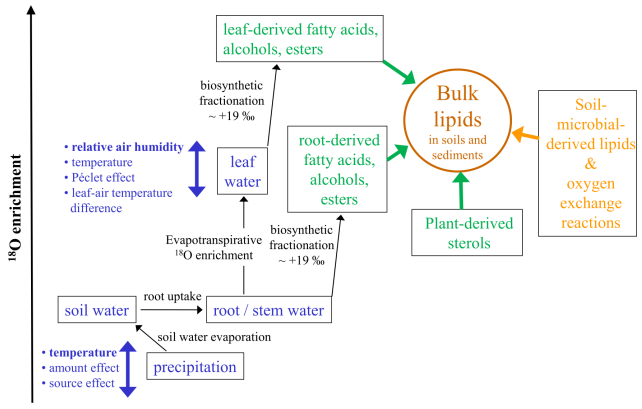

Figure 4. Conceptual diagram illustrating the major factors influencing the oxygen isotopic composition of bulk lipids ($\delta^{18}O_{bulk\,lipid}$) in soils and sediments (modified after Zech et al., 2014). Apart from climatic factors (blue colors) with, e.g., relative air humidity controlling the isotopic enrichment of leaf water by evapotranspiration, "pool effects" (green colors) particularly by the admixture of sterols and root-derived lipids need consideration. Last but not least, the buildup of soil-microbial-derived lipids is also a kind of a pool effect introducing uncertainty, too, and a part of the oxygen bound in lipids is prone to exchange reactions with soil water.

served a strong linear relationship between $\delta^{18}O_{bulk\,lipid}$ and $\delta^{18}O_{cellulose}$. This corroborates that $\delta^{18}O$ values of many plant-derived lipids such as organic acids, carbonyls, alcohols, and esters are water-correlated, although this does not hold true for plant-derived sterols that contain atmospheric-derived oxygen (Schmidt et al., 2001). Accordingly, oxygen from fatty acids or acyl-derived alcohols is about +19 ‰ more positive compared to water. Such systematic offsets are usually described as biosynthetic fractionation factors and are certainly one important factor needing consideration when interpreting $\delta^{18}O_{bulk\,lipid}$ records from LPSs (Fig. 4).

Concerning plant water in which the lipids are biosynthesized, it is generally accepted that the uptake of soil water by plants is not associated with discernible isotopic fractionation. Thus, in cases where significant evaporative enrichment of soil water can be excluded, $\delta^{18}O$ of root and stem water reflects the mean isotopic composition of local precipitation. In high latitudes $\delta^{18}O_{precipitation}$ is primarily temperature-controlled. Hence, it is likely that the temperature effect on $\delta^{18}O_{precipitation}$ is one important factor controlling the glacial–interglacial variability of our Crvenka $\delta^{18}O_{bulk\,lipid}$ record, with more positive/negative values during the warm interglacials/cold glacials (Figs. 2, 3, and 4). However, on the one hand, apart from the temperature effect neither the amount effect nor the source effect can be excluded as possible factors that had influenced $\delta^{18}O_{precipitation}$ in the Crvenka study area during the past. Unfortunately, their quantitative assessment has been rather challenging so far. On the other hand, $\delta^{18}O_{precipitation}$ changes alone can certainly not explain the $\delta^{18}O_{bulk\,lipid}$ amplitude of our Crvenka record, ranging between −10.2 ‰ and +23.0 ‰. Indeed, leaf-(wax-)derived lipids do not reflect the isotopic composition directly of precipitation but instead of isotopically enriched leaf water (Fig. 4). This is well known for $\delta^{2}H$ of leaf-wax-derived *n* alkanes, where due to evaporation leaf water can be isotopically enriched by up to ∼ 50 ‰ compared to xylem water (e.g., Zech et al., 2015). In the case of $\delta^{18}O$, leaf water enrichment of up to ∼ 25 ‰ was for instance reported by Zech et al. (2014). The main controlling factor for this enrichment is relative air humidity (RH), with lower RH values resulting in stronger ^{2}H and ^{18}O enrichment of leaf water. Further minor influencing factors are temperature, leaf–air temperature differences, and the so-called Péclet effect. The latter describes, in simplified terms, the mixing of water from the xylem and from evaporation sites within plant leaves. Water that flows to evaporation sites by transpiration is enriched in $H_2^{18}O$ at the evaporation sites by back diffusion of the enriched water (cf. Farquhar and Lloyd, 1993; Ferrio et al., 2012).

Next to the climatic factors temperature and relative air humidity, also "pool effects" need to be considered when interpreting $\delta^{18}O_{bulk\,lipid}$ values in plants and soils. This is comparable to bulk $\delta^{2}H$ results of soils and sediments, where pool effects exert influence, too (cf. Zech et al., 2015). On the one hand, as mentioned above $\delta^{18}O$ of plant-derived sterols is not water-correlated, and thus sterols dilute the climate signal of the leaf-derived fatty acids and alcohols (Fig. 4). On the other hand, root and stem input of fatty acids and alcohols likely introduces a $\delta^{18}O$ signal that does not carry the ^{18}O enrichment of leaf water (Fig. 4). For instance, in the MIS 2 part of our Crvenka $\delta^{18}O_{bulk\,lipid}$ record, one might have expected more negative values in the case of a mere climate control (Figs. 2 and 3). Hence, postsedimentary Holocene root input of oxygen-bearing lipids into the L1L1 layer could possibly explain the absence of a more pronounced $\delta^{18}O_{bulk\,lipid}$ minimum. Moreover, bulk lipids extracted from soils and sediments not only are plant-derived but also contain soil-microbial-derived lipids. Variable and unknown contributions of such soil-microbial-derived lipids introduce another source of uncertainty that is difficult to quantify based on the current state of knowledge. In addition, a part of the oxygen bound in lipids is prone to exchange reactions with soil water (Fig. 4). For instance, using laboratory incubation studies with isotopically enriched water, Maxwell et al. (2018) found that 22 % of oxygen from bulk soil lipid extracts is exchangeable.

4 Conclusions and outlook

Our pilot study suggests that $\delta^{18}O$ analyses of bulk lipids ($\delta^{18}O_{bulk\,lipid}$) can successfully be applied to loess–paleosol sequences, since absolute bulk lipid yields for the LPS Crvenka ranged between 0.5 and 2.9 mg per 20 g of sample

material. Our Crvenka $\delta^{18}O_{bulk\ lipid}$ record reflects the alternation between loess layers and (paleo-)soils (more negative and more positive $\delta^{18}O_{bulk\ lipid}$ values, respectively) and thus marine oxygen-isotope stage (MIS) 1 to 6. Yet, this does not involve MIS 5 substages a–e, which are not differentiated in the LPS Crvenka. Similarly, our Crvenka $\delta^{18}O_{bulk\ lipid}$ record does not provide evidence for the occurrence of interstadials and stadials comparable to the Dansgaard–Oeschger events known from the Greenland $\delta^{18}O_{ice\ core}$ records. This will require further and higher-resolution data in combination with more robust age models in the future.

Concerning the interpretation of our Crvenka $\delta^{18}O_{bulk\ lipid}$ record, plant-derived lipids such as fatty acids and alcohols are certainly strongly influenced by climatic factors such as temperature (via $\delta^{18}O_{precipitation}$) and relative air humidity (via ^{18}O enrichment of leaf water due to evapotranspiration). However, also pool effects in the form of non-water-correlated lipids such as sterols or the input of root-derived lipids should not be overlooked. Furthermore, also the input of soil-microbial lipids and oxygen exchange reactions represent uncertainties that are challenging quantitative paleoclimate/paleohydrological reconstructions based on $\delta^{18}O_{bulk\ lipid}$ analyses.

Data availability. Underlying data can be found in the Supplement.

Supplement. The supplement related to this article is available online at: https://doi.org/10.5194/egqsj-71-83-2022-supplement.

Author contributions. MZ developed the project idea in consultation with LB, CBR, and JL. The analyzed samples were taken during the fieldwork by RZ in cooperation with MZ. The laboratory work was mainly done by PH and DB with the participation of JL, who prepared the manuscript. SBM and BG, as well as all other co-authors, participated in the interpretation of the results and contributed to the completion of the manuscript.

Competing interests. The contact author has declared that neither they nor their co-authors have any competing interests.

Disclaimer. Publisher's note: Copernicus Publications remains neutral with regard to jurisdictional claims in published maps and institutional affiliations.

Special issue statement. This article is part of the special issue "Quaternary research from and inspired by the first virtual DEUQUA conference". It is a result of the vDEUQUA2021 online conference in September/October 2021.

Acknowledgements. We kindly thank Gerhard Gebauer and his team from the Laboratory of Isotope Biogeochemistry of the BayCEER at the University of Bayreuth as well as Tobias Krause (Institute of Soil Science and Site Ecology, TU Dresden), Erik Michalowski and Amelie Demmer (both Institute of Geography, TU Dresden), Doreen Degenhardt and Patricia Stock (both Institute of Groundwater Management, TU Dresden), and Marianne Zech for their support of laboratory work and isotope analyses. Special thanks go to Hans von Suchodoletz for his editorial handling, as well as to two anonymous reviewers for the valuable suggestions and their constructive reviews.

This paper is dedicated to Ludwig Zöller and Dominik Faust. Ludwig Zöller was born in 1953 and held the Chair of Geomorphology at the University of Bayreuth from 2002 until his retirement in 2018. Dominik Faust was born in 1954 and held the Chair of Physical Geography at the Technische Universität Dresden from 2000 until his retirement in 2020. Ludwig Zöller supervised the dissertation and habilitation of Michael Zech. Both Ludwig Zöller and Dominik Faust were important mentors of Michael Zech and opened the door towards loess research for Michael Zech and his team with their methodological expertise on biomarkers and stable isotopes.

Financial support. This research has been supported by the Deutsche Forschungsgemeinschaft (grant nos. DFG ZE 844/14-1 and DFG FA 239/26-1).

This open-access publication was funded
by the Technische Universität Dresden (TUD).

Review statement. This paper was edited by Hans von Suchodoletz and reviewed by two anonymous referees.

References

Bittner, L., Gil-Romera, G., Grady, D., Lamb, H., Lorenz, E., Weiner, M., Meyer, H., Bromm, T., Glaser, B., and Zech, M.: The Holocene lake-evaporation history of the afro-alpine Lake Garba Guracha in the Bale Mountains, Ethiopia, based on $\delta^{18}O$ records of sugar biomarker and diatoms, Quaternary Res., 105, 23–36, https://doi.org/10.1017/qua.2021.26, 2021.

Dansgaard, W.: Stable isotopes in precipitation, Tellus, 16, 436–468, https://doi.org/10.1111/j.2153-3490.1964.tb00181.x, 1964.

Farquhar, G. D. and Lloyd, J.: 5 – Carbon and Oxygen Isotope Effects in the Exchange of Carbon Dioxide between Terrestrial Plants and the Atmosphere, in: Stable Isotopes and Plant Carbon-water Relations, edited by: Ehleringer, J. R., Hall, A. E., and Farquhar, G. D., Academic Press, San Diego, 47–70, https://doi.org/10.1016/B978-0-08-091801-3.50011-8, 1993.

Ferrio, J. P., Pou, A., Florez-Sarasa, I., Gessler, A., Kodama, N., Flexas, J., and Ribas-Carbo, M.: The Péclet effect on leaf water enrichment correlates with leaf hydraulic conductance and mesophyll conductance for CO_2, Plant, Cell Environ., 35, 611–625, https://doi.org/10.1111/j.1365-3040.2011.02440.x, 2012.

Häggi, C., Eglinton, T. I., Zech, W., Sosin, P., and Zech, R.: A 250 ka leaf-wax δD record from a loess section in Darai

Kalon, Southern Tajikistan, Quaternary Sci. Rev., 208, 118–128, https://doi.org/10.1016/j.quascirev.2019.01.019, 2019.

Lachniet, M. S.: Climatic and environmental controls on speleothem oxygen-isotope values, Quaternary Sci. Rev., 28, 412–432, https://doi.org/10.1016/j.quascirev.2008.10.021, 2009.

Lehmkuhl, F., Nett, J. J., Pötter, S., Schulte, P., Sprafke, T., Jary, Z., Antoine, P., Wacha, L., Wolf, D., Zerboni, A., Hošek, J., Marković, S. B., Obreht, I., Sümegi, P., Veres, D., Zeeden, C., Boemke, B., Schaubert, V., Viehweger, J., and Hambach, U.: Loess landscapes of Europe – Mapping, geomorphology, and zonal differentiation, Earth-Sci. Rev., 215, 103496, https://doi.org/10.1016/j.earscirev.2020.103496, 2021.

Lemma, B., Bittner, L., Glaser, B., Kebede, S., Nemomissa, S., Zech, W., and Zech, M.: $\delta^2H_{n-alkane}$ and $\delta^{18}O_{sugar}$ biomarker proxies from leaves and topsoils of the Bale Mountains, Ethiopia, and implications for paleoclimate reconstructions, Biogeochem., 153, https://doi.org/10.1007/s10533-021-00773-z, 2021.

Lisiecki, L. E. and Raymo, M. E.: A Pliocene-Pleistocene stack of 57 globally distributed benthic $\delta^{18}O$ records, Paleoceanography, 20, https://doi.org/10.1029/2004PA001071, 2005.

Marković, S., Stevens, T., Kukla, G., Hambach, U., Fitzsimmons, K., Gibbard, P., Buggle, B., Zech, M., Guo, Z., Hao, Q., Wu, H., O'Hara-Dhand, K., Smalley, I., Újvári, G., Sümegi, P., Timar-Gabor, A., Veres, D., Sirocko, F., Vasiljevic, D., Vidojko, J., Zdzislaw, J., Anderss, S., Lehmkuhl, F., Kovács, J., and Svirčev, Z.: Danube loess stratigraphy – Towards a pan-European loess stratigraphic model, Earth-Sci. Rev., 148, 228–258, https://doi.org/10.1016/j.earscirev.2015.06.005, 2015.

Maxwell, T. M., Silva, L. C. R., and Horwath, W. R.: Predictable Oxygen Isotope Exchange Between Plant Lipids and Environmental Water: Implications for Ecosystem Water Balance Reconstruction, J. Geophys. Res.-Biogeosc., 123, 2941–2954, https://doi.org/10.1029/2018JG004553, 2018.

NGRIP members: High-resolution record of Northern Hemisphere climate extending into the last interglacial period, Nature, 431, 147–151, https://doi.org/10.1038/nature02805, 2004.

Peel, M. C., Finlayson, B. L., and McMahon, T. A.: Updated world map of the Köppen-Geiger climate classification, Hydrol. Earth Syst. Sci., 11, 1633–1644, https://doi.org/10.5194/hess-11-1633-2007, 2007.

Prud'homme, C., Lécuyer, C., Antoine, P., Moine, O., Hatté, C., Fourel, F., Martineau, F., and Rousseau, D.-D.: Palaeotemperature reconstruction during the Last Glacial from $\delta^{18}O$ of earthworm calcite granules from Nussloch loess sequence, Germany, Earth Planet. Sci. Lett., 442, 13–20, https://doi.org/10.1016/j.epsl.2016.02.045, 2016.

Pustovoytov, K. and Terhorst, B.: An isotopic study of a late Quaternary loess-paleosol sequence in SW Germany, Revista mexicana de ciencias geológicas, ISSN 1026-8774, Vol. 21, No. 1, 2004 (Ejemplar dedicado a: VI International Symposium and Field Workshop on Paleopedology), 21, 88–93 pp., 2004.

Roden, J. S., Lin, G., and Ehleringer, J. R.: A mechanistic model for interpretation of hydrogen and oxygen isotope ratios in tree-ring cellulose, Geochim. Cosmochim. Acta, 64, 21–35, https://doi.org/10.1016/S0016-7037(99)00195-7, 2000.

Schäfer, I., Bliedtner, M., Wolf, D., Faust, D., and Zech, R.: Evidence for humid conditions during the last glacial from leaf wax patterns in the loess–paleosol sequence El Paraíso, Central Spain, Quaternary Int., 407, 64–73, https://doi.org/10.1016/j.quaint.2016.01.061, 2016.

Schmidt, H. L., Werner, R. A., and Rossmann, A.: ^{18}O pattern and biosynthesis of natural plant products, Phytochemistry, 58, 9–32, https://doi.org/10.1016/s0031-9422(01)00017-6, 2001.

Silva, L. C. R., Pedroso, G., Doane, T. A., Mukome, F. N. D., and Horwath, W. R.: Beyond the cellulose: Oxygen isotope composition of plant lipids as a proxy for terrestrial water balance, Geochem. Perspect. Lett., 33–42, https://doi.org/10.7185/geochemlet.1504, 2015.

Sirocko, F., Knapp, H., Dreher, F., Foerster, M., Albert, J., Brunck, H., Veres, D., Dietrich, S., Zech, M., Hambach, U., Röhner, M., Rudert, S., Schwibus, K., Adams, C., and Sigl, P.: The ELSA-Vegetation-Stack: Reconstruction of Landscape Evolution Zones (LEZ) from laminated Eifel maar sediments of the last 60,000 years, Global Planet. Change, 148, 108–135, https://doi.org/10.1016/j.gloplacha.2016.03.005, 2016.

Spötl, C., Mangini, A., and Richards, D. A.: Chronology and paleoenvironment of Marine Isotope Stage 3 from two high-elevation speleothems, Austrian Alps, Quaternary Sci. Rev., 25, 1127–1136, https://doi.org/10.1016/j.quascirev.2005.10.006, 2006.

Stevens, T., Marković, S. B., Zech, M., Hambach, U., and Sümegi, P.: Dust deposition and climate in the Carpathian Basin over an independently dated last glacial–interglacial cycle, Quaternary Sci. Rev., 30, 662–681, https://doi.org/10.1016/j.quascirev.2010.12.011, 2011.

Zech, M., Tuthorn, M., Detsch, F., Rozanski, K., Zech, R., Zöller, L., Zech, W., and Glaser, B.: A 220ka terrestrial $\delta^{18}O$ and deuterium excess biomarker record from an eolian permafrost paleosol sequence, NE-Siberia, Complete, 220–230, https://doi.org/10.1016/j.chemgeo.2013.10.023, 2013.

Zech, M., Mayr, C., Tuthorn, M., Leiber-Sauheitl, K., and Glaser, B.: Oxygen isotope ratios ($^{18}O/^{16}O$) of hemicellulose-derived sugar biomarkers in plants, soils and sediments as paleoclimate proxy I: Insight from a climate chamber experiment, Geochim. Cosmochim. Acta, 126, 614–623, https://doi.org/10.1016/j.gca.2013.10.048, 2014.

Zech, M., Zech, R., Rozanski, K., Gleixner, G., and Zech, W.: Do n-alkane biomarkers in soils/sediments reflect the δ^2H isotopic composition of precipitation? A case study from Mt. Kilimanjaro and implications for paleoaltimetry and paleoclimate research, Isotop. Environ. Health Stud., 51, 508–524, https://doi.org/10.1080/10256016.2015.1058790, 2015.

Zech, R., Zech, M., Marković, S., Hambach, U., and Huang, Y.: Humid glacials, arid interglacials? Critical thoughts on pedogenesis and paleoclimate based on multi-proxy analyses of the loess–paleosol sequence Crvenka, Northern Serbia, Palaeogeogr. Palaeoclim. Palaeoecol., 387, 165–175, https://doi.org/10.1016/j.palaeo.2013.07.023, 2013.

E&G Quaternary Sci. J., 71, 91–110, 2022
https://doi.org/10.5194/egqsj-71-91-2022

Open Access E&G Quaternary Science Journal

Research article

Holocene vegetation reconstruction in the forest–steppe of Mongolia based on leaf waxes and macro-charcoals in soils

Marcel Lerch[1], **Julia Unkelbach**[2], **Florian Schneider**[3], **Michael Zech**[1], **and Michael Klinge**[3]

[1]Heisenberg Chair of Physical Geography with Focus on Paleoenvironmental Research, Institute of Geography, Technische Universität Dresden, Helmholtzstraße 10, 01069 Dresden, Germany
[2]Department of Palynology and Climate Dynamics, Albrecht-von-Haller-Institute for Plant Sciences, University of Göttingen, Untere Karspüle 2, 37073 Göttingen, Germany
[3]Department of Physical Geography, Institute of Geography, University of Göttingen, Goldschmidtstr. 5, 37077 Göttingen, Germany

Correspondence: Michael Klinge (mklinge1@gwdg.de)

Relevant dates: Received: 25 October 2021 – Revised: 20 March 2022 – Accepted: 2 May 2022 – Published: 24 May 2022

How to cite: Lerch, M., Unkelbach, J., Schneider, F., Zech, M., and Klinge, M.: Holocene vegetation reconstruction in the forest–steppe of Mongolia based on leaf waxes and macro-charcoals in soils, E&G Quaternary Sci. J., 71, 91–110, https://doi.org/10.5194/egqsj-71-91-2022, 2022.

Abstract: Vegetation and climate reconstruction in the forest–steppe of Mongolia is still challenging regarding the pattern of forest and grassland distribution during the Holocene. Different sediments containing paleosols and humic layers provide geomorphological archives for landscape development in Mongolia. *n*-Alkane and macro-charcoal ratios represent specific indicators to distinguish the share between grasses and trees. In a preliminary study, we investigated the applicability of these two paleo-proxies from soils for vegetation reconstruction comparing different relief positions and site conditions in the northern Khangai Mountains of Mongolia.

n-Alkanes that are deposited from leaf waxes in the soil have the potential to indicate vegetation composition on a local scale. Depending on site-specific environmental conditions, *n*-alkanes are subjected to different degrees of microbiological decomposition, which is more intensive in soils of dry steppe than of forests. Mongolian forests are often underlain by permafrost that may reduce microbiological activity. In steppe soils, the decomposition of *n*-alkanes increases the quantity of mid-chain *n*-alkanes that adulterate the biomarker proxy signal to indicate more forest share. Macro-charcoals in soils have a site-specific component, but additional eolian input of macro-charcoals from long-distance transport can provide a distinct proportion in sediments. Thus, eolian influx of wood-derived macro-charcoal can dominate the proxy signal at sites where trees were few or had never existed.

Radiometric dating of several paleosols and humic layers has shown that both proxies coincide as evidence for high grassland-to-forest ratios during the Early Holocene. By contrast, the proxy signals diverge for the Late Holocene. For this period, *n*-alkanes generally indicate more grassland, whereas macro-charcoals show increased wood-derived proportions. We imply that this difference is caused by increased forest fires and simultaneously spreading steppe area.

Published by Copernicus Publications on behalf of the Deutsche Quartärvereinigung (DEUQUA) e.V.

A main portion of leaf waxes and charcoal particles in soils directly derive from the covering and nearby vegetation, whereas large lakes and glacier may receive these biomarkers from a larger catchment area. Thus, we conclude that soil archives provide proxies on a more local and site-specific scale than other archives do. Although the temporal resolution of soil archives is lower than for the other ones, biomarker proxies for paleosols and humic layer can be related to periods of distinct geomorphological processes. Further investigations comparing the multi-proxy data of different geomorphological archives are necessary to improve the paleo-ecological reconstruction for landscape development in Mongolia.

Kurzfassung:

Die Rekonstruktion von Klima und Vegetation in der mongolischen Waldsteppe stellt nach wie vor eine große Herausforderung in Hinsicht auf die Verbreitungsmuster von Wald- und Grasslandschaften im Laufe des Holozäns dar. Verschiedenartige Sedimente mit Paläoböden und organischen Schichten können dafür als hervorragende Archive für die Analyse der Landschaftsentwicklung in der Mongolei dienen. Die proportionalen Verhältnisse verschiedener *n*-Alkane und Typen von Holzkohlepartikeln lassen sich als Indikatoren zur Bestimmung der Grass und Baumanteile heranziehen. Im Rahmen einer Vorstudie haben wir die Anwendbarkeit dieser zwei Paläoproxies für die Vegetationsrekonstruktion aus Bodenarchiven untersucht. Dafür wurden Profile mit unterschiedlichen Reliefpositionen und Standortbedingungen aus einem Untersuchungsgebiet im Norden des Khangai-Gebirges in der Mongolei verglichen.

n-Alkane von der Wachsschicht der Blätteroberflächen gelangen in den Boden und bieten die Möglichkeit die Zusammensetzung der Vegetation auf lokaler Ebene zu analysieren. Abhängig von den standortspezifischen Umweltbedingungen werden *n*-Alkane mikrobiell unterschiedlich stark abgebaut, wobei der Abbau in Böden der Trockensteppen intensiver ist als in den Wäldern. In den Wäldern der Mongolei ist häufig Permafrost im Boden vorhanden, der die mikrobiologische Aktivität verringert. In den Steppenböden erhöht sich durch die Zersetzung von *n*-Alkanen den Anteil an mittelkettigen *n*-Alkanen, was das Biomarker-Proxysignal in Richtung eines höheren Waldanteils verfälscht. Holzkohlepartikel in Böden haben eine standortspezifische Komponente. Allerdings kann ein zusätzlicher äolischer Eintrag von Holzkohlepartikeln aus dem Ferntransport einen deutlichen Anteil in den Sedimenten ausmachen. Durch den äolischen Anteil können holzspezifische Kohlepartikel in den Proxysignalen an Standorten dominieren, an denen es nur wenige oder niemals Bäume gab.

Radiometrische Datierungen von Paläoböden und organischen Schichten zeigen, dass beide Proxys einen hohen Anteil von Grasland gegenüber Wald im frühen Holozän aufweisen. Im Gegensatz dazu divergieren die Proxysignale für das späte Holozän. Für diesen Zeitraum deuten *n*-Alkane allgemein auf mehr Grasland hin, während die Holzkohlepartikel einen höheren Waldanteil erkennen lassen. Wir vermuten, dass dieser Unterschied durch vermehrte Waldbrände und die gleichzeitige Ausbreitung von Steppenflächen verursacht wurde.

Allgemein lässt sich folgern, dass Bodenarchive mehr lokale und ortsspezifische Proxies liefern als es bei Archiven aus Seen und Gletschereis zu erwarten ist. Diese Archive erhalten einen Materialeintrag aus wesentlich größeren Einzugsgebieten. Obwohl die zeitliche Auflösung von Bodenarchiven geringer ist als bei den anderen Archiven, können Biomarker aus Paläoböden und humosen Schichten mit Perioden spezifischer geomorphologischer Prozesse verknüpft werden. Weitere Detailuntersuchungen zum Vergleich von Multiproxy-Daten aus verschiedenen geomorphologischen Archiven sind notwendig, um die paläoökologischen Rekonstruktionen zur Landschaftsentwicklung in der Mongolei auf regionaler Ebene zu verbessern.

1 Introduction

The Mongolian forest–steppe represents a zonal ecotone at the southern fringe of the Siberian boreal forests (Breckle et al., 2002; Erdős et al., 2018). Due to the continental and semi-arid climate, the vegetation pattern of forest patches and open grassland is controlled by local geo-ecological conditions (Dulamsuren and Hauck, 2008; Hais et al., 2016; Khansaritoreh et al., 2017). Paleo-environmental reconstruction based on vegetation distribution is the key for interpreting climate and human impact on the Holocene landscape development.

Pollen analyses are most commonly used to produce proxy data for paleo-vegetation. Peat bogs and lake sediments represent efficient archives for pollen analysis that can provide long-term and high-resolution paleo-environmental records (Fowell et al., 2003; Rudaya et al., 2009; Unkelbach et al., 2021). However, the pollen influx depends on near- and long-distance transport and plant-specific pollen productivity. Thus, pollen spectra represent a mixture of different vegetation types from a wide catchment area (Odgaard, 1999; Zech et al., 2010b). Pollen analyses from soil material may be hampered by selective pollen decomposition under aerobic conditions. In contrast, charcoal particles from burned vegetation and long-chain *n*-alkanes originating from leaf waxes (Eglinton and Hamilton, 1967; Kolattukudy, 1976) are relatively resistant against physical, chemical and biological degradation. The long-lasting persistence of charcoal and long-chain *n*-alkanes in soil provides a valuable archive tool for reconstruction of local paleo-vegetation (Patterson et al., 1987; Bliedtner et al., 2020; Thomas et al., 2021).

Few investigations on charcoal and *n*-alkane distribution exist for different paleo-environmental archives in Mongolia and central Asia. Charcoal records from Mongolia have been reported from lacustrine archives (Umbanhowar et al., 2009; Unkelbach et al., 2019, 2021) and glaciers (Brugger et al., 2018). These records have predominantly been used for the reconstruction of fire chronologies. Furthermore, Miehe et al. (2007) found charcoal pieces from birch, willow and coniferous trees in soils of the Gobi Altai Mountains as evidence for forest distribution in southern Mongolia before 4 ka. In addition to charcoal, long-chain *n*-alkane patterns and ratios were used for the reconstruction of past vegetation composition (Zech et al., 2010b; Tarasov et al., 2013). In a case study along several transects in Mongolia, Struck et al. (2020) have shown that the total *n*-alkane concentration (TAC) and the odd-over-even predominance (OEP) from topsoils significantly correlate with climate parameters. OEP and TAC increase with low temperatures and high precipitation. The authors explain low *n*-alkane concentrations in topsoils by low biomass production, enhanced alkane degradation and livestock grazing intensity. Furthermore, Struck et al. (2020) found no climate effect on the average chain length (ACL) and the *n*-alkane ratio ($n\mathrm{C}_{31}/(n\mathrm{C}_{29}+n\mathrm{C}_{31})$) of plants and topsoils. Thus, the authors proposed the applicability of these indices to distinguish between vegetation dominated by grasses and woody shrubs.

According to literature data, vegetation composition consisting of deciduous trees and shrubs is characterized by dominant *n*-alkane chain lengths of $n\mathrm{C}_{27}$ and $n\mathrm{C}_{29}$, whereas grasses and herbs show dominant *n*-alkane chain lengths of $n\mathrm{C}_{31}$ and $n\mathrm{C}_{33}$ (Zech et al., 2010a, b; Schäfer et al., 2016). Apart from leaf waxes, charred biomass and soil, microbial biomass may also contribute to the *n*-alkane fractions in paleosols (Zech et al., 2017). Wiesenberg et al. (2009) investigated the thermal degradation of rye and maize straw and found that short-chain *n*-alkanes in soils may serve as a marker for charred grass biomass. Hence, Zech et al. (2017), who evaluated post-depositional contamination of *n*-alkane biomarkers in paleosols, interpreted $n\mathrm{C}_{18}$ as a proxy for charred sedimentary organic matter. In addition, decomposition by soil microorganisms generates short- and mid-chain *n*-alkanes (Buggle et al., 2010; Zech et al., 2017). In semi-arid regions of central Asia, different relief positions and topographic asymmetries in soil moisture and vegetation cover induce specific variations in soil ecological conditions (Iijima et al., 2012; Kopp et al., 2014; Hais et al., 2016; Pelletier et al., 2018) and control the distribution of discontinuous permafrost (Klinge et al., 2021). The differing geo-ecological conditions lead to differences in the soil formation rate and microbiological activity. Thus, the degree of *n*-alkane decomposition varies between different topographic sites and soil conditions that may influence effectively the *n*-alkane pattern and its relevance for paleo-environmental interpretation in terms of paleo-vegetation.

Geomorphological mapping and investigation of soil profiles for reconstruction of Holocene landscape development comprise a general aim of the research project (Klinge et al., 2022). As part of the general aim, we intended to evaluate the applicability of macro-charcoal and *n*-alkanes for reconstruction of past vegetation composition from paleosols and humic layers in the semi-arid forest-steppe region of Mongolia by executing two different approaches for proxy-data analysis. We calculated macro-charcoal and *n*-alkane ratios for data interpretation. Furthermore, we evaluated mid-chain *n*-alkane contents related to soil properties to estimate microbiological activity and biomass decomposition in humic layers and paleosols and distinguish their paleo-environmental relevance between different site conditions.

2 Material and methods

2.1 Study area

The study area is located near the town of Tosontsengel (48°46′ N, 98°16′ E; 1670 m a.s.l.) in the northern Khangai Mountains of central Mongolia (Fig. 1). At Tosontsengel, the mean monthly temperatures range between −31.7 °C in January and 14.7 °C in July (National Agency for Meteorology and Environment Monitoring of Mongolia, Ulaanbaatar).

The annual precipitation amounts to 220 mm and reaches up to 500 mm in higher altitudes (Academy of Sciences of Mongolia and Academy of Sciences of USSR, 1990). Most of the precipitation occurs in summer during the growing season, whereas winters are mostly dry. Forest–steppe is the dominating vegetation under the continental and semi-arid climate. Cold conditions lead to the distribution of discontinuous permafrost. Permafrost mainly occurs in valley bottoms, on upper mountains and partially on north-facing slopes under large forest stands (Klinge et al., 2021). In the central Khangai Mountains in the south, the mountains reach up to 3200 m a.s.l., whereas the main river in the north, the Ider Gol, is situated around 1600 m a.s.l. The upper treeline rises southward from 2400 to 2600 m a.s.l., while a lower treeline occurs at around 1800 m a.s.l. (Klinge et al., 2018).

Fragmented forests with Siberian larch (*Larix sibirica*) are generally limited to north-facing slopes. Steppe vegetation covers south-facing slopes and the pediments in the basins (*Artemisia* spp., Chenopodiaceae, Poaceae, *Potentilla fruticosa*). Steppe-like grass vegetation spreads into small forest patches and open forest fringes, whereas the ground vegetation of large forests mostly consists of mosses, herbs and shrubs (*Lonicera altaica*, *Vaccinium vitis-idaea*, *Vaccinium myrtillus*). Large forest stands are often accompanied by a belt of broadleaf trees and bushes (*Salix* spp., *Betula* spp.) at toe slopes and in slope depressions, where increased soil moisture is available. Along the rivers, riparian woody vegetation including willow (*Salix* spp.), poplar (*Populus* spp.) and larch (*Larix sibirica*) occurs. The semi-arid conditions promote frequent forest fires in this region, which occur simultaneously with droughts and are often caused by human fire setting (Nyamjav et al., 2007; Hessl et al., 2016). Due to these conditions, tree regrowth on burned sites strongly depends on soil hydrological properties and occurs irregularly (Schneider et al., 2021). Forest distribution in the study area since 9.5 ka has been shown by Unkelbach et al. (2021), and fire intensity increased after 4.5 ka (Klinge et al., 2022). *Epilobium angustifolium* is a common fire indicator that spreads in burned forests (Khapugin et al., 2016).

2.2 Soil sampling and dating

Sampling of soil and vegetation was carried out during fieldwork in Mongolia in the summers of 2018 and 2019. We took sediment samples from 12 soil profiles for analyses. Organic matter from paleosols and humic layers was used for ^{14}C dating, whereas intermediate eolian layers were analyzed by infrared stimulated luminescence (IRSL) dating. Details on dating methods and soil properties and results for geomorphological processes were published by Klinge et al. (2022). All ^{14}C ages are given as calibrated ^{14}C ages in thousands of years before present (ka BP) here. Samples for biomarker and charcoal analyses were taken parallel to soil samples by a separate sampling procedure.

2.3 Sample preparation and element analyses

Analyses of leaf-wax-derived *n*-alkanes were carried out on 35 soil samples and 6 modern vegetation samples that were collected at the study site. *n*-Alkane analyses as well as total carbon and total nitrogen measurements were executed at the laboratory facilities of the Department of Soil Biogeochemistry, Institute of Agricultural and Nutritional Sciences, Martin Luther University Halle-Wittenberg, in Halle (Saale). Soil samples were air-dried and sieved (< 2 mm) for preparation. Vegetation samples were dried, and whole leaves were used for analysis.

The contents of total carbon (TC) and total nitrogen (TN) were measured using a EuroVector EA3000 elemental analyzer (Hekatech, Wegberg, Germany) coupled via a Conflow III interface to a Delta V Advantage isotope ratio mass spectrometer (Thermo Fisher Scientific, Bremen, Germany).

2.4 Lipid biomarker analyses

n-Alkane preparation and quantification followed the procedure described by, e.g., Lerch et al. (2018) and Zech et al. (2013). In brief, the total lipid extracts (TLEs) of all soil and modern vegetation samples were gained using Soxhlet extraction in 24 h and of $\sim$ 180 mL dichloromethane (DCM) : methanol (MeOH) (9 : 1) as the solvent mixture. The necessary sample amount for *n*-alkane analysis depends on the total organic carbon content (TOC). The sample weight for the investigated soil material ranged from $\sim$ 3 to 8 g. A sample weight of $\sim$ 1 g was chosen for plant material, and 5α-androstane was added as an internal standard to each vegetation and soil sample. Additionally, we inserted $\sim$ 1 g of glass wool into extraction thimbles for prevention of the splash effect before extraction started. Afterwards, the TLE was dried with a rotary evaporator and dissolved again with *n*-hexane. For separation of the TLE, aminopropyl silica gel (45 µm; Supelco) pipette columns were used (Struck et al., 2018). The dissolved TLE was separated as well as eluted over these pipette columns into (i) an aliphatic fraction (apolar) including the *n*-alkanes using *n*-hexane (3 $\times$ 1 mL), (ii) an alcoholic fraction (polar) using DCM : MeOH (9 : 1, 3 $\times$ 1 mL) and (iii) an acid fraction using diethyl ether : acetic acid (95 : 5, 3 $\times$ 1 mL) for each sample. Afterwards, separated fractions were dried under nitrogen. The aliphatic fraction was transferred into 1.5 mL gas chromatography vials with 2 $\times$ 0.5 mL *n*-hexane for measurements. *n*-Alkanes were identified and quantified with a gas chromatograph coupled with a flame ionization detector (GC-FID, 2010 series, Shimadzu, Kyoto, Japan). External *n*-alkane standards with a known concentration (*n*-alkane mix nC_8–nC_{40}; Supelco 49452-U) were repeatedly run with each sequence at different concentrations (25, 50 and 100 µg mL^{-1}) for quantification and identification (Hepp et al., 2017; Bliedtner et al., 2018; Bittner et al., 2020). Detailed results of *n*-alkane analysis are shown in Table S2 in the Supplement.

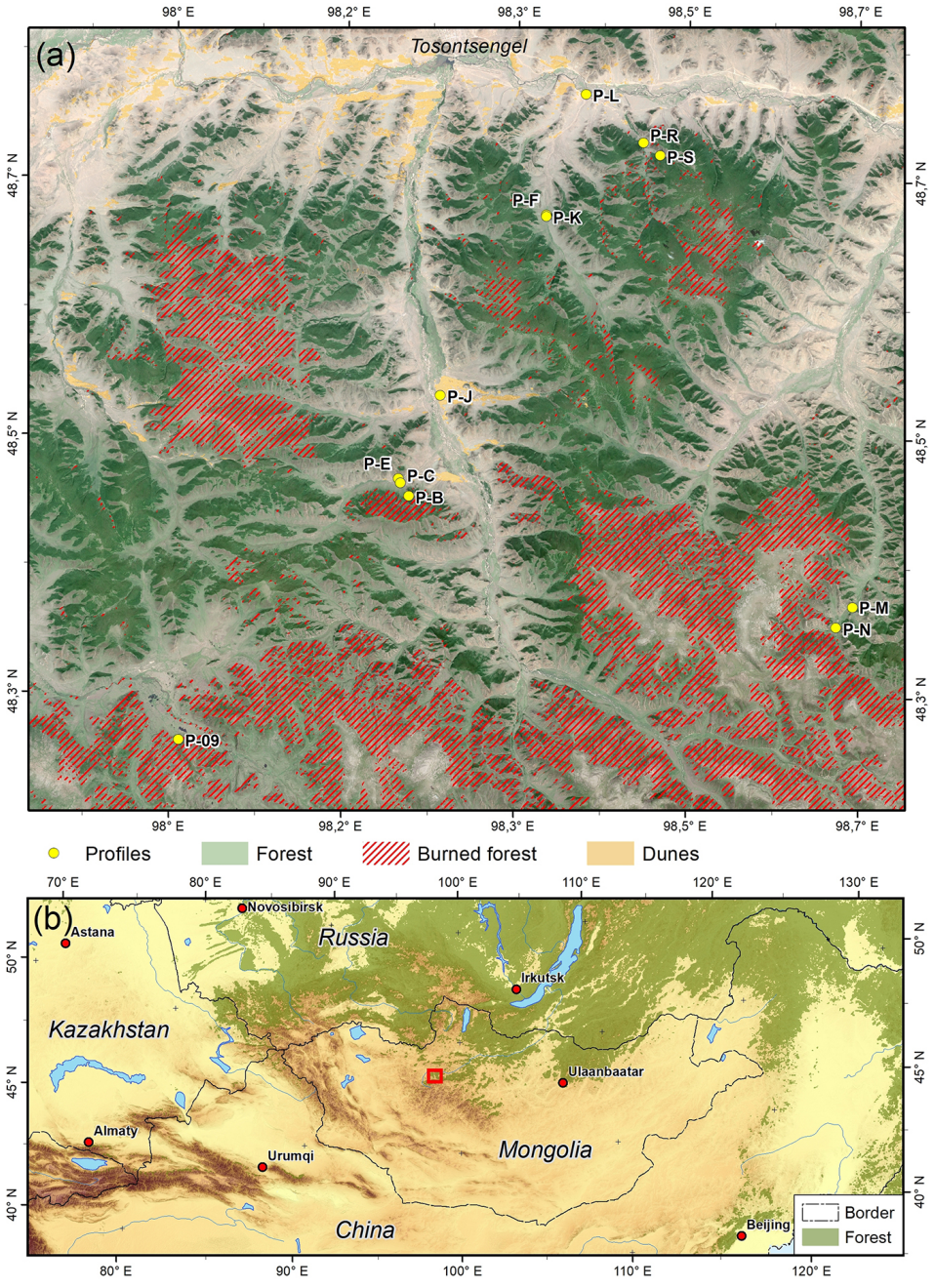

Figure 1. **(a)** Study area and sample sites. The shaded relief is based on TanDEM-X data (© DLR 2011), and the background image is based on Copernicus Sentinel data (31 July 2019). **(b)** Regional overview with red rectangle indicating the position of the study area.

2.5 Macro-charcoal analysis

For macro-charcoal analysis, 27 subsamples of 0.5 cm^3 were taken from organic layers and paleosols. All subsamples were processed based on the method established by Stevenson and Haberle (2005), including KOH (10 %), H_2O_2 (4 %) and wet sieving with low water pressure to avoid further fragmentation of the charcoal material. All charred macroparticles (> 125 µm) of each subsample were counted using a binocular dissecting microscope. To reconstruct dominating vegetation types (forest, steppe), all charred particles were divided into four different morphological types while counting: wood (rather 3-dimensional, long), leaf (rather 2-dimensional, irregularly shaped), grass (rather 2-dimensional, long and mostly rectangular) and other (including mosses, roots, seeds and unidentifiably small fragments). Macro-charcoal identification was based on the examples given in Umbanhowar and Mcgrath (1998) and Mustaphi and

Pisaric (2014). Additionally, macro-charcoal concentrations (particle sum per cubic centimeter) were calculated for each subsample (Supplement File S1).

2.6 Data analysis

Macro-charcoals were classified as originating from wood, leaf and grass. Approx. 25 % of particles could not be identified or had another source and were classified as other and excluded from statistical analysis. The share of charcoal classes was determined to evaluate steppe / forest ratios (C_{sf}) that could indicate vegetation composition:

$$C_{sf} = \frac{\text{grass}}{\text{wood}}. \quad (1)$$

The OEP (odd-over-even predominance) ratio considers long-chain *n*-alkanes and can be used as proxy for *n*-alkane degradation (Zech et al., 2012). High OEP values correspond to fresh plant material, whereas lower OEP values indicate an increased degradation of soil organic matter (Schäfer et al., 2016).

$$\text{OEP} = \frac{nC_{27} + nC_{29} + nC_{31} + nC_{33}}{nC_{26} + nC_{28} + nC_{30} + nC_{32}}, \quad (2)$$

defined as odd-over-even predominance (OEP) according to Hoefs et al. (2002).

The C / N ratio serves as an additional soil parameter for biological decomposition.

Based on *n*-alkane patterns of the analyzed vegetation samples and their dominant *n*-alkane chain lengths, calculated *n*-alkane proxy data can be applied for soils regarding vegetation reconstruction (Zech et al., 2012). Here, we used the ACL (Poynter et al., 1989), defined as the average chain length of *n*-alkanes, in the modified version reported from Schäfer et al. (2016) to address the grassland–woodland composition:

$$\text{ACL} = \frac{27 \times nC_{27} + 29 \times nC_{29} + 31 \times nC_{31} + 33 \times nC_{33}}{nC_{27} + nC_{29} + nC_{31} + nC_{33}}. \quad (3)$$

To indicate fire marker and soil microbial degradation, we checked the short-chain *n*-alkane fraction by elevated values of nC_{18} and $\sum nC_{17}$–nC_{20} to be compared with OEP, C / N and macro-charcoal distribution. Elevated nC_{18} contents along with higher OEP and C / N ratios indicate an input of charred biomass.

The relationship between charcoal and *n*-alkane parameters was assessed by producing bivariate scatterplots and performing a series of correlation analyses. Each relationship was assessed based on correlation coefficients (Pearson's *r*) with a significance threshold (*p* value) set at 0.5.

3 Results and discussion

3.1 Soil profiles and dating results

Paleosols and humic layers containing abundant charcoal were found in various soil profiles in topographic positions on slopes under forest and steppe, dunes, and alluvial plains (Fig. 1). Figure 2 illustrates the soil profiles with positions of samples for soil analyses and dating, which are described in detail in the following section. We classified the soil profiles into three site groups. Group A contains all sites where trees exist or have existed before. Group B comprises sites of exclusively steppe vegetation. All sites with inconsistent dating results and where a mixture of different solum material was found were assigned to group C, which represents problematic profiles for correlation analyses.

Profile P-B (Fig. 2, group A) was located in a toe-slope position inside a dense larch succession at a formerly burned forest site. The profile was composed of colluvial sediments with an imbricated layering that derived from downslope transport of solum after repeated forest fires (Klinge et al., 2021). The solum material was rich in soil organic matter (SOM), and ^{14}C dating of charcoal from different layers provided upward consistent calibrated ^{14}C ages of between 3.8 and 2.0 ka. This dating indicates the ages of the trees that burned in an upslope position during distinct fire events. Two IRSL ages at around 10 ka from intermediate yellowish sand layers pointed to the time of primary eolian deposition further upslope before this sand was transported downslope by colluvial and/or periglacial processes that occurred after 3.3 ka (Klinge et al., 2022). Permafrost occurred at a depth of > 90 cm. Soil profile P-S (Fig. 2, group C) was located at a valley bottom under dense broadleaf vegetation (*Betula*, *Salix*). Intensively cryoturbated colluvial and eolian sediments with paleosols, humic layers and charcoal were found, and permafrost ice occurred at a depth of 70 cm. Carbon-14 dating of charred material and SOM provided calibrated ages of between 2.7 and 0.45 ka, whereas eolian material yielded an IRSL age of 12.1 ka. The time–depth inconsistency of the ages may be due to colluvial, cryoturbation and solifluction processes (Klinge et al., 2022).

Section P-C (Fig. 2, group B) was exposed in a gully in a basin under steppe vegetation. The sediment consisted of two units. The lower unit rested on Pleistocene fanglomerates and was composed of homogeneous eolian sand which provided IRSL ages of between 11.0 and 8.9 ka. Two ^{14}C dating analyses of SOM from a distinct paleosol upon the lower sediment unit provided calibrated ages of 1.8 ± 0.1 and 0.9 ± 0.1 ka, whereas IRSL dating from the upper sediment obtained an age of 1.1 ka (Klinge et al., 2022). In the transition to the upper sediment unit, the paleosol layers diverged into several sub-units, where a humpy upper boundary pointed to enhanced dust trapping around tussock grass. The 60 cm thick upper sediment unit above the paleosol consisted of layered sediments that derived from repeated slope wash processes. A conspicuous black layer at 6 cm depth contained abundant charcoal. Section P-R (Fig. 2, group A) was located at an alluvial fan under steppe vegetation adjacent to an alluvial forest. The sediments consisted of colluvial and slope wash layers including three paleosols with charcoal and several dark brown humic layers. Carbon-14 dating of SOM pro-

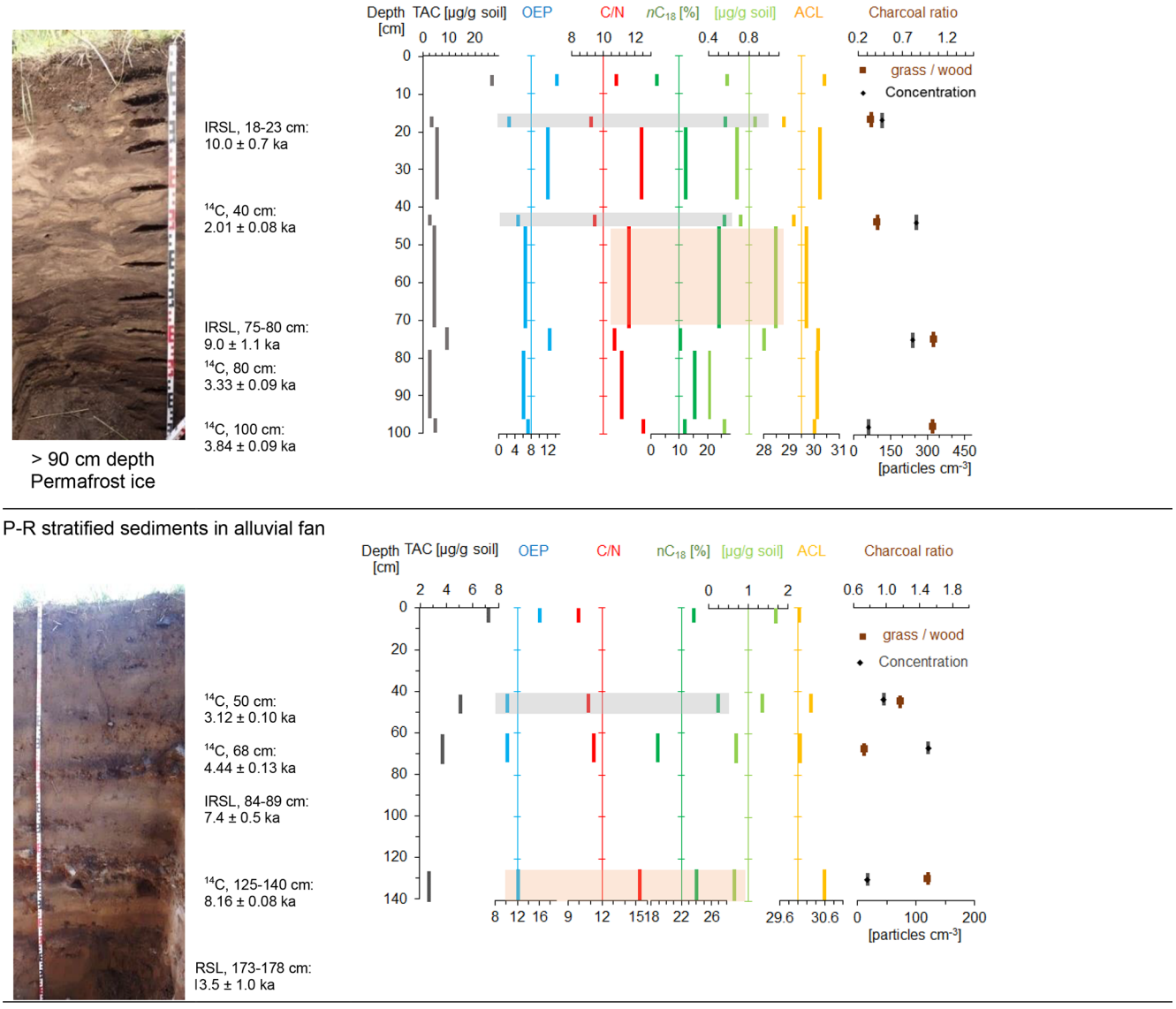

Figure 2.

vided time–depth-consistent calibrated ages of 3.1, 4.4 and 8.2 ka, which were complemented by two IRSL ages of 7.4 and 13.5 ka. In contrast to the profiles P-B and P-S that were located under forest, no permafrost was found at sections P-C and P-R under steppe. This difference in permafrost distribution may have an important influence on biological activity and decomposition.

Section P-J (Fig. 2, group C) was exposed at a dune field upon Pleistocene gravel and under sparse vegetation cover. Carbon-14 dating of a distinct paleosol obtained a calibrated age of 1.3 ka. IRSL dating from sand provided ages of 0.29 ka above the paleosol and 9.2 to 11.7 ka below the paleosol. The eolian sediment of section P-L (Fig. 2, group B) was located in the valley bottom near the Ider Gol under dense steppe. IRSL dating of eolian sand provided ages of 7.1 and 13.8 ka, whereas ^{14}C dating of SOM and charcoal from paleosols obtained calibrated ages of 8.0 and 9.5 ka.

Sections P-F and P-K (Fig. 2, group A) were located in a valley bottom under dense meadow steppe. A paleo-channel cut into alluvial sediments that were composed of eolian and alluvial layers, paleosols, and humic layers, containing charcoal and small pieces of wood. No permafrost was found, whereas slight deformation of sediment layers indicated former weak cryoturbation. At section P-F, several calibrated

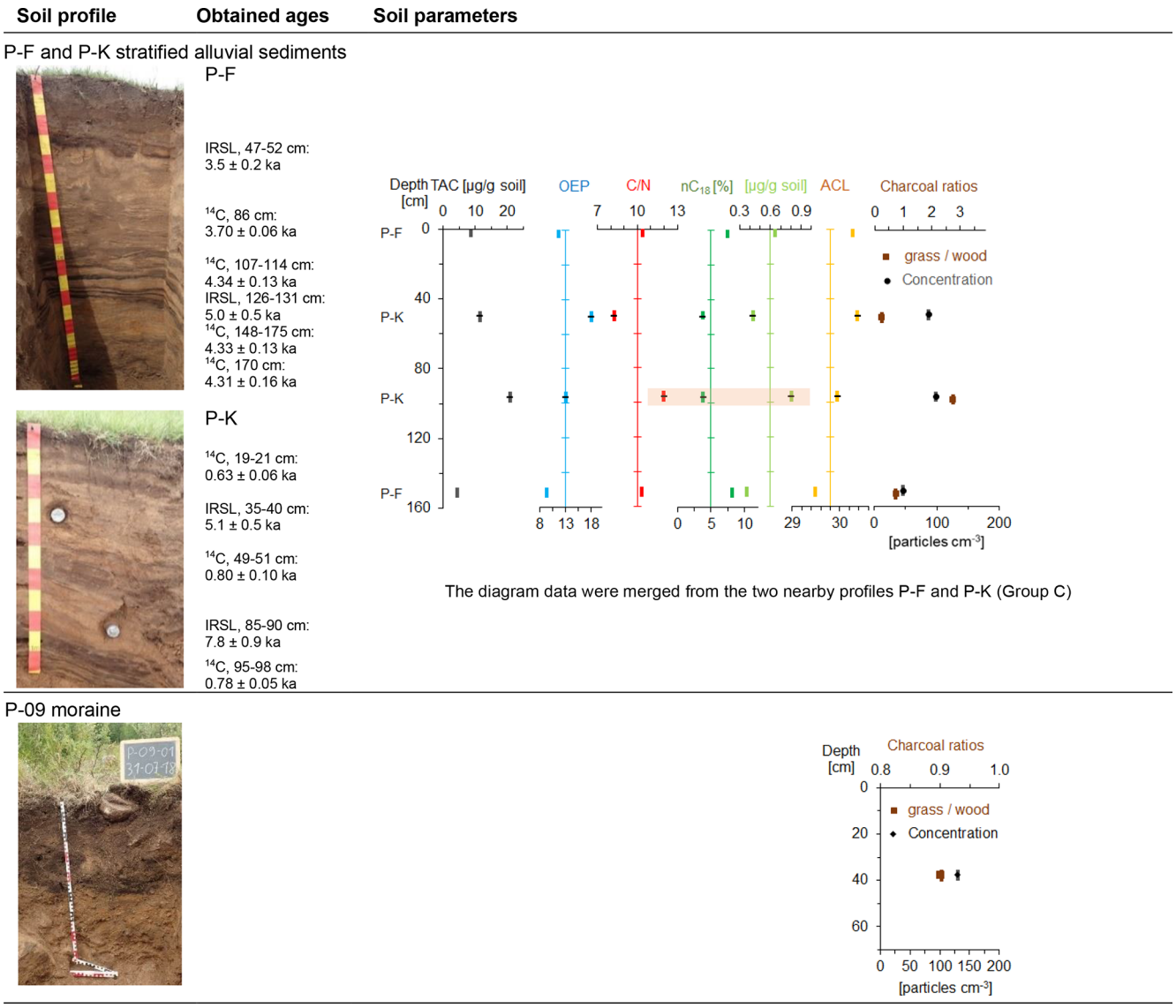

Figure 2.

^{14}C ages of wood and bone artifacts (*Ovis*) provided a consistent chronology between ca. 4.3 and 3.7 ka, which was complemented by two IRSL ages of 3.5 and 5.0 ka. At section P-K, IRSL ages of 5.1 and 7.8 ka were somewhat older compared to section P-F. However, the ^{14}C ages of < 0.8 ka obtained from SOM of three humic layers did not fit into the chronological framework based on the other ages. Contamination by young organic material may have adulterated the dating, and therefore P-K was assigned to group C.

Single samples were taken from three profiles that were not analyzed by radiometric dating. Profile P-M (Fig. 2, group C) was a section in a Pleistocene terrace near a river and was covered by eolian sediments, which contained several cryoturbated paleosols. Profile P-N (Fig. 2, group B) was situated in eolian sand that contained several cryoturbated paleosols above basal moraine. Profile P-09 (Fig. 2, group A) was located at a burned forest site in slope debris above till and contained many charcoals. The paleosol of section P-E (Fig. 2, group A) was developed upon eolian sand and was covered by colluvial sediments. Carbon-14 dating of SOM provided a calibrated age of 12.8 ka. No *n*-alkane analysis was conducted on P-E.

3.2 Macro-charcoal distribution

Macro-charcoal occurred in all samples from paleosols and humic layers. The total amount of macro-charcoal per sample varied between a minimum of 22 and a maximum of 338 particles cm^{-3}, with a mean of 100 particles cm^{-3} (Fig. 3 and Supplement File S1). Charcoal of leaves generally had a lower proportion than charcoal of wood and grass. The ratios

Soil profile	Obtained ages	Soil parameters
Group B: Profiles at steppe sites		
P-C eolian sand and paleosols upon pediment		
	IRSL, 15-20 cm: 1.1 ± 0.1 ka ^{14}C, 45-50 cm: 0.91 ± 0.07 ka ^{14}C, 65-70 cm: 1.77 ± 0.10 ka IRSL, 70-75 cm: 8.9 ± 0.6 ka IRSL, 128-133 cm: 11.0 ± 1.1 ka	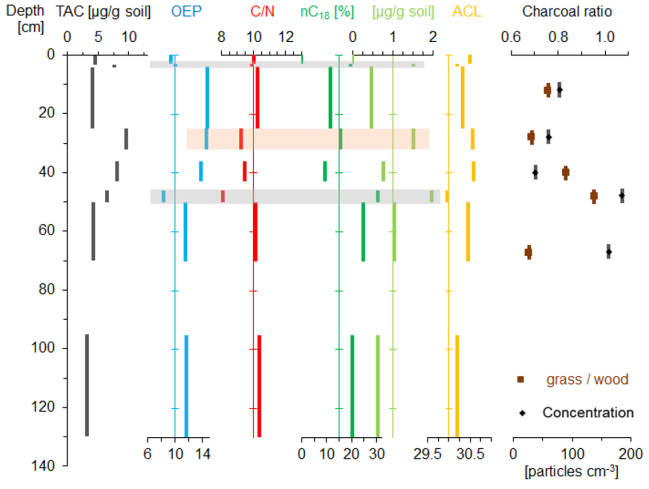
P-L eolian sand and paleosols in basin		
	IRSL, 27-32 cm: 7.1 ± 0.5 ka ^{14}C, 56-61 cm: 7.97 ± 0.06 ka ^{14}C, 114-119 cm: 9.53 ± 0.04 ka IRSL, 122-127 cm: 13.8 ± 0.8 ka	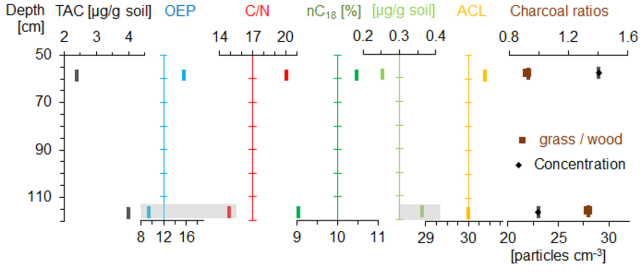
P-N sediment fill in tongue basin of Pleistocene glacier		
		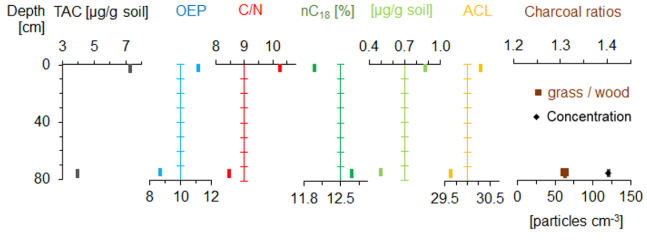
P-E slope debris upon eolian sand		
	IRSL, 77-82 cm: 9.9 ± 0.6 ka ^{14}C, 112 cm: 12.81 ± 0.06 ka IRSL, 180-185 cm: 14.1 ± 1.2 ka IRSL, 218-223 cm: 11.2 ± 1.4 ka IRSL, 250-255 cm: 15.4 ± 1.4 ka IRSL, 290-295 cm: 14.1 ± 1.1 ka	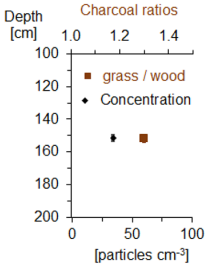

Figure 2.

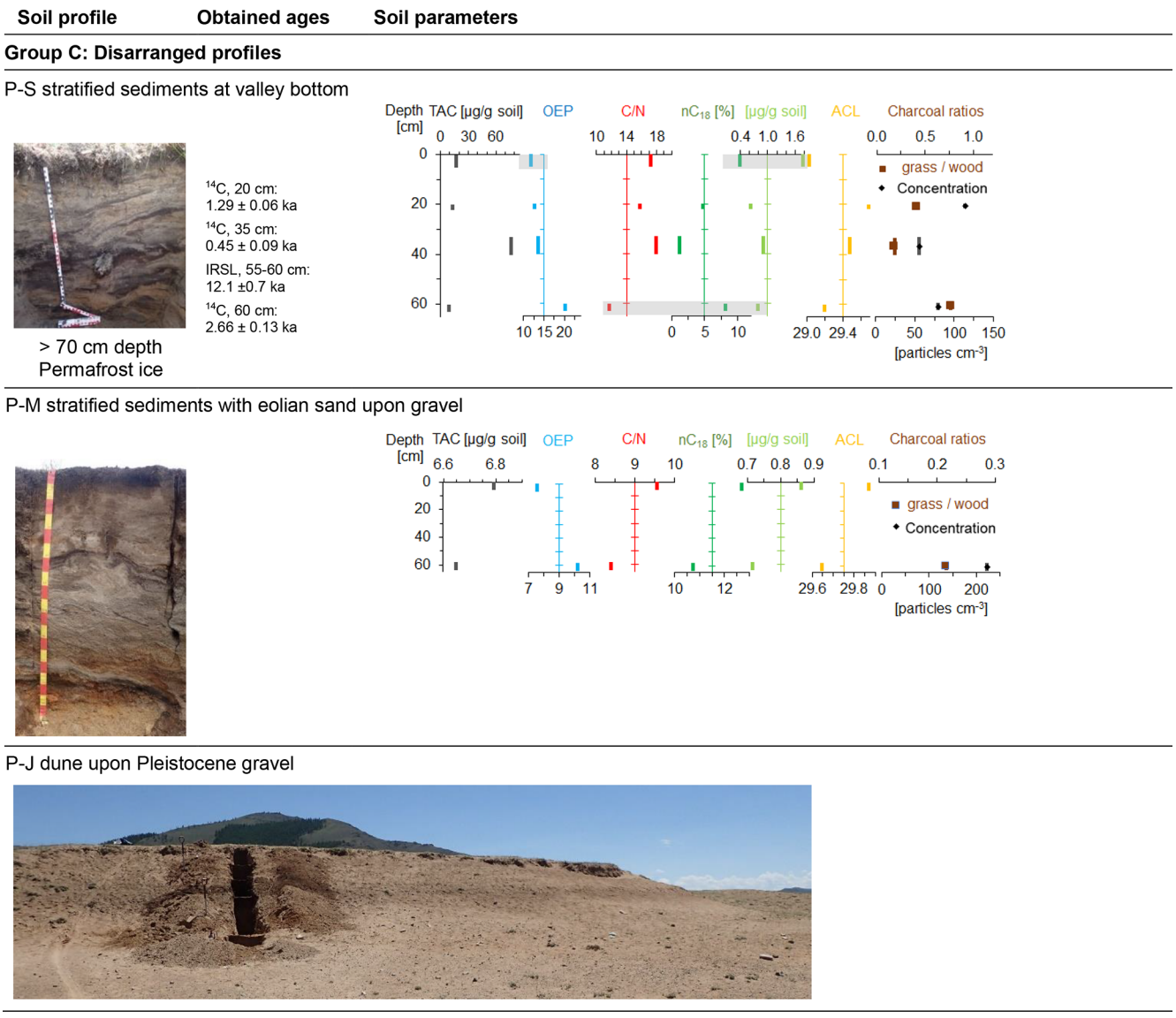

Figure 2. Soil profiles with sampling positions, *n*-alkane and charcoal ratios. Ages for radiometric dating were adapted from Klinge et al. (2022). Grey bars indicate parameters for enhanced biological decomposition, and light brown rectangles indicate parameters for decomposition by fire. Note the different scaling of the horizontal axes.

between charcoal of wood and grass per sample were significantly highly negatively correlated ($r = -0.92$), whereas charcoal of leaves occurred mostly independently from the other two morphotypes (Table 1). The charcoal particle concentration showed no distinct correlation pattern with the site type, sample depth and charcoal type ratio (Fig. 3). At the dune profile P-J, the total amount of charcoal was too low for further interpretations.

Table 1. Correlation coefficient (r) between different charcoal-morphotype distributions ($n = 23$, excluding profile P-J).

Charcoal type	r	p value
Wood–grass	−0.93	< 0.001
Wood–leaf	−0.01	0.969
Grass–leaf	−0.36	0.088

3.3 Patterns of long-chain *n*-alkanes in plants and topsoils

One sample of fresh plant material per species was analyzed for the *n*-alkane distribution from the main species of the study area (Fig. 4). Siberian larch is the dominant tree in the Mongolian forest–steppe, and its *n*-alkane pattern shows dominance in nC_{27} and nC_{29} (Fig. 4), which was also reported by Zech et al. (2010b). In contrast, Struck et al. (2020)

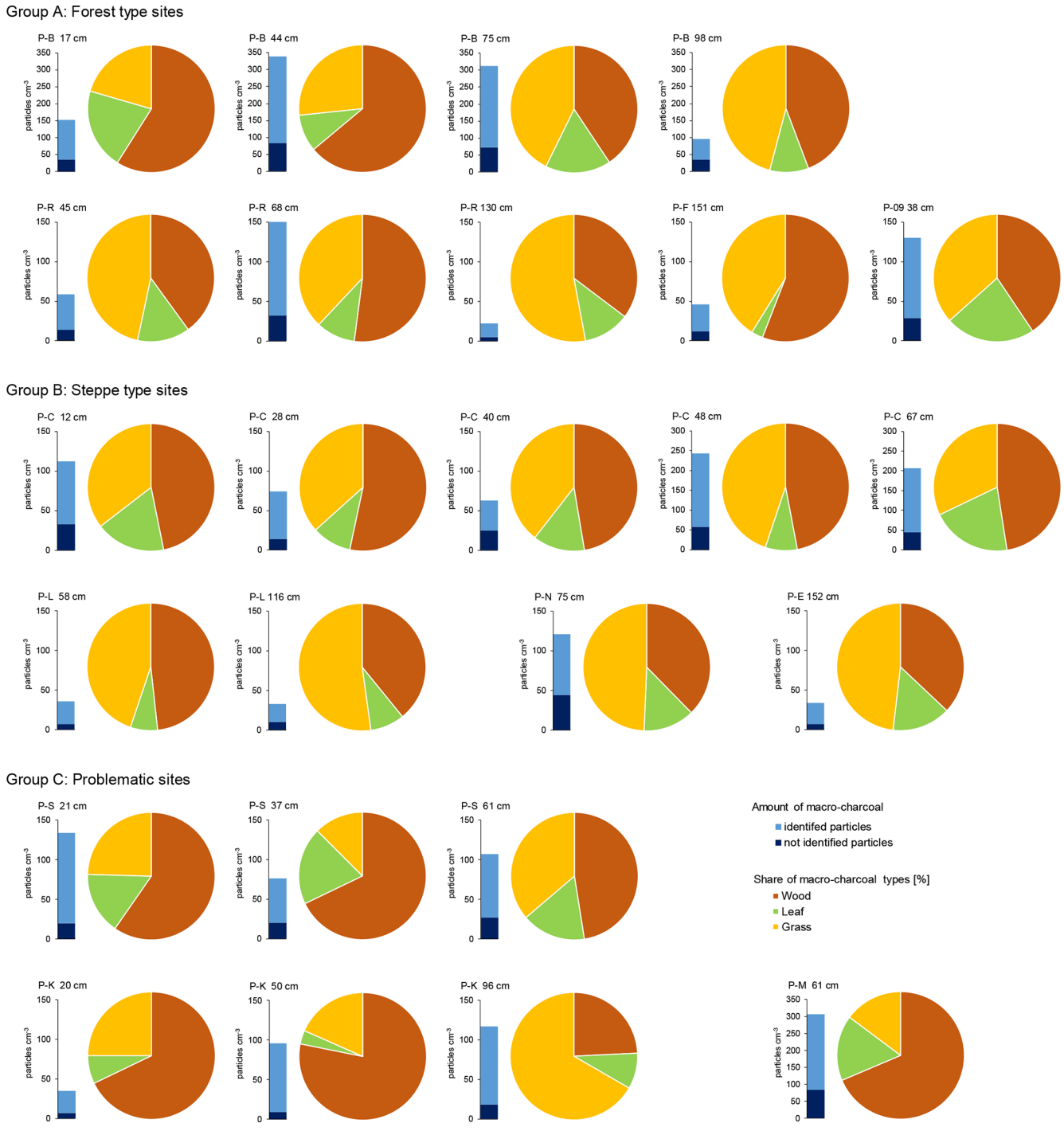

Figure 3. Charcoal concentration and morphotype distribution in paleosols and humic layers at different study sites.

stated a dominance of nC$_{25}$ for their larch samples from Mongolia, whereas Diefendorf et al. (2011) stated a dominance of nC$_{29}$ for *Larix decidua* from North American samples. We detected a low total n-alkane concentration (TAC) of 19.7 µg g^{-1} dry plant material for our Siberian larch sample, which is in agreement with literature data. Thus, larch is unlikely to significantly contribute to the n-alkane patterns of the soils. Birch (*Betula platyphylla*) and willow (*Salix* spp.), which often occur at moist and open sites in forest stands, also have a predominance of nC$_{27}$ and yielded TACs of 248.8 and 96.4 µg g^{-1}, respectively (Fig. 4). Comparable n-alkane distributions with a predominance of nC$_{27}$ for birch species were also reported by Tarasov et al. (2013) (*B. exilis*, *B. fruticosa*) and Zech et al. (2010b) for eastern Siberia and by

Strobel et al. (2021) (*B. nana*) for the Mongolian Altai. Zech et al. (2010b) and Tarasov et al. (2013) also reported a predominance of $n\mathrm{C}_{27}$ for willow, whereas the $n\mathrm{C}_{23}$ content in our sample was exceptionally high. We assume that moist environmental conditions promote the formation of a higher content of mid-chain *n*-alkanes such as $n\mathrm{C}_{23}$ and/or $n\mathrm{C}_{25}$ in leaf waxes of willow (Tarasov et al., 2013). *Lonicera altaica*, *Vaccinium vitis-idaea* and *Vaccinium myrtillus* are common shrubs that are restricted to dense pristine forests and thus may serve as secondary indicators for forests. We found a distinct predominance of $n\mathrm{C}_{29}$ and high TAC of 493.3 µg g^{-1} for *Lonicera altaica* (Fig. 4), whereas a predominance of $n\mathrm{C}_{31}$ was reported for both *Vaccinium vitis-idaea* and *Vaccinium myrtillus* (Tarasov et al., 2013). The authors stated that TAC for *Vaccinium vitis-idaea* was 4070 µg g^{-1} and for *Vaccinium myrtillus* was ∼ 3000 µg g^{-1}.

Poaceae that prevail in the grassland reveal a predominance of $n\mathrm{C}_{31}$ and a TAC of 246.6 µg g^{-1} (Fig. 4), which was also shown by Bush and McInerney (2013) and Struck et al. (2020). The same is true for *Potentilla fruticosa*, which represents a dominant forb in the steppe with a TAC of 1200 µg g^{-1} (Fig. 4), as well as for Cyperaceae (Bush and McInerney, 2013; Struck et al., 2020). Furthermore, *Potentilla fruticosa* as a steppe-dominant plant has an increased relative *n*-alkane contribution of $n\mathrm{C}_{33}$. By contrast, *Artemisia* spp., which contribute many prevalent genera of the steppe, as well as *Caragana* spp. have a predominance of $n\mathrm{C}_{29}$ (Struck et al., 2020).

Most of the long-chain *n*-alkanes detected in the investigated topsoils show similar patterns with increasing relative contributions of odd *n*-alkanes from $n\mathrm{C}_{25}$ to the predominant homologue $n\mathrm{C}_{31}$ (Fig. 5), which confirms the results from Schäfer et al. (2016) and Struck et al. (2020). We observed the highest relative abundances of $n\mathrm{C}_{33}$ in topsoils of the profiles P-B, P-09 and P-C. This finding can be likely explained with the input of litter from *Potentilla fruticosa*, being characterized by high $n\mathrm{C}_{33}$ contents. The OEP ratios of topsoils range between 7.5 and 16.1. A distinct exception of the *n*-alkane pattern in the topsoils occurs at profile P-S. The dominant carbon-chain length for this soil profile is $n\mathrm{C}_{27}$ (Fig. 5). Abundant birch and willow trees at this site may have caused this high content of $n\mathrm{C}_{27}$. TAC ranges from 4.5 to 26.7 µg g^{-1} soil and from 107 to 280 µg g^{-1} TOC for the investigated topsoils.

The ACL (Fig. 5) of different topsoils shows marginal relationships to the modern vegetation. Currently, no trees exist at the sites P-C and P-F and dense larch succession occurs at the site P-B. These sites are among those with the highest ACL values in the topsoils. Leaf trees like willow and birch occur in the vicinity of the steppe-dominated sites P-M and P-N and are mixed with larch at the sites P-09, P-R and P-S. Topsoils of P-09 and P-S are characterized by higher content of $n\mathrm{C}_{27}$ compared to the other topsoils. The high production rate of $n\mathrm{C}_{27}$ of willow and birch produces a distinct signal in the *n*-alkane distribution in topsoil, which decreases the ACL compared to steppe- and larch-dominated sites. Strobel et al. (2021) have shown comparable *n*-alkane patterns in topsoils with $n\mathrm{C}_{31}$ predominance at steppe-dominated sites and with $n\mathrm{C}_{27}$ predominance at sites with *Betula nana*.

3.4 Correlation of *n*-alkane and macro-charcoal ratios in soil profiles

The correlation between *n*-alkane ACL and charcoal ratios as indicators for steppe and forest distribution of all samples without site classification is low (Table 2), although a common trend in the wood- and grass-dominated share exists ($r > 0.5$).

A detailed statistical analysis considering specific *n*-alkanes and charcoal types (Table 2) has shown that correlations of wood-driven charcoal are significantly positive with $n\mathrm{C}_{27}$ and significantly negative with $n\mathrm{C}_{31}$ and $n\mathrm{C}_{33}$, whereas these correlations are inverse for grass charcoal. Charcoals from leaves have no significant correlations, which point to the minor relevance of these morphotypes for vegetation reconstruction.

A closer look at *n*-alkane and macro-charcoal ratios shows that grouping the profiles by vegetation pattern and site conditions increases the statistical correlations significantly (Table 3, Fig. 6). In group A, the profiles P-B and P-R are located at forested sites. At profile P-F no trees occur at present, but the analyzed sample at 151 cm depth included fragments of wood alongside charcoal pieces and alluvial forest grows ca. 1 km upstream. Group A shows highly significant correlations between wood, grass, the grass / wood ratio and C / N on the one hand with ACL and OEP on the other hand (Table 3). Increasing OEP and ACL occurred parallel with the increasing share of grass, which is caused by higher contents of long-chain *n*-alkanes ($n\mathrm{C}_{31}$) in grasses than in other plants and is in agreement with results from Struck et al. (2020) and Strobel et al. (2021). In addition, the C / N ratio correlates positively with C_{sf}, OEP and ACL, which indicates less biological decomposition when the portion of grass vegetation increased at forest-related sites. Permafrost distribution in forest stands, which hampers microbial activity, is related to herb and moss ground vegetation, whereas grass inside forest indicates less canopy closure inducing warmer soil conditions.

Group B includes the profiles P-C and P-L, which are located under dry steppe without any trees, and profile P-N occurs under dense meadow steppe in the vicinity of riparian trees. Group B shows generally lower and inverse correlations between charcoal and *n*-alkane ratios compared to group A (Fig. 6, Table 3). In addition, the total quantity of charcoal particles correlates positively with the short- and mid-chain *n*-alkanes $n\mathrm{C}_{18}$ and $\sum n\mathrm{C}_{17}$–$n\mathrm{C}_{20}$. These *n*-alkane chain lengths can be produced by microbial degradation or in the case of $n\mathrm{C}_{18}$ by charring (Wiesenberg et al., 2009; Zech et al., 2010a). The C / N and OEP values do not show significant correlation with charcoal and *n*-alkane ra-

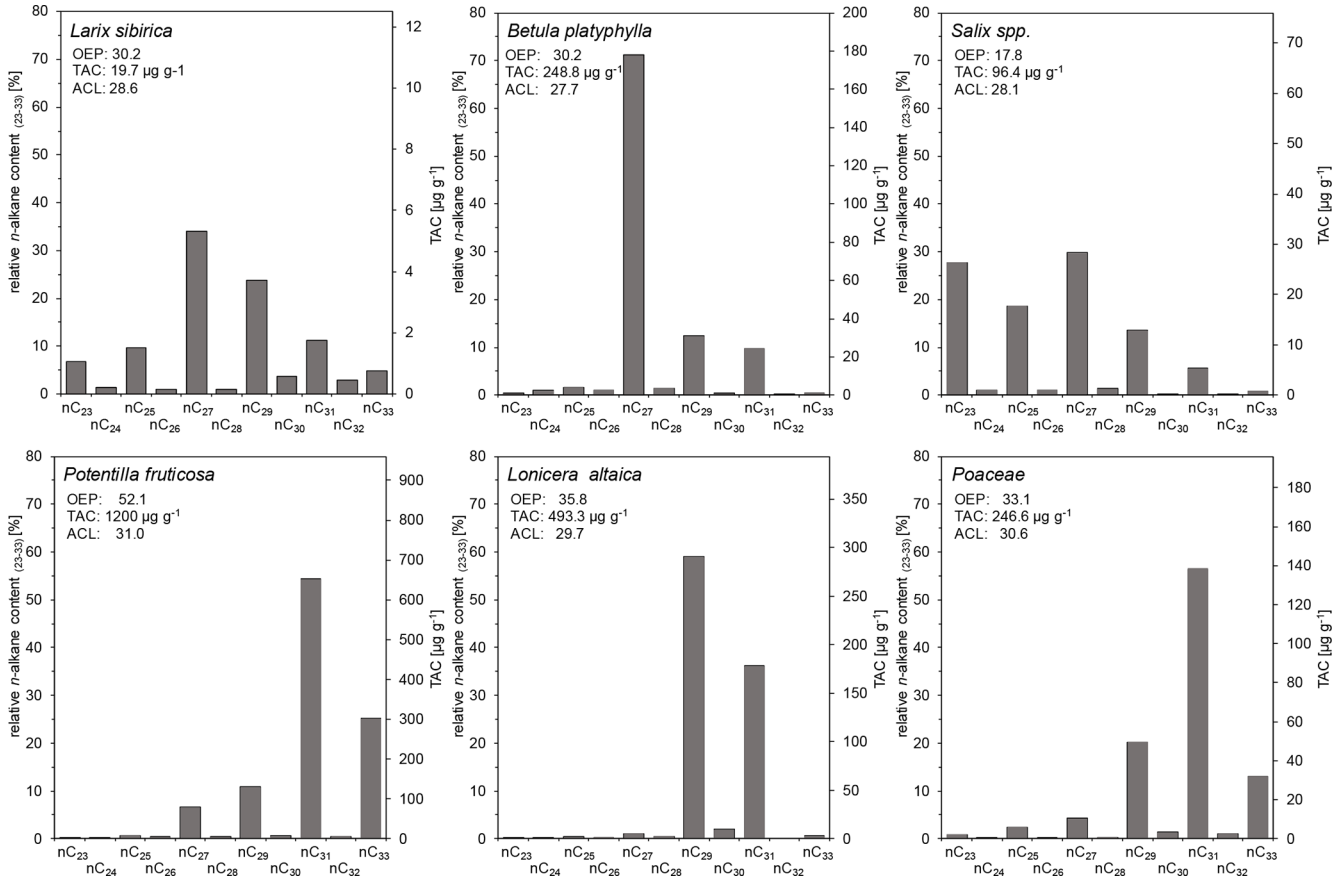

Figure 4. Long-chain n-alkane patterns of plants from the study area at Tosontsengel (OEP, odd-over-even predominance; TAC, total n-alkane concentration of dry plant material; ACL, average chain length of n-alkanes; $n = 1$).

Table 2. Correlation (r) between the relative distribution of charcoal types and ACL (average chain length of n-alkanes, $n = 20$, excluding profile P-K).

Charcoal	nC_{25}	nC_{27}	nC_{29}	nC_{31}	nC_{33}	ACL
Wood	0.20	0.47*	0.23	−0.48*	−0.46*	−0.55*
Leaf	0.03	0.17	−0.08	−0.13	−0.08	−0.17
Grass	−0.18	−0.46*	−0.16	0.45*	0.42	0.53*
Grass / wood (C_{sf})	−0.20	−0.45*	−0.19	0.47*	0.40	0.52*
Grass + leaf / wood	−0.20	−0.44	−0.22	0.48*	0.41	0.51*

* $p < 0.05$.

tios in group B, which may point to less influence of microbial decomposition on these ratios.

Sediment stirring and inverse ages from radiometric dating indicate disturbances and transformations in the organic matter of profiles P-K and P-S, which become visible in the extreme outmost relations between n-alkane and charcoal ratios (Fig. 6). Due to these inconsistencies, these profiles were classified as group C, which is problematic for environmental interpretation.

Figure 2 shows the vertical distribution of charcoal and n-alkane parameters in several soil profiles that were investigated in greater detail. Layers where low values of OEP and C / N and high values of nC_{18} occur are highlighted in grey to indicate the potential of increased microbiological decomposition. Layers where high values of OEP and C / N and nC_{18} occur are highlighted in light brown to indicate the potential of degradation by fire.

The dark-brown-colored humic layers (18–23 cm; 40 cm) of profile P-B show low TAC, OEP and C / N and high nC_{18} and $\sum nC_{17}$–nC_{20} values (Fig. 2), which confirm the assumption of relocated topsoil from an upslope position for these humic layers (Klinge et al., 2021). In contrast,

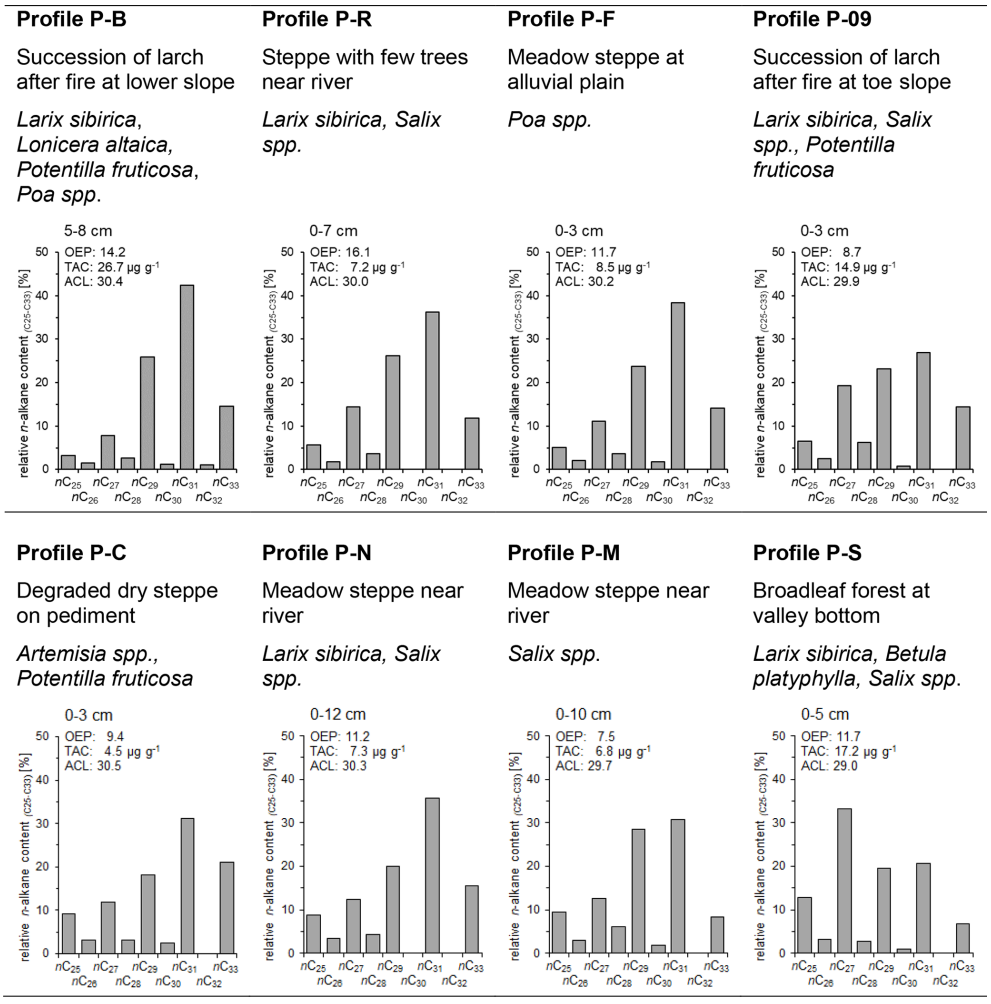

Figure 5. Relative long-chain *n*-alkane content (%), OEP, TAC and ACL of topsoils and mean vegetation at different profiles in the study area (OEP, odd-over-even predominance; TAC, total *n*-alkane concentration of soil; ACL, average chain length of *n*-alkanes).

the bright yellowish sediment (23–38 cm) tends to have increased values for TAC, OEP and C / N and low nC_{18} and $\sum nC_{17}$–nC_{20} values, pointing to more parent material that was subjected to less soil formation. A similar *n*-alkane and C / N pattern occurs in profile P-C, where low OEP and C / N and high nC_{18} of a layer at ∼ 6 cm and a paleosol at 45–50 cm indicated microbiological activity, whereas the other layers were less affected. The inverse distribution of *n*-alkane and macro-charcoal ratios in the pronounced paleosol at 45–50 cm depth in P-C is probably related to the intense decomposition that led to a decrease in long-chain *n*-alkanes and increase in short- and mid-chain *n*-alkanes. The same is true for profile P-L, where the differences in OEP and C / N between the upper layer (58 cm; OEP, 15.6; C / N, 20.1) and lower layer (116 cm; OEP, 9.3; C / N, 14.9) indicate more decomposition related to the decrease in long-chain *n*-alkanes in the latter, which again explains the inverse charcoal ratio (Fig. 2).

At profile P-R, the *n*-alkane pattern is comparable with profile P-B. However, the decomposition rate was already high in the topsoil of profile P-R in contrast to P-B. Although decomposition may have influenced the *n*-alkane pattern of the profiles P-B and P-R, the parallel pattern of macro-charcoal ratios confirms the vegetation proxy. At the top and at the bottom of profile P-F, the OEP, C / N and mid-chain *n*-alkanes indicate similar microbiological activity and soil formation, but ACL points to more forest in the lowest layer.

In the steppe profiles P-C and P-L (group B), higher macro-charcoal ratios that indicate increased grassland share are combined with increased degradation of *n*-alkanes, shown by a lower OEP. This phenomenon is reverse in the forest-related sites (group A, profiles P-B, P-R, P-F). An intensive cryoturbation in profile P-S and substrate infiltration at the profile P-K is underlined by the obtained ages, which diminished the analysis of the *n*-alkane patterns, charcoal ratios and chronology.

Table 3. Correlation matrix between macro-charcoal and *n*-alkane parameters (*r*). TAC denotes total *n*-alkane content; OEP denotes odd-over-even predominance; ACL denotes average chain length of *n*-alkanes.

	nC_{18} (%)	C / N	$\sum nC_{17}$–nC_{20} (%)	TAC	OEP	ACL
Group A: profiles P-B, P-R, P-F; $n = 8$						
Wood	0.18	−0.59	−0.03	−0.40	−0.78*	−0.91**
Leaf	−0.02	−0.51	−0.38	0.23	−0.23	−0.14
Grass	−0.24	−0.37	−0.61	0.27	0.86**	0.93***
Grass / wood; C_{sf}	−0.13	0.85**	−0.28	0.25	0.82*	0.94***
Particles	0.02	−0.55	−0.29	0.35	−0.22	−0.35
C / N	−0.04		−0.11	−0.15	0.59	0.78*
Group B: profiles P-C, P-L, P-N; $n = 8$						
Wood	0.97****	−0.53	0.94***	0.54	0.69	0.83*
Leaf	0.69	−0.43	0.65	−0.10	0.10	0.23
Grass	0.94****	−0.55	0.92**	−0.33	−0.56	−0.75*
Grass / wood; C_{sf}	−0.31	0.19	−0.27	−0.41	−0.66	−0.84**
Particles	0.96****	−0.55	0.93***	0.06	−0.46	−0.17
C / N	−0.45		−0.34	−0.59	0.38	0.13
	Macro-charcoal particle quantity			Macro-charcoal particle proportion		

* $p < 0.05$. ** $p < 0.01$. *** $p < 0.001$. **** $p < 0.0005$.

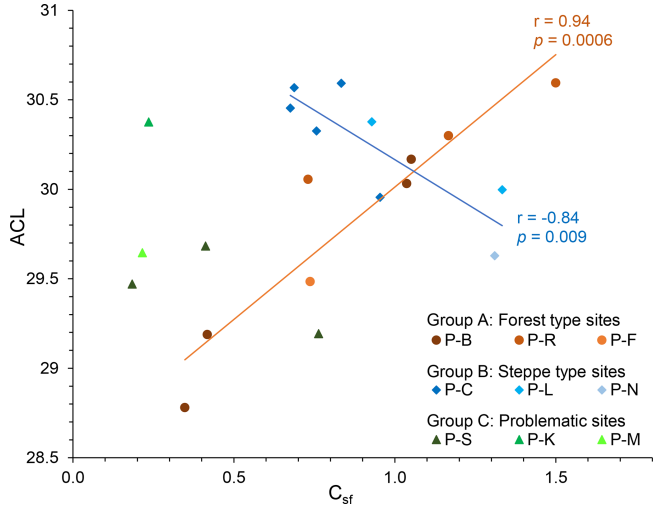

Figure 6. Linear regressions between ACL and C_{sf} grouped by different site conditions (ACL, average chain length of *n*-alkanes; C_{sf}, macro-charcoal grass / wood ratio).

3.5 Evaluating the impact of geomorphological processes, climate and vegetation on *n*-alkanes and macro-charcoal distribution in soils for their suitability as proxy data

The horizontal distribution of *n*-alkane and macro-charcoal ratios in different profiles show parallel patterns in group A and inverse patterns in group B (Fig. 2). A distinct environmental difference between both groups is the occurrence of modern or past forest at the sites of group A, whereas forest was probably absent at the sites of group B. Positive correlations between both ratios may prove the delineation of paleovegetation at the specific sample sites, whereas diverging ratios derive from different sources, pathways and degradation degrees of elements. Irregular biomarker and charcoal distributions in disturbed profiles show inconsistent dating results too, which clearly points to problematic samples that should be interpreted with caution or rejected.

Most of the *n*-alkanes in topsoils originate directly from the litter of the covering vegetation. A paleosol most likely received *n*-alkanes that indicate the local vegetation composition, whereas distinct humic layers as deposits of translocated paleosol contain SOM that comes from distant positions. Thus, *n*-alkanes of colluvial layers represent a mixture of solum material from the upslope area, whereas alluvial layers may receive additional organic material from a larger area of the fluvial catchment. Furthermore, reworked leaf waxes and fossil *n*-alkanes may have deposited along with eolian influx and may have biased the biomarker signals (Haas et al., 2017). However, it can be presumed that the eolian portion of *n*-alkanes in soils is negligible compared to those directly deriving from vegetation.

Paleosols and humic layers contain organic carbon from different sources such as reworked solum material, charcoal, plant material, living roots and dissolved organic matter, which produces uncertainties of > 100 years by ^{14}C dating (Pessenda et al., 2001). Carbon-14 dating of charcoal pro-

vides the age of tree growth before fire. Carbon-14 dating on *n*-alkanes reflects the age of modern vegetation or paleovegetation (i.e., *n*-alkane-producing vegetation) and its input into soils. Therefore, we decided to focus the age determination of our soils using ^{14}C and IRSL dating on bulk material. The *n*-alkane assemblage in the SOM covers the entire period of soil development. Although soil formation may last for a long time, when no soil erosion or sediment covering occurred, the high age frequency of humic layers and paleosols found in our soil profiles (Fig. 2) limits most of the soil formation periods to a few hundred years.

n-Alkanes are subjected to microbiological degradation, which is controlled by different ecological factors relating to moisture and temperature regimes in the investigated soils (Struck et al., 2020). Our results have shown that decomposition of organic matter was generally higher in dry steppe soils and lower under forest that is often underlain by permafrost. The degradation of *n*-alkanes in Mongolian topsoils from semi-arid and arid regions was also investigated for two transects by Struck et al. (2020). OEP values for these topsoils range from 1.5 to 19 and agree with our OEP results (Struck et al., 2020) (Fig. 5).

Although small pieces of charred wood were found in many profiles, the "macro-charcoals" that were analyzed here are particles of microscopic size in the scope of pollen and dust. Thus, macro-charcoals of local origin and eolian input were deposited in different shares. Increasing particle concentration may serve as an indicator for a macro-charcoal source of nearer rather than long-distance fire. Treeless sites of the steppe area (profiles P-C, P-L) must have received their wood-derived macro-charcoal portion in particular by eolian influx. In contrast, the *n*-alkane patterns of steppe soils represent the local vegetation cover consisting of grasses and herbs. The increased share of short- and mid-chain *n*-alkanes (nC_{18}–nC_{26}) in combination with a decreased OEP ratio suggests a more intense microbial degradation of *n*-alkanes (Lerch et al., 2018). Furthermore, statistical analysis (Table 3) proved that a combination of macro-charcoal and *n*-alkanes yields inconsistent results for steppe soils (group B).

The information of macro-charcoal and *n*-alkane distribution (ACL) and the dating results from the paleosols and humic layers provide a chronological framework of the Holocene vegetation evolution in the study area (Fig. 7). Both indices show that grassland dominated in the period before 7.5 ka, although forests had already existed in the Khangai Mountains since at least 9.5 ka (Gunin et al., 1999; Wang et al., 2009; Unkelbach et al., 2021). After 5.0 ka, the indices are more diverse and the vegetation pattern becomes more complex. The site-specific *n*-alkane proxy tends to indicate more grassland compared to the macro-charcoal proxy, which was probably influenced by eolian deposition of allochthonous charcoal particles upon topsoils. The widespread dispersal of charcoal particles after forest and steppe fires represents a distinct sedimentation factor that can even be traced to the high mountains as dust in glacier ice

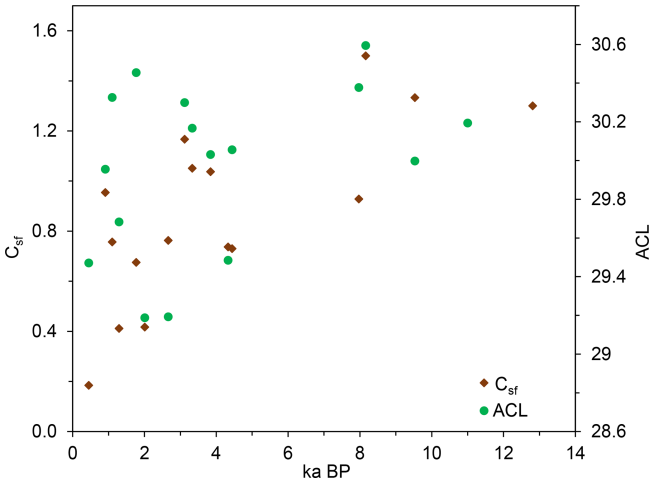

Figure 7. Chronological distribution of macro-charcoal ratio and ACL (ACL, average chain length of *n*-alkanes; C_{sf}, macro-charcoal grass / wood ratio).

(Eichler et al., 2011; Brugger et al., 2018). Thus, the higher share of wood-derived macro-charcoal in soils points to increased forest fires in the region. In addition, the *n*-alkane patterns that represent more local proxies in soils indicate an expanded steppe area for most of the soil profiles, established by a high content of nC_{31}, since the beginning of the Late Holocene. The observed change in the pattern of forest and steppe distribution as well as the increased fire activity in Mongolia since the Late Holocene is related to climatic and/or anthropogenic impact (Klinge and Sauer, 2019). Furthermore, desertification processes and increased geomorphological activity occur concordantly with a cultural change since the early Bronze Age when humans developed a pastoral economy (Fernández-Giménez et al., 2017; Klinge et al., 2022). Nevertheless, these initial findings need further evaluation due to the limited number of samples presented here.

4 Conclusions

Based on our results of comparing two different paleoproxies, *n*-alkanes and macro-charcoals, we have shown that it is essential to consider their different element sources, paths and catchment areas for interpretation of the local and regional paleo-environment. Additional information about soil properties as well as radiometric dating provides further evidence. The analysis of lipid biomarkers, such as *n*-alkanes, on samples from soil profiles of central Mongolia gives insight into local vegetation conditions. *n*-Alkanes, which are organic molecules in leaf waxes, are directly accumulated in the soils by local vegetation (Zech et al., 2010b). Translocation of soil material may occur by slope wash and solifluction processes. Decomposition of organic matter and *n*-alkanes is generally more intense in dry steppe soils and

less intense under forest that is often underlain by permafrost. Macro-charcoals in soils represent a mixture of both local and long-distance sources. Due to the eolian transport, the dominating wind direction frames the catchment area of macro-charcoal influx.

We have shown that paleosols and humic layers represent a valuable archive for reconstruction of the detailed paleo-environment at a high site-specific spatial resolution. The application of lipid biomarker analysis to paleosols can help to prove local differences in topographic site conditions over time such as the aspect-dependent vegetation differentiation of the Mongolian forest–steppe. Charcoal in paleosols indicates periods of increased fire impact on landscape evolution and geomorphology. However, the temporal resolution of paleosol and sediment archives is often low and discontinuous due to irregular deposition intensity and soil-forming periods, but the biomarker proxies are related to distinct geomorphological periods in a local scale. In contrast, lake sediments may provide a more continuous sedimentation chronology, but the sediment input depends on fluvial and eolian catchments. Thus, these archives contain proxy data that represent a larger area than soil archives do. Furthermore, stratified charcoal particles in glacier ice and snow fields solely derive from long-distance eolian transport. Their paleo-proxies depend on the main wind direction that frames the catchment area and thus the region for the paleo-environmental representation of their proxies. In summary, there is further need for multi-proxy analysis (biomarkers, macro-charcoal, pollen, microorganisms, ancient DNA, sediment properties) comparing the different soils, lake and glacier archives in combination with radiometric dating to enhance and refine the paleo-environmental records in Mongolia.

Data availability. All raw data can be provided by the corresponding authors upon request.

Supplement. The supplement related to this article is available online at: https://doi.org/10.5194/egqsj-71-91-2022-supplement.

Author contributions. FS and ML developed the project idea in collaboration with MK and JU. Fieldwork was carried out by FS and MK. ML and JU carried out most of the laboratory work. MK analyzed the data. MK prepared the manuscript, and ML, JU, MZ and FS contributed to the discussion of the results and read and approved the manuscript.

Competing interests. At least one of the (co-)authors is a member of the editorial board of *E&G Quaternary Science Journal*. The peer-review process was guided by an independent editor, and the authors have also no other competing interests to declare.

Disclaimer. Publisher's note: Copernicus Publications remains neutral with regard to jurisdictional claims in published maps and institutional affiliations.

Acknowledgements. We thank our project partners Choimaa Dulamsuren and Markus Hauck (Faculty of Environment and Natural Resources, University of Freiburg) and Uudus Bayarsaikhan (Department of Biology, National University of Mongolia, Ulaanbaatar) for their great support during the fieldwork in Mongolia.

We thank Daramragchaa Tuya (Tarvagatai Nuruu National Park, Tosontsengel Sum, Zavkhan Aimag, Mongolia) for her invaluable support of our research. We wish to express our gratitude to our Mongolian colleagues Amarbayasgalan, Enkhjargal and Enkh-Agar. We greatly appreciated their hospitality and help in the field. Our thanks also go to the German students Jannik Brodthuhn and Tim Rollwage for their assistance during soil sampling in Mongolia.

In particular, we thank Daniela Sauer (Institute of Geography, University of Göttingen) and Manfred Frechen (Leibniz Institute for Applied Geophysics, Hanover) for their professional support and project collaboration. Furthermore, we thank Bruno Glaser and Tobias Bromm (Department of Soil Biogeochemistry, Martin Luther University Halle-Wittenberg) for providing access to laboratory facilities and support of laboratory analyses. We thank Hermann Behling (Albrecht-von-Haller-Institute for Plant Sciences, University of Göttingen) for providing laboratory access.

We also thank Jens Holtvoeth and the anonymous reviewer for their valuable recommendations to improve the manuscript.

Financial support. This research has been supported by the Deutsche Forschungsgemeinschaft (grant no. 385460422).

This open-access publication was funded by the University of Göttingen.

Review statement. This paper was edited by Ingmar Unkel and reviewed by Jens Holtvoeth and one anonymous referee.

References

Academy of Sciences of Mongolia and Academy of Sciences of USSR: National Atlas of the Peoples Republic of Mongolia, Ulan Baatar, Moscow, 144 pp., 1990.

Bittner, L., Bliedtner, M., Grady, D., Gil-Romera, G., Martin-Jones, C., Lemma, B., Mekonnen, B., Lamb, H. F., Yang, H., Glaser, B., Szidat, S., Salazar, G., Rose, N. L., Opgenoorth, L., Miehe, G., Zech, W., and Zech, M.: Revisiting afro-alpine Lake Garba Guracha in the Bale Mountains of Ethiopia: rationale, chronology, geochemistry, and paleoenvironmental implications, J. Paleolimnol., 64, 293–314, https://doi.org/10.1007/s10933-020-00138-w, 2020.

Bliedtner, M., Schäfer, I. K., Zech, R., and von Suchodoletz, H.: Leaf wax *n*-alkanes in modern plants and topsoils from eastern Georgia (Caucasus) – implications for reconstruct-

ing regional paleovegetation, Biogeosciences, 15, 3927–3936, https://doi.org/10.5194/bg-15-3927-2018, 2018.

Bliedtner, M., von Suchodoletz, H., Schäfer, I., Welte, C., Salazar, G., Szidat, S., Haas, M., Dubois, N., and Zech, R.: Age and origin of leaf wax *n*-alkanes in fluvial sediment–paleosol sequences and implications for paleoenvironmental reconstructions, Hydrol. Earth Syst. Sci., 24, 2105–2120, https://doi.org/10.5194/hess-24-2105-2020, 2020.

Breckle, S.-W., Lawlor, G., Lawlor, D. W., and Walter, H. (Eds.): Walter's vegetation of the earth: The ecological systems of the geo-biosphere, 4th edn., Springer, Berlin, 527 pp., ISBN 9783540433156, 2002.

Brugger, S. O., Gobet, E., Sigl, M., Osmont, D., Papina, T., Rudaya, N., Schwikowski, M., and Tinner, W.: Ice records provide new insights into climatic vulnerability of Central Asian forest and steppe communities, Global Planet. Change, 169, 188–201, https://doi.org/10.1016/j.gloplacha.2018.07.010, 2018.

Buggle, B., Wiesenberg, G. L., and Glaser, B.: Is there a possibility to correct fossil *n*-alkane data for postsedimentary alteration effects?, Appl. Geochem., 25, 947–957, https://doi.org/10.1016/j.apgeochem.2010.04.003, 2010.

Bush, R. T. and McInerney, F. A.: Leaf wax *n*-alkane distributions in and across modern plants: Implications for paleoecology and chemotaxonomy, Geochim. Cosmochim. Ac., 117, 161–179, https://doi.org/10.1016/j.gca.2013.04.016, 2013.

Diefendorf, A. F., Freeman, K. H., Wing, S. L., and Graham, H. V.: Production of *n*-alkyl lipids in living plants and implications for the geologic past, Geochim. Cosmochim. Ac., 75, 7472–7485, https://doi.org/10.1016/j.gca.2011.09.028, 2011.

Dulamsuren, C. and Hauck, M.: Spatial and seasonal variation of climate on steppe slopes of the northern Mongolian mountain taiga, Grassl. Sci., 54, 217–230, https://doi.org/10.1111/j.1744-697X.2008.00128.x, 2008.

Eglinton, G. and Hamilton, R. J.: Leaf epicuticular waxes, Science, 1322–1325, 1967.

Eichler, A., Tinner, W., Brütsch, S., Olivier, S., Papina, T., and Schwikowski, M.: An ice-core based history of Siberian forest fires since AD 1250, Quaternary Sci. Rev., 30, 1027–1034, https://doi.org/10.1016/j.quascirev.2011.02.007, 2011.

Erdős, L., Ambarlı, D., Anenkhonov, O. A., Bátori, Z., Cserhalmi, D., Kiss, M., Kröel-Dulay, G., Liu, H., Magnes, M., Molnár, Z., Naqinezhad, A., Semenishchenkov, Y. A., Tölgyesi, C., and Török, P.: The edge of two worlds: A new review and synthesis on Eurasian forest-steppes, Appl. Veg. Sci., 21, 345–362, https://doi.org/10.1111/avsc.12382, 2018.

Fernández-Giménez, M. E., Venable, N. H., Angerer, J., Fassnacht, S. R., Reid, R. S., and Khishigbayar, J.: Exploring linked ecological and cultural tipping points in Mongolia, Anthropocene, 17, 46–69, https://doi.org/10.1016/j.ancene.2017.01.003, 2017.

Fowell, S. J., Hansen, B. C., Peck, J. A., Khosbayar, P., and Ganbold, E.: Mid to late Holocene climate evolution of the Lake Telmen Basin, North Central Mongolia, based on palynological data, Quat. Res., 59, 353–363, https://doi.org/10.1016/S0033-5894(02)00020-0, 2003.

Gunin, P. D., Vastokova, E. A., Dorofeyuj, N. I., Tarasov, P. E., and Black, C. C. (Eds.): Vegetation dynamics of Mongolia, Geobotany, 26, Kluwer Academic Publishers, Dordrecht, Boston, London, 238 pp., https://doi.org/10.1007/978-94-015-9143-0_2, 1999.

Haas, M., Bliedtner, M., Borodynkin, I., Salazar, G., Szidat, S., Eglinton, T. I., and Zech, R.: Radiocarbon Dating of Leaf Waxes in the Loess-Paleosol Sequence Kurtak, Central Siberia, Radiocarbon, 59, 165–176, https://doi.org/10.1017/RDC.2017.1, 2017.

Hais, M., Chytrý, M., and Horsák, M.: Exposure-related forest-steppe: A diverse landscape type determined by topography and climate, J. Arid Environ., 135, 75–84, https://doi.org/10.1016/j.jaridenv.2016.08.011, 2016.

Hepp, J., Zech, R., Rozanski, K., Tuthorn, M., Glaser, B., Greule, M., Keppler, F., Huang, Y., Zech, W., and Zech, M.: Late Quaternary relative humidity changes from Mt. Kilimanjaro, based on a coupled 2H-18O biomarker paleohygrometer approach, Quatern. Int., 438, 116–130, https://doi.org/10.1016/j.quaint.2017.03.059, 2017.

Hessl, A. E., Brown, P., Byambasuren, O., Cockrell, S., Leland, C., Cook, E., Nachin, B., Pederson, N., Saladyga, T., and Suran, B.: Fire and climate in Mongolia (1532–2010 Common Era), Geophys. Res. Lett., 43, 6519–6527, https://doi.org/10.1002/2016GL069059, 2016.

Hoefs, M. J., Rijpstra, W. C., and Sinninghe Damsté, J. S.: The influence of oxic degradation on the sedimentary biomarker record I: evidence from Madeira Abyssal Plain turbidites, Geochim. Cosmochim. Ac., 66, 2719–2735, https://doi.org/10.1016/S0016-7037(02)00864-5, 2002.

Iijima, Y., Ishikawa, M., and Jambaljav, Y.: Hydrological cycle in relation to permafrost environment in forest-grassland ecotone in Mongolia, Journal of Japanese Association of Hydrological Sciences, 42, 119–130, 2012.

Khansaritoreh, E., Dulamsuren, C., Klinge, M., Ariunbaatar, T., Bat-Enerel, B., Batsaikhan, G., Ganbaatar, K., Saindovdon, D., Yeruult, Y., Tsogtbaatar, J., Tuya, D., Leuschner, C., and Hauck, M.: Higher climate warming sensitivity of Siberian larch in small than large forest islands in the fragmented Mongolian forest steppe, Glob. Change Biol., 23, 3675–3689, https://doi.org/10.1111/gcb.13750, 2017.

Khapugin, A. A., Vargot, E. V., and Chugunov, G. G.: Vegetation recovery in fire-damaged forests: a case study at the southern boundary of the taiga zone, Forestry Studies, 64, 39–50, https://doi.org/10.1515/fsmu-2016-0003, 2016.

Klinge, M. and Sauer, D.: Spatial pattern of Late Glacial and Holocene climatic and environmental development in Western Mongolia – A critical review and synthesis, Quaternary Sci. Rev., 210, 26–50, https://doi.org/10.1016/j.quascirev.2019.02.020, 2019.

Klinge, M., Dulamsuren, C., Erasmi, S., Karger, D. N., and Hauck, M.: Climate effects on vegetation vitality at the treeline of boreal forests of Mongolia, Biogeosciences, 15, 1319–1333, https://doi.org/10.5194/bg-15-1319-2018, 2018.

Klinge, M., Schneider, F., Dulamsuren, C., Arndt, K., Bayarsaikhan, U., and Sauer, D.: Interrelations between vegetation, natural and anthropogenic disturbances, and discontinuous permafrost in the forest-steppe of central Mongolia, Earth Surf. Proc. Land., 46, 1766–1782, https://doi.org/10.1002/esp.5116, 2021.

Klinge, M., Schneider, F., Yan, L., Frechen, M., and Sauer, D.: Alternating geomorphological processes in the northern Khangai Mountains, Mongolia since the Late Glacial period, Geomorphology, 401, 108113, https://doi.org/10.1016/j.geomorph.2022.108113, 2022.

Kolattukudy, P. E.: Biochemistry of plant waxes, in: Chemistry and biochemistry of natural waxes, edited by: Kolattukudy, P. E. and Kolattukudy, P. E., Elsevier, Amsterdam, 290–349, ISBN 0444414703, 1976.

Kopp, B. J., Minderlein, S., and Menzel, L.: Soil Moisture Dynamics in a Mountainous Headwater Area in the Discontinuous Permafrost Zone of northern Mongolia, Arct. Antarct. Alp. Res., 46, 459–470, https://doi.org/10.1657/1938-4246-46.2.459, 2014.

Lerch, M., Bliedtner, M., Roettig, C.-B., Schmidt, J.-U., Szidat, S., Salazar, G., Zech, R., Glaser, B., Kleber, A., and Zech, M.: Lipid biomarkers in aeolian sediments under desert pavements – potential and first results from the Black Rock Desert, Utah, USA, and Fuerteventura, Canary Islands, Spain, E&G Quaternary Sci. J., 66, 103–108, https://doi.org/10.5194/egqsj-66-103-2018, 2018.

Miehe, G., Schlütz, F., Miehe, S., Opgenoorth, L., Cermak, J., Samiya, R., Jäger, E. J., and Wesche, K.: Mountain forest islands and Holocene environmental changes in Central Asia: A case study from the southern Gobi Altay, Mongolia, Palaeogeogr. Palaeoclimatol. Palaeoecol., 250, 150–166, https://doi.org/10.1016/j.palaeo.2007.03.022, 2007.

Mustaphi, C. J. C. and Pisaric, M. F.: A classification for macroscopic charcoal morphologies found in Holocene lacustrine sediments, Prog. Phys. Geog., 38, 734–754, https://doi.org/10.1177/0309133314548886, 2014.

Nyamjav, B., Goldammer, G., and Uibrig, H.: Fire situation in Mongolia, in: International Forest Fire News, 46–66, 2007.

Odgaard, B. V.: Fossil pollen as a record of past biodiversity, J. Biogeogr., 26, 7–17, https://doi.org/10.1046/j.1365-2699.1999.00280.x, 1999.

Patterson, W. A., Edwards, K. J., and Maguire, D. J.: Microscopic charcoal as a fossil indicator of fire, Quaternary Sci. Rev., 6, 3–23, https://doi.org/10.1016/0277-3791(87)90012-6, 1987.

Pelletier, J. D., Barron-Gafford, G. A., Gutiérrez-Jurado, H., Hinckley, E.-L. S., Istanbulluoglu, E., McGuire, L. A., Niu, G.-Y., Poulos, M. J., Rasmussen, C., Richardson, P., Swetnam, T. L., and Tucker, G. E.: Which way do you lean? Using slope aspect variations to understand Critical Zone processes and feedbacks, Earth Surf. Proc. Land., 43, 1133–1154, https://doi.org/10.1002/esp.4306, 2018.

Pessenda, L. C. R., Gouveia, S. E. M., and Aravena, R.: Radiocarbon Dating of Total Soil Organic Matter and Humin Fraction and Its Comparison with ^{14}C Ages of Fossil Charcoal, Radiocarbon, 43, 595–601, https://doi.org/10.1017/S0033822200041242, 2001.

Poynter, J. G., Farrimond, P., Robinson, N., and Eglinton, G.: Aeolian-Derived Higher Plant Lipids in the Marine Sedimentary Record: Links with Palaeoclimate, in: Paleoclimatology and Paleometeorology: Modern and Past Patterns of Global Atmospheric Transport, edited by: Leinen, M. and Sarnthein, M., Springer, Dordrecht, 435–462, https://doi.org/10.1007/978-94-009-0995-3_18, 1989.

Rudaya, N., Tarasov, P. E., Dorofeyuk, N., Solovieva, N., Kalugin, I., Andreev, A., Daryin, A., Diekmann, B., Riedel, F., and Tserendash, N.: Holocene environments and climate in the Mongolian Altai reconstructed from the Hoton-Nur pollen and diatom records: A step towards better understanding climate dynamics in Central Asia, Quaternary Sci. Rev., 28, 540–554, https://doi.org/10.1016/j.quascirev.2008.10.013, 2009.

Schäfer, I. K., Lanny, V., Franke, J., Eglinton, T. I., Zech, M., Vysloužilová, B., and Zech, R.: Leaf waxes in litter and topsoils along a European transect, SOIL, 2, 551–564, https://doi.org/10.5194/soil-2-551-2016, 2016.

Schneider, F., Klinge, M., Brodthuhn, J., Peplau, T., and Sauer, D.: Hydrological soil properties control tree regrowth after forest disturbance in the forest steppe of central Mongolia, SOIL, 7, 563–584, https://doi.org/10.5194/soil-7-563-2021, 2021.

Stevenson, J. and Haberle, S.: Macro Charcoal Analysis: A modified technique used by the Department of Archaeology and Natural History, Palaeoworks Technical Papers, 5, http://hdl.handle.net/1885/144170 (last access: 20 May 2022), 2005.

Strobel, P., Struck, J., Zech, R., and Bliedtner, M.: The spatial distribution of sedimentary compounds and their environmental implications in surface sediments of Lake Khar Nuur (Mongolian Altai), Earth Surf. Proc. Land., 46, 611–625, https://doi.org/10.1002/esp.5049, 2021.

Struck, J., Roettig, C. B., Faust, D., and Zech, R.: Leaf waxes from aeolianite–paleosol sequences on Fuerteventura and their potential for paleoenvironmental and climate reconstructions in the arid subtropics, E&G Quaternary Sci. J., 66, 109–114, https://doi.org/10.5194/egqsj-66-109-2018, 2018.

Struck, J., Bliedtner, M., Strobel, P., Schumacher, J., Bazarradnaa, E., and Zech, R.: Leaf wax n-alkane patterns and compound-specific δ^{13}C of plants and topsoils from semi-arid and arid Mongolia, Biogeosciences, 17, 567–580, https://doi.org/10.5194/bg-17-567-2020, 2020.

Tarasov, P. E., Müller, S., Zech, M., Andreeva, D., Diekmann, B., and Leipe, C.: Last glacial vegetation reconstructions in the extreme-continental eastern Asia: Potentials of pollen and n-alkane biomarker analyses, Quatern. Int., 290–291, 253–263, https://doi.org/10.1016/j.quaint.2012.04.007, 2013.

Thomas, C. L., Jansen, B., van Loon, E. E., and Wiesenberg, G. L. B.: Transformation of n-alkanes from plant to soil: a review, SOIL, 7, 785–809, https://doi.org/10.5194/soil-7-785-2021, 2021.

Umbanhowar, C. E. and Mcgrath, M. J.: Experimental production and analysis of microscopic charcoal from wood, leaves and grasses, Holocene, 8, 341–346, https://doi.org/10.1191/095968398666496051, 1998.

Umbanhowar, C. E., Shinneman, A. L., Tserenkhand, G., Hammon, E. R., Lor, P., and Nail, K.: Regional fire history based on charcoal analysis of sediments from nine lakes in western Mongolia, Holocene, 19, 611–624, https://doi.org/10.1177/0959683609104039, 2009.

Unkelbach, J., Kashima, K., Enters, D., Dulamsuren, C., Punsalpaamuu, G., and Behling, H.: Late Holocene (Meghalayan) palaeoenvironmental evolution inferred from multi-proxy-studies of lacustrine sediments from the Dayan Nuur region of Mongolia, Palaeogeogr. Palaeoclimatol. Palaeoecol., 530, 1–14, https://doi.org/10.1016/j.palaeo.2019.05.021, 2019.

Unkelbach, J., Dulamsuren, C., Klinge, M., and Behling, H.: Holocene high-resolution forest-steppe and environmental dynamics in the Tarvagatai Mountains, north-central Mongolia, over the last 9570 cal yr BP, Quaternary Sci. Rev., 266, 107076, https://doi.org/10.1016/j.quascirev.2021.107076, 2021.

Wang, W., Ma, Y., Feng, Z.-D., Meng, H., Sang, Y., and Zhai, X.: Vegetation and climate changes during the last 8660 cal. a BP in central Mongolia, based on a high resolution pollen

record from Lake Ugii Nuur, Chinese Sci. Bull., 54, 1579–1589, https://doi.org/10.1007/s11434-009-0023-8, 2009.

Wiesenberg, G., Lehndorff, E., and Schwark, L.: Thermal degradation of rye and maize straw: Lipid pattern changes as a function of temperature, Org. Geochem., 40, 167–174, https://doi.org/10.1016/j.orggeochem.2008.11.004, 2009.

Zech, M., Buggle, B., Leiber, K., Marković, S., Glaser, B., Hambach, U., Huwe, B., Stevens, T., Sümegi, P., Wiesenberg, G., and Zöller, L.: Reconstructing Quaternary vegetation history in the Carpathian Basin, SE-Europe, using *n*-alkane biomarkers as molecular fossils: Problems and possible solutions, potential and limitations, E&G Quaternary Sci. J., 58, 148–155, https://doi.org/10.3285/eg.58.2.03, 2010a.

Zech, M., Andreev, A., Zech, R., Müller, S., Hambach, U., Frechen, M., and Zech, W.: Quaternary vegetation changes derived from a loess-like permafrost palaeosol sequence in northeast Siberia using alkane biomarker and pollen analyses, Boreas, 4142, 540–550, https://doi.org/10.1111/j.1502-3885.2009.00132.x, 2010b.

Zech, M., Rass, S., Buggle, B., Löscher, M., and Zöller, L.: Reconstruction of the late Quaternary paleoenvironments of the Nussloch loess paleosol sequence, Germany, using *n*-alkane biomarkers, Quat. Res., 78, 226–235, https://doi.org/10.1016/j.yqres.2012.05.006, 2012.

Zech, M., Krause, T., Meszner, S., and Faust, D.: Incorrect when uncorrected: Reconstructing vegetation history using *n*-alkane biomarkers in loess-paleosol sequences – A case study from the Saxonian loess region, Germany, Quatern. Int., 296, 108–116, https://doi.org/10.1016/j.quaint.2012.01.023, 2013.

Zech, M., Kreutzer, S., Zech, R., Goslar, T., Meszner, S., McIntyre, C., Häggi, C., Eglinton, T., Faust, D., and Fuchs, M.: Comparative ^{14}C and OSL dating of loess-paleosol sequences to evaluate post-depositional contamination of *n*-alkane biomarkers, Quat. Res., 87, 180–189, https://doi.org/10.1017/qua.2016.7, 2017.

E&G Quaternary Sci. J., 71, 111–122, 2022
https://doi.org/10.5194/egqsj-71-111-2022

Open Access E&G Quaternary Science Journal

Research article

On the expression and distribution of glacial trimlines: a case study of Little Ice Age trimlines on Svalbard

Camilla M. Rootes and Christopher D. Clark

Department of Geography, University of Sheffield, Sheffield S10 2TN, UK

Correspondence: Christopher D. Clark (c.clark@sheffield.ac.uk)

Relevant dates: Received: 5 May 2021 – Revised: 7 April 2022 – Accepted: 2 May 2022 – Published: 8 June 2022

How to cite: Rootes, C. M. and Clark, C. D.: On the expression and distribution of glacial trimlines: a case study of Little Ice Age trimlines on Svalbard, E&G Quaternary Sci. J., 71, 111–122, https://doi.org/10.5194/egqsj-71-111-2022, 2022.

Abstract: Glacial trimlines are important features for constraining 3-dimensional palaeoglaciological reconstructions, but relatively little is known about the processes of their formation and preservation. A new classification scheme for the expression of glacial trimlines was presented by Rootes and Clark (2020), with the aim to encourage further research into the processes of formation and preservation for trimlines. Here we present the first application of the trimline classification scheme to a case study location in central western Spitsbergen, Svalbard. Little Ice Age trimlines were mapped using remotely sensed imagery and the classification scheme applied. These data are presented and used to examine the factors that may influence the distribution and expression of trimlines in order to explore controls on their formation and preservation. Preliminary analysis suggests that the type of glacier, and geology, particularly the bedrock erodibility, may have an influence over the location and expression of glacial trimlines in Svalbard. These findings open the potential for trimlines to be used as part of diagnostic landsystems for specific types of glacier, such as marine-terminating tidewater glaciers, terrestrial glaciers or surge-type glaciers, and indicates that further research into glacial trimlines may enable these landforms to yield additional information about palaeo-ice masses than has previously been the case.

Kurzfassung: Schliffgrenzen sind wichtige Merkmale für die Ableitung dreidimensionaler paläoglaziologischer Rekonstruktionen, jedoch ist relativ wenig über die Prozesse ihrer Entstehung und Erhaltung bekannt. Ein neues Schema zur Klassifikation der Ausprägung von Schliffgrenzen wurde von Rootes und Clark (2020) vorgestellt, mit dem Ziel, weitere Forschung zu den Prozessen der Bildung und Erhaltung von Schliffgrenzen anzuregen. Hier stellen wir die erste Anwendung des Schliffgrenzen-Klassifikationsschemas auf das Gebiet einer eine Fallstudie im zentralen westlichen Spitzbergen, Svalbard, vor. Die Schliffgrenzen der Kleinen Eiszeit wurden mit Hilfe von Fernerkundungsaufnahmen kartiert und dem Klassifikationsschema unterzogen. Diese Daten werden vorgestellt und dazu verwendet, zu untersuchen, welche Faktoren die Verbreitung und Ausprägung von Schliffgrenzen beeinflussen, um die Kontrollfaktoren ihrer Entstehung und Erhaltung zu identifizieren. Vorläufige Analysen deuten darauf hin, dass der Gletschertyp und die Geologie, insbesondere die Erodierbarkeit des Gesteins, einen Einfluss auf die Lage und Ausprägung der Schliffgrenzen in Spitzbergen haben. Diese Befunde eröffnen die Möglichkeit, Schliffgrenzen als Teil des diagnostischen Formenschatzes

für bestimmte Gletschertypen, wie ins Meer mündende Gezeitengletscher oder terrestrische Gletscher, verwendet werden können. Sie weisen zudem darauf hin, dass bei weiterer Erforschung der Schliffgrenzen diese das Potential haben, mehr Informationen über Paläoeismassen zu liefern als dies bisher der Fall war. (*Abstract was translated by Daniela Sauer.*)

1 Introduction

Glacial trimlines are defined as glaciogenic features expressed as a break or transition in the vegetation, weathered material, erosion pattern, deposited material or truncated slope landforms (e.g. talus cones, gullies) on the slopes of a glacierised or glaciated valley (Rootes and Clark, 2020). These features are important in helping produce 3-dimensional (3D) reconstructions because they provide constraints on both the vertical and horizontal position of palaeo-ice margins (Ballantyne, 2010; Rootes and Clark, 2020).

In spite of the importance of glacial trimlines they remain relatively under-studied in comparison to other glaciogenic landforms which have received far more research regarding their processes of formation and presentation, such as for moraines (e.g. Barr and Lovell, 2014; Reinardy et al., 2013; Lukas, 2012; Lukas et al., 2012; Cooley, 2012). The lack of research means that the processes of trimline formation and preservation remain largely unknown (Rootes and Clark, 2020). This makes it difficult to confidently interpret glacial trimlines and to use them in conjunction with other, better studied glaciogenic features in the production of 3D reconstructions. Trimlines often find themselves in the category of only being seen in the "eye of the beholder", with field parties vigorously arm-waving and debating whether a trimline reliably exists on that flank of valley. Annoyingly, they sometimes disappear the closer you approach them. Some of these problems surely come from a lack of understanding as to how they are manifested in the landscape, which makes it difficult to reliably identify and map trimlines.

A recent attempt at classifying the full range of possible trimline expressions was presented by Rootes and Clark (2020), but this classification scheme has not yet been tested in a case study example. They categorised trimline expression into contrasts in glacial deposition or erosion, in discontinuities in landforms reflecting slope process, or by surface ageing contrasts (see Fig. 3). Here we apply this trimline classification scheme to a case study example in Svalbard. We also investigate the extent to which trimline expression varies with glacier type, such as marine versus terrestrially terminating and surge and non-surging glaciers. The trimlines in the study area have not been the subject of previous research or mapping. The methods used to map and classify the glacial trimlines will be presented, alongside the maps and data files. The utility of the new classification scheme will be assessed, and notable patterns in the expression and distribution of the trimlines across the area will be highlighted and discussed. From these findings we suggest potential directions for further research into the expression, formation and preservation of glacial trimlines.

Study area

The Svalbard archipelago is situated in the Barents Sea and was chosen for this case study because the recent retreat of Svalbard glaciers since their Little Ice Age (LIA) maximum extent has exposed a wide range of glacial trimlines, representing many different trimline expressions. The trimlines are relatively young, with the local LIA maximum ice margin position thought to have been reached between 1850 and 1940 (Ziaja, 2005; Mangerud and Landvik, 2007; Flink et al., 2015; Farnsworth et al., 2020). The relatively recent nature of trimlines on Svalbard mean that these features are generally clear, well-defined and often closely associated with a modern ice margin, making them more straightforward to identify and map than older trimlines.

An area in central western Spitsbergen, the largest of the Svalbard islands, was identified for this study (Fig. 1). Spitsbergen has been well-studied, and the glacial history is reasonably well constrained, particularly along the west coast (Ingólfsson, 2011) where the study area is located. The study area is in a predominantly mountainous area bounded by two prominent fjords: Kongsfjorden in the north and St. Jonsfjorden in the south (Fig. 1). This area was chosen because the glacial geomorphological evidence and stratigraphy have been previously documented, but the trimlines have not been mapped in detail. Previous studies have attempted to produce 3D reconstructions of the LIA ice thickness (e.g. Lønne and Lysså, 2005; Navarro et al., 2005; Ziaja, 2005; Kohler et al., 2007; Mangerud and Landvik, 2007; Nuth et al., 2007) but have made little to no use of glacial trimlines despite the fact that these landforms are very widespread in the study area.

The area is heavily glacierised, with 78 glaciers covering 69 % of the land area (Fig. 2). There are a wide range of valley and cirque glaciers, as well as 15 large marine-terminating valley or icefield outlet glaciers. The study area features 31 surge-type glaciers, which have phases of comparatively rapid flow ("surges") interspersed with longer periods of slower flow (Benn and Evans, 2010). The surge-type glaciers in the study area have been identified either due to being observed during a surge or because they are associated with glacial or geomorphological features that are diagnostic of surging (Heïde Sevestre, personal communication, 2015).

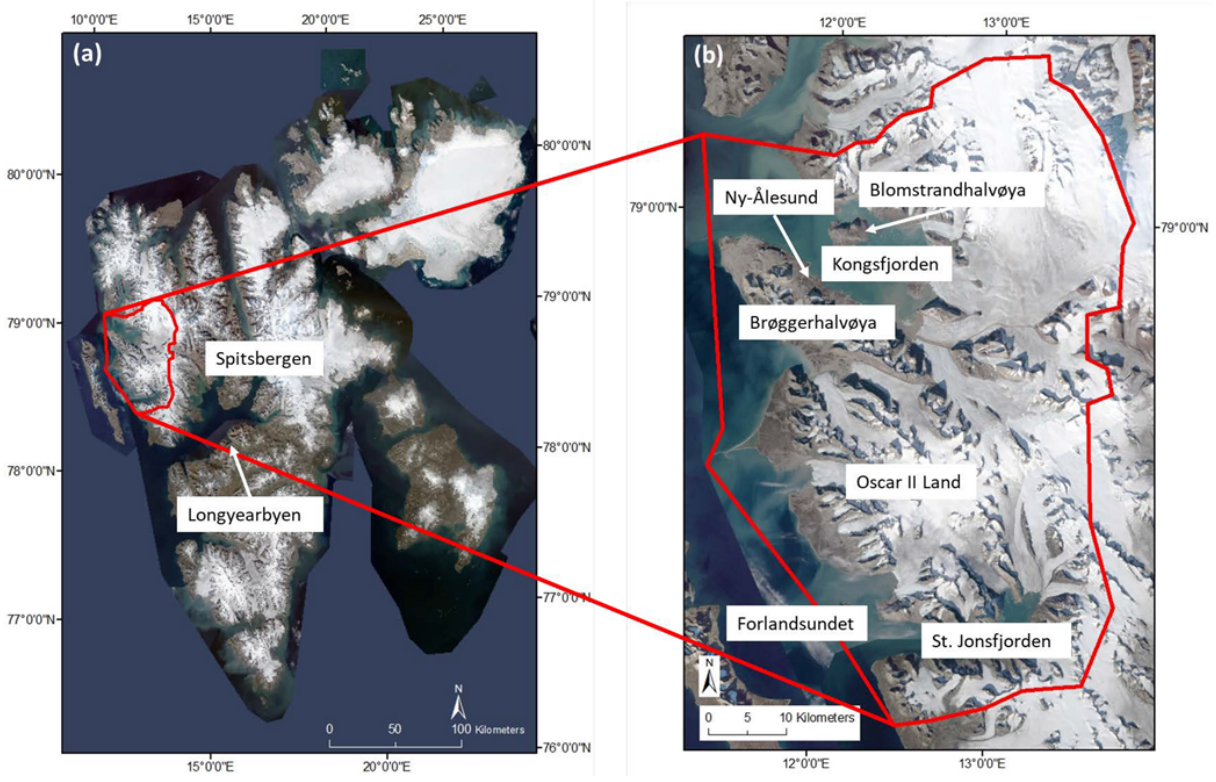

Figure 1. **(a)** The Svalbard archipelago with the study area in central western Spitsbergen outlined in red. **(b)** The study area with place names referred to in the text. Map from the Norwegian Polar Institute.

Central western Spitsbergen has an Arctic maritime climate, which is typical for Svalbard and produces predominately polythermal bed conditions in all but the smallest of cirque glaciers (Nuth et al., 2007). The study area geology can be broadly divided into three categories: (1) metamorphic Precambrian and Caledonian Hecla Hoek basement around St. Jonsfjorden, to the north of Kongsfjorden, and in the mountains of Oscar II Land; (2) sedimentary Permian and Triassic platform cover on the Brøggerhalvøya peninsula; and (3) Tertiary and Quaternary deposits on the coastal plains of Oscar II Land (Dallmann, 2015; Fig. 1). Previous research has suggested that glacial trimlines can be influenced by the underlying geology (e.g. Kelly et al., 2004), so the varied geology of the study area may be expected to be associated with differing patterns of trimline expression and/or distribution.

2 Methodology

2.1 Trimline mapping methodology and data sources

The trimlines of central western Spitsbergen were mapped from remotely sensed imagery using ArcGIS 10.1. The primary mapping was conducted using band 8 (panchromatic) of the Landsat 7 Enhanced Thematic Mapper + scene captured on 1 August 2015. To refine the trimline mapping and to assist in the classification of the modes of trimline expression, the 15 m resolution Landsat scene was compared with very high-resolution (40–50 cm) aerial imagery from the Norwegian Polar Institute (NPI). The aerial images were acquired by the NPI during the summers of 2008–2012. A 20 m resolution digital elevation model (DEM) was also used to provide elevation and slope information for the trimline features and to enable analysis of the surrounding topography. The DEM was produced by the NPI in 2014 from stereo aerial imagery.

Secondary data used in the mapping and analysis of the glacial trimlines included geological maps, acquired from the NPI, and modern glacier margin shapefiles, also acquired from the NPI and produced between 2001 and 2010. A list of the surge-type glaciers in central western Spitsbergen was compiled using Sevestre's Svalbard surging glacier inventory (Sevestre, 2015). Field photographs of several trimlines in central western Spitsbergen were acquired by Mona Henriksen and Camilla M. Rootes during July and August 2015.

All features that could be trimlines or other associated landforms, such as lateral moraines, were identified and mapped onto the Landsat image. Following the terminology outlined in Rootes and Clark (2020), these "apparent trimlines" were then investigated to identify any potentially non-glacial features. This involved consulting the NPI aerial im-

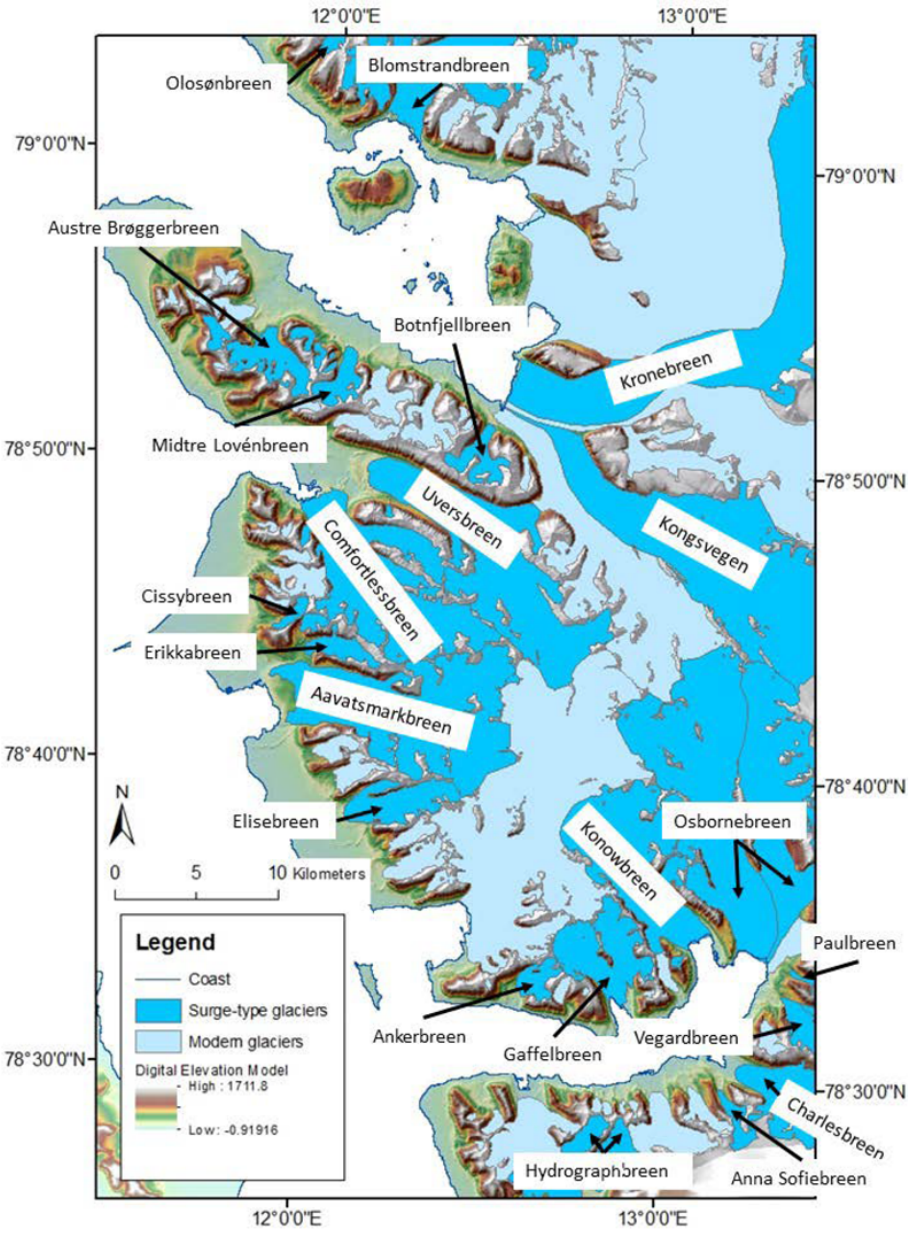

Figure 2. Surge-type (labelled with their names) and non-surging glaciers of central western Spitsbergen. Large surge-type glaciers dominate (many of them with tidewater margins), accounting for roughly half of the glaciated area. Glacier outlines and DEM are from the Norwegian Polar Institute. The surge-type glaciers were identified from Sevestre's inventory of Svalbard surging glaciers (Sevestre, 2015).

agery alongside geological and glacier margin maps to identify any apparent trimlines that were likely to be of geological origin, i.e. marking a fault line or rock boundary, or were probably debris-covered ice margins.

2.2 Classifying trimline expression

The new trimline expression classification scheme (Rootes and Clark, 2020; Fig. 3) was applied to the trimlines in the study area. The classification scheme was used to determine the primary mode of expression for each trimline feature and to separate the glacial trimlines from other associated linear landforms, such as moraines and ice marginal meltwater features (Fig. 3).

The modes of trimline expression were identified by visual analysis using the Landsat scene and the high-resolution NPI aerial imagery. This technique generally allowed one or more of the expression categories to be easily identified for each trimline. In some cases, it was not possible to clearly identify the primary mode of trimline expression, in which case additional methods were applied. For example, a nor-

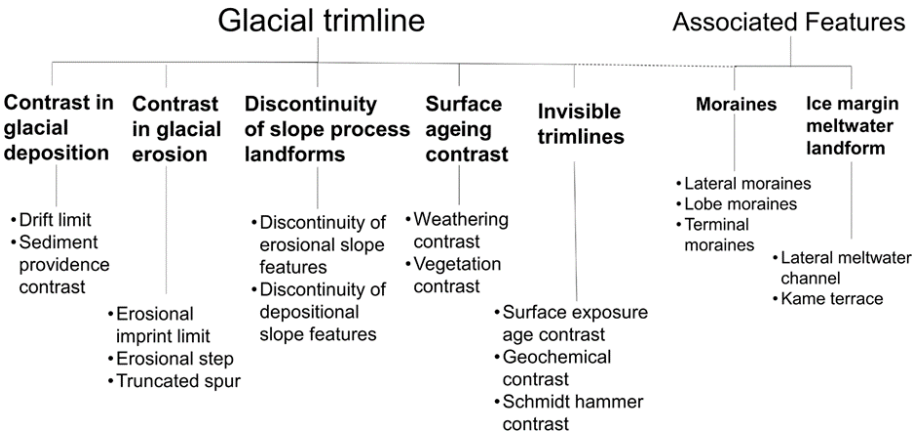

Figure 3. The classification scheme used to determine the mode of expression for glacial trimlines in the study area (Rootes and Clark, 2020). No trimlines were classified in the "invisible trimlines" category. These would need to be identified by analysing soil or rock samples collected in the field, which was beyond the remit of the study. However, all of the remaining trimline expression categories were found to be present in central western Spitsbergen, as well as moraines and ice margin meltwater landforms.

malised difference vegetation index (NDVI), computed from the Landsat data, was used to identify the changes in vegetation that characterised some of the surface ageing trimlines in the study area. Other additional methods involved consulting true and false colour Landsat data composites, the DEM, and any available field photos.

3 Results

The primary mapping identified 407 apparent trimlines, of which 11 were then found to be potentially not glaciogenic landforms. These features were excluded from further analysis, leaving a data set of 396 confirmed glacial trimlines or associated linear glacial features. Of these, 200 apparent trimlines were identified as either moraines or ice marginal meltwater landforms, leaving a final dataset of 196 confirmed glacial trimlines.

Classification of the final dataset determined that the most common mode of expression was as depositional trimlines, such as glacial drift limits, accounting for 93 features, 47 % of all trimlines in the study area. Erosional trimlines, such as limits of warm-based glacial erosion, were also very common; accounting for 90 features or 46 % of all trimlines in the study area. Other modes of expression were found significantly less common, with only eight trimlines expressed primarily as a discontinuity in slope landforms and just five expressed primarily as a contrast in surface ageing. However, both of these less common modes were commonly identified as secondary modes of expression, with either erosional or depositional identified as the feature's primary mode of expression. For example, trimlines primarily identified as depositional were often also found to include discontinuities in slope landforms, whilst primarily erosional trimlines are often associated with surface ageing contrasts. In total, 113 trimlines, representing 58 % of all trimlines in the study area, were identified as composite features that are linked to at least two different modes of expression.

So-called invisible trimlines (Fig. 3), those only apparent from field assessments of relative or absolute dating of the surfaces, were not investigated.

3.1 Trimline distribution and expression

Trimlines were found to be abundant and evenly distributed across the area (Fig. 4a) with most of the modern glaciers having at least one trimline. Four trimlines not associated with any modern glacier were identified: three on Brøggerhalvøya (Fig. 4b) and one in a cirque just west of Comfortlessbreen in Oscar II Land (Fig. 4c). These record the existence of glaciers that likely existed during the Little Ice Age cold event but have since disappeared.

Further evidence for loss of ice mass in the study area is shown by the altitudinal sequences of trimlines associated with several of the larger glaciers, which indicate widespread glacial thinning. A particularly good example are the trimlines on Colletthøgda, defining a nunatak that is emerging as Kongsbreen and Kronebreen lower in elevation (Fig. 4b). Trimline evidence for frontal retreat of glaciers is apparent in that Bullbreen was once a marine-terminating tidewater glacier, but it has retreated and now terminates on land (Fig. 4d). On the coastal plains of Oscar II Land, trimlines along the lateral ice margins can be used in conjunction with the large lateral and frontal moraine complexes to demonstrate both glacial retreat and thinning in large outlet glaciers, such as Aavatsmarkbreen (Fig. 4c). Trimline evidence also points to former confluences between glaciers that are now distinct. For example, following the line of the trimlines of Konowbreen and Osbornebreen in St. Jonsfjorden allows a potential palaeo-confluence point to be identified (marked in Fig. 4d). In some cases, the distribution of trimlines suggests

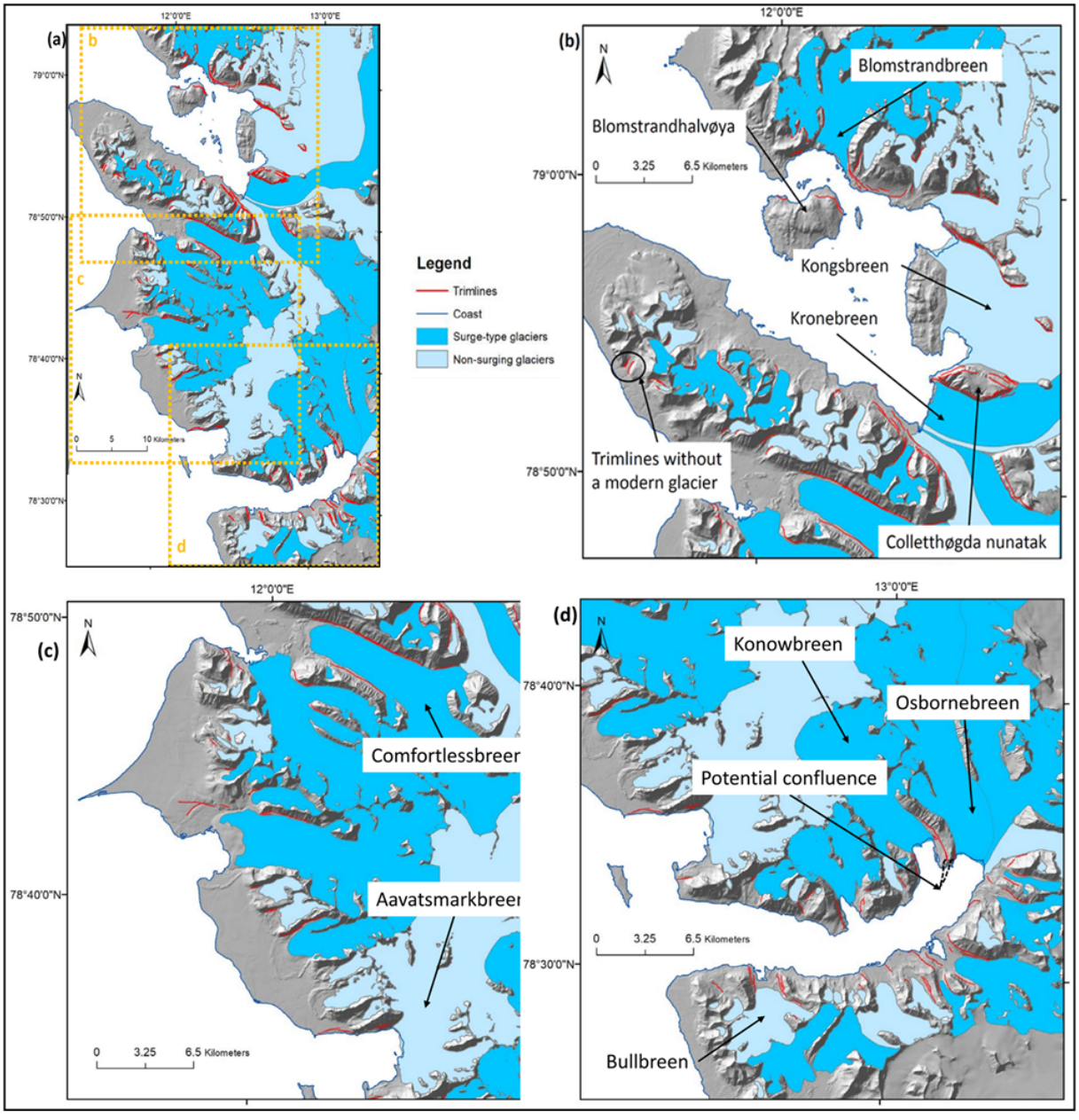

Figure 4. Trimlines and glaciers in central western Spitsbergen. **(a)** Entire study area with areas covered by panels **(b)**, **(c)** and **(d)** indicated in orange; **(b)** greater detail of Kongsfjorden and the Brøggerhalvøya peninsula; **(c)** coastal Oscar II Land; and **(d)** the area around St. Jonsfjorden. These maps show that trimlines are found throughout the ice-free areas of central western Spitsbergen, associated with most glaciers, with many glaciers linked to multiple trimlines. The glacier outlines and background DEM are from the NPI.

possible topographic pinning points, where the shape of the topography stabilised a glacier, such as the frontal margin of Blomstrandbreen on the island of Blomstrandhalvøya in Kongsfjorden (Fig. 4b).

Trimlines of all modes of expression are distributed throughout the study area (Fig. 5a). Depositional and erosional trimlines are often found associated with the same glacier and especially so around the surge-type and tidewater glaciers of St. Jonsfjorden (Fig. 5d) and Kongsfjorden (Fig. 5b). Surface ageing contrasts can also be found primarily in St. Jonsfjorden and Kongsfjorden but are particularly common as secondary classifications of erosional trimlines, in which form they are well distributed throughout the study area. Slope landform discontinuities are mainly found alone in Kongsfjorden and are most often identified as a secondary classification for depositional trimlines, in which form they are well distributed throughout the study area but remain the least common mode of trimline expression. Trimlines of all

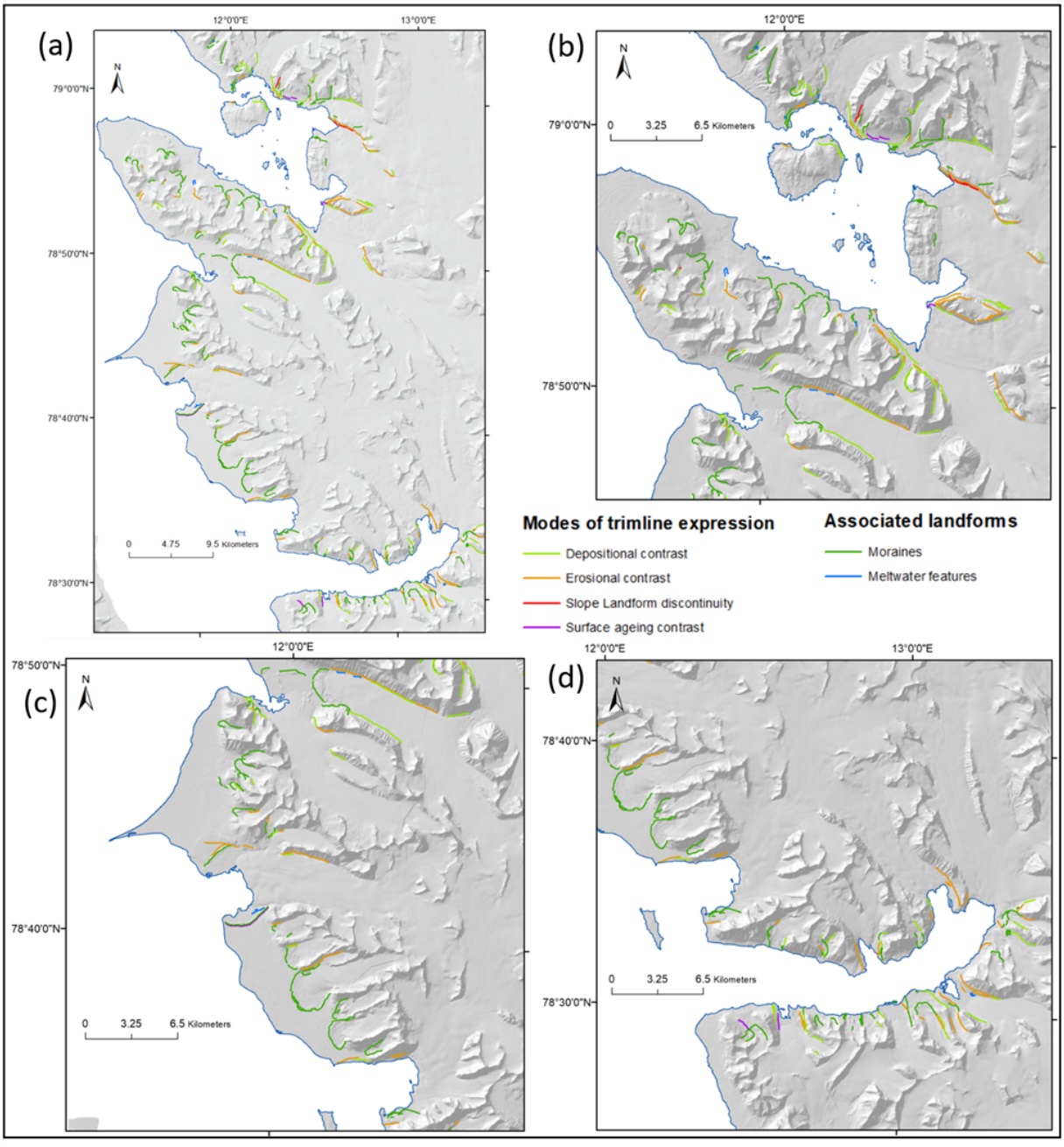

Figure 5. Distribution of the different modes of trimline expression and associated ice marginal landforms. **(a)** Whole study area; **(b)** Kongsfjorden and Brøggerhalvøya; **(c)** coast of Oscar II Land; and **(d)** area around St. Jonsfjorden. Note that many slope landforms and surface ageing trimlines are not visible because the classification here is by the predominant mode of trimline expression, usually erosional or depositional.

types are less common in the coastal plains in Oscar II Land, where limited numbers of mostly erosional and surface ageing trimlines are largely found on the lateral ice margins (Fig. 5c).

3.2 Factors influencing the distribution and expression

Trimlines are most commonly found (55 %) in the regions of the study area underlain by erosion-resistant Hecla Hoek metamorphic basement, which is found around St. Jonsfjorden, to the north of Kongsfjorden, and in the mountains of Oscar II Land. A further 39 % of trimlines are located on sedimentary Permian and Triassic platform cover on the Brøg-

gerhalvøya peninsula, with just 6 % associated with the soft and highly erodible Tertiary and Quaternary deposits that make up the plains of Oscar II Land. This suggests that the resistance to erosion of the bedrock geology may have an influence over the distribution of glacial trimlines, a link that has been previously made (e.g. by Kelly et al., 2004) but which is fraught with the difficulty of disentangling geological from topographical factors given that the two so often co-vary.

Surface ageing contrasts are especially common (63 %) in regions underlain by the erosion-resistant Hecla Hoek basement. In the regions of softer Tertiary and Quaternary deposits, trimlines are relatively uncommon, but erosional trimlines exist in a slightly greater proportion (12 %) compared to all trimlines (6 %), as might be expected.

Slope angle appears to be potentially relevant in influencing the distribution of trimlines and their expression. Trimlines are found across almost the full range of ice-free topographic slopes in the study area but are more common on lower slopes (10–30°) than the typical range of ice-free slope angles (15–35°) (Fig. 6). Trimlines found on slopes steeper than 30° tend to be either erosional, slope landform discontinuities or surface ageing trimlines (Fig. 6). Depositional trimlines can occasionally be found on these steeper slopes, but, as expected, this mode of trimline expression is predominantly found on shallower slopes ($< 30°$) (Fig. 6). This reversal in the most common mode of trimline expression at a slope angle of around 30° may indicate a relationship between topographic slope and the processes of trimline formation or preservation for specific modes of trimline expression.

Trimlines have been previously described as landforms that can form above the equilibrium line altitude (ELA), making them an important tool for reconstructing palaeo-ice surfaces in glacier accumulation areas (Kelly et al., 2004). The local modern ELA in the study area is thought to be at an elevation of 350 m a.s.l. (Nuth et al., 2007), and 8 % of trimline features were found above this elevation. However, the majority of trimlines are thought to be LIA in origin, when the ELA would likely have been lower. The local ELA at the peak of the LIA is estimated to be at around 273 m a.s.l. (Rootes, 2018). Of the trimlines in the study area, 20 % are located above this altitude. Our mapping thus supports previous findings that trimlines can indeed be formed above the ELA. Depositional trimlines (19 %) and slope landform discontinuities (22 %) are slightly more common above the LIA ELA than erosional trimlines or surface ageing contrasts (11 %), the majority of which are found in the LIA ablation zone.

Regarding glaciological factors potentially influencing timeline expression, the study area usefully contains a mix of marine-terminating tidewater (19 %) and terrestrially terminating glaciers, as well as surge-type (40 %) and non-surging glaciers. The majority (53 %), however, are terrestrial and non-surging. These glaciers will be termed "normal" glaciers to distinguish them from "tidewater" or "surge-type" glaciers.

It might be expected that larger glaciers, having longer perimeters, might produce more trimlines. However, whilst there is a weak correlation between glacier size and number of trimlines, neither glacier area nor glacier length is strongly related to the number of trimlines a glacier produces ($r^2 < 0.3$). This appears to be due to a high degree of variability in the number of trimlines associated with medium and large glaciers, which have lengths > 5 km and areas $> 25\,000$ km^2. This variability suggests that another glaciological variable, possibly glacier type, is more important than glacier size for controlling the number of trimlines associated with medium and large glaciers.

The number of trimline features associated with each glacier type was compared to the relative abundance of that glacier type in the study area (Fig. 7). This shows that normal glaciers, despite being the most common type of glacier in the study area (53 %), have a lower proportion of trimlines (26 %) than the other glacier types. Both tidewater and tidewater surge-type glaciers, on the other hand, produce many more trimlines than would be expected given the proportion of these glaciers in the study area. Tidewater glaciers account for 23 % of all trimline features but only 8 % of study area glaciers, whilst tidewater surge-type glaciers produce 26 % of all trimlines from 12 % of glaciers. This suggests that the behaviour or glaciology of tidewater glaciers may promote trimline formation and/or preservation.

Comparing the mode of trimline expression to the type of glacier also suggests a connection between glacier type and how trimlines are expressed. Depositional trimlines exist across all glacier types in roughly equal proportion to their relative abundance, but some other modes of expression are associated with particular glacier types. Erosional trimlines and surface ageing contrasts are slightly more commonly associated with surge-type glaciers compared to non-surging glaciers, but a much stronger connection appears to exist between these modes of trimline expression and tidewater glaciers. Tidewater glaciers, both surge-type and non-surging, are associated with 38 % of all trimlines, but these are predominately erosional trimlines (62 %) or surface ageing contrasts (60 %). Marine-terminating glaciers appear to promote the formation or preservation of these particular modes of trimline expression.

4 Discussion

It is clear that the distribution of glacial trimlines in the area records a wealth of information about the former size, shape and configuration of the local glaciers and is a valuable record of glacier recession.

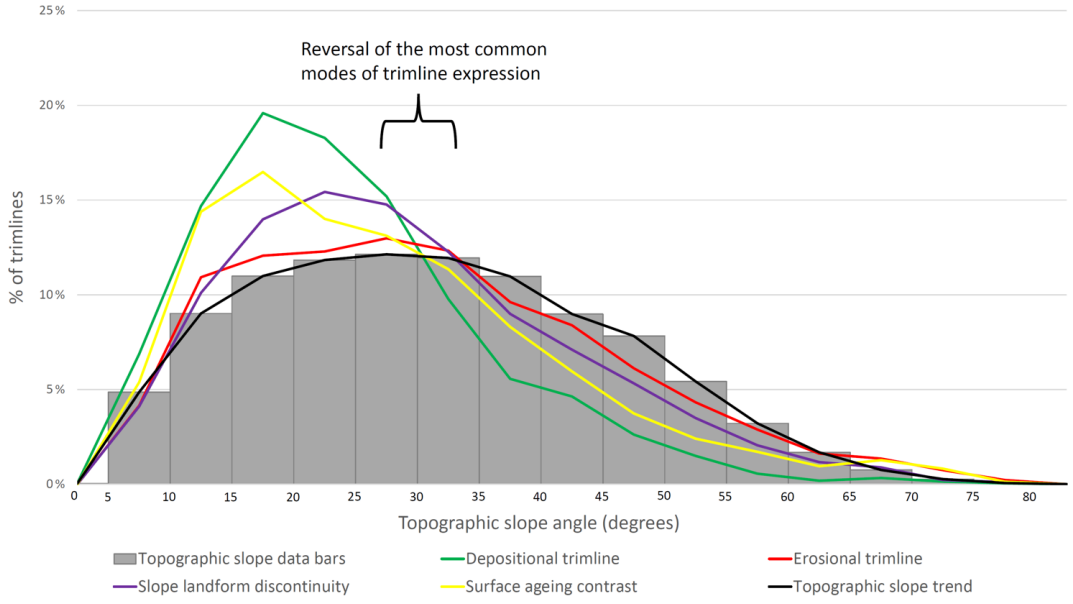

Figure 6. Comparison of types of trimline expression (coloured lines) against the slope angle of the ice-free host landscape (bars and black line). Trimlines of all expressions tend to exist on slightly shallower than average slopes in the study area and with notable preferences per type of trimline expression. There is a reversal in the most common mode of trimline expression at around 30°; below this most trimlines are depositional, whereas the trimlines on steeper slopes are more likely to be expressed as contrasts in erosion, as slope landforms or by surface ageing.

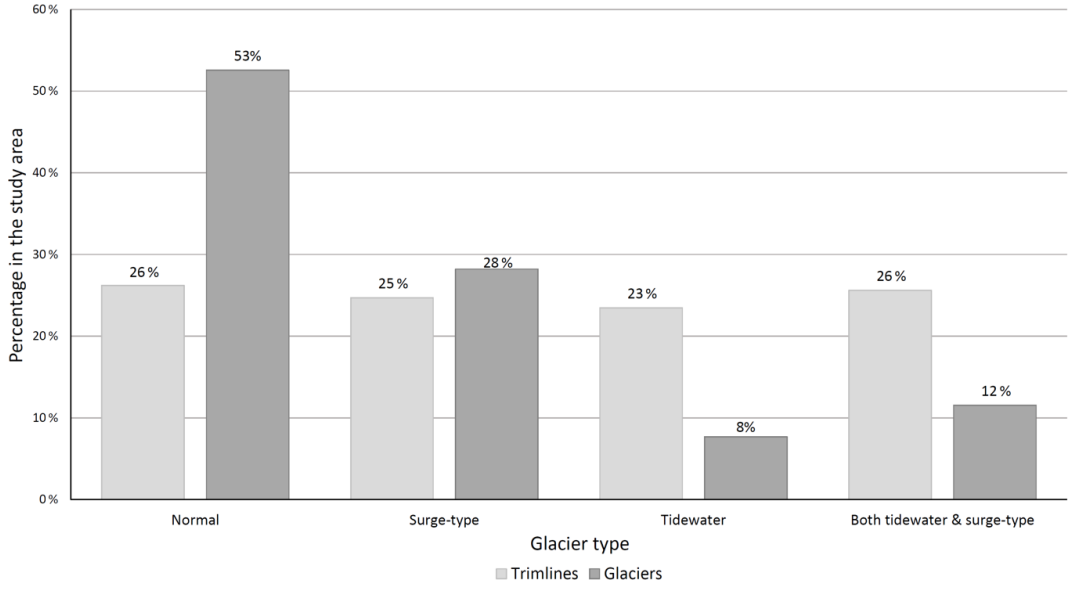

Figure 7. Variation in number of trimlines compared with glacier type, scaled according the abundance of each glacier type in the study area. The main signals are that normal glaciers have fewer trimlines than would be expected and that tidewater glaciers (surge and non-surge) have more than expected given the prevalence of these glacier types in the study area.

4.1 Insights into trimline formation and preservation

Glacial trimlines have been shown to be present both above the modern ELA and above the LIA ELA in central western Spitsbergen. This supports previous suggestions that trimlines can form in the accumulation areas of glaciers (Kelly et al., 2004) and makes these landforms valuable constraints on the vertical dimensions of palaeo-ice masses. This is important for 3D reconstructions and enables the potential to determine rates of thinning in both the ablation and accumulation areas.

Geology, topography and glacier type all appear to influence the distribution and expression of glacial trimlines in central western Spitsbergen. This suggests that these factors may act as controls over either the processes of trimline formation, their preservation or both. Whilst difficult to disentangle between these variables, it appears that underlying geology and glacier type exert a stronger influence than topography on the distribution and expression of glacial trimlines. That trimlines of all expressions are found across nearly the full range of topographic slope angles in the study area may indicate that slope angle is not a strong control over the formation and preservation of glacial trimlines. Since topographic slope may be linked to the rates and mechanics of ice flow and the rates of erosion or deposition of a glacier, it could be that any relationship between trimlines and topographic slope is more a reflection of glaciology than topography.

Alternatively, the location of shallow slope angles within glacial valleys, rather than the slope angle itself, could be the primary influence of topography over glacial trimlines. For example, depositional trimlines may only form where there is sufficient glacially transported material to build a drift limit, which may only be the case at the downstream end of the valley, coinciding with the location of shallower slope angles.

Geology appears to exert a stronger influence than topography, with a clear link identifying a higher prevalence of trimlines in areas of more resistant bedrock. This suggests that trimlines may be better preserved in these environments, a point also made by Kelly et al. (2004) in their study of trimlines in the European Alps. Kelly et al. (2004) also found that erosional trimlines in particular were more common in areas of more resistant bedrock. Erosional trimlines often manifest as a boundary between areas of glacial erosion and regions of periglacial weathering. Therefore, these features may not preserve well in more erodible sediments, where other processes (e.g. fluvial action, mass wasting) could remove or cover erosional trimlines. However, this study has found that, whilst no trimlines were particularly common in the areas of the most easily eroded geology, erosional trimlines were actually the most common mode of expression in these regions. It is hypothesised that this may be due to the relatively young LIA age of the trimlines in central western Spitsbergen compared to the older Last Glacial Maximum trimlines studied by Kelly et al. (2004). It may be that erosional trimlines form relatively easily in areas of more erodible geology but that they are not well preserved in these settings, explaining their relative abundance in these settings on Svalbard compared to areas with older trimline features. The lack of other modes of trimline expression in the coastal area of Oscar II Land, where the geology is very erodible, could indicate that the formation or preservation of most trimlines is hampered by less resistant rocks and sediments. In particular, surface ageing contrasts are likely to take a long time to form and may either not form at all or not be preserved in more rapidly eroding environments, which may explain why these features are markedly more common in the areas of resistant Hecla Hoek basement. Slope landform discontinuities require the presence of existing slope landforms, such as talus cones or gullies, in order to form. These landforms are perhaps less likely to form in areas with softer bedrock because the topography is more likely to be subdued, without steep slopes that encourage the mass wasting and fluvial processes required to form slope landforms.

The finding that tidewater glaciers produced more trimlines than terrestrial glaciers might be due to their greater ice flow velocities, which promote higher levels of glacial erosion and create more material that is then available for glacial deposition. Whilst tidewater surge-type glaciers produced larger numbers of trimlines than might be expected from the number of glaciers, the same is not true of terrestrial surge-type glaciers (Fig. 7). This might be because surge-type glaciers only have high velocities for short periods of time, generally 3–10 years for Svalbard surge-type glaciers, with lower velocities during quiescent phases of 50–500 years (Sevestre and Benn, 2015; Dowdeswell et al., 1991). It appears that high ice flow velocities do not promote greater numbers of trimlines unless velocities are sustained for extended periods of time, as is the case for most tidewater glaciers but not for terrestrial surge-type glaciers.

Erosional and surface ageing trimlines are much more likely to be associated with tidewater glaciers, both surge-type and non-surging. This connection is probably due to the high velocities of these glaciers which promote the processes of glacial erosion that produce these modes of trimline expression.

In summary, we have identified some potentially useful links between the distribution of glacial trimlines, different modes of trimline expression, the underlying geology and the type of glacier. These relationships, if found to hold in further research in a wider range of settings, could enable a more confident interpretation of trimlines and may enable more information to be extracted from them, analogous to landsystem models that have been constructed for terrestrial (Evans and Rea, 2003) and tidewater (Ottesen et al., 2008) surging glaciers in Svalbard. Can trimlines be reliably added to such models?

4.2 Assessment of the trimline expression classification

A new classification scheme for trimline expression (Fig. 3; Rootes and Clark, 2020) was applied here in a case study. No trimlines were identified that could not be matched with one of the modes of trimline expression listed in the classification scheme. In all cases, remotely sensed satellite and aerial images were the primary data used to identify trimline expression, which was carried out by eye. Even when using the lower-resolution (15 m) Landsat imagery, the system worked well and was accurate when compared to the higher-resolution (40–50 cm) aerial images. Identification of the mode of trimline expression using satellite imagery was

aided by the use of minor post-processing to produce composite images, particularly true and false colour images and to conduct NDVI analyses. The use of the digital elevation model (DEM) also assisted in identifying the mode of trimline expression, particularly by altering the angle of illumination in relief shading tools across the trimline. It is therefore recommended that the trimline expression classification system is used with aerial imagery where possible, but it can be applied to lower-resolution satellite imagery, in which DEMs and compound images can be utilised to aid the classification process.

Whilst it was generally possible to separate the different modes of trimline expression, a majority of trimlines (58 %) were found to be expressed in more than one way – these features are referred to as "composite trimlines". The composite trimlines were classified according to their most dominant expression, which was generally easy to identify, but this was necessarily a subjective decision. The most common composite trimlines were dominantly erosional or depositional contrasts, combined with either slope landform discontinuities or surface ageing contrasts. Although the slope landform and surface ageing modes of trimline expression were most commonly used as secondary classifications, both of these modes of expression were found as the sole classification for some trimline features. This suggests that it is worth continuing to identify these modes of expression as distinct from erosional or depositional trimlines.

Overall, the trimline expression classification system was easy to use with both satellite and aerial imagery, although it is best used with higher-resolution images. Utilising DEMs and composite images works well to improve the accuracy of trimline expression classification without significantly adding to the workload required. The insights drawn from exploring the expression of trimlines in central western Spitsbergen suggest that more widespread consideration of the expression of glacial trimlines is likely to be worthwhile. Therefore, the expression classification presented in Rootes and Clark (2020) is recommended as a tool to explore glacial trimline expression, although it would benefit from being tested in more locations. Whilst more time consuming for large areas, field investigation of trimlines can include other types of evidence not visible from remotely sensed data, such as the variable spreads of erratic blocks or striae inscribed on bedrock.

5 Conclusions

Previous research into glacial trimlines has generally not considered the full range of possible trimline expressions, and little attempt has been made to explore the processes of trimline formation and preservation. Rootes and Clark (2020) reviewed the literature of glacial trimline research and suggested a new classification scheme for the various modes of trimline expression (Fig. 3). Here we applied this classification scheme for the first time, using it to investigate glacial trimlines in central western Spitsbergen. Trimlines and associated ice marginal landforms were mapped from aerial and satellite imagery (Fig. 4a) and classified according to the expression classification presented by Rootes and Clark (2020) (Fig. 5a). The classification was found to be straightforward to apply to the remotely sensed imagery and included all of the observable modes of trimline expression in the study area. It is suggested that further applications of the trimline expression classification in a wider range of settings may prove fruitful at illuminating processes of trimline formation and preservation, an area that has seen only limited research.

Preliminary exploration of the possible factors influencing trimline distribution and expression found that the type of glacier and geology, particularly bedrock erodibility, appears to exert control over the distribution and expression of glacial trimlines. Topographic factors were found to have less impact. The findings of this study suggest that analysis of the expression and distribution of glacial trimlines has the potential to shed light on the type of glacier that formed the trimlines, potentially enabling the identification of surge-type and tidewater glaciers in Quaternary settings. This study has also confirmed that trimlines can be formed above the ELA, supporting the conclusions of previous research and validating the use of these features as indicators of palaeo-ice thickness in the accumulation area.

A better understanding of trimline formation and preservation could lead to a significant expansion in the potential uses for glacial trimlines in palaeoglaciological reconstructions. Where previously trimlines have been used only as a constraint on the ice margin position and as a measure of ice thickness, they can now potentially be used to diagnose the type of glacier, but further research is required to confirm this.

Data availability. GIS data of the identified trimlines are not yet available because analysis is ongoing but will be available via a data repository or by request from the second author.

Author contributions. CMR was responsible for the conceptualisation, methodology, investigation, formal analysis, and writing the original draft and producing the figures. CDC was responsible for the conceptualisation, methodology, writing (review, editing and additions), for supervising the PhD, and for submitting and handling the paper.

Competing interests. The contact author has declared that neither they nor their co-author has any competing interests.

Disclaimer. Publisher's note: Copernicus Publications remains neutral with regard to jurisdictional claims in published maps and institutional affiliations.

Acknowledgements. Camilla M. Rootes carried out this work whilst in receipt of a PhD scholarship awarded to her by the Faculty of Social Sciences at the University of Sheffield, and she gratefully acknowledges this support. This work has benefited from funding from the European Research Council (ERC) under the European Union's Horizon 2020 research and innovation programme as part of the PalGlac project (grant agreement no. 787263).

Financial support. This research was supported by a University of Sheffield PhD scholarship scheme and with funding from the European Research Council (ERC) under the European Union's Horizon 2020 research and innovation programme as part of the PalGlac project to Christopher D. Clark (grant agreement no. 787263).

The article processing charge was funded by the Quaternary scientific community, as represented by the host institution of *EGQSJ*, the German Quaternary Association (DEUQUA).

Review statement. This paper was edited by Christopher Lüthgens and reviewed by Margot Böse and one anonymous referee.

References

Ballantyne, C. K.: Extent and deglacial chronology of the last British-Irish Ice Sheet: implications of exposure dating using cosmogenic isotopes, J. Quat. Sci., 25, 515–534, 2010.

Barr, I. D. and Lovell, H.: A review of topographic controls on moraine distribution, Geomorphology, 226, 44–64, 2014.

Benn, D. I. and Evans, D. J.: Glaciers and glaciation, Hodder Education, ISBN 9781138458130, 2010.

Cooley, S. W.: Degradation of moraine slopes with age in Quaternary moraines of eastern California, in: Geological Society of America Abstracts with Programs, p. 1, Geological Society of America, https://our.unc.edu/abstract/cooley-degradation-of-moraine-slopes-with-age-in-quaternary-moraines-of-eastern-ca/ (last access: 7 June 2022), 2012.

Dallmann W. K. (Ed.): Geoscience Atlas of Svalbard, Norwegian Polar Institute, Report 148, Tromsø, http://hdl.handle.net/11250/2580810 (last access: 7 June 2022), 2015.

Dowdeswell, J., Hamilton, G., and Hagen, J.: The duration of the active phase on surge type glaciers: Contrasts between Svalbard and other regions, J. Glaciol., 37, 388–400, 1991.

Evans, D. and Rea, B.: Glacial Landsystems, in: Glacial Landsystems, edited by: Evans, D. J. A., Arnold, London, 259–288, ISBN 9780203784976, 2003.

Farnsworth, W. R., Allaart, L., Ingólfsson, Ó., Alexanderson, H., Forwick, M., Noormets, R., Retelle, M., and Schomacker, A.: Holocene glacial history of Svalbard: Status, perspectives and challenges, Earth-Sci. Rev., 208, 103249, https://doi.org/10.1016/j.earscirev.2020.103249, 2020.

Flink, A. E., Noormets, R., Kirchner, N., Benn, D. I., Luckman, A., and Lovell, H.: The evolution of a submarine landform record following recent and multiple surges of Tunabreen glacier, Svalbard, Quat. Sci. Rev., 108, 37–50, 2015.

Ingólfsson, Ó.: Fingerprints of Quaternary glaciations on Svalbard, Geological Society, London, Special Publications, 354, 15–31, https://doi.org/10.1144/SP354.2, 2011.

Kelly, M. A., Buoncristiani, J.-F., and Schlüchter, C.: A reconstruction of the last glacial maximum (LGM) ice-surface geometry in the western Swiss Alps and contiguous Alpine regions in Italy and France, Eclogae Geol. Helv., 97, 57–75, 2004.

Kohler, J., James, T. D., Murray, T., Nuth, C., Brandt, O., Barrand, N. E., Aas, H. F., and Luckman, A.: Acceleration in thinning rate on western Svalbard glaciers, Geophys. Res. Lett., 34, L18502, https://doi.org/10.1029/2007GL030681, 2007.

Lønne, I. and Lyså, A.: Deglaciation dynamics following the Little Ice Age on Svalbard: Implications for shaping of landscapes at high latitudes, Geomorphology, 72, 300–319, 2005.

Lukas, S.: Processes of annual moraine formation at a temperate alpine valley glacier: insights into glacier dynamics and climatic controls, Boreas, 41, 463–480, 2012.

Lukas, S., Graf, A., Coray, S., and Schlüchter, C.: Genesis, stability and preservation potential of large lateral moraines of Alpine valley glaciers – towards a unifying theory based on Findelengletscher, Switzerland, Quat. Sci. Rev., 38, 27–48, 2012.

Mangerud, J. and Landvik, J. Y.: Younger Dryas cirque glaciers in western Spitsbergen: smaller than during the Little Ice Age, Boreas, 36, 278–285, 2007.

Navarro, F. J., Glazovsky, A. F., Macheret, Y. Y., Vasilenko, E. V., Corcuera, M. I., and Cuadrado, M. L.: Ice-volume changes (1936–1990) and structure of Aldegondabreen, Spitsbergen, Ann. Glaciol., 42, 158–162, 2005.

Nuth, C., Kohler, J., Aas, H. F., Brandt, O., and Hagen, J. O.: Glacier geometry and elevation changes on Svalbard (1936–90): a baseline dataset, Ann. Glaciol., 46, 106–116, 2007.

Ottesen, D., Dowdeswell, J. A., Benn, D. I., Kristensen, L., Christiansen, H. H., Christensen, O., Hansen, L., Lebesbye, E., Forwick, M., and Vorren, T. O.: Submarine landforms characteristic of glacier surges in two Spitsbergen fjords, Quat. Sci. Rev., 27, 1583–1599, 2008.

Reinardy, B. T., Leighton, I., and Marx, P. J.: Glacier thermal regime linked to processes of annual moraine formation at Midtdalsbreen, southern Norway, Boreas, 42, 896–911, 2013.

Rootes, C. M.: The nature and use of trimlines for analysing 3-dimensional glacier change in rugged terrain, PhD thesis, unpublished, The University of Sheffield, 2018.

Rootes, C. M. and Clark, C. D.: Glacial trimlines to identify former ice margins and subglacial thermal boundaries: A review and classification scheme for trimline expression, Earth-Sci. Rev., 210, 103355, https://doi.org/10.1016/j.earscirev.2020.103355, 2020.

Sevestre, H.: Surge-type glaciers: controls, processes and distribution, PhD thesis, unpublished, The University Centre in Svalbard & University of Oslo, 2015.

Sevestre, H. and Benn, D. I.: Climatic and geometric controls on the global distribution of surge-type glaciers: implications for a unifying model of surging, J. Glaciol., 61, 646–662, 2015.

Ziaja, W.: Response of the Nordenskiöld Land (Spitsbergen) glaciers Grumantbreen, Håbergbreen and Dryadbreen to the climate warming after the Little Ice Age, Ann. Glaciol., 42, 189–194, 2005.

E&G Quaternary Sci. J., 71, 123–143, 2022
https://doi.org/10.5194/egqsj-71-123-2022

Open Access E&G Quaternary Science Journal

Research article

A pedo-geomorphological view on land use and its potential in the surroundings of the ancient Hispano-Roman city Munigua (Seville, SW Spain)

André Kirchner[1], Nico Herrmann[2], Paul Matras[1], Iris Müller[3], Julia Meister[3], and Thomas G. Schattner[4]

[1]Department of Geography, University of Hildesheim, Universitätsplatz 1, 31141, Hildesheim, Germany
[2]Department of Soil Protection and Soil Survey, State Authority for Mining, Energy and Geology of Lower Saxony (LBEG), Stilleweg 2, 30655, Hanover, Germany
[3]Institute of Geography and Geology, University of Würzburg, Am Hubland, 97074, Würzburg, Germany
[4]Madrid Department, German Archaeological Institute (DAI), C. Serrano 159, 28002, Madrid, Spain

Correspondence: André Kirchner (andre.kirchner@uni-hildesheim.de), Julia Meister (julia.meister@uni-wuerzburg.de)

Relevant dates: Received: 23 March 2022 – Revised: 6 July 2022 – Accepted: 7 July 2022 – Published: 3 August 2022

How to cite: Kirchner, A., Herrmann, N., Matras, P., Müller, I., Meister, J., and Schattner, T. G.: A pedo-geomorphological view on land use and its potential in the surroundings of the ancient Hispano-Roman city Munigua (Seville, SW Spain), E&G Quaternary Sci. J., 71, 123–143, https://doi.org/10.5194/egqsj-71-123-2022, 2022.

Abstract: This study investigates the surroundings of Munigua (municipium Flavium Muniguense), a small Roman town in the ancient province of Hispania Baetica (SW Spain). The city's economy was based primarily on copper and iron mining, which brought financial prosperity to its citizens. Local production of agricultural goods is thought to have been of little importance, as the regional soil conditions do not seem to be suitable for extensive agriculture.

To evaluate the recent soil agro-potential and to find evidence for prehistoric and historic land use in the surroundings of Munigua, we applied a pedo-geomorphological approach based on the physico-chemical analysis of 14 representative soil and sediment exposures. Selected samples were analyzed for bulk chemistry, texture and phytoliths. The chronostratigraphy of the sequences was based on radiocarbon dating of charcoal samples. The site evaluation of the present-day soil agro-potential was carried out according to standard procedures and included evaluation of potential rootability, available water-storage capacity and nutrient budget within the uppermost 1 m.

The results show that moderate to very good soil agro-potential prevails in the granitic and floodplain areas surrounding Munigua. Clearly, recent soil agro-potential in these areas allows the production of basic agricultural goods, and similar limited agricultural use should also have been possible in ancient times. In contrast, weak to very weak present-day soil agro-potential prevails in the metamorphic landscape due to the occurrence of shallow and sandy to stony soils.

In addition, the study provides pedo-geomorphological evidence for prehistoric and historic land use in pre-Roman, Roman and post-Roman times. Catenary soil mapping in the vicinity of a Roman house complex reveals multi-layered colluvial deposits. They document phases of hillslope erosion mainly triggered by human land use between 4063 ± 82 and 3796 ± 76 cal BP, around

2601 ± 115 cal BP, and between 1424 ± 96 and 421 ± 88 cal BP. Moreover, geochemical and phytolith analyses of a Roman hortic Anthrosol indicate the local cultivation of agricultural products that contributed to the food supply of Munigua.

Overall, the evidence of Roman agricultural use in the Munigua area indicates that the city's economy was by no means focused solely on mining. The production of basic agricultural products was also part of Munigua's economic portfolio. Our geoarcheological study thus supports the archeological concept of economically diversified Roman cities in the province of Baetica and in Hispania.

Kurzfassung:

Diese Studie untersucht die Umgebung von Munigua (municipium Flavium Muniguense), einer kleinen römischen Stadt in der antiken Provinz Hispania Baetica (Südwestspanien). Die Wirtschaft der Stadt basierte in erster Linie auf dem Kupfer- und Eisenbergbau, der den Bürgern finanziellen Wohlstand bescherte. Es wird angenommen, dass die lokale Produktion von landwirtschaftlichen Gütern von geringer Bedeutung war, da insbesondere die regionalen Bodenbedingungen für eine extensive Landwirtschaft nicht geeignet zu sein scheinen.

Um das rezente landwirtschaftliche Potenzial der Böden zu bewerten und mögliche Hinweise für prähistorische und historische Landnutzung in der Umgebung von Munigua zu finden, wurden geoarchäologische Untersuchungen durchgeführt, im Zuge derer 14 repräsentative Boden- und Sedimentaufschlüsse bearbeitet wurden. Ausgewählte Proben wurden auf ihre physikalisch-chemischen Eigenschaften sowie Phytholiten untersucht. Die chronostratigraphische Einordnung erfolgte auf der Grundlage von Radiokohlenstoffdatierungen. Die Standortbewertung des heutigen landwirtschaftlichen Potenzials der Böden wurde nach Standardverfahren durchgeführt und umfasste die Bewertung der potenziellen Durchwurzelbarkeit, der verfügbaren Wasserspeicherkapazität und des Nährstoffhaushalts.

Die Ergebnisse zum landwirtschaftlichen Potenzial der Böden zeigen, dass in Granit- und Auengebieten rund um Munigua ein mäßiges bis sehr gutes Ertragspotenzial vorherrscht, dass die begrenzte Produktion von landwirtschaftlichen Erzeugnissen erlauben würde. Eine vergleichbar begrenzte landwirtschaftliche Nutzung dürfte auch in der Antike möglich gewesen sein. Die Böden in der umgebenden Metamorphitlandschaft besitzen im Gegensatz dazu ein nur schwaches bis sehr schwaches Agrarpotenzial und Hinweise auf eine antike Agrarnutzung sind nicht vorhanden. Darüber hinaus liefert die Studie weitere Hinweise auf prähistorische und historische Landnutzung in vorrömischer, römischer und nachrömischer Zeit. So zeigt eine Catena, die in der Nähe eines römischen Hauskomplexes angelegt wurde, eine reliefabhängige Bodenabfolge mit mehrgliedrigen Hangkolluvien, die anthropogene Bodenerosion zwischen 4063 ± 82 und 3796 ± 76 cal BP, um 2601 ± 115 cal BP, und zwischen 1424 ± 96 und 421 ± 88 cal BP dokumentieren. Darüber hinaus weisen geochemische und Phytolithen-Analysen eines untersuchten römischen Gartenbodens (Hortic Anthrosol) auf den lokalen Anbau landwirtschaftlicher Produkte hin, die zur Nahrungsmittelversorgung von Munigua beitrugen.

Die im Rahmen dieser Untersuchung erzielten Belege für eine landwirtschaftliche Nutzung im Gebiet von Munigua zeigen, dass die Wirtschaft der Stadt keineswegs nur auf den Bergbau ausgerichtet war. Auch die Produktion von landwirtschaftlichen Grunderzeugnissen gehörte zum wirtschaftlichen Portfolio Muniguas. Die Hypothese, dass die lokale Produktion von landwirtschaftlichen Gütern aufgrund eines unzureichenden Ertragspotentials der Böden unbedeutend war, kann somit nicht bestätigt werden. Vielmehr unterstützt diese Studie das archäologische Konzept einer wirtschaftlich diversifizierten römischen Stadt.

1 Introduction

During the imperial period, the economy of small Roman cities in the Roman Empire and particularly in the Roman province of Baetica is assumed to have been very diverse and, depending on the city, typically specialized around a certain economic good (Bowman and Wilson, 2009, 2011). In addition to archeological evidence, abundant historical sources provide a vivid and rich picture of ancient agriculture, fishing and mineral resources, basic foodstuffs, and luxury products (e.g., Blázquez Martinez, 1967; Remesal Rodríguez, 2020).

This study was carried out in the surroundings of the Hispano-Roman municipium Flavium Muniguense, in modern times known as Castillo de Mulva or Munigua (Schattner, 2003), a small urban center in the ancient province of Hispania Baetica. From a historiographic perspective, Munigua is a key site for understanding Roman urbanization on the Iberian Peninsula (Schattner, 2005) since it is one of the few places in Spain that has been systematically excavated for the past 65 years. The local economy was particularly based on copper and iron mining in the surroundings of the town, and Munigua was the largest iron-producer in the Sierra Morena in the 1st and 2nd centuries CE (Schattner, 2019b). Income from the mining activities provided financial prosperity for the citizens and an architectural climax, which culminated in the construction of the impressive terrace sanctuary situated on the highest point in the west of the city (Schattner, 2019a, 2021). In addition to the mining industry, olive oil presses and an oil cellar (*cella olearia*) were located inside the city, indicating the processing of agricultural by-products within the urban area (Schattner, 2003; Peña Cervantes, 2010; Teichner and Peña Cervantes, 2012). Furthermore, wine production and quarrying contributed to economic output even though they were much less significant than the mining operations (Hanel, 1989; Schattner, 2019b).

Current opinion on the food supply strategy of Munigua is based on the assumption that food was obtained in particular from the fertile lower Guadalquivir valley, which was and still is the agricultural center of the region, located just 10 km south of Munigua. Additionally, fish bones and oyster shells indicate connections to the sea (Boessneck and von den Driesch, 1980). In contrast, the local production of agricultural goods is thought to have been of minor relevance (Schattner, 2019b). In this context, it has been suggested that regional soil conditions are currently unsuitable for extensive agriculture and therefore seem to suggest that an ancient agrarian use of the region was also unlikely (Schattner, 2019b). However, so far there has been a lack of evidence-based studies on the agricultural suitability and potential agricultural use of the surroundings of Munigua, and it is only recently that an archeological study has challenged the idea of food imports having been dominant (Krug, 2018). Based on the investigation of small finds, the study stated that tools such as shovels, spades, sickles and billhooks suggest the existence of gardens, meadows for smaller animals and trees which had to be tended and harvested in the wider surroundings of the town (Krug, 2018).

In this paper, we present initial findings from a geoarcheological pilot project and provide new insights into the regional land use history of the Munigua site. Firstly, physicochemical analysis of 14 representative soil and sediment exposures provides a first evidence-based evaluation of present-day agro-potential. Secondly, we present site-specific evidence of prehistoric and historic land use in the surroundings of the city and thus improve understanding of its food supply strategy. In this way we, thirdly, aim to contribute a pedogeomorphological view to the archeological debate on the diversification of the urban economy in the Roman province of Baetica (e.g., Bowman and Wilson 2009, 2011), a topic that has not yet been developed for this region of the Roman Empire.

2 Study area

2.1 Environmental setting

Munigua is located in the southern part of the Sierra Morena about 50 km northeast of the Andalusian capital Seville (Fig. 1a). To the south the region is bordered by the wide valley of the lower Guadalquivir River, which drains large parts of Andalusia and today flows into the Atlantic Ocean southwest of Seville. The region experiences a dry, subhumid, semi-oceanic Mediterranean climate, with arid summers and winter rains due to low-pressure systems from the Atlantic Ocean (Zazo et al., 2008). Average rainfall is around 580 mm yr^{-1}, and the annual average temperature is 18.0 °C (Gómez-Zotano et al., 2015), leading to species-rich Mediterranean vegetation cover with evergreen woody plants such as *Quercus faginea*, *Quercus suber, Quercus rotundifolia, Olea europaea L.* and *Chamaerops humilis* (Frey and Lösch, 2010). In steeper areas, the taller trees are replaced by maquis shrubland, mainly composed of hardwood bushes (e.g., *Cistus* spp.). However, as in the entire Sierra Morena, vegetation has been greatly altered by centuries of agrosilvopastoral farming, in Spanish known as *dehesa* farming (Joffre et al., 1988), resulting in scattered forest cover accompanied by grassland (Fig. 1c and d).

Geologically, the region belongs to the Ossa-Morena Zone (OMZ), a geotectonic unit of the Iberian Massif (Strauss and Madel, 1974; Tornos et al., 2004; Ribeiro et al., 2010). Granite dominates the petrography in the region (Sanz et al., 1973; Schattner et al., 2005). Geomorphologically, the granite area is mainly characterized by flat to slightly undulating landforms with moderately steep slopes, small depressions and ridges (Fig. 1b). They frequently show linear erosion channels (gullies) and are mostly located close to animal pathways. Steep gully flanks and exposed roots of the existing vegetation crossing the gullies indicate modern gully formation (Fig. 1d).

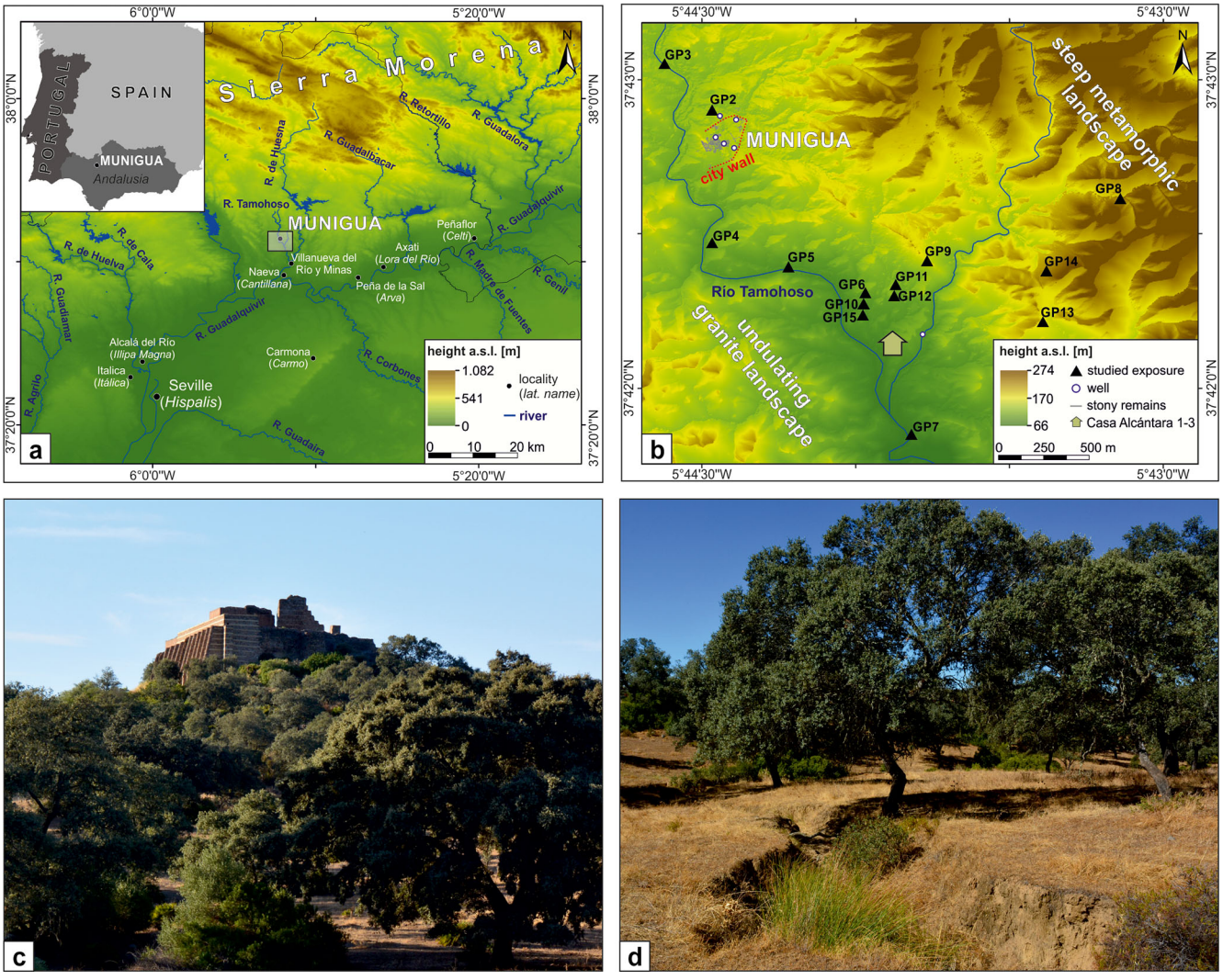

Figure 1. **(a)** Location of Munigua (grey box) in modern SW Spain. **(b)** Investigated soil and sediment exposures within the surroundings of Munigua. GP8, GP13 and GP14 are located in a metamorphic landscape southeast of the city. GP2, GP4, GP6, GP9, GP10, GP11, GP12 and GP15 are in granite areas, and GP3, GP5 and GP7 are within the floodplain of the Tamohoso River. **(c)** South view of Munigua's terrace sanctuary surrounded by scattered forests and grassland. **(d)** Undulated granite landscape with loose holm oak (*Quercus rotundifolia*) and grass understory, typical for the Munigua region. The surface is dissected by a gully about 1.3 m in depth, indicating modern linear soil erosion processes.

The granite landscape is surrounded by mountains consisting of metamorphic Paleozoic rocks, mainly shale, metagreywacke and quartzite (Sanz et al., 1973). This landscape is located in the east of the city and is characterized by much steeper relief, exceeding the altitude of the granite landscape by up to 100 m (Fig. 1b). The main settlement of Munigua with its residential houses and monumental buildings is situated on a morphologically very resistant rhyolite dike (Sanz et al., 1973; Schattner et al., 2005), forming a gently inclined hill that is up to 30 m higher than the adjacent granite landscape (Fig. 1c). Along the Tamohoso River, flowing through the west of Munigua and draining into the Guadalquivir River via the Huesna River (Fig. 1a), a flat alluvial plain has developed in wider valley sections, covering the denudated granite basement (Sanz et al., 1973).

Regional soil investigations in the western sector of the Sierra Morena show poorly developed Regosols, Leptosols and Cambisols. There are frequent erosional features which are often associated with increases in land use over the past two millennia. In consequence, more advanced soil development, leading to the formation of Luvisols or Acrisols, is restricted to small areas (e.g., Paneque and Bellinfante, 1964; Nuñez and Recio, 2002; Recio et al., 2002).

2.2 Archeological background

Munigua is located on the edge of the Iberian Pyrite Belt (IPB), one of the largest and most important volcanogenic polymetallic sulfide districts worldwide, which has been exploited since late prehistoric times (Nocete et al., 2011). The mining importance of Munigua is based in particular on the copper- and iron-bearing ores (e.g., pyrite, chalcopyrite) found near the town (Schattner et al., 2005; Schattner, 2019a).

The oldest archeological finds indicate the presence of humans since the Epipaleolithic period. Especially for the Early (approx. 1750–1550 BCE) and Middle Bronze Age (approx. 1550–1150 BCE), several fortified settlements have been identified and linked to copper mining and the processing and export of mining products to the Guadalquivir valley, a region with limited mineral resources that was highly dependent on continuous supplies from the Sierra Morena mines (Schattner, 2019b). In the 4th century BCE (approx. 360–330 BCE), a small pre-Roman (Turdetan) settlement was founded on the top of the aforementioned rhyolite dike. Traces of urban structure are noticeable from the first half of the 1st century BCE, for instance documented by the construction of thermae (Chic García, 1997; Gutiérrez-Rodríguez et al., 2019; Schattner, 2019b). In 74 CE the settlement was awarded the rank of a municipium after Emperor Vespasian's edict and experienced its heyday. This is revealed by comprehensive urban development and the construction of imposing religious and public buildings like, for example, the terrace sanctuary and the forum. Thus, Munigua possessed a large variety of the typical structural features of a Roman city, although the total size of the settlement was only about 3.8 ha (Ullrich et al., 2007; Schattner, 2019b). Some villas and smaller settlements were established in the surroundings of the city in this period, for example the Roman house complex Casa de Alcántara 1, 2 and 3 located about 1 km southeast of the city (Fig. 1b; Meyer et al., 2007; Schattner, 2019b). At this time, Munigua was part of a dense urban network consisting of some 195 towns and nucleated settlements established in central and western Baetica between approx. 500 BCE and 200 CE (Keay and Earl, 2011).

In the late and post-Roman period (3rd century CE), urban development reached an inflection point expressed by massive depopulation and drastic changes in urban structure. This is thought to be related to seismic activities that caused structural damage to the city, and similar occurrences are also recorded in other Roman cities of the Baetica province (e.g., Rodríguez-Pascua et al., 2011; Giner-Robles et al., 2016; Ruiz-Bueno, 2017). Smaller population groups retreated to the hills in the surroundings where there are traces of a human presence until the end of the 4th century CE (Grünhagen, 1959). The existence of a settlement is documented for Munigua until at least the 7th century CE, even though it is uncertain if ore mining and smelting were still practiced at that time (Eger, 2016). An Arab coin, typical Islamic vessels, oil lamps made of terracotta and burials of Muslim individuals indicate an Islamic settlement on the hill of Munigua from approximately the 8th to the 12th century CE (Teichner, 1998; Eger, 2016). Probably due to its exposed location, Munigua was not reoccupied until its rediscovery in the 16th to 17th century CE (Schattner, 2005). With the industrial expansion of carboniferous coal extraction in the nearby city of Villanueva del Río y Minas (Fig. 1a), regional population density and land use intensity (especially grazing) massively increased during the 19th and 20th centuries CE (Tomás García, 1991).

3 Methods

3.1 Field methods

A total of 14 representative exposures were selected for field investigations: three sites with metamorphic lithology (GP8, GP13 and GP14), eight sites in granite areas (GP2, GP4, GP6, GP9, GP10, GP11, GP12 and GP15) and three floodplain sites (GP3, GP5 and GP7; Fig. 1b). Taking the local relief conditions into account, the soil profiles were arranged in a catenary manner along hillslopes (Semmel, 1977; Evans and Hartemink, 2014; Borden et al., 2020).

Macroscale features were subsequently described by following the German soil mapping instructions (Ad-hoc-AG Boden, 2005). Identified soil horizons were designated according to Jahn et al. (2006) and Zádorová and Penížek (2018). Soil classifications were conducted according to the IUSS Working Group WRB (2015). An exception was made only for colluvium or colluvial deposits, which were used as geoarchives documenting human-induced soil erosion (Dotterweich, 2008; Kittel, 2014), following the definition by Leopold and Völkel (2007, p. 134). Accordingly, colluvium and colluvial deposits are defined as "sediments deposited due to anthropogenic-induced soil erosion, caused by settling, clearing, mining, grazing, and/or farming." According to Zádorová and Penížek (2018) the soil horizon symbol "M" (*migrare* [lat.]; Ad-hoc-AG Boden, 2005) was added, and multiple layers of colluvial deposits within a profile were separated by using suffix numbers, in which the number 1 was always given to the uppermost colluvium. If the overall thickness of colluvial deposits exceeded 50 cm, the soil type was classified as Colluvisol. Otherwise, the term "colluvic" was used as a prefixed qualifier.

In contrast, slope sediments that were mainly mobilized and relocated by natural erosion were classified as slope deposits. Field diagnostic properties have been used to separate colluvial and slope deposits. Slope deposits dominated by properties from the geological subsurface show a denser packing and do not contain anthropogenic remains. In contrast colluvial deposits frequently show a comparable loose packing and anthropogenic remains like pottery shards, slag fragments and bricks.

3.2 Laboratory methods

A total of 57 samples were taken from 10 of the 14 profiles studied in the field and were subjected to further laboratory treatment (Table S1 in the Supplement). Prior to physico-chemical analyses, samples were air dried and the fine-earth fraction (≤ 2.0 mm) was sieved. Grain size analyses utilized a combination of the Köhn pipette method (silt and clay fractions) and wet sieving (sand fractions) (DIN ISO 11277, 2002). Samples were pre-treated with 0.4 M sodium pyrophosphate ($Na_4P_2O_7$) overnight and afterwards shaken for 6 h. When soil organic matter (SOM) exceeded 2.0 %, the samples were additionally pre-treated with 17.5 % hydrogen peroxide (H_2O_2). The sand fraction was divided into coarse (2000–630 µm), medium (630–200 µm) and fine (200–63 µm) sand by wet sieving using the vibratory sieve shaker AS 200 (Retsch). Coarse silt (63–20 µm), medium silt (20–6.3 µm), fine silt (6.3–2.0 µm) and clay (< 2.0 µm) were identified by the Köhn pipette method using the SEDIMAT 4–12 (UGT).

Total carbon (C_t) and total nitrogen (N_t) were measured on milled samples using the CN analyzer vario EL cube (Elementar). Due to the absence of inorganic carbon, as proven in pretests using hydrochloric acid (10 %), the C_t is equal to the amount of total organic carbon (TOC). TOC values were multiplied by 1.724 (Amelung et al., 2018) in order to obtain contents of soil organic matter (SOM). C / N ratio was calculated by dividing TOC by N_t (Blume et al., 2011).

The plant-available macronutrients magnesium (Mg), calcium (Ca), sodium (Na) and potassium (K) were extracted with 1 M NH_4NO_3 and quantified by an atomic absorption spectrophotometer (Perkin Elmer PinAAcle 900T). Additionally, K_2O and P_2O_5 were measured according to the calcium–acetate–lactate method (Schüller, 1969) using a Spectronic C301 spectrophotometer (Milton Roy). The pH value was measured in a 1 : 2.5 suspension in 0.01 M $CaCl_2$ (Jahn et al., 2006).

The content of total phosphorus (P_t), used in archeology as an important indicator for human activity in agricultural and pre-agricultural societies (e.g., Holliday and Gartner, 2007; Weihrauch, 2018), was determined by colorimetry with the spectrophotometer C21 (Milton Roy) following ignition and then acid extraction based on Bleck (1965).

The soil agro-potential of the site was evaluated according to standard procedures (Blume et al., 2011; Amelung et al., 2018), including assessment of potential rootability, the available water-storage capacity and the nutrient budget within the uppermost 1 m. All evaluations consider the total particle-size fractions (coarse and fine-earth fractions) and further take account of the field-estimated bulk density (Ad-hoc-AG Boden, 2005). For stony soils and sediments, deductions have to be made from the available soil volume, which influences the nutrient budget and the water-storage capacity accordingly (Blume et al., 2011). The evaluation was based on a five-step classification including the following classes: (1) very favorable/very good, (2) favorable/good, (3) moderate, (4) unfavorable/weak and (5) very unfavorable/very weak. Blume et al. (2011) suggested the following values for the classification of potential rootability: (1) > 120 cm, (2) 70 to 120 cm, (3) 30 to < 70 cm, (4) 15 to < 30 cm and (5) < 15 cm. The available water-storage capacity was assessed according to the following values: (1) $> 200\,L\,m^{-2}$, (2) 140 to $200\,L\,m^{-2}$, (3) 90 to $< 140\,L\,m^{-2}$, (4) 50 to $< 90\,L\,m^{-2}$ and (5) $< 50\,L\,m^{-2}$. The classification of the nutrient budget was mainly derived from the contents of macronutrients (Mg, Ca, Na and K), grain size distribution, SOM content and pH values, which primarily determine the base saturation and effective cation exchange capacity (Ad-hoc-AG Boden, 2005; Blume et al., 2011). Possible deficiencies in nitrogen and calcium-lactate-soluble phosphorus (P_2O_5) and potassium (K_2O) contents were additionally checked and included in the assessment of the nutrient budget. For GP5, GP9, GP10 and GP14, the evaluation is based on field assessments and conclusions drawn by analogy, considering comparable nearby profiles from this study.

Phytolith extraction followed the procedures outlined by Albert et al. (1999). Approximately 1 g of air-dried sample (< 2 mm) was treated with 3 N HCl, 3 N HNO_3 and H_2O_2 to remove carbonates, phosphates and organic material. The mineral components of the samples were separated according to their densities using $\sim 2.4\,g\,mL^{-1}$ sodium polytungstate solution [$Na_6(H_2W_{12}O_{40})H_2O$]. Slides were prepared by weighing out about 1 mg of sample onto a microscope slide and mounting with Entellan new (Merck). Counting was performed using a KERN OBE-114 microscope at 400× magnification. A total of 200 phytoliths were identified and counted in each sample wherever possible. Unidentifiable phytoliths were counted and recorded as weathered morphotypes. Images of selected phytoliths were recorded using a KERN ODC 825 microscope camera. The numbers of phytoliths per gram of sample were estimated by relating the phytolith amounts and weights of the processed sample material to the initial sample weights. The morphological identification of phytoliths was based on standard literature (Twiss et al., 1969; Brown, 1984; Mulholland and Rapp, 1992; Piperno, 2006), as well as on modern plant reference collections from the Mediterranean area (Albert, 2000; Albert and Weiner, 2001; Tsartsidou et al., 2007; Portillo et al., 2014; Meister et al., 2017). The International Code for Phytolith Nomenclature was followed where possible (Madella et al., 2005; Neumann et al., 2019).

Radiocarbon dating was carried out on 17 charcoal samples at the Curt-Engelhorn-Centre of Archaeometry (MAMS) and at Beta Analytic (BETA) using the accelerator mass spectrometer (AMS) technique (e.g., Hajdas, 2008). Charcoal samples were pretreated using the acid–alkali–acid method to remove contamination by carbonates and humic acids (de Vries and Barendsen, 1954). Conventional ^{14}C ages (BP) were calibrated using the IntCal 13 calibration set (Reimer et al., 2013).

4 Results

4.1 Granite landscape

4.1.1 Casa de Alcántara house complex

A granite area southeast of urban Munigua was chosen for a detailed survey (Fig. 1b) since a Roman rural house complex known as Casa de Alcántara 1–3 and a nearby ancient well document the presence of Roman settlers who may have worked as farmers in ancient times (Meyer et al., 2007; Schattner, 2019b). The schematic catena (Fig. 2) shows shallow Leptosols (GP11) and moderately deep Cambisols (GP15) in upper slope positions and flatter ridge areas. Soil erosion has led to a shallowing of these profiles and frequently to the deposition of a thin colluvial cover (Fig. 2). Here, potential rootability, water-storage capacity and nutrient budget is very weak to weak (Fig. 3, Table S1).

At the transition from upper to middle slopes Cambisols (GP9) and Colluvisols (GP12, GP6, GP10 and GP4) were mapped. They are deeper, favoring potential rootability and improving water-storage capacity (Fig. 3). Essential nutrients (Mg, Ca, Na, K, P_2O_5 and K_2O) are available (Table S1) although with relatively low values of P_2O_5 (median = 5.8 mg kg^{-1}, SD = 10.1, $n = 18$). The pH values range from 4.5 to 6.1 (median = 5.5, SD = 0.5, $n = 18$) and can accordingly be predominantly classified as slightly acidic (Table S1). The SOM (median = 0.5 %, SD = 1.4, $n = 18$) and N_t contents (median = 0.04 %, SD = 0.06, $n = 18$) decrease with depth and are generally low. In sum the nutrient budget of Cambisols and Colluvisols in the surroundings of the Roman house complex Casa de Alcántara 1–3 is moderate (Fig. 3).

For the temporal reconstruction of soil erosion processes around the Casa de Alcántara house complex, seven charcoal samples from three colluvial sequences (GP4, GP10 and GP12) were ^{14}C-dated (Fig. 2, Table 1). The results indicate prehistoric soil erosion phases between around 4063 ± 82 and 3796 ± 76 cal BP (Copper Age to Early Bronze Age), as well as around 2601 ± 115 cal BP (Early Iron Age). Four additional ^{14}C datings from GP10 and GP4 provided ages of 1424 ± 96, 1094 ± 155, 606 ± 51 and 421 ± 88 cal BP.

4.1.2 Profile GP2

Profile GP2 is located less than 100 m north of the fortified urban area of the Muniguan granite landscape (Fig. 1b) in the immediate surroundings of a small, temporary stream and an ancient well (Fig. 4a).

The profile was excavated down to granite-derived slope sediments (3BC horizon) present below approximately 64 cm. The uppermost 23 cm are formed by loosely deposited yellow-brown fluvial sediments (Fig. 4b). Missing pedogenic features and an oral report of a recent flood of the above-mentioned adjacent stream suggest that the sediments were deposited relatively recently. The texture is sandy (sand contents between 61 % and 93 %, Fig. 4), and the fluvial deposits mainly show moderate gravel contents (Table S1). Sharply defined, finer-grained substrate follows below 23 cm. This can be further subdivided into an upper (2MAhub, 23–46 cm) and a lower (2Mub, 46–64 cm) horizon by grain size and minor differences in color (10YR 3/3 vs. 2.5YR 3/3). Both horizons contain numerous pottery shards, slag fragments and bricks, all of which can be assigned to the Roman inventory and thus allow these horizons to be archeologically dated to the Roman period (terminus post quem). A ^{14}C-dated charcoal taken at a depth of 56 cm revealed a Roman age of 2147 ± 147 cal BP (Fig. 4b, Table 1). A second piece of charcoal from a depth of 38 cm could not be dated due to its young age (after 1950). The lowermost profile section (64–70 cm) is formed by yellow-brown slope deposits (3BC horizon) showing a loamy texture and does not contain archeological remains.

Measured pH values are moderately acidic and vary slightly from 5.8 to 5.4 (Fig. 4, Table S1). SOM values are between 0.4 % and 2.3 %, and, interestingly, increased SOM content (1.7 %) is found in the lower section of the Roman horizon (2Mub horizon; 46–64 cm). C / N ratios vary between 10.75 (MAhb2 horizon) and 12.63 (2Mub horizon). Calcium-lactate-soluble phosphorus (P_2O_5) and total phosphorus (P_t) show a first maximum of 108 mg kg^{-1} and 1.895 mg kg^{-1}, respectively, in the uppermost sample (MAh horizon; 0–7 cm), decreasing downwards. However, this trend reverses, and, especially within the lower section of the Roman horizon (2Mub horizon; 46–64 cm), a second maximum is noticeable (123 and 2786 mg kg^{-1}). The same holds true for the macro-nutrient elements Mg, Ca, Na, K and K_2O, which are generally increased in the lower part of the Roman horizon and the lowermost slope deposits (Fig. 4, Table S1). Based on diagnostic criteria (color, determine base saturation, SOM, P_2O_5, thickness) the Roman horizon was classified as a hortic horizon (IUSS Working Group WRB, 2015). In terms of soil agro-potential this site is categorized as good to moderate (Fig. 3).

The amounts of phytoliths in the samples vary considerably, ranging from 6483 phytoliths per gram of sediment to 323 253 phytoliths per gram of sediment, while the highest concentrations were reached in the Roman hortic horizons (Fig. 6a; Table S2.2). A total of 33 different phytolith morphotypes were identified in the six samples studied (Fig. 5, Table S2.1). Overall, the samples are similar in their morphotype assemblages (Fig. 6b, Table S2.2). While about 26.8 % (SD = 3.8, $n = 6$) of the phytoliths were not morphologically identifiable, grass phytoliths, occurring at an average rate of 50.8 % (SD = 4.6, $n = 6$), were the most common group. The amounts of dicotyledonous leaf, wood and bark phytoliths are relatively low, with an average value of 17.1 % (SD = 4.8, $n = 6$). *Parallelepipedal blocky* phytoliths, one of the most common wood/bark morphotypes, for instance, were observed at an average concentration of 10.2 % (SD = 5.9, $n = 6$). *Spheroid echinate* phytoliths, commonly

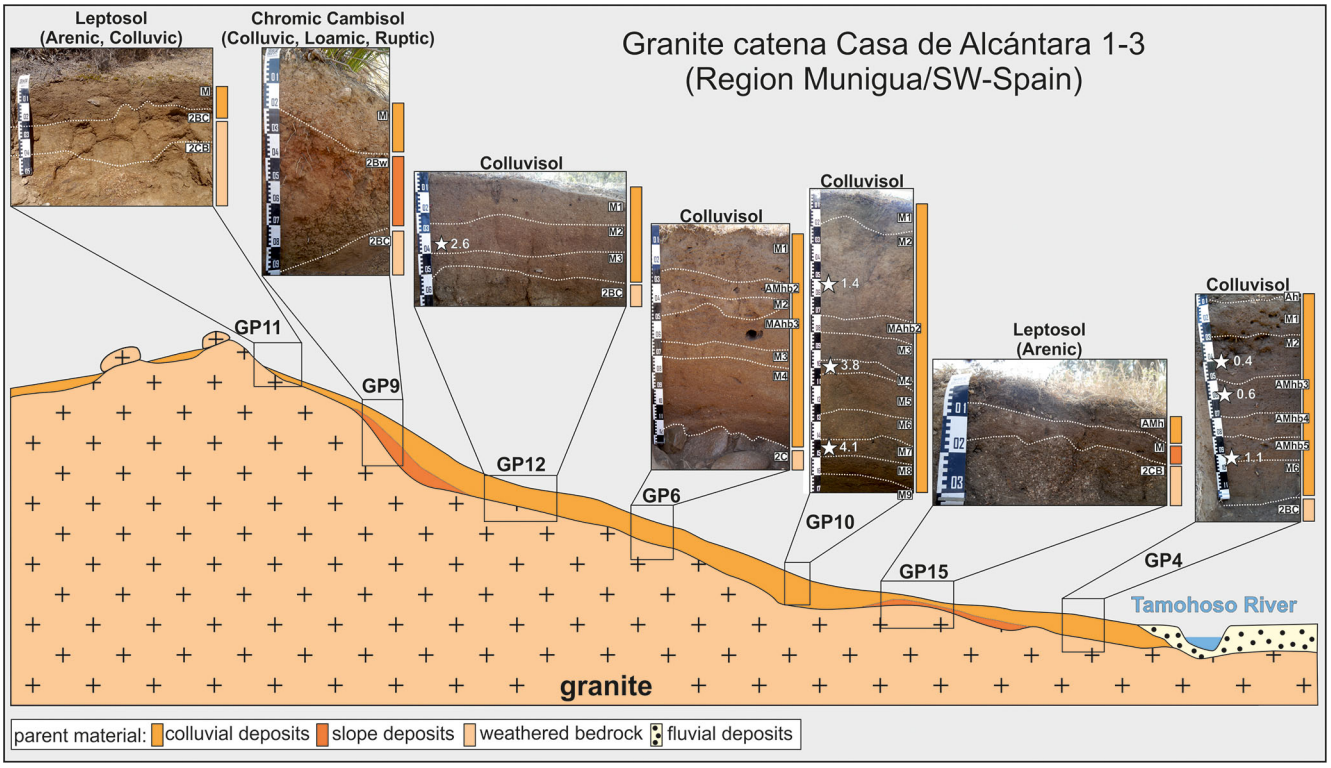

Figure 2. Schematic soil catena for a granite landscape in the surroundings of the Roman house complex Casa de Alcántara 1–3. Soil horizon designations are shown in white boxes. Physico-chemical results are summarized in Table S1. White stars within the photographs indicate the positions of ^{14}C-dated charcoal samples (the calibrated ages are given in ka). The shown catena is exaggerated for illustration purposes.

Table 1. Results of radiocarbon dating in the Munigua region.

Site	Depth (cm)	Facies	Lab. no.	Dated material	^{14}C age BP	Calibrated ^{14}C age BP (2σ range)	δ^{13}C (‰)
GP2	38	hortic	MAMS 43603	charcoal	modern	modern	−31.2
GP2	56	hortic	BETA 551526	charcoal	2120 ± 30	2147 ± 147	−26.0
GP3	44	fluvic	MAMS 43604	charcoal	165 ± 21	196 ± 89	−25.7
GP3	84	fluvic	MAMS 43605	charcoal	121 ± 20	141 ± 128	−19.0
GP3	112	fluvic	MAMS 43606	charcoal	126 ± 21	140 ± 130	−22.8
GP4	40	colluvic	MAMS 43607	charcoal	396 ± 21	421 ± 88	−28.2
GP4	58	colluvic	MAMS 43608	charcoal	622 ± 19	606 ± 51	−25.1
GP4	98	colluvic	MAMS 43609	charcoal	1175 ± 22	1094 ± 84	−32.4
GP7	50	fluvic	MAMS 43610	charcoal	163 ± 18	159 ± 159	−19.4
GP7	115	fluvic	MAMS 43611	charcoal	243 ± 20	157 ± 156	−29.3
GP7	140	fluvic	MAMS 43612	charcoal	172 ± 18	155 ± 155	−24.6
GP7	169	fluvic	MAMS 43613	charcoal	264 ± 20	290 ± 134	−29.6
GP7	190	fluvic	MAMS 43614	charcoal	206 ± 18	157 ± 157	−18.8
GP10	53	colluvic	BETA 562782	charcoal	1510 ± 30	1424 ± 96	−24.3
GP10	100	colluvic	MAMS 43615	charcoal	3525 ± 21	3796 ± 76	−26.8
GP10	145	colluvic	MAMS 43616	charcoal	3710 ± 22	4063 ± 82	−25.8
GP12	39	colluvic	MAMS 43617	charcoal	2481 ± 20	2601 ± 115	−26.4

Geomorphological unit	Geomorphic position	Site	Site evaluation		
			available water-storage capacity	nutrient budget	potential rootability
Granite landscape	Upper slope	GP11	--	-	-
		GP9	+	o	+
	Middle slope	GP12	-	o	o
		GP6	+	o	++
	Lower slope	GP15	--	-	--
		GP10	+	o	++
		GP4	+	o	++
	Plain	GP2	+	o	+
Metamorphic landscape	Upper slope	GP13	--	--	--
	Middle slope	GP14	-	-	-
	Lower slope	GP8	-	-	o
Floodplain	Plain	GP3	++	o	++
		GP5	o	-	+
		GP7	++	o	++

very good	good	moderate	weak	very weak
++	+	o	-	--
very favorable	favorable	moderate	unfavorable	very unfavorable

Figure 3. Site evaluation of investigated soil and sediment exposures in the Munigua area, subdivided according to the studied geological and geomorphological units.

associated with palms (Arecaceae), reached an average concentration of 5.3 % (SD = 4.2, $n = 6$).

The short cell morphologies of the grass phytoliths reveal them to belong mostly to the C3 Pooid subfamily, with *rondel and trapezoid short cells* commonly produced in the leaves, stems and inflorescences of Pooids. Concentrations between 59.1 % in the uppermost sample and 32.7 % in the upper part of the Roman hortic horizon were found (mean = 45.6 %, SD = 9.3, $n = 6$; Fig. 6c; Table S2.2). The proportion of inflorescence phytoliths varies slightly around an average concentration of 15.2 % (SD = 6.2, $n = 6$). The concentrations of phytoliths from grass stems and leaves are higher in the lower profile section (23–70 cm), reaching a maximum of 50.8 % in the upper part of the Roman hortic horizon (mean = 39.2 %, SD = 10.1, $n = 6$). Due to the absence of multicellular phytoliths in the samples, however, it was not possible to identify the type of grasses.

4.2 Metamorphic landscape

The pedo-morphological conditions were also investigated for three sites (GP8, GP14 and GP13) within the metamorphic landscape, located in the southeast of Munigua (Fig. 1b). Here, the lithology is formed by quartzitic metagreywacke, and the soils were classified as Leptosols or Cambisols (Fig. 7). All observed soils in this metamorphic landscape unit are conspicuously shallow and stony (Table S1). Potential rootability, available water-storage capacity and nutrient budget are weak to very weak (Fig. 3). No geomorphological or pedological evidence of prehistoric or historic land use (e.g., colluvial deposits) is preserved in the observed metamorphic landscape so far.

4.3 Tamohoso River floodplain

The investigated fluvial sequence GP3 is located about 500 m upstream of Munigua's urban infrastructure, whereas GP7 is located about 600 m downstream of the Casa de Alcántara

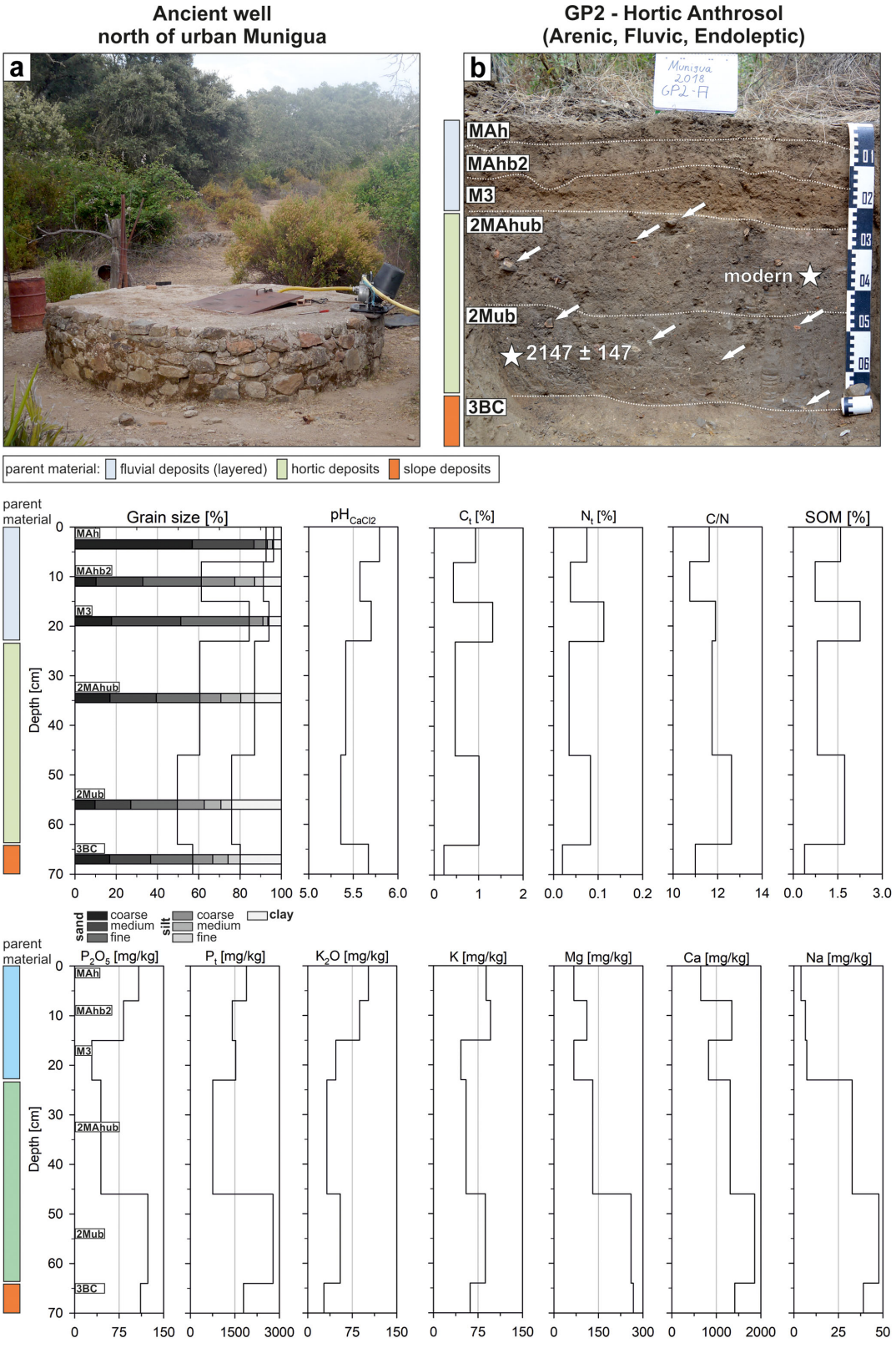

Figure 4. **(a)** Ancient well located outside of Munigua's city wall (Fig. 1b). **(b)** Excavated hortic Anthrosol (arenic, fluvic, endoleptic). Identified parent material is marked on the left of the profile photo. Soil horizon designations are shown in white boxes. White arrows indicate some larger Roman artifacts (e.g., ceramics, brick). Sampling positions and calibrated ^{14}C ages (cal BP) are marked with white stars. Lower section: laboratory results for the hortic Anthrosol (arenic, fluvic, endoleptic).

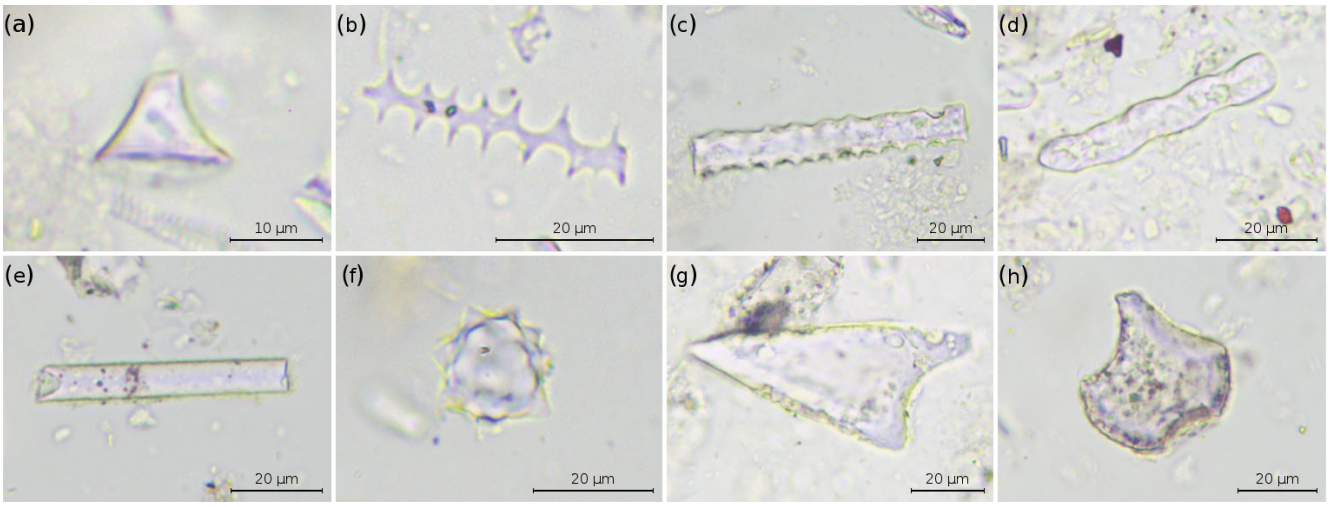

Figure 5. Photomicrographs of selected phytolith morphotypes identified in the GP2 samples. The photographs were taken at 400× magnification. **(a)** Short cell rondel; **(b)** elongate dendritic; **(c)** elongate dentate; **(d)** elongate wavy; **(e)** elongate entire; **(f)** spheroid echinate; **(g)** prickle; **(h)** bulliform.

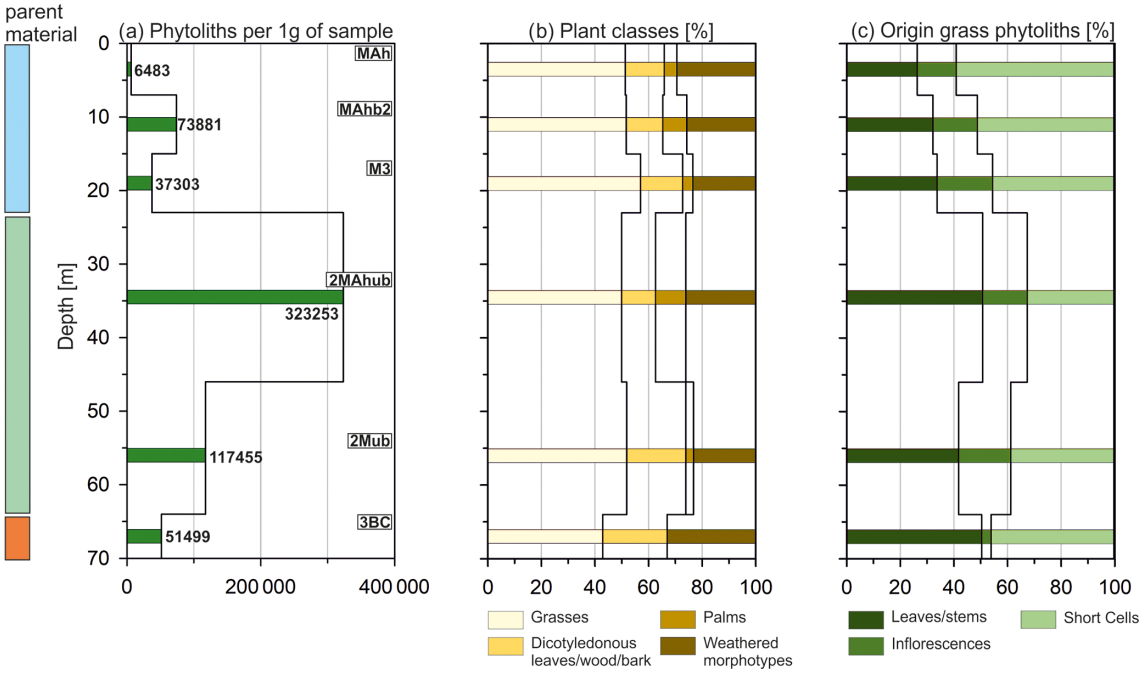

Figure 6. Results of phytolith analyses conducted at site GP2. Identified parent material is marked to the left of the graph according to Fig. 4b. Soil horizon designations are shown in white boxes. **(a)** Phytolith concentrations, **(b)** relative abundances of phytoliths from different plant classes and **(c)** anatomical origin of grass phytoliths.

house complex (Fig. 1b). GP5 is situated between these two sites.

GP3 was excavated to a depth of 145 cm below the surface (Fig. 8). The base of the profile shows coarse-clastic riverbed deposits, classified as moderately rounded gravels or moderately rounded blocks. Upwards, this is followed by alternately deposited, predominantly cross-bedded sands (74 %–84 % sand), which are occasionally interstratified by finer-grained and in particular silty deposits (Figs. 8 and 9). The profile contains charcoal pieces of different sizes in almost all sections, which could indicate the former presence of activities involving fire in the catchment area.

GP7 was excavated to a depth of 250 cm (Fig. 8). Below 220 cm, weakly weathered granite is present and forms

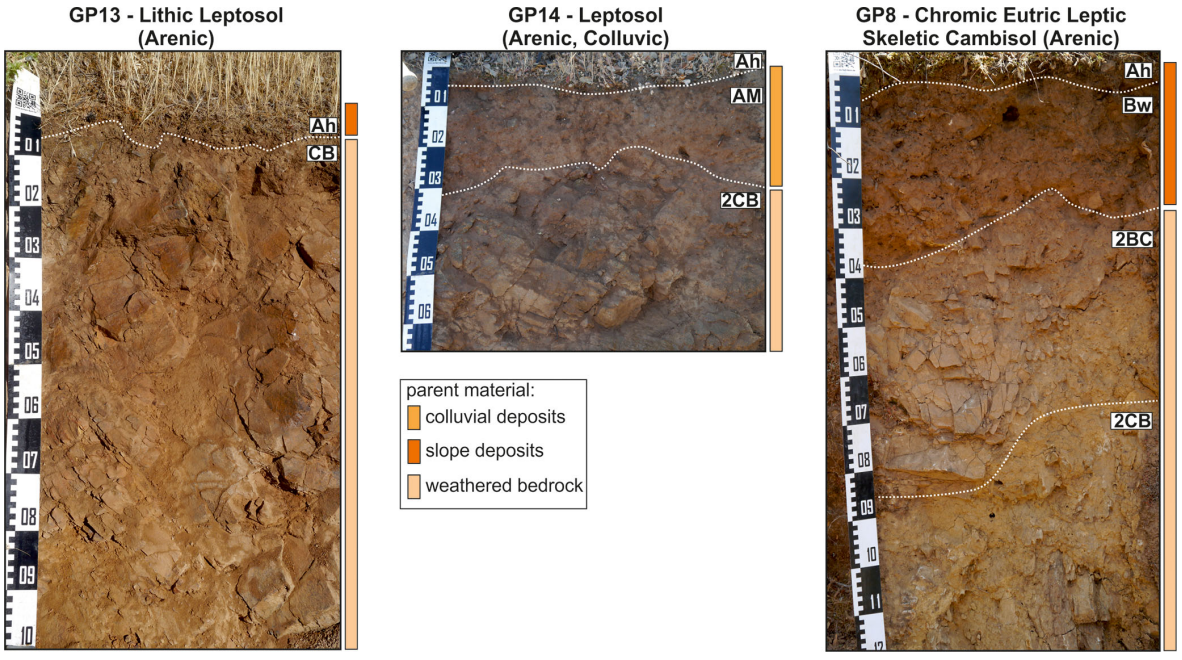

Figure 7. Investigated soil sequences in a metamorphic landscape southeast of Munigua. Soil horizon designations are shown in white boxes. Physico-chemical laboratory results are summarized in Table S1.

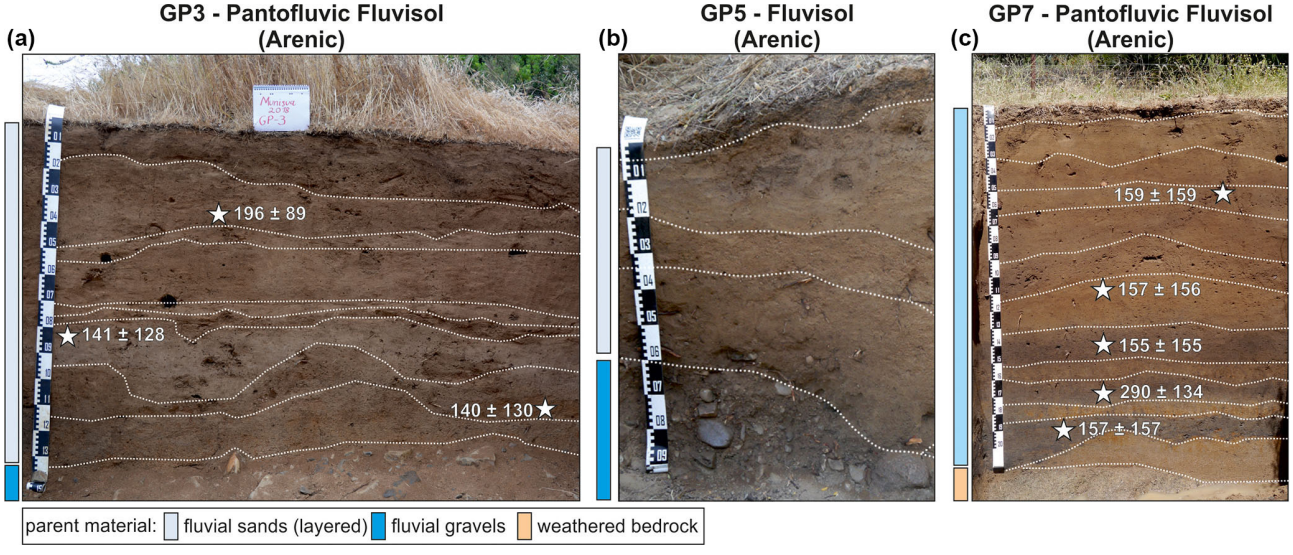

Figure 8. Profile photos of fluvial sequences GP3 **(a)**, GP5 **(b)** and GP7 **(c)**. Identified parent material is marked on the left of the profile photos. Sampling positions for dated charcoal samples and calibrated ^{14}C ages (cal BP) are marked with white stars.

the basis of the profile. Similar to profile GP3, predominantly charcoal-bearing, sand-dominated sediments (59 %–96 % sand) were deposited above 220 cm. Humic sections (Ahb horizons) are preserved at depths of 135–150, 160–175 and 185–200 cm below the surface (Figs. 8 and 10, Table S1).

GP5 is rather shallow and less than 90 cm deep (Fig. 8). Similar to GP3 and GP7, the stratigraphy shows charcoal-bearing brown sands (10YR 3/2 to 4/3) in its upper section. They are relatively loose and overlie rounded gravels and blocks exposed below 60 cm. Due to its stratigraphical similarity to GP3 and GP7, as well as comparably low depth, GP5 was only investigated in the field and not sampled for further laboratory analysis.

Due to the thickness of the fluvial deposits (Fluvisols), potential rootability for plants and available water-storage capacity are very good at sites GP3 and GP7 and are respectively moderate to good at site GP5 (Fig. 3). The nutrient situation of GP3 and GP7 is evaluated as moderate (Ta-

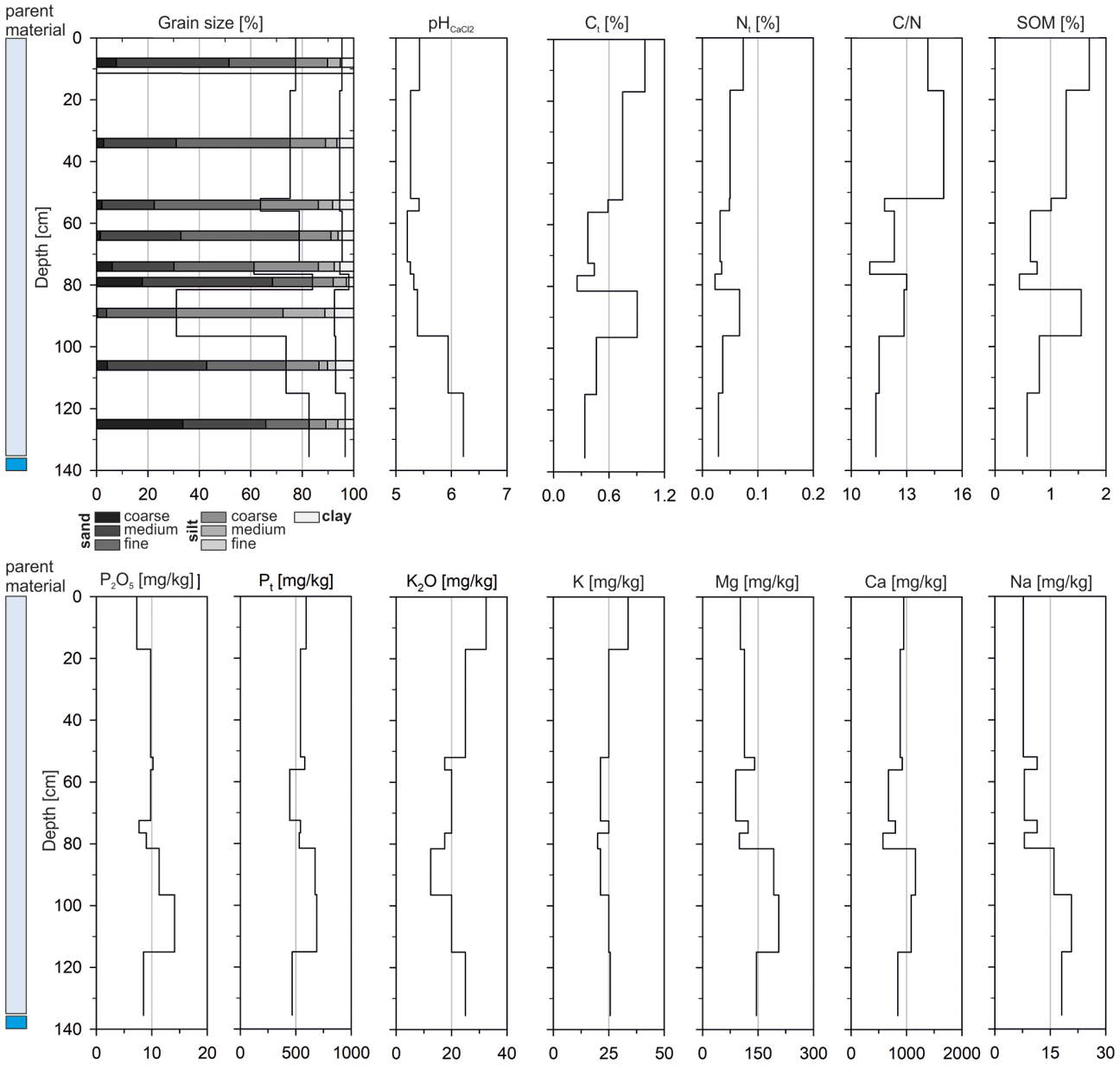

Figure 9. Laboratory results for the pantofluvic Fluvisols (Arenic) at floodplain site GP3. Identified parent material is marked according to Fig. 8.

ble S1, Figs. 9 and 10), and once more only P_2O_5 shows relatively low values (median = 7.5 mg kg^{-1}, SD = 9.4, $n = 22$). The pH values range between 4.9 and 6.5 (median = 5.5, SD = 0.5, $n = 22$). N_t content is low again (median = 0.05 %, SD = 0.13, $n = 22$), and SOM shows average values of 0.83 % (SD = 1.1, $n = 22$).

The ^{14}C dating results from GP3 and GP7 show modern ages for all eight charcoal samples with an oldest age of 290 ± 134 cal BP (Fig. 8, Table 1).

5 Discussion

5.1 Land use and its potential in granite landscape of the Munigua region

Catenary soil mapping in the surroundings of the Roman house complex Casa de Alcántara 1–3 indicates a heterogeneous soil pattern, with soil types clearly depending on geomorphological position (Fig. 2). Most likely this is due to modifications by past soil erosion and related colluviation, leading to profile shallowing in upper slope sites and the deposition of a colluvial cover in middle to lower slope

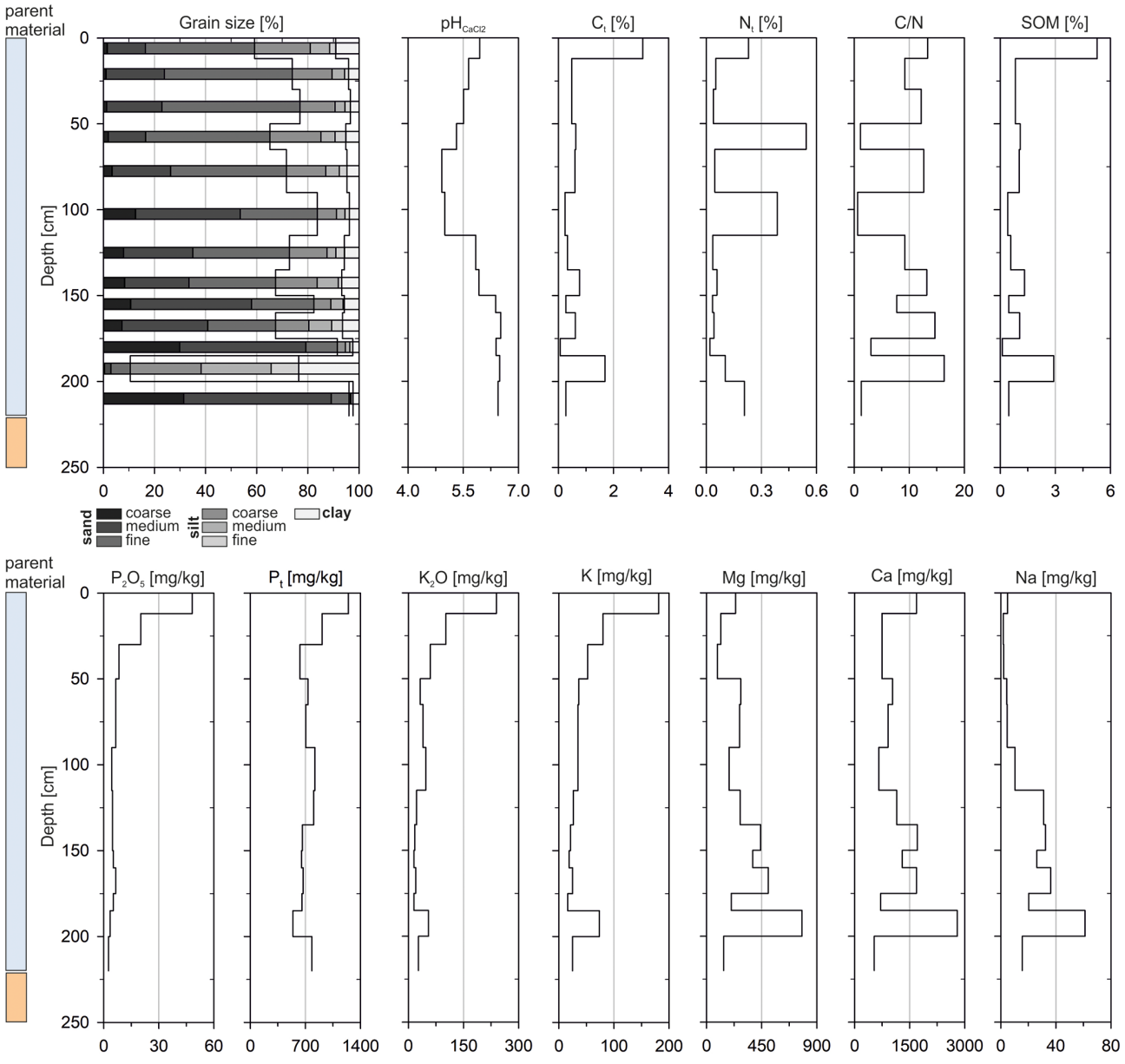

Figure 10. Laboratory results for the pantofluvic Fluvisols (Arenic) at floodplain site GP7. Identified parent material is marked according to Fig. 8.

positions and depressions. Frequent occurrences of embedded bricks, shards and charcoal indicate that mobilization and translocation processes were mainly triggered by anthropogenic factors like settling, clearing and/or local agriculture (Leopold and Völkel, 2007). This is in agreement with other investigations in the western Sierra Morena that highlight erosive processes triggered by accelerated human impact (e.g., Recio Espejo et al., 2002). The ^{14}C dating results of this pilot study (Fig. 2, Table 1) provide evidence for past soil erosion phases in pre-Roman, late Roman and post-Roman times and therefore strongly suggest that farming has recurred within the investigated granite landscape and has been a typical land use strategy over very long periods. This observation chronologically reasonably matches with recent investigations in Spanish river catchments. May et al. (2021) reported on increased fluvial and alluvial deposition during Roman or post-Roman times (after approx. 2100 cal BP) and suggest that this is related to a high anthropogenic impact on the local landscape. Similarly, Faust and Wolf (2017) describe a supply of top soil material to many western Mediterranean floodplains that started about 2.2 kyr ago and seems to be related to anthropogenic influences (e.g., agriculture) especially in the lowest-order catchments. The achieved results of this study support this assumption and therefore re-

fer to larger-scale erosion patterns in the entire region. Along with the in situ evidence for soil erosion triggered by anthropogenic land use activities, this finding furthermore indicates the basic suitability of the granite-derived soils for agricultural purposes. The unexpected fact that no colluvia from Munigua's heyday have been found so far might be related to the limited number of age datings, the applied dating technique and the number of locations investigated in this pilot project. In our opinion it does not necessarily mean that there was no colluviation during this period, and further research is needed for a conclusive assessment on soil erosion and colluviation in the region.

The heterogeneous soil inventory revealed variations in present-day soil agro-potential in the surroundings of Casa de Alcántara 1–3. Truncated Leptosols to moderately deep Cambisols in upper slope positions and flatter ridge areas (Fig. 2) show unfavorable to very unfavorable conditions today (Fig. 3). In particular, the low soil depths of these sites and the sandy soil texture (Table S1) have an unfavorable effect on potential rootability, available water-storage capacity and the nutrient budget. The overall soil agro-potential of these sites can be evaluated as unfavorable to very unfavorable (Fig. 3, Table S1).

In contrast, currently moderate to good soil potential exists in middle to lower slope positions, where multi-layered colluvial deposits almost ubiquitously cover the weathered granite (Fig. 3). Here the potential rootability for cultivated plants ranges from moderate to very good due to increased soil depths at these sites. This also favors available water-storage capacity, which can be evaluated as moderate to good. The nutrient situation is mostly reasonable and would certainly allow the cultivation of agricultural crops. Consequently, the cultivation of cereals, such as emmer, barley or millet, which were part of the Roman diet (Flach, 1990; Gerlach, 2001), as well as vegetables, should definitely be possible at many sites within the regional granite landscape. This assumption is supported by the fact that even today, wild oats grow in this landscape and could also have been cultivated as green fodder or hay in Roman times, if not necessarily for human consumption.

Our observations in the surroundings of the Roman house complex Casa de Alcántara 1–3 therefore do not confirm the aforementioned assumptions that the regional soil conditions (i) are currently unsuitable for extensive agriculture and (ii) generally speak against ancient agricultural use in the region (Schattner, 2019b). Instead, the multiphase deposition of colluvium over longer periods and the moderate to good soil agro-potential rather support archeological assumptions concerning agricultural production (Peña Cervantes, 2010; Teichner and Peña Cervantes, 2012; Krug, 2018) involving fields and gardens, as well as pastures for small animals and trees in the wider surroundings of the town.

However, a challenging question in this context is the extent to which the characteristics of current soils provide information on past soil potential. Extensive studies from the Mediterranean supply clear evidence for soil degradation and decreased soil productivity due to the long-term history of land use (e.g., Redman, 1999; García-Ruiz, 2010; Bellin et al., 2013; García-Ruiz et al., 2013; Dotterweich, 2013). It follows that various areas may have been more productive during Roman times, especially sites in erosion-prone hillslope positions (GP11, GP15) that were evaluated as unfavorable to very unfavorable for the present day. The actual status assigned to the sites thus underestimates the ancient soil agro-potential. Vice versa, it can be assumed that the soil potential in aggradational locations, like flat hillslope positions or slope depressions, has improved. Here, colluviation has led to increased soil thickness, which generally favors potential rootability and available water-storage capacity. However, the ^{14}C-derived chronology provides evidence that colluviation had already taken place, at least in part, before the Roman period (Fig. 2, Table 1), which is why the ancient soil agro-potential in these locations was probably not significantly different to that of the present day. We therefore argue that the prevailing moderate to good soil potential of the granite landscape around Munigua today probably also pertained for antiquity.

Further robust evidence for Roman agriculture was gained in a granite area close to the urban center of Munigua (Fig. 1b). Since this area is located outside the fortified urban area, the withdrawal of water for possible irrigation or livestock seems likely. Less than 5 m away from a Roman well, an enrichment of SOM, P_2O_5, P_t, K_2O and other nutrients (Mg, Ca, Na and K) was detected, especially in the lowermost section of a Roman-dated hortic horizon (Fig. 4, Table S1). We interpret these results as indicating intentional humus or compost fertilization intended to further improve the site and secure yields. In this context, it is assumed that organic, nutrient-enriched waste, settlement residues (e.g., pottery, slag fragments or bricks) and possibly also animal excrements were frequently distributed across the surface after harvesting and mixed into the granitoid slope deposits, leading to the gradual development of the Roman hortic horizon. The lower SOM, phosphate and nutrient contents in the upper part of the hortic horizon (23–46 cm) could be due to multiple causes. On the one hand, the abandonment of the site and the associated lack of phosphate and organically enriched fertilizers could have led to an increased decomposition of SOM and increased phosphate and nutrient consumption by vegetation. On the other hand, it is well-known that larger mammals (e.g., wild boars) and soil organisms impact the physical and chemical properties of soil (e.g., Mohr et al., 2005; Risch et al., 2010; Wirthner et al., 2011). This could have led to a mixing of the substrate in post-Roman times and ultimately to a relative depletion of SOM, phosphate and nutrient concentrations in the upper part of the Roman horizon. Additionally, this mixing process would plausibly explain the incorporation of the modern charcoal at 38 cm (Fig. 4b, Table 1) when this profile section formed the terrain surface.

The greatly enhanced phytolith concentrations within the Roman-dated hortic horizon (Fig. 6a) generally indicate increased plant input and can be plausibly explained by phytolith enrichment through agricultural activities (e.g., Cabanes et al., 2011; Madella and Lancelotti, 2012; Meister et al., 2017). This supports the geochemical interpretation of a Roman hortic soil at site GP2. The observed phytolith assemblages are dominated by Pooids containing some of the major Mediterranean crops, such as barley, wheat or rye (Schiemann, 1948), which could indicate the cultivation of cereals. This is supported by the fact that leaf and stem grass phytoliths within the lower profile section dominate over grass phytoliths formed in the inflorescences or in other plant organs (Fig. 6c). The accumulation of the former could be a consequence of harvesting activities, when only the ears (inflorescences) are collected and the stems and leaves are left on the fields (Flach, 1990; Dietrich et al., 2019; Scherer et al., 2021). It is also conceivable that food crops other than cereals might have been cultivated in this area since, for example, the consumption of vegetables is well documented for the Roman period (Bockisch, 1988; Demandt, 2008). Moreover, in their works on agricultural and horticultural practices, the famous ancient authors Columella (*De re rustica*) and Palladius (*Opus agriculturae*) described a crop rotation system in which different cereals and vegetables were grown in successive years on the same fields (Flach, 1990). However, although phytoliths have been documented, for instance, for numerous specimens from the Fabaceae (Leguminosae) family, phytolith production varies substantially among different subfamilies (Cummings, 1992), while other important vegetable plants (e.g., root vegetables) produce no or only small amounts of phytoliths (Piperno, 2006). Phytolith analysis thus provides no indication of whether the area was used exclusively for cereals or whether vegetables were also cultivated.

Summing up, it can be asserted that both geochemical and phytolith analyses suggest an ancient agrarian use of site GP2. The exclusive use of the site for pasturing or feeding seems rather unlikely since the large number of Roman artifacts incorporated into the Roman hortic horizon clearly document invasive soil cultivation in the sense of digging or hoeing. Since water supply is guaranteed by the nearby well, the site offers suitable conditions for irrigated agriculture almost all year round.

5.2 Land use and its potential in the metamorphic landscape of the Munigua region

A contrasting land use evaluation has to be made for soils within metamorphic landscape, Here, mostly shallow and sandy to stony soils occur (Fig. 7, Table S1), strongly limiting potential rootability and resulting in unfavorable to very unfavorable water-storage capacity and nutrient budget (Fig. 3). Thus the present-day soil agro-potential is evaluated as unfavorable to very unfavorable at these metamorphic sites.

In addition to the pedological limitations, geomorphological circumstances render agriculture rather unprofitable in these areas. The slopes in the metamorphic landscape are generally steeper, and cultivation would be more exhausting in this landscape unit (Fig. 1b). Furthermore, limits on water availability prevent the all-season agricultural use of these sites since streams are commonly deeply incised and natural springs are rare here, rendering irrigation of agricultural areas difficult. These pedological and geomorphological characteristics make it unlikely that the metamorphic landscape was used for agriculture even in Roman times. Lastly, this assumption is supported by the fact that thick colluvial deposits clearly indicate land use in the granitic landscape but are absent in the observed metamorphic landscape. If there had been historical agricultural use, such deposits should have been preserved at least in places.

5.3 Land use and its potential in the Tamohoso floodplain

Floodplains are usually known to be fertile areas and have therefore been used for agriculture around the globe for thousands of years (Brown, 1997). The nearby lower Guadalquivir valley, for example, is a settlement chamber that has been continuously used for agriculture since the Copper Age at the latest and remains a preferred area for agricultural production (Nocete et al., 2008; García Sanjuán et al., 2013). It therefore seems likely that the alluvial deposits of the nearby Tamohoso River could also have been a favored area for agriculture during Roman times, contributing to the food supply of Munigua.

The analyses of the floodplain sites mostly show moderate to good soil agro-potential (Fig. 3). In particular, thicknesses > 1 m (Fig. 8, Table S1) favor potential rootability and available water-storage capacity. Additionally, the nutrient budget is moderate, resulting in the floodplain soils having overall moderate to good agrarian potential from today's perspective. Moreover, in addition to the physico-chemical properties, the flat terrain of the alluvial plain and the easy access to water favor the agricultural use of the floodplain sites.

Nevertheless, so far we have no information on the appearance of the Tamohoso floodplain in Roman times. Eight ^{14}C ages from fluvial sequences indicate deposition within an active meander belt in modern times (Fig. 8, Table 1). This might have been caused by intensified modern land use activities in the 19th and 20th centuries CE (Tomás García, 1991), as also seen in the widespread juvenile gully systems within the area (Fig. 1d). Regarding the ancient situation, it seems likely that comparable conditions existed in the Tamohoso floodplain at least locally during the heyday of Munigua since past soil erosion should already have led to sediment transfer into the streams. However, associated sediments were probably eroded and relocated due to contemporary active meander dynamics.

5.4 A pedo-geomorphological perspective on the Roman economy

The economy of small cities in the Roman province of Baetica was enormously diverse but commonly specialized around a certain economic activity (e.g., Blázquez Martinez, 1967; Chic García, 1997; Bowman and Wilson, 2009, 2011; Remesal Rodríguez, 2020). In the case of Munigua, metallurgy was without doubt the main and most profitable economic activity and led to considerable wealth in the region (Schattner, 2019b). However, multi-layered colluvial deposits in the surroundings of Munigua (Sect. 4.1.1) and a preserved Roman hortic Anthrosol (Sect. 4.1.2) provide proper pedo-geomorphological evidence of prehistoric and historic agrarian land use in granite areas around Munigua. This indicates that there was at least a second economic activity. It can thus rather be assumed that Roman cities were economically diversified rather than being dedicated to a single economic activity. Using a pedo-morphological approach, the present study therefore generally confirms the concept of an economic diversification of Roman towns in the province of Baetica and Hispania.

6 Conclusions

Using a pedo-geomorphological approach, the investigation underlines that the soils around Munigua currently have the potential for at least limited agricultural use in larger areas. The granite landscape and the floodplain areas of the Tamohoso River show conditions that would certainly allow the production of basic agricultural goods, not only today but most likely also in Roman times.

Whereas the existence of tilled floodplain soils during Roman times cannot be proven by this study, clear evidence of agrarian use is detectable in granite areas. Here, profile truncation and multi-layered colluvial deposits indicate multiple soil erosion phases in the surroundings of a Roman rural house complex southeast of the urban center of Munigua. Based on our initial ^{14}C-results, anthropogenic soil erosion and colluviation occurred in pre-Roman, late Roman and post-Roman times, which strongly suggests the long-term agrarian utilization of the area. For a granite area close to Munigua, phytolith and geochemical analyses provide evidence of the existence of a Roman garden, where cereals and vegetables might have been cultivated at least on a small scale. The site was most likely fertilized by humus or compost to improve and secure crop yields, confirming the Roman population's extensive knowledge of agricultural practices, already described by ancient authors like, for instance, Columella or Palladius. Hence, the results of investigations in the granite landscape surrounding Munigua indicate a local cultivation of agricultural products that made an active contribution to the food supply of the area. This seems even more likely if the variety of agricultural equipment (Krug, 2018) and olive oil presses (Peña Cervantes, 2010; Teichner and Peña Cervantes, 2012) excavated in the town are also taken into account. This study thus could not confirm the hypothesis that deficient pedological conditions in the surroundings of Munigua generally prevented the agricultural use of the area during Roman times and that therefore the population was mainly dependent on food imports from the lower Guadalquivir valley (Schattner, 2019b). However, there remain many open questions for future research in the coming years, i.e., concerning the extent and production rates of agricultural activities, the cultivated products, or the adaptation techniques applied to cope with seasonal water deficiencies.

In addition to the site-specific information, the study also provides geoarcheological evidence supporting the concept of an economic diversification of Roman cities in Baetica province and Hispania. Even though metallurgy was without doubt the main and most profitable activity in the Munigua region, the economy was certainly not only dedicated to mining activities. Whereas specialty goods were imported, basic agrarian products (e.g., crops, olive oil, wine) were also part of Munigua's economic portfolio and exemplify the economic diversity of urban settlements in the Roman Baetica province.

Data availability. Data relating to this paper can be found in the Supplement or are available from the corresponding author upon reasonable request.

Supplement. The supplement related to this article is available online at: https://doi.org/10.5194/egqsj-71-123-2022-supplement.

Author contributions. AK, NH and TGS organized the project. AK, NH and PM carried out the fieldwork. The concept and structure of the paper were organized by AK and NH. The laboratory work was mainly done by PM, IM and JM. AK took the lead in writing the manuscript, with input from NH, JM and TGS. All authors discussed the results and contributed to the final manuscript.

Competing interests. At least one of the (co-)authors is a member of the editorial board of *E&G Quaternary Science Journal*. The peer-review process was guided by an independent editor, and the authors also have no other competing interests to declare.

Disclaimer. Publisher's note: Copernicus Publications remains neutral with regard to jurisdictional claims in published maps and institutional affiliations.

Special issue statement. This article is part of the special issue "Quaternary research from and inspired by the first virtual DEUQUA conference". It is a result of the vDEUQUA2021 online conference in September/October 2021.

Acknowledgements. The authors are very grateful to Heinrich Thiemeyer, Doris Bergmann-Dörr and Dagmar Schneider (all Goethe University Frankfurt) for the conscientious implementation of selected soil analyses. Furthermore, Katharine Thomas is acknowledged for improving the language of the manuscript.

Financial support. This research was financially supported by the Madrid Department of the German Archaeological Institute. This publication was supported by the open-access publication fund of the University of Wuerzburg.

Review statement. This paper was edited by Tobias Sprafke and reviewed by two anonymous referees.

References

Ad-hoc-AG Boden: Bodenkundliche Kartieranleitung, 5th edn., Schweizerbart, Stuttgart, 438 pp., ISBN 9783510959204, 2005.

Albert, R. M.: Study of ash layers through phytolith analyses from the Middle Paleolithic levels of Kebara and Tabun caves, Universitat de Barcelona, Barcelona, ISBN 9788459244265, 2000.

Albert, R. M. and Weiner, S.: Study of phytoliths in prehistoric ash layers using a quantitative approach, in: Phytoliths, Applications in Earth Sciences and Human History, edited by: Meunier, J. D. and Colin, F., A.A. Balkema Publishers, Lisse, 251–266, ISBN 9789058093455, 2001.

Albert, R. M., Lavi, O., Estroff, L., Weiner, S., Tsatskin, A., Ronen, A., and Lev-Yadun, S.: Mode of occupation of Tabun Cave, Mt Carmel, Israel during the Mousterian Period: a study of the sediments and phytoliths, J. Archaeol. Sci., 26, 1249–1260, https://doi.org/10.1006/jasc.1999.0355, 1999.

Amelung, W., Blume, H.-P., Fleige, H., Horn, R., Kandeler, E., Kögel-Knabner, I., Kretzschmar, R., Stahr, K., and Wilke, B.-M.: Scheffer/Schachtschabel: Lehrbuch der Bodenkunde, 17th edn., Springer Spektrum, Berlin, Heidelberg, 750 pp., https://doi.org/10.1007/978-3-662-55871-3, 2018.

Bellin, N., Vanacker, V., and De Baets, S.: Anthropogenic and climatic impact on Holocene sediment dynamics in SE Spain: A review, Quatern. Int., 308, 112–129, https://doi.org/10.1016/j.quaint.2013.03.015, 2013.

Blázquez Martínez, J. M.: Estructura económica de la Bética al final de la República romana y a comienzos del Imperio (años 72 a.C.–100 d.C.), Hispania, 27, 7–62, 1967.

Bleck, R.-D.: Zur Durchführung der Phosphatmethode, Ausgrabungen und Funde, 10, 213–218, 1965.

Blume, H.-P., Stahr, K., and Leinweber, P.: Bodenkundliches Praktikum, 3rd edn., Springer Spektrum, Berlin, Heidelberg 255 pp., https://doi.org/10.1007/978-3-8274-2733-5, 2011.

Bockisch, G.: Essen und Trinken im alten Rom, Das Altertum, 34, 87–95, 1988.

Boessneck, J. and von den Driesch, A.: Knochenfunde aus dem römischen Munigua (Mulva), Sierra Morena. Studien über frühe Knochenfunde von der Iberischen Halbinsel, München Uni-Druck, 160–193, 1980.

Borden, W. R., Baillie, I. C., and Hallett, I. C.: The East African contribution to the formalisation of the soil catena concept, Catena, 185, 104291, https://doi.org/10.1016/j.catena.2019.104291, 2020.

Bowman, A. and Wilson, A.: Quantifying the Roman Economy: Methods and Approaches (Oxford Studies on the Roman Economy 1), Oxford University Press, Oxford, 376 pp., https://doi.org/10.1093/acprof:oso/9780199562596.001.0001, 2009.

Bowman, A. and Wilson, A.: Settlement, Urbanization, and Population, Oxford University Press, Oxford, 362 pp., https://doi.org/10.1093/acprof:oso/9780199602353.001.0001, 2011.

Brown, A. G.: Alluvial Geoarchaeology. Floodplain Archaeology and Environmental Change, Cambridge University Press, Cambridge, 377 pp., https://doi.org/10.1017/CBO9780511607820, 1997.

Brown, D. A.: Prospects and limits of a phytolith key for grasses in the central United States, J. Archaeol. Sci., 11, 345–368, https://doi.org/10.1016/0305-4403(84)90016-5, 1984.

Cabanes, D., Weiner, S., and Shahack-Gross, R.: Stability of phytoliths in the archaeological record: a dissolution study of modern and fossil phytoliths, J. Archaeol. Sci., 38, 2480–2490, https://doi.org/10.1016/j.jas.2011.05.020, 2011.

Chic García, G.: Historia económica de la. Bética en la época de Augusto, Padilla Libros, Sevilla, ISBN 84-89769-18-4, 1997.

Cummings, L. S.: Illustrated phytoliths from assorted food plants, in: Phytolith Systematics: Emerging Issues, Advances in Archaeological and Museum Science, edited by: Rapp Jr., G. and Mulholland, S. C., Springer Science & Business Media, 175–192, ISBN 978-1489911575, 1992.

Demandt, A.: Geschichte der Spätantike: Das Römische Reich von Diocletian bis Justinian 284–565 n. Chr., 2nd edn., C. H. Beck, München, 604 pp., ISBN 978-3-406-70032-3, 2008.

de Vries, H. and Barendsen, G. W.: Measurements of age by the carbon-14 technique, Nature, 174, 1138–1141, 1954.

Dietrich, L., Meister, J., Dietrich, O., Notroff, J., Kiep, J., Heeb, J., Beuger, A., and Schütt, B.: Cereal processing at Early Neolithic Göbekli Tepe, southeastern Turkey, PLOS ONE, 14, e0215214, https://doi.org/10.1371/journal.pone.0215214, 2019.

DIN ISO 11277: Soil Quality – Determination of particle size distribution in mineral soil material – method by sieving and sedimentation, Beuth, Berlin, 2002.

Dotterweich, M.: The history of soil erosion and fluvial deposits in small catchments of Central Europe: deciphering the long-term interaction between humans and the environment – a review, Geomorphology, 101, 192–208, https://doi.org/10.1016/j.geomorph.2008.05.023, 2008.

Dotterweich, M.: The history of human-induced soil erosion: Geomorphic legacies, early descriptions and research, and the development of soil conservation – A global synopsis, Geomorphology, 201, 1–34, https://doi.org/10.1016/j.geomorph.2013.07.021, 2013.

Eger, C.: Frühislamische Bestattungen in Munigua (Prov. Sevilla/E), Archäologisches Korrespondenzblatt, 46, 255–269, 2016.

Evans, D. M. and Hartemink, A. E.: Terra Rossa catenas in Wisconsin, USA, Catena, 123, 148–152, https://doi.org/10.1016/j.catena.2014.07.007, 2014.

Faust, D. and Wolf, D.: Interpreting drivers of change in fluvial archives of the Western Mediterranean

– A critical view, Earth-Sci. Rev., 174, 53–83, https://doi.org/10.1016/j.earscirev.2017.09.011, 2017.

Flach, D.: Römische Agrargeschichte, C. H. Beck, München, 347 pp., ISBN 978-3-406-33989-9, 1990.

Frey, W. and Lösch, R.: Geobotanik. Pflanze und Vegetation in Raum und Zeit, 3rd edn., Springer Spektrum, Berlin, Heidelberg, 638 pp., https://doi.org/10.1007/978-3-8274-2336-8, 2010.

García-Ruiz, J. M.: The effects of land use on soil erosion in Spain. A review, Catena, 81, 1–11, https://doi.org/10.1016/j.catena.2010.01.001, 2010.

García-Ruiz, J. M., Nadal-Romero, E., Lana-Renault, N., and Beguería, S.: Erosion in Mediterranean landscapes. Changes and future challenges, Geomorphology, 198, 20–36, https://doi.org/10.1016/j.geomorph.2013.05.023, 2013.

García Sanjuán, L., Luciañez Triviño, M., Schuhmacher, T., Wheatley, D., and Banerjee, A.: Ivory Craftsmanship, Trade and Social Significance in the Southern Iberian Copper Age: The Evidence from the PP4-Montelirio Sector of Valencina de la Concepción (Seville, Spain), Eur. J. Archaeol., 16, 610–635, https://doi.org/10.1179/1461957113Y.0000000037, 2013.

Gerlach, G.: Zu Tisch bei den alten Römern: Eine Kulturgeschichte des Essens und Trinkens, Konrad Theiss, Stuttgart, 112 pp., ISBN 978-3806213539, 2001.

Giner-Robles, J. L., Bardají, T., Rodríguez-Pascua, M. A., Silva, P. G., Roquero, E., Elez, J., Perucha, M. A., Baena, R., Guerrero, I., Fernández-Caro, J. J., Pérez-López, R., and Rodríguez-Escudero, E: Análisis arqueosismológico del conjunto arqueológico romano de Mulva- Munigua (Sevilla, España), Geotemas, 16, 605–608, 2016.

Gómez-Zotano, J., Alcántara-Manzanares, J., Olmedo-Cobo, J.-A., and Martínez-Ibarra, E.: La sistematiza-cíon del clima mediterráneo: identificacíon. Clasificacíon y caracterizacíon climática de Andalucía (España), Rev. Geogr. Norte Gd., 61, 161–180, https://doi.org/10.4067/S0718-34022015000200009, 2015.

Grünhagen, W.: Die Ausgrabungen des Terrassenheiligtums von Munigua, in: Neue deutsche Ausgrabungen im Mittelmeergebiet und im Vorderen Orient, edited by: Boehringer, E., 329–343, 1959.

Gutiérrez-Rodríguez, M., Goldberg, P., Martín Peinado, F. J., Schattner, T. G., Martini, W., Orfila, M., and Bashore Acero, C.: Melting, bathing and melting again. Urban transformation processes of the Roman city of Munigua: the public thermae, Archaeol. Anthropol. Sci., 11, 51–67, https://doi.org/10.1007/s12520-017-0527-0, 2019.

Hajdas, I.: Radiocarbon dating and its applications in Quaternary studies, E&G Quaternary Sci. J., 57, 2–24, https://doi.org/10.3285/eg.57.1-2.1, 2008.

Hanel, N.: Römische Öl- und Weinproduktion auf der Iberischen Halbinsel am Beispiel von Munigua und Milreu, Madrider Mitteilungen, 30, 205–238, 1989.

Holliday, V. T. and Gartner, W. G.: Methods of soil P analysis in archaeology, J. Archaeol. Sci., 34, 301–333, https://doi.org/10.1016/j.jas.2006.05.004, 2007.

IUSS Working Group WRB: World Reference Base for Soil Resources 2014, update 2015. International soil classification system for naming soils and creating legends for soil maps, World Soil Resources Reports No. 106, FAO, Rome, ISBN 978-92-5-108369-7, 2015.

Jahn, R., Blume, H.-P., Asio, V. B., Spaargaren, O., and Schad, P.: Guidelines for soil description, FAO, Rome, 97 pp., ISBN 92-5-105521-1, 2006.

Joffre, R., Vacher, J., del los Llanos, C., and Long, G.: The Dehesa: an agrosilvopastoral system of the Mediterranean region with special reference to the Sierra Morena area of Spain, Agroforest Syst., 6, 71–96, https://doi.org/10.1007/BF02220110, 1988.

Keay, S. and Earl, G.: Towns and Territories in Roman Baetica, in: Settlement, Urbanization, and Population, edited by: Bowman, A., and Wilson, A., Oxford University Press, 276–316, https://doi.org/10.1093/acprof:oso/9780199602353.001.0001, 2011.

Kittel, P.: Slope deposits as an indicator of anthropopressure in the light of research in Central Poland, Quatern. Int., 324, 34–55, https://doi.org/10.1016/j.quaint.2013.07.021, 2014.

Krug, A.: Mulva VI: Die Kleinfunde/ Los hallazgos menores, Madrider Beiträge, 36, 436 pp., ISBN 978-3954902378, 2018.

Leopold, M. and Völkel, J.: Colluvium: definition, differentiation, and possible suitability for reconstructing Holocene climate data, Quatern. Int., 162–163, 133–140, https://doi.org/10.1016/j.quaint.2006.10.030, 2007.

Madella, M. and Lancelotti, C.: Taphonomy and phytoliths: A user manual, Quatern. Int., 275, 76–83, doi10.1016/j.quaint.2011.09.008, 2012.

Madella, M., Alexandre, A., and Ball, T.: International Code for Phytolith Nomenclature 1.0, Ann. Bot., 96, 253–260, https://doi.org/10.1093/aob/mci172, 2005.

May, S. M., Norpoth, M., Pint, A. Shumilovskikh, L., Raith, K., Brill, D., Rixhon, G., Moret, P. Jiménez-Vialás, H., Grau-Mira, I., García-Jiménez, I., Marzoli, D., León-Martín, C., Reicherter, K., and Brückner, H.: Mid- to late Holocene environmental changes and human-environment interactions in the surroundings of La Silla del Papa, SW Spain, Geoarchaeology, 36, 573–600, https://doi.org/10.1002/gea.21846, 2021.

Meister, J., Krause, J., Müller-Neuhof, B., Portillo, M., Reimann, T., and Schütt, B.: Desert agricultural systems at EBA Jawa (Jordan): Integrating archaeological and paleoenvironmental records, Quatern. Int., 434, 33–50, https://doi.org/10.1016/j.quaint.2015.12.086, 2017.

Meyer, C., Ullrich, B., and Barlieb C. D. M.: Archaeological Questions and Geophysical Solutions: Ground-Penetrating Radar and Induced Polarization Investigations in Munigua, Spain, Archaeol. Prospect., 14, 202–212, https://doi.org/10.1002/arp.314, 2007.

Mohr, D., Cohnstaedt, L. D., and Topp, W.: Wild boar and red deer affect soil nutrients and soil biota in steep oak stands of the Eifel, Soil Biol. Biochem., 37, 693–700, https://doi.org/10.1016/j.soilbio.2004.10.002, 2005.

Mulholland, S. C. and Rapp Jr., G.: A morphological classification of grass silica-bodies, in: Phytolith Systematics: Emerging Issues, Advances in Archaeological and Museum Science, edited by: Rapp Jr., G. and Mulholland, S. C., Springer Science & Business Media, 65–89, ISBN 978-1489911575, 1992.

Neumann, K., Strömberg, C. A. E., Ball, T., Albert, R. M., Vrydaghs, L., and Cummings, L. S.: International code for phytolith nomenclature (ICPN) 2.0, Ann. Bot., 124, 189–199, https://doi.org/10.1093/aob/mcz064, 2019.

Nocete, F., Queipo, G., Sáez, R., Nieto, J. M., Inácio, N., Bayona, M. R., Peramo, A., Vargas, J. M., Cruz-Auñón, R., Gil-Ibarguchi,

J. I., and Santos, J. F.: The Smelting Quarter of Valencina de la Concepción (Seville, Spain): The Specialised Copper Industry in a Political Centre of the Guadalquivir Valley During the Third Millennium BC (2750–2500 BC), J. Archaeol. Sci., 35, 717–732, https://doi.org/10.1016/j.jas.2007.05.019, 2008.

Nocete, F., Sáez, R., Bayona, M. R., Peramo, A., Inacio, N., and Abril, D.: Direct chronometry (14C AMS) of the earliest copper metallurgy in the Guadalquivir Basin (Spain) during the third millennium BC: first regional database, J. Archaeol. Sci., 38, 3278–3295, https://doi.org/10.1016/j.jas.2011.07.008, 2011.

Nuñez, M. A. and Recio, J. M.: Holocene pedoenvironmental situations in the eastern Sierra Morena region (Andújar, Spain), Quatern. Int., 93–94, 191–195, https://doi.org/10.1016/S1040-6182(02)00017-4, 2002.

Paneque, G. and Bellinfante, N.: Mediterranean brown forest soils of the Sierra Morena (Spain), their micromorphology and petrography, in: Soil Micromorphology, edited by: Jongerius, A., 189–200, ISBN 978-0444403254, 1964.

Peña Cervantes, Y.: Torcularia: la producción de vino y aceite en Hispania, Tarragona: ICAC, Institut Català d'Arqueologia Clàssica, 284 pp., ISBN 978-84-937734-1-0, 2010.

Piperno, D. R.: Phytoliths: A Comprehensive Guide for Archaeologists and Paleoecologists, Rowman Altamira, Lanham, New York, Toronto, Oxford, 238 pp., https://doi.org/10.1017/S0016756807003159, 2006.

Portillo, M., Kadowaki, S., Nishiaki, Y., and Albert, R. M.: Early Neolithic household behavior at Tell Seker al-Aheimar (Upper Khabur, Syria): a comparison to ethnoarchaeological study of phytoliths and dung spherulites, J. Archaeol. Sci., 42, 107–118, https://doi.org/10.1016/j.jas.2013.10.038, 2014.

Recio Espejo, J. M., Faust, D., and Nuñez Granados, M. A.: The origin of the Sierra de Aracena Hollows in the Sierra Morena, Huelva, Andalucia, Spain, Geomorphology, 45, 197–209, https://doi.org/10.1016/S0169-555X(01)00154-4, 2002.

Redman C. L.: Human impact on ancient environments, University of Arizona Press, Tucson, 256 pp., ISBN 978-0816519637, 1999.

Reimer, P., Bard, E., Bayliss, A., Beck, J. W., Blackwell, P. G., Ramsey, C. B., Buck, C. E., Cheng, H., Edwards, R. L., Friedrich, M., Grootes, P. M., Guilderson, T. P., Haflidason H., Hajdas, I., Hatte, C., Heaton, T. J., Hoffmann, D. L., Hogg, A. G., Hughen, K. A., Kaiser, K. F., Kromer, B., Manning, S. W., Niu, M., Reimer, R. W., Richards, D. A., Scott, E. M., Southon, J. R., Staff, R. A., Turney, C. S. M., and van der Plicht, J.: IntCal13 and Marine13 radiocarbon age calibration curves 0–50 000 years cal BP, Radiocarbon, 55, 1869–1887, https://doi.org/10.2458/azu_js_rc.55.16947, 2013.

Remesal Rodríguez, J.: Die politische und wirtschaftliche Entwicklung der Baetica in der Kaiserzeit, Madrider Mitteilungen, 61, 115–132, 2020.

Ribeiro, A., Munhá, J., Fonseca, P. E., Araújo, A., Pedro, J.C., Mateus, A., Tassinari, C., Machado, G., and Jesus, A.: Variscan ophiolite belts in the Ossa-Morena Zone (Southwest Iberia): Geological characterization and geodynamic significance, Gondwana Res., 17, 408–421, https://doi.org/10.1016/j.gr.2009.09.005, 2010.

Risch, A. C., Wirthner, S., Busse M. D., Page-Dumroese, D. S., and Schütz M.: Grubbing by wild boars (Sus scrofa) and its impact on hardwood forest soil carbon dioxide emissions in Switzerland, Oecologia, 164, 773–784, https://doi.org/10.1007/s00442-010-1665-6, 2010.

Rodríguez-Pascua, M. A., Pérez-López, R., Silva, P. G., Giner-Robles, J. L., Garduño-Monroy, V. H., and Reicherter, K.: A comprehensive classification of Earthquake Archaeological Effects (EAE) for archaeoseismology: application to ancient remains of Roman and Mesoamerican cultures, Quatern. Int., 242, 20–30, https://doi.org/10.1016/j.quaint.2011.04.044, 2011.

Ruiz-Bueno, M. D.: Actividad sísmica en el mediodía ibérico durante el siglo III d.C. La incidencia arqueológica en Corduba (Córdoba), Pyrenae, 48, 29–51, https://doi.org/10.1344/Pyrenae2017.vol48num2.2, 2017.

Sanz, T., Sampelayo, H., and Ledesma Garcia, F.: Mapa Geológica de España. Escala 1 : 50.000, edited by: Instituto geológico y minero de España (IGME), 941, 13–38, 1973.

Schattner, T. G.: Munigua: Cuarenta años de investigaciones, Sevilla: Junta de Andalucía, Instituto Arqueológico Alemán, 335 pp., ISBN 84-8266-364-X, 2003.

Schattner, T. G.: Die Wiederentdeckung von Munigua: Abriss der Forschungsgeschichte, Madrider Mitteilungen, 46, 267–288, 2005.

Schattner, T. G.: Antike "Mondlandschaften", Archäologie Weltweit, 7, 26–31, 2019a.

Schattner, T. G.: Munigua: Un recorrido por la arqueología del Municipium Flavium Muniguense, Editorial Universidad de Sevilla-Secretariado de Publicaciones, Sevilla, 225 pp., ISBN 978-8447219179, 2019b.

Schattner, T. G., Ovejero Zappino, G., and Pérez Macías, J. A.: Avances sobre la producción metalúrgica en Munigua, Habis, 36, 253–276, 2005.

Scherer, S., Höpfer, B., Deckers, K., Fischer, E., Fuchs, M., Kandeler, E., Lechterbeck, J., Lehndorff, E., Lomax, J., Marhan, S., Marinova, E., Meister, J., Poll, C., Rahimova, H., Rösch, M., Wroth, K., Zastrow, J., Knopf, T., Scholten, T., and Kühn, P.: Middle Bronze Age land use practices in the northwestern Alpine foreland – a multi-proxy study of colluvial deposits, archaeological features and peat bogs, SOIL, 7, 269–304, https://doi.org/10.5194/soil-7-269-2021, 2021.

Schiemann, E.: Weizen, Roggen, Gerste. Systematik, Geschichte und Verwendung, Gustav Fischer Verlag, Jena, 102 pp., 1948.

Schüller, H.: Die CAL-Methode, eine neue Methode zur Bestimmung des pflanzenverfügbaren Phosphates in Böden, Zeitschrift für Pflanzenernährung, Düngung und Bodenkunde, 123, 48–63, 1969.

Semmel, A.: Grundzüge der Bodengeographie, Teubner, Stuttgart, 101 pp., ISBN 978-3519134084, 1977.

Strauss, G. K. and Madel, J.: Geology of massive sulphide deposits in the Spanish-Portuguese Pyrite Belt, Geol. Rundsch., 63, 191–211, 1974.

Teichner, F.: Spuren islamischer Besiedlung auf dem Castillo de Mulva (Villanueva del Río y Minas, prov. Sevilla)?, Madrider Mitteilungen, 39, 336–355, 1998.

Teichner, F. and Peña Cervantes, Y.: Archäologisches zur Herstellung von Olivenöl und Wein im römischen Hispanien, Bonner Jahrbücher, 210/211, 375–458, 2012.

Tomás García, L. J.: La Minería sevillana del carbón. Minas de La Reunión y la Compañía de los Ferrocarriles de M.Z.A, Diputación Provincial de Sevilla, Sevilla, ISBN 84-7798-059-4, 1991.

Tornos, F., Inverno, C. M. C., Casquet, C., Mateus, A., Ortiz, G., and Olivera, V.: The metallogenic evolution of the Ossa-Morena Zone, J. Iber. Geol., 30, 143–181, 2004.

Tsartsidou, G., Lev-Yadun, S., Albert, R.-M., Miller-Rosen, A., Efstratiou, N., and Weiner, S.: The phytolith archaeological record: strengths and weaknesses evaluated based on a quantitative modern reference collection from Greece, J. Archaeol. Sci., 34, 1262–1275, https://doi.org/10.1016/j.jas.2006.10.017, 2007.

Twiss, P. C., Suess, E., and Smith, R. M.: Morphological classification of grass phytoliths, Soil Sci. Soc. Am. Pro., 33, 109–115, https://doi.org/10.2136/sssaj1969.03615995003300010030x, 1969.

Ullrich, B., Meyer, C., and Weller, A.: Geoelektrik und Georadar in der archäologischen Forschung: geophysikalische 3D-Untersuchungen in Munigua (Spanien), in: Einführung in die Archäometrie, edited by: Wagner, G. A., Springer, 76–93, https://doi.org/10.1007/978-3-540-71937-3, 2007.

Weihrauch, C.: Phosphor-Dynamiken in Böden. Grundlagen, Konzepte und Untersuchungen zur räumlichen Verteilung des Nährstoffs, Springer Spektrum, Wiesbaden, 369 pp., https://doi.org/10.1007/978-3-658-22348-9, 2018.

Wirthner, S., Frey, B., Busse, M. D., Schütz M., and Risch A. C.: Effects of wild boar (Sus scrofa) rooting on the bacterial community structure in mixed-hardwood forest soils in Switzerland, Eur. J. Soil Biol., 47, 296–302, https://doi.org/10.1016/j.ejsobi.2011.07.003, 2011.

Zádorová, T. and Penížek, V.: Formation, morphology and classification of colluvial soils: A review, Eur. J. Soil Sci., 69, 577–591, https://doi.org/10.1111/ejss.12673 2018.

Zazo, C., Dabrio, C. J., Goy, J. L., Lario, J., Cabero, A., Silva, P. G., Bardají, T., Mercier, N., Borja, F., and Roquero, E.: The coastal archives of the last 15ka in the Atlantic–Mediterranean Spanish linkage area: Sea level and climate changes, Quatern. Int., 181, 72–87, https://doi.org/10.1016/j.quaint.2007.05.021, 2008.

E&G Quaternary Sci. J., 71, 145–162, 2022
https://doi.org/10.5194/egqsj-71-145-2022

Open Access E&G Quaternary Science Journal

Research article

Investigating the loess–palaeosol sequence of Bahlingen-Schönenberg (Kaiserstuhl), southwestern Germany, using a multi-methodological approach

Tabea Schulze[1], Lea Schwahn[1], Alexander Fülling[1], Christian Zeeden[2], Frank Preusser[1], and Tobias Sprafke[3,4]

[1]Institute of Earth and Environmental Sciences, University of Freiburg, Freiburg, Germany
[2]Rock Physics and Borehole Geophysics, Leibniz Institute for Applied Geophysics, Hanover, Germany
[3]Center of Competence for Soils, BFH-HAFL, Zollikofen, Switzerland
[4]Institute of Geography, University of Bern, Bern, Switzerland

Correspondence: Frank Preusser (frank.preusser@geologie.uni-freiburg.de)

Relevant dates: Received: 14 May 2022 – Revised: 6 July 2022 – Accepted: 20 July 2022 – Published: 23 August 2022

How to cite: Schulze, T., Schwahn, L., Fülling, A., Zeeden, C., Preusser, F., and Sprafke, T.: Investigating the loess–palaeosol sequence of Bahlingen-Schönenberg (Kaiserstuhl), southwestern Germany, using a multi-methodological approach, E&G Quaternary Sci. J., 71, 145–162, https://doi.org/10.5194/egqsj-71-145-2022, 2022.

Abstract: Loess–palaeosol sequences (LPSs) are key archives for the reconstruction of Quaternary environmental conditions, but there is a lack of investigated records from the southern Upper Rhine Graben (southwestern Germany). To close this gap, a LPS at Bahlingen-Schönenberg was investigated at high resolution using a multi-method approach. Infrared stimulated luminescence screening reveals a major hiatus in the lower part of the LPS that according to luminescence dating is older than marine isotope stage (MIS) 4. The section above the hiatus formed by quasi-continuous loess sedimentation between ca. 34 and 27 ka, interrupted by phases of weak reductive pedogenesis. The fact that this pedogenesis is much weaker compared to corresponding horizons in the more northerly part of the Upper Rhine Graben could be due to regionally drier conditions caused by a different atmospheric circulation pattern at the time of deposition. Our results reinforce earlier notions that the major environmental shifts leading into the Last Glacial Maximum (LGM) of southern Central Europe significantly predate the transition of MIS 3 to 2 (ca. 29 ka). In particular, the last massive phase of loess accumulation started several thousand years prior to the arrival of glaciers in the foreland of the Alps, which raises questions regarding the source and transport paths of the dust. It is also noted that no loess dating to the LGM or the time thereafter was observed due to either a lack of deposition or later erosion.

Kurzfassung: Löss-Paläoboden Sequenzen (LPS) sind Schlüsselarchive für die Rekonstruktion von quartären Umweltbedingungen, aber es mangelt an der Untersuchung solcher Abfolgen aus dem südlichen Oberrheingraben. Um diese Lücke zu schließen, wurde eine LPS bei Bahlingen-Schönenberg mit einem multimethodischen Ansatz hochauflösend untersucht. Die Untersuchung mit Infrarot Stimulierter Lumineszenz Screening zeigt einen Hiatus im unteren Teil der LPS, der laut Lumineszenzdatierungen älter ist als das Marine Isotopenstadium (MIS) 4. Der Abschnitt oberhalb des Hiatus bildete sich durch quasi-kontinuierliche Lössablagerung zwischen ca. 34 und 27 ka, unterbrochen von Phasen

schwacher reduktiver Pedogenese. Da die Pedogenese im Vergleich zu entsprechenden Horizonten im nördlicheren Teil des Oberrheingrabens viel schwächer ausgeprägt ist, könnte dies auf regional trockenere Bedingungen zurückzuführen sein, verursacht durch ein anderes atmosphärisches Zirkulationsmuster zur Zeit der Ablagerung. Unsere Ergebnisse bestätigen frühere Annahmen, dass die großen Umweltveränderungen, die zum letzten glazialen Maximum (LGM) im südlichen Mitteleuropa führten, deutlich vor dem Übergang von MIS 3 zu 2 (ca. 29 ka) lagen. Insbesondere begann die letzte massive Phase der Lössakkumulation mehrere tausend Jahre vor der Ankunft der Gletscher im Alpenvorland, was Fragen zu den Quellen und Transportwegen des Staubs aufwirft. Es ist auch festzustellen, dass kein Löss aus dem LGM oder der Zeit danach gefunden wurde, entweder aufgrund fehlender Ablagerung oder späterer Erosion.

1 Introduction

Loess is among the most abundant Pleistocene sediments in Central Europe, and thick loess–palaeosol sequences (LPSs) are key archives to reconstruct Quaternary palaeoenvironments (e.g. Lehmkuhl et al., 2016; Sprafke, 2016). On the one hand, a warm to moderately temperate humid climate leads to the formation of different types of soils (depending on the nature and timing of climate conditions). On the other hand, a cool to cold dry climate is often characterised by the accumulation of loess but requires at least a grassland vegetation cover (mammoth steppe) to trap the dust. Furthermore, the subaerially deposited dust undergoes quasi-pedogenic or quasi-diagenetic processes, known as loessification, that result in the typical aggregation of loess (cf. Sprafke and Obreht, 2016; Smalley and Obreht, 2018). Another relevant question regards the source of the dust and its transport paths, which appear rather complex (e.g. Pye, 1995; Smalley, 1995; Wright, 2001; Smalley et al., 2009). For loess deposits found in proximity to formerly glaciated areas, it is usually assumed that dust formation is caused by different forms of grinding related directly to ice contact and meltwater streams, producing fine-grained debris also known as glacier milk. However, fine-grained sediment production is likely also related to different types of periglacial processes including frost shattering and abrasion during slope processes.

Another feature that is common in many LPS, but that has seen very limited attention in loess research, is the presence of hiatuses in the records (e.g. Huayu et al., 2006; Steup and Fuchs, 2017). In fact, most kinds of soil formation will form a break or massive reduction in sediment accumulation. Furthermore, LPSs feature unconformities, i.e. erosional boundaries, when parts of pre-existing loess and palaeosols have been removed (Meszner et al., 2013; Sprafke, 2016; Lehmkuhl et al., 2016; Zöller et al., 2022). In theory, this can be induced by three different processes, soil creep, sheet erosion (by water), and deflation, all of which are related to different climatic conditions.

In Central Europe, the Rhine represents the main drainage of the northwestern Alps with frequent occurrences of LPSs on both sides of the river (Lehmkuhl et al., 2016, 2021). Due to its direct connection to the Alps, the onset of the last phase of loess accumulation along the river Rhine should be directly related to the advance of glaciers towards their last maximum extent (Last Glacial Maximum, LGM). For the Swiss Alps, the chronology of the last advance is rather well constrained, and glaciers did reach the foreland likely shortly after 30 ka (reviewed by Stojakowits et al., 2021). The maximum of the last glaciation was reached around 24–25 ka, followed by rapid decay of ice within a few thousand years (e.g. Gaar et al., 2019). Interestingly, it has been demonstrated that the last massive phase of loess accumulation already started soon after 35 ka, as shown at the sites of Schwalbenberg (Fischer et al., 2021), Nussloch (Antoine et al., 2001, 2009; Moine et al., 2017), and Möhlin (Gaar and Preusser, 2017). A substantial increase in sediment accumulation rate peaking around 32 ka is also observed at Bergsee, a macro-fossil radiocarbon-dated lake record that is only a few kilometres' distance from the Möhlin site in the Rhine Valley (Dupratt-Oualid et al., 2017). In summary, there is a clear offset between the onset and likely even the peak in dust flux, as well as theoretical assumptions regarding dust availability in the context of the last glaciation in this part of Central Europe.

A suitable area to further investigate the above issues would be the southern part of the Upper Rhine Graben, an area located directly downstream of the formerly glaciated areas of the Swiss Alps and the Black Forest (Preusser et al., 2011; Hofmann et al., 2020). In particular the Kaiserstuhl area, an extinct volcanic complex formed during the Miocene (Rotsein and Schaming, 2011), is well-known for its wide-spread loess deposits, mainly on its northern and eastern flanks (Smalley et al., 1973; Guenther, 1961, 1987). However, the most recent studies of the loess deposits in the Kaiserstuhl area were published more than 30 years ago (Guenther, 1987; Zöller et al., 1988; Zöller and Wagner, 1990) and do not represent the present stage of methodology. In particular, there have been substantial improvements in luminescence dating since the late 1980s, which allow for robust age control as a prerequisite to investigate the regional connection between mountain glaciations, glaciofluvial re-

sponse, regional dust dynamics, palaeovegetation, and soil formation.

The LPS Bahlingen-Schönenberg (coordinates: 48.124312° N, 7.731780° E) is located on a small plateau west of the village Bahlingen at the northeastern Kaiserstuhl (Fig. 1), where up to 20 m deep, largely vegetated hollow ways are present. Where the road reaches its highest point, a 7 m high loess cliff without obvious palaeosols is present. The section investigated here is a 5 m thick profile starting 1.5 m below the disturbed top of the loess cliff. In order to develop a robust stratigraphy from this weakly differentiated LPS, we analyse colour (spectrophotometer), granulometry (laser diffraction), magnetic susceptibility, and organic matter and carbonate content (loss on ignition – LOI 550 and 950 °C, respectively) of samples taken at 5 cm resolution. Infrared stimulated luminescence (IRSL) screening at 10 cm resolution is applied to evaluate the chronostratigraphic continuity of the LPS, whereas numerical ages are derived from quartz optically stimulated luminescence (OSL) and feldspar multi-elevated-temperature (MET) post-IR IRSL (pIR). Besides establishing the chronology of the site investigated, this is also a test to check the performance of the applied proxy data and dating approaches and estimate their potential for future studies in the region.

2 Materials and methods

2.1 Profile preparation and sampling

In order to minimise impact to the loess cliff, which is located next to a road, we carefully prepared a 60 cm wide and 30 cm deep trench with spades and scratchers. A general profile description was carried out based on observed colour and structural differences. For sedimentary analyses, including determination of organic and carbonate content, grain size analysis, and colour measurements, samples at 5 cm resolution were taken as continuous column (Antoine et al., 2009; Fig. 2). For luminescence dating, 11 samples were collected using metal tubes with a length of 10–15 cm and a diameter of ca. 7 cm. These were hammered into the profile every 50 cm. These samples were also used for the determination of water absorption capacity. About 51 samples were taken for IRSL screening using small and opaque plastic tubes hammered about 3 cm into the profile every 10 cm (Fig. 2c).

2.2 Colour measurements

For colour measurements at the University of Bern, a ColorLite sph850 spectrophotometer was used on air-dried fine earth (Sprafke, 2016). The measuring diameter is 3.5 mm, the observer angle 10°, and the light source corresponds to D65, emitted from six LEDs. With this spectrophotometer wave lengths from 400 to 700 nm can be measured with a spectral resolution of 3.5 nm. The measuring head was gently pushed into the loose sample material until it was completely sealed from daylight. Between two triplicate measurements at different sample positions, the sample material was stirred. After every 10th measurement the spectrophotometer was calibrated using a white standard disc. All data (various colour variables, remission spectra) were exported to Microsoft Excel© tables with the spectrophotometer software ColorDaTra 1.0.181.5912. After checking for outliers, mean values for each sample were calculated and visualised as real colours based on RGB variables. RGB tuning in three steps was done according to Sprafke et al. (2020) to determine subtle colour variations in the weakly differentiated profile. Variations between oxidative and reductive colours are indicated by the warm–cold value (WCV) according to Sprafke et al. (2013) as the ratio between the spectral reflectance values of 600–700 nm divided by the values of 400–500 nm. Variations in lightness are represented by the L^* value of the CIELAB colour space (Viscarra Rossel et al., 2006).

2.3 Grain size analysis

Grain sizes were determined with laser diffraction spectrometry (LDS), using a Malvern Mastersizer 3000 at the University of Freiburg. The Mastersizer 3000 determines the particle size indirectly by irradiating a suspension with a laser and evaluating the generated angles and intensities of scattered light. For measurements the samples were dried at 105 °C for at least 12 h and sieved through a mesh size of 1 mm. 1–2 g of the subsample < 1 mm was dispersed for 12 h with 50 ml liquid consisting of 33 g $Na_6O_{18}P_6$ and 7 g Na_2CO_3 dissolved in 1 L of distilled water (Abdulkarim et al., 2021). The standard operating procedure for every sample comprised five measurements for each sample and the calculation of grain sizes after the Mie theory of light scattering. After measurements, the data were exported to a Microsoft Excel© worksheet, and average values for each sample were calculated out of the five measurements using MATLAB R2021a. Clay contents determined by LDS strongly underestimate clay contents determined by classical pipette methods; therefore, we use the boundary of 6.3 µm as equivalent to pipette clay measurements (cf. Makó et al., 2017). To interpret changes in wind intensity and dynamics, the grain size index (GSI: [percent between 20 and 63 µm] / [percent < 20 µm]) was calculated (Antoine et al., 2009).

2.4 Determination of organic carbon and carbonate content

After removing the pore water by drying at 105 °C, the samples were pestled with a mortar and sieved through a 2 mm sieve. About 1 g, referred to as dry weight DW_{105}, was weighed out and put in a crucible with known weight. For the determination of organic carbon content, the material was burned in a first cycle at 550 °C for 5 h in a Nabertherm muffle (Heiri et al., 2001). Afterwards the crucible was weighed. The LOI is calculated in weight percentage (wt %) out of the

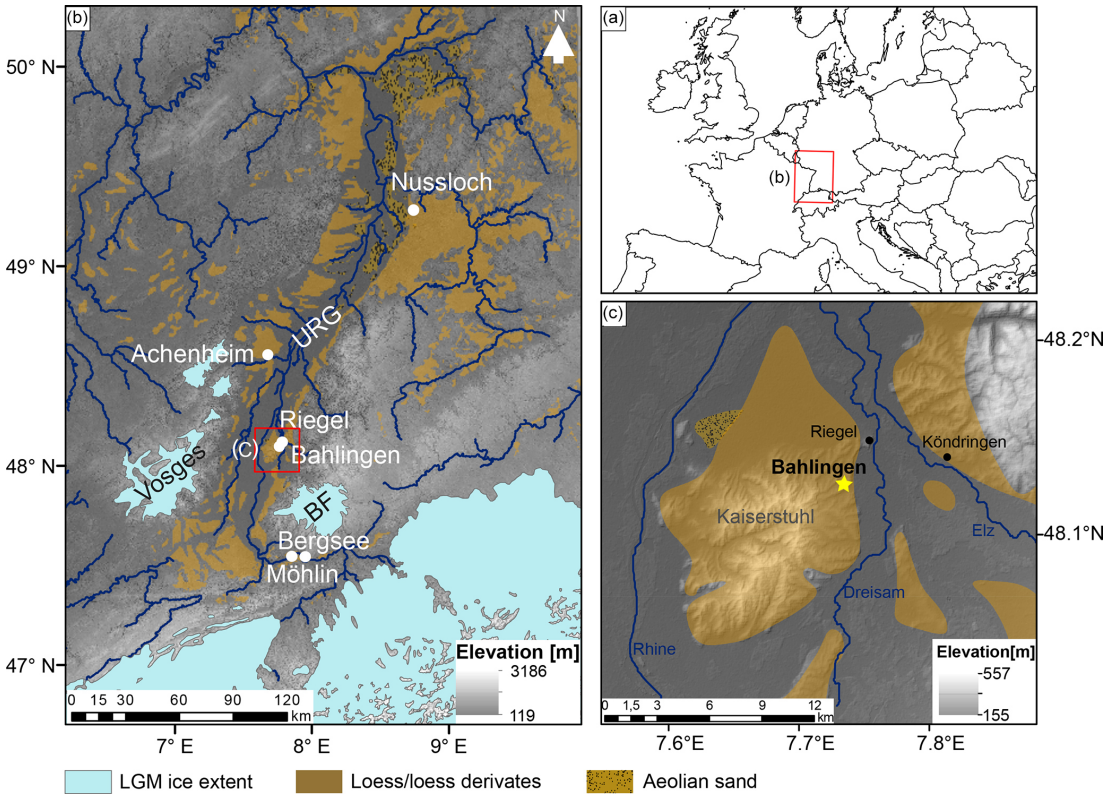

Figure 1. **(a)** Location of the study region in Europe and **(b)** a digital elevation model (DEM) of the Upper Rhine Graben (URG) and its surroundings. The URG is bordered by the Vosges in the west and the Black Forest (BF) in the east. The river Rhine flows along the centre of the graben, and the Kaiserstuhl volcanic range of hills is located in its eastern part. Displayed are also the extent of glaciers during the maximum of the last glaciation (ca. 24 ka) and the aeolian deposits. **(c)** The investigated profile is situated in the northeastern part of the Kaiserstuhl on a plateau (Schönenberg) to the west of the village of Bahlingen (yellow star) (map of Germany from https://www.landkartenindex.de/, last access: 1 April 2022; DEM based on Shuttle Radar Topography Mission (SRTM) data, provided by USGS and processed with ArcMap 10.6.1; distribution of aeolian sediments following Lehmkuhl et al., 2021, and ice extent following Ehlers et al., 2011).

dry weight and the weight measured after the 550 °C burning cycle (Heiri et al., 2001). As per Meyers and Lallier-Verges (1999), the calculated LOI after the 550 °C burning cycle is twice the real organic carbon content. Therefore, the calculated data are bisected to obtain the organic carbon content in a last step. The carbonate content was determined in a second burning cycle, which comprised burning for a further 3 h at 950 °C (Heiri et al., 2001). The LOI after 950 °C can be calculated similarly to the LOI after 550 °C, out of the dry weight, the weight measured after the 550 °C burning cycle, and the weight measured after the 950 °C burning cycle (Heiri et al., 2001). Since carbon dioxide has a molar mass of $\sim 44\,\mathrm{g\,mol^{-1}}$ and carbonate (CO_3^{-2}) has a mass of $60\,\mathrm{g\,mol^{-1}}$, the LOI_{950} has to be multiplied by the ratio of these two masses (1.36) to obtain the carbonate content in the sample (Bengtsson and Enell, 1986; Heiri et al., 2001).

2.5 Magnetic susceptibility

For magnetic susceptibility (weight normalised; χ) measurements, carried out at the Leibniz Institute for Applied Geophysics in Grubenhagen, samples were dried, homogenised, and placed in non-magnetic plastic boxes of $6.4\,\mathrm{cm^3}$ in a way that material is fixed and cannot move. The χ was measured in alternating fields of 505 and 5050 Hz with $400\,\mathrm{A\,m^{-1}}$ using a MAGNON VFSM (variable field susceptibility metre), providing both low-field χ and frequency dependency of the χ. χ is given weight-normalised, taking weights of samples and boxes into account. Temperature-dependent χ was measured following Zeeden et al. (2021) in an Argon atmosphere for five samples (depths: 1.00, 2.60, 2.65, 3.20, 3.95 m) using an AGICO CS3 high-temperature furnace.

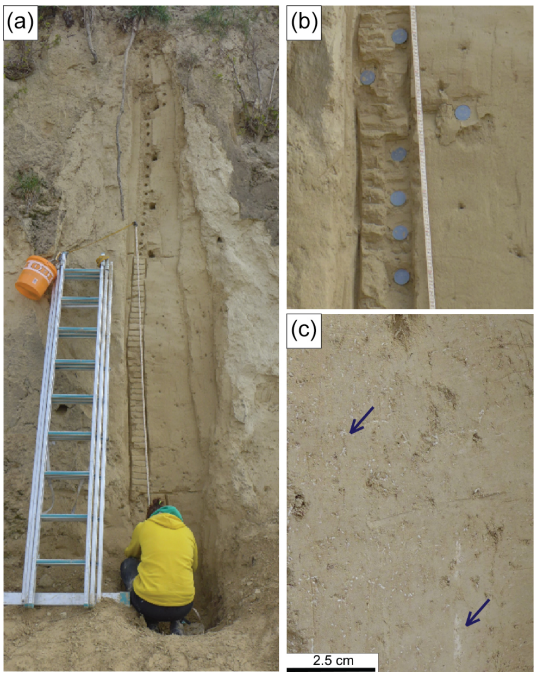

Figure 2. **(a)** The 5 m high loess profile Bahlingen-Schönenberg situated below 1.5 m thick loess disturbed by roots, pedogenesis, and agricultural activity. Note that macroscopically only a few colour changes are visible, mainly related to varying moisture. Small holes at around 1 m height and from 1.8 to 2.6 m were caused by carbonate concretions that fell out. **(b)** Plastic tubes hammered into the loess profile every 10 cm for IRSL screening. **(c)** Examples of pseudomycelia (secondary carbonate of former grass root channels).

2.6 Luminescence screening and dating

2.6.1 Methodological background

During the past decades, luminescence dating has established as key method for constraining the age of LPS (e.g. Roberts, 2008). The advantage of the method is that it allows us to directly determine the age of dust deposition, uses the omnipresent quartz and feldspar minerals, and has a dating range potentially reaching back several hundreds of thousands of years. However, luminescence dating is quite laborious and is affected by several methodological challenges (e.g. Preusser et al., 2008; Rittenour, 2018). While quartz and feldspar overall share the underlying physics, the two minerals have some important differences in luminescence properties. Quartz is known to have an OSL signal that is quickly reset by daylight and to be stable over geological periods (e.g. Preusser et al., 2009). It is hence usually preferred in dating applications. However, depending on provenance, the quartz OSL signal can have problematic properties (e.g. Preusser et al., 2006; Steffen et al., 2009), it may have limited age range due to low saturation dose (e.g. Faershtein et al., 2019), and yet a poorly understood underestimation of quartz has been observed on some occasions (e.g. Lowick et al., 2010; Anechitei-Deacu et al., 2018). Since feldspar usually shows both bright signals and a much higher saturation level, this mineral has attracted a lot of attention over the last 15 years. However, feldspar IRSL is known to contain signal components that are not stable with time. This phenomenon, known as anomalous fading (Wintle, 1973), is explained by the tunnelling of electrons within the crystal structure and will cause underestimation of IRSL ages. While several procedures have been suggested to correct for fading (e.g. Huntely and Lamothe, 2001; Kars et al., 2008), these are all based on measuring signal loss (i.e. the fading rate) over short periods of time (hours to months). The signal loss is then extrapolated to geological time periods (thousand to hundred thousand of years), assuming fading is constant with time and independent of environmental condition such as temperature.

To overcome the need of fading correction, it has been suggested to remove the unstable IRSL component by a first measurement and collect a more stable signal during subsequent stimulations at elevated temperature (Thomsen et al., 2008; Buylaert et al., 2009). This procedure is known as post-IR IRSL and has seen increasingly frequent application since its original development (see review by Zhang and Li, 2020). A modification of the original approach was introduced by Li and Li (2011), who introduced a protocol during which IRSL is subsequently stimulated at increasingly higher temperatures at 50°C increments. The advantage of this MET approach is that it delivers additional information as the degree of stability at higher temperatures is usually at the cost of bleachability of the signal (Kars et al., 2014). Furthermore, higher stimulation temperatures may be affected by changes of sensitivity that may lead to incorrect estimates (e.g. Zhang, 2018). As a consequence, despite the huge potential to expand the dating range, application of the MET post-IR IRSL approach is not always straightforward.

Due to the time and costs required for producing luminescence ages, portable luminescence readers have been used in particular to identify potential breaks in sedimentary sequences in the field (see review by Munyikwa et al., 2021). A similar approach is to take samples to the laboratory but reduce the amount of preparation and simplify the measurement procedures to speed up the required time for receiving preliminary age information (e.g. Roberts et al., 2009; May et al., 2018). This approach is referred to as screening.

2.6.2 IRSL screening

In the red-light laboratory, the outer ca. 1 cm of the sample material from the light-contaminated ends of the sampling tubes was discarded. Samples were then dried at 50 °C for at least 24 h and gently pestled in a mortar. Part of the material gained this way was fixed on small steel sample discs that were previously coated with a thin layer of silicon oil (6 mm stamp) so that the sample material would stick to the surface during measurement. For each sample, three subsamples were generated. Measurements were done on a Lexsyg Smart

device (Freiberg Instruments; Richter et al., 2015) with the detection window centred at 410 nm. The measurement protocol comprised IRSL stimulation (850 nm, 130 mW cm^{-3}) of the natural signal (Ln) and that induced by laboratory irradiation (Tn, ca. 22 Gy, source dose rate ca. 0.1 Gy s^{-1}), both after heating to 250 °C (preheat) and using a stimulation at 50 °C (Table S1 in the Supplement). The ratio Ln/Tn was calculated based on the IRSL emission recorded during the first 20 s of stimulation, after subtracting the last 20 s as background.

2.6.3 Luminescence dating

Under red-light laboratory illumination, 5 cm sample material from the light-contaminated ends of the metal tubes was removed and used for gamma spectrometry and determination of water absorption capacity. From the inner sample material, due to the shortage of sand, the fraction 63–250 µm was gained by wet sieving, first being treated with hydrochloric acid (ca. 20 %) to remove carbonates, followed by treatment with hydrogen peroxide (30 %) to remove organic components. After each chemical treatment the material was washed with distilled water. A feldspar ($\delta < 2.58$ g cm^{-3}) and quartz fraction ($\delta > 2.58$, $\delta < 2.70$ g cm^{-3}) was subsequently isolated by density separation (LST Fastfloat©). The quartz fraction was etched with 40 % hydrofluoric acid for 60 min to dissolve any feldspar contamination and remove the outer layer of the grains. For measurements, grains were mounted on metal discs with a 2 mm stamped spot of silicon oil (ca. 100 grains).

All equivalent dose (D_e) measurements were done on a Lexsyg Standard device (Freiberg Instruments; Richter et al., 2013). Overall, the amount of sand-size grains was quite low which limited the number of replicate measurements. Quartz OSL was measured using a slightly modified version of the single aliquot regenerative dose (SAR) protocol originally developed by Murray and Wintle (2000, 2003; Table S2). Stimulation was done by green LEDs (525 nm, 90 mW cm^{-2}) with application of a detection window centred at 365 nm (Schott BG39 3 mm plus Delta BP 365/50 EX Interference 5 mm). For feldspar, the MET post-IR IRSL following Li and Li (2011) was used (Table S3), with stimulation centred at 850 nm (300 mW cm^{-2}) and detection peak at 410 nm (Schott BG39 3 mm plus AHF BrightLine 414/46 interference filter). For all samples, mean D_e was calculated using the central age model (Galbraith et al., 1999) as individual D_e values are normally distributed and show overdispersion values < 20 % (most between 10 % and 15 %), which is considered to indicate well-bleached samples. The only exceptions apply to quartz OSL of the lower two samples, which is discussed below.

Material for water absorption capacity tests and measurement of dose-rate-relevant elements was dried at 105 °C for at least 12 h, ground, and sieved < 2 mm. Water absorption capacity was determined after DIN 18132 using an Enslin–Neff apparatus. This resulted in an average value of 38 ± 2 %. The present-day water content was measured to 6 ± 3 %, with the highest value of 10 % determined for the lower part of the sequence that was better protected from drying out. While water uptake capability gives the maximum value of the unconsolidated material, present-day water content likely represents a minimum estimate due to drying of sediment close to the surface of the exposure. Hence, an average water content of 20 ± 5 % was used in the calculations.

High-resolution gamma spectrometry was carried out using a high-purity germanium (HPGe) detector (ORTEC GMX30P4-PLB-S, n-type coaxial, 30 % efficiency, 1.9 keV FWHM (full width at half maximum) at 1.33 MeV, detector diameter 54.8 mm, end cap diameter 70 mm, liquid nitrogen cooling). Plastic containers with a volume of ca. 130 cm^3 were completely filled with homogenised sediment, sealed with adhesive tape, and stored for at least a month to build up equilibrium between radon and its daughters. After storage, the sample containers were measured for several days to determine the activities of primordial radionuclides ^{40}K, ^{232}Th, and ^{238}U. The detector is installed in a lead shielding to minimise the influence of the environmental radioactivity. Additionally, a blank sample (empty container) was measured to account for background radiation. The ^{238}U content was determined by analysing the peaks of the ^{226}Ra daughters ^{214}Pb (295.2 and 351.9 keV) and ^{214}Bi (609.3, 1120.3, 1764.5 keV). The ^{234}Th line at 63.3 keV was used to quantify a possible radioactive disequilibrium in the ^{238}U decay chain. The ^{232}Th content was determined by analysing the peaks of the ^{228}Ra daughter ^{228}Ac (338.3, 911.1, 969.1 keV) and the ^{228}Th daughters ^{212}Pb (238.6 keV) and ^{208}Tl (583.2 keV). ^{40}K was measured directly at 1460.8 keV. The weighted mean of all selected peaks was then calculated to determine the activities of the parent radionuclides ^{238}U and ^{232}Th.

Dose rates (Table S4) and ages were calculated using the software ADELE v2017 (Degering and Degering, 2020; https://www.add-ideas.de/, last access: 1 April 2022), which uses the dose rate conversion factors of Guérin et al. (2011). Cosmic-ray dose rates were corrected for geographic position and burial depth following Prescott and Hutton (1994). All ages are given at 1σ level with reference to the year of sampling (2021 CE).

2.6.4 Age–depth modelling

Age–depth models of both OSL and pIR-200 dates were constructed using the model of Zeeden et al. (2018). This method establishes an age–depth model from luminescence ages without making assumptions regarding sedimentation rate or the sedimentation process itself. It involves an inverse model and uses a conservative measure for the random part of the overall uncertainty. In this case, uncertainty is dominantly of random nature because the mean luminescence ages show several inversions which we assign to random uncertainty.

3 Results

3.1 Profile description

The investigated profile consists of silt-dominated loess with only subtle colour differences, notably a slightly darker tone in the lowermost metre (Fig. 3). Throughout the section, there are concretions of iron and/or manganese of 1–3 mm in size, pseudomycelia (secondary carbonate of former grass root channels; Fig. 2c), and snail shells and shell fragments. Sieving to < 250 µm for luminescence dating confirmed that larger components in this profile are mainly calcified root cells, carbonate cemented silty pore walls, and shell fragments. From 1 to 1.35 m several loess dolls were observed with a diameter of ∼ 3 cm, and from 2.1 to 2.8 m their diameter was 1–2 cm. The occurrences of snail shells, manganese concretions, and loess dolls in the profile stratigraphy are shown in Fig. 3. The stratigraphic subdivision into four main units (I–IV), each with four to nine subunits, was finally defined based on quantitative colour and grain size data (cf. Sprafke et al., 2020).

3.2 Colour and stratigraphy

Field and untuned RGB colours indicate a weak stratigraphic differentiation of the profile, which becomes clearer by enhanced RGB colours (Fig. 3). The WCV (range: 1.8–2.1) and the L^* value (range: 64–67) differentiate the main colour components. The inversely plotted WCV and the L^* value show largely similar variations, indicating that major deviations from loess colour are pale blue and slightly darker brownish horizons. Unit VI at the bottom of the sequence has the highest WCV of the profile (> 1.95) due to an overall light brown colour. L^* values from < 65 to 66 indicate a gradient from brown to pale brown colours from bottom to top, leading to the classification of Bw and BC or CB horizons, respectively. Unit III has the highest L^* values (> 66) of the whole profile in its lower part; the WCV differentiates greyish (C[r]) from brownish (CA and CB) horizons. Units II and I have a comparable colour pattern with different C(r) and CA or CB horizons.

3.3 Grain size composition

The granulometry reveals the predominance of coarse silt (20–63 µm; 45 %–60 %) and a mode of 20–25 µm throughout the profile (Fig. 3). Little sand (< 1.6 %) is present, mainly in Units I and IIIe to VI. The mean grain size of the profile is coarse silt, and only in Unit IVd is it partly medium–fine silt (20–6.3 µm). The GSI ranges approximately between 1 and 2.5 and has more or less the same pattern as the mean grain size, with maxima in Units I and III and minima in Units II and IV (Fig. 3). Clay content (LDS particles < 6.3 µm) varies largely parallel to the GSI between 6 % and 12 % in Units I–III and has its maximum (ca. 14 %) in Unit IV. Sand contents vary largely parallel to the GSI. However, in Unit III the GSI has much more pronounced variability compared to sand contents.

3.4 Organic carbon, carbonate content, and magnetic susceptibility

In general, the organic carbon content (C_{org}) varies relatively constant around 1 wt % along the profile, with no clear relation to stratigraphy (Fig. 3). A distinct peak at 3.5 m, along with comparably low carbonate contents, was confirmed by repeated measurement establishing that this is a real sample property. These unusual values may relate to a crotovine with soil material (low carbonate, high C_{org}) not recognised during sampling. Carbonate contents vary between 19 % and 24 %, with the highest values in Unit IV and minima in Units IIIa–c. Small oscillations are usually parallel to the inversely plotted contents of C_{org}, indicating these parameters are rather antagonists. Overall carbonate contents appear largely opposite to the GSI, which means that finer loess has higher carbonate contents. This trend is not confirmed in Unit I, where carbonate contents remain constant, despite the highest sand contents.

Mass-specific χ values oscillate around 12–$14 \times 10^{-8}\,m^3\,kg^{-1}$. The (inversely plotted) χ shows contrasting trends to variations in carbonate content and is opposite to variations of the GSI (Fig. 3). The three χ maxima in Unit III and a distinct peak in Unit IIe, all corresponding to CA horizons, do not follow this general pattern. In these horizons, the carbonate contents are also the lowest. The thin or less pronounced CA horizon IIb and IIg do not show χ maxima and carbonate minima. Generally, χ is low compared to other loess localities in Eurasia but comparable to loess of similar age from Nussloch (Taylor and Lagroix, 2015). The temperature-dependent magnetic susceptibility properties are similar to loess in Willendorf, Austria (Zeeden and Hambach 2021). The susceptibility stays rather constant until 250 °C, increases towards 300 °C, then decreases until ∼ 420 °C, and increases towards ∼ 550 °C. From this maximum during heating, the susceptibility decreases sharply towards ∼ 600 °C and continues to decrease from ∼ 600 to 700 °C (Fig. 4). This pattern is observed for all samples; therefore, only one is shown in Fig. 4.

3.5 IRSL screening

The IRSL screening results show two distinct groups of Ln/Tn values (Fig. 3). The first group comprises Unit IV and is characterised by Ln/Tn values between 5.4 and 6.1. In comparison to the second group the distribution is partly scattered and shows some increase in Ln/Tn values with increasing height. This indicates either a change in dose rate or the presence of partial bleaching of the IRSL signal prior to deposition in some of the samples. The second group comprises Units I to III and is characterised by Ln/Tn values between 1.7 and 2.2, with a single outlier of 2.6 at a height of

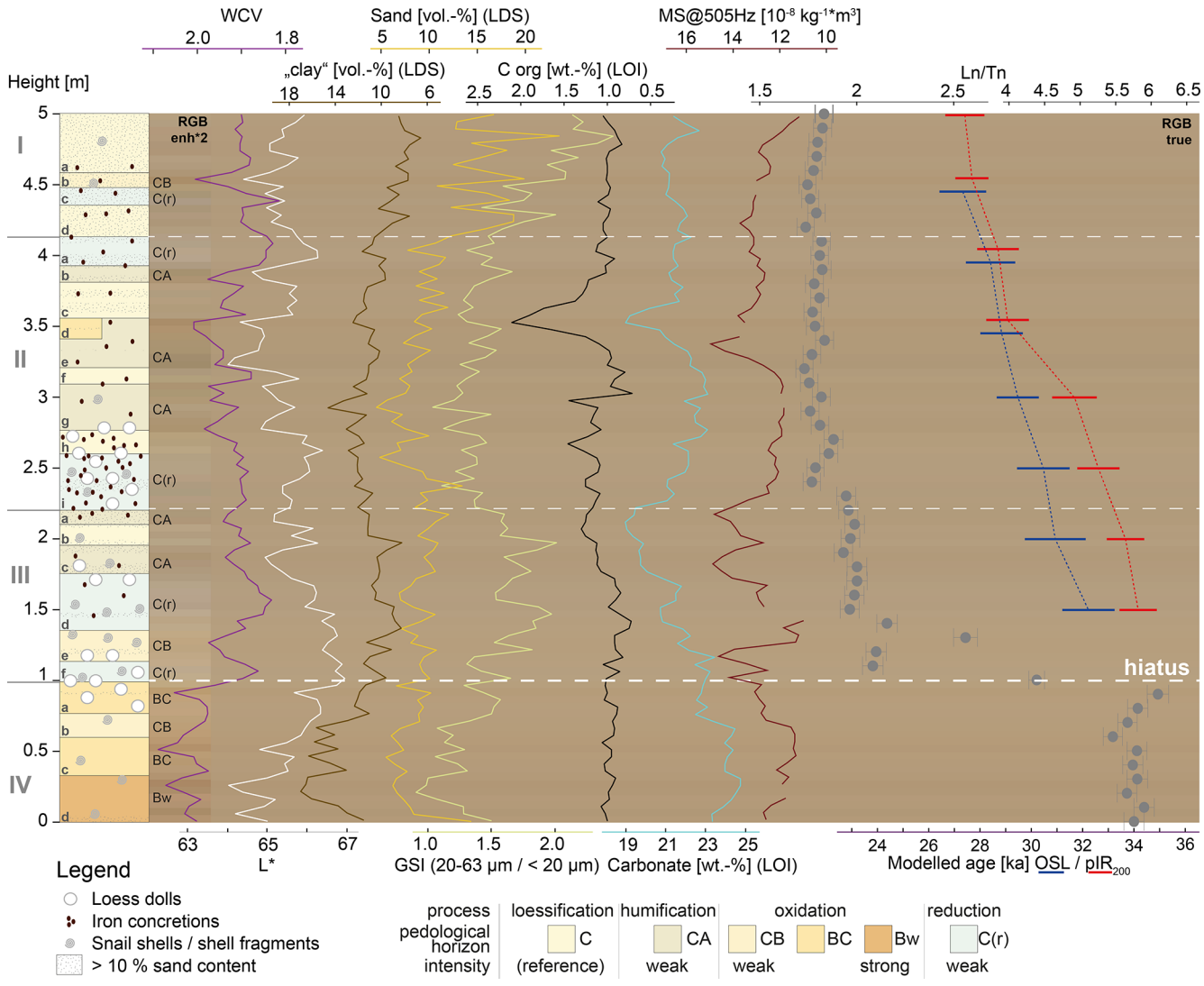

Figure 3. Stratigraphy and main laboratory data with two times enhanced RGB colours behind pedological horizons and true RGB colours behind the data plots. Data peaks oriented to the left indicate enhanced oxidative soil formation, and peaks to the right indicate more aeolian activity and reductive pedogenesis. "Clay" refers to the LDS fractions < 6.3 µm (see "Materials and methods" section). Note the change in scale of the luminescence screening results (Ln/Tn).

1.3 m. The values are not perfectly aligned and show smaller offsets, namely at a height of 1.45, 1.85, 2.35, 2.55, 2.75, 2.95, 3.35, and 4.05 m. However, the second group of values appears overall quite homogeneous with limited variability in the Ln/Tn values. The most likely explanation for the observed two groups of Ln/Tn values appears to be a large hiatus in between Units III and IV. The sample taken across the expected hiatus between Units III and IV, which was not obvious in the field, has a Ln/Tn value of 4.4, which represents the average of the Ln/Tn values directly above and below.

3.6 Luminescence dating

Originally, 11 samples were taken for luminescence dating at intervals of 50 cm along the profile. Due to the likely hiatus within the profile at a height of 1 m, the sample taken at this height (across the hiatus) was discarded. For all investigated samples, the quartz OSL signals are moderately bright and show a rather rapid decay, reaching background within ca. 2 s of stimulation (note that green stimulated OSL decays much slower than blue stimulated OSL). The shape of the OSL decay curves of the natural and artificially irradiated sample is similar, and OSL growth curves fit well when using the sum of exponential saturating functions (Fig. 5a). Unfortunately, the amount of quartz remaining after sample preparation was low for several samples, which limited the number of replicate measurements (Table S5). The feldspar signals are also only moderately bright but much brighter than quartz OSL. Interestingly, the growth curves of IRSL

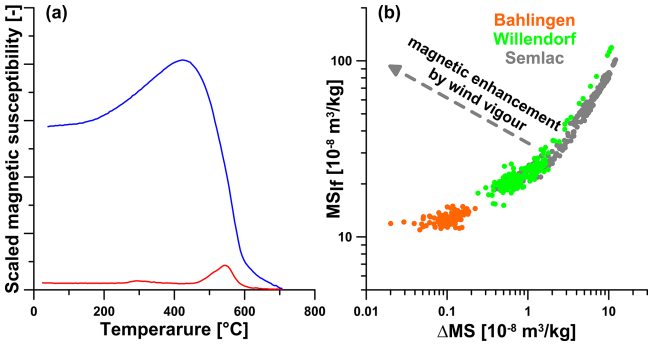

Figure 4. **(a)** Temperature-dependent susceptibility heating (red) and cooling curve (blue). Note that during heating the main decrease in susceptibility occurs around 600 °C, indicative of magnetite. **(b)** Comparison of the magnetic susceptibility and its frequency dependence to the loess sections of Willendorf and Semlac (Zeeden et al., 2016; Zeeden and Hambach, 2021). This shows both the low susceptibility and also the low-frequency dependence. Because the frequency dependence is lower than also pure loess at Semlac, water logging and the associated decrease in at least the frequency-dependent susceptibility are assumed. No strong indication for wind vigour is present.

and the different post-IR IRSL signals show pronounced differences in shape (Fig. 5b). While IRSL and pIR-100 have a quite similar behaviour, pIR-150 shows a much steeper shape of the growth curve. Both the pIR-200 and pIR-250 show a much flatter shape of dose response.

All luminescence ages are presented in Table 1. The determined ages confirm the hiatus between the lower (Unit IV) and upper part (Units I to III) of the profile (Fig. 3). The samples from above the hiatus are internally consistent but show significant differences between the different approaches (Fig. 6). The average ratios in relation to OSL (excluding the top and two bottom samples) are 0.53 ± 0.03 (IRSL), 0.76 ± 0.05 (pIR-100), 0.93 ± 0.05 (pIR-150), 1.04 ± 0.06 (pIR-200), and 1.16 ± 0.08 (pIR-250). The differences are likely explained by signal instability, as well as the effect of partial bleaching and/or thermal transfer, as discussed later in the paper.

For the samples from below the hiatus at 1 m, sample BL-0 has an OSL age of 101.9 ± 13.9 ka and sample BL-50 an OSL age of 96.0 ± 16.1 ka. However, these ages are only based on 3 and 10 replicate measurements, respectively, which calls for caution with regard to the chronological interpretation. The corresponding pIR ages show a significant offset and are internally not consistent; sample BL-50 (pIR-200: 205.7 ± 8.4 ka) shows a clearly older age than the underlying samples BL-0 (pIR-200: 149.8 ± 8.3 ka), as is discussed further below.

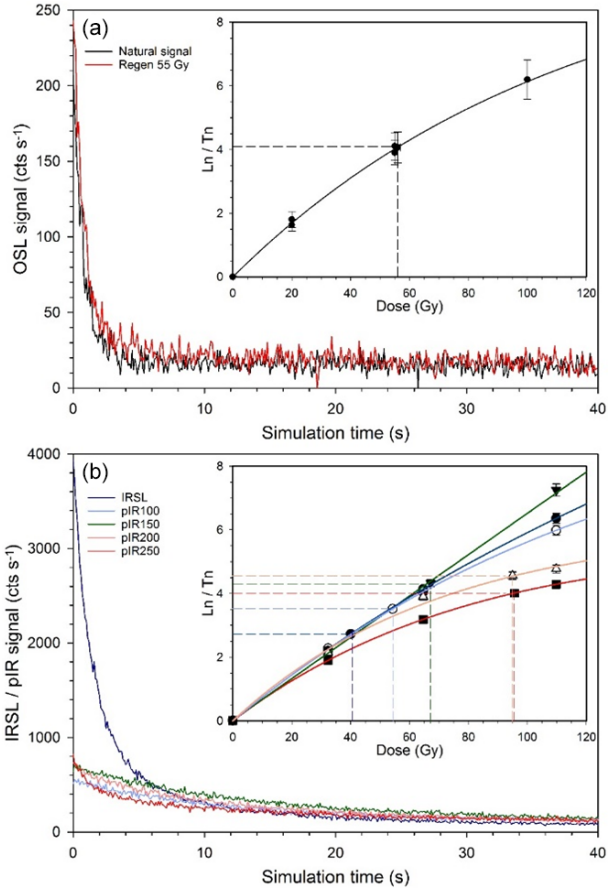

Figure 5. Example of luminescence characteristics. **(a)** Quartz extracted from sample BAL-200 reveals rather weak OSL emissions but a similar decay shape for both the natural and laboratory-induced signal. Dose response curves are well described by a single-exponential saturating function. **(b)** IRSL decay curves are several times brighter than for pIR. The shape of the IRSL and pIR growth curves is significantly different for the different approaches. Both pIR-200 and pIR-250 show a less steep increase compared to lower stimulation temperatures, implying an earlier saturation level.

4 Discussion

4.1 Variations in proxy data

In the field, the LPS Bahlingen gives the impression of weakly differentiated loess with some loess-specific features such as loess dolls, snails shells, and iron/manganese concretions. Luminescence screening, confirmed by the dating results, indicates a major hiatus between Units IV and III. There is no indication of major erosional phases within Units I–III; therefore, this part of the profile will likely have recorded subtle palaeoenvironmental variations during a quasi-constant build-up. While granulometry of weakly differentiated LPSs largely reflects changes in sedimentation dynamics (Antoine et al., 2009; Schulte et al., 2018), changes in colour, χ, C_{org}, and possibly clay content are sensitive to

Table 1. Ages determined at 50 (IRSL), 100, 150, 200, and 250 °C using the MET pIR protocol are shown for the different profile heights, as well as the ages determined using quartz and a SAR protocol (OSL). Ages are given in kiloyears before the year of sampling (2021).

Height (cm)	OSL (ka)	IRSL (ka)	pIR-100 (ka)	pIR-150 (ka)	pIR-200 (ka)	pIR-250 (ka)
500	23.1 ± 2.0	15.6 ± 0.5	19.2 ± 0.7	24.1 ± 1.0	27.6 ± 1.1	30.9 ± 1.3
450	27.0 ± 1.2	14.7 ± 0.5	19.5 ± 0.7	23.6 ± 0.7	27.4 ± 0.9	29.6 ± 1.0
400	29.3 ± 1.4	14.6 ± 0.5	21.7 ± 0.9	25.9 ± 0.9	29.2 ± 1.0	32.0 ± 1.2
350	28.4 ± 1.2	14.9 ± 0.5	20.3 ± 0.7	25.1 ± 0.9	27.5 ± 1.1	30.7 ± 1.0
300	29.4 ± 1.2	15.4 ± 0.5	20.9 ± 0.9	27.4 ± 0.9	31.7 ± 1.2	36.0 ± 1.3
250	31.0 ± 1.4	16.6 ± 0.7	24.7 ± 1.2	29.2 ± 1.3	32.6 ± 1.2	36.9 ± 2.0
200	29.6 ± 1.7	17.3 ± 0.6	25.0 ± 1.1	30.3 ± 1.0	33.7 ± 1.1	37.8 ± 1.8
150	32.7 ± 1.3	17.3 ± 0.6	25.8 ± 0.9	30.8 ± 1.0	34.2 ± 1.1	38.4 ± 1.3
50	96.0 ± 16.1	99.6 ± 5.5	146.8 ± 9.3	185.3 ± 7.1	205.7 ± 8.4	210.3 ± 11.4
0	101.9 ± 13.9	68.4 ± 3.6	110.4 ± 6.7	133.4 ± 6.0	149.8 ± 8.3	157.8 ± 9.6

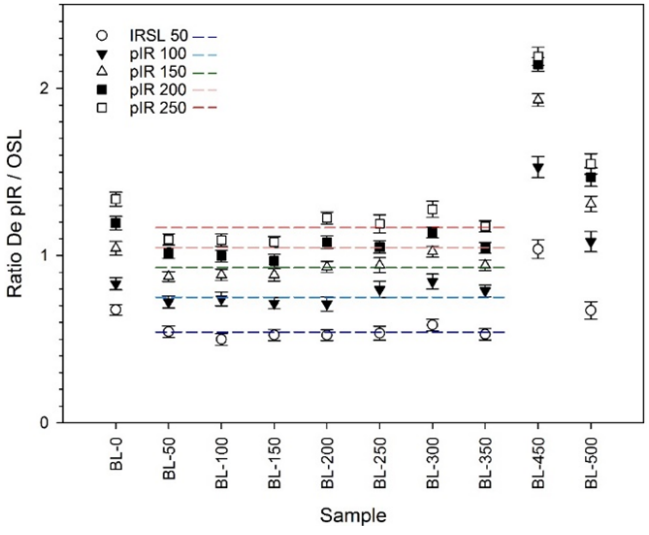

Figure 6. Comparison of IRSL/pIR versus OSL ratios calculated for all samples investigated in this study. Most samples (BL-50 to BL-350) reveal rather similar ratios. The ratio for the two samples from below the lower discontinuity show higher ratios, which reflects either an underestimation of OSL or, more likely, overestimation of IRSL and pIR due to incomplete bleaching of the signal. Furthermore, the top sample (BL-50) also reveals a consistently higher ratio, which is interpreted to reflect an underestimation of the OSL age in this case.

post-sedimentary alteration, i.e. pedogenesis (Sprafke et al., 2020).

Initial soils from loess are usually characterised by enhanced amounts of organic matter, although in palaeosols this is usually lower than in surface soils due to decomposition, while dark colours may persist. Buried dark steppe soils of the LPS Dolní Věstonice have much lower organic carbon contents (0.9 %–1.4 %) than surface steppe soils (ca. 5 %) (Antoine et al., 2013). Advanced development of pedogenesis under warm and humid climate leads to decalcification, oxidation, and clay formation by hydrolysis (Sprafke, 2016); this usually goes along with increasing χ in the course of soil formation (e.g. Heller et al., 1993; Bradak et al., 2021, and references therein). In the presence of permafrost and in the absence of dust deposition, reduced soils form if sufficient soil moisture is present. This will lead to greyish colours, commonly the formation of iron/manganese concretions (Antoine et al., 2009; Terhorst et al., 2015), and possibly the leaching of iron and a reduction of magnetic susceptibility (e.g. Baumgart et al., 2013, and references therein).

Located on a plateau position, the presence of reworked soils and sediments can largely be excluded for the LPS Bahlingen-Schönenberg, and the applied multi-parameter approach is expected to reveal phases of initial pedogenesis (Schulte et al., 2018; Sprafke et al., 2020; Vlaminck et al., 2018). Unit IV appears to be a moderately pigmented pedocomplex with enhanced clay content, but at the same time it contains the highest amount of carbonate throughout the profile and exhibits no increase in χ. This is contrary to common models of pedogenesis on loess, in which oxidation (increase in brownish pigments, higher χ) and clay formation (by hydrolysis) most efficiently take place after decalcification (Stahr et al., 2020). At the LPS Krems-Wachtberg East, loess and brownish (BC) horizons contain 27 % and 18 % of carbonate, respectively, indicating that in the presence of easy weatherable iron-bearing silicates (there: biotite) no complete decalcification is required for brunification (Meyer-Heintze et al., 2018). Yet, at Bahlingen-Schönenberg even higher carbonate values in brownish loess compared to unaltered loess can only be explained by secondary enrichment. We hypothesise that Unit IV was enriched in carbonate during leaching of a formerly superimposed but now eroded and well-developed palaeosol. This does not exclude brunification and changes in magnetic susceptibility in the presence of carbonate. Low magnetic susceptibility may be related to leaching of iron due to high precipitation during pedogenesis (e.g. Ma et al., 2013).

Rather weak colour variations indicate the absence of well-developed palaeosols in Units I–III. It is challenging to link the colour-supported stratigraphy to the other parameter variations as there is no unidirectional pathway of pedogenic alteration, and changes in original sedimentary properties cannot be excluded. It is surprising that Units IIe and IIg share the same colour tone but have distinct differences in C_{org} and carbonate contents, as well as χ. This deviation is independent of some contamination (IId) likely due to a crotovine.

Coarse silt and fine sand content, as well as the GSI, show a rather similar pattern, contrasting with the variations observed for clay to medium silt content. In the absence of significant weathering and reworking, changes in wind speed as represented by the GSI likely explain most variations in granulometry (Antoine et al., 2009). Another explanation could be changing sediment sources or changes in source granulometry and vegetation cover (Sun et al., 2004; Schulte et al., 2016). Units I and III have a higher content of coarse silt to fine sand, possibly indicating more frequent dust storms during their formation (Antoine et al., 2009).

In Units II to III, carbonate contents vary in opposite pattern to the GSI, indicating that coarser grain sizes contain a smaller contribution of carbonate. CA horizons found in Units IIe, IIIa, and IIc do not only have darker pigments but are characterised by higher χ and lower carbonate contents, possibly indicating initial soil formation. Besides these initial terrestrial palaeosols, there are several pale horizons that likely correspond to very weak tundra gley soils that formed under waterlogged conditions (semi-terrestrial) above permafrost (Antoine et al., 2009, Sprafke et al., 2020). Yet, granulometry and magnetic susceptibility show little sensitivity for these initial palaeosols.

The χ values at Bahlingen-Schönenberg are rather low compared to other Central European loess sections, and it has been shown that χ is influenced by a suite of processes (e.g. Baumgart et al., 2013). The low χ is likely partly caused by a high proportion of quartz and other coarse diamagnetic materials diluting the magnetic signal. Yet, χ oscillates in the same range as χ at the LPS Nussloch and also has a close relation to GSI variations. At Nussloch, enhancement of χ, together with a higher GSI, is explained by a higher proportion of relatively dense (i.e. heavier) magnetite minerals delivered from the Rhine floodplain (Antoine et al., 2009). This wind-vigour model of magnetic enhancement in glacial loess is known from Alaska (Begét and Hawkins, 1989) and Siberia (Chlachula et al., 1998), and it likely also explains the present observations. Here, the effect of dissolution of fine magnetic particles most likely contributes to the feature of the low-frequency dependency of χ. Coarse magnetic particles are too large to be completely dissolved during water logging conditions.

We interpret the temperature-dependent susceptibility properties (Fig. 4) as indicative for contributions of both magnetite and hematite. Here, the decrease in the susceptibility at $\sim 580\,^{\circ}C$ is interpreted to represent the Curie temperature of magnetite. The further decrease in χ towards $700\,^{\circ}C$ is interpreted as a contribution of hematite; whether this is an original signal or an effect of heating is at this point uncertain, but sediment colour does not speak for a major contribution of hematite. These properties imply that more or less typical loess is present; a large quantity of the iron is originally not in a strongly magnetic phase.

4.2 Luminescence screening and dating

IRSL screening has proven here as a fast (measurements required only ca. 48 h machine time) and low-cost method to identify qualitative variations in the stored luminescence signal. This helped to quickly identify the substantial hiatus between Units III and IV that was not obvious in the field and to discard the sample that was taken exactly on the hiatus. The age from this sampling tube contains grains from above and below the hiatus, which would have produced a mixed age without much value. Nevertheless, in comparison to actual dating the method only provides semi-quantitative results, and small variations in the measured luminescence signal should not be overinterpreted.

For the upper part of the sequence (Units I to III), the OSL ages are within the time range usually considered to yield reliable results. Hence, the OSL ages are considered as reference. Whereas the lower IRSL, pIR-100, and pIR-150 ages are likely underestimated due to fading (Li and Li, 2011), the higher pIR-250 ages possibly relate to hard-to-bleach components or thermal transfer (Preusser et al., 2014) and may thus overestimate the real age of deposition. As a consequence, it appears that the pIR-200 ages should be regarded as the most reliable, and these indeed fit mainly well with the OSL ages. One exception is the topmost sample BL-500, which shows much higher ratios of IRSL and pIR versus OSL age (Fig. 6). In fact, the OSL age of this sample is some 4000 years younger than those determined for the rest of the sequence above the hiatus. However, neither the IRSL and pIR ages nor the IRSL screening data nor the stratigraphy point towards a major hiatus in this part of the sequence. Hence, it appears appropriate to rather favour the pIR-200 age (27.6 ± 1.1 ka) as being more reliable than the OSL of this sample. While there is no obvious explanation supporting the apparent underestimation of this particular OSL age, it should be noted that it is based on only 10 replicate measurements (due to material shortage), compared to 20 to 30 carried out for most other samples.

Two semi-independent age–depth models were constructed for both OSL and pIR-200 (Fig. 3). We excluded the lower part of the sequence from the age–depth model as, first, including only two samples appears to be too few, second, the number of quartz replicate measurements is very low, and, third, the feldspar ages are inconsistent. While underestimation of quartz has been reported from loess (e.g. Anechitei-Deacu et al., 2018), this is usually for higher D_e

values than those observed here. The higher apparent pIR ages could rather be explained by partial bleaching of the signal prior to deposition, which could be due to short distance reworking of sediment (Yi et al., 2016) in a potentially different geomorphological setting than at present (plateau situation). Due to the limited number of ages and the inconsistency with pIR, we only attribute a minimum age of ca. 100 ka for this part of the sequence. It must be the target of future studies to investigate the nature of the hiatus (soil micromorphology) and its spatial appearance (palaeotopography), as well as to address the chronological position in more detail.

4.3 Upper Pleniglacial chronostratigraphy

The OSL age–depth model indicates quasi-constant loess accumulation from ca. 33 to 27 ka. The pIR-200 age model is largely similar for the sequence above 3 m, whereas below, the mean ages are systematically ca. 2000 years older. According to this age model, loess accumulation may have started around 35 ka and continued until ca. 27 but was interrupted (hiatus) at around 30 ka (Figs. 3 and 7). There is no independent numerical or relative stratigraphic age control in support of either the OSL or the pIR-200 age model. Tundra gley soils and other palaeosols are very weakly developed at the LPS Bahlingen-Schönenberg, challenging pedostratigraphic inferences. The variations in the GSI at Bahlingen largely differ for the GSI of the contemporary part of the LPS Nussloch. At Nussloch the GSI is low before 30 ka and during later interstadials is represented by tundra gley soils, whereas at Bahlingen, the sequence older than 30 ka has distinct GSI peaks and lacks a GSI peak corresponding to the first major Nussloch loess event around 30 ka (Fig. 7). As we did not observe evidence for loess reworking, this pattern is likely related to a distinct aeolian deposition regime at Bahlingen.

Despite the uncertainties related to different age models and the lack of information from the disturbed upper 1.5 m of the outcrop, the available age information from the LPS Bahlingen-Schönenberg clearly shows that the major period of dust deposition predates the Alpine LGM (25–24 ka). Linearly extrapolating the age models to the top of the sequence results in ages of not more than 25 ka. Hypothetically, several metres of previously deposited loess could have been removed by erosion, but our local survey along the hollow lanes did not reveal thick packages of reworked loess. Assuming that the apparent lack of deposition during and after the LGM is real, this is in a way in disagreement with the classical notion that glaciations in the upper reaches of river systems enhance silt production, fluvial and eventually aeolian transport, and deposition (Smalley et al., 2009). A possible scenario would be that during the LGM the local climate at the topographically exposed loess plateau west of Bahlingen was too cold and/or dry (polar-desert-like ecosystem) to support vegetation cover capable of capturing relevant quantities of windblown dust (Sirocko et al., 2016; Sprafke et al., 2020). The hiatus around 30 ka suggested by the pIR-200 age model may be explained in a similar way (Fig. 7), as during the time of Heinrich Event 3 very harsh environmental conditions prevailed from western to Central Europe (Starnberger et al., 2011; Fuhrmann et al., 2021). While the LPS Nussloch likely had sufficient vegetation cover during the Heinrich events and the LGM to collect thick amounts of mineral dust, recorded as loess events (Antoine et al., 2009), the LPS Krems-Wachtberg (Lower Austria) records phases of erosion and reworking attributed to polar-desert-like ecosystems (Sprafke et al., 2020). The lack of loess deposition at Bahlingen-Schönenberg during Heinrich Event 3 and the LGM may equally be explained by the local presence of polar-desert-like ecosystems during these periods.

The OSL age model suggests continuous dust deposition starting around 33 ka, without a clear effect of Heinrich Event 3 (Fig. 7). A slightly earlier onset of loess accumulation around 34–35 ka, as suggested by the pIR-200 model, is in agreement with results from the LPS Nussloch, where loess above the Lohne soil is robustly dated to ca. 35 ka (Gocke et al., 2014; Moine et al., 2017). This represents the transition from the Middle Pleniglacial to the Upper Pleniglacial of the last glacial period, corresponding to the end of Greenland Interstadial 7 (Antoine et al., 2009; Moine et al., 2017). It is possible that at Bahlingen-Schönenberg a Lohne soil equivalent has overprinted the upper part of Unit IV, below the major hiatus, but there are no data to support this assumption. The weak tundra gley soils at 1.0 to 3.5 m height could stratigraphically correspond to the G1 and G2 tundra gley soils at Nussloch that formed before 30 ka, correlative to the Erbenheim soil E0 (Lehmkuhl et al., 2016). These early Upper Pleniglacial tundra gley soils likely correspond to Greenland Interstadials 5 and 6. Taking the OSL age model into account, also the CA horizon at 3 m height may still be part of this suite of weak palaeosols; in this case we can tentatively attribute it to the very weak Greenland Interstadial 5.1 (Fig. 7).

Considerable mineral dust accumulation peaking around 34–29 ka is also reported from the LPS Möhlin (Gaar and Preusser, 2017), ca. 100 km upstream of the Rhine and the nearby Bergsee lacustrine record (Duprat-Oualid et al., 2017). There is no evidence for contemporary major glacier advances into the upstream Swiss Alpine forelands, but Alpine palaeoglacier dynamics and regional palaeoenvironments were likely favourable to contribute to downstream aeolian silt deposition. It appears that Alpine glaciers only advanced into the forelands around 30 ka (Gaar et al., 2019), apparently coinciding with Heinrich Event 3 (Starnberger et al., 2011). Interestingly, none of the dust records in the region (Bahlingen, Bergsee, Möhlin) recorded an increased dust accumulation during and after the LGM, calling for more data to unravel the regional response to the large-scale palaeoclimatic and palaeoenvironmental evolution. Yet, our results strongly support the notion that the Middle to Up-

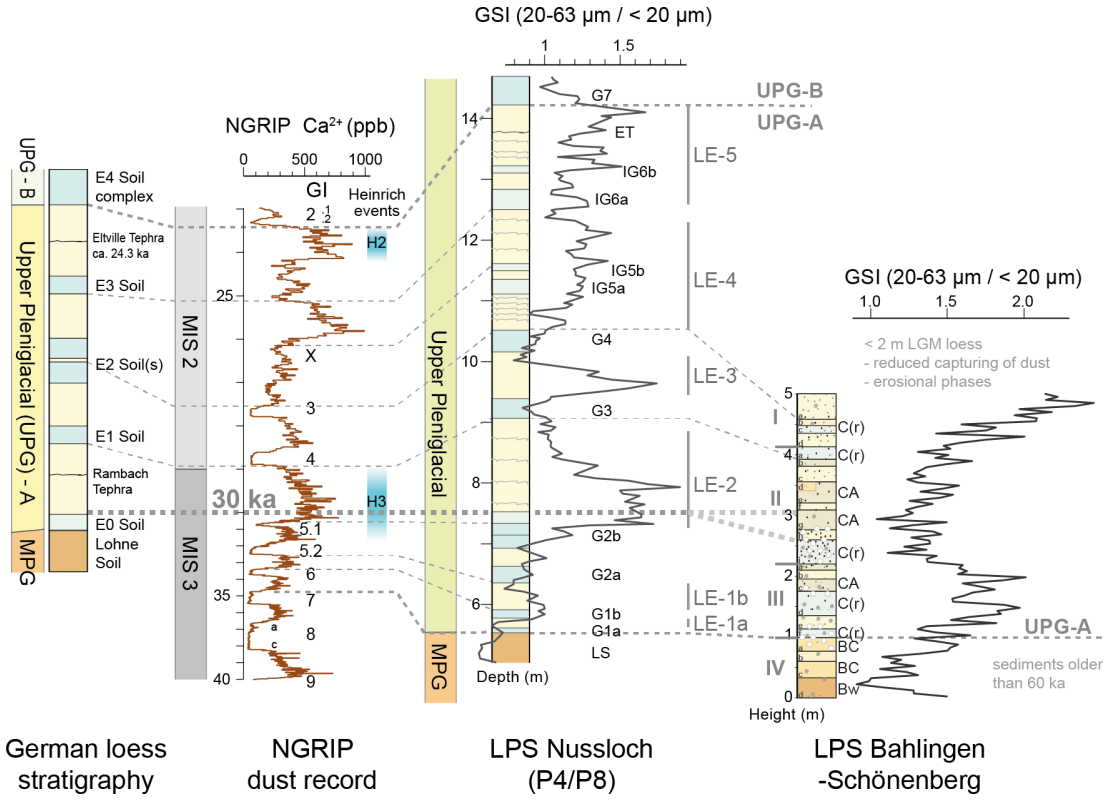

Figure 7. LPS Bahlingen-Schönenberg stratigraphy and GSI record in comparison to the LPS Nussloch (Antoine et al., 2009; Moine et al., 2017), correlated to the North Greenland Ice Core Project (NGRIP) dust record from 40 to 23 ka (Rasmussen et al., 2014), and German loess stratigraphy (Lehmkuhl et al., 2016). UPG = Upper Pleniglacial; MPG = Middle Pleniglacial.

per Pleniglacial transition, as recorded in Central European loess, predates the marine isotope stage (MIS) 3–2 transition (29 ka; Lisiecki and Raymo, 2005) by ca. 5000 years, as also recognised in other LPSs (Antoine et al., 2009, Terhorst et al., 2015, Lehmkuhl et al., 2016, Sprafke et al., 2020).

4.4 Upper Pleniglacial palaeoenvironments

In the classical German loess stratigraphy, originally developed in the northern part of the Upper Rhine Graben (URG; Schönhals et al., 1964; Semmel, 1967), the Upper Pleniglacial often comprises up to five well-developed tundra gleys, named Erbenheim soils after the type locality in southwestern Hesse. The Upper Pleniglacial loess record of Nussloch contains even nine tundra gley complexes of varying intensity. The absence of well-developed tundra gleys at the LPS Bahlingen-Schönenberg is striking but possibly represents a regional phenomenon as such palaeosols have so far not been reported from the southern URG (Guenther, 1987). Krauss et al. (2016) explain weakly developed tundra gleys in LPSs of the northern Harz foreland by drier palaeoclimatic conditions. At present, this region receives less than 600 mm of mean annual precipitation, compared to 600–700 mm in the northern URG and > 800 mm at Nussloch (Institut für Länderkunde, 2003). Bahlingen receives > 800 mm precipitation; therefore, present-day climatic conditions are no adequate reference to explain the absence of tundra gleys in the studied LPS. High dust accumulation rates equally do not explain the absence of palaeosols as the contemporary part of the LPS Nussloch is even thicker, and accumulation rates at Nussloch (1.1 mm yr^{-1}) and Bahlingen-Schönenberg (0.8 mm yr^{-1}) are very similar. Carbonate contents and magnetic susceptibility of the LPS Bahlingen-Schönenberg are also similar to those of the LPS Nussloch; therefore, we can largely exclude an influence of parent material differences on palaeopedogenesis. The absence of tundra gleys in the Pannonian Basin has been related to the lack of continuous permafrost in this region (Terhorst et al. 2015). However, during the Upper Pleniglacial, the Vosges (Mercier and Jeser, 2004), Black Forest (Hofmann et al., 2020), Jura (Buoncristiani and Campy, 2004), and Alps (Preusser et al., 2011) surrounding the southern URG were covered by considerable ice masses; therefore, the absence of permafrost in the area between appears rather unlikely. Yet, this specific topographic and palaeoenvironmental framework likely caused a specific regional palaeoclimate. A possible scenario to explain the absence of tundra gley soils in the Upper Pleniglacial loess of the study region could be a distinct pattern of precipitation during this period. While the missing presence of tun-

dra gleys in the southern URG has to be confirmed, a possible explanation would be the southern advection of precipitation during the LGM, first suggested by Florineth and Schlüchter (2000) and later promoted by several other authors (e.g. Kuhlemann et al., 2008; Monegato et al., 2017; Gribenski et al., 2021). The underlying precipitation pattern would place the southern URG in a rain shadow position north of the Alps that could have been less pronounced further north. However, a robust palaeoenvironmental interpretation of pale horizons in the southern URG requires more detailed studies on this and other regionally distributed loess profiles. For the URG, a reliable pedo- and chronostratigraphic scheme of the Late Pleistocene remains to be established. For the LPS Nussloch, a clear connection of Upper Pleniglacial tundra gley soils to Greenland interstadials was possible only through a very robust age–depth model, based on radiocarbon dating of calcified earthworm casts (Moine et al., 2017).

5 Conclusions

The loess profile of Bahlingen-Schönenberg is the first LPS from the southern Upper Rhine Graben that has been investigated using a multi-method approach. While the site shows little stratigraphic differentiation and no typical response of palaeoenvironmental proxies, it covers a relatively short period of time (ca. 7000 years) at high resolution, covering the onset of the Upper Pleniglacial and the MIS 3–2 transition. IRSL screening has shown its potential as a tool that may help to quickly and cost-efficiently identify gaps in sedimentation and could be used in the future to position samples for luminescence dating more efficiently. Identifying the nature of and possible causes producing the hiatus observed in the lower part of Bahlingen-Schönenberg requires more detailed work in the surroundings. The sequence above the hiatus is characterised by weakly developed tundra gleys that are less intensely developed as tundra gleys found in the same stratigraphic position in the middle and northern part of the Upper Rhine Graben. It is here hypothesised that this could be due to drier regional climate during the time of their formation, possibly caused by the different circulation pattern over the North Atlantic and Europe that has already been deduced from the analyses of glacial features. Another interesting fact is the lack of loess dating to the LGM and the time thereafter. This could be explained either by lack of loess deposition during that time due to wind speed that is too high and/or a lack of vegetation required to fix the dust or by substantial erosion during the late glacial period and early Holocene before the area was occupied by dense vegetation. More regional palaeoenvironmental records are required to further address the above research questions in the future.

Data availability. Relevant data are given either in the main text or in the supplement.

Supplement. The supplement related to this article is available online at: https://doi.org/10.5194/egqsj-71-145-2022-supplement.

Author contributions. FP, ToS, and AF conceptualised this study. Fieldwork and most laboratory analyses were carried out by TaS and LS, under the supervision of FP, ToS, and AF. Luminescence dating was carried out by AF and magnetic susceptibility measurements by CZ. CZ calculated the age models. The original draft was prepared by ToS and FP, based on the MSc thesis written by TaS. All authors contributed by additional writing, reviewing, and editing.

Competing interests. At least one of the (co-)authors is a member of the editorial board of *E&G Quaternary Science Journal*. The peer-review process was guided by an independent editor, and the authors also have no other competing interests to declare.

Disclaimer. Publisher's note: Copernicus Publications remains neutral with regard to jurisdictional claims in published maps and institutional affiliations.

Special issue statement. This article is part of the special issue "Quaternary research from and inspired by the first virtual DEUQUA conference". It is a result of the vDEUQUA2021 online conference in September/October 2021.

Acknowledgements. The authors thank Jan-Hendrik May, University of Melbourne, for inspiring discussions regarding the concepts of landscape dynamics and sediment flux in the Upper Rhine Graben. Many thanks to Robert Peticzka, University of Vienna, for providing the spectrophotometer.

Financial support. This open-access publication was funded by the University of Freiburg.

Review statement. This paper was edited by Hans von Suchodoletz and reviewed by Markus Fuchs and Ludwig Zoeller.

References

Abdulkarim, M., Grema, H. M., Adamu, I. H., Mueller, D., Schulz, M., Ulbrich, M., Miocic, J. M., and Preusser, F.: Effect of using different chemical dispersing agents in grain size analyses of fluvial sediments via laser diffraction spectrometry, Methods and Protocols, 4, 44, https://doi.org/10.3390/mps4030044, 2021.

Anechitei-Deacu, V., Timar-Gabor, A., Constantin, D., Trandafir-Antohi, O., Valle, L. D., Fornós, J. J., Gómez-Pujol, L., and Wintle, A. G.: Assessing the maximum limit of SAR-OSL dating using quartz of different grain sizes, Geochronometria, 45, 146–159, https://doi.org/10.1515/geochr-2015-0092, 2018.

Antoine, P., Rousseau, D.-D., Zöller, L., Lang, A., Munaut, A.-V., Hatte, C., and Fontugne, M.: High-resolution record of the last Interglacial-glacial cycle in the Nussloch loess-palaeosol sequences, Upper Rhine Area, Germany, Quatern. Int., 76/77, 211–229, https://doi.org/10.1016/S1040-6182(00)00104-X, 2001.

Antoine, P., Rousseau, D.-D., Moine, O., Kunesch, S., Hatte, C., Lang, A., Tissoux, H., and Zöller, L.: Rapid and cyclic aeolian deposition during the Last Glacial in European loess: a high-resolution record from Nussloch, Germany, Quaternary Sci. Rev., 28, 2955–2973, https://doi.org/10.1016/j.quascirev.2009.08.001, 2009.

Antoine, P., Rousseau, D.-D., Degeai, J.-P., Moine, O., Lagroix, F., Kreutzer, S., Fuchs, M., Hatte, C., Gauthier, C., Svoboda, J., and Lisa, L.: High-resolution record of the environmental response to climatic variations during the Last Interglacial-Glacial cycle in Central Europe: the loess-palaeosol sequence of Dolní Vestonice (Czech Republic), Quaternary Sci. Rev., 67, 17–38, https://doi.org/10.1016/j.quascirev.2013.01.014, 2013.

Baumgart, P., Hambach, U., Meszner, S., and Faust, D.: An environmental magnetic fingerprint of periglacial loess: records of Late Pleistocene loess–palaeosol sequences from Eastern Germany, Quatern. Int., 296, 82–93, https://doi.org/10.1016/j.quaint.2012.12.021, 2013.

Begét, J. and Hawkins, D.: Influence of orbital parameters on Pleistocene loess deposition in central Alaska, Nature, 337, 151–153, https://doi.org/10.1038/337151a0, 1989.

Bengtsson, L. and Enell, M.: Chemical analysis, in: Handbook of Holocene Palaeoecology and Palaeohydrology, edited by: Berglund, B. E., John Wiley & Sons Ldt., Chichester, 423–451, ISBN 978-1-930665-80-4, 1986.

Bradák, B., Seto, Y., Stevens, T., Újvári, G., Fehér, K., and Költringer, C.: Magnetic susceptibility in the European Loess Belt: New and existing models of magnetic enhancement in loess, Palaeogeogr. Palaeoclimatol. Palaeoecol., 569, 110329, https://doi.org/10.1016/j.palaeo.2021.110329, 2021

Buoncristiani, J. F. and Campy, M.: Expansion and retreat of the Jura Ice sheet (France) during the last glacial maximum, Sediment. Geol., 165, 253–264, https://doi.org/10.1016/j.sedgeo.2003.11.007, 2004.

Buylaert, J. P., Murray, A. S., Thomsen, K. J., and Jain, M.: Testing the potential of an elevated temperature IRSL signal from K-feldspar, Radiat. Meas., 44, 560–565, https://doi.org/10.1016/j.radmeas.2009.02.007, 2009.

Chlachula, J., Evans, M. E., and Rutter, N. W.: A magnetic investigation of a Late Quaternary loess/palaeosol record in Siberia, Geophys. J. Int., 132, 128–132, https://doi.org/10.1046/j.1365-246x.1998.00399.x, 1998.

Degering, D. and Degering, A.: Change is the only constant – Time-dependent dose rates in luminescence dating, Quat. Geochronol., 58, 101074, https://doi.org/10.1016/j.quageo.2020.101074, 2020.

European Standards: DIN 18132:1995-12, Soil, testing procedures and testing equipment – Determination of water absorption, https://www.en-standard.eu/din-18132-soil-testing, last access: 1 April 2022.

Duprat-Oualid, F., Rius, D., Bégeot, C., Magny, M., Millet, L., Wulf, S., and Appelt, O.: Vegetation response to abrupt climate changes in Western Europe from 45 to 14.7k cal a BP: the Bergsee lacustrine record (Black Forest, Germany), J. Quaternary Sci., 32, 1008–1021, https://doi.org/10.1002/jqs.2972, 2017.

Ehlers, J., Gibbard, P. L., and Hughes, P. D. (Eds.): Quaternary Glaciations – Extent and Chronology – A Closer Look, in: Developments in Quaternary Sciences, Elsevier, 15, 1108 pp., ISBN 9780444534477, 2011.

Faershtein, G., Porat, N., and Matmon, A.: Natural saturation of OSL and TT-OSL signals of quartz grains from Nilotic origin, Quat. Geochronol., 49, 146–152, https://doi.org/10.1016/j.quageo.2018.04.002, 2019.

Fischer, P., Jöris, O., Fitzsimmons, K., Vinnepand, M., Prud'homme, C., Schulte, P., Hatté, C., Hambach, U., Lindauer, S., Zeeden, C., Peric, Z., Lehmkuhl, F., Wunderlich, T., Wilken, D., Schirmer, W., and Vött, A.: Millennial-scale terrestrial ecosystem responses to Upper Pleistocene climatic changes: 4D-reconstruction of the Schwalbenberg Loess-Palaeosol- Sequence (Middle Rhine Valley, Germany), Catena, 196, 104913, https://doi.org/10.1016/j.catena.2020.104913, 2021.

Florineth, D. and Schlüchter, C.: Alpine Evidence for Atmospheric Circulation Patterns in Europe during the Last Glacial Maximum, Quaternary Res., 54, 295–308, https://doi.org/10.1006/qres.2000.2169, 2000.

Fuhrmann, F., Seelos, K., and Sirocko, F.: Eolian sedimentation in central European Auel dry maar from 60 to 13 ka, Quaternary Res., 101, 4–12, https://doi.org/10.1017/qua.2020.81, 2021.

Gaar, D. and Preusser, F.: Age of the Most Extensive Glaciation of Northern Switzerland: Evidence from the scientific drilling at Möhliner Feld, E&G Quaternary Sci. J., 66, 1–5, https://doi.org/10.3285/eg.66.1.er1, 2017.

Gaar, D., Graf, H. R., and Preusser, F.: New chronological constraints on the timing of Late Pleistocene glacier advances in northern Switzerland, E&G Quaternary Sci. J., 68, 53–73, https://doi.org/10.5194/egqsj-68-53-2019, 2019.

Galbraith, R. F., Roberts, R. G., Laslett, G. M., Yoshida, H., and Olley, J. M.: Optical Dating of single and multiple Grains of Quartz from Jinmium Rock Shelter, Northern Australia: Part I, Experimental Design and Statistical Models, Archaeometry, 41, 339–364, https://doi.org/10.1111/j.1475-4754.1999.tb00987.x, 1999.

Gocke, M., Hambach, U., Eckmeier, E., Schwark, L., Zöller, L., Fuchs, M., Löscher, M., and Wiesenberg, G. L. B.: Introducing an improved multi-proxy approach for paleoenvironmental reconstruction of loess–paleosol archives applied on the Late Pleistocene Nussloch sequence (SW Germany), Palaeogeogr. Palaeocl., 410, 300–315, https://doi.org/10.1016/j.palaeo.2014.06.006, 2014.

Gribenski, N., Valla, P., Preusser, F., Roattino, T., Crouzet, C., and Buoncristiani J.-F.: Out-of-phase Late Pleistocene glacier advances in the western Alps reflect past changes in North Atlantic atmospheric circulation, Geology, 49, 1096–1101, https://doi.org/10.1130/G48688.1, 2021.

Guenther, E. W.: Sedimentpetrographische Untersuchung von Lössen – Zur Gliederung des Eiszeitalters und zur Einordnung paläolithischer Kulturen – Teil 1 Methodische Grundlagen mit Erläuterung an Profilen, Böhlau Verlag, Köln, Graz, p. 10, Reihe B, Bd. 1, 1961.

Guenther, E. W.: Zur Gliederung der Lösse des südlichen Oberrheintals, E&G Quaternary Sci. J., 37, 67–78, https://doi.org/10.3285/eg.37.1.07, 1987.

Guérin, G., Mercier, N., and Adamiec, G.: Dose-rate conversion factors: Update, Ancient TL, 29, 5–8, 2011.

Heiri, O., Lotter, A. F., and Lemcke, G.: Loss on ignition as a method for estimating organic and carbonate content in sediments: reproducibility and comparability of results, J. Paleolimnol., 25, 101–110, https://doi.org/10.1023/A:1008119611481, 2001.

Heller, F., Shen, C. D., Beer, J., Liu, X. M., Liu, T. S., Bronger, A., Suter, M., and Bonani, G.: Quantitative estimates of pedogenic ferromagnetic mineral formation in Chinese loess and palaeoclimatic implications, Earth Planet. Sc. Lett., 114, 385–390, https://doi.org/10.1016/0012-821X(93)90038-B, 1993.

Hofmann, F. M., Rauscher, F., McCreary, W., Bischoff, J.-P., and Preusser, F.: Revisiting Late Pleistocene glacier dynamics northwest of the Feldberg, southern Black Forest, Germany, E&G Quaternary Sci. J., 69, 61–87, https://doi.org/10.5194/egqsj-69-61-2020, 2020.

Huayu, L., Stevens, S., Shuangwen, Y., and Xuefeng, S.; An erosional hiatus in Chinese loess sequences revealed by closely spaced optical dating, Chinese Sci. Bull., 51, 2253–2259, https://doi.org/10.1007/s11434-006-2097-x, 2006.

Huntley, D. J. and Lamothe, M.: Ubiquity of anomalous fading in K-feldspars and the measurement and correction for it in optical dating, Can. J. Earth Sci., 38, 1093–1106, https://doi.org/10.1139/e01-013, 2001.

Institut für Länderkunde: Nationalatlas der Bundesrepublik Deutschland, Band 3 – Natur und Umwelt II: Klima, Pflanzen und Tierwelt, ISBN 978-3827409560, 2003.

Kars, R. H., Wallinga, J., and Cohen, K. M.: A new approach towards anomalous fading correction for feldspar IRSL dating – tests on samples in field saturation, Radiat. Meas., 43, 786–790, https://doi.org/10.1016/j.radmeas.2008.01.021, 2008.

Kars, R. H., Reimann, T., Ankjærgaard, C., and Wallinga, J.: Bleaching of the post-IR IRSL signal: new insights for feldspar luminescence dating, Boreas, 43, 780–791, https://doi.org/10.1111/bor.12082, 2014.

Krauss, L., Zens, J., Zeeden, C., Schulte, P., Eckmeier, E., and Lehmkuhl, F.: A Multi-Proxy Analysis of two Loess-Palaeosol Sequences in the Northern Harz Foreland, Germany, Palaeogeogr. Palaeocl., 461, 401–417, https://doi.org/10.1016/j.palaeo.2016.09.001, 2016.

Kuhlemann, J., Rohling, E. J., Krumrei, I., Kubik, P., Ivy-Ochs, S., and Kucera, M.: Regional synthesis of Mediterranean atmospheric circulation during the last glacial maximum, Science, 321, 1338–1340, https://doi.org/10.1126/science.1157638, 2008.

Lehmkuhl, F., Zens, J., Krauß, L., Schulte, P., and Kels, H.: Loess-palaeosol sequences at the northern European loess belt in Germany: Distribution, geomorphology and stratigraphy, Quaternary Sci. Rev., 153, 11–30, https://doi.org/10.1016/j.quascirev.2016.10.008, 2016.

Lehmkuhl, F., Nett, J. J., Pötter, S., Schulte, P., Sprafke, T., Jary, Z., Antoine, P., Wacha, L., Wolf, D., Zerboni, A., Hošek, J., Marković, S. B., Obreht, I., Sümergi, P., Veres, D., Zeeden, C., Boemke, B., Schaubert, V., Viehweger, J., and Hambach, U.: Loess landscapes of Europe – Mapping, geomorphology, and zonal differentiation, Earth Sci. Rev., 215, 103496, https://doi.org/10.1016/j.earscirev.2020.103496, 2021.

Li, B. and Li, S.-H.: Luminescence dating of K-feldspar from sediments: A protocol without anomalous fading correction, Quat. Geochronol., 6, 468–479, https://doi.org/10.1016/j.quageo.2011.05.001, 2011.

Lisiecki, L. E. and Raymo, M. E.: A Pliocene-Pleistocene stack of 57 globally distributed benthic d18O records, Paleoceanography, 20, PA10032005, https://doi.org/10.1029/2004PA001071, 2005.

Lowick, S. E., Preusser, F., Pini, R., and Ravazzi, C.: Underestimation of quartz OSL dating towards the Eemian: comparison with palynostratigraphy from Azzano Decimo, northeastern Italy, Quat. Geochronol., 5, 583–590, https://doi.org/10.1016/j.quageo.2009.12.003, 2010.

Ma, M., Liu, X., Pillans, B. J., Hu, S., Lü, B., and Liu, H.: Magnetic properties of Dashing Rocks loess at Timaru, South Island, New Zealand, Geophys. J. Int., 195, 75–85, doi.org/10.1093/gji/ggt206, 2013.

Makó, A., Tóth, G., Weynants, M., Rajkai, K., Hermann, T., and Tóth, B.: Pedotransfer functions for converting laser diffraction particle-size data to conventional values, Eur. J. Soil Sci., 68, 769–782, https://doi.org/10.1111/ejss.12456, 2017.

May, J.-H., Marx, S. K., Reynolds, W., Clark-Balzan, L., Jacobsen, G. E., and Preusser, F.: Establishing a chronological framework for a late Quaternary seasonal swamp in the Australian "Top End", Quat. Geochronol., 47, 81–92, https://doi.org/10.1016/j.quageo.2018.05.010, 2018.

Mercier, J.-L. and Jeser, N.: The glacial history of the Vosges Mountains, Developments in Quaternary Science, 2, 113–118, https://doi.org/10.1016/S1571-0866(04)80061-7, 2004.

Meszner, S., Kreutzer, S., Fuchs, M., and Faust, D.: Late Pleistocene landscape dynamics in Saxony, Germany: Paleoenvironmental reconstruction using loess-palaeosol sequences, Quatern. Int., 296, 94–107, https://doi.org/10.1016/j.quaint.2012.12.040, 2013.

Meyer-Heintze, S., Sprafke, T., Schulte, P., Terhorst, B., Lomax, J., Fuchs, M., Lehmkuhl, F., Neugebauer-Maresch, C., Einwögerer, T., Händel, M., Simon, U., and Solís Castillo, B.: The MIS 3/2 transition in a new loess profile at Krems-Wachtberg East – A multi-methodological approach, Quatern. Int., 464, 370–385, https://doi.org/10.1016/j.quaint.2017.11.048, 2018.

Meyers, P. A. and Lallier-Verges, E.: Lacustrine sedimentary organic matter records of Late Quaternary paleoclimates, J. Paleolimnol., 21, 345–372, https://doi.org/10.1023/A:1008073732192, 1999.

Moine, O., Antoine, P., Hatté, C., Landais, A., Mathieu, J., Prud'homme, C., and Rousseau, D.-D.: The impact of Last Glacial climate variability in west-European loess revealed by radiocarbon dating of fossil earthworm granules, PNAS, 114, 6209–6214, https://doi.org/10.1073/pnas.1614751114, 2017.

Monegato, G., Scardia, G., Hajdas, I., Rizzini, F., and Piccin, A.: The Alpine LGM in the boreal ice-sheets game, Sci. Rep., 7, 2078, https://doi.org/10.1038/s41598-017-02148-7, 2017.

Munyikwa, K., Kinnaird, T. C., and Sanderson, D. C. W.: The potential of portable luminescence readers in geomorphological investigations: a review, Earth Surf. Proc. Land., 46, 131–150, https://doi.org/10.1002/esp.4975, 2021.

Murray, A. S. and Wintle, A. G.: Luminescence dating of quartz using an improved single-aliquot regenerative-dose protocol, Radiat. Meas., 32, 57–73, https://doi.org/10.1016/S1350-4487(99)00253-X, 2000.

Murray, A. S. and Wintle, A. G.: The single aliquot regenerative dose protocol: potential for improvements in reliabil-

ity, Radiat. Meas., 37, 377–381, https://doi.org/10.1016/S1350-4487(03)00053-2, 2003.

Prescott, J. R. and Hutton, J. T.: Cosmic ray contributions to dose rates for luminescence and ESR dating: Large depths and long-term time variations, Radiat. Meas., 23, 497–500, https://doi.org/10.1016/1350-4487(94)90086-8, 1994.

Preusser, F., Ramseyer, K., and Schlüchter, C.: Characterisation of low luminescence intensity quartz from Westland, New Zealand, Radiat. Meas., 41, 871–877, https://doi.org/10.1016/j.radmeas.2006.04.019, 2006.

Preusser, F., Degering, D., Fuchs, M., Hilgers, A., Kadereit, A., Klasen, N., Krbetschek, M., Richter, D., and Spencer, J. Q. G.: Luminescence dating: basics, methods and applications, E&G Quaternary Sci. J., 57, 95–149, https://doi.org/10.3285/eg.57.1-2.5, 2008.

Preusser, F., Chithambo, M. L., Götte, T., Martini, M., Ramseyer, K., Sendezera, E. J., Susino, G. J., and Wintle A. G.: Quartz as a natural luminescence dosimeter, Earth-Sci. Rev., 97, 196–226, https://doi.org/10.1016/j.earscirev.2009.09.006, 2009.

Preusser, F., Graf, H. R., Keller, O., Krayss, E., and Schlüchter, C.: Quaternary glaciation history of northern Switzerland, E&G Quaternary Sci. J., 60, 21, https://doi.org/10.3285/eg.60.2-3.06, 2011.

Preusser, F., Muru, M., and Rosentau, A.: Comparing different post-IR IRSL approaches for the dating of Holocene foredunes from Ruhnu Island, Estonia, Geochronometria, 41, 342–351, https://doi.org/10.2478/s13386-013-0169-7, 2014.

Pye, K.: The nature, origin and accumulation of loess, Quaternary Sci. Rev., 14, 653–667, https://doi.org/10.1016/0277-3791(95)00047-X, 1995.

Rasmussen, S. O., Bigler, M., Blockley, S. P., Blunier, T., Buchardt, S. L., Clausen, H. B., Cvijanovic, I., Dahl-Jensen, D., Johnsen, S. J., Fischer, H., Gkinis, V., Guillevic, M., Hoek, W. Z., Lowe, J. J., Pedro, J B., Popp, T., Seierstadt, I. K., Steffensen, J. P., Svensson, A. M., Vallelonga, P., Vinther, B. M., Walker, M. J. C., Wheatley, J. J., and Winstrup, M.: A stratigraphic framework for abrupt climatic changes during the Last Glacial period based on three synchronized Greenland ice-core records: refining and extending the INTIMATE event stratigraphy, Quaternary Sci. Rev., 106, 14–28, https://doi.org/10.1016/j.quascirev.2014.09.007, 2014.

Richter, D., Richter, A., and Dornich, K.: Lexsyg – A new system for luminescence research, Geochronometria, 40, 220–228, https://doi.org/10.2478/s13386-013-0110-0, 2013.

Richter, D., Richter, A., and Dornich, K.: Lexsyg smart – a luminescence detection system for dosimetry, material research and dating application, Geochronometria, 42, 202–209, https://doi.org/10.1515/geochr-2015-0022, 2015.

Rittenour, T. M.: Dates and rates of earth-surface processes revealed using luminescence dating, Elements, 14, 21–26, https://doi.org/10.2138/gselements.14.1.21, 2018.

Roberts, H.: The development and application of luminescence dating to loess deposits: a perspective on the past, present and future, Boreas, 37, 483–507, https://doi.org/10.1111/j.1502-3885.2008.00057.x, 2008.

Roberts, H. M., Julie A Durcan, J. A., and Duller, G. A. T.: Exploring procedures for the rapid assessment of optically stimulated luminescence range-finder ages, Radiat. Meas., 44, 582–587, https://doi.org/10.1016/j.radmeas.2009.02.006, 2009.

Rotstein, Y. and Schaming, M.: The Upper Rhine Graben (URG) revisited: Miocene transtension and transpression account for the observed first-order structures, Tectonics, 30, TC3007, https://doi.org/10.1029/2010TC002767, 2011.

Schönhals, E., Rohdenburg, H., and Semmel, A.: Ergebnisse neuerer Untersuchungen zur Würmlöß-Gliederung in Hessen, E&G Quaternary Sci. J., 15, 199–206, https://doi.org/10.3285/eg.15.1.15, 1964.

Schulte, P., Lehmkuhl, F., Steininger, F., Loibl, D., Lockot, G., Protze, J., Fischer, P., and Stauch, G.: Influence of HCl pretreatment and organo-mineral complexes on laser diffraction measurement of loess–palaeosol-sequences, Catena, 137, 392–405, https://doi.org/10.1016/j.catena.2015.10.015, 2016.

Schulte, P., Sprafke, T., Rodrigues, L., and Fitzsimmons, K. E.: Are fixed grain size ratios useful proxies for loess sedimentation dynamics? Experiences from Remizovka, Kazakhstan, Aeolian Res., 31, 131–140, https://doi.org/10.1016/j.aeolia.2017.09.002, 2018.

Semmel, A.: Neue Fundstellen von vulkanischem Material in hessischen Lössen, Notizblatt hessisches Landesamt für Bodenforschung, 95, 10–108, 1967.

Sirocko, F., Knapp, H., Dreher, F., Förster, M. W., Albert, J., Brunck, H., Veres, D., Dietrich, S., Zech, M., Hambach, U., Röhner, M., Rudert, S., Schwibus, K., Adams, C., and Sigl, P.: The ELSA-Vegetation-Stack: Reconstruction of Landscape Evolution Zones (LEZ) from laminated Eifel maar sediments of the last 60 000 years, Global Planet. Change, 142, 108–135, https://doi.org/10.1016/j.gloplacha.2016.03.005, 2016.

Smalley, I.: Making the material: The formation of silt sized primary mineral particles for loess deposits, Quaternary Sci. Rev., 14, 645–651, https://doi.org/10.1016/0277-3791(95)00046-1, 1995.

Smalley, I. and Obreht I.: The formation of loess ground by the process of loessification: a history of the concept, Geologos, 24, 163–170, https://doi.org/10.2478/logos-2018-0015, 2018.

Smalley, I., O'Hara-Dhand, K., Wint, J., Machalett, B., Jary, Z., and Jefferson, I.: Rivers and loess: the significance of long river transportation in the complex event-sequence approach to loess deposit formation, Quatern. Int., 198, 7–18, https://doi.org/10.1016/j.quaint.2008.06.009, 2009.

Smalley, I. J., Krinsley, D. H., and Vita-Finzi C.: Observations on the Kaiserstuhl loess, Geol. Mag., 110, 29–36, https://doi.org/10.1017/S0016756800047269, 1973.

Sprafke, T.: Löss in Niederösterreich – Archiv quartärer Klima- und Landschaftsveränderungen, Würzburg University Press, 42–47, ISBN 978-3827409560, 2016.

Sprafke, T. and Obreht, I.: Loess: Rock, sediment or soil – What is missing for its definition?, Quatern. Int., 399, 198–207, https://doi.org/10.1016/j.quaint.2015.03.033, 2016.

Sprafke, T., Terhorst, B., Peticzka, R., and Thiel, C.: Paudorf locus typicus (Lower Austria) revisited: The potential of the classic loess outcrop for Middle to Late Pleistocene landscape reconstructions, E&G Quaternary Sci. J., 62, 59–72, https://doi.org/10.3285/eg.62.1.06, 2013.

Sprafke, T., Schulte, P., Meyer-Heintze, S., Händel, M., Einwögerer, T., Simon, U., Peticka, R., Schäfer, C., Lehmkuhl, F., and Terhorst, B.: Paleoenvironments from robust loess stratigraphy using high-resolution color and grain-size data of the last glacial Krems-Wachtberg record (NE Austria), Quaternary Sci. Rev.,

248, 106602, https://doi.org/10.1016/j.quascirev.2020.106602, 2020.

Stahr, K., Kandeler, E., Herrmann, L. and Streck, T.: Bodenkunde und Standortlehre, 4th edn., Utb. Ulmer, Stuttgart, 327 pp., https://doi.org/10.36198/9783838553450, 2020.

Starnberger, R., Rodnight, H., and Spötl, C.: Chronology of the Last Glacial Maximum in the Salzach Palaeoglacier Area (Eastern Alps), J. Quaternary Sci., 26, 502–510, https://doi.org/10.1002/jqs.1477, 2011.

Steffen, D., Preusser, F., and Schlunegger, F.: OSL quartz age underestimation due to unstable signal components. Quat. Geochronol., 4, 353–362, https://doi.org/10.1016/j.quageo.2009.05.015, 2009.

Steup, R. and Fuchs, M.: The loess sequence at Münzenberg (Wetterau/Germany): A reinterpretation based on new luminescence dating results, Z. Geomorphol. Supp., 61, 101–120, https://doi.org/10.1127/zfg_suppl/2016/0408, 2017.

Stojakowits, P., Mayr, C., Ivy-Ochs, S., Preusser, F., Reitner, J., and Spötl, C.: Environments at the MIS 3/2 transition in the northern Alps and their foreland, Quatern. Int., 581/582, 99–113, https://doi.org/10.1016/j.quaint.2020.08.003, 2021.

Sun, D., Bloemendal, J., Rea, D.K., An, Z., Vandenberghe, J., Lu, H., Su, R., and Liu, T.: Bimodal grain-size distribution of Chinese loess, and its paleoclimatic implications, Catena, 55, 325–340. https://doi.org/10.1016/S0341-8162(03)00109-7, 2004.

Taylor, S. N. and Lagroix, F.: Magnetic anisotropy reveals the depositional and postdepositional history of a loess-paleosol sequence at Nussloch (Germany), J. Geophys. Res.-Sol. Ea., 120, 2859–2876, https://doi.org/10.1002/2014JB011803, 2015.

Terhorst, B., Sedov, S., Sprafke, T., Peticzka, R., Meyer-Heintze, S., Kühn, P., and Solleiro Rebolledo, E.: Austrian MIS 3/2 loess–palaeosol records – Key sites along a west–east transect, Palaeogeogr. Palaeocl., 418, 43–56, https://doi.org/10.1016/j.palaeo.2014.10.020, 2015.

Thomsen, K. J., Murray, A. S., Jain, M., and Bøtter-Jensen, L.: Laboratory fading rates of various luminescence signals from feldspar-rich sediment extracts, Radiat. Meas., 43, 1474–1486, https://doi.org/10.1016/j.radmeas.2008.06.002, 2008.

Viscarra Rossel, R. A., Walvoort, D. J. J., McBratney, A. B., Janik, L. J., and Skjemstad, J. O.: Visible, near infrared, mid infrared or combined diffuse reflectance spectroscopy for simultaneous assessment of various soil properties, Geoderma, 131, 59–75, https://doi.org/10.1016/j.geoderma.2005.03.007, 2006.

Vlaminck, S., Kehl, M., Rolf, C., Franz, S. O., Lauer, T., Lehndorff, E., Frechen, M., and Khormali, F.: Late Pleistocene dust dynamics and pedogenesis in Southern Eurasia - Detailed insights from the loess profile Toshan (NE Iran), Quaternary Sci. Rev., 180, 75–95, https://doi.org/10.1016/j.quascirev.2017.11.010, 2018.

Wintle, A. G.: Anomalous fading of thermoluminescence in mineral samples, Nature, 245, 143–144, https://doi.org/10.1038/245143a0, 1973.

Wright, J. S.: "Desert" loess versus "glacial" loess: quartz silt formation, source areas and sediment pathways in the formation of loess deposits, Geomorphology, 36, 231–256, https://doi.org/10.1016/S0169-555X(00)00060-X, 2001.

Yi, S., Buylaert, J-P., Murray, A. S., Lu, H., Thiel, C., and Zeng, L.: A detailed post-IR IRSL dating study of the Niuyangzigou loess site in northeastern China, Boreas, 45, 644–657, https://doi.org/10.1111/bor.12185, 2016.

Zeeden, C. and Hambach, U.: Magnetic susceptibility properties of loess from the Willendorf archaeological site: Implications for the syn/post-depositional interpretation of magnetic fabric, Front. Earth Sci., 8, 599491, https://doi.org/10.3389/feart.2020.599491, 2021.

Zeeden, C., Kels, H., Hambach, U., Schulte, P., Protze, J., Eckmeier, E., Markovic, S. B., Klasen, N., and Lehmkuhl, F.: Three climatic cycles recorded in a loess-palaeosol sequence at Semlac (Romania) – Implications for dust accumulation in south-eastern Europe, Quaternary Sci. Rev., 154, 130–142, https://doi.org/10.1016/j.quascirev.2016.11.002, 2016.

Zeeden, C., Dietze, M., and Kreutzer, S.: Discriminating luminescence age uncertainty composition for a robust Bayesian modelling, Quat. Geochronol., 43, 30–39, https://doi.org/10.1016/j.quageo.2017.10.001, 2018.

Zeeden, C., Mir, J. A., Vinnepand, M., Laag, C., Rolf, C., and Dar, R. A.: Local mineral dust transported by varying wind intensities forms the main substrate for loess in Kashmir, E&G Quaternary Sci. J., 70, 191–195, https://doi.org/10.5194/egqsj-70-191-2021, 2021.

Zhang, J.: Behavior of the electron trapping probability change in IRSL dating of K-feldspar: A dose recovery study, Quat. Geochronol., 44, 38–46, https://doi.org/10.1016/j.quageo.2017.12.001, 2018.

Zhang, J. and Li, S.-H.: Review of the Post-IR IRSL Dating Protocols of K-Feldspar, Methods and Protocols, 3, 7, https://doi.org/10.3390/mps3010007, 2020.

Zöller, L. and Wagner, G. A.: Thermoluminescence Dating of Loess – Recent Developments, Quatern. Int., 7/8, 119–128, https://doi.org/10.1016/1040-6182(90)90046-7, 1990.

Zöller, L., Stremme, H., and Wagner, G. A.: Thermolumineszenz-Datierung an Löss-Paläoboden-Sequenzen von Nieder-, Mittel- und Oberrhein/Bundesrepublik Deutschland, Chem. Geol., 73, 39–62, https://doi.org/10.1016/0168-9622(88)90020-6, 1988.

Zöller, L., Fischer, M., Jary, Z., Antoine, P., and Krawczyk, M.: Chronostratigraphic and geomorphologic challenges of last glacial loess in Poland in the light of new luminescence ages, E&G Quaternary Sci. J., 71, 59–81, https://doi.org/10.5194/egqsj-71-59-2022, 2022.

E&G Quaternary Sci. J., 71, 163–190, 2022
https://doi.org/10.5194/egqsj-71-163-2022

Open Access E&G Quaternary Science Journal

Research article

Two glaciers and one sedimentary sink: the competing role of the Aare and the Valais glaciers in filling an overdeepened trough inferred from provenance analysis

Michael A. Schwenk[1], **Laura Stutenbecker**[2], **Patrick Schläfli**[1,3], **Dimitri Bandou**[1], **and Fritz Schlunegger**[1]

[1]Institute of Geological Sciences, University of Bern, Bern, Switzerland
[2]Institute of Applied Geosciences, Technical University Darmstadt, Darmstadt, Germany
[3]Institute of Plant Sciences, University of Bern, Bern, Switzerland

Correspondence: Michael A. Schwenk (michael.schwenk@geo.unibe.ch, michi_schwenk@web.de)

Relevant dates: Received: 11 April 2022 – Revised: 13 July 2022 – Accepted: 25 July 2022 – Published: 1 September 2022

How to cite: Schwenk, M. A., Stutenbecker, L., Schläfli, P., Bandou, D., and Schlunegger, F.: Two glaciers and one sedimentary sink: the competing role of the Aare and the Valais glaciers in filling an overdeepened trough inferred from provenance analysis, E&G Quaternary Sci. J., 71, 163–190, https://doi.org/10.5194/egqsj-71-163-2022, 2022.

Abstract: The extent and distribution of glaciers on the Swiss Plateau during the Last Glacial Maximum (LGM) can be determined from the geological record. However, similar reconstructions for the glaciations that preceded the LGM are far more difficult to be made due to the destruction of suitable sedimentary records through recurring glaciations or due to the inaccessibility of preserved records. Here, we explored Quaternary sediments that were deposited during the Marine Isotope Stage (MIS) 8 glaciation at least around 250 ka, and which were recovered in a drilling that was sunk into an overdeepened bedrock trough west of Bern (Switzerland). We analyzed the sediment bulk chemical composition of the deposits to investigate the supply of the material to the area by either the Aare Glacier, the Saane Glacier, or the Valais Glacier, and we complement this investigation with the results of heavy mineral analyses and geochemical information from detrital garnet. The potential confluence of the Valais and the Aare glaciers in the Bern area makes this location ideal for such an analysis. We determined the sediment bulk chemical signal of the various lithological units in the central Swiss Alps where the glaciers originated, which we used as endmembers for our provenance analysis. We then combined the results of this fingerprinting with the existing information on the sedimentary succession and its deposition history. This sedimentary suite is composed of two sequences, Sequence A (lower) and Sequence B (upper), both of which comprise a basal till that is overlain by lacustrine sediments. The till at the base of Sequence A was formed by the Aare Glacier. The overlying lacustrine deposits of an ice-contact lake were mainly supplied by the Aare Glacier. The basal till in Sequence B was also formed by the Aare Glacier. For the lacustrine deposits in Sequence B, the heavy mineral and garnet geochemical data indicate that the sediment was supplied by the Aare and the Saane glaciers. We use these findings for a paleogeographic reconstruction. During the time when Sequence A and the basal till in Sequence B were deposited, the Aare Glacier dominated the area. This strongly contrasts with the situation during the LGM, when the Aare Glacier was deflected by the Valais Glacier towards the northeast. The Valais Glacier was probably less extensive during MIS 8, but it was potentially present

in the area, and it could have been essential for damming a lake in which the material supplied by the Aare and the Saane glaciers accumulated. In conclusion, combining provenance with sedimentological data, we could document how sediment was supplied to the investigated overdeepened basin during the MIS 8 glacial period and how glaciers were arranged in a way that was markedly different from the LGM.

Kurzfassung:

Die Gletscherstände und die Verbreitung der Gletscher im Schweizer Mittelland während des letztglazialen Maximums (LGM) lassen sich aus den erhaltenen Ablagerungen und der Oberflächenmorphologie ableiten. Ähnliche Rekonstruktionen für die dem LGM vorangegangenen Vergletscherungen sind ungleich schwerer anzustellen, da entsprechende Ablagerungen durch die wiederkehrenden Gletschervorstöße zerstört wurden oder da entsprechende Sedimentsequenzen unzugänglich sind. In der vorliegenden Arbeit untersuchten wir Quartäre Sedimente, die während des marinen Isotopenstadiums (MIS) 8 abgelagert wurden. Erbohrt wurden diese Sedimente in einem übertieften Trog, der ins Molassegestein westlich von Bern (Schweiz) erodiert wurde. An diese Stelle konnte Sediment möglicherweise durch einen von drei Gletschern, den Aaregletscher, den Saanegletscher oder den Walliserglетscher transportiert werden. Um zu ermitteln, welche der Gletscher Sediment in den Trog lieferten, untersuchten wir die chemische Zusammensetzung der Ablagerungen und ergänzten diese Untersuchung mit Daten aus der Analyse der Schwermineralzusammensetzung sowie der Analyse detritischer Granate. Da hier möglicherweise der Aare– und der Walliserglетscher zusammenflossen, bietet sich die Gegend um Bern für eine solche Untersuchung an. Um den Ursprung des Sediments feststellen zu können, definierten wir verschiedene lithologische Einheiten der zentralen Schweizer Alpen, in denen die Gletscher sich bildeten, als Endglieder unserer Provenienzanalyse und bestimmten ebenfalls deren chemische Zusammensetzung. Die Ergebnisse aus der Untersuchung dieser chemischen Fingerabdrücke ergänzten wir anschließend mit den bereits vorhandenen Informationen über die Sedimentationsabfolge und deren Ablagerungsverhältnisse. In dieser Abfolge können zwei Sequenzen unterschieden werden, eine untere Sequenz A und eine obere Sequenz B. Beide Sequenzen bestehen aus einer Grundmoräne, die von lakustrischem Sediment überlagert wird. Der Aaregletscher lagerte die Moräne an der Basis der Sequenz A ab. Die Sedimente, die sich anschließend in einem Eisrandsee bildeten, wurden ebenfalls hauptsächlich vom Aaregletscher geliefert. Die basale Moräne der Sequenz B wurde ebenfalls durch den Aaregletscher gebildet. Daraufhin wurde das Seebecken mit Sediment aufgefüllt, das vermutlich durch den Aare– sowie den Saanegletscher herantransportiert wurde, wie die Schwermineralzusammensetzung und Granatgeochemie zeigen. Anhand dieser Ergebnisse erstellen wir eine paläogeographische Rekonstruktion. Es zeigt sich darin die Dominanz des Aaregletschers im Gebiet um Bern während des Ablagerungszeitraums der unteren Sequenz A sowie der Moräne an der Basis der Sequenz B. Dieses Bild der Verbreitung der Gletscher im Raum Bern steht in starkem Kontrast zur Situation während des LGM, als der Aaregletscher vom Walliserglетscher in Richtung Nordost abgedrängt wurde. Augenscheinlich war der Walliserglетscher während der MIS 8 Vergletscherung weniger weit ausgedehnt. Jedoch kann hier die vollständige Abwesenheit des Walliserglетschers nicht ausgeschlossen werden und möglicherweise war er sogar essenziell, um einen See in der Gegend um Bern aufzustauen, in welchen der Aare– und der Saanegletscher ihr mitgeführtes Material schütteten. Letztlich zeichnen die hier präsentierten Ergebnisse, eine Kombination aus Provenienzanalyse und sedimentologischen Daten, ein Bild des Sedimenttransportes in den hier untersuchten übertieften Trog während des MIS 8 Glazials, und den deutlichen Unterschied zur Gletscherverbreitung während des LGM.

1 Introduction

Provenance analysis is a common tool in geology used to determine the origin of sediments and sedimentary rocks, as well as to quantify the relative contribution of material from different parent rocks to the sediment mixture (Weltje and von Eynatten, 2004). Provenance analysis can be used to investigate present-day catchment-wide erosion patterns in fluvial landscapes and the human impact on them (Stutenbecker et al., 2018; Lizaga et al., 2019), and the results offer the basis to infer large-scale denudation patterns and to analyze the resulting impact on the evolution of landscapes (von Eynatten, 2003; Tatzel et al., 2017).

Provenance analysis has been applied in glacial geology, where the lithology of erratic boulders and gravel clasts in glacigenic deposits yields information on the lithologic source of the material and its geographic location. Such information can then be used to identify the motion of ice sheets and the flow patterns of glaciers during past glaciations (e.g., Kjær et al., 2003; Sandroni and Talarico, 2011; Busfield et al., 2015; Braakhekke et al., 2020). Related reconstructions are often based on components that are large enough to allow a petrographic description and the identification of their lithology. However, glacigenic deposits can be entirely composed of silt and sand, which hampers the determination of the provenance by macroscopic tools. Furthermore, the amount of material available for an analysis particularly from drill cores is very limited. In such an instance, where fine-grained glacial deposits have been recovered from a borehole, the source of the material can be determined based on its chemical composition. This has been exemplified by studies that were conducted on the partially fine-grained glacial material recovered from McMurdo Sound in Antarctica (Pompilio et al., 2007; Giorgetti et al., 2009; Sandroni and Talarico, 2011; Monien et al., 2012).

Among the various fingerprinting proxies in the field of sedimentary petrology, such as heavy mineral assemblages, bulk petrography, and geochronological parameters, the analysis of the sediment bulk chemistry provides a geochemical proxy for inferring the origin of sediments (Weltje and von Eynatten, 2004; Garzanti et al., 2012; Vermeesch and Garzanti, 2015; Stutenbecker et al., 2018, 2019). The sediment bulk chemistry is practical in provenance analyses because (i) it can be obtained efficiently so that the smallest aliquots of a sample can be measured quickly with high accuracy and reproducibility, (ii) the chemical analysis of geological samples is an established standard method for commercial applications largely independent from bias such as the operator's experience, and (iii) the statistical analysis of the resulting compositional data can be readily accomplished using various R packages designed specifically to deal with the constant-sum character of such data (Pawlowsky-Glahn and Egozcue, 2006; Vermeesch et al., 2016; Lizaga et al., 2020). Hence, the investigation of the sediment bulk chemistry can be used on large sample sets with high accuracy and swiftness, and related analyses can be utilized on fine-grained material such as glaciolacustrine deposits.

Large amounts of Quaternary glacial deposits of a widely unknown provenance are accumulated in glacially overdeepened valleys, or so-called overdeepenings, in and around the European Alps, including the central Swiss Alps (Preusser et al., 2010). Overdeepenings are bedrock troughs with their thalwegs below the present-day base level, and they can have a U-shaped cross-sectional geometry (Bandou et al., 2022). Hence, they are thought to have formed through glacial rather than fluvial erosion (Cook and Swift, 2012). After the glaciers retreated from the bedrock troughs, these local basins offered accommodation space for sediment to accumulate during glacial and interglacial periods (Buechi et al., 2017). Throughout the Quaternary, the Alpine overdeepenings were repeatedly occupied by glaciers that partially excavated the infill of the overdeepened basins, and thus the sedimentary records within the troughs probably chronicled several of the late Quaternary glaciations during the past 1 million years (Preusser et al., 2010).

Such an overdeepened valley, referred to as the Middle Aare Valley overdeepening (MAV–OD), is located in the Bern area (Swiss Plateau) on the northern side of the Alps. Recently, a scientific drill was sunk into the > 200 m deep Bümpliz trough (Rehhag drilling; WGS84: 46.9326° N, 7.3760° E), which is a lateral trough west of the main MAV–OD. The drilling recovered a 208.5 m long suite of unconsolidated sediment and an additional 3 m thick succession of Molasse bedrock at the base. Schwenk et al. (2022) reported that subglacial till and glaciolacustrine and lacustrine deposits accumulated in this trough during a glaciation between 250 and 300 ka (based on feldspar luminescence dating), which is a period that is equivalent to the global cooling during Marine Isotope Stage (MIS) 8 (Fig. 1). Although the depositional setting has been analyzed in-depth and a general chronology has been established for this succession, the provenance of these sediments and the detailed environmental history are unknown. Particularly, information about the sediment supply by glaciers to the Bern area during glaciations other than the Last Glacial Maximum (LGM) is missing, and such information would be most relevant for the reconstruction of pre-LGM glacial advances. The target region is exceptionally suitable for such reconstructions due to its position in the confluence area of the Aare and the Valais glaciers that originated in different parts of the central Swiss Alps (Bini et al., 2009; Ehlers et al., 2011). It is thus plausible that the sedimentary record in the MAV–OD chronicled the erosion and supply of material by either or both of these glaciers, which we intend to explore through this provenance study.

Here, we present the results of this analysis that we conducted on the predominantly silty and sandy Quaternary deposits encountered in the Rehhag drill core. We determined the bulk (geo-)chemical composition of the drilled sedimentary succession. We then compared the chemical composi-

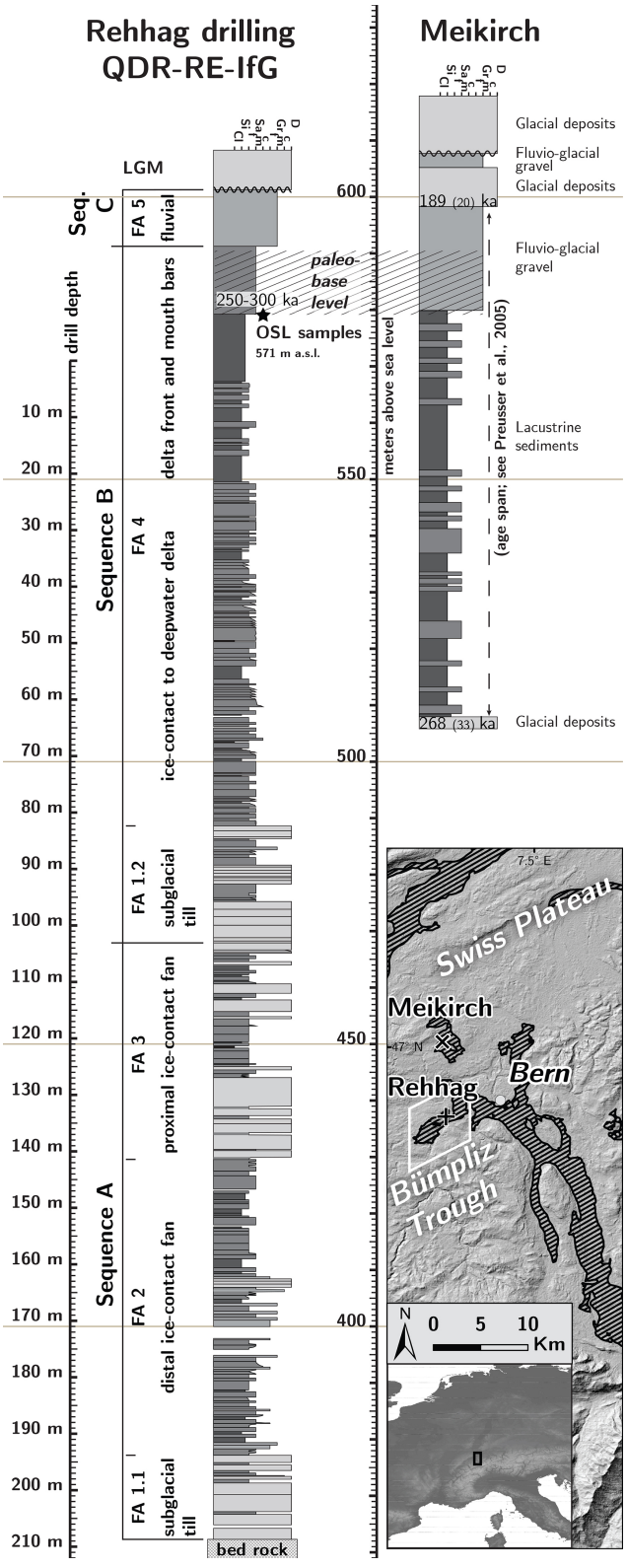

Figure 1. These two logs display the sedimentary succession recovered (left) in the Rehhag drill core with a ca. 40 m extension upsection based on outcrop data (Schwenk et al., 2022) and (right) in the Meikirch drill core (modified from Preusser et al., 2005). In the Rehhag sedimentary suite we focus on the drilled section and the facies assemblages (FA) 1 through 4 (Fig. 5). The inset on the bottom right shows the position of the two scientific drillings, together with the MAV–OD (black hatching). Elevation data from NASA/METI/AIST/Japan Spacesystems and U.S./Japan ASTER Science Team (2019).

tion of the cored material with the bulk chemical composition obtained from source sediment samples that we collected in tributaries of the modern Aare and Rhône rivers. This comparison built the basis for determining the provenance of the sedimentary suite encountered in the drilling. We hypothesize that changes in glacial erosion within the Aare and the Rhône valleys, where the Aare and the Valais glaciers were sourced, respectively, should be reflected in the composition of the sediment in the Bümpliz trough. Our goal is to determine the competing role of these two large Alpine glaciers on the sediment supply and on the filling of this trough. Finally, the provenance information will also be used to reconstruct the details of the paleogeography in the confluence area of the Aare and the Valais glaciers.

2 Setting

2.1 Sedimentological framework of the Rehhag drill core

The Quaternary succession encountered in the Rehhag drilling consists of two sedimentary packages referred to as Sequences A and B, each of which starts with a glacial till (Fig. 1; Schwenk et al., 2022). The basal facies assemblage (FA) 1.1 of Sequence A, composed of a subglacial traction till and intercalated sand layers that were deposited in subglacial conduits, is overlain by cross-bedded and steeply inclined sand, gravel, and diamictic beds referred to as FA 2 & 3. The sedimentary fabric of these latter assemblages was used to infer a deposition from density currents in a subaqueous ice-contact fan environment within a proglacial lake. Furthermore, whereas FA 2 was considered to record a backstepping of the glacier that accumulated the basal till, the overlying "flow–till" deposits of FA 3 were interpreted to indicate a readvance of the same glacier, resulting in the establishment of a proximal ice-contact fan environment (Fig. 1). The overlying Sequence B starts with an assemblage of sedimentary beds containing a subglacial till (FA 1.2), which is overlain by a fining-upward suite of turbidite layers where the bed frequency and thickness decrease upsection (FA 4). Sequence B was considered to have been deposited in a prodelta setting that gradually developed into a delta plain. Although an unconformity that is manifested in the emplacement of a basal till cutting off the underlying inclined beds separates Sequence B from the underlying Sequence A, Schwenk et al. (2022) could neither confirm nor disprove that both sequences were deposited either during two different glacial cycles or the same cycle. Finally, the uppermost deposits at the Rehhag site recorded the transition from the lacustrine setting through a paleo-base level into a fluvial environment (FA 5; Fig. 1). Furthermore, the very low organic carbon content and the absence of pollen grains in Sequence B led Schwenk et al. (2022) to conclude that the lake sediments recorded a depositional environment that was too dynamic for the accumulation of pollen and organic material.

Another scientific drilling was conducted in the Meikirch trough ca. 10 km north of the Rehhag drill site in the 1980s. This drilling regained attention when the yet ambiguous age assignment that resulted from a palynological investigation (Welten, 1982, 1988) was reinterpreted based on luminescence dating. The respective geochronometric investigation (Preusser et al., 2005), together with a recent reevaluation of the pollen record (Schläfli et al., 2021), uncovered that the Meikirch sedimentary succession was most likely deposited during a time interval that spans a phase of ice advance around 270 ka (MIS 8), the subsequent interglacial (MIS 7), and the following glacial period (MIS 6). Furthermore, the sedimentary suites recovered in the Rehhag and the Meikirch drillings both show a transition from a lacustrine environment into a fluvial setting, which is recorded at both locations at an elevation of ca. 580 m a.s.l. (Fig. 1). Schwenk et al. (2022) used this similarity in the development of the sequences to (i) infer the presence of a lake that formed the local base level during the late MIS 8 and to (ii) underpin the luminescence ages obtained at the Rehhag drill site. The records that inform about the extent of this inferred lake have been obscured by the repeated glacial overprinting of the region. Therefore, reconstructions of the spatial extension of this inferred lake can be perceived as speculative, yet this idea has been a long-standing one in the literature about the Quaternary deposits of the region (Gerber, 1923; Beck, 1938). Such a reconstruction of a paleo-lake, which is based on the bedrock topography map of the region by Reber and Schlunegger (2016), is displayed in Fig. 2. This reconstruction shows that two possible outflows north and west of Bern have to be considered to understand the formation of the inferred base level at that time (see "Discussion" below).

2.2 Quaternary glaciations

The European Alps and their adjacent lowlands have been repeatedly affected by glaciations throughout the Quaternary. During these glacial periods, two major ice streams referred to as the Valais and the Aare glaciers advanced into the Bern area multiple times and probably converged perpendicular to each other (Fig. 3; Bachmann, 1870; Favre, 1884; Baltzer, 1896; Schlüchter, 1989; Bini et al., 2009; Preusser et al., 2011; Jouvet et al., 2017). Both glaciers originated in a different part of the Swiss Alps. The ice of the Valais Glacier accumulated in the tributaries of the Rhône Valley in the central Swiss Alps, whereas the Aare Glacier had its sources in the Aare Valley on the northern margin of the Swiss Alps. A third rather small glacier, referred to as the Saane Glacier, originated in an isolated catchment between the Aare and the Rhône valleys on the northern margin of the Alps, and it merged with the Valais Glacier west of Bern (Fig. 3; Favre, 1884; Gilliéron, 1885; Baltzer, 1896; Bini et al., 2009; Ehlers et al., 2011; Becker et al., 2017). Accordingly, this glacier could also have supplied material to the Bümpliz trough.

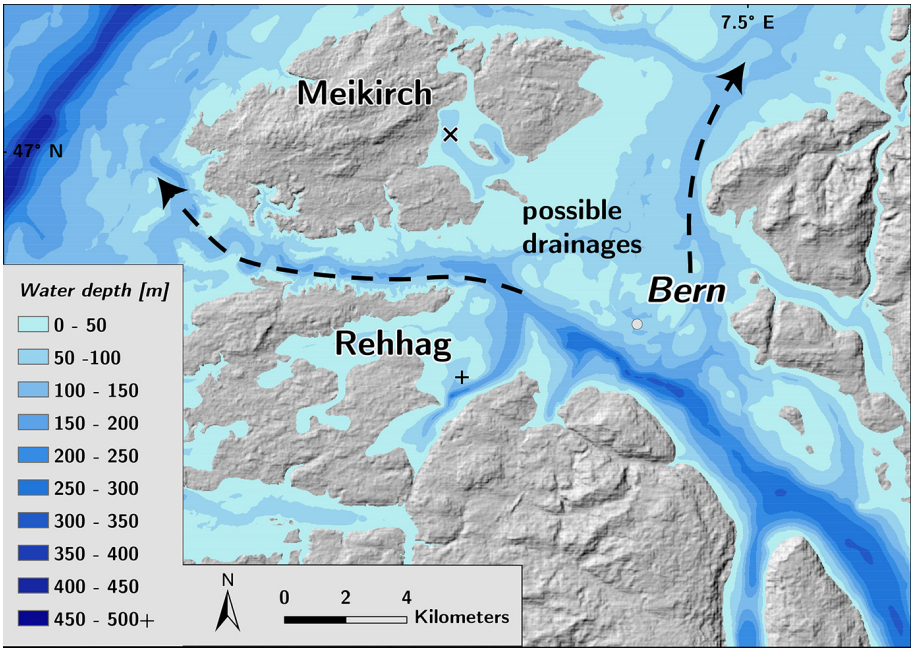

Figure 2. This map depicts the effect in which the topographic raster of the bedrock surface (Bundesamt für Landestopografie swisstopo, 2021a) is filled with water to an elevation of 580 m a.s.l. It reveals two passages through which a lake in the Aare Valley would drain. Accordingly, these passages need to be blocked to allow such a lake to form. The water level is equivalent to the elevation of the paleo-base level that was determined in the scientific drilling at the Rehhag site and inferred for the Meikirch sedimentary succession (Fig. 1; Schwenk et al., 2022). Elevation data from NASA/METI/AIST/Japan Spacesystems and U.S./Japan ASTER Science Team (2019).

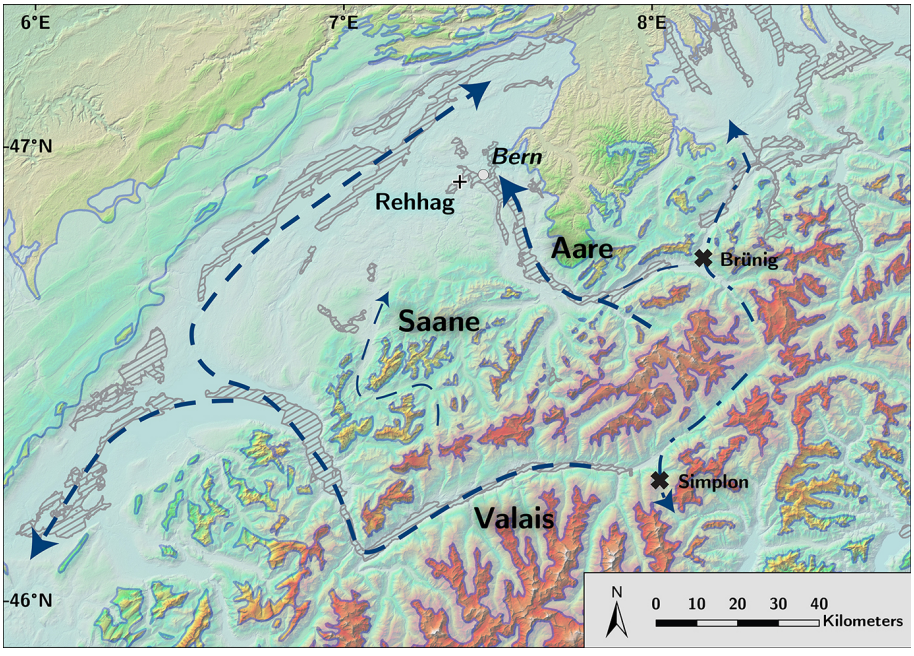

Figure 3. Map of the ice cover in the central Swiss Alps and their northern lowlands during the LGM (Ehlers et al., 2011). Blue arrows indicate the flow patterns of the ice streams. Dashed lines indicate ice flow relevant for sediment transport to the Bern area. Dashed-dotted lines indicate where the ice flow diverged from the main flow (Kelly et al., 2004; Reber et al., 2014; Becker et al., 2017). The Simplon and the Brünig passes, the ice transfluences, are marked with bold crosses. Shaded grey areas indicate the position of overdeepenings in and around the central Swiss Alps (available via Bundesamt für Landestopografie swisstopo, 2021a). Elevation data from NASA/METI/AIST/Japan Spacesystems and U.S./Japan ASTER Science Team (2019).

Reconstructions of the ice distribution and the ice flow during the LGM showed that several ice transfluences existed in the central Swiss Alps (e.g., Kelly et al., 2004; Bini et al., 2009). In the Rhône and the Aare valleys such transfluences were located at the Simplon Pass (Kelly et al., 2004) and the Brünig Pass (e.g., Favre, 1884; Baltzer, 1896; Preusser et al., 2011; Reber et al., 2014), respectively (Fig. 3). In the past years, various authors have used field observations from the Swiss Alps, such as glacial landforms and erosional features, as well as the provenance of erratic boulders, to constrain computer models that calculated the ice extent and ice flow during the LGM (Becker et al., 2017; Jouvet et al., 2017; Seguinot et al., 2018). Both field observations and modeling results suggest that the Valais Glacier in the Bern area was mainly sourced from the lower western part of the Rhône Valley and that the Aare Glacier stretching towards the Bern area was originating from the northwestern part of the Bernese Alps (Fig. 3). Furthermore, these results can be used to explore the distribution of glacier ice and to infer differences in the climate conditions between glaciations, as well as glacials and interglacials (Florineth and Schlüchter, 2000; Becker et al., 2016; Reber and Schlunegger, 2016). In this context and based on the investigation of the bedrock topography in the Bern area, Reber and Schlunegger (2016) suggest that erosion in subglacial conduits below an unobstructed, i.e., free-end, Aare Glacier could effectively contribute to the formation of the MAV–OD. Hence, the aforementioned authors concluded that the Aare and the Valais glaciers were not in an LGM-like arrangement when the MAV–OD was formed and that consequently the climate at that time must have been different from the LGM climate.

2.3 Lithotectonic architecture of the Alpine source area of the target glaciers

The lithotectonic architecture of the Alps is characterized by a large variety of exposed rocks, which offers ideal conditions for allocating the source of the sediments encountered in the Rehhag drilling through fingerprinting. The history of this orogen started with the Mesozoic phase of continental spreading leading to the formation of the Valais and the Piedmont–Liguria oceans (Alpine–Tethys; Stampfli, 2000) with different sedimentary basins, and it culminated in the subsequent closure of these troughs and the following collision of the European, Iberian, and African continental plates (Schmid et al., 2004). Accordingly, in the central part of the Swiss Alps six major lithotectonic units can be distinguished which are relevant in this study. These are from north to south as follows: (i) remnants of the southern stretched margin of the European plate which are referred to as Helvetic units and which are mainly composed of limestone, (ii) the basement of the European plate made up of gneisses and metagranites, (iii) clastic rocks, referred to as flysch and calcshists that accumulated in the Valais and in the Piedmont–Liguria oceans, (iv) limestone sequences that accumulated on the Briançon terrane (part of the Iberian plate), (v) ophiolites and schists that formed in the Piedmont–Liguria ocean between the Iberian and the African plates, and (vi) the basement of the Iberian plate composed of gneisses and mica schists. The closure of these oceans, the subsequent collision of the continental plates, and the metamorphic overprinting of a large portion of the Alps resulted in a significant rearrangement of the lithotectonic units (Hänni and Pfiffner, 2001; Wissing and Pfiffner, 2002; Schmid et al., 2004). The positioning of these lithotectonic units in the source areas, as well as along the course of the Aare, the Saane, and the Valais glaciers, makes them relevant for determining the geochemical fingerprint of each of these glaciers (Fig. 4). In particular, medium-grade metamorphic basement rocks of the Iberian plate, which are referred to as the Penninic crystalline rocks, and ophiolites of the Piedmont–Liguria ocean can mainly be found on the southern flank of the western Rhône Valley and thus form a unit of parent rocks for material that was transported only by the Valais Glacier (Figs. 3 and 4). We here refer to both units as the Penninic domain for simplicity. In contrast, the clastic sedimentary units and limestones of the Valais ocean, the Briançon terrane, and the Piedmont–Liguria ocean were detached from their basement, thrust northward, and currently occur as the so-called Klippen domain on the northwestern margin of the Swiss Alps where they served as parent rocks for the material that was mainly transported by the Saane Glacier. The sedimentary limestone suites of the European margin occur as Helvetic thrust nappes, and either they are exposed on the northern flank of the Rhône Valley and thus in the source area of the Valais Glacier or they delineate the northern Alpine margin to the east of the Klippen belt. There, the Helvetic thrust nappes dominate the source area of the Aare Glacier (Figs. 3 and 4). Finally, crystalline basement rocks of the stretched margin of the European plate occur in the External massifs. These massifs are located in the upstream region of the Rhône and the Aare valleys, yet they probably served as parent rock for material that was mainly transported by the Aare Glacier due to the ice flow setting outlined above (Figs. 3 and 4). The External massifs of the Mont Blanc area (southwest Rhône Valley) probably contributed to the material transported by the Valais Glacier towards the Bern area (Favre, 1884; Baltzer, 1896; Jouvet et al., 2017). However, the fingerprint of the Mont Blanc and the Aiguilles Rouges massifs is most probably accompanied by the fingerprinting signal of the Penninic domain. Because both form a redundancy in the identification of the Valais Glacier provenance signal, we rely on the fingerprint of the Penninic domain to identify material transported by the Valais Glacier. Only small patches of the basement from the African plate are preserved as isolated klippen (Dent Blanche) on top of the Penninic unit. This unit has a very limited areal extent and is thus not relevant for the present study. Table 1 presents an overview of the relative area covered by the respective lithotectonic units in the major catchments that are relevant for this study.

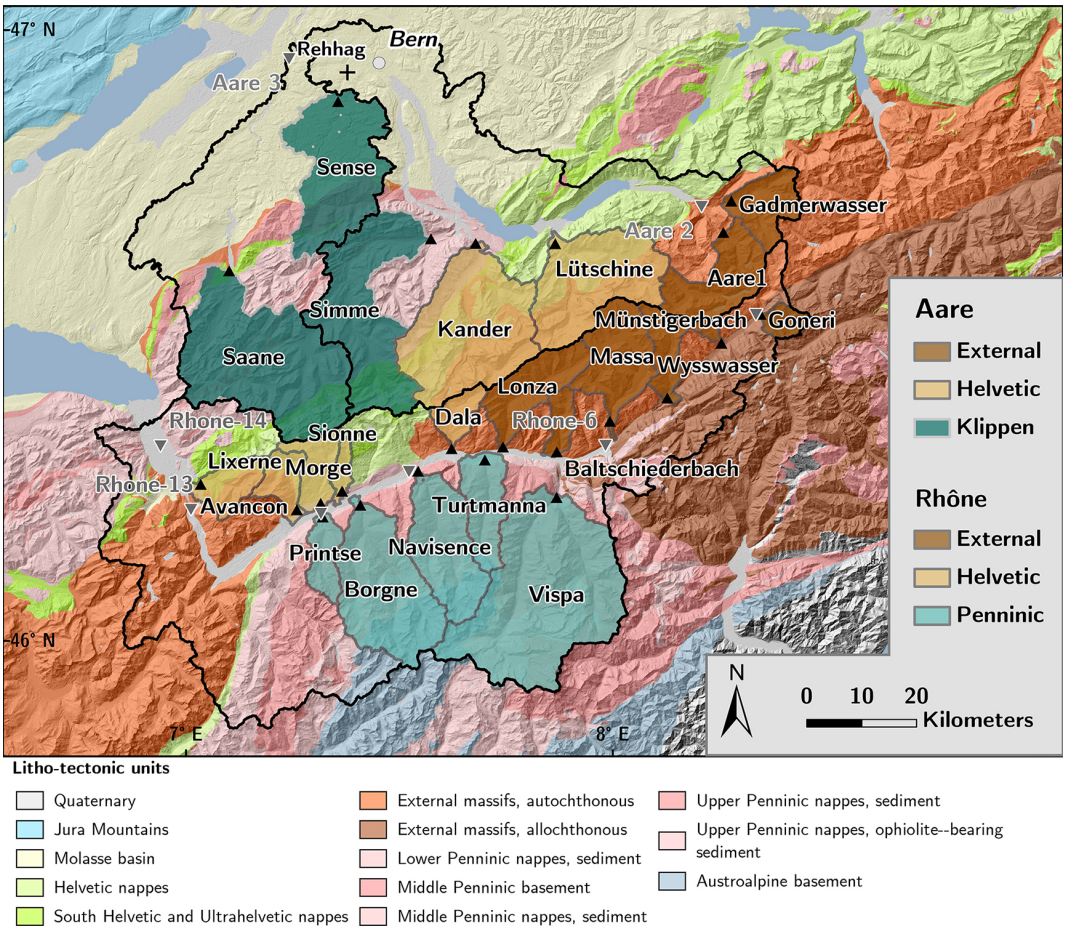

Figure 4. Overview map showing the possible source lithologies for the sediment deposited at the Rehhag drill site in the Bümpliz trough. The major catchments are outlined in black, and within these the minor tributaries are colored according to their attribution to one of the four lithotectonic units. Triangles indicate the locations where samples were collected in the tributary streams (black) and in the Rhône and Aare trunk streams (grey). The location of the Rehhag drill site is marked by a cross. Rhône (Stutenbecker et al., 2018): Gon – Goneri, Mün – Münstigerbach, Wys – Wysswasser, Mas – Massa, Vis – Vispa, Bal – Baltschiederbach, Lon – Lonza, Tur – Turtmanna, Dal – Dala, Nav – Navisence, Bor – Borgne, Sio – Sionne, Mor – Morge, Pri – Printse, Lix – Lixerne, Ava – Avancon; Aare (this study): Gad – Gadmerwasser, Aa1 – Aare 1, Lue – Lütschine, Kan – Kander, Sim – Simme, Sen – Sense, San – Saane. Geological data of the official map (Institut für Geologie, Universität Bern and Bundesamt für Wasser und Geologie, 2005; Bundesamt für Landestopografie swisstopo, 2021b). Elevation data from NASA/METI/AIST/Japan Spacesystems and U.S./Japan ASTER Science Team (2019).

Between the Late Oligocene to Early Miocene, synorogenic Alpine detritus was transported to the northern foreland basin, including the Bern area, where it accumulated to form the clastic sediments of the Swiss Molasse (Fig. 4; e.g., Sinclair and Allen, 1992; Schlunegger et al., 1996; Strunck and Matter, 2002; von Eynatten, 2003). During glacial advances, the surface of the Molasse bedrock was heavily reshaped through subglacial erosion (e.g., Reber and Schlunegger, 2016) and consequently the Molasse provided a sediment source for material transported by both the Aare and the Valais glaciers (Table 1). Provenance tracing revealed that the rocks of Iberian, African, and Piedmont origin constituted the major sediment sources for the Molasse sequences that were deposited in the Bern area (Spiegel et al., 2000, 2001, 2002; von Eynatten, 2003). In contrast, material from the European External massifs was supplied to the Molasse Basin only after their exhumation around 14 Ma (Stutenbecker et al., 2019; Anfinson et al., 2020). Therefore, material derived from the External massifs is absent in the Molasse sequences in the Bern area. The Rhône catchment was separated from the Rhine–Aare system during the latest stage of the Alpine orogeny in the Late Pliocene (ca. 2.9 Ma; Berger et al., 2005; Ziegler and Fraefel, 2009). Since then, material from the Rhône Valley cannot be supplied to the Bern area by fluvial transport, yet a material supply by glaciers (Valais Glacier) did occur during glacial periods (Graf et al., 2015; Jouvet et al., 2017).

Table 1. Overview of the major lithotectonic units and their relative areal cover of the respective catchments. Additionally, an overview of the absolute catchment sizes is provided. a – Quaternary; b – Molasse Basin; c – External massifs, autochthonous; d – External massifs, allochthonous; e – Helvetic nappes; f – South Helvetic and Ultrahelvetic nappes; g – Lower Penninic nappes, sediment; h – Middle Penninic nappes, sediment; i – Upper Penninic nappes, sediment; j – Middle Penninic basement; k – Upper Penninic nappes, ophiolite-bearing sediment; l – Austroalpine basement.

Lithotectonic unit		Rhone (%)	Saane (%)	Aare (%)	Overall (%)
	a	4.67	0.97	6.73	4.64
Molasse Basin	b	0.39	43.77	18.74	13.78
External massifs	c	29.46	1.23	25.97	23.35
	d	7.49			3.85
Helvetic sediments	e	5.97	3.38	22.74	10.67
	f	3.07	3.55	4.6	3.63
Klippen nappe	g	4.68	7.63	8.56	6.40
	h	5.72	23.19	8.47	9.68
	i	0.23	12.27	1.13	2.66
Penninic nappe	j	25.15			12.92
	k	7.31	4.02	3.06	5.41
Austroalpine	l	5.86			3.01
		(km^2)	(km^2)	(km^2)	(km^2)
Catchment size		5359.42	1861.83	3211.80	10 433.05

3 Methods

3.1 Sample collection, preparation, and geochemical analysis

As outlined above, the sedimentary succession in the overdeepened Bümpliz trough is composed of glacial deposits that could have been supplied by one or multiple glaciers, namely the Valais, the Saane, and the Aare glaciers (Fig. 3). These glaciers are expected to have transported material of markedly different composition with distinct bulk chemical signals, which depends on the lithotectonic units (Penninic, Klippen, External, Helvetic) that constitute the parent rocks in the respective source areas. In order to quantify the contribution of the four source units to the Bümpliz sedimentary succession, their chemical fingerprints were established in a first step. We benefited from the availability of a sediment bulk chemistry data set obtained by Stutenbecker et al. (2018) from modern stream samples collected in 16 tributary basins in the Rhône Valley (Fig. 4), which provides an endmember fingerprint of the Valais Glacier. We complemented this data set by collecting riverine material in seven tributaries (Gadmerwasser, Aare 1, Lütschine, Kander, Simme, Sense, and Saane) on the northern side of the Alps to characterize the geochemical fingerprinting signals of the Aare and the Saane glaciers (Fig. 4). We followed closely the sampling strategy of Stutenbecker et al. (2018) to ensure the comparability of our results. In particular, the employed sampling strategy is a tributary sampling approach which relies on the natural mixture of sediment within a tributary and which is tailored towards determining the large-scale provenance of sedimentary material (Garzanti et al., 2012; Vale et al., 2016; Stutenbecker et al., 2018). Thus, this sampling strategy does not yield fingerprints of individual lithologies but allows the combined fingerprint of all lithologies in a tributary to be assessed. Accordingly, the target catchments were chosen such that the bedrock in the respective area consists predominantly of one main lithotectonic unit (Fig. 4). As a second step, we extracted samples from the Rehhag core in intervals < 5 m, yielding a total of 52 samples (Table 2). These 52 core samples, together with the seven riverine samples from the northern part of the Alps, were prepared for the measurement of their sediment bulk chemical composition. The samples were wet-sieved to extract the grain size fraction < 63 µm in accordance with Stutenbecker et al. (2018). Subsequently we also followed the aforementioned authors in the sample analysis to ensure comparability with their data set. The dried samples were analyzed in a whole-rock procedure using a lithium borate fusion coupled with an ICP–ES (inductively coupled plasma emission spectrometer) at Bureau Veritas (Canada). The content of the oxides SiO_2, Al_2O_3, Fe_2O_3, MgO, CaO, Na_2O, K_2O, TiO_2, P_2O_5, MnO, and Cr_2O_3, as well as of the elements Ba, Ni, Sr, Zr, Y, Nb, and Sc, was measured. The results were corrected for the loss on ignition (LOI). The relative contribution from the four source units (Penninic, Klippen, External, Helvetic) to each of the core samples was determined using the respective fingerprints.

3.2 Data analysis and unmixing model

The data were analyzed with the software environment R (v4.1.1; R Core Team, 2022). We used standard packages, as well as the packages `fingerPro` (v1.1; Lizaga et al., 2020) and `provenance` (v4.0; Vermeesch et al., 2016), that were written for the use in provenance analyses. An R script was written to ensure the reproducibility of the results and of each analytical step. Each of the core samples had to be investigated in the context of all riverine samples to determine the changes in the sediment provenance throughout the cored succession. Thus, 52 temporary processing data sets were automatically aggregated from the data sets of the riverine and the core samples. Each of the processing data sets contained the data on the bulk chemical composition of the 23 riverine samples and 1 core sample. The provenance analysis was then performed on each of the 52 individual processing data sets, and the results were combined into a final overview to reveal trends in the sediment composition.

Table 2. The names of all samples collected from the drill core, the according depth along the drill core, and the final set of unmixing results. Please note that the core number and the derived sample names are not exactly equivalent to the depth in the drilling because individual core sections were drilled in 0.5 m intervals. The unmixing results were calculated by the `fingerPro` *unmix()* function. For every sample, the proportion of sediment derived from the respective lithotectonic unit is provided along with the goodness of fit (GOF). These results were plotted to facilitate the comparison with the sedimentary log; see Figs. 5 and 7.

Primary	Secondary	Depth (m)	External (%)	Helvetic (%)	Klippen (%)	Penninic (%)	GOF
V 008.01		007–008	12.46	41.09	32.32	14.13	0.81
	S 012.01	011–012	23.46	27.84	40.14	8.55	0.80
V 013.01		012–013	20.25	45.57	27.39	6.80	0.84
V 018.01		017–018	6.47	47.56	33.81	12.16	0.82
V 024.01		023–024	12.07	45.55	36.00	6.38	0.81
	S 024.01		10.29	33.80	43.78	12.13	0.81
	S 026.01	025–026	9.70	37.86	42.55	9.89	0.78
V 029.01		028–029	17.03	39.37	31.50	12.10	0.82
V 031.01		030–031	6.71	73.94	18.43	0.92	0.86
	S 031.01		13.42	36.22	36.70	13.66	0.81
	S 034.01	033–034	12.26	39.60	35.66	12.47	0.84
V 042.01		038–039	21.86	36.21	30.49	11.43	0.83
	S 044.01	040–041	13.72	36.88	37.13	12.26	0.81
V 047.01		043–044	17.11	38.68	35.93	8.27	0.77
V 052.01		048–049	21.67	34.84	29.20	14.28	0.83
V 057.01		053–054	18.98	36.93	35.48	8.62	0.78
V 062.01		058–059	20.62	35.88	30.35	13.14	0.81
V 067.01		063–064	8.30	42.37	34.29	15.04	0.81
V 072.01		068–069	15.85	38.50	29.56	16.08	0.79
V 077.01		073–074	17.41	35.04	36.01	11.54	0.80
	S 078.01	074–075	29.06	27.94	32.32	10.69	0.80
V 082.01		078–079	17.30	36.47	35.28	10.94	0.80
V 087.01		083–084	45.10	31.58	20.72	2.59	0.81
V 092.01		088–089	40.55	33.74	23.64	2.07	0.78
V 097.01		093–094	18.28	46.85	31.76	3.10	0.72
V 103.01		098–099	31.80	36.06	28.60	3.55	0.83
V 109.01		104–105	7.78	54.80	25.59	11.82	0.78
	S 110.01	105–106	9.56	49.66	29.60	11.18	0.79
V 113.01		108–109	5.29	73.04	20.45	1.22	0.81
V 118.01		113–114	4.40	71.03	21.97	2.59	0.86
V 122.01		117–118	8.68	66.72	23.23	1.37	0.86
	S 123.01	118–119	10.47	72.50	16.32	0.71	0.79
V 128.01		123–124	7.10	73.47	18.92	0.51	0.77
V 138.01		133–134	11.02	70.17	18.39	0.42	0.80
V 143.01		138–139	9.11	70.29	19.20	1.40	0.86
V 148.01		143–144	18.69	60.14	20.21	0.97	0.76
	S 150.01	145–146	12.71	36.99	41.91	8.39	0.82
V 153.01		148–149	12.76	67.10	19.55	0.60	0.77
	S 157.01	152–153	10.42	62.07	25.04	2.47	0.85
V 158.01		153–154	10.42	67.53	21.26	0.79	0.82
V 163.01		158–159	10.90	67.66	20.31	1.13	0.85
V 168.01		163–164	10.26	50.48	32.45	6.81	0.85
V 173.01		168–169	21.74	61.21	16.19	0.86	0.78
V 178.01		173–174	8.46	70.09	20.58	0.87	0.79
	S 179.01	174–175	22.91	57.12	17.83	2.15	0.78
V 184.01		179–180	14.92	68.73	16.01	0.34	0.79
V 188.01		183–184	14.36	62.85	22.01	0.78	0.82
V 193.01		188–189	10.79	71.12	17.19	0.90	0.82
	S 197.01	192–193	17.65	62.95	19.04	0.36	0.75
V 198.01		193–194	7.10	55.68	31.54	5.68	0.84
V 203.01		198–199	18.51	57.74	21.78	1.96	0.84
V 208.01		203–204	50.44	22.11	14.13	13.33	0.72

We used two approaches to prepare the 52 processing data sets and to assess how the selection of variables influences the discrimination between potential source areas. As a first approach, we determined an optimum selection of variables (i.e., oxides and elements) for each processing data set that allows the parent rock domains to be discriminated best. This was achieved through a standard statistical procedure that applies the conservation criterion for each variable, an H test following Kruskal–Wallis (Kruskal and Wallis, 1952), and a stepwise linear discrimination analysis (LDA; e.g., Stutenbecker et al., 2018; Lizaga et al., 2020). This approach yielded a provenance result in one run, and the result is tailored towards each individual core sample. As a second approach, we first determined the variables from the riverine data sets that allowed us to best discriminate between the possible source signals before we explored how different combinations of these source signals could explain the bulk chemical composition of the core samples. In contrast to the first approach, a stepwise LDA was performed on the data from all tributaries (i.e., without the core samples) to identify and remove dispensable variables. Additionally, data of individual tributaries were removed if they were recognized as potential outliers in the respective group of source rocks. These outliers were identified in the PCA (principal component analysis) biplots which were generated for a visual assessment of the data. The data were converted with a centered log-ratio transformation before the PCA. This was a reiterative approach, and a variety of provenance analyses were conducted in different runs.

The processing data sets that resulted from either approach were finally analyzed with the `fingerPro` *unmix()* function (Lizaga et al., 2020). This function determines the contribution of the potential parent rock groups to the relative composition of each core sample. The function applies the following linear multivariate mixing model:

$$\sum_{j=1}^{m} a_{i,j} \cdot \omega_j = b_i, \quad (1)$$

where b_i is the observed relative contribution of one variable i (e.g., SiO_2; $i = 1$ to n) to the sediment mixture (i.e., a core sample), $a_{i,j}$ is the observation of the variable i in the source type j (e.g., Helvetic; $j = 1$ to m), ω_j is the unknown relative contribution of the source type j to the sediment mixture, m is the number of sediment sources (i.e., Helvetic, External, Penninic, and Klippen), and n is the number of observed variables that are allowed in the unmixing procedure (i.e., sediment bulk chemistry measurements). The results of the respective runs were exported to spread sheets and plotted for visual comparison. The unmixing results were plotted in a downhole log in a final step. The *unmix()* function calculates the goodness of fit (GOF) to evaluate the unmixing results and to return the best unmixing solution. An average GOF was determined for each of the 52 processing data sets, and these averages vary with the number of input variables and catchments. Thus, we compared the average GOF of the different runs to evaluate how well the unmixing performed. The final unmixing results were compiled according to the sample position within the stratigraphic succession, and the respective mean values and their standard deviation were calculated.

3.3 Elemental correlations

We additionally used the carbon–nitrogen–sulfur (CNS) data, namely the carbonate content derived from the total inorganic carbon (TIC) and the total organic carbon (TOC) content, as well as the material magnetic susceptibility (MS) data presented in Schwenk et al. (2022). Note that the respective data are available in Schwenk et al. (2021). The unmixing results were then compared to these data to investigate possible correlations. Furthermore, we plotted ratios of measured compounds and elements to facilitate the interpretation of the unmixing results. Additionally, we added the CNS and the multi-sensor core logger (MSCL) data to explore possible correlations with the unmixing results. We selected those compound ratios that were considered by von Eynatten (2003) as diagnostic for fingerprinting the potential sources of Alpine Molasse sediments. According to von Eynatten (2003), the following ratios can be correlated to different parent rock groups: (i) Cr_2O_3 : Ba and Ni : Ba, which allow sources situated in ultramafic rocks to be identified (i.e., ophiolites in the Penninic); (ii) $Na_2O : SiO_2$, which correlates with the input of material from granitoid source rocks; (iii) $MgO : SiO_2$, which correlates with the relative contribution of material from dolomitic source rocks; and (iv) the Cr_2O_3 : Ni ratio, in which a high value (up to 16), caused by the stable and therefore relatively enriched heavy mineral Cr spinel, reflects a flysch source rock component, and in which lower values between 1.2 and 3.5 indicate first-cycle sources in the Penninic domain. We additionally considered the $CaO : SiO_2$ ratio to investigate possible correlations between the results of the ICP–ES measurements and the TIC-derived carbonate contents. We displayed the data in scatter plots to visually assess the correlation between the four components of the unmixing results and the respective compound ratios. Furthermore, we compared the $SiO_2 : Al_2O_3$ ratio to the amplitude of the MS measurements because they are positively correlated to larger grain sizes in the sediment (Weltje and von Eynatten, 2004). Finally, we considered the TOC content in the sedimentary succession because TOC values between 0.1 % and 0.6 % indicate low production rates of autochthonous organic material and point towards a detrital supply of the organic material (Meyers and Teranes, 2001; Larsen et al., 2011).

3.4 Heavy mineral analysis

In addition to the geochemical analysis of the mostly fine-grained sediment fraction, we conducted a heavy mineral

analysis on selected samples from the sandy intervals of the drill core. Heavy mineral analysis was used extensively on Pleistocene sediments and their Mesozoic to Cenozoic sedimentary bedrock in the Swiss Alpine foreland, thus providing a large database for comparison (e.g., Gasser and Nabholz, 1969; Schlunegger et al., 1993; von Eynatten, 2003). In the Pleistocene in particular, heavy mineral spectra have been used to infer the provenance of glaciofluvial deposits (Graf, 1993). However, the heavy mineral spectra supplied by the Aare and the Valais glaciers are very similar, with the only difference of blue sodic amphibole (glaucophane) commonly being attributed to the Valais Glacier source region and titanite being attributed to the Aare Glacier source region. Titanite, however, also occurs in the source area of the Valais Glacier (Stutenbecker et al., 2018). The important contribution of Molasse recycling from the underlying bedrock is further impeding the assignment of heavy minerals to specific source regions (Gasser and Nabholz, 1969).

Because of this complication, we additionally performed single-grain analysis on garnet (Morton, 1985). Detrital garnet geochemistry has been shown to successfully discriminate between source regions of different metamorphic grade and lithology in the Swiss Alps and is particularly effective in distinguishing detritus from the External massifs from that of Penninic origin (Stutenbecker et al., 2017). We chose samples V024, V092, and V203 to represent FA 4, FA 1.2 (both Sequence B), and FA 1.1 (Sequence A), respectively (Fig. 5). Following the approach of Stutenbecker et al. (2018) the grain size fractions 63–250 µm were used to separate heavy minerals. We applied standard heavy mineral separation techniques as outlined in Andò (2020). The heavy minerals were identified using a polarization microscope, and around 200 transparent heavy mineral grains were counted using a Pelcon point counter and an evenly spaced square grid of 0.3 mm step length (Garzanti and Andò, 2019).

From the remaining heavy mineral concentrate, around 100 garnet grains were handpicked using a binocular. The obtained grains were mounted in epoxy resin grain mounts, ground, polished, and analyzed at the University of Tübingen (Germany) using an Agilent 7900 inductively coupled plasma mass spectrometer (ICP–MS) coupled with an Applied Spectra RESOlution-SE laser ablation system with a A155 sample cell. The laser energy was 5 J cm^{-2}, and we used a laser spot size of 30 µm diameter. The ICP–MS was tuned with the NIST SRM612 glass standard. The analysis was time resolved with a total integration time of ca. 0.57 s. The background was measured for 20 s, followed by 30 s of sample measurement. The raw data were cleaned and reduced with an internal software from the University of Tübingen. The garnets were classified using the random forest classification by Schönig et al. (2021) that assigns host rock types based on the concentrations (in wt %) of the element oxides SiO_2, TiO_2, Al_2O_3, Cr_2O_3, FeO total, MnO, MgO, and CaO. The three main host rock types are metamorphic (MM), igneous (IG), and metasomatic (MS). For metamorphic host rocks (MM), the garnets can be further subdivided into those of blueschist/greenschist facies (BS/GS), amphibolite facies (AM), granulite facies (GR), and eclogite facies/ultrahigh-pressure (EC/UHP) metamorphic grade. All three host rock types are furthermore assigned subclasses that in our case fall into three compositional categories: mafic (M), intermediate felsic/sedimentary (IF/S), or calcsilicate (CS). Accordingly, each garnet grain is assigned a combined class consisting of three single abbreviations, e.g., MM GR IF/S refers to a garnet formed in a metamorphic (MM), granulite facies rock (GR) of intermediate felsic or sedimentary composition (IF/S).

In order to compare the obtained heavy mineral and garnet data from the drill core to potential source rock units, we used data from the literature as provided in Table 3. Similar to the geochemistry approach, we defined the Penninic domain and External massifs as endmember sources, and their heavy mineral and detrital garnet signature is provided by modern rivers draining those units (Garzanti et al., 2012; Stutenbecker et al., 2018). The Helvetic nappes were excluded since they have extremely low heavy mineral fertility (Stutenbecker et al., 2018) and are therefore not likely to significantly contribute heavy minerals to the deposits in the Bümpliz trough. The limestones of the Klippen domain are expected to have equally low heavy mineral fertilities; however, this source area also contains garnet-bearing Cretaceous–Eocene flysch (most prominently the so-called Gurnigel flysch; Wildi, 1985), as well as Molasse rocks (Strunck and Matter, 2002). We complemented the existing data with two more samples from the modern Aare and Saane rivers that are expected to provide a fingerprint of the local Molasse around Bern and the mixed flysch/Molasse rocks of the Klippen domain, respectively.

For visual examination of the similarity of the drill core and source rock data, we used the nonmetric multidimensional scaling (MDS) function of Vermeesch et al. (2016).

4 Results

4.1 Geochemistry

The results of the ICP–ES measurements are available in the Supplement. These data reflect the bulk chemical composition of the individual samples and are the basis for the conducted provenance analysis.

Figure 6 shows the PCA results from four different runs (i.e., combinations of variables and tributaries) for which the second approach described above was employed. Overall, the discrimination between the four source groups (lithotectonic units) is good for any of the data sets. The plots in Fig. 6a and c show that one catchment sample in each of the External, the Helvetic, and the Penninic domains is located far off the center of the respective groups, and that these samples could be considered outliers. The discrimination becomes considerably better when individual variables are removed

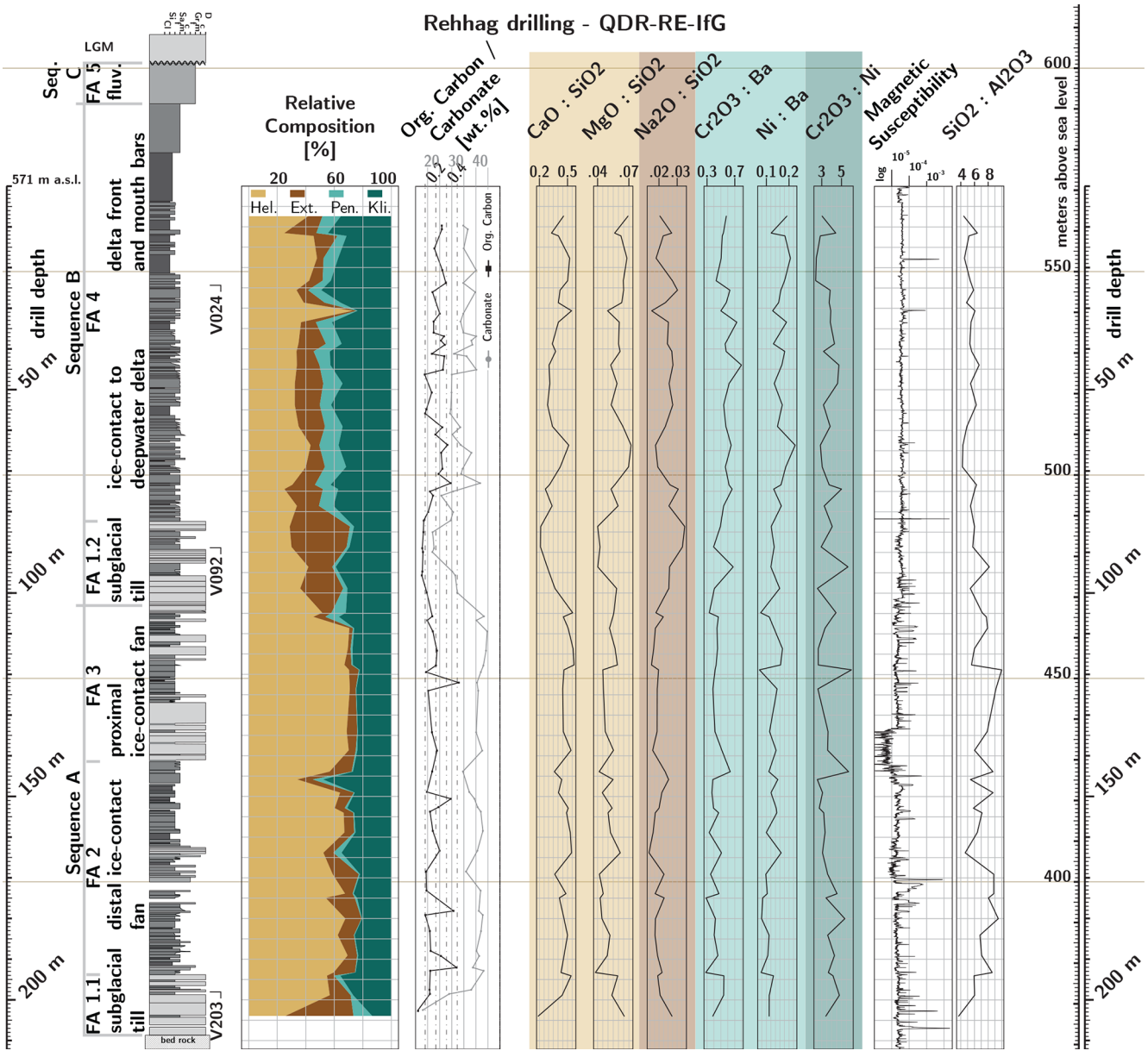

Figure 5. Illustration of the unmixing results presented in Table 2, together with the log of the sedimentary succession recovered in the scientific drilling at the Rehhag site (Schwenk et al., 2022). The sampling depths of the heavy mineral and garnet samples are indicated alongside the log. Additionally, the results of the CNS analysis (TOC and carbonate content) are presented along with the readings of the magnetic susceptibility (MS) that had been reported by the aforementioned authors. Furthermore, the variation in compound ratios that were used to distinguish different source lithologies in the provenance analysis of Swiss Molasse sandstones (von Eynatten, 2003) is presented. The compound ratios are sorted and colored to reflect the lithotectonic units that can potentially be linked to in the sediment mixture. The MS of the sediment and the $SiO_2 : Al_2O_3$ ratio in the sediment mixture can be used to infer the grain size in the respective core sections. Please refer to the text for a detailed discussion.

from the analysis. MgO, Ba, Zr, Nb, and Sc are missing in Fig. 6a, b and lead to a better discrimination in the first principle component (PC1) which is the major axis to distinguish sedimentary from crustal source rocks (Helvetic/Klippen vs. External/Penninic). The removal of individual catchments, for example from the Helvetic group (Fig. 6b, d), does not change the results significantly. Nevertheless, the data set with a reduced set of variables and with one missing catchment is most discriminative in the PCA (Fig. 6b). This finding is corroborated by the comparison of the average GOF that resulted from the unmixing of different data set combinations, the results of which are presented in Table 4.

Table 3. Database from the Central Alps used for the comparison of heavy mineral and detrital garnet data.

Lithotectonic unit	Heavy mineral data	Garnet data
Penninic nappes	Borgne, Vispa, Navisence, Turtmanna, and Printse rivers (Garzanti et al., 2012; Stutenbecker et al., 2018)	Borgne and Vispa rivers (Stutenbecker et al., 2017)
External massifs	Wysswasser, Münstigerbach, and Lonza rivers (Garzanti et al., 2012; Stutenbecker et al., 2018)	Wysswasser and Goneri rivers (Stutenbecker et al., 2017)
"Klippen domain" (including flysch nappes and Molasse)	Molasse bedrock from Frasson (1947) and Strunck and Matter (2002)	Saane River (this study), Ärgera River (Gurnigel flysch; Stutenbecker et al., 2019)
Local Molasse bedrock	Lower Freshwater Molasse near Bern (Lüthy et al., 1963), Lower Freshwater Molasse near Thun (Füchtbauer, 1964)	Aare River (this study)

Table 4. The goodness of fit (GOF) of the unmixing performed with different input data sets. The first GOF value was returned for the unmixing results using the first approach. The remaining six GOF values were returned by the unmixing step in the second approach. The acronyms indicate the number of input variables or if all variables were used (av) and if one catchment was removed (woLue) or if all catchments were used (ac).

	av-ac (1st)	13-woLue	12-woLue	14-woLue	13-ac	av-woLue	av-ac
GOF	0.92	0.82	0.82	0.82	0.81	0.81	0.79

4.2 Unmixing

The unmixing results in Fig. 7a to d were obtained through the procedure described above as the second approach. The unmixing results of the data set that was considered as most representative are presented in Table 2 and Fig. 7c. An account of the variations in the unmixing results with regard to the distinguished Sequences A and B as well as to the different FAs is presented in Table 5. All these plots reveal a significant change in the sediment composition from 99 to 105 m depth that separates the drilled suite in two distinct sections. The lower half is dominated by material derived from the Helvetic sources (65 %). The Klippen nappe contributes a stable background (25 %) to the mixture. A single peak in Klippen material (ca. 40 %) is detected at 145 m depth. The contribution of Penninic material to the mixture (< 3 %) is too low to determine any trends. Material input from the External massifs is prominent at depths > 143 m. A third significant peak of material input from the External massifs can be found at a depth of 203 m. There, between 55 % and 65 % of the material is derived from External sources alone. This 10 % difference is compensated for by material from Penninic sources, yet this depends on the choice of the input variables for the unmixing step. Throughout the lower half of the drilled sedimentary suite the material input from External sources decreases upsection, whereas the relative abundance of sediment from Helvetic sources increases. Between depths of 108 and 139 m the unmixing results show the lowest variability in the sediment composition. The upper half of the drilled suite shows a greater influence of the External, Klippen, and Penninic sources. Between depths of 74 and 99 m material from the External massifs visually dominates the sediment mixture (ca. 32 %), although the material is derived from External, Helvetic, and Klippen sources in about equal proportions. At depths between 7 and 74 m the Penninic and External contribution is relatively stable, and most of the variance is caused by changes in the contribution from Klippen and Helvetic sources. In the same section, the relative abundance of sediment from Penninic sources reaches the highest value (10 %) in all of the sections. A single peak in Helvetic material (ca. 75 %) at a depth of 30 m is counterbalanced by equivalent reductions of material contributions from Klippen and External sources.

Figure 7e depicts the results of the unmixing process based on data that were compiled and analyzed following the first approach outlined above. In this solution, the sediment composition is much more variable. Overall, the contribution of Penninic sources is more pronounced. The trends that were described for the plots in Fig. 7a through d are vaguely present in this fifth plot, yet these trends are attenuated by the large variability in sediment composition determined in the unmixing step. Nevertheless, in this approach the average GOF for all 52 unmixing results was 0.92 (Table 4).

Figure 5 reveals that the unconformity between Sequences A and B at a depth of 103 m is also reflected by a change in the sediment composition. Likewise, transitions

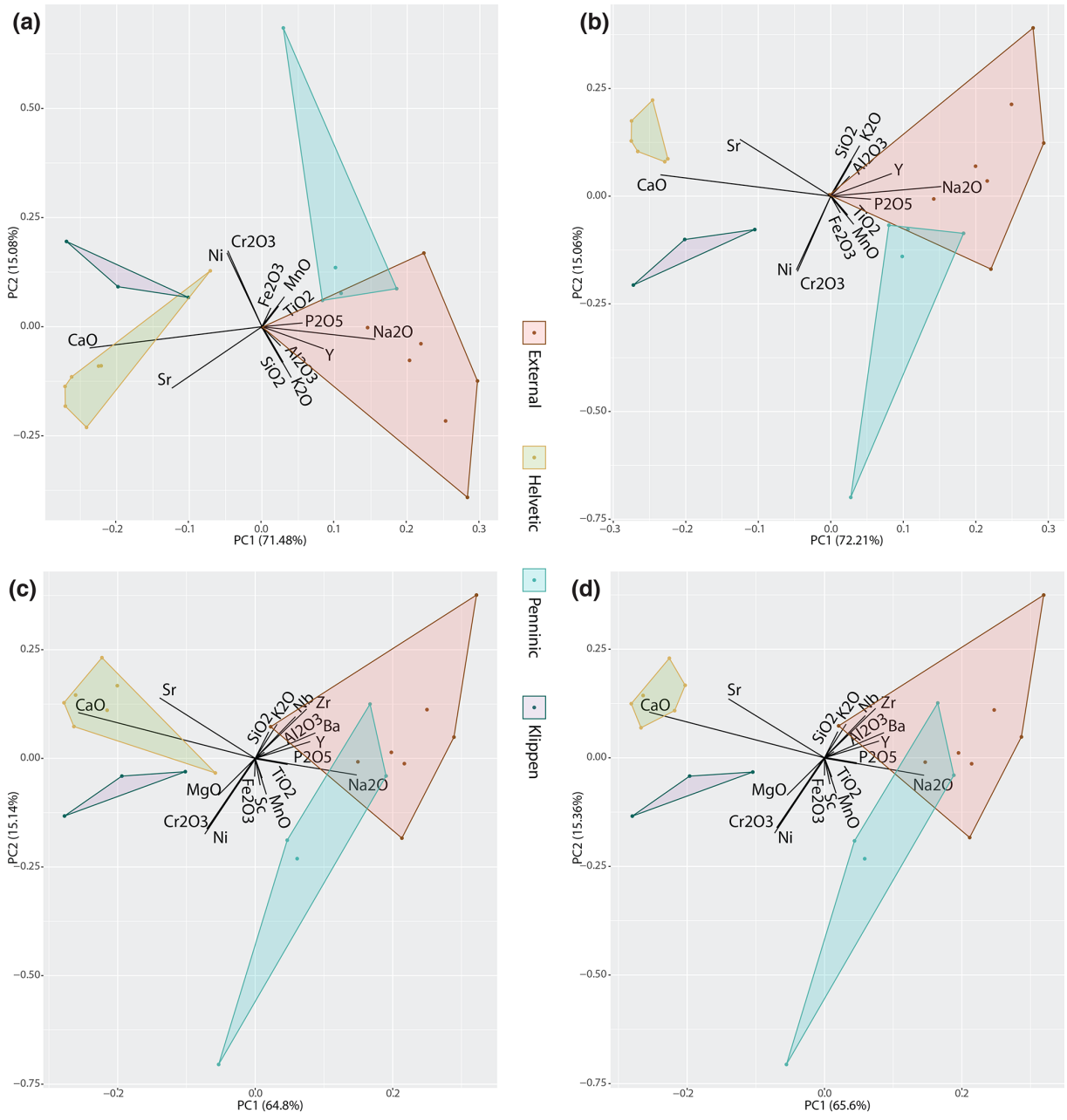

Figure 6. Results of the principal component analyses (PCA) performed exemplarily on four different data sets. The total number of variables was reduced from 18 to 13 in **(a)** and **(b)** by removing MgO, Ba, Zr, Nb, and Sc. The full set of variables was used in **(c)** and **(d)**. The data set of one tributary (Lue – Lütschine) in the Helvetic group was removed in **(b)** and **(d)**. Therefore, the plot in **(c)** shows the PCA results based on the complete data set.

between the distinguished facies assemblages at 83, 141, and 194 m depth correspond well with the described changes in the sediment composition. Henceforth, we describe the results taking into account the unconformity between Sequences A and B.

4.3 Element correlations

Figure 5 additionally displays different compound ratios that can be used to assess the unmixing results (see correlation plots in Appendix Fig. A1). The variability of these compound ratios with regard to the distinguished Sequences A and B as well as to the FAs is presented in Table 5. The carbonate content in the recovered sediment, the CaO : SiO_2 ratio, and the calculated input from the Helvetic units are

Table 5. Mean and standard deviation of the unmixing results determined from the samples in the two sequences and in the five facies assemblages (FAs) distinguished in the sedimentary succession. Similarly, the mean and standard deviation of distinctive compound ratios were determined in the same units to evaluate the unmixing results. Please refer to the text for further descriptions.

Rel. composition (%)	Helvetic	External	Penninic	Klippen
Seq. B	37 ± 10	17 ± 10	9 ± 4	37 ± 6
Seq. A	60 ± 11	10 ± 9	3 ± 4	27 ± 6
FA 4	38 ± 10	14 ± 6	10 ± 3	38 ± 6
FA 1.2	34 ± 6	32 ± 11	3 ± 0	31 ± 5
FA 3	65 ± 10	5 ± 2	3 ± 4	27 ± 5
FA 2	60 ± 9	10 ± 5	2 ± 2	28 ± 7
FA 1.1	41 ± 22	31 ± 23	7 ± 8	20 ± 9

Comp. ratios	$CaO : SiO_2$	$MgO : SiO_2$	$Na_2O : SiO_2$	Cr_2O_3 : Ba	Ni : Ba	Cr_2O_3 : Ni	$SiO_2 : Al_2O_3$
Seq. B	0.37 ± 0.09	0.0584 ± 0.0089	0.0252 ± 0.0045	0.57 ± 0.10	0.16 ± 0.03	3.64 ± 0.85	5.59 ± 0.87
Seq. A	0.47 ± 0.08	0.0508 ± 0.0069	0.0197 ± 0.0030	0.43 ± 0.08	0.12 ± 0.03	3.75 ± 0.94	7.22 ± 1.59
FA 4	0.39 ± 0.08	0.0610 ± 0.0062	0.0243 ± 0.0041	0.59 ± 0.08	0.17 ± 0.03	3.61 ± 0.75	5.44 ± 0.73
FA 1.2	0.27 ± 0.07	0.0452 ± 0.0087	0.0296 ± 0.0046	0.49 ± 0.13	0.13 ± 0.02	3.80 ± 1.39	6.33 ± 1.25
FA 3	0.51 ± 0.05	0.0523 ± 0.0052	0.0184 ± 0.0020	0.43 ± 0.05	0.13 ± 0.04	3.67 ± 1.09	7.49 ± 1.48
FA 2	0.46 ± 0.06	0.0488 ± 0.0070	0.0199 ± 0.0029	0.42 ± 0.10	0.12 ± 0.03	3.75 ± 0.90	7.36 ± 1.49
FA 1.1	0.32 ± 0.18	0.0596 ± 0.0083	0.0239 ± 0.0046	0.46 ± 0.11	0.11 ± 0.00	4.10 ± 0.96	4.86 ± 1.64

positively correlated. In contrast, the $CaO : SiO_2$ ratio is not correlated to the portion of material derived from the Klippen domain. The correlation between the $MgO : SiO_2$ ratio and the relative abundance of material derived from Helvetic units in Sequences A and B is negative or very weak, respectively. Although the apparent input of material from Helvetic sources is higher in Sequence A than in Sequence B, the contrary is the case for the $MgO : SiO_2$ ratio, which is higher in the upper part. For the entire core, a weak positive correlation exists between the $MgO : SiO_2$ ratio and material derived from the Klippen domain. Furthermore, in Sequences A and B the $MgO : SiO_2$ ratio is positively correlated to the portion of material of Penninic origin. However, in Sequence A the calculated contribution from Penninic sources is less than 3 % on average and mostly below 1 %. The $Na_2O : SiO_2$ ratio, which is considered to be representative for the portion of sediment derived from the External units, increases significantly across the unconformity between Sequences A and B. Overall, the $Na_2O : SiO_2$ ratio is positively correlated with the portion of material from the External massifs throughout the core. The Cr_2O_3 : Ba and Ni : Ba ratios in Sequence A do not correlate with the input of material from Penninic sources, yet a slight positive correlation is present in Sequence B. The Cr_2O_3 : Ni ratio cannot be used to infer the input of material from Klippen sources as the ratio is in the range of 2 to 5 and thus too low to make an inference on such an input. Furthermore, this ratio is not correlated with the abundance of material derived from Penninic sources. In Sequence A, the $SiO_2 : Al_2O_3$ ratio is significantly higher than in Sequence B, and likewise the MS amplitude is notably higher in the lower than in the upper half of the core. Hence, the MS amplitude and the $SiO_2 : Al_2O_3$ ratio correlate well, indicating that the sediment in Sequence A is composed of larger clasts than Sequence B, which is consistent with the occurrence of a large number of gravel and diamictic beds in the log. Finally, the low TOC content between 0.2 % and 0.4 % observed in the sediment indicates that the organic material was most likely not produced within the lake itself. This points to the supply of organic material from recycled older sediments or from the bedrock.

4.4 Heavy mineral analysis

The three selected sand samples have heavy mineral concentrations of 1 %–2 % ("moderately poor" following Garzanti and Andò, 2007). The heavy mineral spectra (Fig. 8) of the three selected sand samples are all dominated by epidote group minerals (over 60 %; including epidote, clinozoisite, and rarely zoisite) with moderate contents of garnet (7 %–22 %), hornblende (4 %–11 %), and apatite (3 %–6 %) and minor contents (< 5 %) of staurolite, titanite, zircon, tourmaline, rutile, blue sodic amphibole, chloritoid, and sillimanite. Spurious grains (Garzanti and Andò, 2007) encountered in the concentrates include chlorite, ankerite–dolomite, biotite, and glauconite. Although the three samples are relatively similar in their heavy mineral content, we noted a slight increase in hornblende from the lowermost sample (V203, 4 %) to the uppermost sample (V024, 11 %). Blue sodic amphibole is only present in samples V092 and V024, whereas chloritoid is found in samples V203 and V024 but not in sample V092.

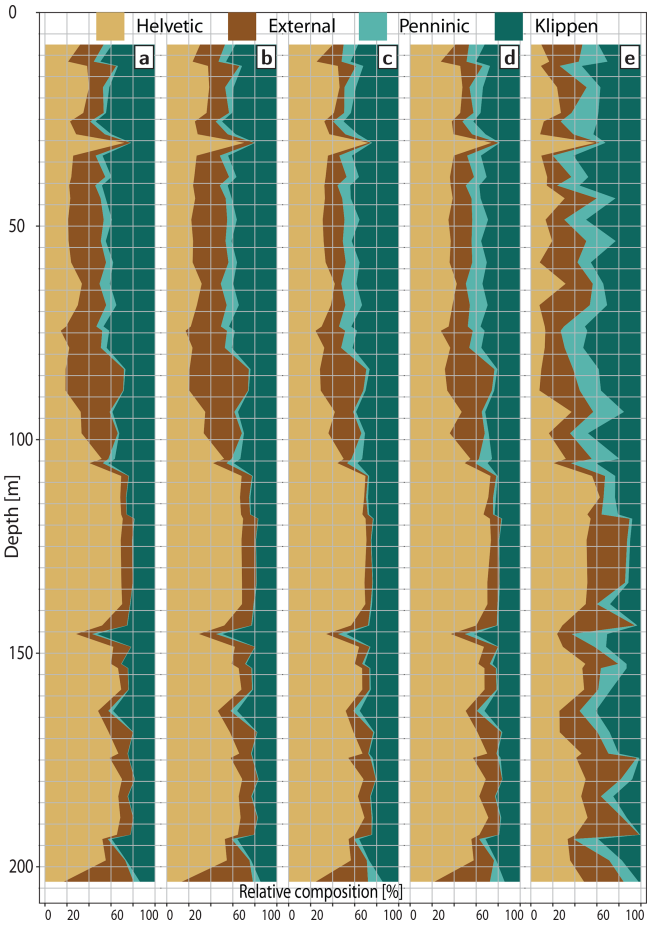

Figure 7. Results of the unmixing step. The graphs in **(a)** through **(d)** are based on the data sets used in their equivalents in Fig. 6. Panel **(e)** shows the results of the procedure described in Sect. 3 as the first approach. The plot in **(c)** shows the results that are finally discussed and that are presented alongside the sedimentary log in Fig. 5.

Figure 9 shows the results from the study of the single-grain garnet variety. In all three core samples, more than 60 % of garnets are derived from intermediate felsic/metasedimentary rocks of amphibolite and blue-/greenschist facies metamorphism (classes MM AM IF/S and MM BS/GS IF/S). From the base (V203) to the top (V024) of the core, the portion of eclogite facies metamorphic mafic garnet (MM EC/UHP M), as well as granulite facies metamorphic garnet (class MM GR IF/S), increases, whereas the amount of blue-/greenschist facies metamorphic mafic garnet (class MM BS/GS M) decreases.

Figure 10 shows the similarity of our data and the literature data (Table 3) as obtained by multidimensional scaling. The comparison of heavy mineral data (Fig. 10a) shows that the three selected core samples plot close together and somewhat in between the two clusters formed by the local Molasse bedrock and the modern streams draining the External massifs and Penninic nappes. The Penninic and External heavy mineral signatures are similar, and the two lithotectonic units are therefore not distinguishable. The detrital garnet data (Fig. 10b), in contrast, allow a distinction of garnets derived from the three considered source units (External massifs, Penninic, Molasse/flysch). Sample V203 is equally similar to all three possible sources, sample V092 plots in between the External massifs and Molasse/flysch sources, and sample V024 is markedly more similar to the Molasse/flysch sources.

5 Discussion

5.1 The selection of tributaries and variables for the unmixing model

The first approach yielded the combinations of most discriminative variables in each of the 52 processing data sets which in turn resulted in the observed clear distinction of the parent rock groups in the individual core samples and accordingly resulted in a very good fitting during the unmixing step (GOF 0.92). Although the trend in the sediment composition that was obtained using the second approach (Fig. 7a through d) is present in the unmixing results of the first approach (Fig. 7e), we disregard the results of the first approach as the solution appears to be overly specific to the individual core samples.

The choice of a distinct set of variables has an impact on the discrimination between the four domains of parent rocks (Fig. 6). In our case, however, the exclusion of specific variables or specific tributary data sets has no distinct advantage for the calculation of the relative composition in the unmixing process and for the calculated level of the unmixing results. This is visible in Fig. 7a through d and also in the minor changes in the GOF as presented in Table 4. In contrast, the unmixing results that were calculated from a reduced set of variables apparently were deprived of their potential to identify Penninic sources, as exemplified by the plots in Fig. 7a and b. Hence, we use the unmixing results from the complete data set (all variables and all tributaries; Figs. 6c, 7c, Table 2) in the following discussion.

5.2 Assessment of the geochemical data and the unmixing results

The unmixing results calculated from the complete set of available chemical data had an average GOF of 0.79. The highest GOF in all data sets which were compiled and analyzed with the second approach was 0.82. However, the dedicated selection of variables and tributaries had minor effects on the unmixing results. Moreover, the $SiO_2 : Al_2O_3$ ratio and the MS data correlate positively, which we regard as evidence that the sediment bulk chemical data in general are related to the sedimentary facies. Furthermore, the comparison of our unmixing results with provenance markers used

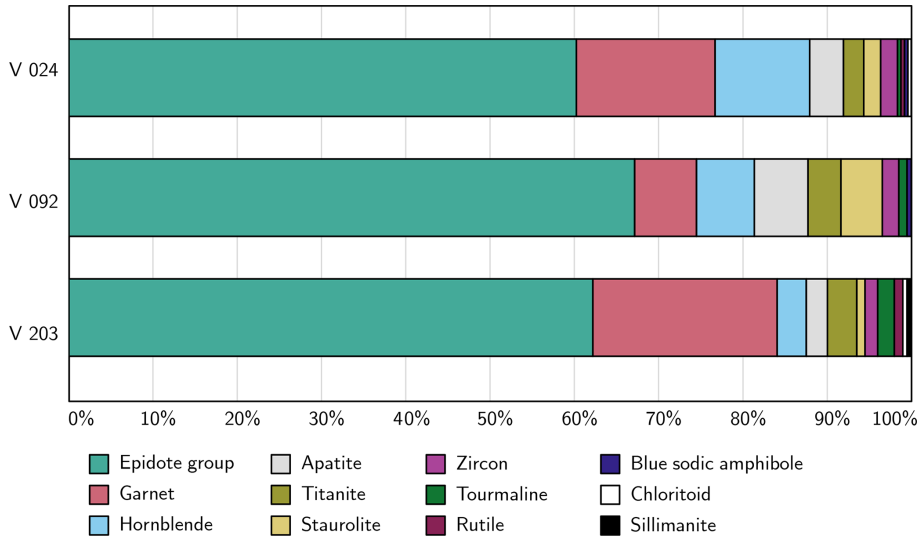

Figure 8. Heavy mineral composition of the three core samples in stratigraphic order. The sampling depth of each of the samples is shown in Fig. 5.

by von Eynatten (2003) showed a good correlation. The positive correlation between the $CaO : SiO_2$ ratio and both the relative contribution of the Helvetic component in the provenance signal and the measured carbonate content indicates that most of the carbonate in the sediment was probably derived from the Helvetic source rocks. Due to the absence of a correlation, the carbonate was not derived from the Klippen domain. A slight correlation between the $MgO : SiO_2$ ratio and the abundance of the Helvetic component is present in Sequence A. However, in the deposits of Sequence B, where more material of Penninic and less detritus of Helvetic provenance were supplied, the $MgO : SiO_2$ ratio is correlated to the abundance of the Penninic component. The positive correlation between material from Penninic sources and the $MgO : SiO_2$ ratio in Sequence A should not be overstated due to the very low input from the Penninic domain. The weak positive correlation of the $MgO : SiO_2$ ratio and the Klippen component indicates a low yet continuous contribution from the latter domain. In combination, this suggests that the $MgO : SiO_2$ ratio reflects the input of material derived from dolomitic source rocks (Klippen, Helvetic) in Sequence A, yet in Sequence B the ratio might reflect a combined contribution of magnesium-rich minerals derived from the ophiolite-bearing bedrock that occurs in the Penninic domain and dolomitic source rocks mainly located in the Klippen domain (cf. von Eynatten, 2003). The positive correlation between the $Na_2O : SiO_2$ ratio and the relative abundance of the External component probably indicates that most of the sodium in the sediment mixture was derived from felsic and feldspar-rich granitoid parent rocks in the External massifs. Both the $Cr_2O_3 : Ba$ and the $Ni : Ba$ ratios show a weak correlation with the abundance of the Penninic component in the provenance signal in Sequence B. Hence, we suggest that nickel and chromium in Sequence B were mainly derived from the ophiolite-bearing parent rocks in the Penninic units, where the ophiolitic bedrock is known to contain chrome spinel and Ni-rich serpentinites. As outlined above, the $Cr_2O_3 : Ni$ ratio in our data can apparently not be used as a proxy for the relative abundance of material derived from the flysch sediments in the Klippen domain. Generally, ratios between 1.2 and 3.5 can be considered as indicative of material derived from ultramafic and metabasaltic rocks located in the Penninic domain (see von Eynatten, 2003, and sources therein). However, the $Cr_2O_3 : Ni$ ratio does not show a particular trend or a correlation with the relative abundance of the Penninic component in the unmixing results. Accordingly, all but one of the geochemical proxies (i.e., compound ratios) that were used by von Eynatten (2003) to distinguish parent rock units in the central Swiss Alps could be used to distinguish between the four domains of parent rocks as material sources for the drilled core. This is a good indicator that the presented sediment bulk chemical data contain a provenance signal that is actually reflected by the unmixing results.

5.3 Provenance interpretation

Henceforth, we use the ice flow patterns of the LGM to infer the possible material composition that was transported by the Valais, the Saane, and the Aare glaciers. During the LGM, the ice streams were arranged in a way that probably impeded the supply of material from the External massifs in the upper Rhône Valley to the Bern area (Fig. 3). Hence, material of Penninic provenance could only be transported by the Valais Glacier, whereas material of External provenance, namely from the Aar Massif, could only have been provided by the Aare Glacier. Please note that the admixture of material derived from the Mont Blanc Massif to the sediment

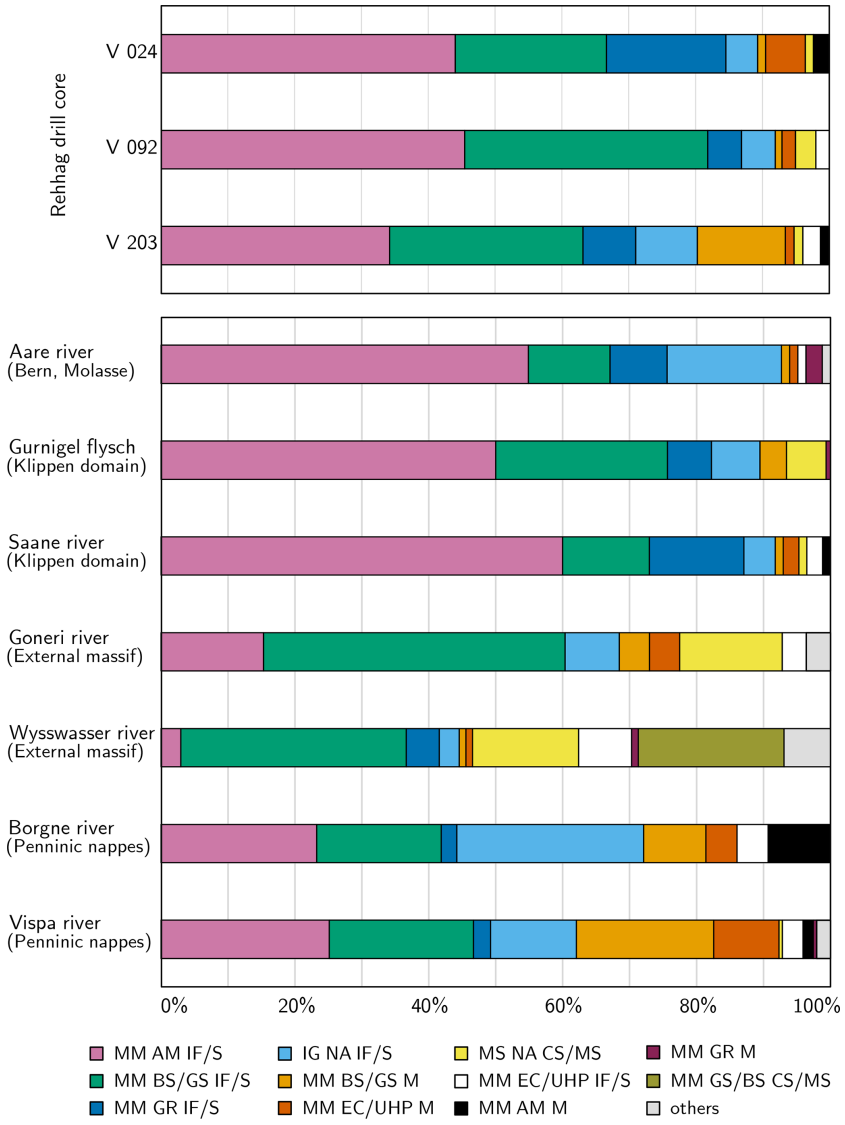

Figure 9. Classification results of detrital garnet based on geochemistry in the core samples and seven reference tributaries located in the possible source rocks. The sampling depth of each of the core samples is shown in Fig. 5. The garnet classes are composed of the abbreviations of the three groups (host rock, metamorphic grade, and composition) as defined by Schönig et al. (2021); MM – metamorphic, IG – igneous, MS – metasomatic, AM – amphibolite facies, GR – granulite facies, BS/GS – blueschist/greenschist facies, EC/UHP – eclogite facies/ultrahigh-pressure, NA – not defined (for rocks without metamorphic overprint), M – mafic, IF/S – intermediate felsic/sedimentary, CS/MS – calcsilicate/metasomatic.

transported by the Valais Glacier would result in a signal that contains both an External and a Penninic component. As a consequence, for sections (such as Sequence A) where a Penninic signal is missing, we can confidently attribute the material derived from the External domain to the Aare Glacier. In the same sense, material from Helvetic sources was most likely also transported by the Aare Glacier as can be deduced from the abundance of this lithotectonic unit within the Aare catchment (Table 1). Therefore, we interpret the admixture of material from External and Penninic sources as evidence for the sediment supply by the Aare Glacier or the Valais Glacier, respectively. The Klippen domain could effectively contribute material to either ice stream; however, this part of the Alps was occupied by the Saane Glacier to a large extent during the LGM (Fig. 3). Consequently, this glacier is expected to transport a sediment mixture dominated by material of Klippen provenance (Table 1). Furthermore, reconstructions imply that in a full glacial setting such as during the LGM (Fig. 3) or any preceding glaciation, the Aare Glacier was pushed and deflected in a northeast direction upon its confluence with the Valais Glacier. In such a case, material from the Klippen domain could probably only

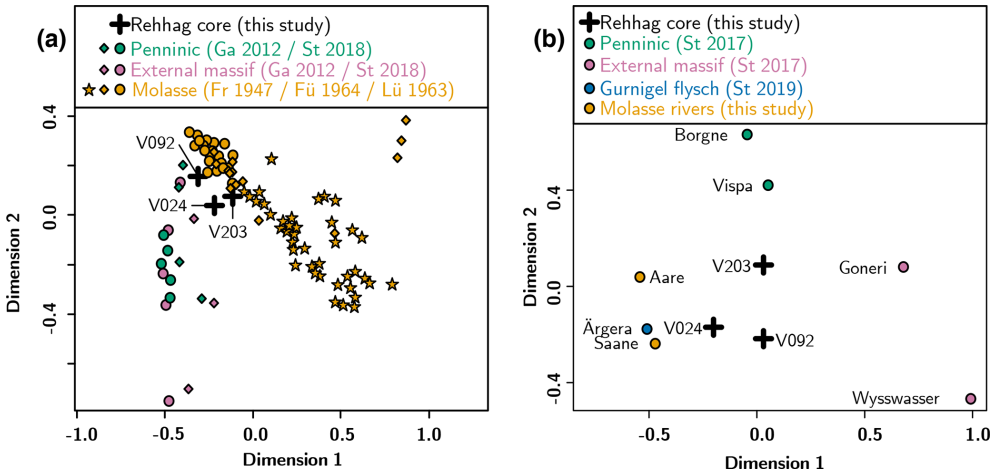

Figure 10. Results of the multidimensional scaling (MDS) of **(a)** the heavy mineral composition and **(b)** the garnet geochemical composition of three core samples compared to a database aggregated from published literature (see Table 3). The sampling depth of each of the core samples is shown in Fig. 5. The abbreviations of the literature used refer to Ga 2012 – Garzanti et al. (2012); St 2017, 2018, 2019 – Stutenbecker et al. (2017, 2018, 2019); Fr 1947 – Frasson (1947); Fü 1964 – Füchtbauer (1964); Lü 1963 – Lüthy et al. (1963).

be supplied by the Valais and mainly the Saane glaciers, and correspondingly a provenance signal from the Aare Valley would be missing in the sediment composition. Conversely, the absence of material of Penninic origin could indicate that the Valais Glacier did not advance to the Bern area and that material from Klippen sources was probably supplied by the Aare Glacier and mainly by the Saane Glacier. Finally, the bedrock that underlies the Quaternary succession at the Rehhag drill site consists of the Lower Freshwater Molasse (Schwenk et al., 2022), which is composed of the clastic sediment that was derived from the Klippen and the Penninic domains during the Late Oligocene and the Early Miocene (Schlunegger et al., 1993; Spiegel et al., 2002; von Eynatten, 2003; Anfinson et al., 2020). Therefore, it is likely that the distinction between a first-cycle Klippen and Penninic source signal and a Molasse signal is not straightforward if only the unmixing results are used.

However, heavy mineral analysis provides important insights into the role of Molasse recycling. Modern sediment supplied by most Alpine units, including the External massifs and Penninic nappes, carries abundant hornblende (usually 20 %–30 %; Garzanti et al., 2012; Stutenbecker et al., 2018). In contrast, hornblende rarely makes up more than 1 % of the heavy mineral spectra in the Swiss Molasse (Füchtbauer, 1964; Schlunegger et al., 1993; von Eynatten, 2003). The low percentage of hornblende in the lowermost core sample V203 indicates an important contribution from the hornblende-poor Molasse, which is confirmed by the overall similarity of its heavy mineral spectrum to that of the local bedrock in the Bern area (Fig. 10a). The higher hornblende content in the upper samples V092 and V024 (Fig. 8) points toward an increasingly important input of first-cycle sediment from hornblende-rich sources. Based on the heavy mineral data alone, the origin of this first-cycle detritus remains ambiguous, since the External massifs and Penninic nappes supply indistinguishable heavy mineral spectra (Fig. 10a; Stutenbecker et al., 2018). However, the similarity of the detrital garnet spectra (Fig. 10b) suggests that this first-cycle material in samples V092 and V024 was derived from the External massifs rather than from the Penninic nappes. Nevertheless, the garnet data suggest an evident contribution from (local) Molasse bedrock, especially in sample V024.

5.4 Combining the sedimentary processes and the provenance signals

Here, we combine information provided by the provenance signals with the sedimentary information elaborated by Schwenk et al. (2022) to develop a scenario of how the different glaciers contributed to the filling of the targeted trough.

5.4.1 Subglacial till in Sequence A

The geological history recorded by the sedimentary succession started with the deposition of the till assemblage at the base of Sequence A (FA 1.1), which shows the lowest admixture of the Helvetic and Klippen components and an apparent exceptional contribution of External and Penninic material. However we consider the Penninic signal as a record of recycled material derived from the Molasse bedrock and not as a first-cycle signal from the Central Alps on the basis of the heavy mineral spectra and the following three sedimentological observations (Schwenk et al., 2022): (i) the till beds overlying the bedrock contact (in FA 1.1) contain large rafts of the Lower Freshwater Molasse bedrock, (ii) the color of the till resembles that of the bedrock, and (iii) the FA1.1 sediments are depleted in carbonate content similar to

the Molasse bedrock (Fig. 5; 0 %–20 %; Blaser et al., 1994). Furthermore, the large portion (> 45 %) of material from the External massifs encountered in the basal till of FA 1.1 suggests that this till was most likely supplied by the Aare Glacier and not by the Valais Glacier. Farther upsection, yet within the lower till assemblage (i.e., upper FA 1.1), where the sediment was probably deposited in subglacial conduits (Schwenk et al., 2022), the input from the Molasse bedrock apparently decreased. This section is similar in composition to the overlying assemblages.

5.4.2 Ice-contact fan deposits in Sequence A

The unmixing results show that the Aare Glacier was likely the main source of material during the deposition of the upper section of FA 1.1 and the deposition in the following proglacial lake setting recorded by FA 2 & 3. Overall, a stable background signal (> 25 %) related to the material supply of apparently Klippen provenance suggests that the sediment could have been supplied by the Aare Glacier, as well as by the Saane Glacier. Material supply to the lacustrine deposits by the Valais Glacier or input of detritus from the Molasse bedrock is unlikely due to the absence of a Penninic component in the provenance signal throughout most of FA 2 & 3. Isolated peaks pointing towards an occasional input of material with a Penninic origin and of more material with a Klippen origin (meters 175, 164, 153, 146, and 116 to 106) could indicate that a limited connection existed between the Bümpliz trough and the Valais Glacier, or alternatively it could point to an occasional supply of material from the surrounding Molasse bedrock. In general, the stable signal of Aare Valley provenance (Helvetic and External > 60 %) throughout FA 2 & 3 implies that the material supply was dominated by the initially retreating and then readvancing Aare Glacier.

5.4.3 Subglacial till in Sequence B

The Aare Glacier was also the ice stream that dominated the formation of the till assemblage (FA 1.2) at the base of Sequence B. In contrast to the underlying deposits of the ice-contact fan, this till contains a relatively large portion of material derived from the External massifs (> 40 %). Similar to the lower till, a Penninic contribution suggests an admixture of either Molasse material or material from the Valais Glacier. The heavy mineral spectra, as well as the detrital garnet data of sample V092, suggest no first-cycle Penninic source but rather a mixed contribution from External sources and Molasse recycling. We explain the stable Klippen background signal (> 25 %), which is also present in this assemblage, by the input of material through the Aare Glacier with a contribution from reworked sedimentary substratum. Combining the sedimentological evidence and the unmixing results, we suggest that the second till assemblage had most probably been formed by the Aare Glacier.

5.4.4 Lacustrine sediments in Sequence B

The provenance signal in the sediment of FA 4 is significantly different from the underlying assemblages. Within FA 4, the unmixing results imply material input from Helvetic and External sources which is > 50 % on average, and material from Klippen sources is at the highest level with an average of 38 %. Based on the occurrence of these three components, we interpret the material supply to have been strongly controlled by the Aare Glacier and the Saane Glacier. Furthermore, the highest admixture (ca. 10 %) of material with a Penninic origin in this section is most relevant because it could only have been supplied to the depositional site through the transport by the Valais Glacier or in response to a substantial increase in material derived from the Molasse bedrock. The heavy mineral and garnet data of sample V024 favor an origin from Molasse and possibly flysch sources in the Klippen domain that may have been supplied by the Saane Glacier.

5.5 Landscape evolution during the shallowing-up period of the Bümpliz trough

Because the Valais Glacier was not involved in the formation of the till at the base of Sequence A, we propose that the Aare Glacier was the dominant glacier in the Bern area. Accordingly, we envision a scenario in which the Valais Glacier had not reached the Bern area and did not deflect the Aare Glacier towards the northeast (Fig. 11a), which is different from the situation proposed for the LGM (Fig. 3; Favre, 1884; Baltzer, 1896; Bini et al., 2009; Ehlers et al., 2011).

Following the retreat of the Aare Glacier the Bümpliz trough was filled with water forming a lake that remained in contact with the glacier (Fig. 11b). However, the Valais Glacier or the Saane Glacier probably was still present on the Swiss Plateau as far east as our study area (i) to block the Bümpliz trough allowing the temporary formation of an ice-dammed lake and thus (ii) to allow the deposition of lacustrine sediments in Sequence A. Furthermore, the observed very low TOC content corroborates this scenario of an ice-dominated landscape free of terrestrial or aquatic plant life.

After the small basin had been filled with sediment, supplied mainly by the Aare Glacier and partially by the Saane Glacier, the Aare Glacier must have readvanced into the Bümpliz trough once more. During this advance an unknown amount of sediment was removed, which resulted in the formation of the truncation surface between Sequences A and B. Because the till sequence overlying this truncation was formed again by the Aare Glacier, the glacial environment surrounding the Bümpliz trough was once more different from the situation during the LGM (see above and Fig. 11c). Additionally, the inference that the Aare Glacier readvanced into the Bümpliz trough during the deposition of Sequence A and that it also formed the basal till of Sequence B lets us suggest that Sequences A and B were formed during two glacial advances within the same glacial period.

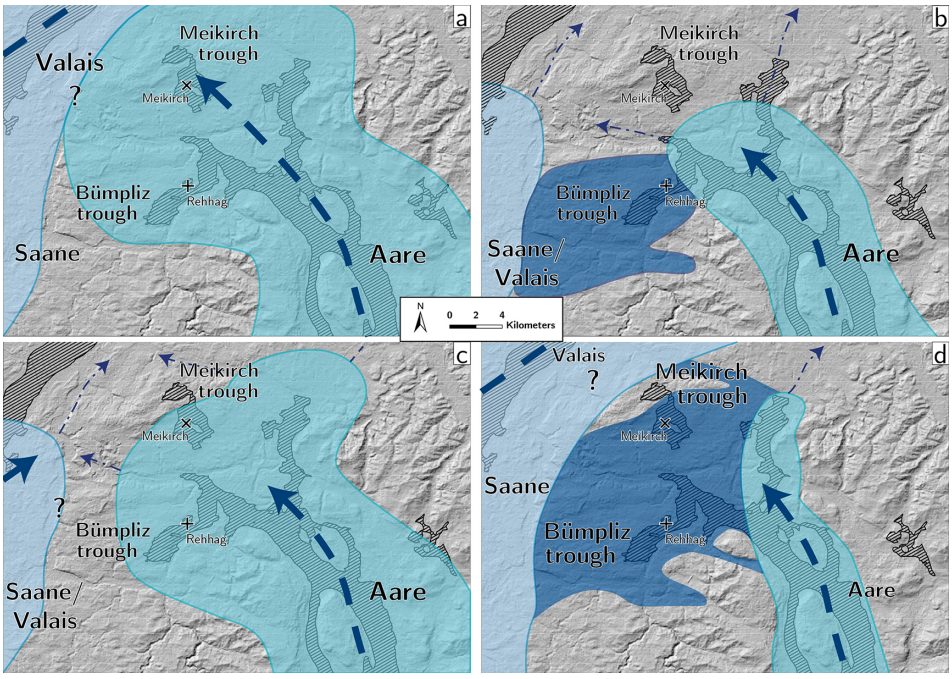

Figure 11. Proposed distribution of glacier ice in the Bern area based on the presented provenance analysis. **(a)** The Bümpliz trough is covered entirely by the Aare Glacier during the first glacial advance (FA 1.1). **(b)** The Aare Glacier retreated from the Bümpliz trough, yet remained in very close proximity, which led to the formation of ice-contact fans and an almost exclusive supply of material by the Aare Glacier (FA 2 & 3). **(c)** Readvance of the Aare Glacier into the Bümpliz trough (FA 1.2). **(d)** Rearranged distribution of the glacier lobes, when water was effectively blocked to form a lake (Fig. 2) and when the sediment was mainly by the Aare Glacier and partially by the Saane Glacier (FA 4). Shaded black areas indicate the position of overdeepenings in the Bern area (available via Bundesamt für Landestopografie swisstopo, 2021a). Elevation data from NASA/METI/AIST/Japan Spacesystems and U.S./Japan ASTER Science Team (2019). Please refer to the text for a detailed discussion.

Similar to the lower Sequence A, material supply by the Valais Glacier was minor or negligible during the deposition of Sequence B because heavy mineral and garnet data suggest that the Penninic component rather reflects a signal related to the recycling of the Molasse bedrock than a first-cycle signal. Nevertheless, we propose that the presence of the Valais Glacier in the study area was again, similar to the depositional environment proposed for Sequence A, a prerequisite to allow the formation of an ice-dammed lake which collected the meltwater of the adjacent ice streams (Fig. 11d). Potentially it was a single lake that spread out across the Bümpliz depression and that also occupied the Meikirch trough farther north. In fact, a late MIS 8 depositional age, based on luminescence dating, was suggested for a large suite of lacustrine deposits (ca. 40 m) within the sedimentary sequence in the Meikirch trough (Preusser et al., 2005). Considering the minimum depositional age between 250 to 300 ka (MIS 8; Schwenk et al., 2022) for the Bümpliz trough sequence, such a lacustrine connection between the two troughs seems possible.

In summary, the provenance data let us suggest that in the Bern area a LGM-like glacial setting of the glacier lobes had not been established during the period the investigated sedimentary sequence was deposited (ca. 250 to 300 ka, MIS 8; Preusser et al., 2005; Schwenk et al., 2022) because the evolution of the landscape in this region and the deposition of sediment was not dominated by the Valais Glacier but by the Aare Glacier.

6 Conclusions

Based on the results of the presented provenance analysis, we showed that glacier lobes in the Bern area were positioned in a different pattern during the MIS 8 glaciation than during the LGM. In particular, the dominance of material supplied by the Aare Glacier contradicts a scenario in which the Aare Glacier was deflected in a northeast direction by the Valais Glacier as was the case during the LGM. Furthermore, the provenance data provide additional evidence that the entire sedimentary sequence was deposited within a single glaciation yet during two separate glacial advances. Although the Valais Glacier had been present and could have supplied material occasionally, it might have never been relevant for the sediment supply during the deposition of the investigated sedimentary sequence. It appears that the Aare and the Saane glaciers were dominating the sediment supply

towards the Bümpliz trough, when a larger area in the vicinity of the glacier lobes was occupied by a lake.

The results of our provenance analysis thus substantiate the findings of Reber and Schlunegger (2016) in that the positioning of glacier lobes in the Bern area during an earlier glaciation was different than during the LGM. As a consequence, these differences could have been caused by variations in climate that affected the ice accumulation in the central Swiss Alps. Hence, the presented results could be used to constrain future ice flow and erosion models that focus on pre-LGM glaciations and the formation of overdeepenings on the Swiss Plateau.

Methodologically, we showed that the sediment bulk chemical data obtained from a drill core allow the stratigraphic architecture to be reproduced, which in our case is an architecture that was previously established based on the sedimentological analysis of these sediments. Certainly, the presented study benefits from the fact that two glaciers with sources in two lithologically different parts of the central Swiss Alps supplied the investigated sediment. Nevertheless, after the large-scale domains of potential parent rocks are identified, the bulk chemical data alone offer a strong fingerprinting proxy based on which the sediment provenance in drill cores can be determined, which then offers the basis to improve our understanding of how the landscape surrounding the drill site has evolved. Where the above prerequisites are met, it seems plausible that the presented workflow offers a robust, fast, and affordable way to determine changes in the sediment provenance for the fine-grained sedimentary infill of overdeepenings or for other glacial deposits. Potentially, the resolution of such provenance results is suitable to correlate sedimentary sequences across multiple boreholes apart from determining the depositional age of the recovered sediment.

Appendix A

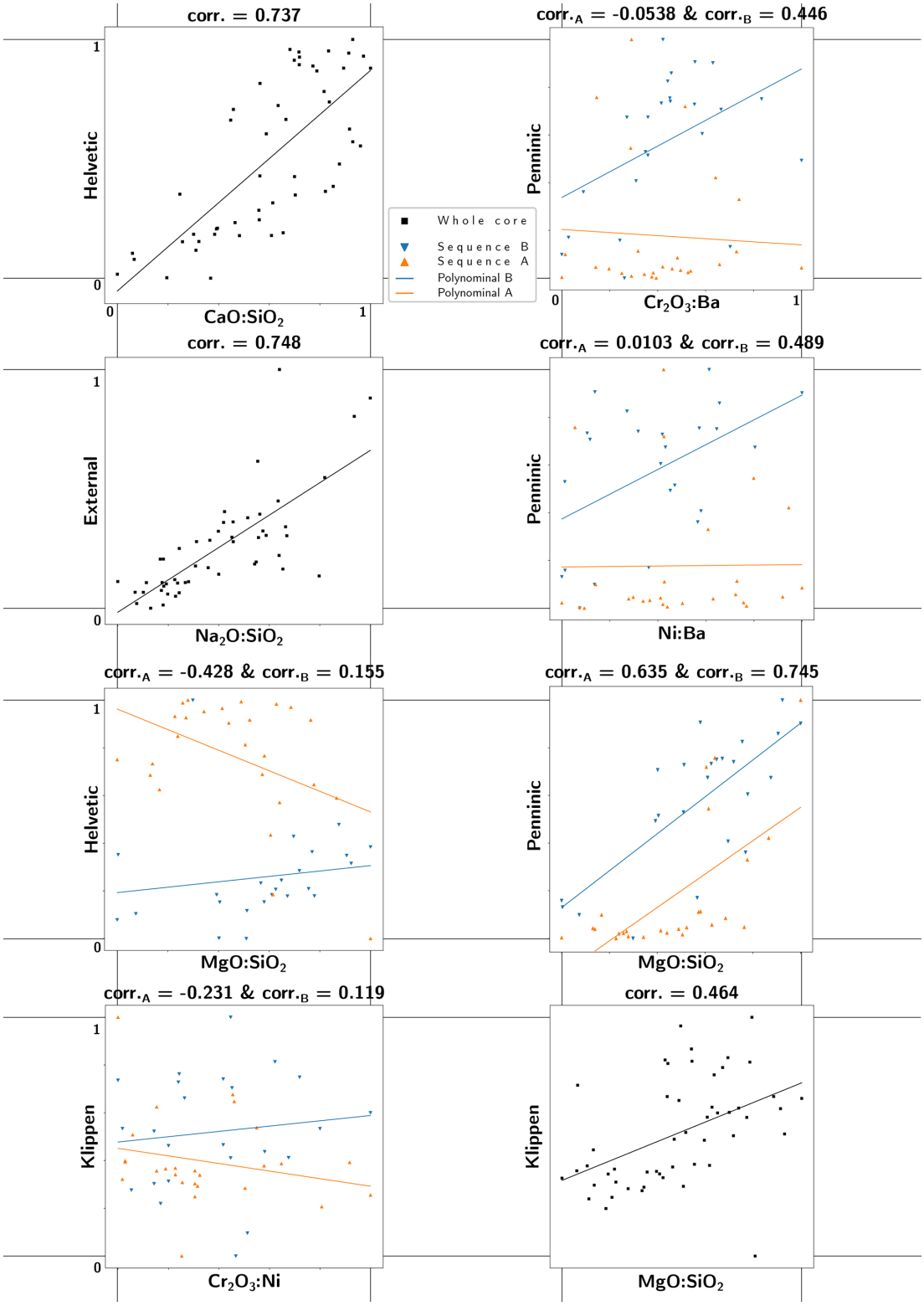

Figure A1. Different correlation plots showing the relation between the unmixing results and compound ratios used by von Eynatten (2003) and displayed in Fig. 5. The data were normalized, and the displayed trends were fitted with a first-degree polynomial.

Code and data availability. The petrochemical data and the R script used for their analysis are provided in the Supplement. The results of the heavy mineral and garnet analyses are also available in the Supplement.

Supplement. The supplement related to this article is available online at: https://doi.org/10.5194/egqsj-71-163-2022-supplement.

Author contributions. MAS collected and prepared the samples, analyzed the petrochemical data, and wrote the paper with support from FS. LS provided the heavy mineral and garnet measurements and the respective sections in the text, as well as helped with the analysis of the petrochemical data. MAS designed the core and field sampling campaign, and FS organized the funding. PS helped with the core sampling and the statistical analyses, and DB helped with field work, sample preparation, and improving the R script. All authors approved the text and the figures.

Competing interests. The contact author has declared that none of the authors has any competing interests.

Disclaimer. Publisher's note: Copernicus Publications remains neutral with regard to jurisdictional claims in published maps and institutional affiliations.

Acknowledgements. We acknowledge the friendly support and sample analyses by Bureau Veritas (CA). We thank the editor in charge, Gilles Rixhon, and two reviewers, Andreas Dehnert and Christoph Mayr, for helping improve our manuscript.

Financial support. This research has been supported by the Schweizerischer Nationalfonds zur Förderung der Wissenschaftlichen Forschung (grant no. 175555).

Review statement. This paper was edited by Gilles Rixhon and reviewed by Andreas Dehnert and Christoph Mayr.

References

Andò, S.: Gravimetric Separation of Heavy Minerals in Sediments and Rocks, Minerals, 10, 273, https://doi.org/10.3390/min10030273, 2020.

Anfinson, O. A., Stockli, D. F., Miller, J. C., Möller, A., and Schlunegger, F.: Tectonic exhumation of the Central Alps recorded by detrital zircon in the Molasse Basin, Switzerland, Solid Earth, 11, 2197–2220, https://doi.org/10.5194/se-11-2197-2020, 2020.

Bachmann, I.: Die Kander im Berner Oberland ein ehemaliges Gletscher- und Flussgebiet, Dalp'sche Buch- und Kunsthandlung, Bern, 1870.

Baltzer, A.: Der diluviale Aargletscher und seine Ablagerungen in der Gegend von Bern mit Berücksichtigung des Rhonegletschers, in: Der diluviale Aargletscher und seine Ablagerungen in der Gegend von Bern mit Berücksichtigung des Rhonegletschers, Beiträge zur Geologischen Karte der Schweiz Lieferung 30, Schmid, Francke & Co., Bern, 1896.

Bandou, D., Schlunegger, F., Kissling, E., Marti, U., Schwenk, M., Schläfli, P., Douillet, G., and Mair, D.: Three-dimensional gravity modelling of a Quaternary overdeepening fill in the Bern area of Switzerland discloses two stages of glacial carving, Sci. Rep., 12, 1441, https://doi.org/10.1038/s41598-022-04830-x, 2022.

Beck, P.: Bericht über die ausserordentliche Frühjahrsversammlung der Schweizerischen Geologischen Gesellschaft in Thun, Eclogae Geol. Helv., 31, 173–197, https://doi.org/10.5169/seals-159820, 1938.

Becker, P., Seguinot, J., Jouvet, G., and Funk, M.: Last Glacial Maximum precipitation pattern in the Alps inferred from glacier modelling, Geogr. Helv., 71, 173–187, https://doi.org/10.5194/gh-71-173-2016, 2016.

Becker, P., Funk, M., Schlüchter, C., and Hutter, K.: A study of the Würm glaciation focused on the Valais region (Alps), Geogr. Helv., 72, 421–442, https://doi.org/10.5194/gh-72-421-2017, 2017.

Berger, J.-P., Reichenbacher, B., Becker, D., Grimm, M., Grimm, K., Picot, L., Storni, A., Pirkenseer, C., and Schaefer, A.: Eocene-Pliocene time scale and stratigraphy of the Upper Rhine Graben (URG) and the Swiss Molasse Basin (SMB), Int. J. Earth Sci., 94, 711–731, https://doi.org/10.1007/s00531-005-0479-y, 2005.

Bini, A., Buoncristiani, J., Couterrand, S., Ellwanger, D., Felber, M., Florineth, D., Graf, H., Keller, O., Kelly, M., and Schlüchter, C.: Die Schweiz während des letzteiszeitlichen Maximums (LGM) (1 : 500 000), Bundesamt für Landestopografie swisstopo, Bern–Wabern, ISBN 978-3-302-40049-5, 2009.

Blaser, P., Gubler, T., Küpfer, T., Marschall, P., Matter, A., Matyas, J., Meier, B., Müller, W., Schlanke, S., Schlunegger, F., Siber, N., and Wyss, E.: Geothermiebohrung Bassersdorf. Charakterisierung der Oberen Meeresmolasse und Unteren Süsswassermolasse, Tech. Rep. NTB 94-01, Nagra, Wettingen, https://www.nagra.ch/de/technischer-bericht-94-01 (last access: 17 August 2022), 1994.

Braakhekke, J., Ivy-Ochs, S., Monegato, G., Gianotti, F., Martin, S., Casale, S., and Christl, M.: Timing and flow pattern of the Orta Glacier (European Alps) during the Last Glacial Maximum, Boreas, 49, 315–332, https://doi.org/10.1111/bor.12427, 2020.

Buechi, M. W., Frank, S. M., Graf, H. R., Menzies, J., and Anselmetti, F. S.: Subglacial emplacement of tills and meltwater deposits at the base of overdeepened bedrock troughs, Sedimentology, 64, 658–685, https://doi.org/10.1111/sed.12319, 2017.

Bundesamt für Landestopografie swisstopo: Höhenmodell der Felsoberfläche, Bundesamt für Landestopografie swisstopo, https://www.swisstopo.admin.ch/de/geodata/geology/models/bedrock-elevation.html, last access: 3 November 2021a.

Bundesamt für Landestopografie swisstopo: Tektonische Karte der Schweiz 1 : 500 000, Bundesamt für Landestopografie swisstopo, https://data.geo.admin.ch/ch.swisstopo.geologie-tektonische_karte/, last access: 3 November 2021b.

Busfield, M. E., Lee, J. R., Riding, J. B., Zalasiewicz, J., and Lee, S. V.: Pleistocene till provenance in east Yorkshire: reconstruct-

ing ice flow of the British North Sea Lobe, P. Geologist. Assoc., 126, 86–99, https://doi.org/10.1016/j.pgeola.2014.12.002, 2015.
Cook, S. J. and Swift, D. A.: Subglacial basins: Their origin and importance in glacial systems and landscapes, Earth-Sci. Rev., 115, 332–372, https://doi.org/10.1016/j.earscirev.2012.09.009, 2012.
Ehlers, J., Gibbard, P. L., and Hughes, P. D. (Eds.): Supplementary data to Quaternary Glaciations – Extent and Chronology – A Closer Look, in: Developments in Quaternary Sciences, Elsevier, https://booksite.elsevier.com/9780444534477/ (last access: 26 November 2021), 2011.
Favre, A.: Carte du phénomène erratique et des anciens glaciers du versant nord des Alpes suisses et de la chaîne du Mont-Blanc, Archives des sciences physiques et naturelles, A Cherbuliez, Geneva, 12, 1884.
Florineth, D. and Schlüchter, C.: Alpine evidence for atmospheric circulation patterns in Europe during the Last Glacial Maximum, Quaternary Res., 54, 295–308, https://doi.org/10.1006/qres.2000.2169, 2000.
Frasson, B. A.: Geologie der Umgebung von Schwarzenburg (Kanton Bern), Beiträge zur Geologischen Karte der Schweiz – Neue Folge, vol. 88, 62 pp., Kümmerli & Frey AG, Bern, Switzerland, 1947.
Füchtbauer, H.: Sedimentpetrographische Untersuchungen in der älteren Molasse nördlich der Alpen, Eclogae Geol. Helv., 57, 157–298, https://doi.org/10.5169/seals-163140, 1964.
Garzanti, E. and Andò, S.: Chapter 20 Heavy Mineral Concentration in Modern Sands: Implications for Provenance Interpretation, in: Heavy Minerals in Use, edited by: Mange, M. A. and Wright, D. T., vol. 58 of Developments in Sedimentology, Elsevier, 517–545, https://doi.org/10.1016/S0070-4571(07)58020-9, 2007.
Garzanti, E. and Andò, S.: Heavy Minerals for Junior Woodchucks, Minerals, 9, 148, https://doi.org/10.3390/min9030148, 2019.
Garzanti, E., Resentini, A., Vezzoli, G., Andò, S., Malusà, M., and Padoan, M.: Forward compositional modelling of Alpine orogenic sediments, Sediment. Geol., 280, 149–164, https://doi.org/10.1016/j.sedgeo.2012.03.012, 2012.
Gasser, U. and Nabholz, W.: Zur Sedimentologie der Sandfraktion im Pleistozän des schweizerischen Mittellandes, Eclogae Geol. Helv., 62, 467–516, https://doi.org/10.5169/seals-163708, 1969.
Gerber, E.: Einige Querprofile durch das Aaretal mit Berücksichtigung der letzten Bohrungen und Tunnelbauten, Mitteilungen der Naturforschenden Gesellschaft Bern, XXIV–XXXI, 1923.
Gilliéron, V.: Description géologique des territoires de Vaud, Fribourg et Berne, in: Description géologique des territoires de Vaud, Fribourg et Berne compris dans la feuille XII entre le lac de Neuchâtel et la crête du Niesen, Matériaux pour la carte géologique de la Suisse Livraison 18, Schmid, Francke & Co., Berne, 1885.
Giorgetti, G., Talarico, F., Sandroni, S., and Zeoli, A.: Provenance of Pleistocene sediments in the ANDRILL AND-1B drillcore: Clay and heavy mineral data, Global Planet. Change, 69, 94–102, https://doi.org/10.1016/j.gloplacha.2009.03.018, 2009.
Graf, A., Akçar, N., Ivy-Ochs, S., Strasky, S., Kubik, P. W., Christl, M., Burkhard, M., Wieler, R., and Schlüchter, C.: Multiple advances of Alpine glaciers into the Jura Mountains in the Northwestern Switzerland, Swiss J. Geosci., 108, 225–238, https://doi.org/10.1007/s00015-015-0195-y, 2015.
Graf, H. R.: Die Deckenschotter der zentralen Nordschweiz, PhD thesis, ETH Zürich, Zürich, Switzerland, 187 pp., https://doi.org/10.3929/ethz-a-000899302, 1993.
Hänni, R. and Pfiffner, O.-A.: Evolution and internal structure of the Helvetic nappes in the Bernese Oberland, Eclogae Geol. Helv., 94, 161–171, https://doi.org/10.5169/seals-168886, 2001.
Institut für Geologie, Universität Bern and Bundesamt für Wasser und Geologie: Tektonische Karte der Schweiz 1 : 500 000 = Carte tectonique de la Suisse 1 :500 000, Institut für Geologie, Universität Bern and Bundesamt für Wasser und Geologie, ISBN 3-906723-56-9, 2005.
Jouvet, G., Seguinot, J., Ivy-Ochs, S., and Funk, M.: Modelling the diversion of erratic boulders by the Valais Glacier during the last glacial maximum, J. Glaciol., 63, 487–498, https://doi.org/10.1017/jog.2017.7, 2017.
Kelly, M. A., Buoncristiani, J.-F., and Schlüchter, C.: A reconstruction of the last glacial maximum (LGM) ice-surface geometry in the western Swiss Alps and contiguous Alpine regions in Italy and France, Eclogae Geol. Helv., 97, 57–75, https://doi.org/10.1007/s00015-004-1109-6, 2004.
Kjær, K. H., Houmark-Nielsen, M., and Richardt, N.: Ice-flow patterns and dispersal of erratics at the southwestern margin of the last Scandinavian Ice Sheet: signature of palaeo-ice streams, Boreas, 32, 130–148, https://doi.org/10.1111/j.1502-3885.2003.tb01434.x, 2003.
Kruskal, W. H. and Wallis, W. A.: Use of Ranks in One-Criterion Variance Analysis, J. Am. Stat. Assoc., 47, 583–621, https://doi.org/10.1080/01621459.1952.10483441, 1952.
Larsen, D. J., Miller, G. H., Áslaug Geirsdóttir, and Thordarson, T.: A 3000-year varved record of glacier activity and climate change from the proglacial lake Hvítárvatn, Iceland, Quaternary Sci. Rev., 30, 2715–2731, https://doi.org/10.1016/j.quascirev.2011.05.026, 2011.
Lizaga, I., Gaspar, L., Blake, W. H., Latorre, B., and Navas, A.: Fingerprinting changes of source apportionments from mixed land uses in stream sediments before and after an exceptional rainstorm event, Geomorphology, 341, 216–229, https://doi.org/10.1016/j.geomorph.2019.05.015, 2019.
Lizaga, I., Latorre, B., Gaspar, L., and Navas, A.: FingerPro: an R Package for Tracking the Provenance of Sediment, Water Resour. Manage., 34, 3879–3894, https://doi.org/10.1007/s11269-020-02650-0, 2020.
Lüthy, H., Matter, A., and Nabholz, W. K.: Sedimentologische Untersuchung eines temporären Quartäraufschlusses bei der Neubrügg nördlich Bern, Eclogae Geol. Helv., 56, 119–145, https://doi.org/10.5169/seals-163032, 1963.
Meyers, P. A. and Teranes, J. L.: Sediment Organic Matter, Springer Netherlands, Dordrecht, 239–269, https://doi.org/10.1007/0-306-47670-3_9, 2001.
Monien, D., Kuhn, G., von Eynatten, H., and Talarico, F. M.: Geochemical provenance analysis of fine-grained sediment revealing Late Miocene to recent Paleo-Environmental changes in the Western Ross Sea, Antarctica, Global Planet. Change, 96-97, 41–58, https://doi.org/10.1016/j.gloplacha.2010.05.001, 2012.
Morton, A. C.: A new approach to provenance studies: electron microprobe analysis of detrital garnets from Middle Jurassic sandstones of the northern North Sea, Sedimentology, 32, 553–566, https://doi.org/10.1111/j.1365-3091.1985.tb00470.x, 1985.

NASA/METI/AIST/Japan Spacesystems and U.S./Japan ASTER Science Team: ASTER Global Digital Elevation Model V003, LPDAAC Data Pool [data set], https://doi.org/10.5067/ASTER/ASTGTM.003, 2019.

Pawlowsky-Glahn, V. and Egozcue, J. J.: Compositional data and their analysis: an introduction, Geological Society, London, Special Publications, 264, 1–10, https://doi.org/10.1144/GSL.SP.2006.264.01.01, 2006.

Pompilio, M., Dunbar, N., Gebhardt, A. C., Helling, D., Kuhn, G., Kyle, P., McKay, R., Talarico, F., Tulaczyk, S., Vogel, S., Wilch, T., and the ANDRILL-MIS Science Team: Petrology and Geochemistry of the AND-1B Core, ANDRILL McMurdo Ice Shelf Project, Antarctica, Terra Antartica, 14, 255–288, 2007.

Preusser, F., Drescher-Schneider, R., Fiebig, M., and Schlüchter, C.: Re-interpretation of the Meikirch pollen record, Swiss Alpine Foreland, and implications for Middle Pleistocene chronostratigraphy, J. Quaternary Sci., 20, 607–620, https://doi.org/10.1002/jqs.930, 2005.

Preusser, F., Reitner, J. M., and Schlüchter, C.: Distribution, geometry, age and origin of overdeepened valleys and basins in the Alps and their foreland, Swiss J. Geosci., 103, 407–426, https://doi.org/10.1007/s00015-010-0044-y, 2010.

Preusser, F., Graf, H. R., Keller, O., Krayss, E., and Schlüchter, C.: Quaternary glaciation history of northern Switzerland, E&G Quaternary Sci. J., 60, 21, https://doi.org/10.3285/eg.60.2-3.06, 2011.

R Core Team: R: A Language and Environment for Statistical Computing, R Foundation for Statistical Computing, Vienna, Austria, https://www.R-project.org/, last access: 17 August 2022.

Reber, R. and Schlunegger, F.: Unravelling the moisture sources of the Alpine glaciers using tunnel valleys as constraints, Terra Nova, 28, 202–211, https://doi.org/10.1111/ter.12211, 2016.

Reber, R., Akçar, N., Ivy-Ochs, S., Tikhomirov, D., Burkhalter, R., Zahno, C., Lüthold, A., Kubik, P. W., Vockenhuber, C., and Schlüchter, C.: Timing of retreat of the Reuss Glacier (Switzerland) at the end of the Last Glacial Maximum, Swiss J. Geosci., 107, 293–307, https://doi.org/10.1007/s00015-014-0169-5, 2014.

Sandroni, S. and Talarico, F. M.: The record of Miocene climatic events in AND-2A drill core (Antarctica): Insights from provenance analyses of basement clasts, Global Planet. Change, 75, 31–46, https://doi.org/10.1016/j.gloplacha.2010.10.002, 2011.

Schlunegger, F., Matter, A., and Mange, M. A.: Alluvial fan sedimentation and structure of the southern Molasse Basin margin, Lake Thun area, Switzerland, Eclogae Geol. Helv., 86, 717–750, https://doi.org/10.5169/seals-167260, 1993.

Schlunegger, F., Burbank, D., Matter, A., Engesser, B., and Mödden, C.: Magnetostratigraphic calibration of the Oligocene to Middle Miocene (30–15 Ma) mammal biozones and depositional sequences of the Swiss Molasse Basin, Eclogae Geol. Helv., 89, 753–788, https://doi.org/10.5169/seals-167923, 1996.

Schläfli, P., Gobet, E., van Leeuwen, J. F., Vescovi, E., Schwenk, M. A., Bandou, D., Douillet, G. A., Schlunegger, F., and Tinner, W.: Palynological investigations reveal Eemian interglacial vegetation dynamics at Spiezberg, Bernese Alps, Switzerland, Quaternary Sci. Rev., 263, 106975, https://doi.org/10.1016/j.quascirev.2021.106975, 2021.

Schlüchter, C.: The most complete quaternary record of the Swiss Alpine Foreland, Palaeogeogr. Palaeocl., 72, 141–146, https://doi.org/10.1016/0031-0182(89)90138-7, 1989.

Schmid, S. M., Fügenschuh, B., Kissling, E., and Schuster, R.: Tectonic map and overall architecture of the Alpine orogen, Eclogae Geol. Helv., 97, 93–117, https://doi.org/10.1007/s00015-004-1113-x, 2004.

Schönig, J., von Eynatten, H., Tolosana-Delgado, R., and Meinhold, G.: Garnet major-element composition as an indicator of host-rock type: a machine learning approach using the random forest classifier, Contrib. Mineral. Petr., 176, 98, https://doi.org/10.1007/s00410-021-01854-w, 2021.

Schwenk, M. A., Schlunegger, F., Gribenski, N., Schläfli, P., Bandou, D., Douillet, G. A., and Krbanjevic, J.: Stratigraphic and Multi Scanner Core Logging (MSCL) data plus supplementary luminescence dating material obtained from the scientific drilling QDR-RE-IfG and its drill site in the Aare Valley, Bern, Switzerland, GFZ Data Services [data set], https://doi.org/10.5880/fidgeo.2021.021, 2021.

Schwenk, M. A., Schläfli, P., Bandou, D., Gribenski, N., Douillet, G. A., and Schlunegger, F.: From glacial erosion to basin overfill: a 240 m-thick overdeepening–fill sequence in Bern, Switzerland, Sci. Dril., 30, 17–42, https://doi.org/10.5194/sd-30-17-2022, 2022.

Seguinot, J., Ivy-Ochs, S., Jouvet, G., Huss, M., Funk, M., and Preusser, F.: Modelling last glacial cycle ice dynamics in the Alps, The Cryosphere, 12, 3265–3285, https://doi.org/10.5194/tc-12-3265-2018, 2018.

Sinclair, H. D. and Allen, P. A.: Vertical versus horizontal motions in the Alpine orogenic wedge: stratigraphic response in the foreland basin, Basin Res., 4, 215–232, https://doi.org/10.1111/j.1365-2117.1992.tb00046.x, 1992.

Spiegel, C., Kuhlemann, J., Dunkl, I., Frisch, W., Von Eynatten, H., and Balogh, K.: The erosion history of the Central Alps: evidence from zircon fission track data of the foreland basin sediments, Terra Nova, 12, 163–170, https://doi.org/10.1046/j.1365-3121.2000.00289.x, 2000.

Spiegel, C., Kuhlemann, J., Dunkl, I., and Frisch, W.: Paleogeography and catchment evolution in a mobile orogenic belt: the Central Alps in Oligo–Miocene times, Tectonophysics, 341, 33–47, https://doi.org/10.1016/S0040-1951(01)00187-1, 2001.

Spiegel, C., Siebel, W., Frisch, W., and Berner, Z.: Nd and Sr isotopic ratios and trace element geochemistry of epidote from the Swiss Molasse Basin as provenance indicators: implications for the reconstruction of the exhumation history of the Central Alps, Chem. Geol., 189, 231–250, https://doi.org/10.1016/S0009-2541(02)00132-8, 2002.

Stampfli, G. M.: Tethyan oceans, Geological Society, London, Special Publications, 173, 1–23, https://doi.org/10.1144/GSL.SP.2000.173.01.01, 2000.

Strunck, P. and Matter, A.: Depositional evolution of the western Swiss Molasse, Eclogae Geol. Helv., 95, 197–222, https://doi.org/10.5169/seals-168955, 2002.

Stutenbecker, L., Berger, A., and Schlunegger, F.: The potential of detrital garnet as a provenance proxy in the Central Swiss Alps, Sediment. Geol., 351, 11–20, https://doi.org/10.1016/j.sedgeo.2017.02.002, 2017.

Stutenbecker, L., Delunel, R., Schlunegger, F., Silva, T. A., Šegvić, B., Girardclos, S., Bakker, M., Costa, A., Lane, S. N., Loizeau,

J.-L., Molnar, P., Akçar, N., and Christl, M.: Reduced sediment supply in a fast eroding landscape? A multi-proxy sediment budget of the upper Rhône basin, Central Alps, Sediment. Geol., 375, 105–119, https://doi.org/10.1016/j.sedgeo.2017.12.013, 2018.

Stutenbecker, L., Tollan, P. M. E., Madella, A., and Lanari, P.: Miocene basement exhumation in the Central Alps recorded by detrital garnet geochemistry in foreland basin deposits, Solid Earth, 10, 1581–1595, https://doi.org/10.5194/se-10-1581-2019, 2019.

Tatzel, M., Dunkl, I., and von Eynatten, H.: Provenance of Palaeo-Rhine sediments from zircon thermochronology, geochemistry, U / Pb dating and heavy mineral assemblages, Basin Res., 29, 396–417, https://doi.org/10.1111/bre.12155, 2017.

Vale, S. S., Fuller, I. C., Procter, J. N., Basher, L. R., and Smith, I. E.: Application of a confluence-based sediment-fingerprinting approach to a dynamic sedimentary catchment, New Zealand, Hydrol. Process., 30, 812–829, https://doi.org/10.1002/hyp.10611, 2016.

Vermeesch, P. and Garzanti, E.: Making geological sense of "Big Data" in sedimentary provenance analysis, Chem. Geol., 409, 20–27, https://doi.org/10.1016/j.chemgeo.2015.05.004, 2015.

Vermeesch, P., Resentini, A., and Garzanti, E.: An R package for statistical provenance analysis, Sediment. Geol., 336, 14–25, https://doi.org/10.1016/j.sedgeo.2016.01.009, 2016.

von Eynatten, H.: Petrography and chemistry of sandstones from the Swiss Molasse Basin: an archive of the Oligocene to Miocene evolution of the Central Alps, Sedimentology, 50, 703–724, https://doi.org/10.1046/j.1365-3091.2003.00571.x, 2003.

Welten, M.: Pollenanalytische Untersuchungen im Jüngeren Quartär des nördlichen Alpenvorlandes der Schweiz, Beiträge zur Geologischen Karte der Schweiz-Neue Folge, 156, 210 pp., 1982.

Welten, M.: Neue pollenanalytische Ergebnisse über das Jüngere Quartär des nördlichen Alpenvorlandes der Schweiz (Mittel- und Jungpleistozän), Beiträge zur Geologischen Karte der Schweiz-Neue Folge, 162, 52 pp., 1988.

Weltje, G. J. and von Eynatten, H.: Quantitative provenance analysis of sediments: review and outlook, Sediment. Geol., 171, 1–11, https://doi.org/10.1016/j.sedgeo.2004.05.007, 2004.

Wildi, W.: Heavy mineral distribution and dispersal pattern in penninic and ligurian flysch basins (Alps, northern Apennines), Giornale di Geologia, 47, 77–99, 1985.

Wissing, S. and Pfiffner, O.-A.: Structure of the eastern Klippen nappe (BE, FR): Implications for its Alpine tectonic evolution, Eclogae Geol. Helv., 95, 381–398, https://doi.org/10.5169/seals-168966, 2002.

Ziegler, P. A. and Fraefel, M.: Response of drainage systems to Neogene evolution of the Jura fold-thrust belt and Upper Rhine Graben, Swiss J. Geosci., 102, 57–75, https://doi.org/10.1007/s00015-009-1306-4, 2009.

E&G Quaternary Sci. J., 71, 191–212, 2022
https://doi.org/10.5194/egqsj-71-191-2022

Open Access E&G Quaternary Science Journal

Research article

Morpho-sedimentary characteristics of Holocene paleochannels in the Upper Rhine alluvial plain, France

Mubarak Abdulkarim[1,2], Stoil Chapkanski[3], Damien Ertlen[4], Haider Mahmood[1], Edward Obioha[1], Frank Preusser[1], Claire Rambeau[4], Ferréol Salomon[4], Marco Schiemann[1], and Laurent Schmitt[4]

[1]Institute of Earth and Environmental Science, University of Freiburg, Freiburg, Germany
[2]Department of Geology, Federal University Birnin Kebbi, Kebbi, Nigeria
[3]Laboratoire de Géographie Physique (UMR-8591), CNRS/Université Paris 1, Meudon, France
[4]Laboratoire Image, Ville, Environnement (LIVE UMR 7362), CNRS/Université de Strasbourg/ENGEES, Strasbourg, France

Correspondence: Mubarak Abdulkarim (mubarak.abdulkarim@geologie.uni-freiburg.de)

Relevant dates: Received: 23 May 2022 – Revised: 26 July 2022 – Accepted: 9 August 2022 – Published: 8 September 2022

How to cite: Abdulkarim, M., Chapkanski, S., Ertlen, D., Mahmood, H., Obioha, E., Preusser, F., Rambeau, C., Salomon, F., Schiemann, M., and Schmitt, L.: Morpho-sedimentary characteristics of Holocene paleochannels in the Upper Rhine alluvial plain, France, E&G Quaternary Sci. J., 71, 191–212, https://doi.org/10.5194/egqsj-71-191-2022, 2022.

Abstract: The French Upper Rhine alluvial plain is characterized by a complex system of paleochannels inherited from Late Glacial to Holocene fluvial dynamics of the Rhine and Ill river systems, among other smaller rivers. These paleochannels represent valuable archives for understanding and reconstructing the fluvial and landscape evolution of the area. However, the Holocene temporal trajectories of the paleochannels, in response to a range of environmental changes, remain poorly understood. This study presents a detailed and systematic mapping and characterization of an extensive network of paleochannels spanning the entire width (19 km) of a reach of the central French Rhine plain. Based on qualitative and quantitative lidar analysis, field investigations, and provenance investigations of paleochannel infill sequences, five distinct paleochannel groups (PG 1 to PG 5) were identified in the study area. These paleochannel groups differ considerably regarding their channel patterns, morphological characteristics, and sedimentary sources of the infilling sediments. The interpretation of the different datasets indicates that the development of these different paleomorphologies is attributed to significant changes in hydro-geomorphodynamic processes in the area during the Holocene, especially lateral migrations of the Rhine and Ill rivers. The findings reported here are promising and will have significant implications for reconstructing the long-term (Late Glacial to Holocene) evolution of the Upper Rhine fluvial hydrosystem in response to various controlling factors.

Kurzfassung: Die französische Oberrheinebene ist durch ein komplexes System von ehemaligen Fließrinnen gekennzeichnet, die aus der spätglazialen bis holozänen fluvialen Dynamik des Rhein- und Ill-Systems sowie einiger anderer kleinerer Flüsse stammen. Diese Fließrinnen stellen wertvolle Archive dar, die für das Verständnis und die Rekonstruktion der fluvialen und landschaftlichen Entwicklung des Gebietes von zentraler Bedeutung sind. Die zeitliche Entwicklung der Fließrinnen im Holozän, als Reaktion auf die Veränderung einer Reihe von Umweltbedingungen, ist jedoch nach wie vor nur unzureichend bekannt. Diese Studie präsentiert eine detaillierte und systematische Kartierung

und Charakterisierung eines ausgedehnten Netzwerks von ehemaligen Fließrinnen, das sich über die gesamte Breite (19 km) eines Abschnitts der zentralen französischen Rheinebene erstreckt. Auf Grundlage von qualitativen und quantitativen lidar-Analysen, sowie durch Feld- und Provenienzuntersuchungen von Sedimentfüllungen wurden im Untersuchungsgebiet fünf verschiedene Rinnengruppen (PG 1 bis PG 5) identifiziert. Diese Gruppen unterscheiden sich erheblich in Bezug auf ihre Rinnenmuster, morphologischen Merkmale und Sedimentherkunft. Die Interpretation der verschiedenen Datensätze deutet darauf hin, dass die Entwicklung dieser unterschiedlichen Paläo-Morphologien auf signifikante Veränderungen der hydro-geomorphodynamischen Prozesse in diesem Gebiet während des Holozäns zurückzuführen ist, insbesondere auf die seitlichen Verlagerungen von Rhein und Ill. Die hier vorgestellten Ergebnisse sind vielversprechend und bilden die Basis für eine Rekonstruktion der langfristigen (spätglazialen bis holozänen) Entwicklung des fluvialen Oberrhein-Hydrosystems in Abhängigkeit von verschiedenen Einflussfaktoren.

1 Introduction

The French Upper Rhine alluvial plain (eastern France) is characterized by a complex pattern of paleochannels inherited from the Late Glacial to Holocene fluvial dynamics of the Rhine and Ill rivers, as well as some other tributaries or sub-tributaries of the Rhine (Hirth, 1971; Carbiener, 1983a; Striedter, 1988). From Colmar to Sélestat, which is a part of the so-called "Ried central d'Alsace" (Carbiener, 1983a), the formation and evolution of the paleochannel network is attributed to significant landscape changes throughout the Holocene, as exemplified by the narrowing and eastward lateral migration of the Rhine fluvial hydrosystem and a westward displacement for its main tributary, the Ill River (Schmitt et al., 2016). Consequently, these paleochannels inherited from these lateral displacements preserve a comprehensive record of Holocene environmental changes, which is invaluable for understanding past landscape evolution and fluvial processes, as well as providing insights into the factors that controlled these changes (Bowler, 1978; Page et al., 1996; Dambeck and Thiemeyer, 2002; Sylvia and Galloway, 2006; Kemp and Spooner, 2007; Bisson et al., 2011; Nandini et al., 2013; Resmi et al., 2017). However, both the internal structure and organization of the extensive and well-preserved network of paleochannels, as well as the temporal development of trajectories in response to environmental change during the Holocene remain poorly understood.

Around the world, paleochannels have been extensively studied using a variety of methodological approaches in order to reconstruct the evolution of fluvial hydrosystems and associated landscapes in the geological and historical past (e.g., Page et al., 1996; Dambeck and Thiemeyer, 2002; Bos et al., 2008; Rossetti and Góes, 2008; Erkens et al., 2011; Plotzki et al., 2015; Jotheri et al., 2016; Resmi et al., 2017; Scorpio et al., 2018; Candel et al., 2020; Khosravichenar et al., 2020; von Suchodoletz et al., 2022). Likewise, in the Ried central d'Alsace, pioneering studies (e.g., Carbiener, 1969, 1983a; Hirth, 1971; Al Siddik, 1986; Boës et al., 2007; Schmitt et al., 2016) have investigated paleochannels and paleoenvironments with the aim to reconstruct the Holocene evolution of the landscape and/or study past human–river interactions. However, these research efforts lacked precision (e.g., no location of the sampling sites, no provenance study of fine sediments) or were, in many cases, concentrated around some archeological sites located close the village of Mussig (Boës et al., 2007) and focused on a rather limited number of paleochannels between the Rhine and Ill rivers. No study has yet extensively mapped and characterized systematically the paleochannel network over the entire width of the large and complex alluvial plain.

Against this backdrop, the present study aims at providing new insights into the formation and evolution of the paleochannels. The study specifically aims to (1) map the paleochannels and measure their morphometric properties using remote sensing data, (2) characterize paleochannel geometry and stratigraphic infillings of selected paleochannels using hand-augured core data, and (3) determine the provenance of paleochannel infillings through mid-infrared spectroscopic analysis. In addition, as the chosen research tools have barely been used, this study may also provide some methodological outputs.

2 Geological and geomorphological setting

The study area is located in the French Rhine alluvial plain, within the Upper Rhine Graben (URG). The URG is a 30–40 km wide rift valley extending 300 km from the Jura Mountains to the southern border of the Rhenish Massif (Fig. 1). The valley is bounded to the west by the Vosges and Pfälzerwald (Palatinate Forest) mountains and to the east by the Black Forest and Odenwald mountains. This rift structure ensued from the formation of the Alps starting during the middle Eocene, with the main phase of its rifting occurring during the Oligocene and Miocene, as well as extending into the Pleistocene and Holocene (Przyrowski and Schäfer, 2015). Today, it forms a down-faulted trough through which the Rhine has flown continuously since the start of the Pleistocene (Preusser, 2008). During this time period, the URG

was an important sink for sediments from the Rhine River and its tributaries, mostly unconsolidated fluvial sediments of up to several hundreds of meters thickness (e.g., Haimberger et al., 2005; Gabriel et al., 2013). In the French Rhine alluvial plain, the Pleistocene sediments, primarily gravel and sand deposited during glacial periods, intercalate with fine-grain layers (sand, silt, and clay) attributed to warm periods. Hence, the superficial Holocene deposits generally have finer textures than the Pleistocene sediments (Simler et al., 1979), except on the historical Rhine braided belt (Schmitt, 2001; Schmitt et al., 2016).

Following the Older Dryas (13.9 ka cal BP; van Raden et al., 2013), the longitudinal profile of the Rhine readjusted in response to several controlling factors: (i) a decrease in water and sediment fluxes due to Holocene climate warming (Hirth, 1971); (ii) trapping of sediment in Swiss lakes (e.g., Lake Constance) for 60 % of the Rhine basin area upstream of Basel after their formation by the retreat of Alpine glaciers, which decreased the sediment load and intensity of floods (Walser, 1959; Hirth, 1971); and (iii) positive tectonic movements (uplift) upstream and downstream of Mulhouse (Nivière et al., 2006; Kock et al., 2009) and negative (downward) tectonic movements around Marckolsheim (Jung and Schlumberger, 1936; Illies and Greiner, 1978) or even over the entire Marckolsheim–Strasbourg sector and north of Strasbourg (Jung and Schlumberger, 1936; Illies and Greiner, 1978; Vogt, 1992).

Consequently, the longitudinal profile of the Rhine became more incised between the Basel–Neuf-Brisach and Strasbourg–Lauterbourg sections during the Holocene and remained unchanged or even rose slightly in the Neuf-Brisach–Strasbourg section (Carbiener, 1969, 1983a). Thus, the Holocene Upper Rhine and its alluvial plain are classified into four major longitudinal sections based on geomorphological characteristics and dynamics (Carbiener, 1969, 1983a; Schmitt et al., 2016; Fig. 2). The upstream sector (from Basel to Neuf-Brisach) is characterized by a braided channel pattern, while a braided-anastomosing channel pattern characterizes the middle sector, from Neuf-Brisach to Strasbourg. The downstream sector (from Strasbourg to Karlsruhe–Maxau) is distinguished by a combination of anastomoses and incipient meanders, whereas further north, beyond the French Rhine Plain, the Rhine River is characterized by an almost pure meandering style. It has to be noted that the natural channel pattern and dynamics have been completely destroyed by human regulation works (correction, regularization, and canalization) since the 19th century (e.g., Eschbach et al., 2018).

The central study area of our research, within the French Rhine alluvial plain, corresponds roughly to a large transect (14 km) from Houssen to Baltzenheim along which paleochannels were cored (Fig. 1b). To gain insight into the channel pattern of these paleochannels, we studied the surface topography using a light detection and ranging (lidar) digital elevation model (DEM) over a larger spatial scale, which corresponds to an extended studied area (Fig. 1b). The area stretches between the villages of Neuf-Brisach and Sainte-Croix-en-Plaine in the south and Illhaeusern and Marckolsheim in the north, covering an area of approximately 572 km^2 (Fig. 1b). This area corresponds mainly to the braided-anastomosing sector and is delimited by the Rhine River in the west and the Ill River in the east. It corresponds also to the southern part of the so-called "Grand Ried central d'Alsace", which extends up to south of Strasbourg and corresponds to a large, wet alluvial area whose biodiversity is extremely rich (Carbiener, 1983a). The Fecht River represents a major western tributary of the Ill River in this area, which joins the Ill at Illhaeusern. Until the end of the Pleistocene, the Ill River did not exist as the Rhine fluvial hydrosystem (with mostly braided channel pattern) occupied almost the entire width of the plain (Schmitt et al., 2016). At the start of the Holocene, a change in the dynamics and narrowing of the Rhine fluvial hydrosystem resulted in the formation of the Ill River (Schmitt et al., 2016).

The Rhine and Ill rivers then continuously moved laterally across the plain until human interference, with fine sediments deposited on the alluvial plain with an average thickness of 0.5–1 m but reaching several meters in channel structures (Schmitt et al., 2016). As a consequence, the current floodplain features a complex network of paleochannels. These paleochannels are generally embedded into the Rhine gravels, incompletely filled, and are therefore visible as geomorphological features (depressions and levees) in the surface topography. The former channels have been filled with clastic and organic sediments and are mainly bereft of flowing water, although some remain active today due to perennial or intermittent upstream hydrological connection to the Ill or Rhine rivers or to groundwater (Carbiener, 1983a, b; Trémolières et al., 1993; Schmitt, 2001; Schmitt et al., 2016), forming phreatic and semi-phreatic rivers (Carbiener, 1983a, b; Schmitt et al., 2007). These streams support an abundance of biodiversity, in particular aquatic macrophytes (Carbiener, 1983b; Trémolières et al., 1993).

The alluvial plain is generally categorized into two main geomorphological units based on geomorphological, hydrological, pedological, and ecological properties: the "Hardt" and the "Ried" (Carbiener, 1969; Hirth, 1971; Ollive et al., 2006, Fig. 3). The "Hardt" is an area with gravelly islands associated with the Late Pleistocene alluvial fan of the Rhine, primarily located in the central part of the alluvial plain. The "Ried" comprises low-lying, swampy areas primarily consisting of fine sand, silt, clay, and organic matter, which may be mixed together (Hirth, 1971; Kremer et al., 1978; Al Siddik, 1986; Ollive et al., 2006). These two zones are further subdivided into six subunits: "Hardt Rouge", "Hardt Grise", "Ried Blond", "Ried Brun", "Ried Noir", and "Ried Gris" (Hirth, 1971; Kremer et al., 1978, Fig. 3).

The Hardt Rouge represents the intact Pleistocene alluvial fan, whereas the Hardt Grise has been remobilized at the surface. The Ried Blond is the sub-modern floodplain of the

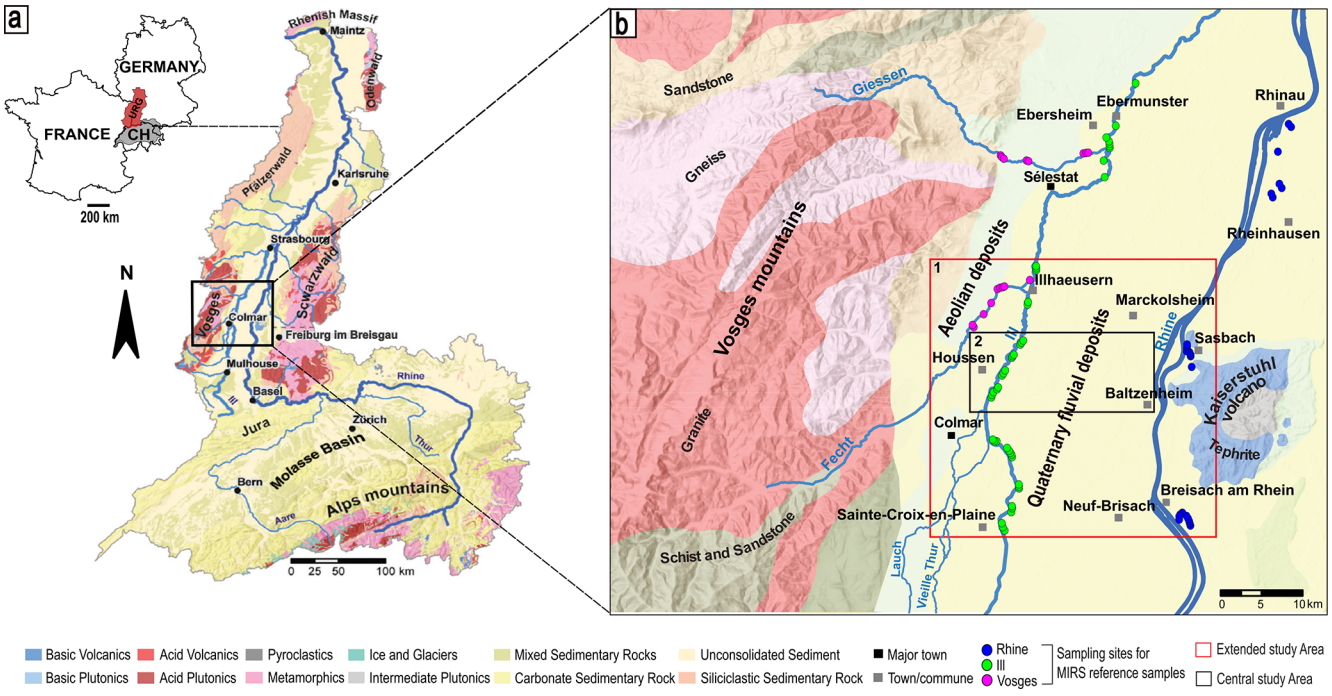

Figure 1. **(a)** Geological setting and location of the Upper Rhine Graben (URG). **(b)** Location of the two spatial scales of the study area within the French Rhine alluvial plain: (1) the extended study area (red) on which the lidar DEM was studied and (2) the central study area (black) on which the paleochannels were bored by hand auger. The figure also shows the sampling sites for MIRS reference samples. Modified from Chapkanski et al. (2020). Source of data: ESRI, BRGM.

Rhine prior to the correction works (width of about 5–7 km), composed of sandy/silty and calcareous alluvium and in some places overlapped by young soils (Kremer et al., 1978). Ried Brun corresponds to a series of moderately overhanging post-Roman Rhine levees and terraces located within the sub-modern floodplain of the Rhine, with limestone-rich soils and highly mineralized organic matter. The Ried Noir, situated further to the west of the plain, corresponds to marshy depressions with permanent or semi-permanent contact to groundwater. It is composed of black hydromorphic soils rich in organic matter and locally peat (Carbiener, 1969, 1983a; Hirth, 1971). The westernmost component, the Ried Gris, represents the area regularly flooded by the Ill River, consisting of fine floodplain sediments, mainly fine sand, silt, and clay (Carbiener, 1969, 1983a; Hirth, 1971; Al Siddik, 1986).

3 Methods

3.1 Remote sensing

Paleochannels within the study area were identified and comprehensively mapped through the combined use of a lidar-derived DEM, a photogrammetric digital terrain model (DTM), aerial photos, and historical maps from the 18th and 19th centuries. The elevation data, aerial photos, and historical maps are found in the Supplement. The primary data used are a lidar-generated DEM with a resolution of 50 cm and pixel values ranging from 132.47 to 556.82 m. However, a portion of the research area (approximately 65 km^2) currently lacks lidar coverage (Fig. 4); it is covered by a photogrammetric DTM with a 1 m resolution. The photogrammetric DTM was developed in 2018 and obtained from the RGE ALTI® database of the National Institute of Geographic and Forestry Information, France (IGN-F). In addition to the elevation data, aerial photographs, and historical maps dating from 1702 CE to 1838 CE were geo-referenced and digitized to complement the identification and mapping of paleochannels. Prior to mapping, the datasets were processed, and enhancement techniques (e.g., contrast stretching, hill shading, and slope maps) were applied to improve visualization and enhance the appearance of the microtopography and detectability of the geomorphologic features of interest (paleochannels).

After their mapping, the paleochannels were further characterized in relation to their surface topographic properties, including channel width, channel depth, width / depth ratio, sinuosity, and orientation (paleochannel direction). For the determination of these geometrical properties, four transect lines were drawn across the study area, perpendicular to the orientation of the main valley (Fig. S3 in the Supplement). Based on the surface topography, paleochannel width and depth were measured at points where they intersect with these profile lines using the *Measure* tool and *3D Analyst*

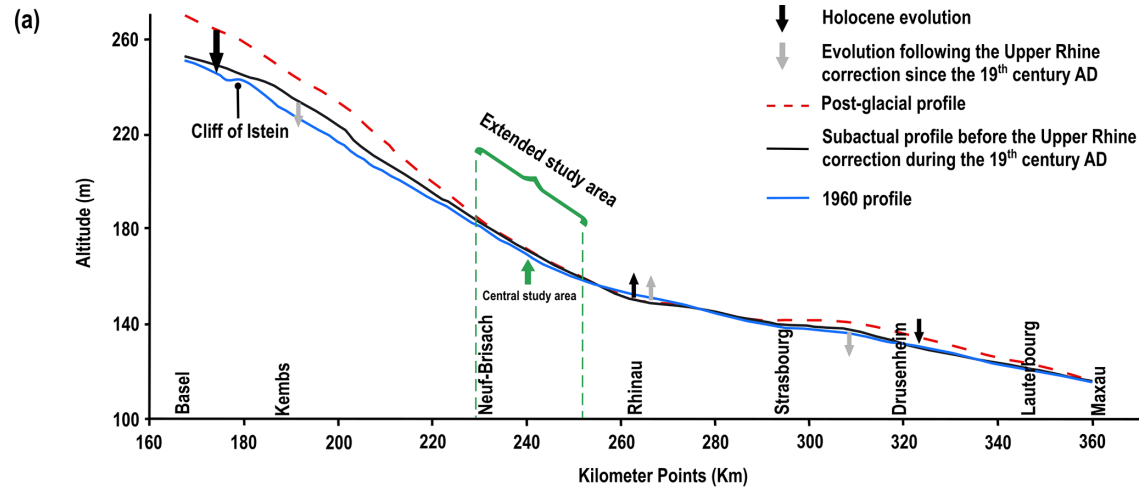

(b)

Variable \ Sector	Braided	Braided and anastomosing	Anastomosing and meandering	Meandering
Width of the hydrosystem	2.9 Km	5.9 Km	4.9 Km	5.5 Km
Slope	0.93 %	0.66 %	0.46 %	0.31 %
Specific stream power	45 W.m^{-2}	33 W.m^{-2}	26 W.m^{-2}	22 W.m^{-2}
Number of braided channels	7.1	7.4	5.6	–
Number of anasto. channels	2.6	4.6	2.8	–
Sinuosity	1.11	1.22	1.33	1.45

Figure 2. **(a)** Post-glacial and Holocene Upper Rhine longitudinal profiles. **(b)** Some hydromorphological characteristics according to the Upper Rhine sectorization (adapted from Commission Internationale de l'Hydrologie du Bassin du Rhin, 1977; Carbiener and Dillmann, 1992; Schmitt, 2001; and Schmitt et al., 2019).

tool in ArcMap 10.4. The sinuosity index (P) of the paleochannels was also estimated using the *Measure* tool in ArcMap 10.4, following the method of Fuller et al. (2013). All morphometric parameters were determined three times, with the average values reported. Except for the measurements of paleochannel orientations, which were performed using the open-source GIS program QGIS V10.3, all dataset processing, paleochannel mapping, and planform measurements were carried out using ESRI ArcGIS 10.4.1.

3.2 Paleochannel coring

A total of 16 paleochannels within the alluvial plain were originally chosen for this study. The selection strategy was designed to include all paleochannels from the Rhine to the left (western) side of the Ill River (Figs. 4a; 5a). Furthermore, the paleochannels were chosen based on a number of criteria, including the absence of significant anthropogenic disturbances and whether or not they had been previously investigated. Only 12 of the 16 paleochannels could be investigated (Fig. 4) due to inaccessibility or the lack of authorization by landowners. The paleochannels with current activity were given names based on their present streams, while others that are completely abandoned and filled were assigned names reflecting their geographical location. Borings with an Edelman hand auger were used to characterize the subsurface geometry and sedimentary infillings of the selected paleochannels. The cores were placed at irregular (3–5 m) intervals along transects that spanned the entire width of the paleochannels, while the thickness of fine sediment infill determined the depth of the cores. Almost every coring penetrated fine sediment (clay, silt, and sand) and terminated in underlying gravel beds. The gravel deposits were encountered at depths ranging from less than 0.5 m near the channel margins to depths up to 5 m at the deepest portions of some paleochannels. Sediment samples were collected at 20 cm depth intervals and described in terms of dominant grain size, color, and organic matter content (qualitatively). These data were compiled to delineate stratigraphic units filling the paleochannels.

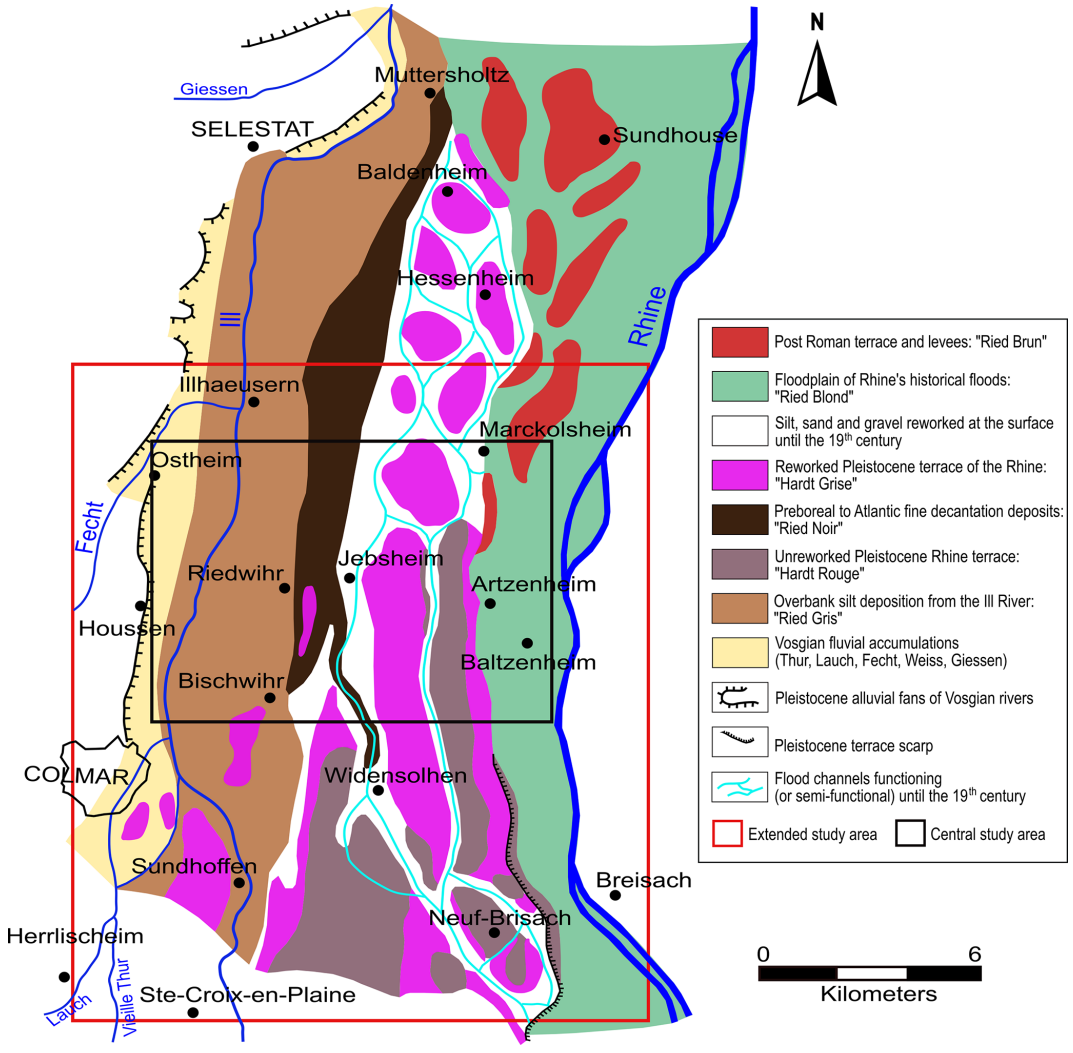

Figure 3. Geomorphological map of a part of the French Rhine alluvial plain whose southern part corresponds to our extended study area (Colmar-Sélestat; Hirth, 1971, modified by Schmitt, 2001, and Schmitt et al., 2016). Figure modified from Schmitt et al. (2016).

3.3 Provenance analysis

The source region of sediments and the contributions from different drainage basins within the same sedimentary basin can be determined by performing provenance studies (Haughton et al., 1991). The data from these analyses will facilitate a better understanding of fluvial paleodynamics at large spatiotemporal scales (Chapkanski et al., 2020). Following Chapkanski et al. (2020), the provenance of paleochannel infills and basal gravel deposits was determined by combining mid-infrared spectroscopy (MIRS) measurements and discriminant analyses (DAs). MIRS is a molecular-based, non-destructive and rapid method permitting the characterization of both mineralogical and bio-chemical properties of sediments (Bertaux et al., 1998). Therefore, using mid-infrared spectra to feed discriminant analysis allows mineralogical similarities to be established between samples from a sedimentary reference dataset and samples from paleochannel infills (Chapkanski et al., 2020). The reference dataset used in this study contains 196 (sub-)surface samples covering the main potential sedimentary sources in the study area (i.e., Rhine River, Ill River, and Vosges tributaries; Chapkanski et al., 2020; see also Fig. 1b). A total of 46 additional reference samples were collected and incorporated into the original reference dataset. A total of 73 samples from the paleochannel infills (referred to as target samples) were collected in the 12 paleochannels from different stratigraphic units.

Both the reference and target samples were dried for 7 d at 30 °C before sieving through a 2 mm sieve. The samples were then ground for 3 min using a vibratory disc mill equipped with an agate grinding set to obtain a fine, homogenous powder. Spectroscopic measurements were performed on a Fourier-transform infrared spectroscopy (FT-IR) frontier spectrometer (PerkinElmer, USA) with KBr beam split-

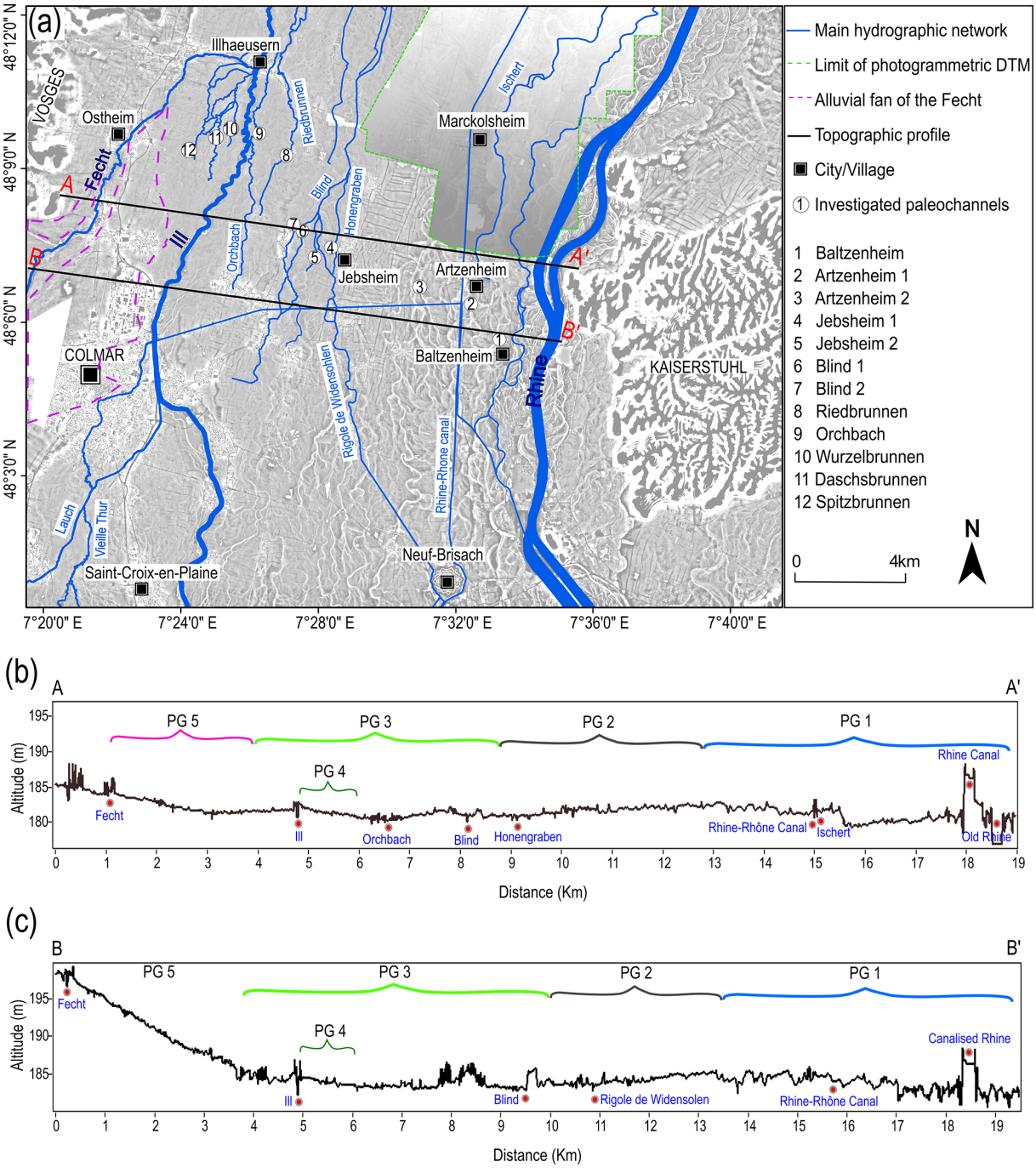

Figure 4. **(a)** Lidar DEM and photogrammetric DTM of the study area, with the main river network and coring sites of the investigated paleochannels. **(b)** Topographic profile along line A–A′. **(c)** Topographic profile along line B–B′. Data sources: lidar DEM: Regional Council of Grand Est and the European Collectivity of Alsace; photogrammetric DTM: IGN France.

ter equipped with a diffuse reflectance sampling accessory. The powdered samples were scanned from 4000 to 450 cm^{-1} with a 2 cm^{-1} resolution. Each spectrum is the average of 20 scans of each sample. Following Chapkanski et al. (2020), spectra resolution was averaged over a 16 cm^{-1} interval to improve spectra pattern recognition. Standard normal variates, baseline, and second derivate pre-treatments were performed to reduce scatter effects and improve the spectral alignment. Moreover, only the fingerprint mid-infrared spectral region (from 1500 to 450 cm^{-1}) was selected prior to statistical treatments in order to reduce misleading results due to organic matter absorbing in the regions between

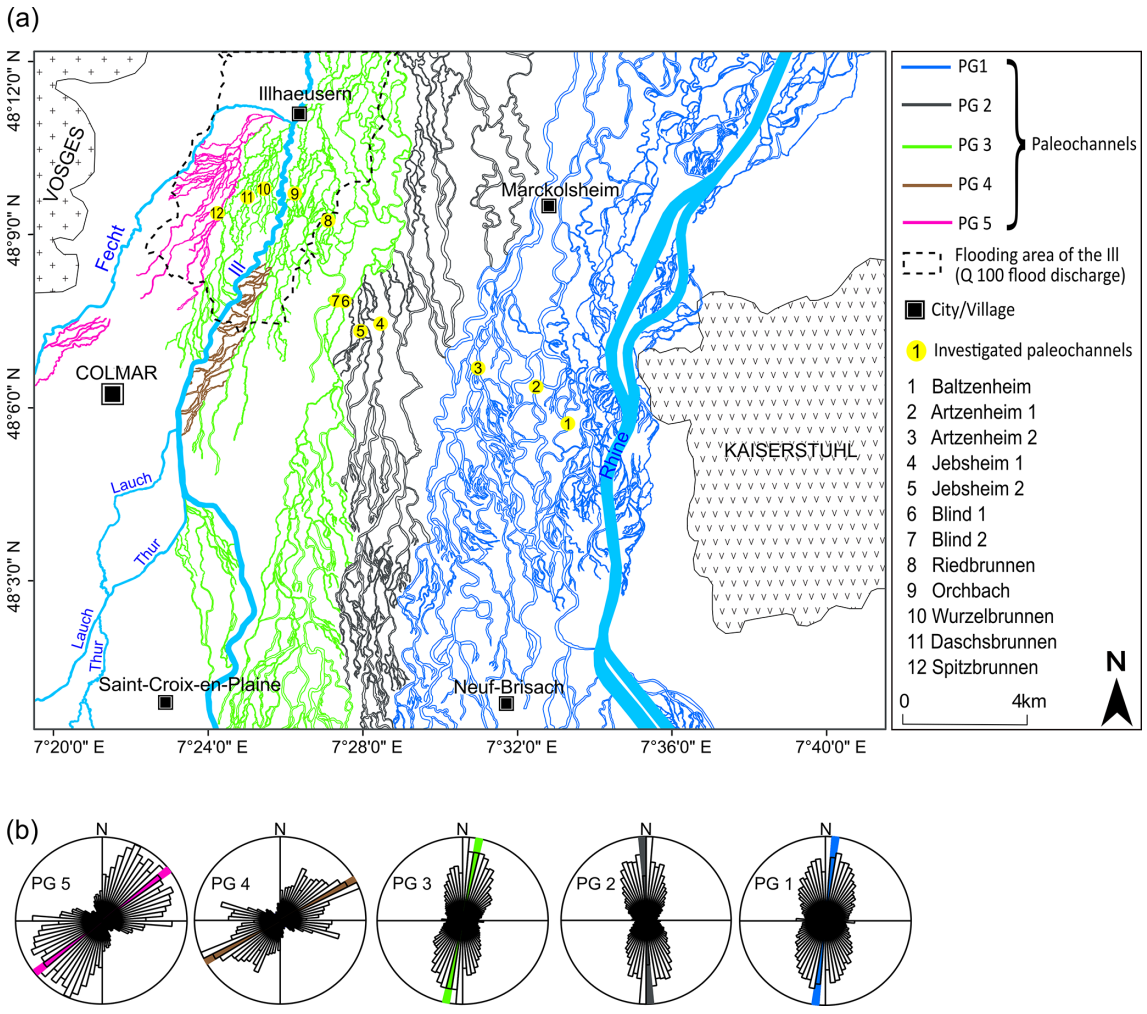

Figure 5. **(a)** Map showing the paleochannel network in the extended study area based on the surface topography, as well as the spatial delineation of five paleochannel groups (PG 1 to PG 5). **(b)** Distribution of the directions of the five paleochannel groups.

3750–3450 cm^{-1} (Bertaux et al., 1998) and 2950–2850 cm^{-1} (Kaufhold et al., 2012). A stepwise discriminant analysis was applied using the Mahalanobis distance to assess the spectral resemblances between the reference and the target samples. The sedimentary provenance of target samples was deduced as the function of the nearest barycenter of reference groups. Detailed statistical treatments are described by Ertlen et al. (2010) and Chapkanski et al. (2020).

In order to evaluate the effect of organic matter on spectra and thus misleading provenance prediction, samples collected in paleochannels (target samples) were analyzed before and after organic matter removal by hydrogen peroxide (H_2O_2). The deviation of the Mahalanobis distance of samples before and after organic matter removal was used to assess the effects of organic matter on provenance determination.

4 Results

4.1 Remote-sensing-based mapping and analysis

We were able to map a detailed and extensive network of paleochannels (about 19 km wide) covering the entire study area by integrating elevation data and aerial images. A map of the area was created (Fig. 5), revealing far more information about the paleochannels than the lidar data provided. The area was divided into five paleochannel groups (PG 1 to PG 5) based on the expected genesis of the paleochannels by showing where the channels are coming from, their location within the alluvial plain, direction, and general channel pattern. Quantitative (lidar) analyses revealed further differences in the surface topographical properties (channel width, depth, sinuosity, and orientation) of these paleochannel groups (Figs. 5 and 6, Table 1).

PG 1. The paleochannels span a 7 km wide corridor in the eastern section of the study area, close to the current Rhine

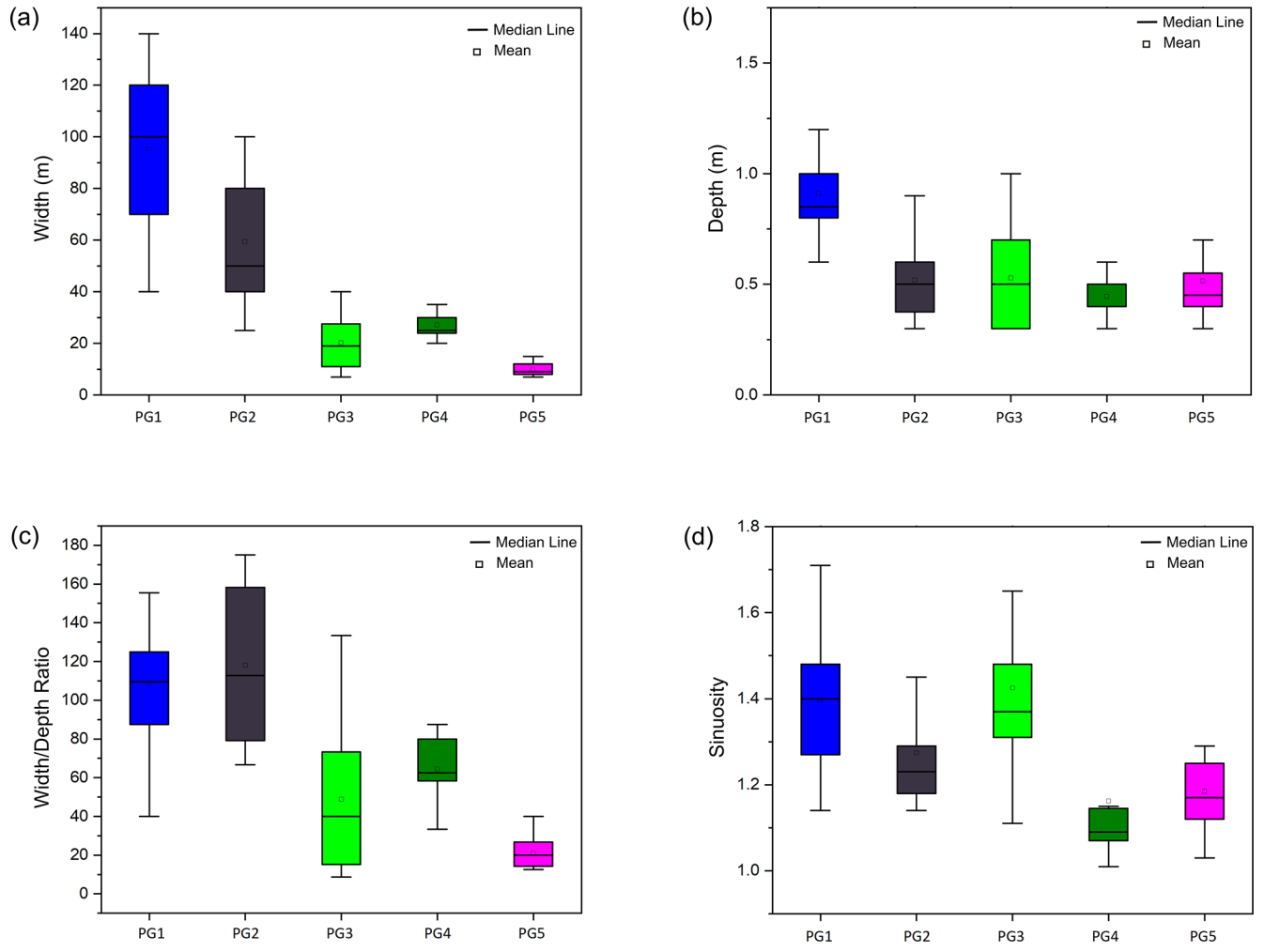

Figure 6. Box plot diagrams of four morphometric parameters for the five paleochannel groups. **(a)** Channel width, **(b)** channel depth, **(c)** width / depth ratio, and **(d)** sinuosity.

Table 1. Summary data of four morphometric parameters for the surface topography of the paleochannel groups (PG 1 to PG 5). The values of each morphometric parameter are arithmetic means and variation coefficients (in brackets).

	Paleochannel groups				
	PG 1	PG 2	PG 3	PG 4	PG 5
Mean channel width	95.38 (27.66)	59.38 (40.89)	20.16 (53.5)	27.11 (21.06)	9.81 (29.3)
Mean channel depth	0.91 (26.37)	0.52 (34.61)	0.53 (43.39)	0.44 (25.00)	0.50 (44.46)
Mean width / depth ratio	108.88 (28.14)	117.88 (33.09)	48.83 (72.30)	64.44 (29.38)	20.93 (35.9)
Sinuosity	1.40 (11.42)	1.27 (11.81)	1.42 (12.67)	1.16 (15.52)	1.18 (8.47)

fluvial hydrosystem. This group comprises multi-threaded channel networks with a high degree of sinuosity (average 1.40). The paleochannels follow a south-southwest–north-northeast trend and are on average 95 m wide and 1 m deep (surface topography). The majority of these paleochannels are located on the lowest topographical level of the alluvial plain, but there is a general increase in surface elevation moving east to west, with a sharp elevation increase in the center of the group (Fig. 4b).

PG 2. This paleochannel group is located in the central sector of the study area and is generally south-southeast–north-northwest trending. Similar to PG 1, the paleochannels exhibit a multi-threaded channel pattern but are less sinuous (average 1.27) than the paleochannels of PG 1. The paleochannel surface topography exhibits an average width

of 60 m and an average depth of 0.5 m. The trace of these paleochannels becomes less visible downstream around the village of Jebsheim due to agricultural activity in the area, which has smoothed the microtopography over time. The PG 2 paleochannels are situated on the same topographical level as the western portion of the PG 1 paleochannels, but the elevation decreases progressively from east to west (Fig. 4b and c).

PG 3. These paleochannels extend approximately 6 km from the central portion of the study area, where they appear to intersect the paleochannels of PG 2, to the western side of the Ill River. The paleochannels exhibit both single- and multi-threaded channel patterns, as well as a high degree of sinuosity (average 1.43). They run south-southwest–north-northeast and are significantly smaller than PG 1 and PG 2 paleochannels, with the channel size decreasing from east to west. Their widths range from less than 10 to 45 m, with an average width of 20 m and a depth of 0.5 m. The PG 3 paleochannels are on a similar topographic level as PG 2, but the elevation increases towards the current channel of the Ill River.

PG 4. The paleochannels are localized very close to the current channel of the Ill River and are associated with the paleochannels of PG 3. Although these paleochannels are associated with the PG 3 paleochannels, they all originate on the Ill River's eastern bank, where they cut into the Ill levee before connecting to the PG 3 paleochannels. In comparison to PG 3 paleochannels, these are low sinuosity (average 1.16), single-thread channels that average 27 m in width and 0.4 m in depth. The PG 4 paleochannels are at a relatively high elevation, which corresponds to the levee of the Ill River. However, there is a progressive decrease in elevation from west to east (Fig. 4b and c). These channels are only visible with lidar. They are barely noticeable in the field or in aerial photos, as they are hidden by dense grassland or in some sectors by the dike of the Ill River.

PG 5. These paleochannels are limited to the northwestern sector of the study area, covering an area of about 2.5 km width. The paleochannels originate on the Fecht River's western bank, from where they flow northeast towards the current channel of the Fecht around Illhaeusern, where they coalesce and gradually taper out (Fig. 5). The paleochannels are mainly multi-threaded to meandering channels (average sinuosity of 1.18) and are much smaller compared to the paleochannels of the other groups. They have an average width of 10 m and a depth of 0.5 m. These paleochannels are located on the highest topographical level of the alluvial plain, which corresponds to the downstream extremity of the alluvial fan of the Fecht River (Fig. 4b and c).

4.2 Paleochannels cross sections, infill sedimentary characteristics, and provenance

The geometry and internal architecture of the investigated paleochannels vary significantly across the study area. The paleochannels range from shallow and narrow channels less than 30 m wide to deep (ca. 5 m) and wide channels with lateral extents exceeding 80 m. The paleochannel infills (sequences) vary across the channels as well, but generally sequences fining upward are observed regardless of channel geometry. For nearly all paleochannels, sandy deposits at the basal parts are overlain by a heterogeneous succession of fine materials (silt, clay), interrupted by peat and organic mud units at some locations (Fig. 7).

4.2.1 PG 1: Channel 1: Baltzenheim (48°05′53.6″ N, 7°33′1.9″ E)

The paleochannel of Baltzenheim is located 2 km west of the current Rhine channel. It is the most eastern of the paleochannels investigated, located within the historical floodplain of the Rhine ("Ried Blond"), and is part of PG 1. This paleochannel has a width of about 80 m and a maximum depth of 2.8 m. The base of the channel infill is composed of 1.5 m thick beige medium sand that extends the entire width of the channel. This unit gradually changes into a subsequent thin layer of beige silty sand. The sandy deposits (medium sand and silty sand) are overlain by brown clayey silt, capped by dark brown silt with some sand that covers the entire width of the channel. MIRS provenance studies indicate that the sedimentary infills of this paleochannel are primarily attributed to the Rhine catchment (Figs. 7a and 8b).

4.2.2 PG 1: Channel 2: Artzenheim 1 (48°06′28.8″ N, 7°32′15.2″ E)

This paleochannel is located 2.5 km west of the present-day Rhine channel within the historical floodplain of the Rhine River and is part of PG 1. However, it exhibits a more complex morphologic and stratigraphic character than the Baltzenheim paleochannel. The paleochannel reaches a maximum depth of around 5 m and a maximum width of 60 m. The lowermost section of the channel is formed of beige-colored fine to medium sand that extends the channel's entire width. Peat and organic mud which range in color from dark brown to black and are approximately 1.5 m thick overlie the sand unit but are restricted to the western and deepest portion of the channel. This peat unit contains abundant plant macrorests and is interbedded with thin, laterally discontinuous clay and carbonate layers (carbonate concretions and shell fragments). The peat/organic mud is topped by a dark gray clayey silt unit marked by shell fragments, pebbles, and thin layers of bright orange coarse sand. On the eastern side of the channel, adjacent to the clayey silt unit, is a layer of beige silty sand with a maximum thickness of 0.8 m. The succession of medium sand, peat, clay, and silty sand is overlain by dark brown clayey silt that spans the entire width of the paleochannel. All units are capped by a 0.5 m thick dark brown organic-rich silt and sand, replete with pebbles, plant macrorests, and traces of plowing. Similar to the sediments

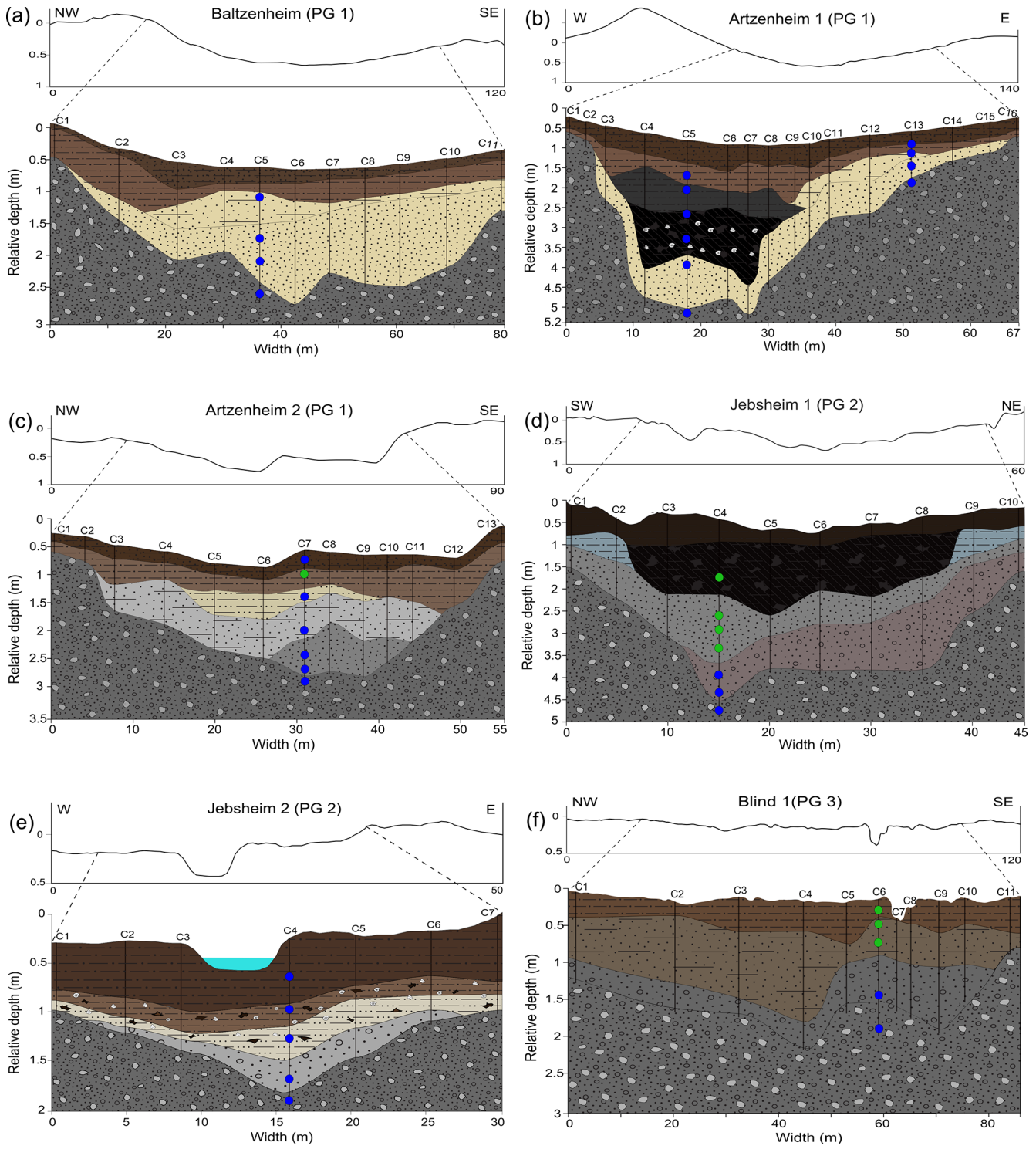

Figure 7.

of the Baltzenheim paleochannel, all the stratigraphic units of this paleochannel also show a complete Rhine provenance affinity (Figs. 7b and 8b).

4.2.3 PG 1: Channel 3: Artzenheim 2 (48°06′50.3″ N, 7°30′46.3″ E)

This paleochannel is located about 5 km west of the present-day Rhine channel and is associated with PG 1. The pale-

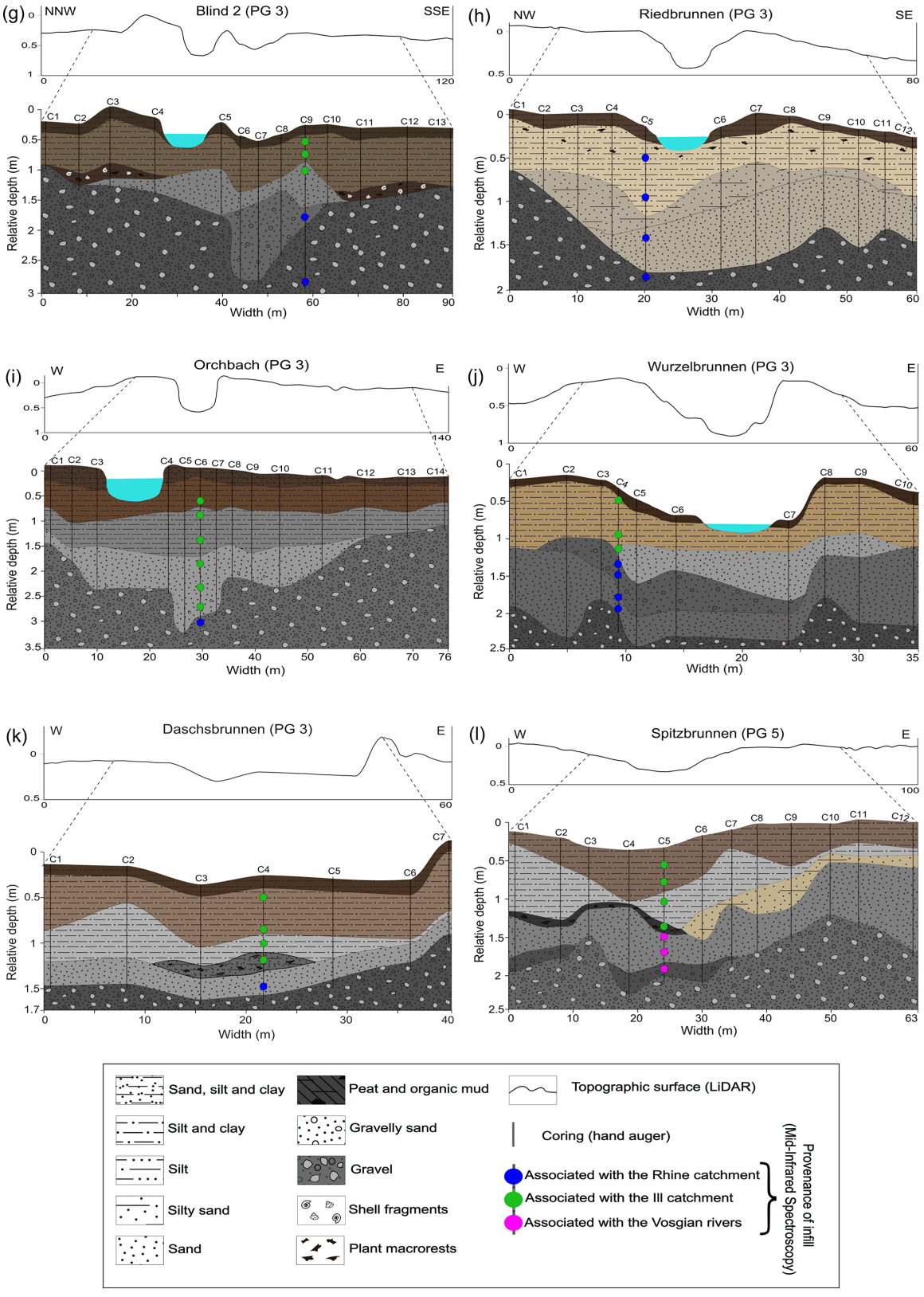

Figure 7. Cross-sections of investigated paleochannels showing internal architecture and stratigraphy based on augured boreholes, as well as description and interpretation of the stratigraphical units. Using lidar data, surface topographical profiles were drawn beyond the limit of the corings to show the full extent of the banks and levees. The figure also shows the provenance of the sediments based on mid-infrared spectroscopy analysis (MIRS) (see also Fig. 8).

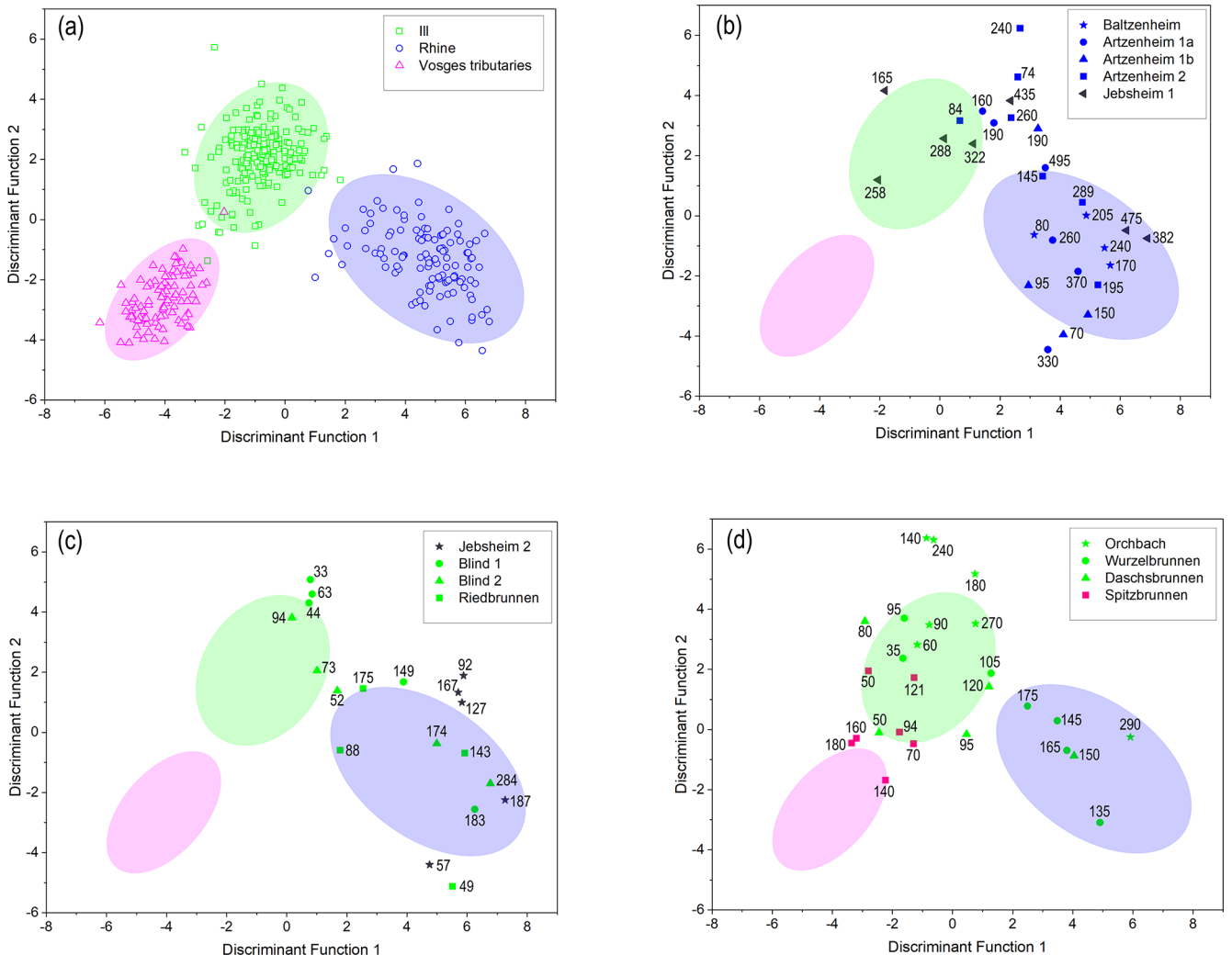

Figure 8. **(a)** Two-dimensional scatter plots showing the MIRS reference samples classified into three distinct source groups based on discriminant analysis (DA). Panels **(b)**, **(c)**, and **(d)** show the DA scores of the paleochannel (target) samples compared to reference samples. The ellipses show the area where 90 % of the different reference samples are concentrated, while the numbers indicate the depths (in cm) at which the target samples were taken.

ochannel has a maximum recorded depth of 2.8 m and is approximately 50 m wide. The sequence of units consists of gray medium sand with intermittent pebbles at the lowermost part of the channel, which is confined to the eastern portion of the channel. The unit gradually changes to gray silty-fine sand with a maximum thickness of ca. 1 m which extends almost the full width of the channel. A thin (ca. 0.5 m thick) beige silt unit follows but is confined only to the center of the channel. This silt is completely covered by a greyish-brown clayey silt unit that spans the channel's width. A dark brown sandy clayey silt with pebbles and plant macrorests completes the sequence. MIRS investigations indicate a Rhine origin for all the stratigraphic units, except for the silt unit, which shows an Ill provenance affinity (Figs. 7c and 8c).

4.2.4 PG 2: Channel 4: Jebsheim 1 (48°07′33.3″ N, 7°28′06.1″ E)

This paleochannel is located in a forested area and belongs to PG 2. The paleochannel is approximately 4.5 m deep but relatively narrow (ca. 40 m wide). The basal channel fills are composed of reddish-gray gravelly sand at the lowest level, which gradually changes to an overlying unit of gray medium sand with occasional gravel lenses. The sandy deposits are overlain by a 1 m thick layer of dark brown to black peat with intermittent layers of organic mud and clay. Numerous plant macrorests and shell fragments are found in the peat layer. Laterally adjacent to the peat on both sides is a bluish-gray clayey silt unit with a maximum thickness of 0.5 m. The peat and clayey silt layers are topped with a dark brown organic-rich clayey silt. The unit contains roots, partially decomposed

organic debris, and shell fragments. MIRS data indicate that the gravelly sand unit at the base of this paleochannel is Rhine-sourced. In contrast, the overlying medium sand and peat units are in good correspondence with an Ill provenance source (Figs. 7d and 8b).

4.2.5 PG 2: Channel 5: Jebsheim 2 (48°07′23.7″ N, 7°27′42.1″ E)

This paleochannel is located 600 m southwest of the Jebsheim 1 paleochannel and is also classified as PG 2. This paleochannel, which serves as the course of an unnamed stream, is relatively narrow (about 25 m wide) and shallow, with a maximum recorded depth of 1.7 m. The infill succession of the paleochannel begins with coarse gravelly sand at its lowermost section, followed by beige silt with abundant plant fragments, and eventually a transition to brown organic-rich clayey silt. This clayey unit contains abundant shell fragments and plant macrorests, capped by a dark brown clayey silt with some pebbles. In contrast to the Jebsheim 1 paleochannel, which contains sediments from both the Rhine and Ill systems, Jebsheim 2 shows only Rhine-derived infill sediments (Figs. 7e and 8c).

4.2.6 PG 3: Channels 6 and 7: Blind River (Blind 1 and Blind 2)

This location comprises two paleochannels: one that serves as the course for an inactive tributary of the Blind River (Blind 1: 48°07′52.9″ N, 7°27′13.4″ E), colloquially named "Old Blind", and another that serves as the current course for the Blind River (Blind 2: 48°07′55.7″ N, 7°27′08.3″ E). Both paleochannels are classified as PG 3 and are located within the "Ried Gris".

The "Old Blind" paleochannel (Blind 1) is relatively wide (about 80 m) but shallow, reaching a maximum depth of 1.8 m. The infill sediment sequence shows a basal gravelly sand unit (maximum thickness 0.7 m) overlain by a 1 m thick brownish-gray silty sand unit which gradually transitions to a brown clayey silt unit that caps the sequence. The gravelly sand at the base of the paleochannel has a Rhine origin, while the overlying units are composed of Ill-derived sediments (Figs. 7f and 8c).

The paleochannel of Blind 2 is also relatively wide (approximately 80 m) and has a depth of 2.8 m. The Blind River does not flow through the deepest section of the paleochannel but rather around 10 m to the west. The flowing channel of Blind 2 appears to be artificial, with a regular trapezoidal shape and an artificial right bank levee. Furthermore, at the top of the deepest part of the paleochannel, the surface topography preserves a former channel that likely corresponds to the natural channel (Fig. 7g). At Blind 2, the paleochannel infill sequence consists of, from bottom to top, a 1 m thick gravelly sand unit concentrated in the middle of the paleochannel, overlain by gray fine to medium sand that reaches a maximum thickness of 0.6 m. Overlying the medium sand on both the eastern and western channel margins is a layer of dark brown organic clay with shell fragments and some pebbles. A brown clayey silt unit (0.8 m thick) lies above the organic clay, followed by an organic-rich silty-clay unit. MIRS results show an origin from the Rhine for the gravelly sand unit, while the overlying fine sand and clayey silt units have an Ill origin (Figs. 7g and 8c).

4.2.7 PG 3: Channel 8: Riedbrunnen (48°09′19.4″ N, 7°26′46.2″ E)

The Riedbrunnen paleochannel is classed as PG 3 and contains the current course of the Riedbrunnen River, which flows near the deepest section of the paleochannel. The paleochannel is relatively shallow and narrow, reaching a maximum depth of 1.9 m and a width of about 60 m. At the channel's base, a greige color, fine to medium sand unit (maximum thickness 0.8 m) is overlain by a greige silty sand unit (maximum thickness 0.5 m). Following this unit is a succession of beige to light gray sandy silt with abundant plant detritus in its upper part. The upper 0.2 m of the channel infill is formed of dark brown organic-rich silty clay with partially decomposed plant macrorests. Sediment provenance analyses indicate that all the infill sediments of the Riedbrunnen paleochannel originate from the Rhine catchment (Figs. 7h and 8c).

4.2.8 PG 3: Channel 9: Orchbach (48°09′45.7″ N, 7°25′54.7″ E)

The Orchbach is another PG 3 paleochannel within the floodplain of the Ill ("Ried Gris"). This paleochannel is located about 350 m east of the Ill River and contains the current course of the Orchbach River. The paleochannel has a maximum depth of 3.2 m and a width of approximately 65 m. The Orchbach River's current channel is about 10 m west of the center of the paleochannel. The lowest section of the paleochannel comprises gray medium to coarse sand with a maximum recorded thickness of 1.5 m. A 1 m thick gray clayey silt unit covering the entire channel width overlies the sand, followed progressively by a brown clayey silt (0.7 m thick) unit with shell fragments and plant macrorests. Dark brown clayey silt with some sand caps the infill succession. Unlike the sediments of the nearby Riedbrunnen paleochannel, which have a Rhine origin, all of the infill sediments of the Orchbach paleochannel are of Ill provenance (Figs. 7i and 8d).

4.2.9 PG 3: Channel 10: Wurzelbrunnen (48°09′51.6″ N, 7°25′07.9″ E)

Wurzelbrunnen is the first of three paleochannels that have been investigated west of the Ill River. It is also of PG 3 and located around 450 m west of the Ill River in the "Ried Gris". The paleochannel is currently active and serves as the course

of the shallow Wurzelbrunnen stream. The paleochannel is roughly 35 m wide and reaches a maximum depth of 2.4 m. The infill of the paleochannel begins with a gray medium sand unit with a maximum thickness of 1.2 m, which is overlain by gray gravelly sand concentrated in the western and central sections of the paleochannel. The gravelly sand is overlain by another unit of gray medium sand (maximum thickness 1.2 m) that runs the channel's central and eastern sections. The medium sand is covered by a beige-brown clayey silt unit that extends the full width of the paleochannel and is topped by dark brown clayey silt with root fragments and traces of plowing. MIRS analysis indicates that the first two sandy units at the base of the paleochannel are composed of sediments derived from the Rhine provenance area. In contrast, the upper sand unit is primarily associated with the Ill, albeit with a little Rhine influence. The clayey silt has a pure Ill origin (Figs. 7j and 8d).

4.2.10 PG 3: Channel 11: Daschsbrunnen (48°09′44.8″ N, 7°24′43.0″ E)

The Daschsbrunnen paleochannel is located 450 m west of Wurzelbrunnen and is also a part of PG 3 on the western side of the Ill River. The paleochannel is approximately 40 m wide and 1.6 m deep. The basal 0.5 m are gray fine to medium sand with scattered pebbles, followed by 0.2 m of dark brown to gray silty sand with abundant plant fragments. This silty sand unit is restricted to the mid-section of the paleochannel. The overlying unit consists of gray 1.2 m thick clayey silt, which gradually changes to greyish brown in the upper 0.5 m. The topmost 0.2 m of the paleochannel is built up of dark brown clayey silt. MIRS data reflect a Rhine origin for the basal sand infill, while the overlying silty sand is Ill-derived with some Rhine influence. In contrast, the clayey silt units bear a pure Ill signature (Figs. 7k and 8d).

4.2.11 PG 5: Channel 12: Spitzbrunnen (48°09′25.5″ N, 7°24′0.8″ E)

Spitzbrunnen is the westernmost of the studied paleochannels, located about 1.9 km west of the Ill River and 2.2 km east of the Fecht River. It is the only paleochannel of PG 5 that has been investigated. The paleochannel reaches a maximum depth of 2.2 m and is approximately 65 m wide. At its base, the paleochannel is filled with dark gray gravelly sand localized in the middle of the channel. A gravel bank separates this gravelly sand from an identical unit on the western side of the channel. The unit directly overlying the gravelly sand is made of gray medium to coarse sand that reaches a thickness of about 1 m. Above the medium sand is a layer of beige silty sand that extends from the center of the channel to the eastern bank. This layer is flanked by a dark gray, organic-rich silty sand that gradually changes to gray clayey silt that stretches the entire channel width. All the units are then topped by brownish-gray clayey silt with a maximum thickness of 0.6 m. Provenance analysis (MIRS) shows that the basal sand units (gravelly sand and medium to coarse sand) of the Spitzbrunnen paleochannel originated primarily from the Vosges source area. In contrast, the overlying silty units are composed of Ill-derived sediments (Figs. 7l and 8d).

5 Discussion

5.1 Consolidation of the MIRS method to identify sediment provenance

Chapkanski et al. (2020) pioneered the use of MIRS and discriminant analysis (DA) to identify the provenance of paleochannel infills within the Upper Rhine alluvial plain. However, since the methodology was only tested on one paleochannel, it remained unknown whether the MIRS–DA technique could be widely applied to determine the provenance of paleochannel infillings across a large part of the alluvial plain. As a result, we employed the MIRS–DA approach to determine the provenance of several paleochannel infillings over the whole width of the French Upper Rhine plain. Our findings clearly demonstrate the robustness of this method in identifying the sources of paleochannel infilling, which may have changed during the filling for some paleochannels. The Baltzenheim 1 and Baltzenheim 2 paleochannels, for example, are entirely filled with Rhine sediments, whereas the Orchbach paleochannel is filled with Ill sediments. In contrast, the filling of paleochannels such as Blind, Wurzelbrunnen, and Daschsbrunnen began with Rhine sediments and subsequently transitioned to Ill deposits (Figs. 7 and 8).

While the MIRS–DA technique has demonstrated great potential for determining the provenance of sediments, Chapkanski et al. (2020) suggested that high organic matter (more than 5 % to 10 %) in sediment samples might affect the mid-infrared spectra, resulting in less accurate measurements. To address this potential constraint, we pre-treated target samples with an organic matter content of more than 5 % (see Sect. 3.3). The results (Table 2) show that the deviations of the samples from their initial position before OM removal remain within a reasonable range of < 1.5 (Mahalanobis distance). However, those samples containing more than 10 % of organic matter recorded deviations ranging from 1.5 to 5, which could induce modification of provenance attribution. However, the results here showed no significant inconsistencies in the attribution of sediment provenance except for two samples (Az1_260 and Az1_330) from peaty deposits and two other samples (NB_73 and L'O_90) from organic-rich units. Therefore, these confirm suggestions provided by Chapkanski et al. (2020), and we recommend systematically pre-treating samples containing more than 10 % of organic matter.

Overall, our findings confirm that the MIRS–DA technique is capable of determining the provenance of paleochannel infills within the French Rhine alluvial plain with high specificity. Moreover, the method is a low-cost and ef-

Table 2. Provenance attribution of target samples containing more than 5 % organic matter (OM) before and after organic matter treatment. The table also shows the deviation of each sample after organic matter removal. F1: discriminant function 1; F2: discriminant function 2.

Sample ID	Depth (cm)	Paleochannel	OM before treatment (%)	Deviation from F1 after treatment	Deviation from F2 after treatment	Provenance before organic matter treatment	Provenance after organic matter treatment
Bz_80	80	Baltzenheim	15.38	1.71	1.58	Rhine	Rhine
Az1_260	260	Artzenheim 1	16.86	3.60	3.11	Ill	Rhine
Az1_330	330	Artzenheim 1	14.91	3.44	4.58	Ill	Rhine
Az2_145	145	Artzenheim 2	5.79	0.02	1.43	Rhine	Rhine
Jebs1_165	165	Jebsheim 1	6.89	0.09	0.17	Ill	Ill
Jebs2_57	57	Jebsheim 2	11.77	0.07	2.79	Rhine	Rhine
OB_44	44	Blind 1	8.25	1.96	1.13	Rhine	Rhine
NB_73	73	Blind 2	12.21	5.14	4.79	Vosges	Ill
NB_94	94	Blind 2	6.62	0.63	0.44	Ill	Ill
Ried_88	88	Riedbrunnen	6.73	1.22	1.19	Rhine	Rhine
L'O_60	60	Orchbach	12.24	1.96	0.81	Ill	Ill
L'O_90	90	Orchbach	11.85	3.14	0.34	Rhine	Ill
Wz_35	35	Wurzelbrunnen	11.34	1.53	2.58	Ill	Ill
Spt_94	94	Spitzbrunnen	9.93	0.92	0.88	Ill	Ill
Spt_121	121	Spitzbrunnen	10.47	0.58	2.30	Ill	Ill

ficient alternative for provenance investigations of deposits in large and complex fluvial systems. The MIRS–DA technique, however, has so far only been applied in the Upper Rhine Valley, and it remains to be tested in other large river floodplains.

5.2 Establishment of sedimentary facies

The subsurface morphology of the investigated paleochannels exhibits a range of geometric forms, as well as varied sedimentary infill (Fig. 7). Several other paleochannels within the French Rhine alluvial plain have shown a similar pattern of varying subsurface morphology and infill stratigraphy (e.g., Schmitt et al., 2016; Chapkanski et al., 2020). These differences in internal sedimentary infills across the plain indicate infilling by rivers with varying dynamics, reflecting lateral dynamics of the Rhine, Ill, and Fecht rivers. To better understand the various dynamics and channel activity over time, we classified the stratigraphic units of our investigated paleochannels into four genetic groups ("Gravel", "Active", "Infill", and "Surficial" facies). These classifications are based on the characterization and interpretations of various Late Pleistocene and Holocene fluvial deposits from the Upper Rhine Valley (Dambeck and Thiemeyer, 2002; Schirmer et al., 2005; Erkens et al., 2009, 2011; Schmitt et al., 2016). By deciphering the different stages of channel activity and assigning a provenance of filling dynamics to the stages, we determined the river system(s) that contributed to the infilling of the investigated paleochannels.

The gravelly sediments at the very bottom of the paleochannels are categorized as "Gravel" deposits. These sediments form the base and lateral limits of the paleochannels and are easily differentiated from the overlying fill sediments by their significantly larger grain sizes, with gravel dominating. This facies is interpreted to have formed by high-energy depositional conditions via non-selective bedload transport (Chardon et al., 2021). Moreover, Gravel is ubiquitously present throughout the study area, and MIRS spectroscopy reveals an unambiguous Rhine origin for these deposits (Figs. 7 and 8). The ubiquity of these gravels, as well as their sedimentary characteristics and provenance, indicates that they are deposits of the Rhine braided belt, which covered nearly the entire plain of the URG during the Late Pleistocene (Lang et al., 2003; Kock et al., 2009). It is worth noting that these sediments do not directly constitute the infilling sequences of the paleochannels. However, some fluvial reworking of the sediments and their deposition within the stratigraphic infills may occur, thus forming essential components for understanding channel dynamics.

The "Active" facies constitute the sand-rich stratigraphic units (gravelly sands, sands, and silty sands) at the basal parts of the paleochannels and overlying the Pleistocene gravel (Gravel). These sandy strata are interpreted as channel deposits, comprising gravelly channel lags (bedload) and sandy channel fills (bedload and graduated suspension; Plotzki et al., 2015; Delile et al., 2016). The deposits indicate deposition during moderate- to high-energy periods of flow at the beginning of infill. So this facies reveals deposition during a permanent or intermittent connection to a basin-fed river. Bank accretion may also have occurred during such periods. Thus, by identifying the Active deposits and their provenance, we were able to discern which rivers were active in infilling of each paleochannel. In contrast to the gravel deposits, which are exclusively Rhine-sourced, the sandy channel deposits (Active) show Rhine, Ill, and Vosges signatures

as revealed by MIRS (Figs. 7 and 8). This disparity in provenance sources indicates that the infilling sources changed over time in some cases, highlighting active past lateral dynamics of the main rivers within the alluvial plain.

The succession of silty and clayey layers, interspersed with peat and organic mud, are classified as "Infill" facies. Unlike the Active channel deposits, which are generally restricted to the paleochannels' deepest and central sections, the Infill sediments mostly form a blanket of fine-grained materials that covers the whole width of the paleochannels (Fig. 7). Furthermore, these units are characterized by an abundance of plant macrorests and shell fragments. Accordingly, these units' stratigraphic position and sedimentary characteristics represent low- (silt) to very low-energy (clay, organic mud, peat) depositional environments. Silt and clay transport (and deposition) also indicates a homogeneous suspension (Delile et al., 2016). In such a context, channels have no (or a weak) upstream connection to a basin-fed river. The peat and organic mud, which can be considered a sub-class of the Infill facies (given the close association in the successions), indicate autochthonous sedimentation and starvation or minimal input of clastic sediments in the channels (Hoffmann et al., 2008; Toonen et al., 2012).

Consequently, the Infill sediments serve as key stratigraphic markers for determining an important filling phase associated with reduced fluvial activity and a partial or total disconnection from feeding rivers. Such depositions occurred mostly during floods which extended to the channels. Furthermore, establishing the provenance of these sediments was critical for determining which river(s) contributed to the paleochannel filling phase (after their abandonment). Provenance (MIRS) investigations reveal a mixture of Rhine, Ill, and Vosges signatures for the Infill sediments (Figs. 7 and 8), confirming the lateral movements of the basin-fed rivers across the alluvial plain.

The uppermost sequences of the paleochannels are classed as "Surficial" facies and are typically formed of clays and silts (and in some places, reworked floodplain sands and gravel). Additionally, this facies contains biogenic materials and some anthropogenic materials locally. Typically, the uppermost portion of these floodplain surface deposits shows organic soils and traces of agricultural activity (plowing). The pedogenesis indicates (quasi-)total channel abandonment and a very weak sedimentation rate for centuries. In the cases where a current stream runs in the paleochannels, the presence of this surface facies indicates that the current channel is in a (quasi-)steady state (which may be linked in some cases to some human dredging activities; Schmitt, 2001; Schmitt et al., 2007, 2011). Considering the Upper Rhine valley is highly anthropized (Lang et al., 2003; Wantzen et al., 2021), these units are considered to be affected by direct human alteration. Hence, they are only used to develop an understanding of soil formation processes and agricultural practices in the immediate environment. They are not used to make direct inferences regarding the fluvial processes within the alluvial plain.

5.3 Reconstructing the temporal trajectories of the five paleochannel groups

Remote sensing combined with qualitative and quantitative morphometric analysis of the surface topography provided a basis for classifying five paleochannel groups within our study area. Additional datasets from the fieldwork and provenance analysis provide information into further complexities amongst these paleochannel groups. In the following section, we combine all of the datasets, as well as information from earlier studies, to provide insights into the origins and the temporal trajectories of these paleochannel groups and speculate on the various basin-fed rivers with which they may be associated.

5.3.1 PG 1

The PG 1 paleochannels in the easternmost sector of the study area are clearly visible in the landscape, with the highest values of width and depth of all the paleochannel groups (Fig. 6; Table 1). These paleochannels exhibit a relatively high degree of sinuosity (average 1.4), as well as a multi-threaded channel pattern, and are almost entirely composed of Rhine-sourced infill sediments, as shown by the paleochannels Baltzenheim, Artzenheim 1, and Artzenheim 2 (Fig. 7a–c). The topographic surfaces and lidar analysis indicate a braided channel pattern. However, the remaining streams in this part of the alluvial plain exhibit an anastomosing channel pattern (Schmitt et al., 2007, 2011). Furthermore, as depicted on historical maps, the sub-modern Rhine system in this region was characterized by a similar anastomosing channel pattern (see Supplement). Thus, we consider the PG 1 paleochannels to consist of two main generations of paleochannels: an initial system with a braided channel pattern, which metamorphosed (fluvial metamorphosis) to the current anastomosing (and paleo-anastomosing, i.e., disconnected upstream) system. Accordingly, the PG 1 paleochannel group can be described as a palimpsest, consisting of the current and paleo-anastomosing patterns, with a low level of flow energy, superimposed on – and controlled by – the former braided channel pattern of the highly dynamic (with a high level of energy) Late Glacial Rhine fluvial hydrosystem (Schmitt, 2010).

5.3.2 PG 2

The south-southeast–north-northwest-oriented PG 2 paleochannels exhibit a similar multi-threaded pattern to PG 1. They are, however, less sinuous (average 1.27) than the PG 1 paleochannels. The surface channel pattern of these paleochannels is obscured by agricultural activity in the area, which has smoothed much of the microtopography. However, visual inspection of the elevation data and aerial pho-

tographs reveals traces of some features that appear to reflect a braided channel pattern. This is reinforced by high values of the width / depth ratio (Schmitt et al., 2007). Furthermore, the PG 1 and PG 3 paleochannels to the east and west respectively appear to cross and intersect the PG 2 paleochannels, which may indicate an older age for the PG 2 paleochannels. Based on these observations, it can thus be suggested that the PG 2 paleochannels are relicts of the Late Glacial braided Rhine system, with a more south–north flow direction. This fluvial style was the dominant character of the Rhine system during the Late Pleistocene, occupying almost the entirety of the alluvial plain (Lang et al., 2003; Schmitt et al., 2016). At the start of the Holocene, the individualization of the Rhine and Ill rivers resulted in the abandonment and partial filling up of the PG 2 paleochannels.

In comparison to the PG 1 paleochannels, which contain only Rhine-sourced sediments, it is worth noting that the Active facies of the Jebsheim 1 paleochannel show both Rhine and Ill sediments. Gravelly sand at the basal part of paleochannel is Rhine-sourced, while the overlying medium sand has an ill origin (Fig. 7). In contrast, all the stratigraphic units of the Jebsheim 2 paleochannel are Rhine-sourced (Figs. 7 and 8). A similar mixed Rhine–Ill sediment infilling pattern was observed in a northwest-trending paleochannel about 3 km north (downstream) of the Jebsheim 1 paleochannel (Chapkanski et al., 2020). Thus, the presence of Ill-derived sediments in the braided Rhine paleochannels can be explained by branches of the ensuing Holocene anastomosing Ill system re-occupying parts of the paleochannels before it migrated westward as well (Schmitt et al., 2016). Following the lateral migrations of the Rhine and Ill systems and the abandonment of the PG 2 paleochannels, the central area of the alluvial plain most likely remained dry except for periodic large floods.

The channel pattern is relatively more anastomosing in the downstream part of this group (north of Colmar), which is likely due to a general slope decrease.

5.3.3 PG 3

The PG 3 paleochannels are generally south-southwest–north-northeast trending and correspond to paleochannels of the main course of the Ill River, as well as former main and flood channels of this river at the eastern and western banks of the Ill. The surface topography shows these paleochannels to be narrower (average 20.13) than those of the PG 1 and PG 2 groups. The channel pattern shows a relatively high sinuosity, with a general multi-threaded channel pattern (Fig. 5). These paleochannels correspond to Ill-inherited geomorphic features. However, there are significant differences in their internal stratigraphy and sediment provenance. The Blind paleochannels, for example, are first filled by Rhine sediments and afterward by Ill sediments (Fig. 7f and g). The Riedbrunnen paleochannel is entirely filled by Rhine deposits, whereas the nearby Orchbach paleochannel is completely filled with Ill sediments (Figs. 7 and 8). On the western side of the Ill River, a similar Rhine sequence, followed by an Ill infilling sequence, is also recorded for the smaller Wurzelbrunnen and Daschsbrunnen paleochannels. Based on these findings, we propose that the PG 3 paleochannels are actually a mixture of Rhine and Ill paleochannels. The Rhine not only transported and deposited gravelly Active sediments, but Rhine discharge also shaped some of the paleochannels. However, there is no prior record of coeval activity of the Rhine and Ill systems in this area. Following the individualization of the Rhine and Ill, the Rhine shifted westwards progressively, and the channels were abandoned after some of them were more or less filled by Rhine sediments. The ensuing Ill system then reoccupied and modified several of these ancient Rhine paleochannels, depositing Ill sediments.

The investigated PG 3 paleochannels provide an excellent illustration of these dynamics. The Blind paleochannels, for instance, are defined by a meandering/anastomosing channel pattern in the lidar DEM, suggestive of the Ill system. However, the fill stratigraphy reveals "a wide paleochannel" with coarse-grained Active deposits from the Rhine, overlain by Active and Infill sediments bearing an Ill signature. Thus, we presume that the Blind paleochannel was created and used by the Rhine. Following its abandonment, the Ill re-occupied and modified the channel, depositing Ill sediments. This conjecture is consistent with the findings of Carbiener (1969), Hirth (1971), and Schmitt et al. (2016), the latter suggesting that the current Blind River is flowing in a former main channel of the Ill River.

In comparison, the Riedbrunnen paleochannel, located close to the contemporary Ill River, is completely filled with Rhine-derived sediments. This atypical sediment provenance can be explained by a former Rhine channel that was abandoned and completely filled by the Rhine, probably before it moved far further east. As a result, this paleochannel was not re-occupied by the Ill system. Interestingly, the Orchbach paleochannel, 1.5 km east of the Riedbrunnen, contains only Ill-derived sediments. Looking at the spatial position, planform morphology, and infilling of the Orchbach paleochannel, it appears that the Orchbach paleochannel was a former main channel of the Ill River that was created and used solely by the Ill River.

Other paleochannels documented in this section of the alluvial plain (Al Siddik, 1986; Schmitt et al., 2016) show paleochannels of mixed origin, as well as those of pure Rhine and pure Ill origin. Some with a pure Ill provenance were also recorded further downstream of our study area. Based on these findings, we can conclude that the PG 3 paleochannels are best described as a mixture of older Rhine and younger Ill paleochannels. This distribution pattern is also the result of the Ill being relatively smaller than the Rhine, and it did not wholly occupy large areas of the Holocene alluvial plain. This explains why a small part of the Rhine "Hardt Grise"

exists close to the Ill River, southwest of the village of Bischwihr (Fig. 3; Hirth, 1971).

5.3.4 PG 4

The PG 4 paleochannels constitute distinctively southwest–northeast-trending paleochannels that originate from the eastern bank of the current Ill River channel. Although field investigations and provenance analysis remain to be undertaken for these paleochannels, analysis of their surface topography and spatial distribution indicates that they are most likely natural flood channels cutting the eastern bank of the Ill River. They were most likely only active during high floods, diverting floodwaters away from the Ill River towards the floodplain. Owing to the lack of a temporal context for these paleochannels, it is unknown if they are contemporaneous with some PG 3 paleochannels or if they were periodically active during historical times. These paleochannels are predominantly concentrated along the regulated reach of the Ill River (where no floods occur anymore), upstream of the Ill River floodplain ($Q100$ flood discharge; Fig. 5). Therefore, these paleochannels are not currently active, but they were probably active prior to the mid-19th century regulation of the Ill River.

5.3.5 PG 5

The PG 5 paleochannels, the westernmost component, are the narrowest (average 10 m), primarily single-threaded channels with low sinuosity (average 1.18). These paleochannels have a southwest–northeast orientation and a fluvial style different from those of the Rhine and Ill, which may reflect a link with the Fecht River fluvial hydrosystem. Moreover, the infilling of the Spitzbrunnen paleochannel shows an Active facies with Vosges signature, overlain by Infill sediments of Ill provenance (Fig. 7l). This filling pattern indicates that the Spitzbrunnen paleochannel was carved by a Vosgian river and later filled with overbank sediments from the Ill following its abandonment. A detailed examination of the Spitzbrunnen's surface topography indicates parallels to the modern Fecht River. As a result, it can be argued that the Spitzbrunnen paleochannel was most likely a former bed of the Fecht River. Considering the morphology and infill of the Spitzbrunnen, as well as the character and placement of the other PG 5 paleochannels, we propose that the PG 5 paleochannels are very likely to be the former channels and side channels of the Fecht River. Accordingly, we assume that the Fecht River was located farther east within the alluvial plain, and it moved westwards towards its current position over the course of its evolution, naturally and/or by human activities (Schmitt, 2001).

This delineation of a putative Fecht paleochannel cluster and the absence of true Ill paleochannels beyond the Spitzbrunnen imply that the Ill River did not extend beyond the Spitzbrunnen paleochannel in its western lateral migration. This observation is consistent with the suggestion of Schmitt et al. (2016) that the Ill River's western migration during the Holocene was limited to somewhere near the Wurzelbrunnen paleochannel. However, our findings show that the Ill did migrate slightly westward, up to the Daschsbrunnen paleochannel. As a result, we assume that the Ill River's Holocene displacement limit was somewhere between the Daschsbrunnen and Spitzbrunnen paleochannels. This boundary corresponds to an area near the eastern limit of the Fecht's alluvial fan.

6 Conclusions

Using remote sensing data, we identified and mapped a detailed and extensive network of paleochannels spanning a 19 km wide corridor within the French Upper Rhine alluvial plain. The mapped paleochannels exhibit a range of surface morphological characteristics, including planform character, geometry, and paleo-flow orientations. Additional data from field investigations and provenance analysis revealed considerable differences in the sedimentary characteristics and provenance of the infillings of the paleochannels, indicating significant changes in hydro-geomorphodynamic processes, especially lateral displacements of the main rivers.

Five paleochannel groups (PG 1 to PG 5) were delineated in the study area based on assessments and interpretations of the remotely sensed data, hand-augured core data, and mid-infrared spectroscopic analysis. The PG 1 paleochannels correspond to remnants of the Holocene braided Rhine hydrosystem which is currently predominantly an anastomosing system, while the PG 2 paleochannels represent relicts of the Late Pleistocene braided Rhine. The PG 3 paleochannels, on the other hand, are a complex mixture of paleochannels from the Ill hydrosystem superimposed on the Rhine braided channels. The PG 4 paleochannels are ancient Ill flood channels, while the Fecht river system formed the PG 5 paleochannels.

While our findings unequivocally establish the presence of at least five paleochannel groups in the area, their temporal trajectory remains vague. Age assignments for the paleochannel systems, as well as additional sedimentological analyses, need to be established. Accordingly, further studies on these paleochannels will be carried out to develop these datasets, which will provide new insights into the chronology of paleochannel development, the paleoenvironments in which they formed, and the processes that controlled their formation, all mainly linked to the Holocene lateral dynamics of the Rhine, Ill, and Fecht rivers.

Data availability. All data relevant for this study are either presented in the main text or the Supplement.

Supplement. The supplement related to this article is available online at: https://doi.org/10.5194/egqsj-71-191-2022-supplement.

Author contributions. FP and LS designed and supervised the study. Funding was acquired by FP and MA. Fieldwork was carried out by MA, HM, EO, MS, CR, and FS. MA, CR, FS, SC, and DE were responsible for methodology and formal analysis under the supervision of LS. EO, HM, and MS assisted with methodology. MA wrote the original draft with input from SC. The manuscript was reviewed and edited by LS and FP. All authors commented on and approved the final version of the manuscript.

Competing interests. The contact author has declared that none of the authors has any competing interests.

Disclaimer. Publisher's note: Copernicus Publications remains neutral with regard to jurisdictional claims in published maps and institutional affiliations.

Special issue statement. This article is part of the special issue "Quaternary research from and inspired by the first virtual DEUQUA conference". It is a result of the vDEUQUA2021 online conference in September/October 2021.

Acknowledgements. Special thanks to Alexander Fülling, Elijah Fon, Armelle Ballian, and Amir Bangash for their assistance in the field. Thanks go to Grégoire Skupinski and Jérome Houssier for processing and treating the raw lidar data. We thank the local administrators of the various communes for giving us permission to conduct the fieldwork. We also express our gratitude to the landowners who permitted us to drill on their property. The Regional Council of Grand Est and the European Collectivity of Alsace are also acknowledged for providing the lidar data.

Financial support. This research has been supported by the Landesgraduiertenförderung Baden-Württemberg (state graduate funding) through a PhD scholarship to Mubarak Abdulkarim.

This open-access publication was funded
by the University of Freiburg.

Review statement. This paper was edited by Christian Zeeden and reviewed by Dominik Faust and one anonymous referee.

References

Al Siddik, A. M.: Contribution à l'étude de la dynamique de l'humification des sols hydromorphes du Ried Ello-Rhénan (Région d'Illhaeusern, Haut-Rhin), PhD thesis, Nancy 1 University, France, 95 pp., unpublished, 1986.

Bertaux, J., Frohlich, F., and Ildefonse, P.: Multicomponent analysis of FTIR spectra; quantification of amorphous and crystallized mineral phases in synthetic and natural sediments, J. Sediment. Res., 68, 440–447, https://doi.org/10.2110/jsr.68.440, 1998.

Bisson, M., Piccinini, S., and Zanchetta, G.: A multidisciplinary GIS-Based approach for mapping paleoriver migration: A case study of the Serchio River (Lucca Alluvial Plain, Tuscany), GIsci Remote Sens., 48, 566–582, https://doi.org/10.2747/1548-1603.48.4.566, 2011.

Boës, E., Schmitt, L., Schwartz, D., Gebhardt, A., Goepp, S., and Lasserre, M.: L'anthropisation des zones humides de la plaine d'Alsace au cours de la Protohistoire: problématiques d'études à partir des fouilles récentes menées sur les tumulus de Mussig Plaetze (Bas-Rhin), in: L'âge du Fer dans l'arc jurassien et ses marges. Dépôts, lieux sacrés et territorialité à l'âge du Fer. Annales Littéraires, Série "Environnement, sociétés et archéologie", edited by: Barral, P., Daubigney, A., Dunning, C., Kaenel, G., and Roulière-Lambert, M. J., Presses Universitaires de Franche-Comté, 113–118, ISBN 978-2848672014, 2007.

Bos, J. A. A., Dambeck, R., Kalis, A. J., Schweizer, A., and Thiemeyer, H.: Palaeoenvironmental changes and vegetation history of the northern Upper Rhine graben (southwestern Germany) since the Lateglacial, Neth. J. Geosci., 87, 67–90, https://doi.org/10.1017/S0016774600024057, 2008.

Bowler, J. M.: Quaternary climate and tectonics in the evolution of the Riverine Plain, southeastern Australia, in: Landform evolution in Australasia, edited by: Davies, J. L., and Williams, M. A. J., Australian National University Press, Canberra, 70–112, ISBN 978-0-7081-1194-9, 1978.

Candel, J. H., Makaske, B., Kijm, N., Kleinhans, M. G., Storms, J. E., and Wallinga, J.: Self-constraining of low-energy rivers explains low channel mobility and tortuous planforms, Depos. Rec., 6, 648–669, https://doi.org/10.1002/dep2.112, 2020.

Carbiener, R.: Le Grand Ried d'Alsace, Ecologie d'un paysage, Bull. Soc. Ind. Mulhouse, 1, 15–44, 1969.

Carbiener, R.: Le grand Ried central d'Alsace: ecologie et évolution d'une zone humide d'origine fluviale rhénane, Bull. Écol., 14, 249–277, 1983a.

Carbiener, R.: Brunnenwasser, Encyclopedie de l'Alsace, 2, Publitotal, Strasbourg, 891–900, 1983b.

Carbiener R. and Dillmann E.: Cas type de Rhinau-Daubensand: l'évolution du paysage rhénan dans la région de Rhinau, au coeur du secteur des Giessen, des Muhlbach et Brunnenwasser, in: Die Auen am Oberrhein/Les Zones alluviales du Rhin Supérieur, edited by: Gallusser, W. A., and Schencker, A, Birkhäuser, Switzerland, 113–136, https://doi.org/10.1007/978-3-0348-6237-0_13, 1992.

Chapkanski, S., Ertlen, D., Rambeau, C., and Schmitt, L.: Provenance discrimination of fine sediments by mid-infrared spectroscopy: Calibration and application to fluvial palaeoenvironmental reconstruction, Sedimentology, 67, 1114–1134, https://doi.org/10.1111/sed.12678, 2020.

Chardon, V., Schmitt, L., Arnaud, F., Piégay, H., and Clutier A.: Efficiency and sustainability of gravel augmentation to restore large regulated rivers: insights from three experiments on the Rhine River (France/Germany), Geomorphology, 380, 107639, https://doi.org/10.1016/j.geomorph.2021.107639, 2021.

Commission Internationale de l'Hydrologie du Bassin du Rhin: Le bassin du Rhin: monographie hydrologique, ISBN 978-90-12-01775-6, 1977.

Dambeck, R. and Thiemeyer, H.: Fluvial History of the northern Upper Rhine river (south-western Germany) during the Lateglacial and Holocene times, Quatern. Int., 93–94, 53–63, https://doi.org/10.1016/S1040-6182(02)00006-X, 2002.

Delile, H., Schmitt, L., Jacob-Rousseau, N., Grospretre, L., Privolt, G., and Preusser, F.: Headwater valley response to climate and land use changes during the Little Ice Age in the Massif Central (Yzeron basin, France), Geomorphology, 257, 179–197, https://doi.org/10.1016/j.geomorph.2016.01.010, 2016.

Erkens, G., Dambeck, R., Volleberg, K. P., Bouman, M. T. I. J., Bos, J. A. A., Cohen, K. M., Wallinga, J., and Hoek, W. Z.: Fluvial terrace formation in the northern Upper Rhine Graben during the last 20 000 years as a result of allogenic controls and autogenic evolution, Geomorphology, 103, 476–495, https://doi.org/10.1016/j.geomorph.2008.07.021, 2009.

Erkens, G., Hoffmann, T., Gerlach, R., and Klostermann J.: Complex fluvial response to Lateglacial and Holocene allogenic forcing in the Lower Rhine Valley (Germany), Quaternary Sci. Rev. 30, 611–627, https://doi.org/10.1016/j.quascirev.2010.11.019, 2011.

Ertlen, D., Schwartz, D., Trautmann, M., Webster, R., and Brunet, D.: Discriminating between organic matter in soil from grass and forest by near-infrared spectroscopy, Eur. J. Soil Sci., 61, 207–216, https://doi.org/10.1111/j.1365-2389.2009.01219.x, 2010.

Eschbach, D., Schmitt, L., Imfeld, G., May, J.-H., Payraudeau, S., Preusser, F., Trauerstein, M., and Skupinski, G.: Long-term temporal trajectories to enhance restoration efficiency and sustainability on large rivers: an interdisciplinary study, Hydrol. Earth Syst. Sci., 22, 2717–2737, https://doi.org/10.5194/hess-22-2717-2018, 2018.

Fuller, I. C., Reid, H. E., and Brierley, G. J.: Methods in geomorphology: investigating river channel form, in: Treatise on geomorphology, edited by: Shroder, J. F., Academic Press, San Diego, 73–91, https://doi.org/10.1016/B978-0-12-374739-6.00374-2, 2013.

Gabriel, G., Ellwanger, D., Hoselmann, C., Weidenfeller, M., and Wielandt-Schuster, U.: The Heidelberg basin, Upper Rhine Graben (Germany): A unique archive of Quaternary sediments in Central Europe, Quatern. Int., 292, 43–58, https://doi.org/10.1016/j.quaint.2012.10.044, 2013.

Haimberger, R., Hoppe, A., and Schäfer, A.: High-resolution seismic survey on the Rhine River in the northern Upper Rhine Graben, Int. J. Earth Sci. (Geol. Rundsch.), 94, 657–668, https://doi.org/10.1007/s00531-005-0514-z, 2005.

Haughton, P. D. W., Todd, S. P., and Morton, A.C.: Sedimentary provenance studies, Geol. Soc. London. Spec. Publ., 57, 1–11, https://doi.org/10.1144/GSL.SP.1991.057.01.01, 1991.

Hirth, C.: Eléments d'explication à la formation des Rieds ellorhénans au nord de Colmar du début du Post-glaciaire à la canalisation du Rhin au XIXè siècle, Bull. Soc. Hist. nat. Colmar, 54, 21–44, 1971.

Hoffmann, T., Lang, A., and Dikau, R.: Holocene river activity: analysing 14C-dated fluvial and colluvial sediments from Germany, Quaternary Sci. Rev., 27, 2031–2040, https://doi.org/10.1016/j.quascirev.2008.06.014, 2008.

Illies, J. H. and Greiner, G.: Rhinegraben and the Alpine system, Geol. Soc. Am. Bull., 89, 770–782, https://doi.org/10.1130/0016-7606(1978)89<770:RATAS>2.0.CO;2, 1978.

Jotheri, J., Allen, M. B., and Wilkinson, T. J.: Holocene avulsions of the Euphrates River in the Najaf area of western Mesopotamia: Impacts on human settlement patterns, Geoarchaeology, 31, 175–193, https://doi.org/10.1002/gea.21548, 2016.

Jung, J. and Schlumberger, C.: Soulèvement des alluvions du Rhin par des intrusions salines diapires de Haute-Alsace: déformation de la surface de la basse terrasse du Rhin et tectonique du bassin salifère de Haute-Alsace, Bull. du Service de la Carte géologique d'Alsace et de Lorraine, 3, 77–86, 1936.

Kaufhold, S., Hein, M., Dohrmann, R., and Ufer, K.: Quantification of the mineralogical composition of clays using FTIR spectroscopy, Vib. Spectrosc., 59, 29–39, https://doi.org/10.1016/j.vibspec.2011.12.012, 2012.

Kemp, J. and Spooner, N. A.: Evidence for regionally wet conditions before the LGM in southeast Australia: OSL ages from a large palaeochannel in the Lachlan Valley, J. Quaternary Sci., 22, 423–427, https://doi.org/10.1002/jqs.1125, 2007.

Khosravichenar, A., Fattahi, M., Amini, H., and von Suchodoletz, H.: The potential of small mountain river systems for paleoenvironmental reconstructions in drylands – An example from the Binaloud Mountains in Northeastern Iran, Geosci., 10, 448, https://doi.org/10.3390/geosciences10110448, 2020.

Kock, S., Huggenberger, P., Preusser, F., Rentzel, P., and Wetzel, A.: Formation and evolution of the Lower Terrace of the Rhine River in the area of Basel, Swiss J. Geosci., 102, 307–321, https://doi.org/10.1007/s00015-009-1325-1, 2009.

Kremer, M., Rieb, J.-P., Rebholtz, C., and Delecolle, J.-C.: Écologie des Cératopogonidés de la plaine d'Alsace – I. – Le genre Culicoides des sols humides du Ried, Ann. Parasitol. Hum. Comp., 53, 101–115, https://doi.org/10.1051/parasite/1978531101, 1978.

Lang, A., Bork, H. R., Mäckel, R., Preston, N., Wunderlich, J., and Dikau, R.: Changes in sediment flux and storage within a fluvial system: some examples from the Rhine catchment, Hydrol. Process., 17, 3321–3334, https://doi.org/10.1002/hyp.1389, 2003.

Nandini, C. V., Sanjeevi, S., and Bhaskar, A. S.: An integrated approach to map certain palaeochannels of South India using remote sensing, geophysics, and sedimentological techniques, Int. J. Remote Sens., 34, 6507–6528, https://doi.org/10.1080/01431161.2013.803629, 2013.

Nivière, B., Giamboni, M., Innocent, C., and Winter, T.: Kinematic evolution of a tectonic wedge above a flat-lying décollement: The Alpine foreland at the interface between the Jura Mountains (Northern Alps) and the Upper Rhine graben, Geology, 34, 469–472, https://doi.org/10.1130/G22334.1, 2006.

Ollive, V., Petit, C., Garcia, J. P., and Reddé, M.: Rhine flood deposits recorded in the Gallo-Roman site of Oedenburg (Haut-Rhin, France), Quatern. Int., 150, 28–40, https://doi.org/10.1016/j.quaint.2006.01.006, 2006.

Page, K., Nanson, G., and Price, D.: Chronology of Murrumbidgee River palaeochannels on the River-

ine Plain, southeastern Australia, J. Quaternary Sci., 11, 311–326, https://doi.org/10.1002/(SICI)1099-1417(199607/08)11:4<311::AID-JQS256>3.0.CO;2-1, 1996.

Plotzki, A., May, J. H., Preusser, F., Roesti, B., Denier, S., Lombardo, U., and Veit, H.: Geomorphology and evolution of the late Pleistocene to Holocene fluvial system in the south-eastern Llanos de Moxos, Bolivian Amazon, Catena, 127, 102–115, https://doi.org/10.1016/j.catena.2014.12.019, 2015.

Preusser, F.: Characterisation and evolution of the River Rhine system, Neth. J. Geosci., 87, 7–19, https://doi.org/10.1017/s0016774600024008, 2008.

Przyrowski, R. and Schäfer, A.: Quaternary fluvial basin of northern Upper Rhine Graben, Z. Dtsch. Ges. Geowiss., 166, 71–98, https://doi.org/10.1127/1860-1804/2014/0080, 2015.

Resmi, M. R., Achyuthan, H., and Jaiswal, M. K.: Middle to late Holocene paleochannels and migration of the Palar River, Tamil Nadu: Implications of neotectonic activity, Quatern. Int., 443, 211–222, https://doi.org/10.1016/j.quaint.2016.05.002, 2017.

Rossetti, D. F. and Góes, A. M.: Late Quaternary drainage dynamics in northern Brazil based on the study of a large paleochannel from southwestern Marajó Island, An. Acad. Bras. Cienc., 80, 579–593, https://doi.org/10.1590/s0001-37652008000300017, 2008.

Schirmer, W., Bos, J. A., Dambeck, R., Hinderer, M., Preston, N., Schulte, A., Schwalb, A., and Wessels, M.: Holocene fluviatile processes and valley history in the River Rhine catchment, Erdkunde, 59, 199–215, https://doi.org/10.3112/erdkunde.2005.03.03, 2005.

Schmitt, L.: Typologie hydro-géomorphologique fonctionnelle de cours d'eau: recherche méthodologique appliquée aux systèmes fluviaux d'Alsace, PhD thesis, University of Strasbourg, France, 348 pp., unpublished, 2001.

Schmitt, L.: Dynamiques fluviales et gestion environnementale durable des hydrosystèmes. Application à une grande plaine alluviale (Rhin-Ill, Alsace) et à hydrosystème périurbain (Yzeron, Ouest Lyonnais), Habilitation thesis, Lumière University Lyon 2, France, 296 pp., unpublished, 2010.

Schmitt, L., Tremolieres, M., Nobelis, P., and Maire, G.: Complémentarité entre typologies hydro-géomorphologique et biologique de rivières dans l'hydrosystème fluvial ello-rhénan français, in: Protéger, restaurer et gérer les zones alluviales. Pourquoi et comment?/Floodplain protection, restoration, management. Why and How?, edited by: Tremolieres, M., Schnitzler, A., and Silan, P, Editions TEC & DOC, Lavoisier, Paris, 123–136, ISBN 978-2-7430-1011-9, 2007.

Schmitt, L., Lafont, M., Tremolieres, M., Jezequel, C., Vivier, A., Breil, P., Namour, P., Valin, K., and Valette, L.: Using hydro-geomorphological typologies in functional ecology: preliminary results in contrasted hydrosystems, Phys. Chem. Earth, 36, 539–548, https://doi.org/10.1016/j.pce.2009.11.011, 2011.

Schmitt, L., Houssier, J., Martin, B., Beiner, M., Skupinski, G., Boës, E., Schwartz, D., Ertlen, D., Argant, J., Gebhardt, A., Schneider, N., Lasserre, M., Trintafillidis, G., and Ollive, V.: Paléo-dynamique fluviale holocène dans le compartiment sud-occidental du fossé rhénan (France), Rev. Archéologique l'Est, 42, 15–33, 2016.

Schmitt, L., Beisel, J. N., Preusser, F., de Jong, C., Wantzen, K. M., Chardon, V., Staentzel, C., Eschbach, D., Damm, C., Rixhon, G., Salomon, F., Glaser, R., Himmelsbach, I., Meinard, Y., Dumont, S., Hardion, L., Jérôme, H., Rambeau, C., Chapkanski, S., and Brackhane, S.: Sustainable management of the Upper Rhine River and its alluvial plain: Lessons from interdisciplinary research in France and Germany, in: Sustainability research in the Upper Rhine region, concepts and case studies, edited by: Hamman, P. and Vuilleumier, S., Presses Universitaires de Strasbourg, Strasbourg, 201–226, ISBN 978-2-86820-549-0, 2019.

Scorpio, V., Surian, N., Cucato, M., Dai Prá, E., Zolezzi, G., and Comiti, F.: Channel changes of the Adige River (Eastern Italian Alps) over the last 1000 years and identification of the historical fluvial corridor, J. Maps, 14, 680–691, https://doi.org/10.1080/17445647.2018.1531074, 2018.

Simler, L., Valentin, L., and Duprat A.: La nappe phréatique de la plaine du Rhin en Alsace, Sci. Geol., 60, 1–266, 1979.

Striedter, K.: Holozäne Talgeschichte im Unterelsass, PhD thesis, University of Düsseldorf, Germany, 235 pp., unpublished, 1988.

Sylvia, D. A. and Galloway, W. E.: Morphology and stratigraphy of the late Quaternary lower Brazos valley: Implications for paleoclimate, discharge and sediment delivery, Sediment. Geol., 190, 159–175, https://doi.org/10.1016/j.sedgeo.2006.05.023, 2006.

Toonen, W. H., Kleinhans, M. G., and Cohen, K. M.: Sedimentary architecture of abandoned channel fills, Earth Surf. Proc. Land., 37, 459–472, https://doi.org/10.1002/esp.3189, 2012.

Trémolières, M., Eglin, I., Roeck, U., and Carbiener, R.: The exchange process between river and groundwater on the Central Alsace floodplain (Eastern France), Hydrobiologia, 254, 133–148, https://doi.org/10.1007/bf00014108, 1993.

Van Raden, U. J., Colombaroli, D., Gillia, A., Schwander, J., Bernasconi, S.M., van Leeuwen, J., Leuenberger, M., and Eicher, U.: High-resolution late-glacial chronology for the Gerzensee lake record (Switzerland): δ^{18}O correlation between a Gerzensee-stack and NGRIP, Palaeogeogr. Palaeoclimatol. Palaeoecol, 391, 13–24, https://doi.org/10.1016/j.palaeo.2012.05.017, 2013.

Vogt, H.: Le relief en Alsace. Etude géomorphologique du rebord sud-occidental du fossé rhénan, Oberlin, Strasbourg, 239 pp., ISBN 9782853691284, 1992.

von Suchodoletz, H., Pohle, M., Khosravichenar, A., Ulrich, M., Hein, M., Tinapp, C., Schultz, J., Ballasus, H., Veit, U., Ettel, P., Werther, L., Zielhofer, C., and Werban, U.: The fluvial architecture of buried floodplain sediments of the Weiße Elster River (Germany) revealed by a novel method combination of drill cores with two-dimensional and spatially resolved geophysical measurements, Earth Surf. Proc. Land., 47, 955–976, https://doi.org/10.1002/esp.5296, 2022.

Walser, E.: Le bassin du Rhin à l'amont de Bâle et l'influence des lacs sur le régime du fleuve, Houille Blanche, 45, 115–124, https://doi.org/10.1051/lhb/1959028, 1959.

Wantzen, K. M., Uehlinger, U., Van der Velde, G., Leuven, R. S. E. W., Schmitt, L., and Beisel, J. N.: The Rhine River basin, in: Rivers of Europe, 2nd edn., edited by: Tockner, K., Zarfl, C., and Robinson, C. T., Academic Press, London, 331–389, ISBN 9780081026137, 2021.

E&G Quaternary Sci. J., 71, 213–226, 2022
https://doi.org/10.5194/egqsj-71-213-2022

Open Access E&G Quaternary Science Journal

Research article

Fluvial activity of the late-glacial to Holocene "Bergstraßenneckar" in the Upper Rhine Graben near Heidelberg, Germany – first results

Max Engel[1], **Felix Henselowsky**[1,2], **Fabian Roth**[1], **Annette Kadereit**[1], **Manuel Herzog**[1], **Stefan Hecht**[1], **Susanne Lindauer**[3], **Olaf Bubenzer**[1], **and Gerd Schukraft**[1,†]

[1]Institute of Geography, Heidelberg University, Im Neuenheimer Feld 348, 69120 Heidelberg, Germany
[2]Institute of Geography, Johannes Gutenberg University Mainz, Johann-Joachim-Becher-Weg 21, 55099 Mainz, Germany
[3]Curt-Engelhorn-Centre Archaeometry, D6, 3, 68159 Mannheim, Germany
†deceased, April 2020

Correspondence: Max Engel (max.engel@uni-heidelberg.de) and Felix Henselowsky (felix.henselowsky@uni-mainz.de)

Relevant dates: Received: 9 February 2022 – Revised: 13 July 2022 – Accepted: 20 July 2022 – Published: 8 September 2022

How to cite: Engel, M., Henselowsky, F., Roth, F., Kadereit, A., Herzog, M., Hecht, S., Lindauer, S., Bubenzer, O., and Schukraft, G.: Fluvial activity of the late-glacial to Holocene "Bergstraßenneckar" in the Upper Rhine Graben near Heidelberg, Germany – first results, E&G Quaternary Sci. J., 71, 213–226, https://doi.org/10.5194/egqsj-71-213-2022, 2022.

Abstract: The term "Bergstraßenneckar" (BSN) refers to an abandoned course of the river Neckar. It flowed in a northern direction east of the river Rhine in the eastern part of the northern Upper Rhine Graben in southwestern Germany. The former meandering course merged with the Rhine ca. 50 km further north of the site of the present-day confluence near Mannheim. The palaeo-channels are still traceable by their depressional topography, in satellite images and by the curved boundaries of adjacent settlements and land parcels. In the plan view, satellite and aerial images reveal a succession of meander bends, with older bends being cut off from younger channels. Based on stratigraphic investigations of the channel infill in the northern part of the BSN, fluvial activity is assumed from ca. 14 500 years ago until the onset of the Holocene. We present results of the first stratigraphic investigations at two sites in the southern part of the BSN near Heidelberg (Rindlache, Schäffertwiesen), together with results from granulometric, carbonate and organic content analyses, as well as electrical resistivity tomography (ERT) measurements. The data clearly show a change from high-energy fluvial bedload (sand, gravel) to low-energy fluvio-limnic suspended load (organoclastic and calcareous mud) and to peat formation. Radiocarbon dating indicates a time lag of ca. 1500 years between the cut-off meander site (Schäffertwiesen) and the younger site (Rindlache) that was possibly still active until the present-day confluence near Mannheim was established and the BSN eventually became abandoned. Our preliminary data conform with the pedo-sedimentary evidence from the northern BSN, but slight differences in the stratigraphic pattern of the youngest channels are identified: whilst for the younger channel sections of the northern BSN the channel-bottom facies (sand, gravel) is directly overlain by peat, the channel at Rindlache shows substantial intervening mud deposition, which is interpreted as suspension load from flooding by the new Neckar channel nearby. The study shows that more

chronostratigraphic data from channel sections of the southern BSN are needed to better constrain the timing of the fluvial activity and to decipher the reasons for the abandonment of the BSN. These data are also necessary to better understand the pattern of temporary reactivation of the BSN channels across the Holocene and their usage by humans, which can be deduced from historical sources and archaeological data.

Kurzfassung:

Mit dem Begriff Bergstraßenneckar (BSN) wird der heute inaktive mäandrierende Lauf des Neckars bezeichnet, der im Spätglazial dem östlichen Rand des nördlichen Oberrheingrabens folgte. Von dort floss der BSN dem Rhein bei Trebur zu, bevor er sein Mündungsgebiet um ca. 50 km nach Süden in den Raum Mannheim verlegte. Die morphologischen Strukturen der verlandeten Neckarbetten sind in Satellitenbildern, im Mikrorelief und am Verlauf von Flurgrenzen erkennbar. Auf Basis von stratigraphischen Untersuchungen an Rinnenfüllungen des nördlichen BSN wird die Aktivität dieses Flusslaufs von ca. 14 500 Jahren vor heute bis zum Beginn des Holozäns angenommen. Hier präsentieren wir die ersten stratigraphischen Untersuchungen zweier Lokalitäten im südlichen Bereich des BSN (Rindlache, Schäffertwiesen) gemeinsam mit granulometrischen, Organik-, Karbonat- und widerstandsgeoelektrischen Daten. Die Ergebnisse reflektieren deutlich den Übergang von einer aktiv durchflossenen Rinne (Sand- und Kiesfazies) hin zu Verlandung unter fluvio-limnischen Bedingungen (organoklastische und kalkreiche Feinkornablagerungen) mit abschließendem Torfwachstum. Die bislang verfügbaren ^{14}C-Daten deuten auf einen zeitlichen Versatz der Aktivität von ca. 1500 Jahren zwischen der morphologisch älteren Mäanderschlinge (Schäffertwiesen) und der jüngeren Lokalität (Rindlache) hin, die möglicherweise noch zu der Zeit die Hauptrinne bildete, als die Mündung nach Süden in den Raum Mannheim verlagert wurde. Die hier präsentierten vorläufigen Daten sind mit der bestehenden Chronologie am nördlichen BSN vereinbar, wenngleich auch Unterschiede in der stratigraphischen Abfolge der Verlandungssedimente in den zuletzt aktiven Rinnen identifiziert werden: Während im Norden die fluviale Sand- und Kiesfazies unmittelbar von Niedermoortorf überlagert wird, sind in den jüngeren Rinnen im Süden Feinkornablagerungen zwischengeschaltet, die als Suspensionsfracht periodischer Überflutungen möglicherweise ausgehend vom nur wenige Kilometer entfernten neuen Neckarlauf interpretiert werden. Die Ergebnisse verdeutlichen, dass weitere chrono-stratigraphische Untersuchungen an Rinnenstandorten des südlichen BSN erforderlich sind, um den Zeitrahmen und die Abfolge der fluvialen Aktivität besser eingrenzen und die Ursachen für die Laufverlagerung besser definieren zu können. Zudem ergäben sich so detailliertere Hinweise auf die temporäre Reaktivierung bestimmter Abschnitte des BSN über das gesamte Holozän hinweg sowie auf deren Nutzung durch den Menschen, die in historischen Quellen und durch archäologische Daten belegt ist.

1 Introduction

The term "Bergstraßenneckar" (BSN) refers to an abandoned course of the river Neckar in the eastern part of the northern Upper Rhine Graben in southwestern Germany. Whilst the modern river Neckar flows in a western direction to connect with the river Rhine at Mannheim after leaving the Odenwald Mountains at Heidelberg, the BSN flowed from Heidelberg almost 50 km in a northern direction to join the river Rhine near Trebur (Fig. 1a). The palaeo-meanders of the BSN run parallel to the foothill zone ("Bergstraße") connecting the Odenwald Mountains and the Upper Rhine Graben (Mangold, 1892; Bernhard and Hickethier, 1966; Dambeck, 2005; Dambeck and Bos, 2002; Dambeck and Thiemeyer, 2002; Beckenbach, 2016). The palaeo-meanders can be identified by their sinuous courses, lowered surface and the typically curved boundaries of adjacent settlements and roads, as well as cadastral boundaries. Satellite and aerial images reveal a relative chronology of younger and older meander bends, with younger bends truncating the older bends and older bends being cut off from younger channel sections. Since early modern times, it has been contentious whether natural or anthropogenic processes caused the Neckar to abandon the BSN riverbed. The hypothesis of a man-made diversion of the lower Neckar from a northern flow direction (i.e., the BSN) to a western direction towards Mannheim (i.e., the modern Neckar) in the late Middle Ages (after 1354 CE) as a flood protection measure (e.g. Saur, 1593; Winkelmann, 1697; Mone, 1826) was later rejected (Mangold, 1892; Barsch and Mäusbacher, 1979, 1988). Some palaeo-channel sections of the BSN may have still served as waterways in historical times, particularly in the Roman period (Eckoldt, 1985; Wirth, 2011). Systematic chronolog-

ical and sedimentological investigations from the northern Upper Rhine Graben indicate drainage of the lower Neckar catchment through the BSN during a short period between ca. 14 500 years ago and the onset of the Holocene (see Große-Brauckmann et al., 1990; Dambeck, 2005; Dambeck and Thiemeyer, 2002; Bos et al., 2008, 2012). This phase of fluvial activity encompasses the formation and abandonment of different meanders, a relative chronology of which has been established by Dambeck (2005). Here, we aim to generate an initial chronostratigraphy of palaeo-meanders in the southern part of the BSN near Heidelberg (hereafter: southern BSN). We compare our results to meander activity phases as identified for the northern BSN by Dambeck (2005), Dambeck and Bos (2002), and Dambeck and Thiemeyer (2002) to establish working hypotheses for detailed investigations on the southern BSN in the future.

2 Regional setting

Two palaeo-meanders were investigated at the field sites Rindlache (RL) and Schäffertwiesen (SW). The sites are located 1 km apart, ca. 15 km northwest of Heidelberg and ca. 10 km northeast of Mannheim, at the border between the German federal states of Baden-Württemberg and Hesse near Viernheim (Fig. 1b). The study area is part of the eastern Upper Rhine Graben and located between the river Rhine and the eastern graben shoulder, formed by the southern Odenwald with a Palaeozoic basement covered by (among others) Triassic Buntsandstein sandstone (Barsch and Mäusbacher, 1979, 1988; Nickel and Fettel, 1979; Eisbacher and Fielitz, 2010). Quaternary subsidence rates of the eastern Upper Rhine Graben near Heidelberg of $\sim 0.2\,\mathrm{mm\,yr^{-1}}$ are an order of magnitude higher compared to other parts of the graben and lead to high sedimentation rates and a thick late Quaternary infill (Peters and van Balen, 2007; Buness et al., 2009; Gabriel et al., 2013).

The study sites are located north of the alluvial fan of the Neckar, which forms where the river leaves the Odenwald and enters the surface of the last-glacial Lower Terrace inside the Upper Rhine Graben (Fig. 1b) (Barsch and Mäusbacher, 1979, 1988). In the northernmost part of the Upper Rhine Graben, the Lower Terrace is categorised into an upper Lower Terrace (t6, early to middle Würm) underlying the fluvial landscape of the northern BSN and a lower Lower Terrace (t7, late Würm) underlying the Rhine and its floodplain (Scheer, 1978; Dambeck, 2005; Erkens et al., 2009). In the area of the southern BSN no such distinction is made (Schottler, 1906; Kupfahl et al., 1972; Holzhauer, 2013). The Lower Terrace around the study sites shows varying ratios of sand and gravel, has an irregular surface, is cut by BSN channels, and is overlain by up to several metres of BSN-related sand- and silt-dominated flood deposits (Barsch and Mäusbacher, 1979; Löscher, 2007). During the late Pleistocene–Holocene transition, dunes formed on top of the silt- and sand-covered Lower Terrace (Löscher, 2007; Löscher et al., 1989) as elements of a larger regional dune system covering substantial parts of the northern Upper Rhine Graben (Dambeck, 2005; Holzhauer, 2013; Holzhauer et al., 2017; Pflanz et al., 2022).

The meandering course of the former BSN is reflected in the spatial distribution of peat deposits in Fig. 1a corresponding to morphological depressions of a depth of $\sim$ 2–4 m (Fig. 1b) (Barsch and Mäusbacher, 1979). The two study sites are situated in the most prominent palaeochannels of the southern BSN (Fig. 1b) with distinct channel morphologies of inwardly convex and outwardly concave banks, and with diameters (half-meander path lengths sensu Howard and Hemberger, 1991) of 800–900 m. The two sites have been chosen as representative examples of (1) the presumably youngest course of the BSN (meander Rindlache) and (2) an earlier fluvial phase (cut-off meander Schäffertwiesen) (see maps in Mangold, 1892; Barsch and Mäusbacher, 1979) (Fig. 1b). The historical field names indicate that the sites were formerly used for pasture (*Rind* = cattle; *Wiese* = meadow) likely due to waterlogging (*Lache* = marsh/swamp) caused by a high groundwater table. The formerly high groundwater table in the Upper Rhine Graben has lowered significantly due to major regulation measures on the Neckar and Rhine since the early 19th century and subsequent river incision. More recently, the intensified exploitation of drinking and irrigation water added to groundwater level fall (see Barsch and Mäusbacher, 1979; Dister et al., 1990).

3 Methods

The stratigraphy at both sites was studied using 2-D electrical resistivity tomography (ERT) and sediment cores. ERT profiles were measured using a GeoTom MK1E100 device with Schlumberger configuration, 100 electrodes and 1 m spacing, as in Kneisel (2003). The composite ERT profile 6–7–8–11 at Rindlache consists of four separate profiles integrated with an overlap of 25 m (profiles 6–8) and 66 m (profiles 8 and 11), respectively. ERT profile 1–2 (112.5 m long) at Schäffertwiesen combines two separate profiles overlapping for 37.5 m. Post-processing of ERT data comprises the calculation of standard inversions without filtering using Res2Dinv software. Erroneous data points, e.g. resulting from disconnected electrodes during the measurement, were removed from the raw data prior to data modelling.

Along the ERT profiles, sediment cores were taken using a vibracorer and two different stainless-steel sampling tubes (Table S1 in the Supplement): (1) open percussion gouges (ø 6 cm) (Figs. S1, S2) and (2) closed percussion gouges equipped with PVC liner tubes (ø 5 cm) (Figs. S3–S7). Sediment cores taken in the open gouges were documented and sampled in the field according to Ad-hoc-AG Boden (2005) and the Munsell Soil Color Charts (Munsell Color Labo-

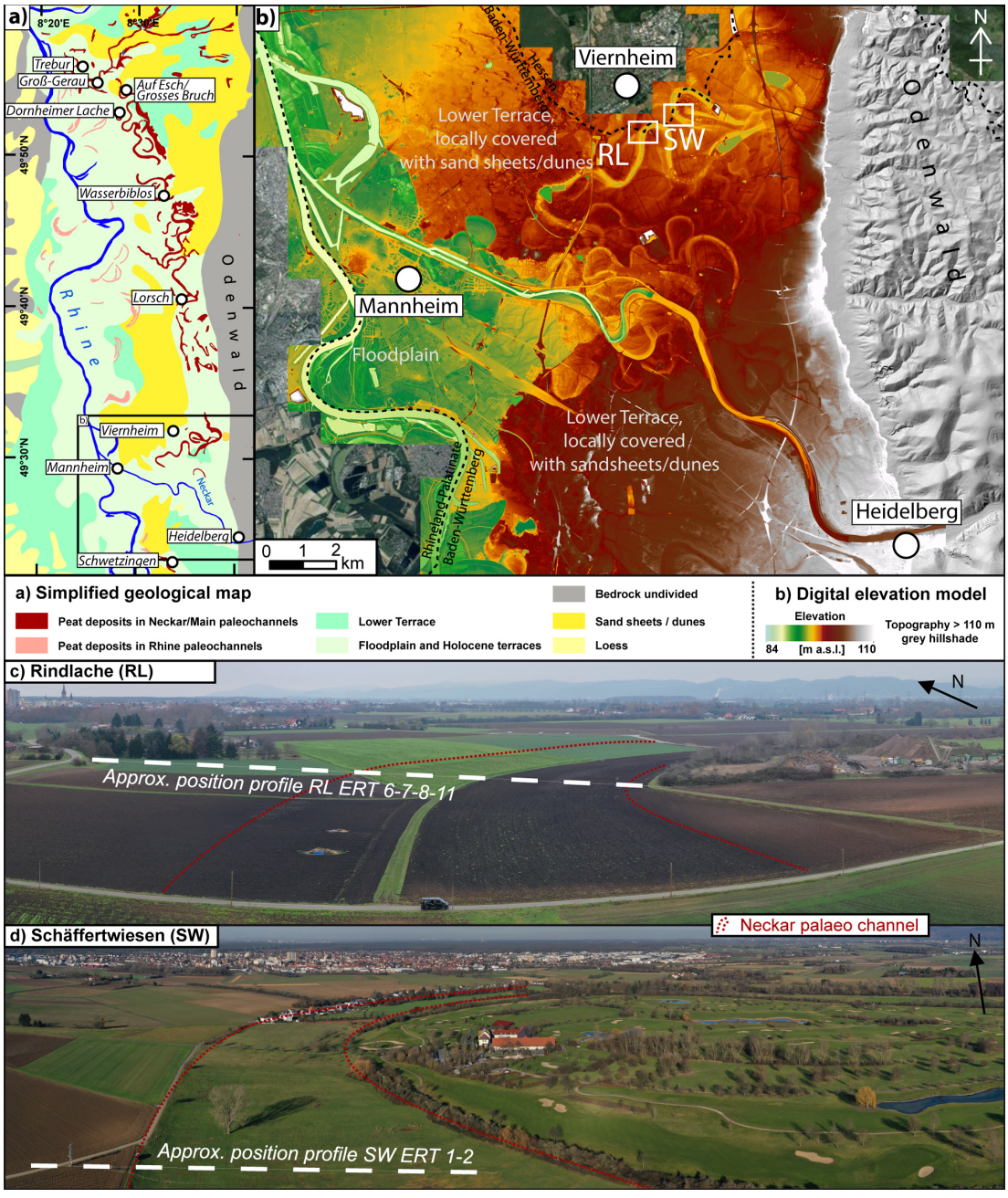

Figure 1. Overview of the study area. **(a)** Simplified geological map of the northern Upper Rhine Graben based on the Geological Map of Germany 1 : 1 000 000 (GK1000) and, for the peat deposits, the General Geological Map of Germany 1 : 200 000 (GUEK200), sheets CC 6310 Frankfurt/Main – West and CC 7110 Mannheim. Data source: Bundesanstalt für Geowissenschaften und Rohstoffe (BGR). **(b)** High-resolution digital elevation model emphasising relief variation at 84–110 m NHN to highlight the active and abandoned fluvial channels of the BSN between Heidelberg and Mannheim. RL = Rindlache; SW = Schäffertwiesen. Data source: DGM1 of the Federal State of Baden-Württemberg provided by Landesamt für Geologie, Rohstoffe und Bergbau (LGBR) and established in 2000–2005. **(c)** Drone-based photograph of the Rindlache site (9 November 2020). **(d)** Drone-based photograph of the Schäffertwiesen site (17 January 2020).

ratory, 2000) (Table S2). The upper part of each core segment is prone to disturbances from material collapsing inside the borehole or from the recovery process. These disturbances were identified based on comparison with the lowermost part of the overlying core segment and removed from the record. The PVC liners were opened and the sediment documented (Munsell Color Laboratory, 2000; Ad-hoc-AG Boden, 2005) and sampled in the Laboratory for Geomorphology and Geoecology, Institute of Geography, Heidelberg University (Table S3). One additional core (RL01) was

taken using an Edelman-type corer. At each site one core was analysed in more detail in the laboratory to support facies interpretation. All depths reported in the result section follow the original documentation and correspond to the core photographs in Figs. S1–S7. Additionally, adjusted depths of unit boundaries of the uppermost compressed metre are given in Tables S2 and S3. Samples were dried, carefully pestled by hand and sieved for the < 2 mm fraction. Grain-size distributions of the < 2 mm fraction were measured using a laser particle sizer (Fritsch Analysette P22) with a measurable range of 0.8–2000 µm at the Laboratory of Sedimentology, Institute of Geosciences, Heidelberg University. All samples were pre-treated with 10 mL H_2O_2 (30 %) to remove organic carbon and $Na_4P_2O_7$ (55.7 g L^{-1}) for aggregate dispersion. Univariate statistical measures were calculated using the Excel sheet GRADISTAT v9.1 (Blott and Pye, 2001). Organic matter was determined by loss-on-ignition (LOI) following a protocol slightly modified from Heiri et al. (2001). Samples of 3–5 g were combusted at 550 °C for 4 h in a muffle furnace. The carbonate content was measured using the Scheibler method according to DIN ISO 10693.

Four samples of autochthonous peat were dated by ^{14}C accelerator mass spectrometry (AMS) at the Curt-Engelhorn-Centre Archaeometry in Mannheim, Germany. The absence of allochthonous root material was verified under a binocular microscope prior to sample submission to the dating laboratory. All samples were pre-treated with HCl, NaOH and HCl according to the acid–base–acid (ABA) method, during which the "base" step eliminates ex situ humic acids (Wild et al., 2013). The non-dissolved residual was then used for dating. The analysis was carried out on a MICADAS type AMS system (Kromer et al., 2013). Results were calibrated using CALIB 8.2 (Stuiver et al., 2022) and the IntCal20 dataset (Reimer et al., 2020). For age interpretation, the 2σ error was considered (Table S4). The reference date for all calibrated ^{14}C data is 1950 CE.

The positions of all sediment cores and ERT electrodes, as well as topographic corrections, were determined using a Leica GS16 differential global navigation satellite system (DGNSS) and the satellite positioning service of the Federal State of Baden-Württemberg (SAPOS BW) in real-time kinematic (RTK) mode (lateral error: 1–2 cm; vertical error: 2–3 cm). Elevations are given in metres above NHN (*Normalhöhen-Null*: official vertical datum used in Germany signifying mean sea level in reference to *Normaal Amsterdams Peil* or Amsterdam Ordnance Datum) within the DHHN2016 (*Deutsches Haupthöhennetz*: official German height reference system, newly levelled and introduced in 2016–2017; AdV, 2018).

4 Results

4.1 The Rindlache site

4.1.1 Stratigraphic record

Sediment core RL09 represents the stratigraphy of the BSN at Rindlache and was taken on a harvested crop field in the central part of the assumed palaeo-channel (Fig. 1b). The bottom unit of 5.45–5.20 m b.s. (below surface) is dominated by sand of changing colour and shows only minor amounts of silt and fine gravel (Figs. 2, S2). Between 5.20 and 4.50 m b.s., it is grain-supported, and coarser components of up to 5 cm (long axis) contribute up to > 50 %. The sorting varies. The LOI values are very low, and the carbonate content is around 8 %. The section 4.50–2.30 m b.s. shows medium to coarse sand with lower amounts of coarser components and with improved sorting. The organic content is equally low, and the carbonate content decreases to 5 %–7 %. This unit is overlain by light greyish brown mud with upward-increasing carbonate content, culminating in a high value of > 90 % in the uppermost part at 1.50 m b.s. Sand or coarser components are absent, whereas reddish brown vertical root casts are visible. Unfortunately, the lower boundary could not be identified due to core loss (2.30–2.00 m b.s.); however, it is abrupt in parallel core Gerd 1b (Fig. S3). The LOI values up to 1.36 m b.s. increase slightly to levels of 3 %–4 %. Above a sharp contact, black peat was found, most of which was lost during the core recovery (core loss: 1.30–1.00 m b.s.). The LOI values reach up to > 40 %. In the parallel core Gerd 1b, peat from this unit at 1.05 m b.s. was dated to 6539–6402 cal yr BP (MAMS 43 986). The peat is overlain by dark grey, well-sorted organic-rich mud (0.92–0.80 m b.s.) showing LOI values of 13 %, a very low carbonate content and many fine roots. From 0.80 to 0.57 m b.s., the grey mud contains a few terrestrial gastropod shells and shell fragments, as well as some fine vertical roots. The carbonate content is slightly increased, whereas the LOI value is lower. Above this unit, the clayey silt has a light yellowish-brown colour, still containing gastropod shell fragments exhibited as higher carbonate content. The uppermost unit (0.46–0.15 m b.s.; for decompacted values see Table S3) is silt-dominated with increased LOI values representing the anthropogenically turbated plough horizon.

4.1.2 Electrical resistivity tomography (ERT)

The ERT profile 6–7–8–11 runs perpendicular to the BSN channel, indicated by a surface depression (Fig. 2a, c). It includes the flanks on both sides and intersects with core RL09 at 183 m horizontal distance (h.d.). In the northwest, the ERT profile starts at the foot of a late Pleistocene dune (Bettenberg, Fig. 2c; mapped in Barsch and Mäusbacher, 1979) at ca. 102 m NHN, running down a slightly concave slope with a small terrace bordering the outer bank at approximately 75–95 m h.d. It reaches the lowest elevations of the palaeo-

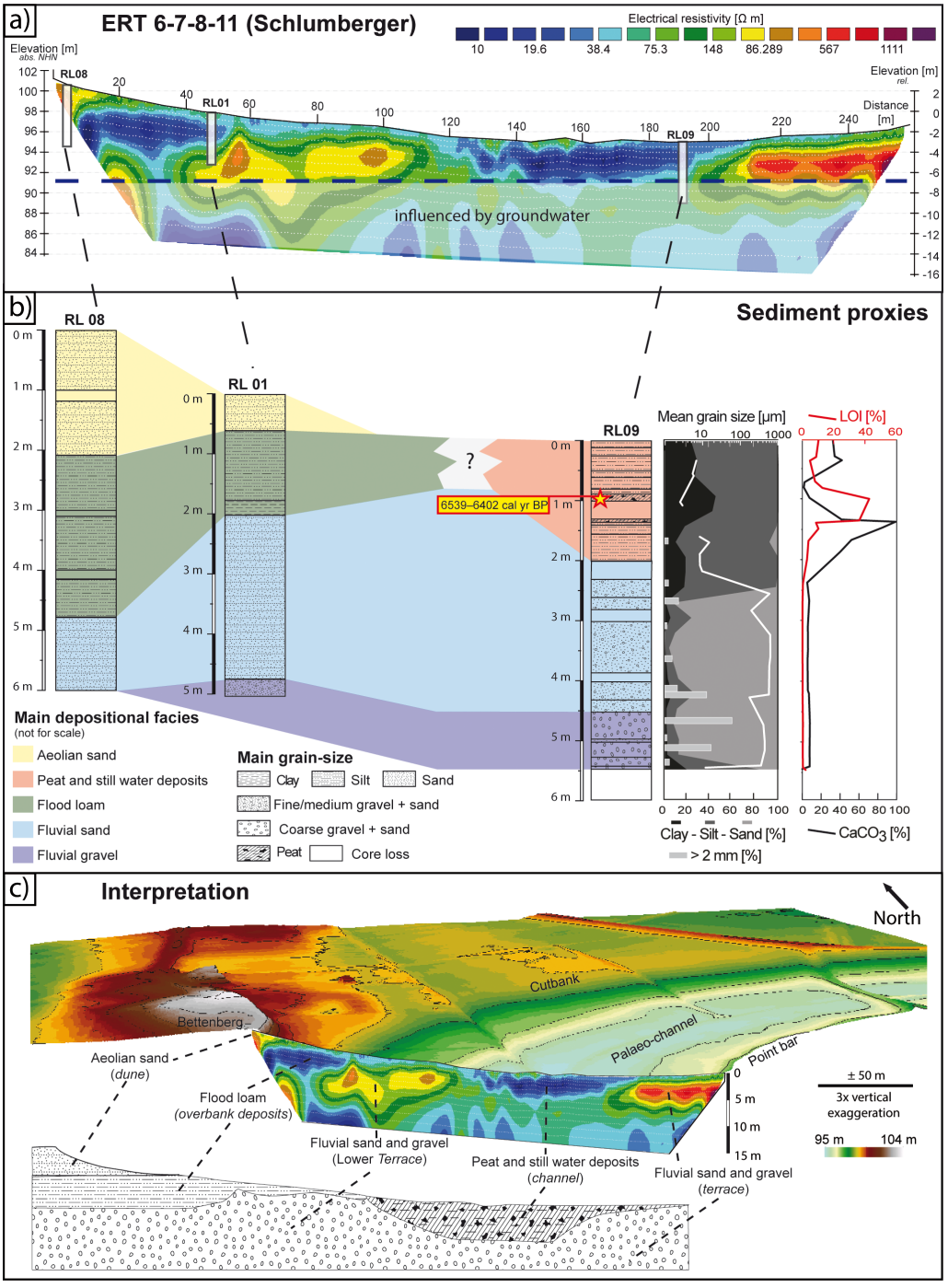

Figure 2. BSN meander at Rindlache. **(a)** Transect ERT 6–7–8–11 crossing the palaeo-river channel and showing the distribution of fine-grained deposits in blue (low resistivity values) and coarse-grained deposits in green, yellow, brown and red (intermediate to high resistivity values). **(b)** Synopsis of sediment cores RL08, RL01 and RL09 with tentative facies interpretation. For RL09, grain-size distributions, mean grain size, LOI values and $CaCO_3$ content are displayed. **(c)** Oblique view of the BSN meander in combination with the transect ERT 6–7–8–11 and tentative facies interpretation. A legend for the bottom drawing is provided in panel **(b)**. Data source: DGM1 of the Federal State of Baden-Württemberg provided by LGBR and established in 2000–2005.

meander channel at ca. 95 m NHN (ca. 125 to 210 m h.d.) and terminates at the inner bank of the palaeo-meander. The root mean square error (RMSE) is 4.1 % after three iterations of data modelling. The maximum difference in elevation across the entire profile is 6.5 m. The measured resistivity ranges between ∼ 10 and ∼ 1100 Ωm, and a depth of ca. 20 m b.s. was reached (Fig. 2a). The central channel between 125 and 210 m h.d. shows the lowest resistivity in the uppermost 4–6 m. This is in strong contrast to values which are an order of a magnitude higher at the southeastern end of the ERT profile between 210 and 260 m h.d. The slope at the foot of the Bettenberg dune also shows higher resistivities of 200–500 Ωm with a slightly thicker wedge of low-resistivity materials on top. Between 10 and 55 m h.d. this pattern is reversed, with ca. 1 m of medium resistivities (50–100 Ωm) at the top above very low resistivities, similar to the palaeo-meander channel infill.

4.2 The Schäffertwiesen site

4.2.1 Stratigraphic record

The sediment cores from Schäffertwiesen were taken along an ERT profile oriented perpendicular to the meander channel including the outer bank and a part of the channel (Figs. 1b, 3b, c). Sediment core SW01 was taken on the slope of the outer bank and reaches a depth of 4 m b.s. (Fig. S4). The lower part from 4.00 m to 1.74 m b.s. is characterised by a medium to coarse sand matrix and varying amounts of well-rounded gravel components, the latter mostly below 2.68 m b.s. This lowermost section is clast-supported between 3.45 m and 3.00 m b.s. (mostly limestone of Middle Triassic Muschelkalk, Upper Jurassic Weißjurakalk and red sandstone of Lower to Middle Triassic Buntsandstein, as well as other limestone and quartzite varieties). It shows increased carbonate content of up to 10 % and very low LOI values (< 0.3 %). Between 2.75 m and 2.40 m b.s. some finer and darker laminae occur. From 2.40 m to 2.00 m b.s., the core is disturbed by collapsed material. A sharp boundary separates the sand to gravel deposits from sandy to clayey mud (1.74–0.84 m b.s.), where LOI values increase to up to 6 %, and carbonate content reaches up to 25 %. A thin sand layer resembling the bottom facies is intercalated at 1.61–1.57 m b.s. Plant remains from a depth of 1.67 m b.s. were dated to 11 258–11 195 cal yr BP (MAMS 46037). The carbonate-rich mud is overlain by peat (0.84–0.59 m b.s.) with LOI values of up to 57 % and a very low carbonate content of < 1 %. Peat-derived ^{14}C data range from 11 079–10 722 cal yr BP (0.80 m b.s., MAMS 46036) to 7920–7701 cal yr BP (0.60 m b.s., MAMS 46035). This peat section is separated from the organic-rich topsoil (0.28–0.11 m b.s.; LOI values up to 24 %) by a brownish grey sandy mud section.

The coarse sand and gravel unit was found in the basal parts of all cores from Schäffertwiesen, where it varies in thickness (Fig. 3b). Its sharp upper boundary rises from 93.11 m NHN in the west (SW03) to 93.72 m b.s. (SW01), 94.22 m b.s. (SW04) and 96.17 m b.s. (SW02) in the east. The overlying poorly sorted sandy mud from SW01 (1.74–0.84 m b.s.) was not found in SW02 and SW04 but can be correlated with a much thicker occurrence in the western part of the profile (SW03; 4.45–0.55 m b.s.). The peat, however, is only present in SW04, close to the top of the sequence, in similar thickness as observed in SW01.

4.2.2 Electrical resistivity tomography (ERT)

The stratigraphic correlations between the cores are reflected by the ERT profile 1–2 at Schäffertwiesen (Fig. 3a). It has a length of 112.5 m and an RMS error of 3.9 % after three iterations of data modelling. Resistivity values are in the same range as in ERT profile 6–7–8–11 at Rindlache. From its southwestern end, the profile traverses over a flat terrace for ca. 30 m at ca. 98 m NHN before following a concave slope down to ca. 95.5 m NHN in the lowest part of the profile, which is also where core SW01 was taken. Between 45 m h.d. and the northeastern end, the profile gradually rises in the form of a slightly convex slope to ca. 96.5 m NHN. The flat part of the profile in the southwest, represented by core SW03, shows very low resistivity values (10–40 Ωm) correlating with the sandy mud facies. Here, resistivity only increases below ca. 5 m b.s., where the sand and gravel deposits were encountered in SW03. Likewise, in the topographically lowest part of the profile, corresponding to SW01, the basal sand and gravel deposits are reflected by medium resistivity values of around 80 Ωm, compared to 20–50 Ωm in the sandy mud and peat of the uppermost 1.70 m of the sequence. In the northeastern part of the profile, medium to high resistivity values reach close to the surface, following the rising boundary between the sand and gravel unit and the peat.

5 Discussion

5.1 Fluvial activity as reconstructed from facies patterns

The sand and gravel deposits found in the basal part of all cores from both palaeo-meander sites consist of varying ratios of predominantly medium to coarse sand and rounded to well-rounded gravel components. They represent the bedload of the BSN deposited at the bottom of the formerly active meander channel. Primary deposition of the material in pre-late-glacial times, perhaps in a braided system in Pleniglacial times of the last-glacial period, and subsequent reworking of these deposits in late-glacial times by a single meandering channel is plausible. As the channels are incised into the Lower Terrace of the Rhine, it is possible that Rhine deposits were reactivated by the BSN. Although a quantitative petrographic analysis to discriminate between Rhine and Neckar deposits is still pending, the visual inspection of basal gravel components in both master cores RL09 and SW01 already shows a dominance of Muschelkalk, Weißjura and other

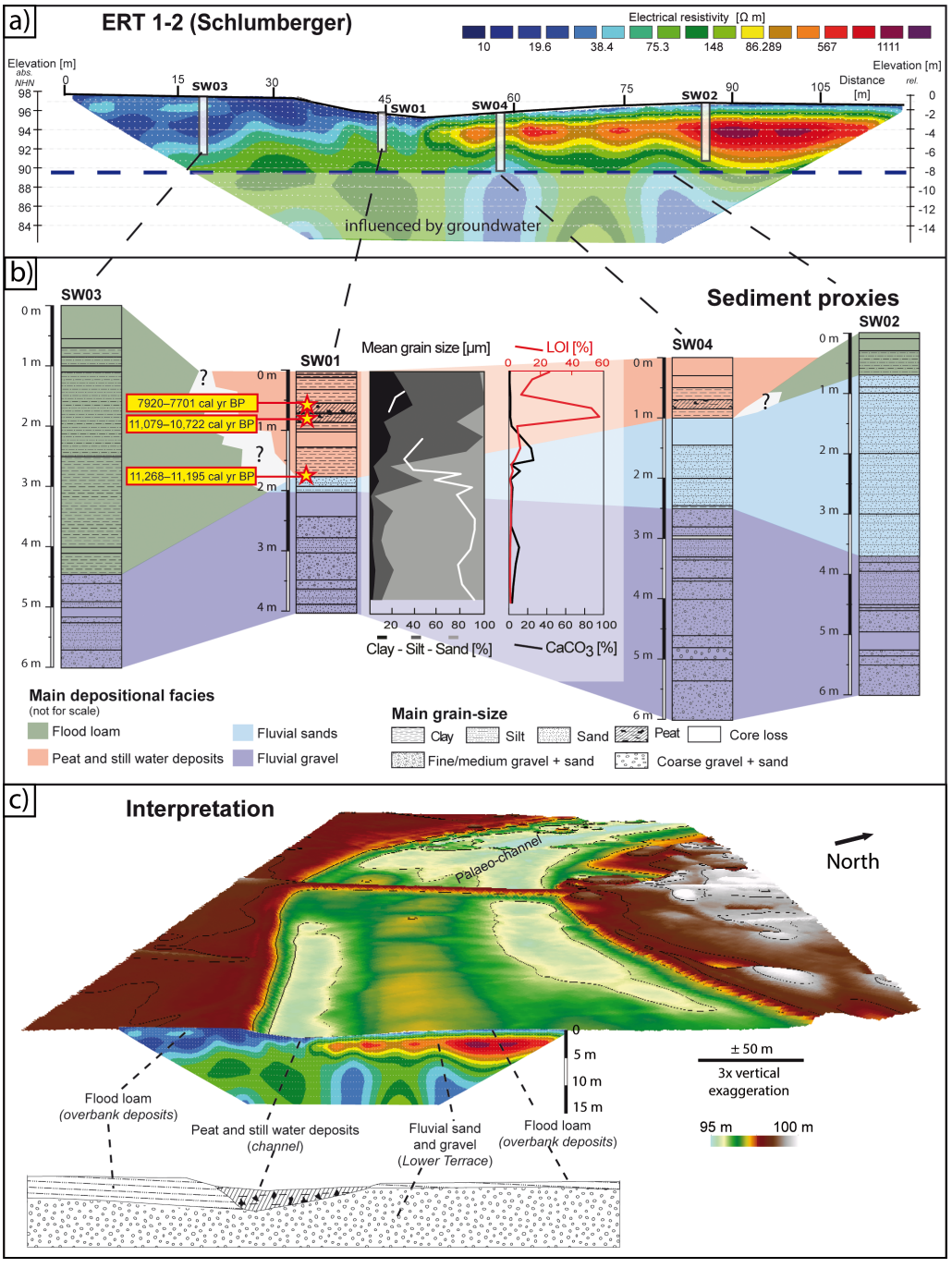

Figure 3. BSN meander at Schäffertwiesen. **(a)** Transect ERT 1–2 crossing the palaeo-river channel and showing the distribution of fine-grained deposits in blue (low resistivity values) and coarse-grained deposits in green, yellow, brown and red (intermediate to high resistivity values). **(b)** Synopsis of sediment cores SW03, SW01, SW04 and SW02 with tentative facies interpretation. For SW04, grain-size distributions, mean grain size, LOI values and $CaCO_3$ content are displayed. **(c)** Oblique view of the BSN meander in combination with the transect ERT 6–7–8–11 and tentative facies interpretation. A legend for the bottom drawing is provided in panel **(b)**. Data source: DGM1 of the Federal State of Baden-Württemberg provided by LGBR and established in 2000–2005.

limestones, as well as Buntsandstein sandstone, collectively representing the main erosional products of the Neckar catchment (Barsch and Mäusbacher, 1979; Fezer, 1997; Bibus and Rähle, 2003; Löscher, 2007; LGBR, 2021). These deposits shape the youngest part of the wide alluvial fan of the Neckar (Löscher et al., 1980; Barsch and Mäusbacher, 1988), which belongs to the Mannheim Formation (LGBR, 2021) and, at its northern boundary, almost reaches the study area (Fezer, 1997; Beckenbach, 2016).

The typical sediment sequence of palaeo-meander channels of the northern BSN (e.g. site of "Wasserbiblos" in Dambeck, 2005; Dambeck and Bos, 2002) also starts with fluvial sands and few pebbles. The general fining-up gradient from a sand and gravel mixture (in the southern BSN with some clast-supported sections) to matrix-supported units and pure fluvial sands indicates a decrease in fluvial transport capacity at the end of the phase of fluvial activity of the BSN. This decrease is either related to lower discharge or a thalweg shifting away from the coring site. However, it cannot be excluded that the increasing medium sand component in the upper part of the fining-up sequence is partially related to reactivated aeolian processes and input during the Younger Dryas (Löscher et al., 1989; Dambeck and Thiemeyer, 2002; Pflanz et al., 2022). The poorly sorted greyish-brown sandy mud overlying the in-channel fluvial sands in RL09 (boundary at 2.30 m b.s.) and SW01 (boundary at 1.74 m b.s.) reflects a distinct shift from a fluvial channel carrying bedload – until then presumably the main active channel of the BSN – to a cut-off channel restricted to suspension-load settling during stages of overbank flow by an adjacent active channel (Barsch and Mäusbacher, 1979). At Schäffertwiesen, this adjacent channel was the Rindlache channel. After the BSN was entirely abandoned, the Rindlache site was subject to flooding and received suspension load from a new Neckar course close by. This might have been the current channel heading straight to the Rhine near Mannheim, although this assumption requires verification with future research. Along the northern BSN this type of fluvio-limnic deposition is observed for the older meander generation before peat formation commenced, whereas at the younger meander sites peat deposits immediately overlie the coarse-grained channel-bottom deposits (Dambeck, 2005; Dambeck and Bos, 2002). Thus, the sedimentary sequences at Rindlache and Schäffertwiesen both resemble the infill of the older meander sites along the northern BSN. At some palaeo-channel sites of the northern BSN (e.g. "Auf Esch", "Großes Bruch"), as well as at Rindlache, peat formation is interrupted by organic-rich black clays that may represent a reactivation of overbank deposition and indicate increased input of fine-grained material into the inactive fluvial system (Dambeck, 2005; Dambeck and Thiemeyer, 2002).

Dambeck and Bos (2002) and Dambeck and Thiemeyer (2002) refer to the sandy mud overlying the fluvial channel-bottom facies at the older meander sites as clays, silts, loam or gyttja with occasional fine sandy laminae, depending on the site. The very high carbonate content in the uppermost part of this fine-grained unit (> 90 % in RL09) right below the overlying peat, also referred to as calcareous gyttja along the northern BSN (Dambeck and Bos, 2002; Bos et al., 2008), was identified as secondary carbonate precipitation. At present, two models for the formation of this carbonate precipitation are considered.

- The first is precipitation within the sediment body at distinct substrate boundaries in the groundwater fluctuation zone, along the capillary fringe, as described for the so-called *Rheinweiß* in similar contexts (Dambeck, 2005; Holzhauer, 2013; Holzhauer et al., 2017). Being this close to the present-day land surface, the *Rheinweiß* represents a relict feature. It predates the river regulation measures in the Upper Rhine Graben from 1817 CE on that led to rapid linear incision of the Rhine and to lowering of groundwater levels by several metres in the entire graben area (Barsch and Mäusbacher, 1979; Dister et al., 1990).

- The second is precipitation in the fluvio-limnic environment of the cut-off meander by photosynthesising Charophyceae and aquatic plants, aided by the uptake of CO_2 from bicarbonate (HCO_3^-) dissolved in the water (e.g. Bohnke and Hoek, 2007). The general model, according to which carbonate ions (CO_3^{2-}) are released and attract Ca^{2+} ions to form Ca_2CO_3 in the immediate vicinity of the photosynthesising organisms, is described in, for example, Merz (1992).

Whilst in both the southern and the northern (site "Wasserbiblos" in Dambeck and Bos, 2002) parts of the BSN these calcareous muds mostly date into the Preboreal (11.7–10.3 kyr ago) (Fig. 4), they are also well recognised to have formed earlier during the Alleröd (13.4–12.7 kyr ago) elsewhere in Central Europe (e.g. Bohncke and Hoek, 2007; Pawłowski et al., 2016). They may in general be associated with warmer phases of the late-glacial to Holocene transition with more abundant (aquatic) vegetation, shifting the carbonate balance and leading to increased carbonate precipitation (Waldmann, 1989; Dambeck, 2005).

5.2 Timing of fluvial activity of the southern BSN

There are diverging assumptions regarding the timing of the fluvial activity of the BSN. Its relatively short existence has been associated with the late-glacial formation of the north–south-directed dune belt between Schwetzingen and Lorsch (Fig. 1a) (e.g. Dambeck, 2005), which is assumed to have blocked the direct connection with the Rhine between Heidelberg and Mannheim. Yet, none of the palaeo-channels of the northern BSN are covered by any significant drift sands, the formation of which terminated mostly before the Older Dryas (13.6–13.4 kyr ago). Instead, drift sands were eroded by the BSN in some places, indicating that fluvial activ-

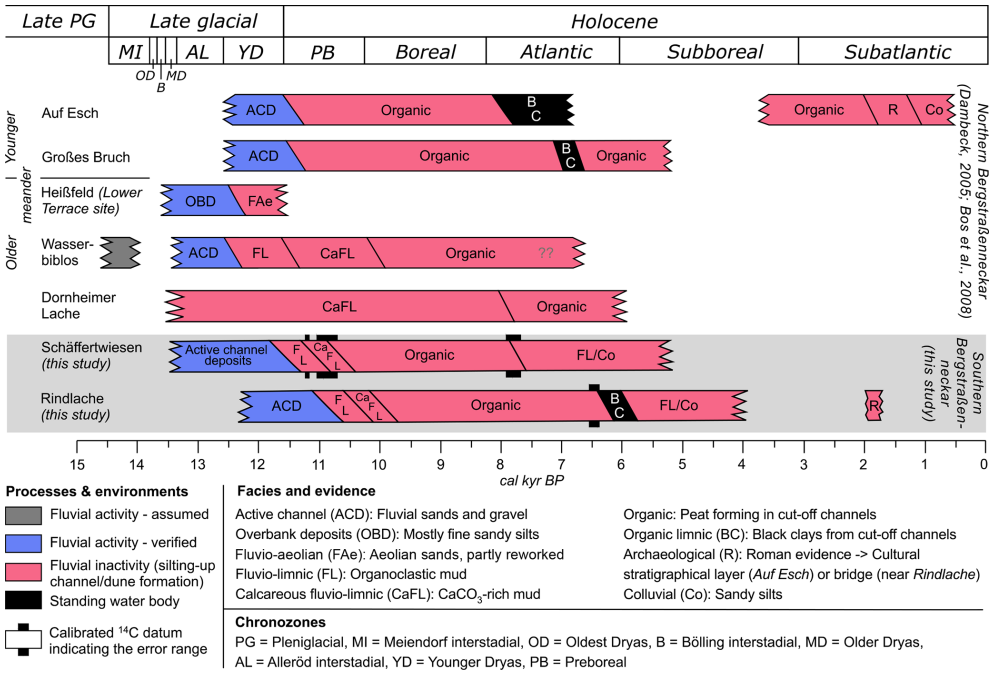

Figure 4. Assumed timeline of fluvial activity and inactivity of the Bergstraßenneckar (BSN). All sites refer to profiles from palaeo-channels, apart from Heißfeld (profile on the Lower Terrace adjacent to a BSN palaeo-channel). Results from the northern BSN (upper part) were taken from Dambeck (2005) and Bos et al. (2008). Preliminary data and interpretation from the southern BSN (this study) are shown in the lower part on the grey background. Wetland or temporary standing-water conditions at Rindlache during Roman times are inferred from the partially excavated wooden bridge across the same BSN channel ca. 1 km to the south (Wirth, 2011).

ity postdates the period of main aeolian activity. Initial activity of the BSN is tentatively dated to ca. 14 500 years ago (Dambeck, 2005). At the site "Fasanerie" near Groß-Gerau (Dambeck, 2005) and near Schwanheim (Hoffmann and Kzyzanowski, 1984) (Fig. 1a), Laacher See tephra, now dated to 13 006 ± 9 cal yr BP (Reinig et al., 2021), was identified in overbank deposits of the northern BSN. The detailed stratigraphic investigations in the northern part of the BSN indicate a dune breach of the Neckar towards the Rhine at approximately 12 800 to 11 500 years ago during the Younger Dryas (12.7–11.7 kyr ago) and an end to fluvial activity of the BSN channels at some point between ca. 11 600 and 10 120 years ago (Haupt, 1928; Wagner, 1981; Große-Brauckmann et al., 1990; Dambeck, 2005; Dambeck and Bos, 2002; Bos et al., 2008, 2012). However, there are several historical accounts and archaeological data pointing to the reactivation of certain sections of the BSN by smaller tributaries draining the western Odenwald Mountains and their use as waterways for the transport of goods, in particular during Roman times (Eckoldt, 1985; Wirth, 2011).

For the northern BSN, two palaeo-meander generations have been classified. Whilst the relatively younger meander generation forms a more or less continuous course to the former mouth west of Trebur, the relatively older meanders are morphologically detached (Kupfahl et al., 1972; Dambeck, 2005). Based on palynostratigraphical evidence and radiocarbon data, mud deposition in cut-off meanders of the older generation started in Alleröd times (site "Dornheimer Lache" in Bos et al., 2008) or by the end of the Younger Dryas (site "Wasserbiblos" in Dambeck, 2005; Dambeck and Bos, 2002; Bos et al., 2012). Elsewhere, it is assumed that sands were blown out from the inactive point bars of cut-off meanders to form proximal dunes on the Lower Terrace (HLfB, 1990), e.g. at the site "Heißfeld" (Dambeck, 2005; Dambeck and Thiemeyer, 2002) at a time, during the Younger Dryas, when aeolian dunes and drift sands of the northern Upper Rhine Graben were reactivated to a limited extent (Löscher et al., 1989; Dambeck and Bos, 2002; Pflanz et al., 2022). The younger meander sites show a distinct shift from fluvial sands to peat growth roughly at the beginning of the Preboreal (Fig. 4), possibly reflecting the abandonment of the BSN and confluence of the Neckar with the Rhine further to the south near Mannheim (Dambeck, 2005).

The basic stratigraphic patterns of the northern and southern BSN show striking similarities, but presently, very few radiocarbon ages are available for the southern BSN. However, if these are used as chronometric tie points as illustrated in Fig. 4 (lower part), the similarities become even more obvious. As the clastic mud deposits at the site Schäffertwiesen may date to the Younger Dryas to Preboreal period, we assume that the coarse-grained channel-bottom deposits underneath date to late-glacial times. The shift from mud sedimen-

tation to peat growth may have been induced by a denser vegetation cover at the onset of the Preboreal (Dambeck and Bos, 2002; Bos et al., 2008) leading to reduced suspension load during flood events and termination of the silting-up process. At the site "Wasserbiblos", northern BSN, sedimentation of similar silty and calcareous mud, reflecting a change in fluvial conditions from in-channel bedload transport and accumulation at the channel bottom to fluvio-limnic conditions inside a cut-off meander, is also dated to the end of the late-glacial period. A temporal overlap of changing fluvial dynamics at the Schäffertwiesen meander (between 12 000 and 11 500 cal yr BP) at the southern BSN and the older meander generation at the northern BSN, represented by the site "Wasserbiblos" (Dambeck, 2005; Dambeck and Bos, 2002; Bos et al., 2012), is likely. Yet peat formation at the northern BSN started earlier, during Preboreal times, and lasted until the end of the Boreal or beginning of the Atlantic period (ca. 8000–7500 cal yr BP). The peat at Rindlache continued to form until ca. 1500 years later (ca. 6500–6000 cal yr BP) (Fig. 4). The deposition of organic-rich black clays inside the channels and as overbank fines during the Atlantic period may represent an initial signal of anthropogenic soil erosion by Middle Neolithic communities (Große-Brauckmann et al., 1990; Dambeck and Thiemeyer, 2002). This interpretation is supported by the first occurrence of *Cerealia* in pollen spectra of northern BSN sites as an indicator of the introduction of agriculture and a decrease of *Ulmus*, which is related to the Neolithic Linear Pottery and Rössen cultures using this type of wood for fire and construction (Bos et al., 2012). In the area of the southern BSN people of the Late Neolithic Michelsberg (ca. 4400–3500 BCE; Lang, 1996) and/or the end Neolithic Corded Ware ceramic cultures (ca. 2900–2350 BCE; König, 2015) may have intensified soil erosion resulting in a subsequent increase in suspension load and the formation of the black clays.

Assuming that the Rindlache site – in contrast to the cut-off meander of Schäffertwiesen – represented the active channel until the modern Neckar channel was established and the BSN finally abandoned, the entire chronostratigraphy may be offset by ca. 1500 years. Thus, it would overlap with the chronostratigraphy of northern BSN sites representing the younger meander generation, sensu Dambeck (2005), even though the Rindlache site shows an interim sequence of fluvio-limnic sandy mud, which in the north is characteristic of only older meander sites (Fig. 4).

6 Conclusions and outlook

Palaeo-meanders of the southern BSN are an understudied geomorphological archive. This is all the more surprising as studies along the northern BSN in Hesse proved to reveal detailed aspects of the late-glacial to Holocene history of the Upper Rhine Graben riverscape (e.g. Dambeck, 2005; Dambeck and Thiemeyer, 2002; Bos et al., 2008). The palaeo-meander channels of the southern BSN can still be morphologically identified in the field, as well as from satellite imagery and digital elevation models (Beckenbach, 2016), representing a sequence of relatively older meanders which have been cut off from younger channels. Our pilot study at the relatively older Schäffertwiesen meander and the younger Rindlache meander shows a stratigraphic sequence reaching from partially clast-supported sand and gravel in-channel facies to muds and peat representing the phase after which the meanders were cut off, and the Neckar shifted its course entirely. The ^{14}C data of the upper boundaries of the peat deposits at both sites, Schäffertwiesen (cut-off meander) and Rindlache (part of the latest course), are offset by ca. 1500 years, reflecting the overall older age of the Schäffertwiesen sequence. In comparison with the abandoned riverscape of the northern BSN (Dambeck, 2005), both sites studied here resemble the stratigraphic pattern of the older meander phase with fluvio-limnic mud deposition which is vertically confined by coarse-grained in-channel facies (below) and peat and black clays (above). The chronology of the Schäffertwiesen site tentatively correlates with the older meander generation, while the Rindlache site has more of a chronological overlap with the younger meander generation of the northern BSN, where, however, the intermittent mud is absent. Therefore, the presence of fluvio-limnic sediments in the abandoned river channel may be a function of flooding frequency and proximity to a still active channel. Whilst this was the case for both of the southern sites after the final abandonment of the BSN as they were still close to the new Neckar course, the northern BSN channel sites were cut off from a regular flooding regime.

Evidently, more palaeo-channel stratigraphies of the southern BSN need to be investigated and correlated, in combination with an extended chronological dataset of ^{14}C ages for the organic-rich sediments and optically stimulated luminescence ages for the sand-dominated in-channel facies, for which no data are available to date. In particular, the palaeoenvironments of the fluvio-limnic muds, along with any potential anthropogenic impact, require further attention and need to be reconstructed in more detail. Deciphering a chronology of fluvial activity in the southern BSN domain will provide the basis for investigating the reactivation of some reaches of and human interaction with the BSN across the Holocene, in particular during Roman times and later historical periods, for which only fragmented historical and archaeological information is available so far (e.g. Eckoldt, 1985).

Data availability. All data from this study can be found in the Supplement.

Supplement. The supplement related to this article is available online at: https://doi.org/10.5194/egqsj-71-213-2022-supplement.

Author contributions. The concept of the study was jointly developed by all authors at the Institute of Geography, Heidelberg University, in the context of field courses held at the two study sites. All these authors were involved in the fieldwork. Sedimentary laboratory analyses were carried out by FR, GS and ME. FR contributed results from his master of science thesis. Processing and analysis of ERT data were carried out by MH, FH and SH. The GIS for this project was set up by FH. SL performed the ^{14}C dating. A first draft of the manuscript was written by ME, FH and AK. ME, FH, FR, AK, MH, SH, SL and OB commented on and approved the manuscript.

Competing interests. The contact author has declared that none of the authors has any competing interests.

Disclaimer. Publisher's note: Copernicus Publications remains neutral with regard to jurisdictional claims in published maps and institutional affiliations.

Special issue statement. This article is part of the special issue "Quaternary research from and inspired by the first virtual DEUQUA conference".

Acknowledgements. We thank Peter Müller (Mannheim-Straßenheim) and the Bach family (Heddesheim) for permission to conduct fieldwork on their properties. Undergraduate students of the geography programmes at Heidelberg University are thanked for their engagement during field courses. Nicola Manke kindly provided support during one field course and during the laboratory analyses. Support and permission to use the laser particle sizer of the Sedimentology and Marine Paleoenvironmental Dynamics research group at the Institute of Geosciences at Heidelberg University by Andre Bahr are greatly appreciated. Finally, we would like to thank the Landesamt für Geologie, Rohstoffe und Bergbau (LGBR) for providing the digital elevation model DGM1 of the state of Baden-Württemberg. We are thankful for the helpful reviews of one anonymous person and of Rainer Dambeck, who provided highly detailed comments, plenty of ideas and improved the manuscript by sharing his great regional expertise.

Gerd Schukraft was a driving force of the research on the southern Bergstraßenneckar and one of the initiators back in 2019. He sadly passed away in April 2020.

Financial support. This research was supported by funds of Heidelberg University. For the publication fee we acknowledge financial support by Deutsche Forschungsgemeinschaft within the funding programme "Open Access Publikationskosten", as well as by Heidelberg University.

Review statement. This paper was edited by Julia Meister and reviewed by Rainer Dambeck and one anonymous referee.

References

Ad-hoc-AG Boden: Bodenkundliche Kartieranleitung, 5th edn., Schweizerbart, Hannover, 438 pp., 2005.

AdV (Arbeitsgemeinschaft der Vermessungsverwaltungen der Länder der Bundesrepublik Deutschland): DHHN2016 – Die Erneuerung des Deutschen Haupthöhennetzes und der einheitliche integrierte geodätische Raumbezug 2016, Landesamt für Digitalisierung, Breitband und Vermessung Bayern, München, 2018.

Barsch, D. and Mäusbacher, R.: Erläuterungen zur Geomorphologischen Karte 1:25 000 der Bundesrepublik Deutschland – GMK 25 Blatt 3, 6417 Mannheim-Nordost, in: GMK Schwerpunktprogramm, Geomorphologische Detailkartierung in der Bundesrepublik Deutschland, edited by: Barsch, D., Fränzle, O., Leser, H., Liedtke, H., and Stäblein, G., Berlin, 1–56, 1979.

Barsch, D. and Mäusbacher, R.: Zur fluvialen Dynamik beim Aufbau des Neckarschwemmfächers, Berlin. Geogr. Abh., 47, 119–128, https://doi.org/10.23689/fidgeo-3194, 1988.

Beckenbach, E.: Geologische Interpretation des hochauflösenden digitalen Geländemodells von Baden-Württemberg, PhD thesis, University of Stuttgart, Germany, https://doi.org/10.18419/opus-8846, 2016.

Bernhard, H. and Hickethier, H.: Beitrag zur Kenntnis des alten Neckarlaufs am Westrand des Odenwalds bei Bensheim, Notizbl. Hess. L.-Amt Bodenforsch., 94, 385–389, 1966.

Bibus, E., and Rähle, W.: Stratigraphische Untersuchungen an molluskenführenden Terrassensedimenten und ihren Deckschichten im mittleren Neckarbecken (Württemberg), E&G Quaternary Sci. J., 53, 94–113, https://doi.org/10.3285/eg.53.1.06, 2003.

Blott, S. J., and Pye, K.: GRADISTAT: a grain size distribution and statistics package for the analysis of unconsolidated sediments, Earth Surf. Proc. Landf., 26, 1237–1248, https://doi.org/10.1002/esp.261, 2001.

Bohncke, S. J. P. and Hoek, W. Z.: Multiple oscillations during the Preboreal as recorded in a calcareous gyttja, Kingbeekdal, The Netherlands, Quaternary Sci. Rev., 26, 1965–1974, https://doi.org/10.1016/j.quascirev.2007.02.017, 2007.

Bos, J. A. A., Dambeck, R., Kalis, A. J., Schweizer, A., and Thiemeyer, H.: Palaeoenvironmental changes and vegetation history of the northern Upper Rhine Graben (southwestern Germany) since the Lateglacial, Neth. J. Geosci., 87, 67–90, https://doi.org/10.1017/S0016774600024057, 2008.

Bos, J. A. A., Dambeck, R., and Bouman, M. I. T. J.: Paläoökologische Untersuchungen im nördlichen Oberrheingraben vom Spätglazial bis Atlantikum; Vegetationsgeschichte und anthropogene Einflüsse, Frankfurt. Archäol. Schr., 18, 59–90, 2012.

Buness, H., Gabriel, G., and Ellwanger, D.: The Heidelberg Basin drilling project: Geophysical pre-site surveys, E&G Quaternary Sci. J., 57, 338–366, https://doi.org/10.3285/eg.57.3-4.4, 2009.

Dambeck, R.: Beiträge zur spät- und postglazialen Fluss- und Landschaftsgeschichte im nördlichen Oberrheingraben, PhD thesis, University of Frankfurt/Main, Germany, 438 pp., 2005.

Dambeck, R. and Bos, J. A. A.: Lateglacial and Early Holocene landscape evolution of the northern Upper Rhine River valley, south-western Germany, Z. Geomorph. Suppl., 128, 101–127, 2002.

Dambeck, R., and Thiemeyer, H.: Fluvial history of the northern Upper Rhine River (southwestern Germany) during the

Lateglacial and Holocene times, Quaternary Int., 93, 53–63, https://doi.org/10.1016/S1040-6182(02)00006-X, 2002.

Dister, E., Gomer, D., Obrdlik, P., Petermann, P., and Schneider, E.: Water management and ecological perspectives of the upper Rhine's floodplains, Regul. River., 5, 1–15, https://doi.org/10.1002/rrr.3450050102, 1990.

Eckoldt, M.: Schiffahrt auf kleinen Flüssen. T. 2, Gewässer im Bereich des "Odenwaldneckars" im ersten Jahrtausend n. Chr., Deutsch. Schiffahrtsarch., 8, 101–116, 1985.

Eisbacher, G. H. and Fielitz, W.: Karlsruhe und seine Region. Nordschwarzwald, Kraichgau, Neckartal, südlicher Odenwald, Oberrhein-Graben, Pfälzerwald und westliche Schwäbische Alb. Sammlung Geologischer Führer Vol. 103, Bornträger, Stuttgart, 2010.

Erkens, G., Dambeck, R., Volleberg, K. P., Bouman, M. T., Bos, J. A., Cohen, K. M., Wallinga, J., and Hoek, W. Z.: Fluvial terrace formation in the northern Upper Rhine Graben during the last 20 000 years as a result of allogenic controls and autogenic evolution, Geomorphology, 103, 476–495, https://doi.org/10.1016/j.geomorph.2008.07.021, 2009.

Fezer, F.: 220 m Altpleistozän im "Heidelberger Loch", E&G Quaternary Sci. J., 47, 145–153, https://doi.org/10.3285/eg.47.1.10, 1997.

Gabriel, G., Ellwanger, D., Hoselmann, C., Weidenfeller, M., Wielandt-Schuster, U., and The Heidelberg Basin Project Team: The Heidelberg Basin, Upper Rhine Graben (Germany): A unique archive of Quaternary sediments in Central Europe, Quaternary Int., 292, 43–58, https://doi.org/10.1016/j.quaint.2012.10.044, 2013.

Große-Brauckmann, G., Malchow, G., and Streitz, B.: Makrofossil- und pollenanalytische Befunde vom Altneckarbett bei Riedstadt-Goddelau, in: Die Holzbrücken bei Riedstadt-Goddelau, Kreis Groß-Gerau, edited by: Wagner, P., Mater. Vor- u. Frühgesch. Hessen, 5, 111–132, 1990.

Haupt, O.: Die Pfahlbausiedlung am Phillipshospital bei Goddelau im hessischen Ried sowie das Alter der Neckarbetten und des Modauschuttkegels an der Bergstraße, Notizbl. Ver. Erdk. Hess. Geol. L.-Anst., V(10), 239–245, 1928.

Heiri, O., Lotter, A. F., and Lemcke, G.: Loss on ignition as a method for estimating organic and carbonate content in sediments: reproducibility and comparability of results, J. Paleolimnol., 25, 101–110, https://doi.org/10.1023/A:1008119611481, 2001.

HLfB (Hessisches Landesamt für Bodenforschung): Bodenkarte der nördlichen Oberrheinebene 1:50000, Wiesbaden, 1990.

Hoffmann, J. and Krzyzanowski, J.: Laacher-Bimstuff-Vorkommen im Bereich des ehemaligen Neckarlaufs bei Zwingenberg (Bergstraße), Geol. Jb. Hessen, 112, 77–81, 1984.

Holzhauer, I.: Landschaftsgeschichte und menschlicher Einfluss im Umfeld der Schwetzinger Hardt seit dem Würm-Hochglazial, PhD thesis, Heidelberg University, Germany, https://doi.org/10.11588/heidok.00015714, 2013.

Holzhauer, I., Kadereit, A., Schukraft, G., Kromer, B., and Bubenzer, O.: Spatially heterogeneous relief changes, soil formation and floodplain aggradation under human impact – geomorphological results from the Upper Rhine Graben (SW Germany), Z. Geomorph., 61 (Suppl. 1), 121–158, https://doi.org/10.1127/zfg_suppl/2017/0357, 2017.

Howard, A. D. and Hemberger, A. T.: Multivariate characterization of meandering, Geomorphology, 4, 161–186, https://doi.org/10.1016/0169-555X(91)90002-R, 1991.

Kneisel, C.: Electrical resistivity tomography as a tool for geomorphological investigations – some case studies, Z. Geomorph. Suppl., 132, 37–49, 2003.

König, P.: Eine vorgeschichtliche und frühmittelalterliche Siedlung von Heddesheim, Rhein-Neckar-Kreis, Fundber. Baden-Württemb., 35, 141–204, https://doi.org/10.11588/fbbw.2015.0.44523, 2015.

Kromer, B., Lindauer, S., Synal, H. A., and Wacker, L.: MAMS – a new AMS facility at the Curt-Engelhorn-Centre for Achaeometry, Mannheim, Germany, Nucl. Instr. Meth., 294, 11–13, https://doi.org/10.1016/j.nimb.2012.01.015, 2013.

Kupfahl, H.-G., Meisl, S., and Kümmerle, E.: Erläuterungen zur geologischen Karte von Hessen 1:25000, Blatt 6217 Zwingenberg an der Bergstraße, Hessisches Landesamt für Bodenforschung, Wiesbaden, 276 pp., 1972.

Lang, A.: Die Infrarot-Stimulierte-Lumineszenz als Datierungsmethode für holozäne Lössderivate. Ein Beitrag zur Chronometrie kolluvialer, alluvialer und limnischer Sedimente in Südwestdeutschland, Heidelb. Geogr. Arb., 103, 1–137, 1996.

LGBR (Landesamt für Geologie, Bergbau und Rohstoffe): Kiese und Sande des Neckars im Oberrheingraben, https://lgrbwissen.lgrb-bw.de/rohstoffgeologie/rohstoffe-des-landes/kiese-sandig/kiese-sande-des-neckars-im-oberrheingraben, last access: 27 August 2021.

Löscher, M.: Die quartären Ablagerungen auf der Mannheimer Gemarkung, in: Mannheim vor der Stadtgründung. Teil 1 Band 1, edited by: Probst, H., Friedrich Pustet Verlag, Regensburg, 28–47, 2007.

Löscher, M., Haag, T., and Münzing, K.: Zum Alter der Dünen im nördlichen Oberrheingraben bei Heidelberg und zur Genese ihrer Bänderparabraunerden, E&G Quaternary Sci. J., 39, 98–108, https://doi.org/10.3285/eg.39.1.10, 1989.

Löscher, M., Becker, B., Bruns, M., Hieronymus, U., Mäusbacher, R., Münnich, M., Münzing, K., and Schedler, J.: Neue Ergebnisse über das Jungquartär im Neckarschwemmfächer bei Heidelberg, E&G Quaternary Sci. J., 30, 89–100, https://doi.org/10.3285/eg.30.1.07, 1980.

Mangold, A.: Die alten Neckarbetten in der Rheinebene, Abh. Großherzogl. Hess. Geol. Landesanst. Darmstadt, 2, 75–114, 1892.

Merz, M. U. E.: The biology of carbonate precipitation by cyanobacteria, Facies, 26, 81–102, https://doi.org/10.1007/BF02539795, 1992.

Mone, F. J.: Ueber den alten Flußlauf im Oberrheintal, Badisch. Arch. z. Vaterlandsk. in allseit. Hinsicht, 1, 1–47, 1826.

Munsell Color Laboratory: Munsell Soil Color Chart, New Windsor, 2000.

Nickel, E. and Fettel, M.: Odenwald – Vorderer Odenwald zwischen Darmstadt und Heidelberg, Sammlung Geologischer Führer Vol. 65, Bornträger, Stuttgart, 1979.

Pawłowski, D., Borówka, R. K., Kowalewski, G. A., Luoto, T. P., Milecka, K., Nevalainen, L., Okupny, D., Tomkowiak, J., and Zieliński, T.: Late Weichselian and Holocene record of the paleoenvironmental changes in a small river valley in Central Poland, Quaternary Sci. Rev., 135, 24–40, https://doi.org/10.1016/j.quascirev.2016.01.005, 2016.

Peters, G. and van Balen, R. T.: Tectonic geomorphology of the northern Upper Rhine Graben, Germany, Global Planet. Change, 58, 310–334, https://doi.org/10.1016/j.gloplacha.2006.11.041, 2007.

Pflanz, D., Kunz, A., Hornung, J., and Hinderer, M.: New insights into the age of aeolian sand deposition in the northern Upper Rhine Graben (Germany), Quaternary Int., 625, 1–13, https://doi.org/10.1016/j.quaint.2022.03.019, 2022.

Reimer, P. J., Austin, W. E., Bard, E., Bayliss, A., Blackwell, P. G., Ramsey, C. B., and Grootes, P. M.: The IntCal20 northern hemisphere radiocarbon age calibration curve (0–55 cal kBP), Radiocarbon, 62, 725–757, https://doi.org/10.1017/RDC.2020.41, 2020.

Reinig, F., Wacker, L., Jöris, O., Oppenheimer, C., Guidobaldi, G., Nievergelt, D., Adolphi, F., Cherubini, P., Engels, S., Esper, J., Land, A., Lane, C., Pfanz, H., Remmele, S., Sigl, M., Sookdeo, A., and Büntgen, U.: Precise date for the Laacher See eruption synchronizes the Younger Dryas, Nature, 595, 66–69, https://doi.org/10.1038/s41586-021-03608-x, 2021.

Saur, A.: Parvum theatrum urbium, Frankfurt, 1593.

Scheer, H.-D.: Gliederung und Aufbau der Niederterrassen von Rhein und Main im nördlichen Oberrheintalgraben, Geol. Jb. Hessen, 106, 273–289, 1978.

Schottler, W.: Erläuterungen zur geologischen Karte des Grossherzogtums Hessen im Maßstabe 1:25000, Hessischer Staatsverlag, 1906.

Stuiver, M., Reimer, P. J., and Reimer, R. W.: CALIB 8.2 (WWW program), http://calib.org, last access: 19 January 2022.

Wagner, P.: Riedstadt-Goddelau, Kreis Groß-Gerau. Holzbrücken im alten Neckarbett, Ausgrabungen im Hessischen Ried 1976–1977, Archäol. Denkm. Hessen, 20, 1–12, 1981.

Waldmann, F.: Beziehungen zwischen Stratigraphie und Bodenbildungen aus spätglazialen und holozänen Sedimenten in der nördlichen Oberrheinebene, PhD thesis, University of Freiburg, Germany, 1989.

Wild, E. M., Steier, P., Fischer, P., and Höflmayer, F.: ^{14}C dating of humic acids from Bronze and Iron Age plant remains from the eastern Mediterranean, Radiocarbon, 55, 599–607, https://doi.org/10.1017/S003382220005774X, 2013.

Winkelmann, J. J.: Gründliche Beschreibung der Fürstenthümer Hessen und Hersfeld, Brauer, Bremen, 1697.

Wirth, K.: Ein Bohlenweg oder eine Sumpfbrücke aus römischer Zeit in Mannheim-Straßenheim, in: Archäologie der Brücken, Vorgeschichte, Antike, Mittelalter, Neuzeit, edited by: Pflederer, T. and Sommer, C., Friedrich Pustet Verlag, Regensburg, 102–105, 2011.

E&G Quaternary Sci. J., 71, 227–241, 2022
https://doi.org/10.5194/egqsj-71-227-2022

Open Access E&G Quaternary Science Journal

Research article

Comparison of bulk and sequential sampling methodologies on mammoth tooth enamel and their implications in paleoenvironmental reconstructions

Zuorui Liu[1], **Amy Prendergast**[1], **Russell Drysdale**[1], **and Jan-Hendrik May**[1,2]

[1]School of Geography, Earth and Atmospheric Sciences (SGEAS), University of Melbourne, Melbourne, VIC, Australia
[2]GeoQuest Research Centre, School of Earth, Atmospheric and Life Sciences, University of Wollongong, Wollongong, NSW, Australia

Correspondence: Zuorui Liu (zuoruil@student.unimelb.edu.au), Amy Prendergast (amy.prendergast@unimelb.edu.au), and Jan-Hendrik May (janhendrikmay@unimelb.edu.au)

Relevant dates: Received: 29 March 2022 – Revised: 18 August 2022 – Accepted: 30 August 2022 – Published: 30 September 2022

How to cite: Liu, Z., Prendergast, A., Drysdale, R., and May, J.-H.: Comparison of bulk and sequential sampling methodologies on mammoth tooth enamel and their implications in paleoenvironmental reconstructions, E&G Quaternary Sci. J., 71, 227–241, https://doi.org/10.5194/egqsj-71-227-2022, 2022.

Abstract: Mammoth teeth have been widely investigated using stable-isotopic analysis for paleoenvironmental and paleoecological reconstructions due to their large size and frequent discoveries. Many past investigations sampled the tooth enamel with the "bulk" method, which involves drilling one sample from the occlusal surface to the root for each tooth. Some of the more recent studies applied the "sequential" method, with a sequence of samples drilled following the dominant enamel growth direction to produce a time series of isotopic oscillations that reflects high-resolution environmental changes, as well as changes in mammoth dietary behavior. Although both the bulk and mean sequential $\delta^{18}O$ values are expected to represent the averaged signal over the time of tooth formation, it is uncertain whether their paleoenvironmental records were formed during similar periods of time. In this study, we applied both sampling methods (sequential drilling first followed by a thin layer of bulk drilling) on the same enamel ridges of multiple mammoth teeth and compared their respective $\delta^{18}O$ values. The results indicated that, in most enamel ridges, the bulk samples have more negative $\delta^{18}O$ values compared to the average sequential values, and some of the bulk values even fall outside the range of sequential values. The most likely explanation for the differences is the structure and formation stages of enamel that caused uneven distributions of different seasons recorded in the samples. This finding provides insights into current limitations of the two sampling methods and the applicability of cross-method data comparison from past studies.

Kurzfassung: Aufgrund ihrer relativen Fundhäufigkeit und Grösse werden Mammuthmolare vielfach für paläoökologische Zwecke und Umweltrekonstruktionen mit Hilfe von stabilen Isotopen herangezogen. Bei vielen der bislang publizierten Arbeiten wurde dabei Zahnschmelz mit der "Bulk"-Methode beprobt, bei der für jeden Zahn eine einzelne Probe von der Kaufläche bis zur Wurzel gebohrt wird. Neuere Studien wenden nun die "sequenzielle" Methode an, bei der eine Reihe von Proben entlang der Hauptwachstumsrichtung des Zahnschmelzes gebohrt wird, um die Variation der Isotopenwerte über

die Zeit zu bestimmen, welche sowohl hochauflösende Umweltveränderungen als auch Veränderungen im Ernährungsverhalten der Mammuts widerspiegeln kann. Obwohl sowohl "Bulk"- als auch die gemittelten sequenziellen δ^{18}O-Werte ein zeitlich gemitteltes Signal der Zahnbildung repräsentieren sollten, ist bislang nicht klar, inwieweit diese Werte tatsächlich den selben, direkt vergleichbaren Zeitraum wiederspiegeln. In dieser Studie haben wir beide Methoden der Probenahme (zuerst sequenzielle Proben, dann eine dünne Schicht von "Bulk"-Proben) an denselben Schmelzkämmen mehrerer Mammutzähne angewandt und ihre jeweiligen δ^{18}O-Werte verglichen. Die Ergebnisse zeigen, dass in den meisten Schmelzkämmen die "Bulk"-Proben im Vergleich zu den mittleren sequenziellen Werten negativere δ^{18}O-Werte aufweisen, und einige der "Bulk"-Werte sogar außerhalb der Variationsbreite der sequenziellen Werte liegen. Die wahrscheinlichste Erklärung für diese Unterschiede liegt in der Struktur sowie den Bildungsraten und -stadien des Zahnschmelzes, welche eine ungleichmäßige Verteilung der verschiedenen in den Proben erfassten Jahreszeiten verursachen. Die Ergebnisse geben Einblick in die derzeitigen Grenzen der beiden Probenahmeverfahren und ermöglichen damit einen kritischeren und verbesserten methoden-übergreifenden Datenvergleich.

1 Introduction

Stable-isotopic analysis on mineralized tissues of animals has added great knowledge to our understanding of past environments and climates. Among all the animal tissues, Pleistocene mammoth teeth and tusks are of special interest for paleoenvironmental and paleoclimatic reconstructions over the past decades due to their large size and frequent discoveries. Oxygen-isotope ratios in mammoths can represent their surrounding environmental properties because they are directly related to the isotopic ratios of their ingested environmental water, which in turn primarily reflects regional temperature and water balance (Dansgaard, 1964; Longinelli, 1984; Luz et al., 1984). Previous studies of oxygen isotopes in mammoth remains have provided paleoenvironmental records in Europe and North America from Marine Isotope Stage (MIS) 5 to MIS 2 (130–22 ka cal BP). In most previous studies, the sampling method has been drilling one "bulk" sample from each tooth from the occlusal surface to the root (Genoni et al., 1998; Tütken et al., 2007; Ukkonen et al., 2007; Iacumin et al., 2010; Kovács et al., 2012; Pryor et al., 2013). The purpose of bulk sampling is to try to cover the longest possible period of time of tooth formation (Pryor et al., 2013), as the sample should represent an averaged isotopic signal across the tooth formation time (Fricke and O'Neil, 1996; Sharp and Cerling, 1998; Hoppe, 2004). Although this method can effectively reconstruct the averaged paleoclimatic conditions over several years, the temporal resolution of reconstruction is limited to decadal scale, and consequently, a very small amount of data exist on sub-annual environmental conditions and climatic variations during the Quaternary from these regions. Such data, however, are crucial in understanding how the highly variable climate of the Late Pleistocene translated into regional- to local-scale environmental conditions, ultimately affecting a range of animal–environmental and human–environmental interactions (Denton et al., 2005; Bradtmöller et al., 2012; Prendergast and Schöne, 2017; Prendergast et al., 2018).

To address this issue, a "sequential" approach has also been applied to mammoth and isotope research in some studies (Koch et al., 1989; Fisher and Fox, 2007; Metcalfe and Longstaffe, 2012; Widga et al., 2021; Wooller et al., 2021). Like most mammal species, mammoth tooth enamel has a dominant growth direction from the occlusal surface to the roots at a relatively constant rate (Metcalfe and Longstaffe, 2012). Therefore, it has the potential to yield highly resolved time series of paleoenvironmental information over the course of tooth formation. In several recent studies, multiple sequential samples were drilled from the same mammoth tooth following its growth direction with a resolution up to 1mm per sample, forming a time series of isotopic oscillations that likely reflects paleoenvironmental changes at sub-annual scales (Metcalfe and Longstaffe, 2012; Wooller et al., 2021; Miller et al., 2022). The mean value of the sequential samples should therefore reflect the averaged isotopic signal during the period of time of tooth growth, which is also what the bulk sample is expected to represent. However, this remains untested, and it is unknown whether the mean sequential value and the bulk value obtained from the same mammoth tooth yield similar isotopic compositions, as well as whether they have recorded the environmental properties during approximately the same period of time. Due to this limitation, it is still uncertain whether isotopic results obtained from bulk and sequential sampling methods can be directly compared, interpreted, and used for paleoenvironmental reconstruction.

In this study, we explored the potential differences between the sequential and the traditional bulk sampling methods. We obtained four mammoth teeth of MIS 3 age from southwestern Germany and applied both sampling methods on each tooth. The bulk and average sequential δ^{18}O values from the same tooth were then compared.

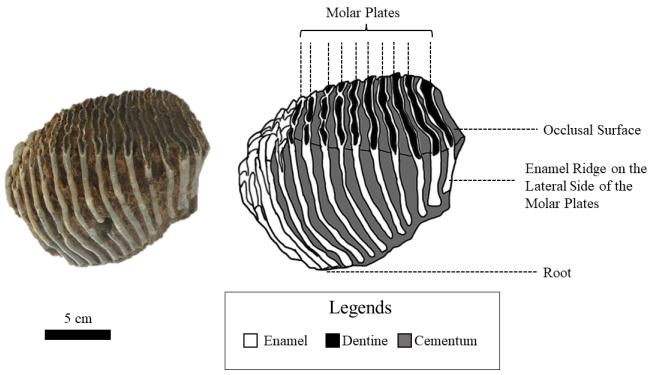

Figure 1. A photograph and its corresponding schematic diagram of a mammoth molar tooth used in this study (UW-1).

2 Background

2.1 Mammoth tooth growth

Similar to modern elephants, the woolly mammoths (*Mammuthus primigenius*) had six sets of teeth and a total number of 24 molar teeth throughout their lifespan. At any one time only one tooth was fully in operation in each of the four jaws (Maschenko, 2002; Lister and Bahn, 2007). Each molar tooth of *M. primigenius* is a combination of 22–24 molar plates (Lister and Bahn, 2007), which are flat thin sections of dentine folded in enamel. Each molar plate is adhered by cementum (Ferretti, 2003). The apex of these molar plates forms the occlusal surface for grinding food, and their lateral outer surface is exposed, forming separate enamel ridges (Fig. 1).

Within each molar plate, mammoth tooth enamel has primary and secondary stages of formation (Smith, 1998; Smith and Tafforeau, 2008). During the secretory (primary) stage, daily incremental features grow from the enamel-dentine junction (EDJ) to the outermost surface, and these incremental lines are parallel to the EDJ under microscopic view (Metcalfe and Longstaffe, 2012). Tooth increments formed during the primary stage take up only about 20 %–30 % of the entire enamel weight (Passey and Cerling, 2002; Passey et al., 2005). The maturation (secondary) stage starts after the secretory stage ends, and it takes up most enamel weight and formation time (approximately two-thirds of total formation time) (Smith, 1998). During this stage, enamel formation starts at the apex (occlusal surface) near the EDJ side, growing dominantly along the tooth height to the root while extending to the outermost surface simultaneously. Secondary daily incremental features captured by microscopic analysis indicated that enamel growth direction is inclined at an angle of 55–60° to the EDJ (Metcalfe and Longstaffe, 2012).

2.2 Oxygen isotopes and mammoth water source

Oxygen isotopic composition in animal bioapatite can be used as an indicator of past climates and environmental conditions. For large-sized homeothermic animals (animals which can keep a constant body temperature) such as the mammoths, the $\delta^{18}O$ values in their enamel carbonate are solely determined by the $\delta^{18}O$ values in their body water (Longinelli, 1984; Luz et al., 1984). Mammoths were obligate drinkers, with more than two-thirds of their body water being obtained from direct consumption of environmental water (Koch et al., 1989; Ayliffe et al., 1992). Therefore, their body water $\delta^{18}O$ values directly reflect those in their ingested environmental water, which are in turn primarily controlled by local- to regional-scale environmental factors such as discharge, precipitation, and air temperature (Dansgaard, 1964). A cyclicity of oxygen isotopic variations is expected from the sequentially drilled mammoth enamel samples, since they should reflect regional surface water $\delta^{18}O$ values, and nearly all natural water bodies, including streams, estuaries, and lakes, experience seasonal oscillations of $\delta^{18}O$ values due to seasonally differing water balances (Rozanski et al., 2001; Theakstone, 2003). The surface water isotopic content of any given water body is determined by the isotopic composition and amount of its water sources (input), as well as those of the water output (Rozanski et al., 2001; Benson and Paillet, 2002). In the context of the late Pleistocene Rhine River catchment (Fig. 2), the main input water sources for the catchment would have included groundwater, precipitation sourced from the Atlantic ocean, and snow and glacier melt, and output is primarily runoff and evaporation. These input water sources have different effects on the $\delta^{18}O$ values in surface water. Glacier and snow meltwater usually have the most depleted $^{18}O/^{16}O$ ratio (Theakstone, 2003), and the $^{18}O/^{16}O$ ratio in precipitation and groundwater is usually more enriched than surface water (Theakstone, 2003; Yeh and Lee, 2018; Bedaso and Wu, 2021). We also analyzed modern hydrological data of the Rhine River (for the period 2005–2010 at Lobith, Netherlands) to better constrain the mechanism of isotopic oscillations. In the modern Rhine River, $\delta^{18}O$ values show seasonal variations, with $\delta^{18}O$ values being approximately 1 ‰ more negative during summer than in winter months (Rozanski et al., 2001). Under interglacial (Holocene) climatic conditions, the summer $^{18}O/^{16}O$ depletion is caused by increased contributions of meltwater from alpine glaciers (Rozanski et al., 2001). Therefore, in the sequential $\delta^{18}O$ records from the mammoth teeth, local troughs (minima) in a curve are expected to correspond to the summer months when glacier melt is highest, and local peaks (maxima) are the coldest winter month. A cycle of isotopic variation should thus closely approximate the range of climatic variability throughout a year, with the distance between two neighboring maxima (or minima) corresponding to one "hydrological year" of tooth growth (Metcalfe and Longstaffe, 2012; Prendergast and Schöne, 2017).

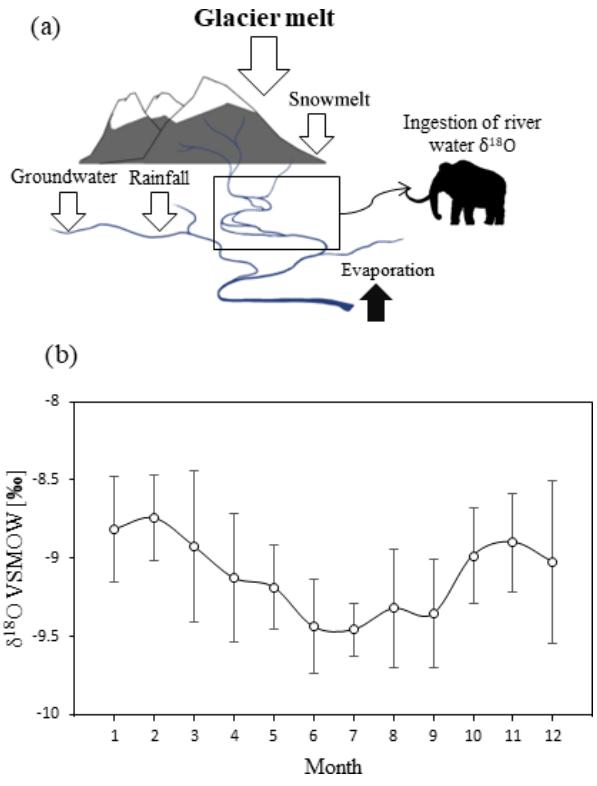

Figure 2. **(a)** A schematic diagram of mammoth water source model during the Late Pleistocene; **(b)** average modern monthly water $\delta^{18}O$ values of the Rhine River (Lobith, Netherlands, 2005–2010). Error bars represent standard deviation. Data collected from local IAEA stations and retrieved from https://nucleus.iaea.org/wiser/index.aspx (last access: 24 March 2022).

3 Methodology

3.1 Study location and materials

Three complete molar teeth (one M1 and two M3 molars) and one fragmentary molar of woolly mammoths (*Mammuthus primigenius*) were recovered from a gravel quarry called Hardtsee, which is located in Ubstadt-Weiher, Upper Rhine Graben, southwestern Germany (49.17694° N, 8.622163° E; Fig. 3). The quarry lake where the teeth were discovered is approximately 2 km east of the Rhine River, and gravel mining occurs underwater via dredging at controlled depths. The teeth were recovered from various depths between 5 and 15 m, and they stem from fluvial sediments that were predominantly transported to the Upper Rhine Graben by meltwater discharge from an upstream alpine glacier advance (Preusser et al., 2021). The enamel on the outermost surface was preserved with no indication of erosion, which suggests they were not likely transported over long distances. Therefore, we essentially interpret the Hardtsee location as the death location of the mammoths and the Rhine catchment as their primary water source. The teeth were radiocarbon dated, and the resulting ages fit into four different time windows during Marine Isotope Stage 3, approximately 43–34 ka cal BP (Table 1).

3.2 Analytical methods

A 1 mm cylindrical diamond-coated drill bit attached to a low speed hand drill and a state drill model were used to drill the enamel and collect its powder. Two sampling methods were applied. The first method was bulk drilling, which involves taking one sample from one enamel ridge by scraping down the entire enamel length, and only a thin layer (< 1 mm) of powder was collected. The second method is sequential sampling. For this, we drilled each enamel ridge by taking successive samples along a horizontal line perpendicular to the tooth height at a resolution between 1.5 and 2 mm, starting from the occlusal surface and moving downward (Fig. 4). Both methods were applied to all available enamel ridges of the four samples. We first used the drill bit to remove the outermost surface of all enamel ridges, followed by sequentially sampling the enamel, and finally we took one bulk sample from each enamel ridge in the same trench as the sequential sampling. The mass of each sample was approximately 15 mg.

We then conducted chemical pretreatment, following the protocol developed by Snoeck and Pellegrini (2015), which involves soaking the samples in acetic acid (1 M, buffered with sodium acetate, pH = 4.5) for 30 min and rinsing in distilled water before drying overnight at 40°C. Pretreated samples were analyzed using an Analytical Precision AP2003 continuous-flow stable-isotope ratio mass spectrometer at the SGEAS, University of Melbourne. Containers were first placed on a hot plate set to 70 °C. Then they were purged with ultrapure helium gas, followed by injection of 0.5–1 mL of 104 % orthophosphoric acid with syringes. Samples were left to react with the acid for 30 min, and the headspace CO_2 gas produced was introduced to the mass spectrometer for analysis. Results are presented in delta (δ) notation and in units of per mil (‰) in relation to the Vienna Pee Dee Belemnite (VPDB) standard. The AP2003 mass spectrometer analyzed both $\delta^{18}O$ and $\delta^{13}C$ values for each sample; however, our main focus is only the oxygen isotopic values in this study. Three inorganic standards, NEW1, NEW12, and NBS 18, were used to set the calibration scale. The analytical precision was approximately 0.12 ‰ for $\delta^{18}O$ and 0.08 ‰ for $\delta^{13}C$, which was the standard deviation calculated based on the replicate analysis of in-house standards.

3.3 Statistical analysis

The similarity of bulk and mean sequential values was first assessed by their offset. If the offset is less than the analytical precision of the mass spectrometer (0.12 ‰), the two values are considered the same, and *t* tests were also performed to examine the statistical differences between the bulk and mean sequential values in each tooth.

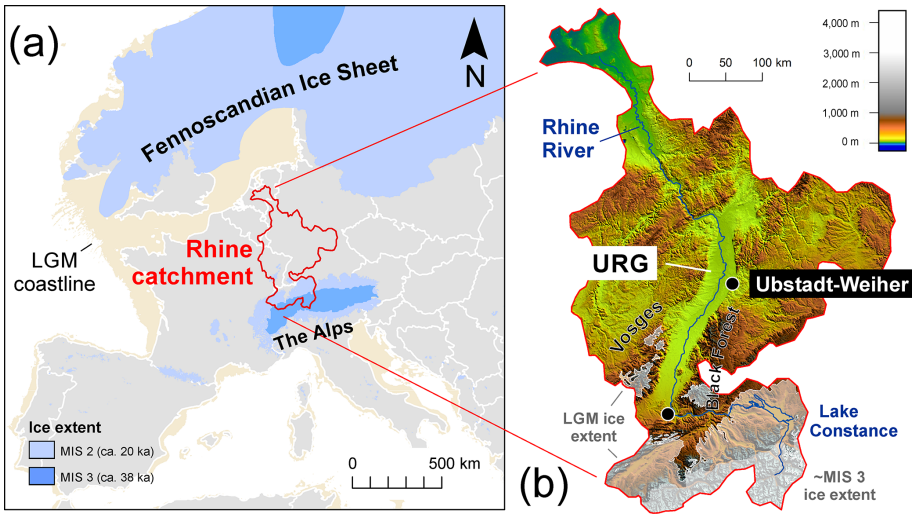

Figure 3. **(a)** Geographic context of the Rhine catchment during MIS 3 and MIS 2 (Ehlers et al., 2011; Hughes et al., 2015; Seguinot et al., 2018). **(b)** Topographic map of the Rhine catchment highlighting of study location site at Ubstadt-Weiher at a resolution of 15 arcsec (Tozer et al., 2019).

Table 1. Information on the mammoth teeth used in this study. Radiocarbon dating was undertaken at the Research School of Earth Science, Australian National University, and calibrated with Calib (http://calib.org/calib/calib.html, last access: 27 August 2020). Samples were dated to stadial/interstadial phases by comparing their ages with Greenland ice-core records (GISP2) (Grootes and Stuiver, 1999).

Sample name	Depth (m)	Radiocarbon dates (ka cal BP, median)	Radiocarbon dates (ka cal BP, 95 % CI)	Phase in MIS 3	No. of enamel ridges assessed
UW-1	5	33.7	34.6–32.7	Stadial	6
UW-2	10	36.4	38.0–34.7	Interstadial	10
UW-3	15	39.7	40.8–38.2	Interstadial	7
UW-3b	15	42.3	45.1–40.2	Uncertain	1

In addition to offsets, we also used a "modified seasonal method" to analyze where the bulk value sits in relation to the range of values from the sequential samples. This method is based on the season of mollusk collection method from Prendergast et al. (2016), in which four seasons can be differentiated from the sequential records by generating quartiles in the range of δ^{18}O values. However, in this study we applied this method not for reconstructing seasons; instead it is being adapted as a way of comparing the data distributions of bulk and sequential values. We differentiated the sequential δ^{18}O values from each enamel ridge into four quartiles with equal data distributions. Based on the Late Pleistocene hydrological model we built in Fig. 2a and by reference to seasonal variations in δ^{18}O values in the current Rhine River, we defined the lower quartile ($<$ 25th percentile) in the sequential results to reflect the warmest summer months when an increased amount of glacier meltwater was mixed in the river discharge; consequently, the upper quartile ($>$ 75th percentile) reflects the coldest winter months, and the middle quartiles (25–75th percentile) reflect intermediate environmental conditions during autumn or spring. Although this method can effectively analyze various paleoenvironmental aspects (e.g., seasonality and season of death) in the sequential records (Koch et al., 1989; Fisher and Fox, 2007; Prendergast and Schöne, 2017), it may be inappropriate for the comparison between bulk and sequential values due to two arguments. First, the bulk value is not from the same dataset as the sequential results, and consequently it has the possibility of falling outside the sequential data distribution. Also, the four seasons interpreted from the quartiles are based on the sequential δ^{18}O values within 1 year of records. One enamel ridge of a mammoth tooth may hold several either complete or incomplete years of records. The median and quartile values may skew when an incomplete year was recorded. For instance, if the enamel ridge contains 2.5 years of records, there are unequal numbers of warming and cooling seasons, which may skew the data distribution to one direction.

To address the two issues, this seasonal method was further modified, and we decided to calculate a "relative percentile" of bulk values compared to sequential data distribu-

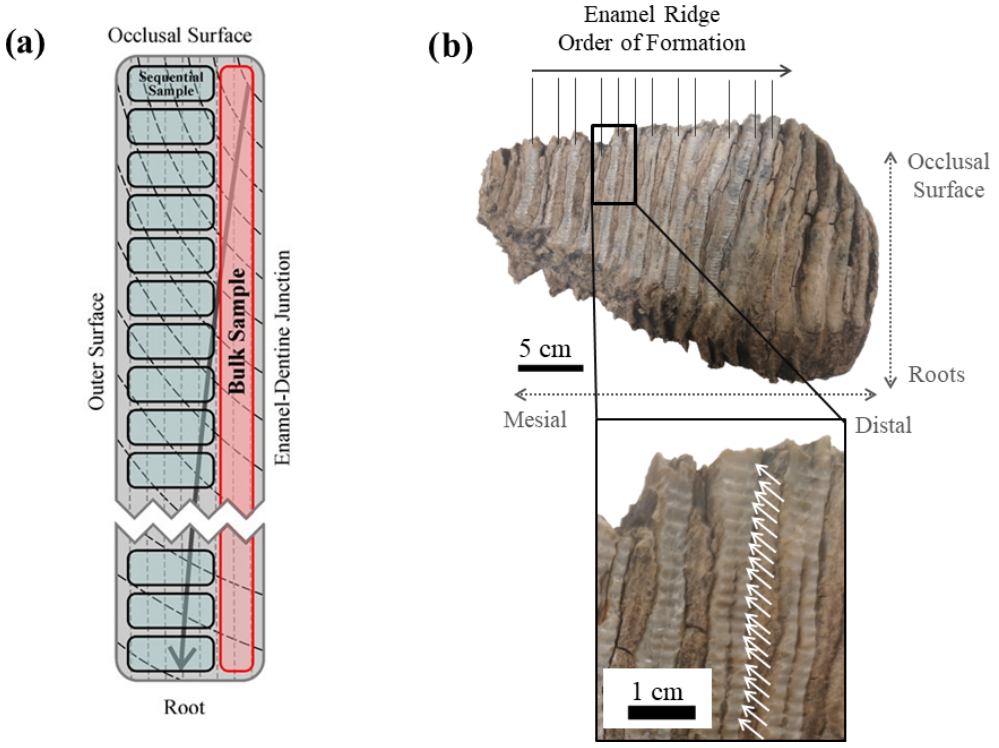

Figure 4. **(a)** A schematic diagram of an enamel section showing the difference between bulk and sequential sampling methods. Vertical dashed lines represent primary incremental lines of enamel, and black curves represent secondary incremental lines of enamel, with the arrow indicating the growth direction. **(b)** Photograph of sampled tooth UW-2 as an illustration of the sequential sampling technique. White arrows highlight the drilling spots.

tions with the following equation:

$$\text{Relative Percentile (\%)} = \frac{\text{Bulk Value} - \text{Min (Seq. Value)}}{\text{Max (Seq. Value)} - \text{Min (Seq. Value)}} \times 100.$$

In this equation, we defined the minimum and maximum sequential values along one enamel ridge to be between 0 % and 100 %, respectively, and this range was equally divided into 100 units. Within this range, we still divided the data into four quartiles. The bulk value is expected to fall within the middle quartiles, as the averaged signal over several years is unlikely to reflect environmental conditions during extreme summer or winter months.

4 Results

4.1 Data distribution

In total, 24 bulk and 1114 sequential samples were drilled out of 24 enamel ridges. The results for each enamel ridge are summarized in Table 2 and plotted in Fig. 5. In the sequential results, we removed the outliers with boxplots. The data distributions of each tooth were box-plotted separately, and values that are smaller than the 25th percentile minus 1.5 interquartile ranges and greater than the 75th percentile plus 1.5 interquartile ranges were considered as outliers and removed ($n = 16$). After removing outliers, the bulk $\delta^{18}O$ values range from -10.4 ‰ to -7.6 ‰, and sequential values are between -11.3 ‰ and -5.7 ‰. Both the bulk and sequential values for all teeth are significantly different to each other based on t tests ($p < 0.05$). The fragmentary molar UW-3b is excluded from bulk comparison since there is only one value.

For both bulk and average sequential values, more positive $\delta^{18}O$ values were found in teeth UW-2 and UW-3, which are dated to interstadials, compared to tooth UW-1, which is dated to a stadial period (Fig. 4a). Tooth UW-1 is also the youngest sample; therefore, the three complete molar teeth show progressively more negative mean $\delta^{18}O$ values from the oldest to the youngest between 39 and 33 ka cal BP. The bulk $\delta^{18}O$ value of UW-3b is more positive than the younger UW-1 and UW-2, and it is intermediate to those of UW-3. The mean sequential $\delta^{18}O$ value of UW-3b, however, is the most negative value among all four teeth.

4.2 Intra-enamel isotopic variations

The cyclicity of all enamel ridges was assessed to identify features of seasonal environmental changes. For UW-1, UW-2, and UW-3, the intra-tooth sequential $\delta^{18}O$ exhibits mul-

Table 2. The list of results of the study, including the length, number of identifiable years, and the bulk and sequential $\delta^{18}O$ values of all sampled enamel ridges (outliers removed).

	Enamel ridge	Length (mm)	No. of years identified	Bulk value (‰)	Seq. value mean (‰)	Offset (bulk seq. mean) (‰)	Seq. value min (‰)	Seq. value max (‰)	Relative percentile (%)
UW-1	1	136	5	−9.90	−9.27	−0.64	−10.46	−8.3	25.78
	2	150	6.5	−10.41	−9.39	−1.02	−10.55	−8.1	5.93
	3	150	8	−9.72	−9.25	−0.47	−10.44	−8.51	37.41
	4	160	8	−10.03	−9.23	−0.81	−10.12	−8.17	4.51
	5	152	9.5	−9.49	−9.46	−0.03	−10.29	−8.52	45.10
	6	146	7.5	−9.66	−9.35	−0.31	−10.32	−8.38	34.09
UW-2	1	32	2	−8.54	−7.88	−0.66	−8.9	−7.45	24.93
	2	42	1.5	−8.77	−8.09	−0.68	−8.67	−7.68	−10.06
	3	54	3	−8.64	−8.1	−0.54	−8.76	−7.43	9.01
	4	54	4	−8.70	−8.43	−0.28	−8.96	−7.9	24.23
	5	72	5	−8.50	−8.38	−0.12	−9.11	−7.54	39.01
	6	74	6	−8.36	−8.49	0.13	−8.98	−7.92	58.41
	7	80	6	−8.63	−8.24	−0.39	−9.22	−7.48	34.21
	8	84	6.5	−8.44	−8.29	−0.15	−9.14	−7.52	43.07
	9	92	8	−8.57	−8.33	−0.24	−9.12	−7.63	37.19
	10	100	8	−8.41	−8.61	0.20	−9.35	−7.88	63.88
UW-3	1	60	2.5	−8.31	−6.93	−1.38	−7.9	−6.03	−21.80
	2	78	3.5	−8.19	−6.98	−1.21	−7.63	−6.07	−36.28
	3	78	3.5	−8.50	−7.12	−1.38	−8.06	−6.03	−21.77
	4	82	3.5	−8.54	−7.28	−1.26	−8.4	−6.49	−7.20
	5	90	3.5	−7.86	−7.15	−0.71	−8.15	−6.1	14.17
	9	112	5	−8.19	−7.1693	−1.02	−8.17	−6	−1.06
	10	108	5	−7.63	−7.13	−0.50	−7.98	−6.31	20.56
UW-3b	1	37.5	NA	−8.25	−9.6	1.35	−11.29	−8.14	96.63

NA: not available.

tiple local maxima and minima along the entire ca. 100–150 mm of enamel length, and examples are plotted in Fig. 6. The data resemble cyclic oscillations, with the $\delta^{18}O$ values of maxima being approximately 0.8 ‰ to 1.1 ‰ higher than those of the minima. Among these three teeth, the sequential values of UW-3 show the clearest oscillations, with five complete cycles of similar incremental lengths identified. In teeth UW-1 and UW-2, however, the cyclicity is more difficult to identify, as both selected enamel ridges have a reduced amplitude of isotopic variation in the middle of the enamel ridge. The enamel ridge of the fragmentary molar UW-3b has the most difficult isotopic variation to interpret. Although we can identify one maximum and minimum (and potentially a second maximum), it is uncertain whether these data cover a full year of records considering the incremental length is only 37.5 mm. The number of cycles in each enamel ridge ranges from one to eight, and they are correlated to the incremental length of enamel ridges ($r^2 = 0.60$, $n = 23$), with longer enamel ridges generally containing more interpreted hydrological years.

4.3 Comparison of bulk and sequential values

Significant differences ($p < 0.05$) were detected between bulk and mean sequential $\delta^{18}O$ values in all complete teeth based on t tests (i.e., UW-1, UW-2, UW-3), with the difference varying from 0.03 ‰ to 1.35 ‰. One enamel ridge from UW-1 has a difference of less than 0.12 ‰. The differences of three enamel ridges from UW-2 are between 0.1 ‰ and 0.15 ‰. All other samples have differences greater than 0.2 ‰ (Table 2). Overall, the mean differences in the younger teeth UW-1 (0.54 ‰) and UW-2 (0.34 ‰) are smaller compared to the older UW-3 (1.06 ‰) and UW-3b (1.35 ‰). For all enamel ridges of teeth UW-1 and UW-3, the bulk values are more negative than the mean sequential values. The bulk values of most enamel ridges (8 out of 10) of UW-2 are more negative, and the other two are slightly more positive. The bulk value of UW-3b is 1.35 ‰ more positive than the sequential value, which is the greatest among all enamel ridges.

The relative percentile values were also analyzed and shown in Table 2 and Fig. 7. The bulk values of most enamel ridges of teeth UW-1 (4 out of 6) and UW-2 (6 out of 10) are located between the 25th and 75th percentiles within the mid-

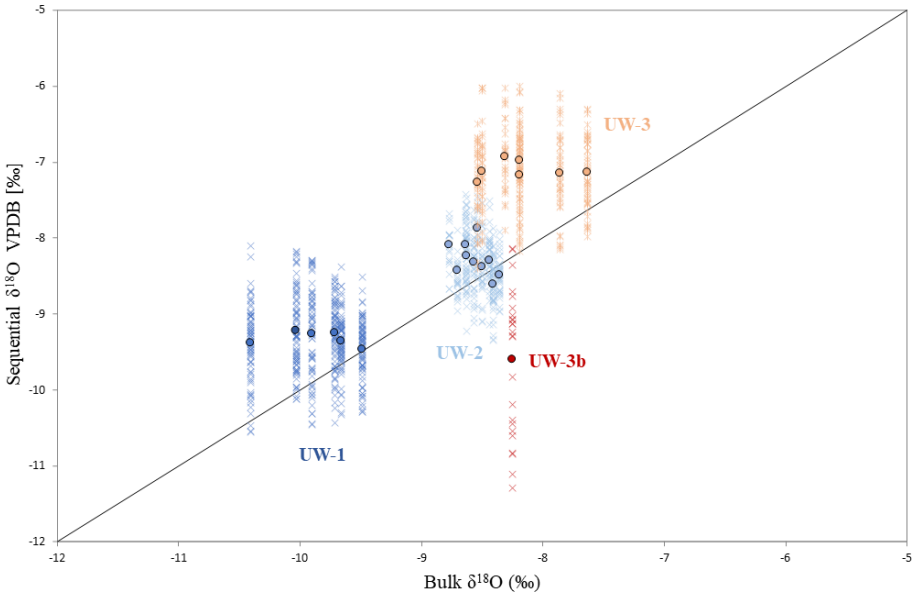

Figure 5. Data distribution of the four teeth and comparison between bulk and sequential results. Each cross represents the $\delta^{18}O$ value of one sequential spot, and dots are bulk (x axis) and averaged sequential (y axis) $\delta^{18}O$ values of different enamel ridges. The diagonal line represents data points for which bulk and sequential means are equal; if a dot is located above this line, the mean sequential $\delta^{18}O$ value of this enamel ridge is more positive than the bulk value, and vice versa.

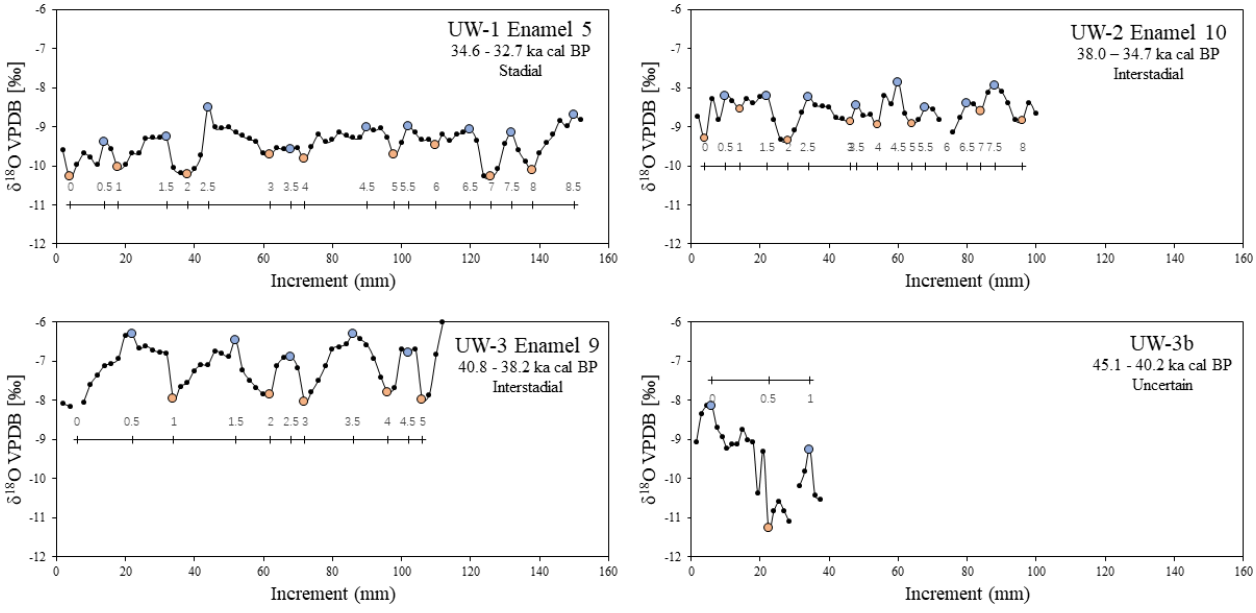

Figure 6. Examples of $\delta^{18}O$ variations along one enamel from each tooth with expected years. Local maxima (winter) and minima (summer) are highlighted with blue and orange dots, respectively.

dle quartile with the remaining values falling below the 25th percentile including one value for UW-2 being more negative than the minimal sequential value. The bulk values of all enamel ridges of tooth UW-3 are below the 25th percentile, with the majority (5 out if 7) being more negative than the minimal sequential value. The relative percentile of UW-3b is 96.3 %, the only data point above the 75th percentile.

5 Discussion

5.1 Sample preservation

It is essential to evaluate whether physical and chemical transformations of sample materials may lead to isotopic exchange and loss of primary isotopic signal (Keenan, 2016;

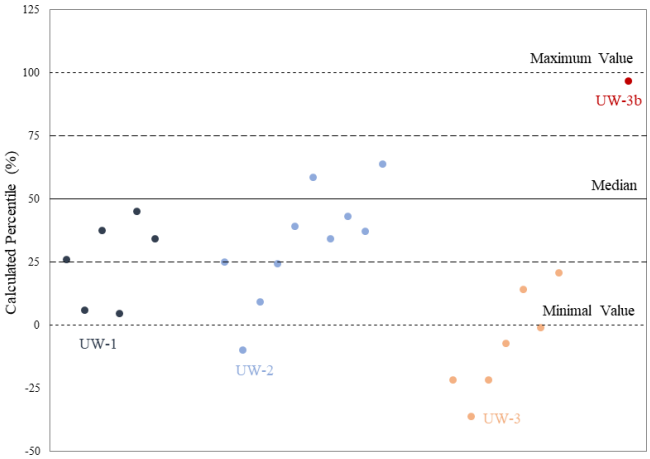

Figure 7. The plot of relative percentiles of bulk values from all the enamel ridges of the four teeth.

Goedert et al., 2016). The preservation condition of our mammoth teeth was assessed, and based on three pieces of evidence, at least part of their original materials seems to have been preserved. The first piece of evidence is the sequential $\delta^{18}O$ values which show variations that mimic seasonal patterns. The $\delta^{18}O$ values of all sequential samples would likely be homogenized if all material had been completely recrystallized (Metcalfe and Longstaffe, 2012; Goedert et al., 2016); therefore, this supports the point that at least some of the primary enamel material is preserved and still holds records of paleoenvironmental changes, but it is not a full proof. The carbon isotopic compositions, although not analyzed in detail in this study, provide additional evidence of primary material preservation. Carbon isotopes of herbivorous animals are incorporated from the vegetation they consumed (Arppe and Karhu, 2006; Kovács et al., 2012; Prendergast and Schöne, 2017), with the $\delta^{13}C$ values of animals which forage upon C_3 and C_4 plants to be -20 ‰ to -8 ‰ and from 0 ‰ to +5 ‰, respectively (Kohn and Cerling, 2002). The $\delta^{13}C$ values of the four teeth range between -13.13 ‰ and -11.21 ‰ (Liu, 2020), which falls within the C_3 foraging range, and this agrees with mammoth dietary behavior observed from their fecal remains (Kirillova et al., 2016). Therefore, both oxygen and carbon isotopic results suggest that at least some primary isotopic signal is preserved. In addition, we drilled additional enamel powder from each tooth, and the powder was sub-divided into pretreated and non-pretreated groups. The isotopic values of both groups were tested, and no statistically significant differences were detected between the $\delta^{18}O$ values of these two groups.

Although there is still a possibility of diagenetic alteration, all samples were pretreated with acetic acid to remove any secondary carbonates. Additionally, due to its low porosity and low organic contents, tooth enamel is one of the most resistant materials to diagenetic alteration and is capable of preserving primary isotopic signals for millions of years. Based on all the above considerations, we assume our mammoth teeth have at least partially preserved their original isotopic signals, and the acquired $\delta^{18}O$ values reflect their living environmental properties.

5.2 Comparison between bulk and mean sequential values

Differences between bulk and sequential results are present in all four mammoth teeth, with the bulk values being generally more negative than the mean sequential values. There is only one exception, which is the enamel ridge of UW-3b, with the bulk value being 1.35 ‰ more positive. This may be caused by the absence of a complete annual cycle, as only 37.5 mm of material was sampled. The incomplete hydrological year in the records of UW-3b could also cause the data distribution of sequential samples to taper. Older tooth samples also have generally greater offsets. Only one enamel ridge from UW-1 has a difference less than 0.12 ‰, which is within the precision of the mass spectrometer. Therefore, the bulk and sequential values for this sample can be considered as equal. Three enamel ridges from UW-2 show slightly greater offsets between 0.12 ‰ and 0.15 ‰, which may still be considered as similar. Most other enamel ridges in teeth UW-1 and UW-2 ($n = 11$) have offsets between 0.2 ‰ and 0.81 ‰, with only one enamel ridge from UW-1 having a difference value over 1 ‰. All enamel ridges from teeth UW-3 and UW-3b have difference values of at least 0.5 ‰, and most of them (6 out of 8) are greater than 1 ‰. The relative percentiles for all UW-3b enamel ridges are located in the lower quartile, while most enamel ridges from teeth UW-1 and UW-2 are within the middle quartile. However, even if some samples are located within the middle quartile, most of them in UW-2 and all samples in UW-1 are more negative than the median. The uneven distributions suggest that bulk and sequential samples reflect different environmental conditions in these two teeth.

One explanation for the difference is the geometry of incremental lines. Our two sampling methods each predominantly cover one growth direction: a bulk sample covering the entire enamel height with only a thin layer of enamel collected, whereas each sequential sample includes a deeper sampling pit covering the majority of the enamel thickness but with only a small proportion of the enamel height. Neither of the two methods followed the exact enamel growth direction: the incremental lines of mammoth secondary enamel material are inclined at an angle of 55–60° to the enamel-dentine junction (EDJ). The inconsistency between drilling orientation and enamel growth direction can cause "damping" of the isotopic signal due to time averaging (Passey et al., 2005; Metcalfe and Longstaffe, 2012). A simplified model is presented in Fig. 8 to illustrate how the angle of incremental lines can cause potential isotopic damping. In this model, although we assumed the four seasons in a year

have the same incremental distance in a section of the enamel ridge, the seasonal distribution in the bulk sample is uneven with an incomplete representation of increments formed during the last summer and autumn. The sequential samples have the same issue, with the first autumn incompletely represented in our model. Therefore, this may result in bulk results more similar to the isotopic signals near the occlusal surface and mean sequential values more similar to those near the root. However, the seasonal distribution of the combination of all sequential samples is slightly more even as they occupy more enamel thickness (and much more enamel material overall). If only one method is applied and it covers the entire enamel thickness, then the obtained samples would theoretically have even distributions of the four seasons.

This problem may be more significant in enamel ridges of shorter lengths. In Fig. 9, we plotted the difference values against the incremental lengths of each enamel ridge. Teeth UW-2 and UW-3 have enamel ridges of different lengths, varying from 32 to 112 mm, and both of them show strong negative relationships between enamel length and difference value. No correlation was detected from the enamel ridges of UW-1. This could be due to their similar lengths (136–160 mm). Inter-tooth comparison also indicates that enamel ridges with longer lengths generally have smaller differences between bulk and mean sequential values: greater difference values (> 1 ‰) predominantly occurred in enamel ridges less than 100 mm in length. When the bulk sample recorded uneven distributions of seasons, it mainly occurred at the apex and root of the enamel (Fig. 8); therefore, a longer enamel ridge with more annual records in the middle would theoretically reduce this impact. However, despite the correlation between the offsets and incremental lengths, the primary deciding factor of the offsets is still inter-tooth difference given that (1) the inter-tooth difference of values is greater than intra-tooth variations especially between UW-2 and UW-3 and (2) the offset values of UW-1 have a variation of nearly 1 ‰, although all of its enamel ridges are more than 100 mm.

The geometry of incremental lines may have another consequence, which is reduced seasonal amplitude in sequential isotopic records (Passey et al., 2005). In Fig. 8, one sequential sample may contain increments formed during more than one season, especially those formed during seasonal transitions. In fact, oxygen and carbon isotopic cyclicity has been detected from the EDJ to the outer surface, indicating that there was tooth growth through the enamel thickness, although the growth rate was much slower compared to the growth along tooth height. Therefore, each sequential sample obtained in this study may hold an averaged isotopic signal of one or multiple seasons, and the isotopic variation in environmental water would have potentially greater amplitude.

Another possible explanation for the difference between bulk and sequential results is that the two methods collect enamel formed during different times. Reade et al. (2015) sampled the tooth enamel of Barbary sheep (*Ammotragus lervia*) with both bulk and sequential sampling strategies. They also found different bulk and mean sequential $\delta^{18}O$ values. The main difference between the two studies is that the locations of the two sampling methods are the opposite: their bulk samples were taken before the sequential samples and therefore are closer to the outer surface. They proposed an explanation, which is that the bulk samples in their study contain a greater proportion of enamel mineralized later because the enamel mineralization process at their sampling locations (outer surface) is slower than the sequential samples obtained near the EDJ (Suga, 1979, 1982). In our case, the bulk samples are then expected to contain more enamel mineralized earlier, and this argument agrees with the impact caused by the angle of incremental lines (Fig. 8). Therefore, there could be an offset in the formation time of the material collected by the two methods, and in turn this caused differences in isotopic compositions due to different time averaging in the samples.

A third explanation is the mixture of primary and secondary enamel increments in the samples. We primarily sampled the secondary incremental lines in the teeth. However, there was also a primary mineralization phase in mammoth tooth formation, although it only took up 20 %–30 % of the total enamel mass (Passey and Cerling, 2002; Passey et al., 2005). Primary mineralization forms vertical incremental lines under microscopic view, indicating the material grows from the EDJ to the outer surface (Metcalfe and Longstaffe, 2012). Therefore, the thin layer of enamel powder collected by the bulk sampling method may also contain primary mineralized material formed during a short period of time. This period of time could be during any season; consequently, if the collected primary increments were formed during extreme summer or winter months, the mixture of primary and secondary enamel material might skew the isotopic signal to one direction. This could be the cause of the bulk values of several enamel ridges falling outside the data distribution of sequential values, since primary increments were formed during a different time to the secondary increments. If the collected primary increments were formed during spring or autumn months with the isotopic signal in environmental water closer to the annual average, there is less impact from primary material, and the bulk and mean sequential values would be more similar. The sequential samples again are less influenced by the primary mineralization, as more enamel thickness is sampled, covering primary increments formed during a longer period of time and maybe including multiple seasons.

5.3 Comparison of sampling methods

The bulk and mean sequential results obtained in this study show both similar and different values. Here we discuss how these differences may help us decide the optimal sampling methods for future research. The bulk samples, at least those obtained through the method applied in this study, do not always reflect an averaged isotopic signal at decadal scales.

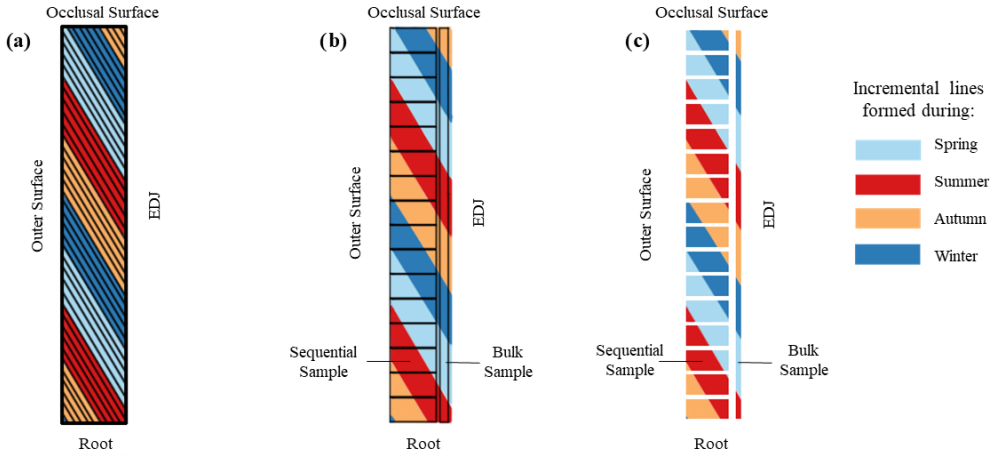

Figure 8. A simplified model showing secondary incremental lines formed during different seasons and the sampling spots. **(a)** A schematic diagram of an enamel section with the assumption of the four seasons having equal incremental lengths, **(b)** sampling spots for both bulk and sequential sampling methods, and **(c)** the duration and distribution of different seasons included in each sample.

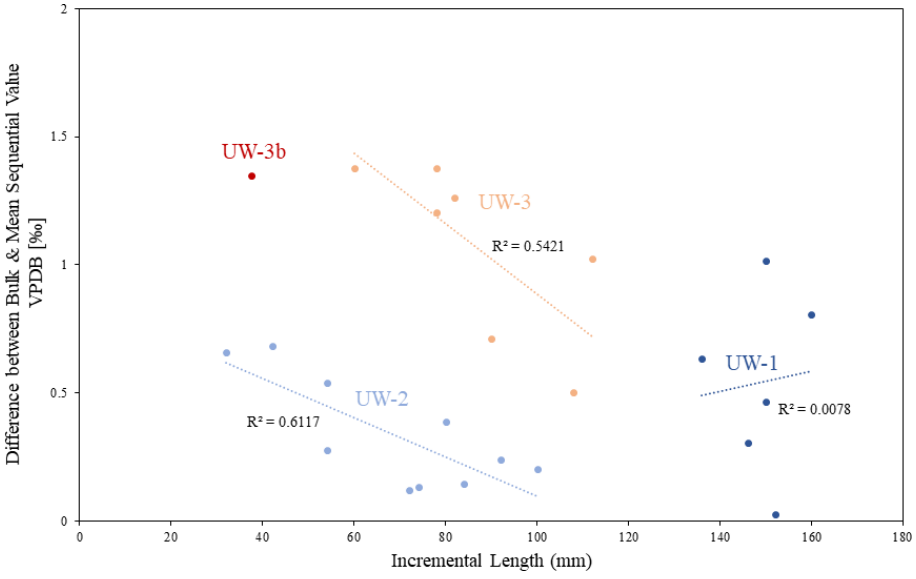

Figure 9. Plot of difference values against incremental lengths of all enamel ridges.

Instead, it is more likely a reflection of either extreme summer/winter environmental conditions or spring/autumn isotopic compositions which are close to the annual mean value. In comparison, the sequential method is less influenced by the primary increments and the geometry of secondary incremental lines. We do not suggest the sequential sampling method itself can more accurately reflect paleoenvironmental conditions. The main reason it does in this study is that with our drilling method, the combination of all sequential samples covers the entire enamel length and the majority of enamel thickness, which included increments formed during a longer period of time than the thin layer of the bulk sample. Reade et al. (2015) suggested sampling the entire tooth height, as well as the enamel thickness, to reduce isotopic damping caused by the enamel growth pattern. We also recommend that future studies which involve surface sampling on mammoth teeth drill all available enamel material in both directions, regardless of which sampling method will be applied.

However, this means we can only apply one method to each enamel ridge. We suggest the sequential sampling method is more optimal because it provides not only an averaged multi-annual-scale isotopic composition (mean sequential value) but more importantly a time series of high-

resolution paleoenvironmental records. Such records are crucial for understanding the highly variable climatic conditions of the Late Pleistocene and deciphering human–environmental interactions (Denton et al., 2005; Bradtmöller et al., 2012; Prendergast et al., 2018). In addition, the sequential $\delta^{18}O$ variations that reflect seasonal environmental changes can also indicate whether there is a complete annual cycle, and if so, how many of them are recorded in each enamel ridge. A fragmentary enamel ridge without one annual cycle may not provide an accurate annual mean $\delta^{18}O$ value, so the temporal duration of the record is unsuitable for the bulk sampling method. This also indicates that the completeness and size of mammoth teeth should be important criteria considered during sample selection. Mammoth teeth with complete and long enamel ridges should have the highest priority because long enamel ridges generally contain more annual cycles of $\delta^{18}O$ oscillations. Although offsets between bulk and mean sequential values may still be detected in long ridges, the difference value is likely smaller than those of short enamel ridges, as the long sequence of isotopic records reduces the impact of uneven seasonal distributions in both bulk and sequential samples.

Although we recommend using complete and large-sized mammoth molar teeth as the preferred study material, we are aware that such samples are not always available at certain sites. Mammoth teeth may have been weathered and transported by surrounding environments, and consequently they may break into fragments and lose enamel thickness through erosion. Due to this limitation, it is unclear which part of the enamel and how much enamel thickness and tooth height were sampled in many past stable-isotope studies on mammoth teeth, especially those which employed bulk sampling methods. Given that the bulk values in some of our samples fall outside the range of sequential values, we recommend only comparing results obtained from sequential sampling methods with other sequential sampling studies. If results obtained from two different methods are compared directly, the potential isotopic offset between bulk and sequential samples may be falsely concluded to reflect different environmental conditions.

5.4 Limitations and future research

The main limitation of this study is the different locations of the two sampling methods. Although the sampling spots are from the same trenches, bulk and sequential samples are powder from different parts of the enamel ridge. A possible improvement in further studies is to use only part of the powder in each sequential sample and combine all the remaining powder along one enamel ridge to form the bulk sample. In this case, enamel powder taken from the two methods would have covered roughly the same incremental length of enamel thickness and tooth height. Another possible improvement is applying the two methods on the enamel ridges at two sides of the same molar plate. However, this method assumes that enamel ridges on both sides grow simultaneously. Nonetheless, this study has provided insights into the degree to which we can compare past studies, as it is likely that different parts of enamel ridges were sampled in different studies, and some studies might have only sampled a thin layer of enamel material as the bulk samples.

Another limitation is that we considered primary enamel mineralization as a factor that caused differences in bulk and sequential results, but we are uncertain about the proportion of primary mineralization collected in each sample and its degree of impact. These questions require further investigations into mammoth dental morphology and separate isotopic analysis of primary and secondary incremental materials.

In addition, although the sequential samples provide high-resolution records of likely seasonal environmental changes, they are not perfect reflections of paleoenvironments. The geometry of secondary incremental lines potentially caused several different seasons recorded in one sequential sample, averaging the isotopic signal and in turn reducing the amplitude of isotopic oscillations. In future sequential sampling of mammoth teeth, we may section the teeth to expose the enamel thickness, identify incremental features under microscopic views so that we can perform spot-drilling on each incremental line to avoid seasonal averaging.

6 Conclusion

We applied both bulk and sequential sampling methods to mammoth enamel and compared the results. Both similar and different $\delta^{18}O$ values between bulk and mean sequential results were discovered, and in most samples, they are different, with the bulk samples having more negative $\delta^{18}O$ values. Multiple potential factors might have jointly caused the offsets, including the geometry of secondary incremental lines, the mixture of primary increments, and different periods of time formation near the EDJ and outer surface. In this study, the mean sequential values may be more accurate reflections of decadal-scale paleoenvironmental conditions because their samples include most material in both tooth height and enamel thickness direction. A thin layer of enamel material collected by the bulk sampling method may have uneven distributions of different seasons, and consequently the $\delta^{18}O$ values may reflect either an annual average or conditions in only a certain season. Choosing long enamel ridges that contain more annual cycles as study materials may reduce the impact of uneven seasonal distribution caused by incremental line geometry. Therefore, we recommend that future isotopic analysis on mammoth teeth selects complete and large-sized samples and drills the entire tooth height and enamel thickness if possible. Considering that the sampling locations are unknown in many past studies, a cross-method data comparison is not recommended.

We also effectively obtained high-resolution paleoenvironmental records of sub-seasonal resolution. These records

hold the potential of reconstructing paleo-climate and paleo-hydrology for various aspects, such as seasonality and inter-annual differences, in future studies. However, we must be aware that the amplitude of isotopic signal obtained from this sequential sampling method might be reduced, since the drilling direction has an angle against the incremental lines so that enamel materials formed during more than one season could be mixed in each sample. This issue may be improved by combining the sequential sampling method with micro-scopic analysis on mammoth dental morphology to achieve spot-drilling on each incremental line in future research.

Data availability. The data that support the findings of this study will be uploaded to the PANGAEA database and be open to other researchers in the near future.

Author contributions. The research idea was conceived by JHM and AP; sample acquisition was carried out by JHM; experiment planning was carried out by ZL, AP, and JHM; laboratory work was carried out by ZL; isotopic data processing was carried out by RD; data analysis and interpretation were carried out by ZL, AP, and JHM; ZL drafted the manuscript. All co-authors reviewed and made inputs to the manuscript.

Competing interests. At least one of the (co-)authors is a member of the editorial board of *E&G Quaternary Science Journal*. The peer-review process was guided by an independent editor, and the authors also have no other competing interests to declare.

Disclaimer. Publisher's note: Copernicus Publications remains neutral with regard to jurisdictional claims in published maps and institutional affiliations.

Special issue statement. This article is part of the special issue "Quaternary research from and inspired by the first virtual DEUQUA conference". It is a result of the vDEUQUA2021 online conference in September/October 2021.

Acknowledgements. We would like to thank Frank Kiesewetter from the Ubstadt-Weiher gravel quarry for collecting and providing the mammoth teeth for this research, and we thank Rachel Wood from Australian National University for undertaking the radiocarbon dating of the samples. We are also grateful for Niels de Winter and another anonymous reviewer for providing valuable feedback.

Review statement. This paper was edited by Christian Zeeden and reviewed by Niels de Winter and one anonymous referee.

References

Arppe, L. M. and Karhu, J. A.: Implications for the Late Pleistocene climate in Finland and adjacent areas from the isotopic composition of mammoth skeletal remains, Palaeogeogr. Palaeocl., 231, 322–330, https://doi.org/10.1016/j.palaeo.2005.08.007, 2006.

Ayliffe, L. K., Lister, A. M., and Chivas, A. R.: The preservation of glacial-interglacial climatic signatures in the oxygen isotopes of elephant skeletal phosphate, Palaeogeogr. Palaeocl., 99, 179–191, https://doi.org/10.1016/0031-0182(92)90014-V, 1992.

Bedaso, Z. and Wu, S.-Y.: Linking precipitation and groundwater isotopes in Ethiopia – Implications from local meteoric water lines and isoscapes, J. Hydrol., 596, 126074, https://doi.org/10.1016/j.jhydrol.2021.126074, 2021.

Benson, L. V. and Paillet, F.: HIBAL: A hydrologic-isotopic-balance model for application to paleolake systems, Quaternary Sci. Rev., 21, 1521–1539, https://doi.org/10.1016/S0277-3791(01)00094-4, 2002.

Bradtmöller, M., Pastoors, A., Weninger, B., and Weniger, G.-C.: The repeated replacement model – Rapid climate change and population dynamics in Late Pleistocene Europe, Quatern. Int., 247, 38–49, https://doi.org/10.1016/j.quaint.2010.10.015, 2012.

Dansgaard, W.: Stable isotopes in precipitation, Tellus, 16, 436–468, https://doi.org/10.3402/tellusa.v16i4.8993, 1964.

Denton, G., Alley, R., Comer, G., and Broecker, W.: The role of seasonality in abrupt climate change, Quaternary Sci. Rev., 24, 1159–1182, https://doi.org/10.1016/j.quascirev.2004.12.002, 2005.

Ehlers, J., Gibbard, P. L., and Hughes, P. D. (Eds): Quaternary Glaciations – Extent and Chronology: A Closer Look, Elsevier, ISBN: 9780444534477, 2011.

Ferretti, M. P.: Structure and evolution of mammoth molar enamel, Acta Palaeontol. Pol., 48, 383–396, 2003.

Fisher, D. C. and Fox, D. L.: Season of death of the Dent mammoths distinguishing single from multiple mortality events, in: Frontiers in Colorado Paleoindian Archaeology: From the Dent Site to the Rocky Mountains, University Press of Colorado, 123–153, ISBN: 9781607323549, 2007.

Fricke, H. C. and O'Neil, J. R.: Inter- and intra-tooth variation in the oxygen isotope composition of mammalian tooth enamel phosphate: implications for palaeoclimatological and palaeobiological research, Palaeogeogr. Palaeocl., 126, 91–99, https://doi.org/10.1016/S0031-0182(96)00072-7, 1996.

Genoni, L., Iacumin, P., Nikolaev, V., Gribchenko, Yu., and Longinelli, A.: Oxygen isotope measurements of mammoth and reindeer skeletal remains: an archive of Late Pleistocene environmental conditions in Eurasian Arctic, Earth Planet. Sc. Lett., 160, 587–592, https://doi.org/10.1016/S0012-821X(98)00113-7, 1998.

Goedert, J., Amiot, R., Boudad, L., Buffetaut, E., Fourel, F., Godefroit, P., Kusuhashi, N., Suteethorn, V., Tong, H., Watabe, M., and Lécuyer, C.: Preliminary investigation of seasonal patterns recorded in the oxygen isotope compositions of theropod dinosaur tooth enamel, PALAIOS, 31, 10–19, https://doi.org/10.2110/palo.2015.018, 2016.

Grootes, P. M. and Stuiver, M.: GISP2 Oxygen Isotope Data, PANGAEA [dataset], https://doi.org/10.1594/PANGAEA.56094, 1999.

Hoppe, K. A.: Late Pleistocene mammoth herd structure, migration patterns, and Clovis hunting strategies inferred from isotopic analyses of multiple death assemblages, Paleobiology, 30, 129–145, https://doi.org/10.1666/0094-8373(2004)030<0129:LPMHSM>2.0.CO;2, 2004.

Hughes, A. L., Gyllencreutz, R., Lohne, Ø. S., Mangerud, J., and Svendsen, J. I.: DATED-1: compilation of dates and time-slice reconstruction of the build-up and retreat of the last Eurasian (British-Irish, Scandinavian, Svalbard-Barents-Kara Seas) Ice Sheets 40-10 ka, PANGAEA [dataset], https://doi.org/10.1594/PANGAEA.848117, 2015.

Iacumin, P., Di Matteo, A., Nikolaev, V., and Kuznetsova, T. V.: Climate information from C, N and O stable isotope analyses of mammoth bones from northern Siberia, Quatern. Int., 212, 206–212, https://doi.org/10.1016/j.quaint.2009.10.009, 2010.

Keenan, S. W.: From bone to fossil: A review of the diagenesis of bioapatite, Am. Mineral., 101, 1943–1951, https://doi.org/10.2138/am-2016-5737, 2016.

Kirillova, I. V., Argant, J., Lapteva, E. G., Korona, O. M., van der Plicht, J., Zinovyev, E. V., Kotov, A. A., Chernova, O. F., Fadeeva, E. O., Baturina, O. A., Kabilov, M. R., Shidlovskiy, F. K., and Zanina, O. G.: The diet and environment of mammoths in North-East Russia reconstructed from the contents of their feces, Quatern. Int., 406, 147–161, https://doi.org/10.1016/j.quaint.2015.11.002, 2016.

Koch, P. L., Fisher, D. C., and Dettman, D.: Oxygen isotope variation in the tusks of extinct proboscideans: A measure of season of death and seasonality, Geology, 17, 515–519, https://doi.org/10.1130/0091-7613(1989)017<0515:OIVITT>2.3.CO;2, 1989.

Kohn, M. J. and Cerling, T. E.: Stable Isotope Compositions of Biological Apatite, Rev. Mineral. Geochem., 48, 455–488, https://doi.org/10.2138/rmg.2002.48.12, 2002.

Kovács, J., Moravcová, M., Újvári, G., and Pintér, A. G.: Reconstructing the paleoenvironment of East Central Europe in the Late Pleistocene using the oxygen and carbon isotopic signal of tooth in large mammal remains, Quatern. Int., 276–277, 145–154, https://doi.org/10.1016/j.quaint.2012.04.009, 2012.

Lister, A. and Bahn, P.: Mammoths: Giants of the Ice Age Hardcover – 15 November 2007, University of California Press, ISBN: 0520253191, 2007.

Liu, Z.: Reconstruction of Paleo-Environments in Southern Germany during the Last Glacial Maximum with Mammoth Teeth, Honors thesis, School of Geography, Earth and Atmospheric Sciences, University of Melbourne, Australia, https://doi.org/10.13140/RG.2.2.32020.63361, 147 pp., 2020.

Longinelli, A.: Oxygen isotopes in mammal bone phosphate: A new tool for paleohydrological and paleoclimatological research?, Geochim. Cosmochim. Ac., 48, 385–390, https://doi.org/10.1016/0016-7037(84)90259-X, 1984.

Luz, B., Kolodny, Y., and Horowitz, M.: Fractionation of oxygen isotopes between mammalian bone-phosphate and environmental drinking water, Geochim. Cosmochim. Ac., 48, 1689–1693, https://doi.org/10.1016/0016-7037(84)90338-7, 1984.

Maschenko, E. N.: Individual development, biology and evolution of the woolly mammoth, Cranium, 19, 4–120, 2002.

Metcalfe, J. Z. and Longstaffe, F. J.: Mammoth tooth enamel growth rates inferred from stable isotope analysis and histology, Quaternary Res., 77, 424–432, https://doi.org/10.1016/j.yqres.2012.02.002, 2012.

Miller, J. H., Fisher, D. C., Crowley, B. E., Secord, R., and Konomi, B. A.: Male mastodon landscape use changed with maturation (late Pleistocene, North America), P. Natl. Acad. Sci. USA, 119, e2118329119, https://doi.org/10.1073/pnas.2118329119, 2022.

Passey, B. H. and Cerling, T. E.: Tooth enamel mineralization in ungulates: Implications for recovering a primary isotopic time-series, Geochim. Cosmochim. Ac., 66, 3225–3234, https://doi.org/10.1016/S0016-7037(02)00933-X, 2002.

Passey, B. H., Cerling, T. E., Schuster, G. T., Robinson, T. F., Roeder, B. L., and Krueger, S. K.: Inverse methods for estimating primary input signals from time-averaged isotope profiles, Geochim. Cosmochim. Ac., 69, 4101–4116, https://doi.org/10.1016/j.gca.2004.12.002, 2005.

Prendergast, A. L. and Schöne, B. R.: Oxygen isotopes from limpet shells: Implications for palaeothermometry and seasonal shellfish foraging studies in the Mediterranean, Palaeogeogr. Palaeocl., 484, 33–47, https://doi.org/10.1016/j.palaeo.2017.03.007, 2017.

Prendergast, A. L., Stevens, R. E., O'Connell, T. C., Fadlalak, A., Touati, M., al-Mzeine, A., Schöne, B. R., Hunt, C. O., and Barker, G.: Changing patterns of eastern Mediterranean shellfish exploitation in the Late Glacial and Early Holocene: Oxygen isotope evidence from gastropod in Epipaleolithic to Neolithic human occupation layers at the Haua Fteah cave, Libya, Quatern. Int., 407, 80–93, https://doi.org/10.1016/j.quaint.2015.09.035, 2016.

Prendergast, A. L., Pryor, A. J. E., Reade, H., and Stevens, R. E.: Seasonal records of palaeoenvironmental change and resource use from archaeological assemblages, J. Archaeol. Sci. Rep., 21, 1191–1197, https://doi.org/10.1016/j.jasrep.2018.08.006, 2018.

Preusser, F., Büschelberger, M., Kemna, H. A., Miocic, J., Mueller, D., and May, J.-H.: Exploring possible links between Quaternary aggradation in the Upper Rhine Graben and the glaciation history of northern Switzerland, Int. J. Earth Sci., 110, 1827–1846, https://doi.org/10.1007/s00531-021-02043-7, 2021.

Pryor, A. J. E., O'Connell, T. C., Wojtal, P., Krzemińska, A., and Stevens, R. E.: Investigating climate at the Upper Palaeolithic site of Kraków Spadzista Street (B), Poland, using oxygen isotopes, Quatern. Int., 294, 108–119, https://doi.org/10.1016/j.quaint.2011.09.027, 2013.

Reade, H., Stevens, R. E., Barker, G., and O'Connell, T. C.: Tooth enamel sampling strategies for stable isotope analysis: Potential problems in cross-method data comparisons, Chem. Geol., 404, 126–135, https://doi.org/10.1016/j.chemgeo.2015.03.026, 2015.

Rozanski, K., Froehlich, K., and Mook, W. G.: Environmental isotopes in the hydrological cycle: principles and applications, IHP-V, Technical Documents in Hydrology, No. 39, vol. III: Surface water, UNESCO, Paris, 2001.

Seguinot, J., Ivy-Ochs, S., Jouvet, G., Huss, M., Funk, M., and Preusser, F.: Modelling last glacial cycle ice dynamics in the Alps, The Cryosphere, 12, 3265–3285, https://doi.org/10.5194/tc-12-3265-2018, 2018.

Sharp, Z. D. and Cerling, T. E.: Fossil isotope records of seasonal climate and ecology: Straight from the horse's mouth, Geology, 26, 219–222, https://doi.org/10.1130/0091-7613(1998)026<0219:FIROSC>2.3.CO;2, 1998.

Smith, C. E.: Cellular and Chemical Events During Enamel Maturation, Crit. Rev. Oral Biol. M., 9, 128–161, https://doi.org/10.1177/10454411980090020101, 1998.

Smith, T. M. and Tafforeau, P.: New visions of dental tissue research: tooth development, chemistry, and structure, Evol. Anthropol., 17, 213–226, https://doi.org/10.1002/evan.20176, 2008.

Snoeck, C. and Pellegrini, M.: Comparing bioapatite carbonate pretreatments for isotopic measurements: Part 1–Impact on structure and chemical composition, Chem. Geol., 417, 394–403, https://doi.org/10.1016/j.chemgeo.2015.10.004, 2015.

Suga, S.: Comparative Histology of Progressive Mineralization Pattern of Developing Incisor Enamel of Rodents, J. Dent. Res., 58, 1025–1026, https://doi.org/10.1177/00220345790580021401l, 1979.

Suga, S.: Progressive mineralization pattern of developing enamel during the maturation stage, J. Dent. Res., 61, 1532–1542, 1982.

Theakstone, W. H.: Oxygen isotopes in glacier-river water, Austre Okstindbreen, Okstindan, Norway, J. Glaciol., 49, 282–298, https://doi.org/10.3189/172756503781830700, 2003.

Tozer, B., Sandwell, D. T., Smith, W. H. F., Olson, C., Beale, R., and Wessel, P.: Global Bathymetry and Topography at 15 Arc Sec: SRTM15+, OpenTopography [data set], https://doi.org/10.5069/G92R3PT9, 2019.

Tütken, T., Furrer, H., and Vennemann, T. W.: Stable isotope compositions of mammoth teeth from Niederweningen, Switzerland: Implications for the Late Pleistocene climate, environment, and diet, Quatern. Int., 164–165, 139–150, https://doi.org/10.1016/j.quaint.2006.09.004, 2007.

Ukkonen, P., Arppe, L., Houmark-Nielsen, M., Kjær, K. H., and Karhu, J. A.: MIS 3 mammoth remains from Sweden–implications for faunal history, palaeoclimate and glaciation chronology, Quaternary Sci. Rev., 26, 3081–3098, https://doi.org/10.1016/j.quascirev.2007.06.021, 2007.

Widga, C., Hodgins, G., Kolis, K., Lengyel, S., Saunders, J., Walker, J. D., and Wanamaker, A. D.: Life histories and niche dynamics in late Quaternary proboscideans from midwestern North America, Quaternary Res., 100, 224–239, https://doi.org/10.1017/qua.2020.85, 2021.

Wooller, M. J., Bataille, C., Druckenmiller, P., Erickson, G. M., Groves, P., Haubenstock, N., Howe, T., Irrgeher, J., Mann, D., Moon, K., Potter, B. A., Prohaska, T., Rasic, J., Reuther, J., Shapiro, B., Spaleta, K. J., and Willis, A. D.: Lifetime mobility of an Arctic woolly mammoth, Science, 373, 806–808, https://doi.org/10.1126/science.abg1134, 2021.

Yeh, H.-F. and Lee, J.-W.: Stable Hydrogen and Oxygen Isotopes for Groundwater Sources of Penghu Islands, Taiwan, Geosciences, 8, 84, https://doi.org/10.3390/geosciences8030084, 2018.

E&G Quaternary Sci. J., 71, 243–247, 2022
https://doi.org/10.5194/egqsj-71-243-2022

Open Access E&G Quaternary Science Journal

Express report

A new Google Earth Engine tool for spaceborne detection of buried palaeogeographical features – examples from the Nile Delta (Egypt)

Tobias Ullmann[1,2], **Eric Möller**[2], **Roland Baumhauer**[2], **Eva Lange-Athinodorou**[3], **and Julia Meister**[2]

[1]Remote Sensing, Institute of Geography and Geology, University of Würzburg, 97074 Würzburg, Germany
[2]Physical Geography, Institute of Geography and Geology, University of Würzburg, 97074 Würzburg, Germany
[3]Institute of Egyptology, University of Würzburg, 97070 Würzburg, Germany

Correspondence: Tobias Ullmann (tobias.ullmann@uni-wuerzburg.de)
and Julia Meister (julia.meister@uni-wuerzburg.de)

Relevant dates: Received: 27 July 2022 – Revised: 12 October 2022 – Accepted: 27 October 2022 – Published: 18 November 2022

How to cite: Ullmann, T., Möller, E., Baumhauer, R., Lange-Athinodorou, E., and Meister, J.: A new Google Earth Engine tool for spaceborne detection of buried palaeogeographical features – examples from the Nile Delta (Egypt), E&G Quaternary Sci. J., 71, 243–247, https://doi.org/10.5194/egqsj-71-243-2022, 2022.

1 Introduction

With the opening of the Landsat archive in 2002, the largest remote sensing archive became available to the public (Wulder et al., 2012). This record presents the most comprehensive civil database on the Earth's surface, and it has stimulated research across the globe for many disciplines (Wulder et al., 2016). Several spaceborne remote sensing missions have since then been launched (Belward and Skøien, 2015), some of them operating now for more than 20 years, such as the highly successful missions carrying the MODIS instrument. Furthermore, recent spaceborne earth observation missions not only continue the building of global remote sensing archives using various sensors but also significantly increased the temporal and spatial resolution (e.g. the Sentinel-2 mission), allowing the dynamics of the Earth to be studied at so far unprecedented spatio-temporal resolution on a global scale. These datasets have also contributed to the field of geomorphology and geoarchaeology. Exemplarily, Brandolini et al. (2021) and Orengo and Petrie (2017) used time series of the Sentinel-2 or Landsat mission to infer and map differences in soil and moisture properties related to historic or palaeogeographical features. Further, Ullmann et al. (2020) have investigated long-term differences in the normalized difference water index (NDWI) in the Nile Delta to map buried palaeogeographical features, i.e. related to former river branches of the Nile, or buried Pleistocene sand hills ("geziras") often used as settlement mounts. While these archives and datasets certainly offer new opportunities, the handling and analyses come with challenges, most strikingly arising from the enormous data load and the high computing effort. Fortunately, some of these limitations can be overcome by recently available cloud-computing capacities, exemplary offered by the Google Earth Engine (GEE) (Gorelick et al., 2017). These capacities allow processing and analysing large stacks of earth observation data in a cloud environment in a very fast and efficient manner without the need of downloading and processing the raw data. To make these new developments applicable for users with less experience in remote sensing, we present here a freely available GEE tool that allows the processing of remote sensing archive data from Landsat, MODIS, and Sentinel-2 in a user-friendly way. The tool is based on the GEE efforts of previ-

ous research (Ullmann et al., 2020) but provides an improved and ready-to-use browser-based application that is suitable for users who are less familiar with GEE. In this contribution, we exemplarily show the processing results of the tool for the entire Nile Delta for Landsat, MODIS, and Sentinel-2 and continue mapping buried palaeogeographical features using the long-term differences in NDWI (see Ullmann et al., 2020).

2 Study area

The Egyptian Nile Delta covers about 24 000 km^2 and is the largest delta of the Mediterranean Sea. Historic textual sources witness up to seven major Nile branches that flowed through the delta, while today only the Rosetta and Damietta branches exist (Fig. 1; Bietak, 1975). In antiquity, these waterways were of high significance for intra-Egyptian trade and traffic, and major ancient Egyptian cities are exclusively found in their immediate surroundings. Hence, the reconstruction of the Holocene delta environments is also crucial for studying the human–environment interactions of ancient Egypt (Butzer, 1976; Pennington et al., 2017; Bietak, 1975). For protection against the seasonal Nile floods, settlements were either built on Pleistocene sand mounds ("geziras") or on the embankments of the river branches. However, due to the long-term dynamics of the riverine system, the landscape of the Nile Delta has constantly changed. Water courses have been silted up and are no longer visible in the modern landscape. Knowing about the importance of localizing the route of former Nile branches, several geophysical and geoarchaeological investigations were carried out in the past, of which some also rely on remotely sensed imagery, e.g. Ginau et al. (2017) and El-Fadaly et al. (2019).

3 Material and methods

In continuation of these efforts, the processing of remote sensing time series of Landsat (including Landsat 9 and Collection 2 data), Sentinel-2 and MODIS was conducted using the cloud-based processing capacities of the GEE. For this purpose, we developed a script which allows the generation of cloud-free surface reflectance products and various spectral indices for a user-defined period, region of interest, and for the earth observation data of the respective sensors. The source code of this tool is freely available on GitHub (https://github.com/EricMoeller96/master_thesis, last access: 9 November 2022) and comes with documentation on the most important settings. The tool requires a minimum of user inputs for the execution and can be executed for a user-defined region. Exemplarily, the datasets, specified in Table 1, were processed to generate median RBG composites for the entire Nile Delta (Fig. 1). In addition, multispectral indices, such as the normalized difference vegetation index (NDVI), NDWI (Gao, 1996), and normalized difference snow index (NDSI), are calculated and processed by default. Following the approach presented in a preceding work (Ullmann et al., 2020), in this study we exemplarily focus on two median NDWI images which were calculated from the time series: one for the winter (January/February) and one for the summer (July/August) seasons and for each sensor. These NDWI images were then differenced (summer minus winter) to draw the long-term seasonal difference (ΔNDWI; Fig. 2).

4 First results and discussion

The GEE script allows cloud-free summer and winter mosaics to be processed for the entire Nile Delta in a fast manner and for all sensors (Fig. 1) using analysis-ready products (i.e. surface reflectance). Processing time in the GEE was about 10 to 30 min, which would not be achievable using standard computing facilities given the high number of scenes (e.g. more than 1900 scenes for Landsat).

Thus, the analyses are not limited to the spectral indices, but the multispectral information can also be utilized, which opens possibilities for further investigations apart from the differentiation of spectral indices, e.g time series analysis or land cover classification. The ΔNDWI images of all three sensors show corresponding positive and negative anomalies on the broadest scale (Fig. 2), which follow the general systematic outlined in Ullmann et al. (2020). As such, the largest and strongest anomalies likely display distinctive features of the general (palaeo-)environmental setting as sketched by Butzer (1976). For instance, strong negative anomalies of the ΔNDWI somewhat match the proposed location of sands at or near the surface at several locations between the modern course of the Rosetta and the Damietta branches and between Tanta and Cairo. In all datasets negative ΔNDWI values are found in the western Nile Delta (south of Alexandria and west of Damanhur), the central Nile Delta (south of Tanta towards Cairo), and in the northern Nile Delta (in the vicinity of Lake Burullus). Positive ΔNDWI values are less frequent, and the largest patches are found near Lake Burullus (north) and Lake Manzala (east). Obviously, the higher spatial resolution of Landsat and Sentinel-2 allows a more detailed picture to be depicted; in both datasets spatially varying positive and negative anomalies are found in the delta west of the Rosetta branch. Overall, Sentinel-2 data deliver a better geometric resolution revealing more details (e.g. as exemplified for Geziret Sineita in Fig. 2d–f); however, due to the rather short time series of 4 years (compared to 36 years offered by Landsat), anomalies are less clear, and the ΔNDWI image shows more heterogeneities compared to the results of Landsat. This is also displayed by the higher deviation used to scale the ΔNDWI images (Fig. 2). It is likely that this issue is linked to the short time series as seasonal differences in NDWI become best visible when long timescales are analysed (Ullmann et al., 2020). As such, a long observation

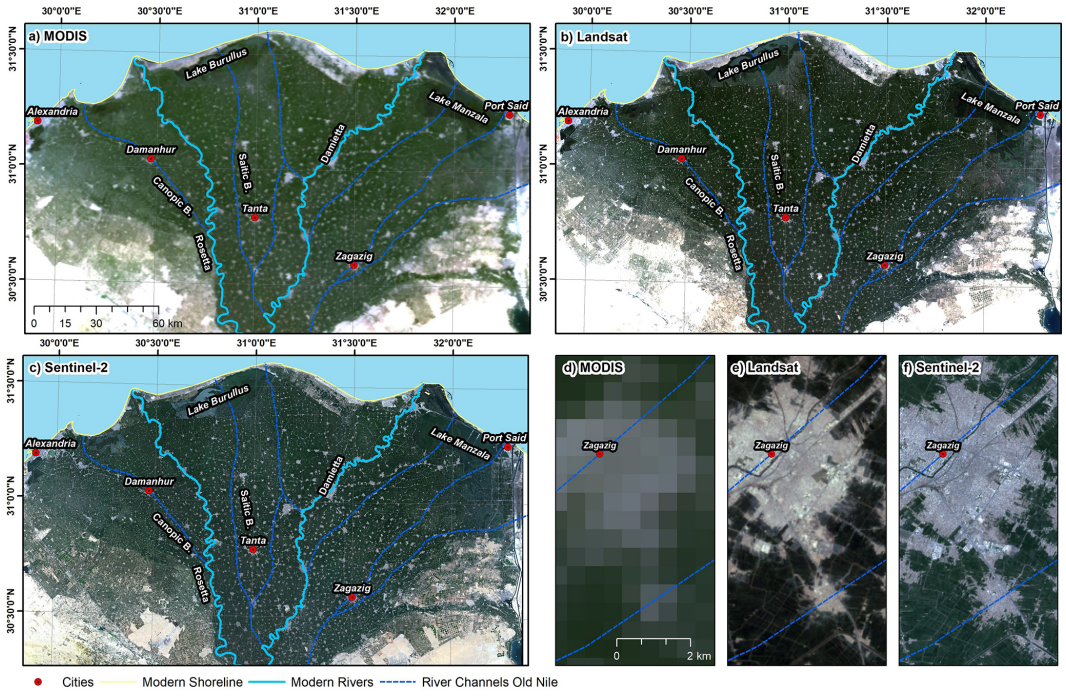

Figure 1. Comparison of cloud-free summer (July/August) median RGB composites of the Nile Delta: **(a)** MODIS (2001–2021), **(b)** Landsat (1985–2021), **(c)** Sentinel-2 (2017–2021), and **(d–f)** detailed views of the city of Zagazig. Ancient river channels of the Nile are drawn according to Pennington et al. (2017).

Table 1. Overview of investigated remote sensing datasets which were processed using the Google Earth Engine. Bands refer to B = blue, G = green, R = red, NIR = near infrared, and SWIR = short-wave infrared. Multispectral indices and products are as follows: NDVI = normalized difference vegetation index, NDWI = normalized difference water index, NDSI = normalized difference snow index, NBR = normalized burn ratio, and LST = land surface temperature. Composites of each band, index, and product were generated using the median operator; as such, a pixel shows the median value over the entire stack of all cloud-free acquisitions within the period of investigation.

Mission	Resampled geometric resolution (m)	Bands	Multispectral indices and products	Period of investigation	Number of images
MODIS	500	B, G, R, NIR1, NIR2, SWIR1, SWIR2	NDVI, NDWI, NBR, NDSI, LST	January/February 2001 to 2021	1240
MODIS	500	B, G, R, NIR1, NIR2, SWIR1, SWIR2	NDVI, NDWI, NBR, NDSI, LST	July/August 2001 to 2021	1363
Landsat	30	B, G, R, NIR, SWIR1, SWIR2	NDVI, NDWI, NBR, NDSI	January/February 1985 to 2021	620
Landsat	30	B, G, R, NIR, SWIR1, SWIR2	NDVI, NDWI, NBR, NDSI	July/August 1985 to 2021	1310
Sentinel-2	20	B, G, R, Red Edge 1, Red Edge 2, Red Edge 3, NIR, Red Edge 4, SWIR1, SWIR2	NDVI, NDWI, NBR, NDSI	January/February 2017 to 2021	412
Sentinel-2	20	B, G, R, Red Edge 1, Red Edge 2, Red Edge 3, NIR, Red Edge 4, SWIR1, SWIR2	NDVI, NDWI, NBR, NDSI	July/August 2017 to 2021	814

period is important to identify rather weak anomalies in the ΔNDWI. Thus for now, the Landsat archive appears to be the most useful and promising record for identifying ΔNDWI anomalies associated with surface and near-surface discontinuities in soil properties. Taking this further, Fig. 3 shows preliminary results from the continued mapping efforts. The visual analysis of the Landsat ΔNDWI revealed several additional linear and meandering anomalies, especially between Damanhur and Tanta and in the surroundings of Zagazig. Some of them correspond remarkably well with the general

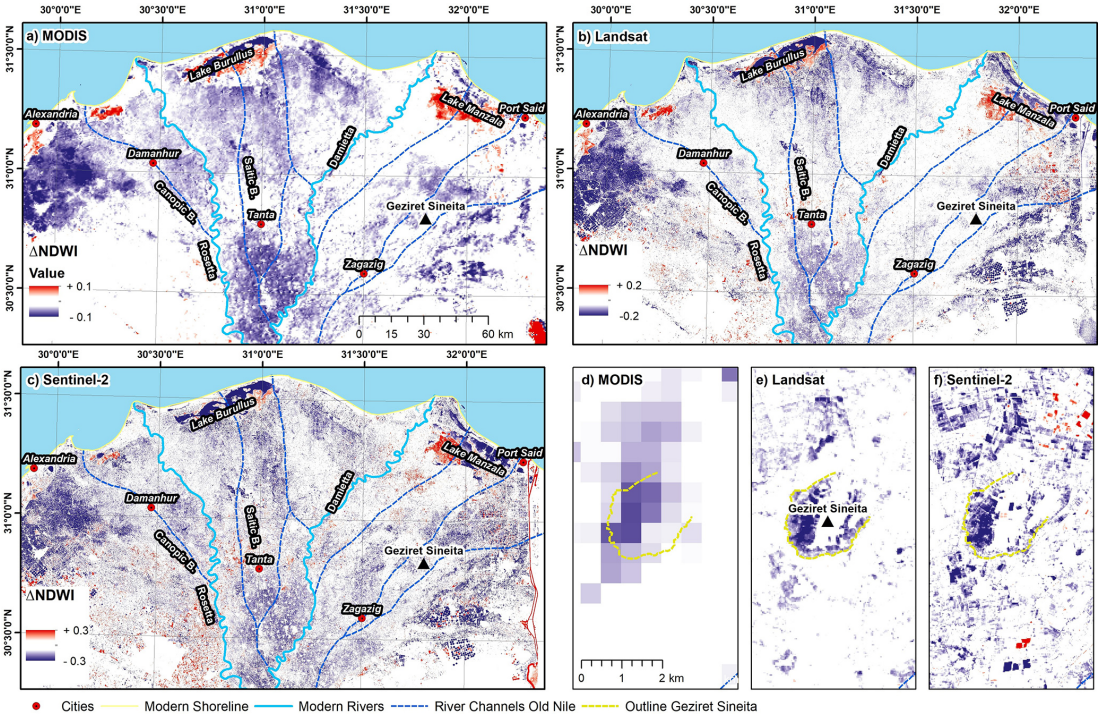

Figure 2. Comparison of ΔNDWI anomalies of the Nile Delta: **(a)** MODIS (2001–2021), **(b)** Landsat (1985–2021), **(c)** Sentinel-2 (2017–2021), and **(d–f)** detailed views of Geziret Sineita (Tell es-Sunayta) (see van den Brink, 1987). Ancient river channels of the Nile are drawn according to Pennington et al. (2017).

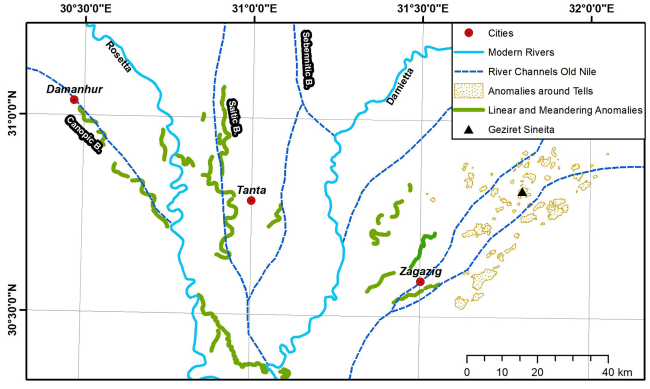

Figure 3. Preliminary mapping results of ΔNDWI anomalies in the central Nile Delta based on Landsat imagery (1985–2021). Ancient river channels of the Nile are drawn according to Pennington et al. (2017).

flow directions and river routes indicated by Pennington et al. (2017). These anomalies could therefore indicate former courses of the Canopic Branch and Saitic Branch.

5 Conclusion

The increased number and availability of spaceborne remote sensing records, their enhanced spatio-temporal resolution, and latest cloud-based processing capacities open new opportunities to study the nature and dynamics of the land surface on a local to global scale. This opens opportunities in the field of geomorphology and geoarchaeology, e.g. in the context of landscape archaeology. In the present contribution, we highlight as an example the application of a freely available Google Earth Engine (GEE) tool to process cloud-free composites for the Nile Delta using the archives of MODIS, Landsat, and Sentinel-2. Following a preliminary approach, seasonal differences in the NDWI were investigated and interpreted in the context of buried palaeogeographical features. Among the investigated data, the Landsat archive offers the most promising record to identify spectral anomalies related to surface and surficial discontinuities of soil and land properties. Given the global availability of remote sensing data from Sentinel-2, Landsat, and MODIS, as well as the capacities that arise from the Google Earth Engine, a transfer to other sites with similar environmental conditions (e.g. continuous rather that homogeneous land cover) seems certainly feasible and of interest for future investigations.

Code and data availability. Data relating to this paper are available from the corresponding authors upon reasonable request. The Google Earth Engine code is available at https://doi.org/10.5281/zenodo.7313130 (EricMoeller96, 2022).

Author contributions. The methodology was developed by TU and EM. The formal analysis was conducted by TU and EM. TU, EM, RB, ELA and JM interpreted the results jointly. Funding was acquired by TU and JM. The manuscript was prepared by TU and JM with contributions from all authors.

Competing interests. At least one of the (co-)authors is a member of the editorial board of *E&G Quaternary Science Journal*. The peer-review process was guided by an independent editor, and the authors also have no other competing interests to declare.

Disclaimer. Publisher's note: Copernicus Publications remains neutral with regard to jurisdictional claims in published maps and institutional affiliations.

Special issue statement. This article is part of the special issue "Quaternary research from and inspired by the first virtual DEUQUA conference". It is a result of the vDEUQUA2021 online conference in September/October 2021.

Acknowledgements. We are grateful to Janek Walk for providing valuable feedback.

Financial support. This research has been supported by the Deutsche Forschungsgemeinschaft (DFG, German Research Foundation; grant no. 507687060).

This open-access publication was funded by Julius-Maximilians-Universität Würzburg.

Review statement. This paper was edited by Christian Zeeden and reviewed by Janek Walk.

References

Belward, A. S. and Skøien, J. O.: Who launched what, when and why; trends in global land-cover observation capacity from civilian earth observation satellites, ISPRS J. Photogramm., 103, 115–128, https://doi.org/10.1016/j.isprsjprs.2014.03.009, 2015.

Bietak, M.: Tell El-Dab'a II: Der Fundort im Rahmen einer archäologisch-geographischen Untersuchung über das ägyptische Ostdelta, in: Untersuchungen der Zweigstelle Kairo des Österreichischen Archäologischen Instituts, Verlag der Österreichischen Akademie der Wissenaschaften, Wien, 236 pp., ISBN 978-3-7001-0136-9, 1975.

Brandolini, F., Domingo-Ribas, G., Zerboni, A., and Turner, S.: A Google Earth Engine-enabled Python approach for the identification of anthropogenic palaeo-landscape features, Open Res Europe, 1, 22, https://doi.org/10.12688/openreseurope.13135.2, 2021.

Butzer, K. W.: Early hydraulic civilization in Egypt: a study in cultural ecology, University of Chicago Press, Chicago, 134 pp., ISBN: 0-226-08634-8, 1976.

El-Fadaly, A., Abouarab, M. A. R., El Shabrawy, R. R. M., Mostafa, W., Wilson, P., Morhange, C., Silverstein, J., and Lasaponara, R.: Discovering Potential Settlement Areas around Archaeological Tells Using the Integration between Historic Topographic Maps, Optical, and Radar Data in the Northern Nile Delta, Egypt, Remote Sens., 11, 3039, https://doi.org/10.3390/rs11243039, 2019.

EricMoeller96: EricMoeller96/master_thesis: Script_by_Eric_Moeller_v6, Version V6, Zenodo [code], https://doi.org/10.5281/zenodo.7313130, 2022.

Gao, B.: NDWI–A normalized difference water index for remote sensing of vegetation liquid water from space, Remote Sens. Environ., 58, 257–266, https://doi.org/10.1016/S0034-4257(96)00067-3, 1996.

Ginau, A., Schiestl, R., Kern, F., and Wunderlich, J.: Identification of historic landscape features and settlement mounds in the Western Nile Delta by means of remote sensing time series analysis and the evaluation of vegetation characteristics, Journal of Archaeological Science: Reports, 16, 170–184, https://doi.org/10.1016/j.jasrep.2017.09.034, 2017.

Gorelick, N., Hancher, M., Dixon, M., Ilyushchenko, S., Thau, D., and Moore, R.: Google Earth Engine: Planetary-scale geospatial analysis for everyone, Remote Sens. Environ., 202, 18–27, https://doi.org/10.1016/j.rse.2017.06.031, 2017.

Orengo, H. and Petrie, C.: Large-Scale, Multi-Temporal Remote Sensing of Palaeo-River Networks: A Case Study from Northwest India and its Implications for the Indus Civilisation, Remote Sens., 9, 735, https://doi.org/10.3390/rs9070735, 2017.

Pennington, B. T., Sturt, F., Wilson, P., Rowland, J., and Brown, A. G.: The fluvial evolution of the Holocene Nile Delta, Quaternary Sci. Rev., 170, 212–231, https://doi.org/10.1016/j.quascirev.2017.06.017, 2017.

Ullmann, T., Nill, L., Schiestl, R., Trappe, J., Lange-Athinodorou, E., Baumhauer, R., and Meister, J.: Mapping buried paleogeographical features of the Nile Delta (Egypt) using the Landsat archive, E&G Quaternary Sci. J., 69, 225–245, https://doi.org/10.5194/egqsj-69-225-2020, 2020.

van den Brink, E. C. M.: A Geo-Archaeological Survey in the North-Eastern Nile Delta, Egypt; the First Two Seasons, a Preliminary Report, Mitteilungen des Deutschen Archäologischen Instituts, Abteilung Kairo, 43, 7–31, 1987.

Wulder, M. A., Masek, J. G., Cohen, W. B., Loveland, T. R., and Woodcock, C. E.: Opening the archive: How free data has enabled the science and monitoring promise of Landsat, Remote Sens. Environ., 122, 2–10, https://doi.org/10.1016/j.rse.2012.01.010, 2012.

Wulder, M. A., White, J. C., Loveland, T. R., Woodcock, C. E., Belward, A. S., Cohen, W. B., Fosnight, E. A., Shaw, J., Masek, J. G., and Roy, D. P.: The global Landsat archive: Status, consolidation, and direction, Remote Sens. Environ., 185, 271–283, https://doi.org/10.1016/j.rse.2015.11.032, 2016.

E&G Quaternary Sci. J., 71, 249–265, 2022
https://doi.org/10.5194/egqsj-71-249-2022

Open Access E&G Quaternary Science Journal

Research article

The lithostratigraphic formations of the coastal Holocene in NE Germany – a synthesis

Reinhard Lampe

Institut für Geographie und Geologie, Universität Greifswald, Greifswald, 17486, Deutschland

Correspondence: Reinhard Lampe (lampe@uni-greifswald.de)

Relevant dates: Received: 14 December 2021 – Revised: 28 September 2022 – Accepted: 14 October 2022 – Published: 1 December 2022

How to cite: Lampe, R.: The lithostratigraphic formations of the coastal Holocene in NE Germany – a synthesis, E&G Quaternary Sci. J., 71, 249–265, https://doi.org/10.5194/egqsj-71-249-2022, 2022.

Abstract: Based on extensive investigations along the coast and in the coastal waters of NE Germany, a lithostratigraphic classification of the Holocene coastal deposits is presented. Their characteristics, i.e. the lithofacies, reflect the spatial change in hydrodynamics, sediment supply, salinity, bioproduction, etc. in the accumulation space. The displacement of the facies associated with the sea-level rise of the Baltic Sea led to the formation of regularly occurring vertical depositional sequences. From these regular profiles, four lithostratigraphic formations and two subformations of the coastal deposits can be delineated as approximately homogeneous sedimentary bodies, which are described in detail, defined in terms of their spatial extent and classified with regard to the time of accumulation.

Kurzfassung: Auf der Grundlage umfangreicher Untersuchungen entlang der Küste und in den inneren Küstengewässern NE-Deutschlands wird eine lithostratigraphische Gliederung der holozänen Küstenablagerungen vorgestellt. Deren Merkmale, d.h. die Lithofazies, spiegeln den räumlichen Wandel der Hydrodynamik, Sedimentzufuhr, Salinität, Bioproduktion, etc. im Akkumulationsraum wider. Die mit dem Meeresspiegelanstieg der Ostsee einhergehende Verlagerung der Fazies führte zur Herausbildung regelhaft auftretender vertikaler Depositionssequenzen. Aus diesen Regelprofilen lassen sich als annähernd homogene Sedimentkörper vier lithostratigraphische Formationen und zwei Subformationen des Küstenholozäns ausgliedern, die detailliert beschrieben, in ihrer räumlichen Ausdehnung definiert und deren Akkumulation zeitlich eingestuft werden.

1 Introduction

Lithostratigraphy is the branch of stratigraphy that correlates rock units exclusively on the basis of rock properties (lithofacies) and their changes in space (within a sedimentation area) and time (within the vertical profile). Any fossil content is taken into account as a rock property. According to the stratigraphic principle, the lithofacies of coastal sediments reflect environmental conditions such as hydrodynamics, salinity and bioproductivity in the accumulation areas and trace their temporal changes and spatial displacements due to shoreline shifts, which can be caused by an unbalanced sediment budget but mainly by rising or falling sea levels (Kraft, 1978).

The basic unit in the lithostratigraphic hierarchy is the formation, which is defined by its lithology, its internal heterogeneity/anisotropy and facies-change-related boundaries. Since the properties of formations are identifiable with field methods and because they can be traced in the landscape

without any additional stratigraphic information, they build the primary mapping units in geological surveys (Ad-hoc-Arbeitsgruppe Geologie, 2002). For land-use planning, construction, mineral resource exploitation, water management, and coastal and landscape conservation, it is important to know the spatial distribution of geological and geotechnical properties in the sub-ground. Maps of formations reflect this information and mirror the distribution of the parameters needed for planning purposes (Weerts et al., 2005).

According to Remane et al. (2005), a formation represents a lithologically sufficiently homogeneous rock unit that can be mapped on the ground surface or in the subsurface and represented at a scale of at least 1 : 10 000. Terrain morphological criteria can also be taken into account. The boundaries of the formation are determined by a distinct change in lithological characteristics, which are usually diachronic due to the spatial displacement of the sedimentation areas. Formations can be grouped together on account of common lithological features. It is also possible to separate subformations due to their specific characteristics.

This paper deals with the lithostratigraphic formations and subformations of the coastal Holocene along the SW Baltic shoreline in Mecklenburg-Vorpommern. Although the term "coastal Holocene" is commonly used, no explicit definition exists. Therefore, the following definition is here proposed: the coastal Holocene comprises the subaqueous and subaerial accumulations whose formation is determined by littoral processes and brackish-marine environments. In the subaqueous part of the coast, those depositions are to be considered which accumulated above a critical water depth where wind waves cause sediment transport due to bottom contact. In the subaerial part, all accumulations count as coastal Holocene which formed directly under the influence of seawater or under environmental conditions which are characteristic for the proximity to the sea (wind regime, salt and sediment inputs, flooding).

On the coast of Mecklenburg-Vorpommern, the critical water depth is about 10 m (Ministerium für Landwirtschaft, Umwelt und Verbraucherschutz Mecklenburg-Vorpommern, 2009). Since the Holocene global sea-level rise reached the Baltic Sea basin around 8800 years ago, the water level has risen by about 25 m (Niedermeyer et al., 2011). Therefore, coastal Holocene sediments are also to be expected beyond the current 10 m isobath. Although comprehensive seabed data are available (Bundesamt für Seeschifffahrt und Hydrographie, 2012, 2016), they only reflect the conditions close to the ground surface. Since the sediments and their bounding surfaces in the deeper sub-ground remain widely unknown, such data are not sufficient for the definition of formations. The explanations presented in this paper are therefore limited to the near-coastal area, which is comparatively better explored (Fig. 1).

In the past, studies to subdivide the German coastal Holocene lithostratigraphically were made only for the North Sea coast of Lower Saxony (Brand et al., 1965; Sindowski, 1968; Barckhausen et al., 1977; Streif, 1979). The underlying principles, however, are hardly transferable to the North Frisian coast (Ahrendt, 2006) and not applicable to the Baltic Sea coast due to different sediment layering. Further, the studies mentioned do not include any aeolian accumulations, which are important coastal landforms along the SW Baltic region (Niedermeyer et al., 2011). For the coast of Mecklenburg-Vorpommern a spatial representation of lithologically defined units was given by the Quaternary lithofacies map 1 : 50 000 LKQ50 (Cepek, 1999) produced in the German Democratic Republic (GDR). As the map series was designed for the entire national territory, the coastal Holocene as such is not shown separately but is integrated into the Holocene horizon map and shown with signatures as marine brackish, telmatic or aeolian accumulation and differentiated as gravel, sand, silt and clay, marine or limnic mud, fen peat, or aeolian sand.

Currently, the descriptions of lithostratigraphic units used for geological maps in Germany are collected in a unified way. This posed the challenge to subdivide the coastal Holocene into formal units that correspond to the criteria of the lithostratigraphic lexicon LithoLex. LithoLex – a joint project of the German Stratigraphic Commission and the Federal Institute for Geosciences and Natural Resources (DSK and BGR, 2021) – was initiated in 1999 as a collection that records all defined lithostratigraphic units of Germany. Since 2006 LithoLex has established a dynamic database which is publicly accessible via the internet. It complements the Stratigraphic Table of Germany 2016 (STD 2016) and should provide descriptions of all units mentioned there, and these are also the mapping units of the geological maps of the state geological surveys.

The formations of the coastal Holocene on the SW Baltic coast were defined and evaluated by the Subcommission on Quaternary Stratigraphy for the first time in 2014. However, the standard forms used in LithoLex allow only short descriptions which need to be amplified and explained separately.

Therefore, the aim of the paper is

- to summarise the available lithological information by defining homogeneous sedimentary units (formations), describing their general lithological properties, their occurrence, boundaries, mean thickness and spatial interrelations;
- to relate the accumulation of these units to specific phases of the regional Baltic sea-level development and to show their genetic and chronostratigraphic correlations;
- to contribute an exemplary solution within the efforts for a comprehensive and uniform definition of lithostratigraphic units in Germany (LithoLex) as a basis for future geological maps.

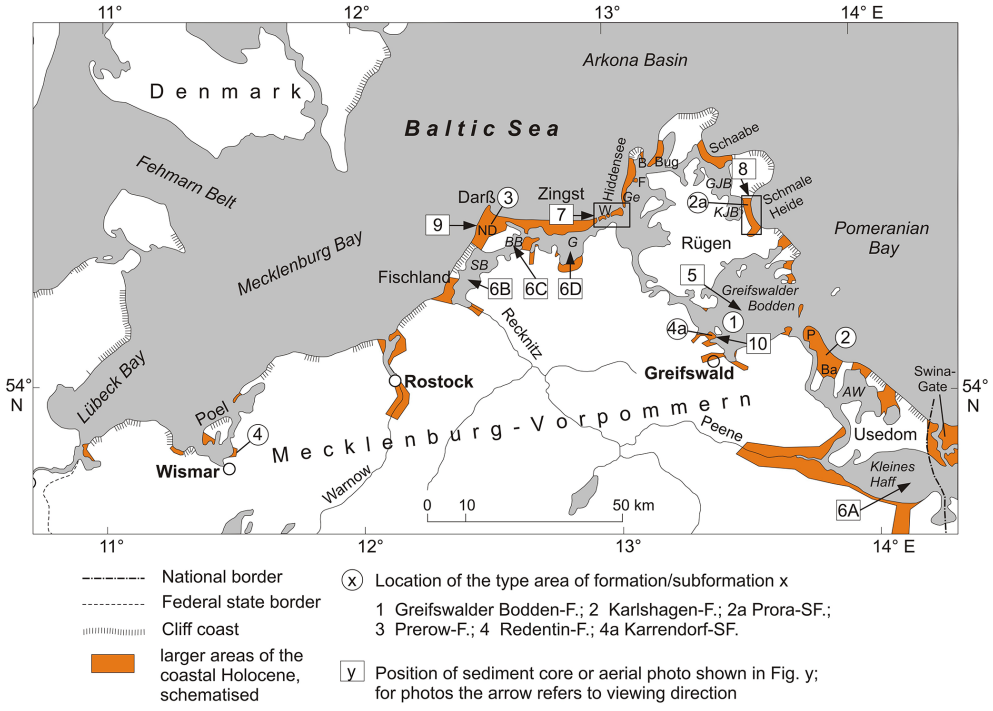

Figure 1. Occurrences of larger coherent areas of the coastal Holocene in Mecklenburg-Vorpommern (schematised), locations of the type areas of the formations and subformations, and the sediment cores and photos used for their description. SB: Saaler Bodden; BB: Bodstedter Bodden; G: Grabow; GJB: Großer Jasmunder Bodden; KJB: Kleiner Jasmunder Bodden; AW: Achterwasser; ND: Neudarß; W: Werder islands and sandflat; Ge: Gellen and Gellenschaar; F: Fährinsel; B: Bessin and Bessinsche Schaar; P: Peenemünder Haken; Ba: Banneminer Niederung.

2 Data sources and methods

The definitions and descriptions of the coastal formations of the SW Baltic region rely mainly on data from investigations which were conducted at the University of Greifswald during the past decades, among them unpublished project reports and diploma and PhD theses. They document more than 600 descriptions of on- and offshore sampled sediment cores (sampled onshore mostly with motor-hammer-driven core devices and offshore with shipborne vibrocorer or gravity corers) and related lithological investigations (colour, grain size distribution by sieving or with a laser particle sizer, content of organic matter as loss on ignition (LOI) at 550 °C, carbonate according to Scheibler or as the difference of LOI at 1100 °C and LOI at 550 °C, trace elements using X-ray fluorescence spectroscopy (XRF), or inductively coupled plasma (ICP), as well as macroscopically identifiable remains of organisms), which were used to derive the general lithology of the coastal sediment bodies and to gain cross sections of the coastal landforms. In some cases ground penetrating radar (GPR) or sediment echo sounder records provide supplementary information regarding the spatial layering. Additionally, for many samples or cores radiocarbon or optically stimulated luminescence (OSL) datings and analyses of pollen, diatoms, molluscs or macro-remains are available which provide information about the deposition period, environmental conditions, accumulation rates and human impact. Almost all of these investigations were conducted to reconstruct the sea-level development and/or the evolution of the coastal landscape.

From the lithological and topographical information contained in these data, supplemented by the data documented in the drilling data repository of the State Geological Survey of Mecklenburg-Vorpommern, the general layering structure of the coastal morphogenetic units, such as strandplain, coastal mire, barrier, lagoonal infill, etc., is known, and from this a useful classification into lithostratigraphical formations can be derived. The characteristic of a formation is essentially determined by its position in the accumulation space relative to the shoreline. This position might be temporarily shifted due to sea-level or sediment budget variations, and thus, the formations as pure lithostratigraphic units can be linked to chronostratigraphy to some extent.

3 Outline of the Holocene evolution

With few exceptions, the morphogenetic framework for the development of today's coastal landscape was formed during the Weichselian Glacial. The sediment and relief legacy of this glaciation determined the spatial distribution of the ele-

vations and depressions of the ground surface, as well as the type and volume of the sediment that built up the later coastal landforms and is responsible for the development of regionally predominant coastal types (Hurtig, 1957). After the deglaciation of northern Germany about 14 500 years ago, the present coastal area remained under terrestrial-limnic conditions until the Atlantic (Kolp, 1976; Verse et al., 1998; Schumacher and Bayerl, 1999). The precursors of the Baltic Sea – the Baltic Ice Lake, the Yoldia Sea and the Ancylus Lake – did not exceed a level of −18 m NHN (standard elevation zero) according to present knowledge (Lemke, 1998; Lampe et al., 2005); only sediments of local waters have survived. Therefore, in today's coastal area, deposits of the coastal Holocene are always separated from those of the terrestrial-limnic Late Pleistocene or Early Holocene by an erosional unconformity.

The development of the coastal landscape started with the Littorina transgression, i.e. the time when the postglacially rising ocean flooded the connecting sounds between the Baltic Sea and the Kattegat and entered the Baltic Sea basin (Fig. 2). There are differing opinions about the exact time. Rößler et al. (2011) give an age of 8 ka b2k (all ages are converted to millennia before 2000 CE (ka b2k) and rounded) for the onset of marine sedimentation in the Mecklenburg Bay and 7.2 ka b2k for the Arkona Basin, while Andrén et al. (2000) found an age of 7.8 ka b2k for the Bornholm Basin. For today's coastal areas, however, most researchers describe marine sediments from as early as 8.8–8.0 ka b2k (e.g. Kliewe and Janke, 1982; Berglund et al., 2005; Lampe et al., 2010; Rosentau et al., 2021).

The further development of sea level is also interpreted somewhat differently depending on the investigator. In general, however, it can be divided into four phases, which are characterised by different rates of rise and the formation of characteristic coastal landscape units (Niedermeyer et al., 2011). Depending on the regional context and the dating methods used, the information on the time intervals of the phases can vary by several hundred years; the following information follows Lampe and Lampe (2021).

During the Littorina-1 Transgression (L1T; Fig. 2), ca. 8.8–7.5 ka b2k, a very rapid water-level rise occurred at a rate of 6–9 mm a^{-1} on average; for more precise data, the regionally varying isostatic movements of the coastal sections must be taken into account (Dietrich and Liebsch, 2000). The abrasion of the inundated land areas remained relatively low, it can rather be assumed that the landscape drowned (cf. Schwarzer et al., 2019). In the depressions of the present-day lagoons (Bodden), which were protected by surrounding Pleistocene uplands, mud accumulated rich in shell hash. Over the Littorina-2 Transgression (L2T), ca. 7.5–6.3 ka b2k with a gradual transition to the next phase, the rate of rise decreased to about 1–2 mm a^{-1}. This was associated regionally with an increase in abrasion and locally with the filling of the near-shore submarine areas with shallow-water sands. Towards the end of the phase, the first stable coastal landforms emerged. The Post-Littorina Retardation (PLR), ca. 6.3–1.2 ka b2k, was characterised by a largely stable sea level, but several decimetre-scale fluctuations were found (Fig. 2). The phases of falling or at least stagnating sea level coincide with known climate variations such as the Homeric Minimum (ca. 2.9–2.6 ka b2k; Martin-Puertas et al., 2012; Mayewski et al., 2004) and the Dark Age Cold Period (ca. 1.6–1.2 ka b2k; Helama et al., 2017). The mean rate of rise was about 0.2–0.4 mm a^{-1}. During this phase, coastal equilibration was largely completed, with the aforementioned water-level fluctuations appearing as intervals of varying shoreline progradation or retreat. The fourth phase began at about 1.2 ka b2k, when the rate of rise increased again with the onset of the Late Sub-Atlantic Transgression (LSAT). Due to the interruption during the Little Ice Age (LIA), which in Central Europe is mostly dated to 0.55–0.15 ka b2k, the mean rate of rise for the entire period was 0.5–0.7 mm a^{-1} but reached 1.0–1.5 mm a^{-1} before and after the LIA (Fig. 2). Initially, the phase was characterised by increased abrasion on the cliffs and an increase in shoreline progradation along the coastal barriers. At the same time, extensive mires developed on the back-barrier sand flats and on other low-exposure sections of the coast. After the end of the LIA, erosive tendencies generally intensified. Currently about 70 % of the formerly prograding coastline has a negative sediment balance (Schwarzer, 2003). An accelerated sea-level rise will exacerbate this trend in the future.

4 Lithofacies of the coastal Holocene

Lithofacies differentiation is mainly determined by the position of depositional areas in relation to sea level and shoreline, hydrodynamic exposure, and sediment availability. As a result of the transgression- or regression-related shifts in the facies spaces, characteristic vertical sequences of lithofacial units developed in the course of the coastal evolution which can be defined as standard profiles.

For example, with the inundation of the pre-Littorina relief gravelly or blocky residual sediments formed on elevated till deposits, which were covered by marine-brackish shallow-water sand and later by dunes or cover peat (Fig. 4: Barrier). In contrast, basal organic sediments indicating ponding accumulated in the depressions of the relief shortly before the arrival of the transgressing sea (Kliewe and Janke, 1978). After inundation, they were covered by thin strata of shallow-water sand (which can also be missing and is therefore not shown in Figs. 3 and 4) and lagoonal mud after a sufficient water depth was reached (Fig. 4: Lagoon). Where elongating spits evolved, the mud was overlain by shallow-water and beach sand or pebbles, on which dunes of different generations could develop as the shoreline started to prograde (Fig. 4: Barrier).

The depositional sequences (standard profiles) empirically proven by sediment cores are marked by arrows in Fig. 3.

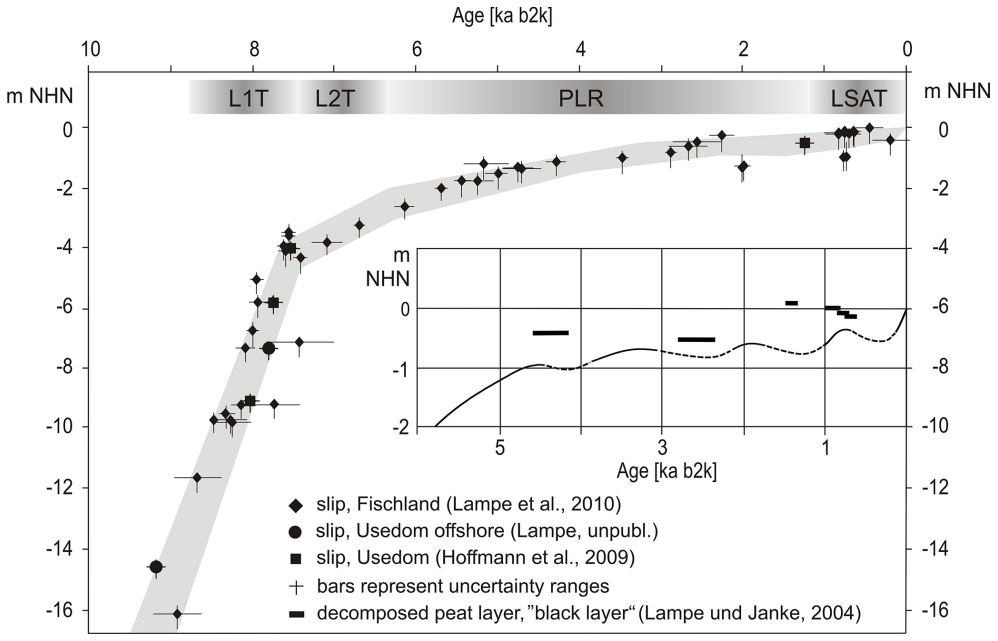

Figure 2. Relative sea-level curve for the Fischland and northern Usedom coastal sections (see Fig. 1). L1T/L2T: Littorina-1/Littorina-2 Transgression; PLR: Post-Littorina Retardation; LSAT: Late Sub-Atlantic Transgression; for explanation see text. Due to different glacio-isostatic movements, the curve is flatter north of Fischland and Usedom and steeper to the south (see Lampe et al., 2010). For the period after 6 ka b2k, a curve derived from degraded peat layers in the coastal mires is additionally given, which better reflects the small-scale sea-level fluctuations (after Lampe and Janke, 2004; modified). Dashed curve sections mark periods of sea-level fall as deduced from degraded peat layers. The amplitude of the lowerings is not known. For a detailed description of the sea-level index points (slip) see the database in Rosentau et al. (2021).

More specifically, however, the depicted sequences do not have to be fully developed but can end before any facies change. They form the framework in which the lithofacial units (formations) are to be defined. Since for practical reasons the number of formations should be kept as low as necessary (Piller et al., 2003), the thin basal peats and the residual sediments are not kept as separate formations but are added to the subsequent facies unit. In addition, the dunes of different generations are combined into one unit. This results in four formations:

1. basal peat or lag sediment and brackish lagoonal mud (Greifswalder Bodden Formation),
2. basal peat or lag sediment and marine-brackish shallow-water and beach sediment (sand, gravel, boulder) (Karlshagen Formation),
3. aeolian sand (Prerow Formation),
4. cover peat and sediments of the coastal mires (Redentin Formation).

4.1 Greifswalder Bodden Formation (GBF)

Lithologically, the GBF is predominantly characterised by lagoonal mud (*Schlick*). Although Möbus (2000) designated the formation as *Mudde-Sequenz*, it is recommended to use the term *Schlick* to emphasise the distinction from *Mudde* as a limnic sediment (Ad-hoc-Arbeitsgruppe Boden, 2005). Different approaches to the definition of lagoonal mud can be found in Kolp (1966), Lindner (1972), Schlungbaum (1979), Leipe (1986), and Lampe and Meyer (1995). In the revision of the "Definitions of Geogenetic Term of the Geological Mapping Guide" (AG Geologie, 2021), mud is described in general terms, GeolKAID 323, and again under the term lagoonal deposits, GeolKAID 29, in a narrower sense to denote fine-grained basin sediments.

The muddy sediments of the GBF consist mainly of silt (40 %–95 % dry weight) with variable admixtures of fine sand and to a lesser extent also clay, as well as organic matter between 5 % and 30 % dry weight. Within the individual lagoons, the composition is relatively uniform due to intensive wind-driven resuspension. In contrast, there are clear differences when comparing different lagoons, which are mainly due to hydrographic conditions such as water exchange with the Baltic Sea, river input, land use in the catchment area, bioproductivity and resuspension conditions (Lampe and Meyer, 1995). Lagoons having a high water exchange with the Baltic Sea (outer lagoons: Greifswalder Bodden, Großer Jasmunder Bodden, Grabow; Fig. 1) show lower concentrations of organic matter and higher proportions of fine sand.

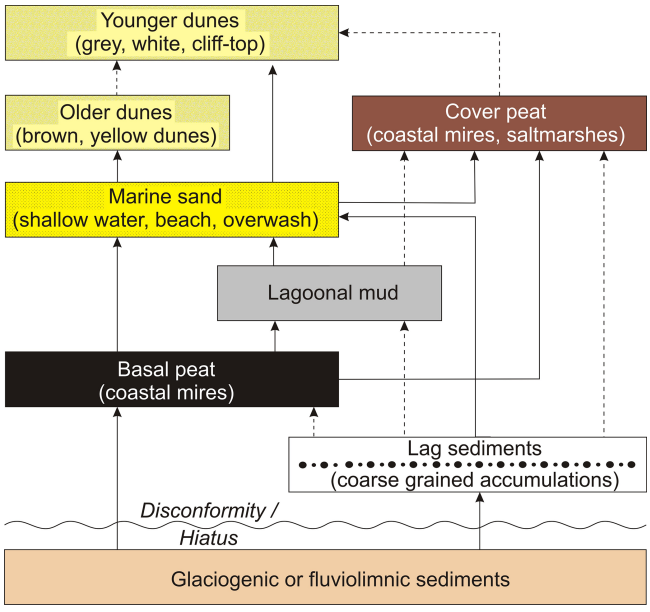

Figure 3. Sediment and facies sequences in the coastal Holocene of Mecklenburg-Vorpommern, empirically proven by sediment cores. The sequences do not have to be completely developed but can end at each facies change. Transitions marked with broken lines occur only rarely. Note that the vertical sequence of facies units is not necessarily equivalent to the temporal sequence.

Below a brownish oxidised surface layer a few millimetres thick (which may also be absent at times of oxygen deficit), the colour of the mud is black or olive-black due to the formation of iron–sulfur compounds. Characteristic is the intensive smell of H_2S. The $FeS_x \times nH_2O$ content may reach more than 7.5 % dry weight (Neumann et al., 2005). The formation can be traced into the lower sections of the coastal rivers where it interlocks with peat and gyttja of the river floodplains. The Greifswalder Bodden as the largest water body of the Western Pomeranian lagoons has been best studied sedimentologically and stratigraphically (Kolp, 1976; Leipe, 1986; Verse, 2001) and represents the type area of the formation.

The lower boundary of the formation represents the transgression surface of the Littorina Sea (Verse et al., 1998) during L1T (Fig. 2). Its age depends on the time of flooding, and it varies in its character depending on the exposure, sediment and morphology of the flooded area. As a result of the sea-level rise, at first the development of shallow paludification mires (*Versumpfungsmoor*) started in the coastal lowlands (this refers to the term *Basistorf* as defined by Lange and Menke, 1967; detailed descriptions can be found in Kliewe and Janke, 1978; Strahl, 1997; Verse et al., 1999). These basal peats (see Figs. 3 and 4) mark the upper limit of the sea level at the time of their growth, and, if reliably dated, they can be used as sea-level indicators (sea-level index points, slip; see Figs. 2 and S2 in the Supplement). For the indicative meaning of sea-level indicators, methodological limitations and uncertainties the reader is referred to the literature, e.g. Dörfler et al. (2009), Hijma et al. (2015), and Khan et al. (2019).

The transgression contact representing the transition from the terrestrial to the marine environment is formed as a change from this peat to a sandy and peaty mud or as an interbedding of these sediments (Janke and Kliewe, 1990). As an erosive reworking horizon, it is usually less suitable for dating. In accordance with the landward shift of the facies, marine shallow-water sand follows on top (Fig. 7). Due to the fast sea-level rise and the resulting rapid increase in the landward distance of the accumulation area, the sandy deposits generally have a low thickness and may even be missing. In hydrodynamically more exposed areas, an abrupt sediment change can be observed, where superficially eroded glaciogenic or fluviolimnic sediments of the Pleistocene or Early Holocene are followed by the typical lagoonal mud. Such a transition corresponds to an erosive ravinement surface (Verse et al., 1998) and – if till is the underlying sediment – might be accompanied by the formation of coarse-grained lag sediments (Figs. 3, 4 and S3). According to the little available ^{14}C data, the hiatus associated with the change from terrestrial-telmatic to marine-brackish conditions can cover a period of several hundred to more than a thousand years (see also Kliewe and Janke, 1978).

In the central areas of the basins, lagoonal mud accumulation began with a thin layer that still contains little amounts of shell hash of marine species. Above this, a several-decimetre-thick section with a high concentration of mollusc shells is generally observed. The detritus of mainly *Cerastoderma*, *Mytilus* and *Hydrobia* shells can reach up to 50 % of the sediment mass (molluscan shell breccia, sensu Kolp, 1976). This shell accumulation marks the phase of maximum inundation, greatest land distance and lowest sediment input and is an expression of a sediment deficit in which relatively little clastic material reached the accumulation area (Figs. 5, S3). The extent to which a trophic favouring of the zoobenthos took place during this period has not yet been investigated. The massive shell hash accumulation in the Greifswalder Bodden began around 7.1 ka b2k (Poz#2-91310) and ended around 5 ka b2k (Poz#2-91309, possible reservoir effect not included in either case). In the Oder Lagoon, Borówka et al. (2005) rank the marine-influenced section between 7.1 ka b2k (Gd-16027) and ca. 5 ka b2k by estimate. Age estimates can also be derived from pollen analyses of cores from other lagoons. They show that in the sediment columns, the pollen zones VII (late Atlantic) and especially VIII (Sub-Boreal, according to Franz Firbas) are characterised by low mass accumulation rates (Schumacher et al., 1998). Temporally, this largely coincides with the PLR (Fig. 2).

A noticeable growth of the spit and barrier system started about 5 kyr ago and increasingly separated the lagoons from the Baltic (Reimann et al., 2011; Lampe and Lampe, 2021). During this phase, which lasted until about 2 ka b2k, mud ac-

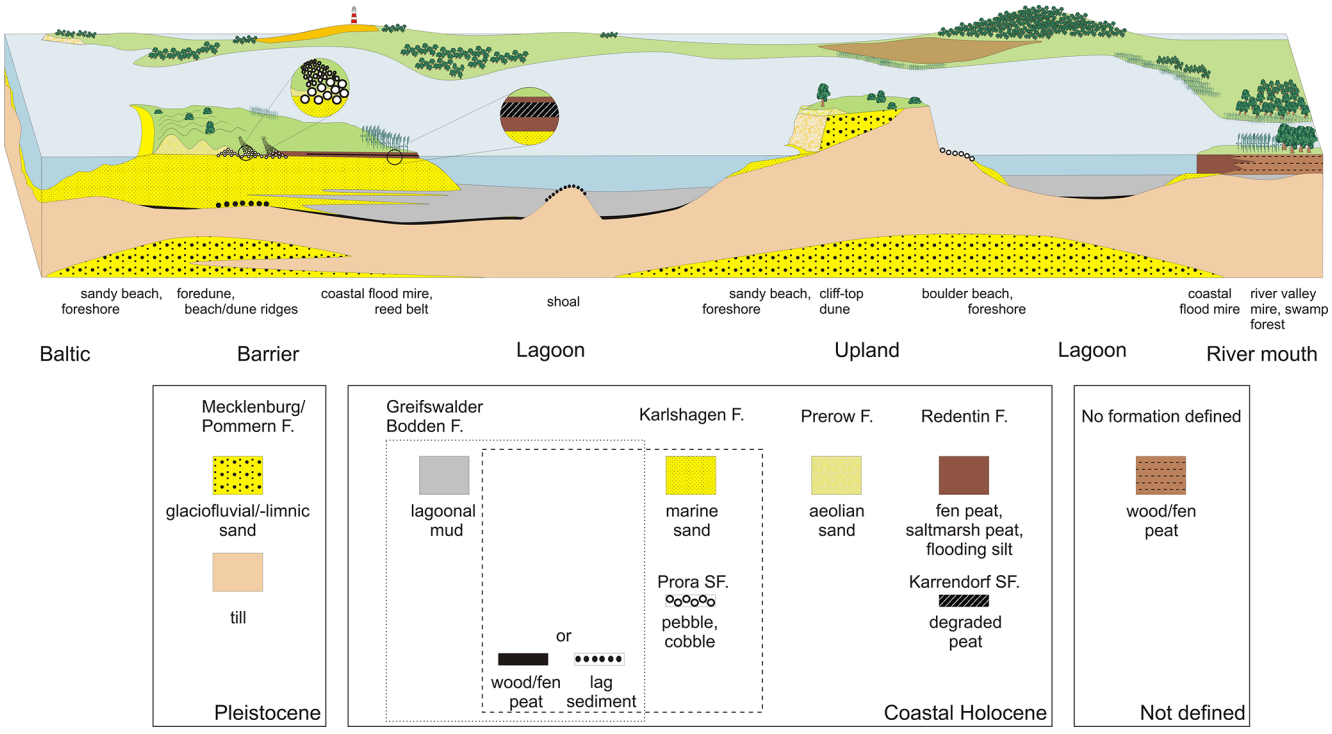

Figure 4. Schematised cross section (not to scale) through the SW Baltic coast illustrating the main coastal landforms, their typical vertical sediment sequences (including the formations and subformations as described in this synthesis), and the lateral sediment interlocking, also with sediments, not belonging to the coastal Holocene. Note that not all possible depositional sequences (see Fig. 3) are shown.

cumulation in the lagoons increased relative to the deposition of shell hash. Storm-wave-induced resuspension and subsequent re-sedimentation of the uppermost sediment layer led to the separation of mud and hash and thus to the formation of numerous tempestite layers (Verse, 2001; Fig. S4).

For the period 2.1–0.75 ka b2k, another strong increase in the mass accumulation rate is documented for the lagoons. The onset of the LSAT (Fig. 2) and the related shoreline erosion, an increased separation from the Baltic Sea, and advancing deforestation in the catchment area can be assumed as causes, but the relative significance remains unclear (Schumacher et al., 1998). As the dating of the period is based on pollen data, the above timing does not necessarily represent the interval of increased accumulation; it merely gives the limits within which the rate was calculated.

The mollusc fauna reconstructed from the shell hash suggests several salinity changes. Although marine-brackish conditions developed rapidly with the flooding, the salinity maximum appears to be offset by several hundred years due to the backwater of the rivers. Characteristically, large and thick shells of mainly *Cerastoderma glaucum*, *Scrobicularia plana* and *Mytilus edulis* appear then. *Littorina littorea* – as it prefers to colonise harder ground – is rarely found in the mud probably due to redeposition.

With the ongoing isolation of the lagoons from the sea and the increasing importance of river discharge in the water exchange, the species spectrum adapted to the respective salinity. In the lagoon Kleines Haff, the accumulation of mud containing shells of marine species in appreciable quantities ended at about 4 ka b2k, in the Saaler Bodden at about 2 ka b2k and in the Großer Jasmunder Bodden (for locations see Fig. 1) at about 1 ka b2k (Schumacher et al., 1998; ages are derived from pollen data and can be several hundred years higher than calibrated ^{14}C ages of corresponding samples, uncorrected for a reservoir effect). In contrast, due to the intensive water exchange with the Baltic, the salinity development in the Greifswalder Bodden rather reflects that in the Pomeranian Bay (Fig. 1). So far, two special regional events can be inferred from diatom analyses: the local maximum salinity with 12–14 PSU lasted until about 4 ka b2k, then decreased to 10–12 PSU and dropped to the current level of 7–8 PSU between 1.6 and 1.3 ka b2k (Janke, unpublished). Increased salinity over shorter periods in recent times (e.g. between 1.8 and 0.8 ka b2k in the Kleiner Jasmunder Bodden; Fig. 1, Lampe et al., 2002) is possibly related to temporary modifications in the water exchange with the Baltic Sea. The last occurrence of the species *Scrobicularia plana*, typical for Littorina-age sediments and indicating salinities $\geq$ 8 PSU (Frenzel, 2006) or $\geq$ 10 PSU (Jaeckel, 1952), is dated to 1.8 ka b2k in the Greifswalder Bodden (Poz#2-91305, not including a reservoir effect). In the coastal section of the river Ryck, which flows into the Greifswalder Bodden (Fig. 1),

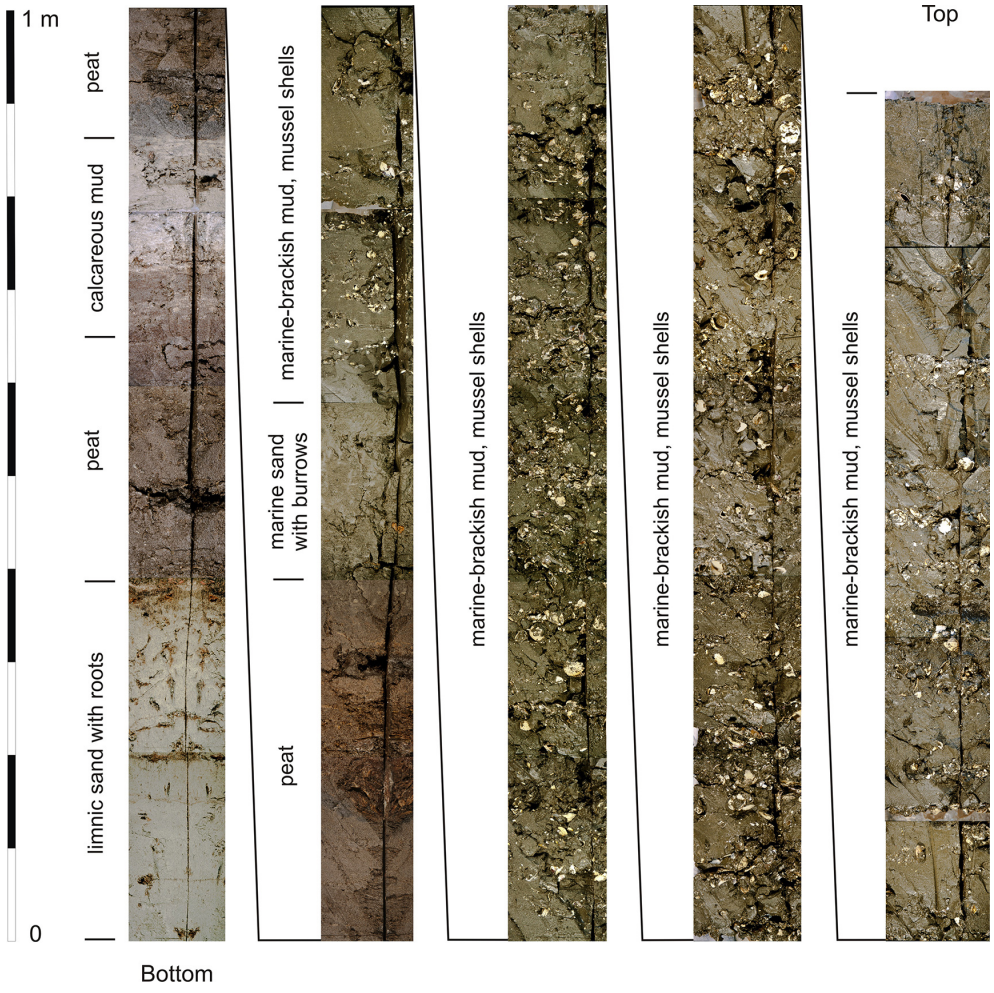

Figure 5. Composite photo of the 5.9 m long sediment core GB95-2 from the northern Greifswalder Bodden, water depth 8.2 m; for the position see Fig. 1. Above late glacial/Early Holocene sediments (sand, peat, calcareous mud, peat), the lower boundary of the Greifswalder Bodden Formation is situated within the upper peat at the transition from a terrestrialisation mire (*Verlandungsmoor)* to a paludification mire (*Versumpfungsmoor*). Above marine sand in shallow-water facies (which is mostly of low thickness or missing) lagoonal mud (*Schlick*) with numerous shells (molluscan shell breccia, sensu Kolp, 1976) follows, forming storm surge layers (tempestites) towards the top. Due to the sampling method, the uppermost ca. 0.3 m of the core is missing (photo: Reinhard Lampe, 1995).

S. plana is recorded up to the middle of pollen zone IXa (Janke, unpublished), which corresponds to an age of ca. 2.0–1.8 ka.

The youngest mud strata, about 300–500 years old, are nearly free of mollusc remains, which indicates a considerable deterioration of the living conditions. The occurrence of *Mya arenaria* in the lagoons with a higher salinity is restricted to sandier sediments in the transition to the Karlshagen Formation. An age of ≤ 0.5 ka is usually assumed for this species being introduced from North America. Its first occurrence in the Greifswalder Bodden was dated to about 0.7 ± 0.07 ka b2k by Behrends et al. (2005) based on amino acid racemisation. However, probably due to temperature effects, this age may be too high. As another neozoon, *Dreissena polymorpha* has populated the inner lagoons with the lowest salinity (Saaler Bodden, Kleines Haff) since about 200 years ago (Gruszka, 1999).

Particularly characteristic is the increase in concentration of organic matter, phosphorus and the metals Zn, Pb and Cu in the uppermost decimetres of the sediment column, which, according to Leipe et al. (1998), began with the industrial and agricultural development in the catchment around 1850 CE (cf. Borówka et al., 2005). Although this increase varies in the individual lagoons depending on the river water input, it is detectable in all of them (Fig. 6). In the highly eutrophic waters of the Kleines Haff and the Saaler Bodden (Fig. 6a, b), which belong to the inner lagoons and are both strongly influenced by the rivers Oder and Recknitz, chalk contents of about 20 % and 10 % on average, respectively, are also characteristic and are based on summer calcite precipitation as a result of photosynthesis of the phytoplankton. This *anthro-*

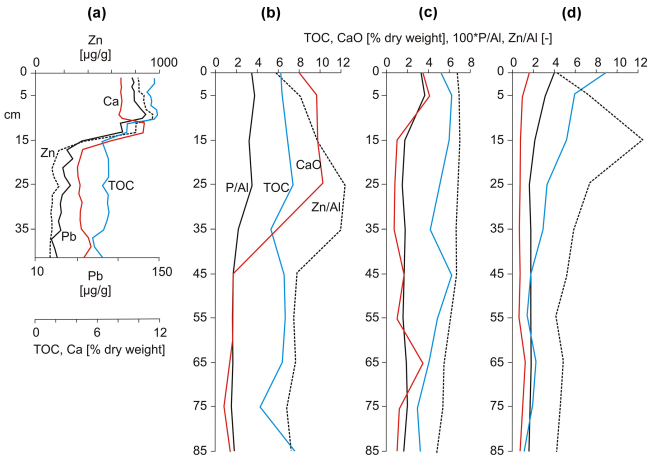

Figure 6. Concentrations of selected elements in short sediment cores from the Kleines Haff (**a**, sample interval 1 cm, based on Leipe et al., 1998), the Saaler Bodden, Bodstedter Bodden and the Grabow (**b, c, d**; sample interval 10 cm, the P and Zn contents are normalised to the Al concentration; TOC = total organic carbon; based on Hensel et al., 2006). For the positions of the cores see Fig. 1.

pogenically modified layer (Hensel et al., 2006) can comprise the uppermost 10 to > 100 cm, depending on the sedimentation rate and redistribution intensity; an average of 20 cm is to be expected.

The GBF forms the surface of the coastal Holocene in the mud-filled central areas of the lagoons. The mean thickness is probably about 3 m, and the maximum thickness known so far is 9 m (Kleiner Jasmunder Bodden). Only the older part of the formation is found under the coastal barriers. Here, due to the distance of the depocentre from the shoreline and the compaction due to the overburden, the characteristic black, mollusc-rich mud is mostly found below −8 m NHN. In sheltered areas or in the coastal sections of the rivers, the formation is somewhat more complete and may already be present at −1 to −3 m NHN (Janke and Kliewe, 1990). When covered by littoral shallow-water sand, the upper boundary of the GBF is indistinctly marked by an alternating bedding of sand and mud, which represents the transition to the Karlshagen Formation. The age of the upper boundary is diachronic and ranges from the beginning of the progradational coastal development to the present.

It has to be noted that the marine mud of the much deeper Baltic Sea basins differs significantly from the lagoonal mud in terms of grain size distribution, fossil content, concentration of organic matter and trace elements and is not represented by the GBF.

4.2 Karlshagen Formation (KF)

During the phase of rapid sea-level rise, a large part of the material eroded from the uplands reached the seaward edge of the coastal zone comparatively quickly. Thus, it was not available for long-shore transport or only available with a time lag. Under these conditions, neither an equilibrium profile normal to the coast could develop nor could a significant shoreline adjustment parallel to the coast take place. As a result, the moraine landscape with its uplands and depressions developed into an archipelago with deficient sedimentation in the inundated basins (see GBF). With the declining sea-level rise rate in the L2T (Fig. 2) the volume of coastal long-shore transport started to grow. The material eroded from the active cliffs and the still unbalanced foreshore areas was increasingly transported parallel to the coast and accumulated where the shoreline turned landward and the coastal long-shore transport led into deeper water (Hoffmann and Lampe, 2007; Lampe and Lampe, 2021). Wide, sandy shallow-water accumulations with subaerial spits growing into the basins developed (Figs. 7, S5 and S6). At the same time, the filling of the basins intensified due to increased supply of silty material transported beyond the shallow-water areas.

These shallow-water and beach sediments form the Karlshagen Formation (KF; *Obere Sandfolge* according to Möbus, 2000). They consist predominantly of grey, silty fine and medium sands in varying mixtures. Coarse sands, gravels and pebbles are, with exceptions, bound to (formerly) subaerial beach ridges and berms. In general, the transition from subaqueous to subaerially deposited sand is gradual. Grain coarsening tendencies towards the ground surface (coarsening upward) are regularly observed, as well as from the back-barrier to the front-barrier area (Kliewe, 1960; Hoffmann and Barnasch, 2005; Hoffmann et al., 2005). Channel and overwash formations lead to local variations (Fig. 7). The subaquatic sands contain small amounts of shell hash. Plant remains occur regularly. Occasionally, they are concentrated in platy detritus layers and should not be confused with thin peat strata, which would be recognisable from a rooting horizon below.

The diachronous lower boundary of the formation is marked by the transition to glaciogenic sediments of the Pleistocene or fluviolimnic sediments of the Early Holocene, which often show a fossil soil or a basal peat on top. If the KF is underlain by the GBF, the lower boundary is indistinct due to alternating bedding of sand and mud at the transition. So far, only a few absolute dates are available for the Banneminer Niederung/Usedom (Fig. 1), where the sands of the KF have a maximum OSL age of 6530 ± 470 years (Lampe and Lampe, 2021). Thus, the age of the lower boundary extends from the end of the L2T to the present at sites where spits and related foreshore and sandflat sediments (e.g. Bessin with the Bessinsche Schaar/Hiddensee, Gellen/Hiddensee with Gellenschaar, Zingst with the Werder sandflat; Figs. 1 and 7) accumulate over non-marine late glacial/Early Holocene sediments or muds of the GBF or where strandplains prograde over marine sands of the Baltic Sea (Peenemünder Haken/Usedom, Neudarß; Fig. 1). The distinction from the latter, which are mostly marine redeposited sands of glaciofluvial

Figure 7. Sandflat east of the Zingst peninsula (Z) with the islands Großer Werder (GW), Kleiner Werder (KW) and Bock (B) and in the background the southern tip of Hiddensee with Gellenschaar (Ge) and Rügen (R); M marks the mainland (see Fig. 1 for the position of the image section). The sandflat and the bases of the islands are made up of shallow-water sand up to 4 m thick and the islands of prograding beach ridges. Between them overwash deposits (O) are recognisable. All deposits belong to the Karlshagen Formation. Dunes (D) of the Prerow Formation are deposited on the seaward beach ridges of the Zingst peninsula (photo: Reinhard Lampe, 2007).

Figure 8. Aerial view of the Schmale Heide/Rügen spit from the northwest, with the towns of Prora and Binz in the background (see Fig. 1 for the position of the image section). The marine and beach sands forming the spit, including the sands of the adjoining foreshore areas in the Baltic and the lagoon, belong to the Karlshagen Formation. The light-coloured beach ridges in the image centre consist mainly of flint pebbles (Prora Subformation). The dunes adjoining the Baltic Sea (to the left in the image), covered with forest, belong to the Prerow Formation. On the right two bays of the Kleiner Jasmunder Bodden are recognisable. The peat of their reed belts belongs to the Redentin Formation (photo: Reinhard Lampe, 2007).

or glaciolacustrine origin, is problematic because the grain size spectrum and fossil content are very similar.

On the barriers of the Vorpommern coast, the average thickness of the KF is about 8 m; the maximum thickness observed so far amounts to 15 m. In the drilling data repository of the Geological Survey of Mecklenburg-Vorpommern even higher values are found, also in Kliewe (1960), but the marine origin of the sands described there seems uncertain. Lithofacially, the thin beach deposits in front of the cliffs, which border the barriers and represent their main sediment source, also belong to the KF (Fig. S7). The thickness of these sediments hardly exceeds 1–1.5 m on average.

As a special feature, the Prora Subformation (PSF) is differentiated. It is characterised by beach ridges consisting predominantly of pebbles. At the type location on the barrier Schmale Heide/Rügen, the beach ridges with a thickness of up to 4 m and a height of up to 2.5 m NHN consist of approximately 95 % flint pebbles and cobbles, which probably originated from a glaciofluvial concentration in a neighbouring shoal (Fig. 8). In the north of the barrier, they overlie a peat layer of the Redentin Formation, which yielded a ^{14}C age of 4.4 ka b2k (Hoffmann, 2004), but for morphological reasons a somewhat older age must be assumed for the oldest ridges. Similar beach ridge formations, consisting mainly of flint, exist on Schaabe/Rügen and on the Fährinsel near Hiddensee (Fig. 1).

For consistency reasons, all pebble and cobble beaches are combined in the PSF and together with the sandy beaches assigned to the KF. Likewise, the *coastal sand migration zone*, i.e. the foreshore with its sand bars, belongs to the KF (Figs. S8 and S9). The *offshore residual sediment zone* is to be regarded as the seaward boundary, where the shoreward sand transport separates from the seaward transport of finer material (Pratje, 1948; Kolp, 1966). However, such a residual sediment zone is clearly pronounced only where sediments with a wider grain size spectrum, e.g. till, are eroded and depleted of fine particles. In the case of a purely sandy foreshore, delineation is difficult. The upper boundary of the formation is either equal to the ground surface or coincides with the lower boundary of the dune sands of the Prerow Formation or the lower boundary of the coastal mires of the Redentin Formation.

4.3 Prerow Formation (PF)

The PF comprises exclusively aeolian sediments. Most of the sediments are dunes that rest on underlying beach ridges belonging to the KF (Figs. 3 and 4). They consist mainly of well to very well sorted, non-calcareous fine to medium sands. The transition from the beach ridges to the overlying drift sand is usually gradual, especially if the beach sand is well sorted. Otherwise, the absence of coarse sand, gravel and mollusc detritus is a useful criterion to distinguish them from the beach sediment.

Usually, all sandy beach ridges, which are no longer reshaped by annual storm floods, have a drift sand cover and are raised to a greater or lesser extent. Dunes form from them

Figure 9. Brown dune of the Prerow Formation with pronounced iron–humus podsol in Neudarß (for the position see Fig. 1; photo: Reinhard Lampe, 1995).

where sand is delivered from the beach for a sufficiently long time and is subsequently fixed by vegetation. With a prograding shoreline due to a positive sand balance or a falling sea level, a new beach ridge forms in front of the dune within a few decades. This increasingly focuses the sand input on a new foredune, whereby the older dune successively becomes inactive and finally covered by forest.

Keilhack (1912) gave a comprehensive description and first subdivision of the beach ridges and the coastal dunes on top of them, using the Świna Gate between the islands of Usedom and Wolin as an example (see also Reimann et al., 2011). According to the occurrence of typical soil horizons and their colour, he distinguished between brown dunes with iron–humus podzols (Bhs/Bs horizon; Fig. 9), yellow dunes with humus podzols (Bh/Bsh horizons) and white dunes (syrozems with O/Ai/Ah horizons) and concluded that their age decreased in this order. Janke (1971) separated the grey dunes with a distinct Ah horizon (regosols; see Ad-hoc-Arbeitsgruppe Boden, 2005) from the white dunes and placed them between the yellow and white dunes in terms of age.

First attempts to date the dune generations are based on ^{14}C data from swale peats (Prusinkiewicz and Noryskiewicz, 1966) between the dunes of the Świna Gate (see Fig. 1). The results, however, are to be regarded as minimum ages. Reliable absolute chronological data can only be obtained with the OSL method. So far, the oldest ages (6.6 ± 0.4 ka b2k) within the KF have been found at the dunes of the Świna Gate (Reimann et al., 2011) and fall into the L2T phase with clearly decreasing water-level rise. Thereafter, the formation of dunes remains closely linked to the sediment budget of the coastal section. Rapid progradation of the shoreline is coupled with the formation of relatively numerous beach ridges with low dunes on top, while slow or no progradation results in fewer beach ridges covered by higher dunes (Lampe and Lampe, 2018). The grey dunes formed during the LIA. In contrast to the uniform, linear walls of the other dune generations, they have an irregular, hummocky and elevated relief with heights of up to 15 m. Fossil soils, lidar surveys and OSL dating show that grey dunes often dispersed, developing individual barchanoid forms and transgressed over older, lower linear dunes (Lampe and Lampe, 2021). Janke (1971) attributes the development of this dune type, which can be found on all SW Baltic strandplains, to the destruction of the vegetation cover by humans and to the special climatic conditions of the LIA. Today, they are mostly stabilised by forests, but in some cases they are still active (Fig. S10).

Cliff-top dunes also belong to the aeolian landforms of the coastal area. They form where cliffs predominantly consist of non-cohesive, sandy sediments, which are blown out by landward-directed winds and deposited behind the upper cliff edge (Fig. S11). Like the cliff itself, they erode and shift landward with the retreat of the cliff's edge. Thus, cliff-top dunes are subject to a constant recycling process and are always relatively young accumulations. Although the mechanism of development is different from that of strandplain dunes, the lithological differences, such as the smaller grain size and a chalk content of 2 %–3 % (Kliewe, 1973), are not striking. It seems therefore appropriate to include the cliff-top dunes in the PF. If necessary, their special position can be taken into account by defining a subformation.

The lower boundary of the PF at the transition to the underlying KF can be very gradual and indistinct but can be estimated by its position relative to the sea level. For the cliff-top dunes, the lower boundary is clearly marked by the soil of the sub-ground over which the dune migrated. The average thickness of the KF is difficult to determine due to the unstable relief but is probably around 2 m; the maximum thickness is around 15 m in the transgressive grey dunes of the LIA. In the case of the cliff-top dunes, a maximum thickness of 25 m (which can no longer be verified) was observed at Streckelsberg/Usedom (Wernicke, 1930); here, too, the mean thickness is probably in the range of a few metres. The upper limit of the formation is always equal to the ground surface.

4.4 Redentin Formation (RF)

In sheltered areas of the inner lagoons and in the lower reaches of the coastal rivers, siliciclastic sedimentation was not yet possible during the phases L1T and L2T of the sea-level rise. With the onset of inundation, lagoonal mud accumulated under marine influence (GBF), while gyttja predominantly deposited in fluvially affected sections. In places, the backwater into the river valleys temporarily led to the development of lake-like waters in the lower reaches, in which calcareous fine detritus gyttja accumulated, e.g. in the Recknitz valley (Succow, 2001). After the end of the rapid rise, *Phragmites* peat accumulation prevailed in the river valley mires (*Flusstalmoore*), in which the decreasing influence of seawa-

ter is accompanied by a decreasing sulfur content (Kliewe and Janke, 1978; Janke, 1978; Succow, 2001).

At the transition of the valleys into the lagoons, the river valley mires interlock with the coastal mires, which are usually only shallow and continuously influenced by brackish water. In small sheltered depressions their accumulation started at about 7 ka b2k, while the largest increase in area is linked to the LSAT, which began at about 1.2 ka b2k (Fig. 2). This new transgression led to a widespread rise of the groundwater table, to ponding in the lowlands surrounding the lagoons and to the development of coastal terrestrialisation mires (*Küstenverlandungsmoore*; Slobodda, 1989; Fig. S12). Unlike in inland reed beds, however, the growth zone of the *Phragmites* reed along the lagoon shores is confined in the vertical to a small interval of ±0.2 m around mean sea level (Krisch, 1978; Slobodda, 1989). Because of this close relationship, only a rising sea level can lead to an aggradation in the coastal mires dominated by *Phragmites*, while even a slight lowering may lead to desiccation, mineralisation and associated peat shrinkage. This results in a highly decomposed peat (*Fen* or *Mulm* according to the German classification), which is characterised by the absence of macroscopically recognisable plant remains and by a conspicuously dark colour (*Schwarze Schicht*; Fig. S13). Where thicker peat strata accumulated in sheltered depressions, two and in one case even three black layers within the uppermost 1.5 m have been detected (Lampe and Janke, 2004). Palynostratigraphically and chronostratigraphically, these layers were assigned to cooler climatic phases, which apparently were associated with sea-level recession or retardation (see Fig. 2). The conspicuous and typically formed uppermost black layer is designated as the Karrendorf Subformation (KSF; Fig. 10). The phenomenon probably corresponds to the *Humus-Dwog* horizon in the marsh soils of the North Sea coast (Behre, 1986; Scheder et al., 2018), but comparative studies are still lacking.

In some areas, a further type of peatland occurs in the form of coastal flood mires (*Küstenüberflutungsmoore*; Fig. S14). Phenologically it differs from the coastal terrestrialisation mires, which are characterised by reed beds, by the dominance of grassland communities, and morphologically by a higher position above the mean water level and sedimentologically by the occurrence of flooding silt (*Überflutungsschlick*), which is characterised by a higher content of mineral matter. Typically, the content of organic matter varies between 20 % and 30 % (*Antorf*), but locally up to 80 % has been observed. *Phragmites* largely recedes as peat-forming vegetation; radicells of rushes (above all *Juncus gerardii*) and grasses are predominantly observed as the main peat former, but sedges occur too. Jeschke and Lange (1992) described this sediment, which is characteristic of coastal mires used as pastures or meadows, as saltmarsh peat; on the geological map GK25 it is designated as flooding silt. The flooding silt layer reaches thicknesses of 2 to 4 dm and typically occurs above the KSF.

Figure 10. Between underlying *Phragmites* peat and overlying saltmarsh peat, which together form the Redentin Formation, the Karrendorf Subformation is recognisable as a black layer of heavily degraded peat. Shore of the Karrendorfer Wiesen near Greifswald during low water (for the position see Fig. 1; photo: Reinhard Lampe, 2003).

According to Jeschke and Lange (1992), the development of the sequence black layer with covering saltmarsh peat (flooding silt) is the result of the coincidence of a sea-level fluctuation and a land-use change. Hence, the regression at the transition from the Medieval Climate Anomaly (MCA) to the LIA led to the development of the black layer as a result of the desiccation and oxidation of the peat that had developed during the previous phase of rising sea level. Subsequently, the use of the desiccated reed belt areas as mowing meadows and cattle pastures, which began in the 13th century, promoted the establishment of saltmarsh vegetation and prevented a potentially renewed growth of *Phragmites* reeds during the subsequent phase of sea-level rise. The compaction of the substrate by cattle trampling and the production of H_2S promoted by the saltwater influence ensured that the grass roots were inhibited from decomposing. In combination with the more frequent flooding during the LIA and the resulting increase in clastic sediment input, this led to the saltmarsh growing up to 60 cm above the mean water level. The saltmarsh peat (flooding silt) accumulation should therefore be regarded as an anthropo-zoogenic formation.

Lampe and Janke (2004) have shown that flooding silt already occurred in earlier phases of coastal mire evolution. In such cases, too, it was the successor sediment of a black layer (see Fig. 2) but, like the latter, not as typically formed as the deposits built in the MCA and in the LIA. Mostly, it is merely silty peat. Information about the mean content of mineral matter is not meaningful for detection, as the values vary greatly depending on the (palaeo-)exposure. However, the deviation becomes clear in comparison to the under- and overlain strata, and this may be used as an indicator.

In areas not affected by dyking, drainage or land use change the flooding silt accumulated in the LIA is followed

by a shallow saltmarsh peat as the uppermost layer, which has a much higher organic content than the saltmarsh peat below (Fig. S15). This transition to an increased accumulation of organic matter is probably caused both by a reduced sediment input from the lagoons and a decreased removal of above-ground biomass of the mire through mowing and grazing. The extent to which this also reflects an accelerated sea-level rise is currently still open.

The RF includes two types of peatlands: coastal terrestrialisation mires and coastal flood mires. Lithologically, they consist of moderately to highly decomposed reed, sedge and saltmarsh peats with a variable content of mineral matter (*Antorf*, *Halbtorf* or *Volltorf*), as well as moderately to strongly degraded peat (*Fen* or *Mulm*) and flooding silt (*Überflutungsschlick*), the latter both being restricted to the upper section of the depositional sequence. Towards the shore, increasingly silty and fine sandy admixtures occur in the peat. Especially in the immediate shoreline area, wide, shallow sandy embankments can sit on top of the mires and can be interpreted as beach ridges.

The coastal mires rarely reach a thickness of more than 1.5 m, in many areas considerably less. Due to drainage measures and the associated subsidence and oxidation, the mires are severely degraded, especially in the back-barrier areas. Only in the lower reaches of rivers and creeks have thicknesses of up to 4 m been observed locally (Niederes Fischland; Lampe et al., 2010; Redentin/Groß Strömkendorf; Lampe et al., 2005; coastal sections of the rivers Recknitz; Peene and Uecker, Janke, 1978; Endtmann, 2006; Michaelis and Joosten, 2009). In the back-barrier areas, the formation overlies the KF, which defines the lower boundary of the RF. On the mainland side of the lagoons, the RF is underlain by Pleistocene sands and till, mostly of the Mecklenburg Formation or Pommern Formation. The upper boundary is usually defined by the ground surface, but in rare cases older parts of the RF may be overlain by sediments of the KF and PF. In sheltered bays and river valleys, the RF interlocks with river valley mires (Fig. 4), which are difficult to differentiate. Apart from vegetation remains or foraminifera indicating the influence of brackish water, a higher sulfur content is a possible indicator for the coastal Holocene.

5 Summary and final remarks

The four lithostratigraphic formations and two subformations described above represent all Holocene littoral deposits accumulated in the near-coastal SW Baltic realm since the region was reached by the Littorina transgression. The Greifswalder Bodden Formation started at first to accumulate, is dominated by fine-grained mud and includes underlying thin transgression contact deposits like basal peat or lag sediment. It mainly represents calm-water conditions, but tempestite layers mark occasional erosion and redeposition during storm floods.

The Karlshagen Formation started to accumulate not earlier than about 7 kyr ago when the rate of the sea-level rise declined. Sandy shallow-water accumulations with subaerial spits evolved and developed into prograding beach-ridge plains. The Prora Subformation as part of the Karlshagen Formation comprises all accumulations that are particularly coarse (pebble to boulder). All sediments reflect the effects of waves and currents.

Many beach ridges of the Karlshagen Formation and the Prora Subformation are covered by wind-driven sand. The Prerow Formation comprises exclusively these aeolian deposits, including the cliff-top dunes. The formation started to develop somewhat later than the Karlshagen Formation, as it needs dry, subaerial sand accumulations to form dunes.

The Redentin Formation is dominated by organic deposits as *Phragmites* peat or saltmarsh peat. In a few sheltered areas it started to accumulate somewhat after the Greifswalder Bodden Formation, which it may overlie. The formation has the widest distribution on the low-lying coastal belt of the mainland and on the back-barrier areas of the coastal barriers. Here, the accumulation started mainly about 1.2 kyr ago with the onset of the Late Sub-Atlantic Transgression. The Karrendorf Subformation is a layer of degraded peat, which developed shortly before the Little Ice Age due to a falling sea level. Except for the Karrrendorf Subformation, all formations are still in development.

The lithostratigraphic units are defined in a way that they are easy to recognise in the field from sediment cores and without any methods, which are not usually available in field surveys. However, it was not intended to test the suitability of the defined formations for mapping. Mapping is the task of the competent State Geological Survey, and thus, the usefulness and applicability can only be assessed within the survey's mapping practice. With the mapping experience gained, it might become necessary to revise and adjust the subdivision of the units and their definitions.

The formations as described above are well backed by the results of many investigations of the coastal barriers, the lagoons and the near-coastal offshore area of Mecklenburg-Vorpommern. Since the environmental conditions and the related facial characteristics increasingly diverge because of the growing extent of an accumulation area, the validity of a formation's definition is spatially limited. For neighbouring regions, the definitions can not be adopted without reservation and must be verified in each case. For instance, different remains of organisms or ages of accumulation must be expected even over shorter distances in the SW Baltic region, as the environmental conditions vary greatly. Also, lithofacially deviating characteristics are anticipated for lagoonal sediments and coastal mires elsewhere, which may require a more comprehensive characterisation of the existing formations in the future. Practicable solutions also need to be found to separate the set of coastal formations from inland formations, especially in areas of valleys and lowlands, and from marine formations of the open sea.

Data availability. The drilling data repository of the State Geological Survey of Mecklenburg-Vorpommern can be accessed at https://www.umweltkarten.mv-regierung.de/atlas/script/index.php (last access: 22 November 2022; LUNG MV, 2022). All other data are available from the author upon reasonable request.

Supplement. The supplement related to this article is available online at: https://doi.org/10.5194/egqsj-71-249-2022-supplement.

Competing interests. The author has declared that there are no competing interests.

Disclaimer. Publisher's note: Copernicus Publications remains neutral with regard to jurisdictional claims in published maps and institutional affiliations.

Acknowledgements. This article is mainly based on data collected since 1992 at the Chair of Physical Geography, University of Greifswald. The author would like to express his sincere thanks to all who have contributed. Therefore, the students and PhD students who have not been cited should be mentioned here: Susanne Angelstein, Anke Barthel, Johann Bastrop, Käthe Effenberger, Ulrike Kerstan, Steffen Koch, Elke Mandelkow, Mathias Möller, Anne Müller, Andreas Musolff, Michael Naumann, Susanne Rohleder, Annette Roßdeutscher, Nico Schmedemann, Christian Svensson, Henning Tiarks, Peter Voss and Björn Wohlrab. Particularly valuable contributions were made by my former colleagues Hinrich Meyer and Wolfgang Janke. Thanks also to Matthias Lampe for his support during the completion of the manuscript.

The main part of the data summarised in this paper was collected within projects mentioned below, the funding of which is thankfully acknowledged.

The author gratefully acknowledges critical comments and useful suggestions from the managing editor, Michael Zech; from the Copernicus editorial team; from the anonymous reviewer; and especially from Friederike Bungenstock as the second reviewer. They all helped to improve the paper.

Financial support. This research has been supported by the EU Commission (project no. PL-910398), the Federal Ministry for Research and Technology (BMBF; grant no. 01LK9405/4), State Mecklenburg-Vorpommern, the German Federal Environmental Foundation (DBU; project no. 20000/134), Federal State Mecklenburg-Vorpommern, and Deutsche Forschungsgemeinschaft (DFG; project no. FOR 488).

The article processing charges for this open-access publication were covered by the University of Greifswald.

Review statement. This paper was edited by Michael Zech and reviewed by Friederike Bungenstock and one anonymous referee.

References

Ad-hoc-Arbeitsgruppe Boden: Bodenkundliche Kartieranleitung KA5, Schweizerbart, Stuttgart, 438 pp., ISBN 978-3-510-95920-4, 2005.

Ad-hoc-Arbeitsgruppe Geologie: Geologische Kartieranleitung. Allgemeine Grundlagen, Geologisches Jahrbuch, G9, 135 pp., 2002.

AG Geologie: https://www.geokartieranleitung.de/Fachliche-Grundlagen/Genese/Petrogenetische-Gesteinsbezeichnung/Lockergesteine/entry/ last access: 6 April 2021.

Ahrendt, K.: Ein Beitrag zur holozänen Entwicklung Nordfrieslands, Die Küste, 71, 1–32, https://hdl.handle.net/20.500.11970/101554 (last access: 14 May 2022), 2006.

Andrén, E., Andrén, T., and Sohlenius, G.: The Holocene history of the southwestern Baltic Sea as reflected in a sediment core from Bornholm Basin, Boreas, 29, 233–250, 2000.

Barckhausen, J., Preuss, H., and Streif, H.: Ein lithologisches Ordnungsprinzip für das Küstenholozän und seine Darstellung in Form von Profiltypen, Geologisches Jahrbuch, A44, 45–74, 1977.

Behre, K.-E.: Meeresspiegelverhalten und Besiedlung während der Zeit um Christi Geburt in den Nordseemarschen, Offa, 43, 45–53, 1986.

Behrends, B., Hertweck, G., Liebezeit, G., and Goodfriend, G.: Earliest Holocene occurrence of the soft-shell clam, Mya arenaria, in the Greifswalder Bodden, Southern Baltic, Mar. Geol., 216, 79–82, 2005.

Berglund, B. E., Sandgren, P., Barnekow, L., Hannon, G., Jiang, H., Skog, G. and Yu, S.-Y.: Early Holocene history of the Baltic Sea, as reflected in coastal sediments in Blekinge, southeastern Sweden, Quatern. Int., 130, 111–139, https://doi.org/10.1016/j.quaint.2004.04.036, 2005.

Borówka, R. K. Osadczuk, A., Witkowski, A., Wawrzyniak-Wydrowska, B., and Duda, T.: Late Glacial and Holocene depositional history in the eastern part of the Szczecin Lagoon (Great Lagoon) basin–NW Poland, Quatern. Int., 130, 87–96, https://doi.org/10.1016/j.quaint.2004.04.034, 2005.

Brand, G., Hageman, B. P., Jelgersma, S., and Sindowski, K.-H.: Die lithostratigraphische Unterteilung des marinen Holozäns an der Nordseeküste, Geologisches Jahrbuch, 82, 365–384, 1965.

Bundesamt für Seeschifffahrt und Hydrographie (BSH): Meeresbodensedimente in der deutschen Ostsee, 1 : 100 000, BSH Nr. 2931–2939, 2012.

Bundesamt für Seeschifffahrt und Hydrographie (BSH): Anleitung zur Kartierung des Meeresbodens mittels hochauflösender Sonare in den deutschen Meeresgebieten, BSH Nr. 7201, 147 pp., 2016.

Cepek, A. G.: Die Lithofazieskarten Quartär 1 : 50 000 (LKQ 50)–eine Erläuterung des Kartenkonzepts mit Hinweisen für den Gebrauch, Brandenburgische Geowissenschaftliche Beiträge, 6, 3–38, 1999.

Dietrich, R. and Liebsch, G.: Zur Variabilität des Meeresspiegels an der Küste von Mecklenburg-Vorpommern, Zeitschrift für Geologische Wissenschaften, 28, 615–624, 2000.

Dörfler, W., Jakobsen, O., and Klooß, S.: Indikatoren des nacheiszeitlichen Meeresspiegelanstiegs der Ostsee. Eine methodische Diskussion am Beispiel der Ostseeförde Schlei,

Schleswig-Holstein, Universitätsforschungen zur prähistorischen Archäologie, 165, 177–186, 2009.

Endtmann, E.: Häufige botanische Makroreste in Ablagerungen des südlichen Ostseeraumes und das Küstenmoor Körkwitz nahe Ribnitz-Damgarten (Saaler Bodden), Meyniana, 58, 57–74, 2006.

Frenzel, P.: Organismenreste aus holozänen Sedimenten der Ostsee als Paläomilieuindikatoren, Meyniana, 58, 97–128, 2006.

German Stratigraphic Commission (DSK) and the Federal Institute for Geosciences and Natural Resources (BGR): Litholex – "Lithostratigraphisches Lexikon Deutschland", BGR, https://www.bgr.bund.de/DE/Themen/GG-Stratigraphie/LithoLex/litholex_node.html last access: 6 April 2021.

Gruszka, P.: The River Odra Estuary as a Gateway for Alien Species Immigration to the Baltic Sea Basin, Acta Hydroch. Hydrob., 27, 374–382, 1999.

Helama, S., Jones, P. D., and Briffa, K. R.: Dark ages cold period: A literature review and directions for future research, The Holocene, 27, 1600–1606, https://doi.org/10.1177/0959683617693898, 2017.

Hensel, R., Meyer, H., and Lampe, R.: Untersuchungen an Schlickkernen in der Darss-Zingster Boddenkette, Final project report, Umweltplan GmbH, Stralsund, 56 pp., 2006.

Hijma, M. P., Engelhart, S. E., Törnqvist, T. E., Horton, B. P., Hu, P., and Hill, D. F.: A protocol for a geological sea-level database, in: Handbook of Sea-Level Research, edited by: Shennan, I., Long, A. J., and Horton, B. P., Wiley, 536–553, 2015.

Hoffmann, G.: Rekonstruktion und Modellierung der Küstenevolution im Bereich der Pommerschen Bucht in Abhängigkeit von holozänen Meeresspiegelschwankungen, PhD thesis, University of Greifswald, Germany, 129 pp., 2004.

Hoffmann, G. and Barnasch J.: Late Glacial to Holocene coastal changes of SE Rügen Island (Baltic Sea, NE Germany), Aquat. Sci., 67, 132–141, https://doi.org/10.1007/s00027-005-0763-8, 2005.

Hoffmann, G. and Lampe, R.: Sediment budget calculation to estimate Holocene coastal changes on the southwest Baltic Sea (Germany), Mar. Geol., 243, 143–156, https://doi.org/10.1016/j.margeo.2007.04.014, 2007.

Hoffmann, G., Lampe, R., and Barnasch, J.: Postglacial evolution of coastal barriers along the West Pomeranian coast, NE Germany, Quatern. Int., 133/134, 47–59, https://doi.org/10.1016/j.quaint.2004.10.014, 2005.

Hoffmann, G., Schmedemann, N., and Schafmeister, M.-T.: Relative sea-level curve for SE Rügen and Usedom Island (SW Baltic Sea coast, Germany) using decompacted profiles, Zeitschrift der deutschen Gesellschaft für Geowissenschaften, 160, 69–78, 2009.

Hurtig, T.: Physische Geographie von Mecklenburg, Deutscher Verlag der Wissenschaften, Berlin, 252 pp., 1957.

Jaeckel, S.: Zur Ökologie der Molluskenfauna in der westlichen Ostsee, Schriften des Naturwissenschaftlichen Vereins für Schleswig-Holstein, 26, 18–50, 1952.

Janke, W.: Beitrag zur Entstehung der Dünen der Lubminer Heide sowie der Peenemünde-Zinnowitzer Seesandebene, Wissenschaftliche Zeitschrift der Ernst-Moritz-Arndt-Universität Greifswald, mathematisch-naturwissenschaftliche Reihe, 1/2, 39–54, 1971.

Janke, W.: Untersuchungen zu Aufbau, Genese und Stratigraphie küstennaher Talungen und Niederungen Nordost-Mecklenburgs als Beitrag zu ihrer geoökologischen und landeskulturellen Charakteristik, Habilitation treatise, University of Greifswald, Germany, 172 pp., 1978.

Janke, W. and Kliewe, H.: Genese und Sedimentabfolge einiger ausgewählter Bodden, Wissenschaftliche Zeitschrift der Ernst-Moritz-Arndt-Universität Greifswald, mathematisch-naturwissenschaftliche Reihe, 39, 3, 7–11, 1990.

Jeschke, L. and Lange, E.: Zur Genese der Küstenüberflutungsmoore im Bereich der vorpommerschen Boddenküste, in: Jungquartäre Landschaftsräume. Aktuelle Forschungen zwischen Atlantik und Tienschan, edited by: Billwitz, K., Jäger, K.-D., and Janke, W., Springer, Berlin, Heidelberg, Germany, 208–215, 1992.

Khan, N. S., Horton, B. P., Engelhardt, S., Rovere, A., Vacchi, M., Ashe, E. L., Törnquist, T. E., Dutton, A., Hijma, M. P., Shennan, I., and HOLSEA working group: Inception of a global atlas of sea levels since the Last Glacial Maximum, Quaternary Sci. Rev., 220, 359–371, https://doi.org/10.1016/j.quascirev.2019.07.016, 2019.

Keilhack, K.: Die Verlandung der Swinepforte, Jahrbuch der Preußischen Geologischen Landesanstalt, 32, part II/2, 209–244, 1912.

Kliewe, H.: Die Insel Usedom in ihrer spät- und nacheiszeitlichen Formenentwicklung, Deutscher Verlag der Wissenschaften, Berlin, 277 pp. 1960.

Kliewe, H.: Zur Genese der Dünen im Küstenraum der DDR, Petermanns Geographische Mitteilungen, 117, 161–168, 1973.

Kliewe, H. and Janke, W.: Zur Stratigraphie und Entwicklung des nordöstlichen Küstenraumes der DDR; Petermanns Geographische Mitteilungen, 122, 2, 81–91, 1978.

Kliewe, H. and Janke, W.: Der holozäne Wasserspiegelanstieg der Ostsee im nordöstlichen Küstengebiet der DDR, Petermanns Geographische Mitteilungen, 126, 65–74, 1982.

Kolp, O.: Die Sedimente der westlichen und südlichen Ostsee und ihre Darstellung, Beiträge zur Meereskunde, 17/18, 9–60, 1966.

Kolp, O.: Die submarinen Terrassen der südlichen Ost- und Nordsee und ihre Beziehungen zum eustatischen Meeresanstieg, Beiträge zur Meereskunde, 35, 5–48, 1976.

Kraft, J. C.: Coastal stratigraphic sequences, in: Coastal sedimentary environments, edited by: Davis Jr., R. A., Springer, New York, 361–384, ISBN 0-387-90300-3, 1978.

Krisch, H.: Die Abhängigkeit der Phragmites-Röhrichte am Greifswalder Bodden von edaphischen Faktoren und der Exponiertheit des Standortes, Archiv für Naturschutz und Landschaftsforschung, 18, 121–144, 1978.

Lampe, M. and Lampe, R.: Evolution of a large Baltic beach ridge plain (Neudarss, NE Germany): A continuous record of sea-level and wind-field variation since the Homeric Minimum, Earth Surf. Proc. Land., 43, 3042–3056, https://doi.org/10.1002/esp.4468, 2018.

Lampe, R. and Janke, W.: The Holocene sea-level rise in the southern Baltic as reflected in coastal peat sequences, Polish Geological Institute Special Papers, 11, 19–30, 2004.

Lampe, R. and Lampe M.: The role of sea-level changes in the evolution of coastal barriers – An example from the southwestern Baltic Sea, The Holocene, 31, 515–528, https://doi.org/10.1177/0959683620981703, 2021.

Lampe, R. and Meyer, H.: Sedimentqualität und hydrographische Bedingungen – ein Vergleich verschiedener Boddengewässer, BODDEN, 2, 7–26, 1995.

Lampe, R., Janke, W., Ziekur, R., Schuricht, R., Meyer, H., and Hoffmann, G.: The Late glacial/Holocene evolution of a barrier spit and related lagoonary waters – Schmale Heide, Kleiner Jasmunder Bodden and Schmachter See, Greifswalder Geographische Arbeiten, 27, 75–88, 2002.

Lampe, R., Endtmann, E., Janke, W., Meyer, H., Lübke, H., Harff, J., and Lemke, W.: A new relative sea-level curve for the Wismar Bay, N-German Baltic coast, Meyniana, 57, 5–35, 2005.

Lampe, R., Endtmann, E., Janke, W., and Meyer, H.: Relative sea-level development and isostasy along the NE German Baltic Sea coast during the past 9 ka, E&G Quaternary Sci. J., 59, 3–20, https://doi.org/10.3285/eg.59.1-2.01, 2010.

Lange, W. and Menke, B.: Beiträge zur frühpostglazialen erd- und vegetationsgeschichtlichen Entwicklung im Eidergebiet, insbesondere zur Flussgeschichte und zur Genese des sogenannten Basistorfes, Meyniana, 17, 29–44, 1967.

Leipe, T.: Beiträge zur Geochemie und Ökologie rezenter Sedimente der Boddengewässer im Nordosten der DDR, PhD thesis, University of Greifswald, Germany, 85 pp., 1986.

Leipe, T., Eidam, J., Lampe, R., Meyer, H., Neumann, T, Osadczuk, A., Janke, W., Puff, T., Blanz, T., Gingele, F. X., Dannenberger, D., and Witt, G.: Das Oderhaff–Beiträge zur Rekonstruktion der holozänen geologischen Entwicklung und anthropogenen Beeinflussung des Oder-Ästuars, Meereswissenschaftliche Berichte, 28, 61 pp., ISSN 0939-396X, 1998.

Lemke, W.: Sedimentation und paläogeographische Entwicklung im westlichen Ostseeraum (Mecklenburger Bucht bis Arkonabecken) vom Ende der Weichselvereisung bis zur Litorinatransgression, Habilitation treatise, University of Greifswald, Germany, 186 pp., 1998.

Lindner, A.: Soziologisch-ökologische Untersuchungen an der submersen Vegetation in der Boddenkette südlich des Darßes und des Zingst. PhD thesis, University of Rostock, Germany, 137 pp., 1972.

LUNG MV (Landesamt für Umwelt, Naturschutz und Geologie M-V: Historische Karten: WebAtlasDE (Graustufen), 1:1367390, LUNG MV, https://www.umweltkarten.mv-regierung.de/atlas/script/index.php, last access: 22 November 2022.

Martin-Puertas, C., Matthes, K., Brauer, A., Muscheler, R., Hansen, F., Petrick, C., Aldahan, A., Possnert, G., and van Geel, B.: Regional atmospheric circulation shifts induced by a grand solar minimum, Nat. Geosci., 5, 397–401, https://doi.org/10.1038/NGEO1460, 2012.

Mayewski, P. A., Rohling, E. E., Stager, J. C., Karlén, W., Maasch, K. A., Meeker, L. D., Meyerson, E. A., Gasse, F., van Kreveld, S., Holmgren, K., Lee-Thorp, J., Rosqvist, G., Rack, F., Staubwasser, M., Schneider, R. R., and Steig, E. J.: Holocene climate variability, Quaternary Res., 62, 243–255, https://doi.org/10.1016/j.yqres.2004.07.001, 2004.

Michaelis, D. and Joosten, H.: Mire development, relative sea-level change, and tectonic movement along the Northeast-German Baltic Sea coast, Bericht der Römisch-Germanischen Kommission 2007, 101–134, 2009.

Ministerium für Landwirtschaft, Umwelt und Verbraucherschutz Mecklenburg-Vorpommern (Ed.): Regelwerk Küstenschutz Mecklenburg-Vorpommern, Übersichtsheft, Schwerin, 102 pp., https://www.stalu-mv.de/mm/Themen/Küstenschutz/Regelwerk-Küstenschutz-Mecklenburg-Vorpommern/ (last access: 22 November 2022), 2009.

Möbus, G.: Geologie der Insel Hiddensee (südliche Ostsee) in Vergangenheit und Gegenwart – eine Monographie, Greifswalder Geowissenschaftliche Beiträge, 8, 150 pp., 2000.

Neumann, T., Rausch, N., Leipe, T., Dellwig, O., Berner, Z., and Böttcher, M.: Intense pyrite formation under low-sulfate conditions in the Achterwasser lagoon, SW Baltic Sea, Geochim. Cosmochim. Ac., 69, 3619–3630, 2005.

Niedermeyer, R.-O., Lampe, R., Janke, W., Schwarzer, K., Duphorn, K., Kliewe, H., and Werner, F.: Die deutsche Ostseeküste, Sammlung geologischer Führer, Vol. 105, 2nd edn., Gebr. Bornträger, Stuttgart, 370 pp., 2011.

Piller, W. E., van Husen, D., and Schnabel, W.: Zur lithostratigraphischen Handhabung quartärer Sedimente und deren Darstellung auf geologischen Karten, in: Stratigraphia Austriaca, edited by: Piller, W. E., Österreichische Akademie der Wissenschaften, Schriftenreihe der Erdwissenschaftlichen Kommission, Wien, 16, 7–10, 2003.

Pratje, O.: Die Bodenbedeckung der südlichen und mittleren Ostsee und ihre Bedeutung für die Ausdeutung fossiler Sedimente, Deutsche Hydrographische Zeitschrift, 1, 45–61, 1948.

Prusinkiewicz, K. and Noryśkiewicz, B.: Zagadnienie wieku bielic na wydmach brunatnych Mierzei Świny w świetle analizy palynologicznej i datowania radioweglem ^{14}C, Zeszyty Naukowe Uniwersytetu Mikołaja Kopernika w Toruniu, Geografia, 5, 75–88, 1966.

Reimann, T., Tsukamoto, S., Harff, J., Osadczuk, K., and Frechen, M.: Reconstruction of Holocene coastal foredune progradation using luminescence dating – An example from the Świna barrier (southern Baltic Sea, NW Poland), Geomorphology, 132, 1–16, https://doi.org/10.1016/j.geomorph.2011.04.017, 2011.

Remane, J., Adatte, T., Berger, J.-P., Burkhalter, R., Dall'Agnolo, S., Decrouez, D., Fischer, H., Funk, H., Furrer, H., Graf, H.-R., Gouffon, Y., Heckendorn, W., and Winkler, W.: Richtlinien zur stratigraphischen Nomenklatur, Eclogae Geol. Helv., 98, 385–405, https://doi.org/10.1007/s00015-005-1167-4, 2005.

Rosentau, A., Klemann, V., Bennike, O., Steffen, H., Wehr, J., Latinovic´, M., Bagge, M., Ojala, A., Berglund, M., Peterson Becher, G., Schoning, K., Hansson, A., Nielsen, L., Clemmensen, L. B., Hede, M. U., Kroon, A., Pejrup, M., Sander, L., Stattegger, K., Schwarzer, K., Lampe, R., Lampe, M., Uścinowicz, S., Bitinas, A., Grudzinska, I., Vassiljev, J., Nirgi, T., Kublitskiy, Y., and Subetto, D.: A Holocene relative sea-level database for the Baltic Sea, Quaternary Sci. Rev., 266, 107071, https://doi.org/10.1016/j.quascirev.2021.107071, 2021.

Rößler, D., Moros, M., and Lemke, W.: The Littorina transgression in the southwestern Baltic Sea: new insights based on proxy methods and radiocarbon dating of sediment cores, Boreas, 40, 231–241, https://doi.org/10.1111/j.1502-3885.2010.00180.x, 2011.

Scheder, J., Engel, M., Bungenstock, F., Pint, A., Siegmüller, A., Schwank, S., and Brückner, H.: Fossil bog soils ("dwog horizons") and their relation to Holocene coastal changes in the Jade Weser region, southern North Sea, Germany, J. Coast. Conserv., 22, 51–69, https://doi.org/10.1007/s11852-017-0502-z, 2018.

Schlungbaum, G.: Untersuchungen über die Sedimentqualität der Darß-Zingster Boddenkette unter besonderer Berücksichtigung der Stoffaustauschverhältnisse zwischen Wasser und Sediment, Habilitation treatise, University of Rostock, Germany, 129 pp., 1979.

Schumacher, W. and Bayerl, K.-A.: The shoreline displacement curve of Rügen Island (Southern Baltic Sea), Quatern. Int., 56, 107–113, 1999.

Schumacher, W., Lampe, R., Janke, W., Bayerl, K., Reisch, F., Müller, A., and Gusen, R.: Klimaänderung und Boddenlandschaft–KLIBO, Verbundvorhaben des BMFT, Fördernr. 01 LK9405/4, Final project report 1994–1998, 34 pp., 1998.

Schwarzer, K.: 4.2 Beeinflussung der Küstenmorphodynamik durch Wasserstandsänderungen, in: Die Wasserstände an der Ostseeküste. Entwicklung–Sturmfluten–Klimawandel, edited by: Hupfer, P., Harff, J., and Sterr, H., Die Küste, 66, 223–243, 2003.

Schwarzer, K., Ricklefs, K., Lohrberg, A., and Valerius, J.: Die geologische Entwicklung von Nord- und Ostsee, Die Küste, 87, 343–376, https://doi.org/10.18171/1.087114, 2019.

Sindowski, K.-H.: Gliederungsmöglichkeiten im sandig ausgebildeten Küsten-Holozän Ostfrieslands, Eiszeitalter und Gegenwart, 19, 209–218, 1968.

Slobodda, S.: Landschaftsökologische Kennzeichnung und Typisierung von Bodden-Verlandungsufern an den inneren Seegewässern der DDR unter Einbeziehung vegetationsökologischer Untersuchungen, Habilitation treatise, University of Greifswald, Germany, 156 pp., 1989.

Strahl, J.: Pollenanalytische Untersuchungen von Sedimentkernen aus dem Seegebiet des Greifswalder Boddens (NE-Deutschland, südliche Ostsee), Zeitschrift der deutschen geologischen Gesellschaft, 148, 81–93, 1997.

Stratigraphische Tabelle von Deutschland 20016 (STD 2016): http://www.stratigraphie.de/std/Bilder/5_2.pdf, last access: 14 May 2022.

Streif, H.: Die Profiltypenkarte des Holozän–eine neue geologische Karte zur Darstellung von Schichtenfolgen im Küstenraum für praktische und wissenschaftliche Zwecke, Die Küste, 34, 79–86, https://hdl.handle.net/20.500.11970/101151 (last access: 14 May 2022), 1979.

Succow, M.: 6. Durchströmungsmoore, in: Landschaftsökologische Moorkunde, edited by: Succow, M. and Joosten, H., Fischer, Jena, 365–379, ISBN 978-3-510-65198-6, 2001.

Verse, G.: Sedimentation und paläogeographische Entwicklung des Greifswalder Boddens und des Seegebietes der Greifswalder Oie (südliche Ostsee) seit dem Weichsel-Spätglazial, PhD thesis, University of Greifswald, Germany, 135 pp., 2001.

Verse, G., Niedermeyer, R.-O., Flemming, B., and Strahl, J.: Seismostratigraphie, Fazies und Sedimentationsgeschichte des Greifswalder Boddens (südliche Ostsee) seit dem Spätglazial, Meyniana, 50, 213–236, 1998.

Verse, G., Niedermeyer, R.-O., and Strahl, J.: Kleinskalige holozäne Meeresspiegelschwankungen an Überflutungsmooren des NE-deutschen Küstengebietes (Greifswalder Bodden, südliche Ostsee), Meyniana, 51, 153–180, 1999.

Weerts, H. J. T., Westerhoff, W. E., Cleveringa, P., Bierkens, M. F. P., Veldkamp, J. G., and Rijsdijk, K. F.: Quaternary geological mapping of the lowlands of the Netherlands, a 21st century perspective, Quatern. Int., 133–134, 159–178, https://doi.org/10.1016/j.quaint.2004.10.011, 2005.

Wernicke, W.: Die Küste der Insel Usedom und Wollin vom Peenemünder Haken bis zum Swinhöft, 1. Beiheft zum 47./48. Jahrbuch der Pommerschen Geographischen Gesellschaft 1929/1930, Greifswald, 113 pp., 1930.

E&G Quaternary Sci. J., 71, 267–274, 2022
https://doi.org/10.5194/egqsj-71-267-2022

Open Access E&G Quaternary Science Journal

Research article

Tunnel valleys in the southeastern North Sea: more data, more complexity

Arne Lohrberg, Jens Schneider von Deimling, Henrik Grob, Kai-Frederik Lenz, and Sebastian Krastel

Institute for Geosciences, Christian-Albrechts-Universität zu Kiel, 24118 Kiel, Germany

Correspondence: Arne Lohrberg (arne.lohrberg@ifg.uni-kiel.de)

Relevant dates: Received: 15 June 2022 – Revised: 23 November 2022 – Accepted: 1 December 2022 – Published: 22 December 2022

How to cite: Lohrberg, A., Schneider von Deimling, J., Grob, H., Lenz, K.-F., and Krastel, S.: Tunnel valleys in the southeastern North Sea: more data, more complexity, E&G Quaternary Sci. J., 71, 267–274, https://doi.org/10.5194/egqsj-71-267-2022, 2022.

Abstract: Large Pleistocene ice sheets have produced glacial structures both at and below the surface in northern Europe. Some of the largest and most erosive structures are so-called tunnel valleys (TVs): large and deep channels (typically up to 5 km wide and up to 400 m deep, with lengths up to 100 km), which formed below ice sheets. Although the subject of many studies, the details of their formation and fill are still not well understood. Here, we present an update on the distribution of TVs in the southeastern North Sea between Amrum and Heligoland based on a very dense grid of high-resolution 2D multi-channel reflection seismic data (400 m line spacing). The known tunnel valleys (TV1–TV3) in that area can now be traced in greater detail and further westwards, which results in an increased resolution and coverage of their distribution. Additionally, we were able to identify an even deeper and older tunnel valley, TV0, whose orientation parallels the thrust direction of the Heligoland Glacitectonic Complex (HGC). This observation implies a formation of TV0 before the HGC during an early-Elsterian or pre-Elsterian ice advance. For the first time, we acquired high-resolution longitudinal seismic profiles following the thalweg of known TVs. These longitudinal profiles offer clear indications of an incision during high-pressure bank-full conditions. The fill indicates sedimentation in an early high-energy environment for the lower part and a subsequent low-energy environment for the upper part. Our results demonstrate that a very dense profile spacing is required to decipher the complex incisions of TVs during multiple ice advances in a specific region. We also demonstrate that the time- and cost-effective acquisition of high-resolution 2D reflection seismic data holds the potential to further our understanding of the incision and filling mechanisms as well as of the distribution, complexity and incision depths of TVs in different geological settings.

Kurzfassung: Große pleistozäne Eisschilde haben in Nordeuropa glaziale Strukturen sowohl an der Oberfläche als auch unter der Oberfläche hinterlassen. Einige der größten und erosivsten Strukturen sind sogenannte Tunneltäler (TV); große und tiefe Rinnen (typischerweise bis zu 5 km breit, bis zu 400 m tief, mit einer Länge von bis zu 100 km), die sich unter Eisschilden gebildet haben. Die Bedingungen ihrer Entstehung und Verfüllung sind jedoch noch immer nicht genau verstanden. Hier zeigen wir eine Erweiterung der Verteilung von Tunneltälern in der südöstlichen Nordsee zwischen Amrum und Helgoland auf der Grundlage eines sehr dichten Netzes von hochauflösenden 2D-Mehrkanal-Reflexionsseismikdaten (400 m Profilabstand). Die bekannten Tunneltäler (TV1–TV3) in diesem Ge-

biet können nun detaillierter und weiter westlich verfolgt werden, was zu einer erhöhten Auflösung und Abdeckung ihrer Verteilung führt. Darüber hinaus konnten wir ein tieferes und älteres Tunneltal TV0 identifizieren, dessen Ausrichtung parallel zur Schubrichtung des Helgoland Glazialtektonischen Komplex (HGC) verläuft. Diese Beobachtung deutet auf eine Entstehung von TV0 vor dem HGC während eines früh- oder vor-elsterzeitlichen Eisvorstoßes hin. Zum ersten Mal haben wir hochauflösende seismische Profile genau entlang des Verlaufs der bekannten Tunneltäler aufgenommen. Diese Längsprofile liefern eindeutige Hinweise auf einen Einschnitt unter hohen Drücken. Die Füllung deutet auf eine Sedimentation während einer frühen hochenergetischen Phase für den unteren Teil und einer nachfolgenden niederenergetischen Phase für den oberen Teil hin. Unsere Ergebnisse zeigen, dass ein sehr dichter Profilabstand erforderlich ist, um die komplexen Einschnitte von Tunneltälern während mehrerer Eisvorstöße in einer ausgewählten Region zu entschlüsseln. Wir zeigen auch, dass die zeit- und kosteneffiziente Erfassung von hochauflösenden 2D-reflexionsseismischen Daten das Potenzial hat, unser Verständnis für die Erosions- und Füllmechanismen sowie für die Verteilung, Komplexität und Einschnitttiefen von Tunneltälern in verschiedenen geologischen Umgebungen zu verbessern.

1 Introduction

Extensive seismic studies have shown a high abundance of subglacially produced channels – so-called tunnel valleys (TVs) – in many regions of the North Sea (Fig. 1; Huuse and Lykke-Andersen, 2000; Lonergan et al., 2006; Kristensen et al., 2007; Lutz et al., 2009; Andersen et al., 2012; Hepp et al., 2012; Stewart et al., 2013; Lohrberg et al., 2020; Kirkham et al., 2021). TVs typically have widths of 1 to 5 km, incision depths of up to 400 m and lengths of up to 100 km (van der Vegt et al., 2012). Widths of up to 10 km and depths of up to 500 m have been observed locally in the North Sea (Ottesen et al., 2020). In the German sector of the North Sea in particular, Lutz et al. (2009) reported lengths of up to 60 km, widths of up to 8 km and depths of up to 400 m. Most of these TVs are now filled with sediments and often buried beneath a drape of glacial and interglacial deposits. The evaluation of their distribution with respect to different subsoil conditions may provide details on their incision process assuming that glacial conditions may have been comparable for larger regions of the North Sea. Constraints on the maximum incision depth and widths of TVs are needed to evaluate the long-term stability and safety of subsurface storage sites in formerly glaciated terrain due to the potential of direct hydraulic connections to otherwise sealed systems as a consequence of erosion and subsequent filling. Considering that glaciations of similar magnitude to those of the Pleistocene are likely to occur in the future (Loutre and Berger, 2000), this factor has increased in significance during the site selection process for radioactive waste. This is due to the fact that radioactive waste has half-lives of millions of years, such that German legislation requires safe storage for at least 1 million years.

Many stages of advancing and retreating ice sheets are known from the Pleistocene and correlated with the so-called marine isotope stages (MISs) derived from the analysis of ice and sediment cores all over the globe. Using the MISs, the remnants of glacially produced structures were used to correlate the cover of ice sheets in different regions during different stages of glaciations. In particular, the Scandinavian Ice Sheet (SIS) advanced into the North Sea during MIS 2 (Weichsel), MIS 6–8 (Saale), MIS 10 (Elster) and possibly MIS 16 (Cromer) (Ehlers, 1990; Ehlers et al., 2011; Batchelor et al., 2019). Only the latest glaciation during MIS 2 did not result in the full coverage of the North Sea as evidence for Weichselian ice sheets is missing in the southeastern North Sea (Batchelor et al., 2019).

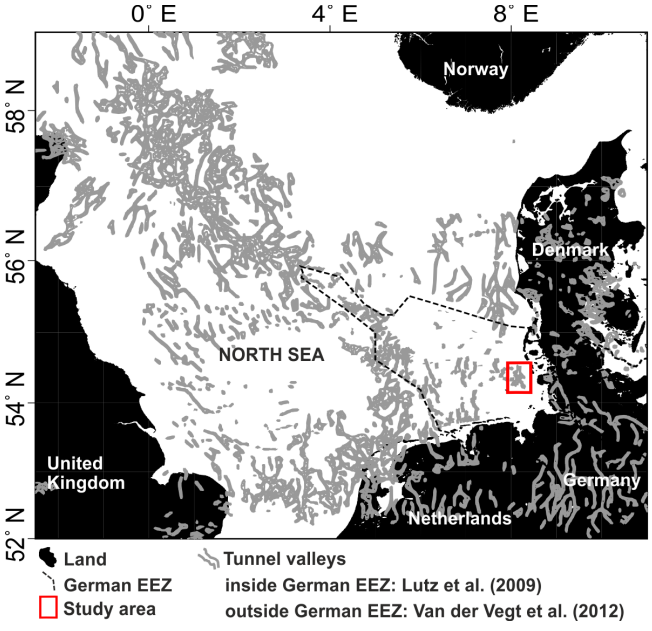

Figure 1. Location of the study area and distribution of tunnel valleys (TVs) in the North Sea and adjacent countries (adapted from Lohrberg et al., 2020).

Based on 3D seismic data, several authors showed that TVs often cross-cut and that they exist in different stratigraphic levels, such that a sequence of their formation can be derived (Kristensen et al., 2007, 2008; Stewart and Lonergan, 2011; Kirkham et al., 2021). In fact, Stewart and Lonergan (2011) were able to show that the formation of all TVs in their study area in the central North Sea can be correlated with at least seven phases of ice advance-and-retreat cycles in different directions. These results imply that TVs tend to form in multiple phases during a number of ice advances. As a consequence, a clear attribution of single TVs to the maximum extents of the three major ice advances in the North Sea (i.e. Elster, Saale and Weichsel) is not feasible. Instead, the occurrence of different phases of TVs likely represents a multitude of different ice advances and ice lobes in a specific area (Kehew et al., 1999).

The multitude of extensive 3D and high-resolution 2D seismic data provided good detail on the distribution of TVs in the North Sea (Huuse and Lykke-Andersen, 2000; Kristensen et al., 2007; Lutz et al., 2009; Stewart et al., 2013; Ottesen et al., 2020). Yet, this distribution has wide blank spots where costly 3D seismic data are not available and where 2D seismic data were acquired with a focus on potentially hydrocarbon-bearing structures hundreds of metres deeper than Pleistocene sediments. Extensive high-resolution 2D seismic studies using dense profile spacing of 800 m or less were able to show that a high-density 2D approach is well suited to assessing buried TVs (Hepp et al., 2012; Lohrberg et al., 2020). Here, we provide an update of the tunnel valley distribution between Amrum and Heligoland in the southeastern North Sea (Lohrberg et al., 2020; Fig. 2a). For the first time, we have acquired longitudinal seismic profiles following the thalweg of known TVs to image their fill over several kilometres in high resolution and to evaluate existing hypotheses for the incision and filling mechanism.

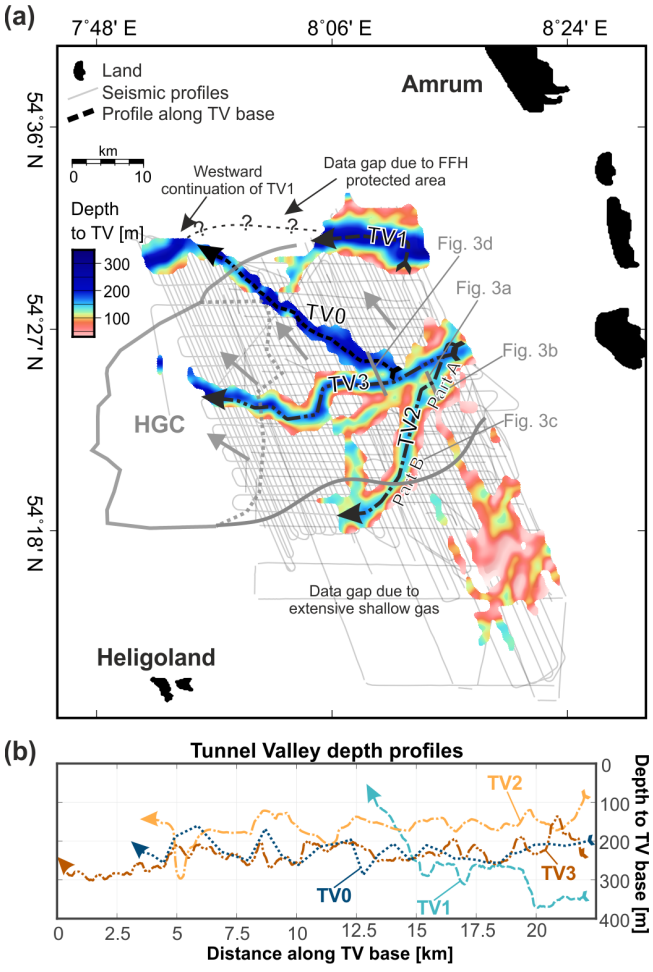

Figure 2. Overview of the study area. **(a)** Detailed distribution of large tunnel valleys (TVs) in the study area in the form of a depth grid based on all available high-resolution 2D reflection seismic profiles (with the sea level as depth reference). The limits of the Heligoland Glacitectonic Complex (HGC) are plotted for reference, where the arrows indicate the thrust direction towards the northwest (Winsemann et al., 2020; Lohrberg et al., 2022). **(b)** Depth profiles for the base of TV1–TV3 inferred from longitudinal seismic profiles following the thalweg of the TVs. Note that the depth profile for TV0 has been generated from the updated tunnel valley grid as it was unknown during data acquisition.

2 Materials and methods

We acquired 2D reflection seismic data to image subsurface structures and landforms from 0 to 800 ms two-way travel time (approximately 600 m) beneath the seafloor between Amrum and Heligoland in the southeastern North Sea. During cruise AL496 with R/V *Alkor* in July 2017, we acquired a total of 1058 km of 2D high-resolution multi-channel reflection seismic data in a closely spaced 2D grid covering approximately 800 km^2 with a mean profile spacing of 800 m. During cruise MSM98/2 with R/V *Maria S. Merian* in February 2021, we acquired an additional 1600 km of 2D high-resolution multi-channel reflection seismic data filling the gaps of the previous survey (AL496) to achieve a combined line spacing of approx. 400 m and to extend the data set westwards. Based on earlier results (Lohrberg et al., 2020), we were able to plan selected survey lines precisely along the thalweg of known TVs to produce longitudinal seismic profiles.

The acquisition setup and data processing were highly similar for both surveys, and details are described in Lohrberg et al. (2020, 2022). We used a sound velocity of 1600 m s^{-1} for the depth conversion for lack of a detailed velocity model, and depths are provided in reference to the water level. The frequencies used to image the subsurface range between 70 and 1000 Hz with the main frequency around 300 Hz, which results in a vertical resolution in the metre range for the upper tens of metres below the seafloor,

whereas the resolution decreases with increasing penetration due to the absorption of high frequencies.

The fully processed seismic sections were loaded into IHS Markit Kingdom software (2018) for interpretation. The Kingdom software was used to trace the horizons and the morphology of the subsurface landforms. The horizons were then exported for interpolation and plotting using the Generic Mapping Tools (GMT) open-source software.

3 Results

We updated our previous results for the distribution of TVs for the study area (Lohrberg et al., 2020) using the newly acquired data, which resulted in an updated map (Fig. 2a). Due to the increased profile density, we were able to close gaps that previously led to an ambiguous tracing of the TVs. Although similar to the results of Lohrberg et al. (2020), the updated map allows for the tracing of previously identified TV1, TV2 and TV3 in greater detail and approx. 10 km farther towards the west. Based on the updated map, we are confident that we imaged the westward continuation of TV1 in the northwest of the study area (Fig. 2a). Furthermore, TV2 can now be traced along its thalweg over 17 km and TV3 can now be traced along 22 km (Fig. 2b). Owing to the increased profile density, we were able to identify a new tunnel valley, TV0, which lies in a deeper stratigraphic level than TV1–TV3. The average depth of its thalweg is around 250 m, and the thalweg shows minor undulation. The fill of TV0 shows less stratification, yet it can be separated into a lower and an upper part in some profiles, despite strongly undulating reflectors in its upper part. Its flanks show more gentle slopes than the flanks of TV1–TV3, and both its beginning and its end have been crossed and eroded by other TVs. In contrast to TV1–TV3, TV0 does not show clear "shoulders" at its top, and its orientation differs. TV0 is oriented in a SE–NW direction and therefore parallels the identified thrust direction of the Heligoland Glacitectonic Complex (HGC) towards the northwest postulated in that area (Fig. 2; Winsemann et al., 2020; Lohrberg et al., 2022).

For the first time, we were able to generate high-resolution seismic profiles oriented along the thalweg of TVs by planning profiles based on earlier results (Lohrberg et al., 2020). Figure 3a shows a typical transverse profile of TV2 in which the TV infill can be delineated into two parts based on its acoustic properties (TV2f1 and TV2f2). Figure 3b and c display longitudinal profiles following TV2's thalweg, in which we traced the base of the two fills (TV2e1 and TV2e2). From Fig. 3b and c it is evident that TV2's thalweg (TV2e1) significantly undulates along the profile. The depth profiles for the thalwegs of TV1–TV3 are shown in Fig. 2b for comparison, and Table 1 provides basic values for the incision depth with respect to sea level. Based on our data, it is clear that TV2 incised through Miocene and late Paleogene strata while overcoming significant barriers of over 75 m height difference during incision (Fig. 3b and c). Part A of the longitudinal profile following TV2 (Fig. 3b) shows increased undulation and partly very deep incision of the thalweg. The dip of the thalweg parallels the dip of the underlying strata in limited areas with frequent deeper incisions on several occasions (Fig. 3b and c). The base of the upper fill (TV2f2) follows this trend and undulates more strongly in areas of deeper incision (Fig. 3b). Part B further towards the west of the study area shows slightly less undulation of the thalweg and an almost flat base of the upper fill (TV2f2; Fig. 3c). Neither TV2f1 nor TV2f2 shows a distinct stratigraphic pattern, except for a faint layering, which follows TV2e2. Excluding the undulation of the thalweg (TV2e1), the mean incision depth of TV2 is close to 160 m over the whole course of the TV, despite a significant dip of the underlying strata towards the west (Fig. 3b and c).

Table 1. Basic values for the incision depth of the largest TVs in the study area with respect to sea level.

	Minimum depth (m)	Mean depth (m)	Maximum depth (m)
TV0	161	226	288
TV1	73	271	372
TV2	75	162	297
TV3	110	237	301

4 Discussion and conclusions

Different incision mechanisms have been described for TVs, and there has long been a debate about whether the incision could be explained with fluvial erosion (Donovan, 1972; Salomonsen, 1995; Sørensen and Michelsen, 1995) or whether pressurized subglacial erosion is the more likely mechanism (Jentzsch, 1884; Kuster and Meyer, 1979; Piotrowski, 1994). Our high-resolution longitudinal profiles along a single-incision TV show that the incision has overcome significant morphological highs of over 75 m over a 500 m distance, which is a significant gradient when compared to earlier studies by Stewart et al. (2013), who showed a maximum gradient of approx. 100 m over a 1 km distance. These large gradients are impossible to reconcile with a gravity-driven fluvial erosion, as any water flow would stagnate at either of the morphological barriers (Ó Cofaigh, 1996; van der Vegt et al., 2012). Therefore, we conclude that fluvial erosion is not the primary process that led to the formation of the TVs in our study area. Instead, we conclude and confirm interpretations that bank-full pressurized drainage beneath an ice sheet was responsible for their formation (Piotrowski, 1994; Huuse and Lykke-Andersen, 2000) as bank-full conditions would be capable of overflowing such barriers. High hydraulic heads beneath kilometre-thick ice sheets in combination with abrasion at their base provided a high

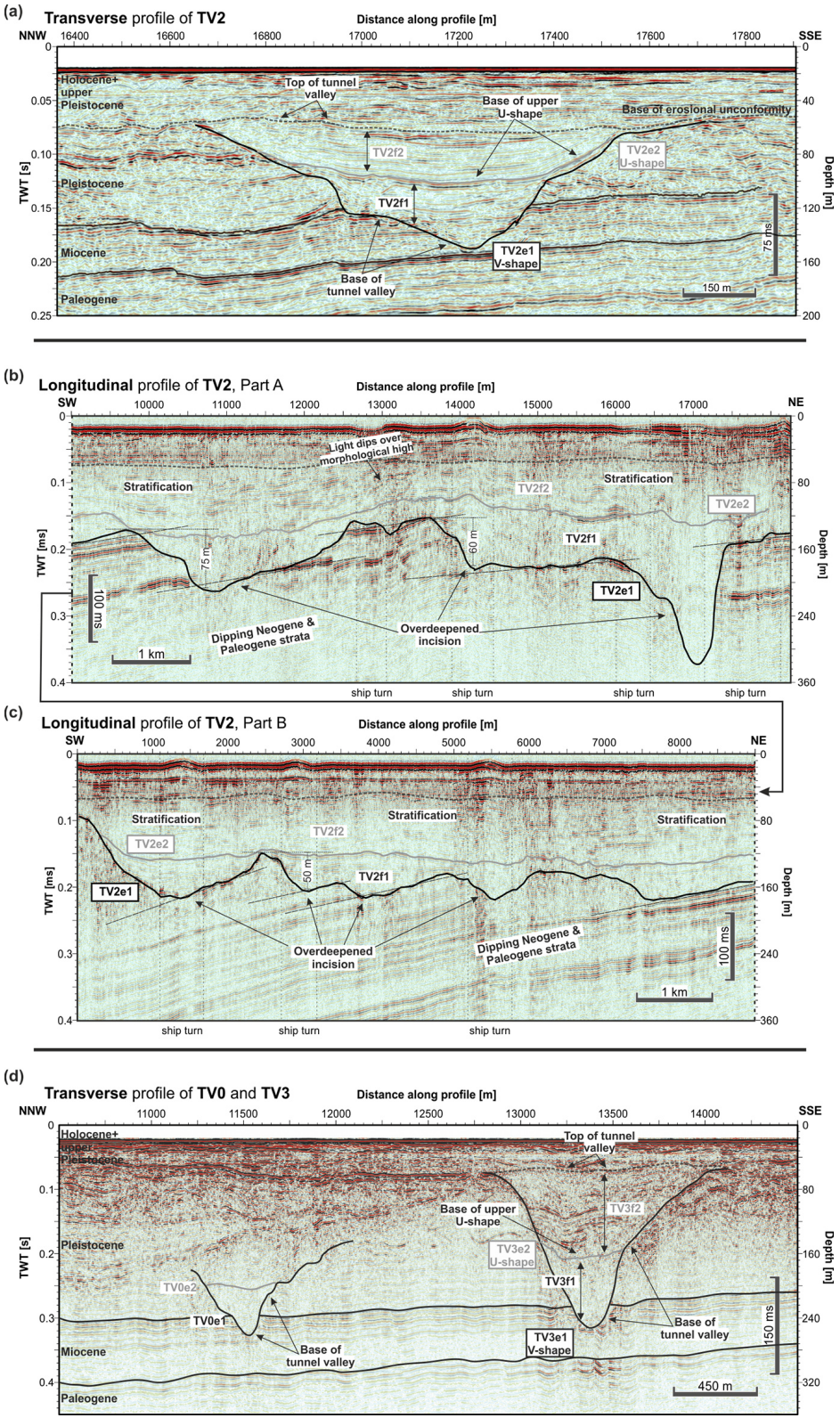

Figure 3. Seismic sections showing transverse and longitudinal profiles of a tunnel valley (TV2). The location of the profiles is indicated in Fig. 2a. **(a)** Typical transverse profile imaging TV2 perpendicular to its thalweg. **(b)** Part A and **(c)** Part B of a longitudinal profile following the thalweg of TV2 known from earlier results. **(d)** Transverse profile imaging TV0 and TV3 perpendicular to their thalweg. Turns of the ship needed to follow the TV introduce a slight decrease into the imaging quality and are marked in the figure. TV#e# refers to the respective erosional base of the respective upper or lower fill of the TV denoted as TV#f#, where # denotes a number.

efficiency for the erosion of the underlying strata. Based on the morphology of the thalweg and on the lower fill of the TVs alone, we are unable to answer whether the incision followed a "catastrophic" or rather a longer-term "steady-state" erosion process. Yet, the strongly undulating thalweg and barriers can be seen as strong indications of different stages of catastrophic erosion during different cycles of glacier retreat and advance, which would directly control the meltwater pressures at the base. Because of these observations, we consider a catastrophic meltwater outburst scenario more likely than steady-state erosion of the thalweg.

Following their incision, most TVs of the North Sea have been filled. Contrary to our expectation, we do not observe patterns that are a diagnostic for specific sedimentary processes in the fill of the TVs along their thalweg, except for a segmentation into an upper part with increased stratification and a lower part with decreased or absent stratification (TV2f1, TV2f2; Fig. 3b and c). In particular, we do not observe clinoforms or other structures postulated before as a diagnostic for the process of "backfilling" (Praeg, 1996), which refers to the near-simultaneous up-ice-directed meltwater erosion and deposition of the soil during ice sheet retreat. Rather the increased stratification in the fill's upper part (TV2f2) indicates a contemporaneous filling of the valley in a low-energy environment, possibly paralleling water level rise during melting ice sheets (Piotrowski, 1994; Huuse and Lykke-Andersen, 2000; Stewart et al., 2012; van der Vegt et al., 2012). Considering the decreased stratification in the lower part of the fill (TV2f1), we consider it likely that the early/lower fill of the TVs was deposited in a high-energy environment, which explains larger and less sorted grain sizes, such as coarse sands, gravels and boulders, being often observed in drilling campaigns in northern Germany (Hepp et al., 2012). The absence of glaciotectonic deformation along the thalweg precludes the sedimentation of TV2f1 and TV2f2 during the ice advance (van der Vegt et al., 2012). Consequently, we see evidence only for the hypothesis of filling during ice retreat in a glaciomarine or glaciolacustrine environment.

Owing to the increased density of seismic profiles, we were able to identify the hitherto unknown deep tunnel valley TV0. Likely due to a subsequent overriding ice sheet, TV0's shoulders were eroded, and only its middle and lower parts are preserved. Yet, its NW–SE orientation can be clearly derived from the data. This orientation parallels the thrust direction postulated for the HGC (Winsemann et al., 2020; Lohrberg et al., 2022). Combining its deeper stratigraphic location with thrusts occurring stratigraphically higher/later than the top of TV0, it seems likely that its incision dates back to the same ice lobe responsible for the formation of the HGC or is older (Fig. 2a). The clear separation from TV1–TV3, both in depth and in orientation, also indicates a substantial time between the formation of TV0 and TV1–TV3 as observed for other TVs in the North Sea (Stewart and Lonergan, 2011). These observations further strengthen the conclusion that an early-Elsterian or pre-Elsterian ice lobe reached the study area from the southeast (Winsemann et al., 2020; Lohrberg et al., 2022). Consequently, these chronospatial relationships indicate that TV0 may reflect this early-Elsterian or pre-Elsterian ice advance into the southeastern North Sea. Considering recent modelling results for global ice sheets (Fig. 4; Batchelor et al., 2019), we hypothesize that TV0 may be a relic of the Cromer glaciation (MIS 16). These considerations show that the distributions and the depth of TVs are major factors when trying to attribute their formation to specific glaciations in specific regions. Furthermore, the anomalous fill of TVs dictates that detailed knowledge of their distribution and depth as well as sedimentological composition is critical for offshore operations, such as construction sites for wind turbines or infrastructure for carbon capture and storage (CCS).

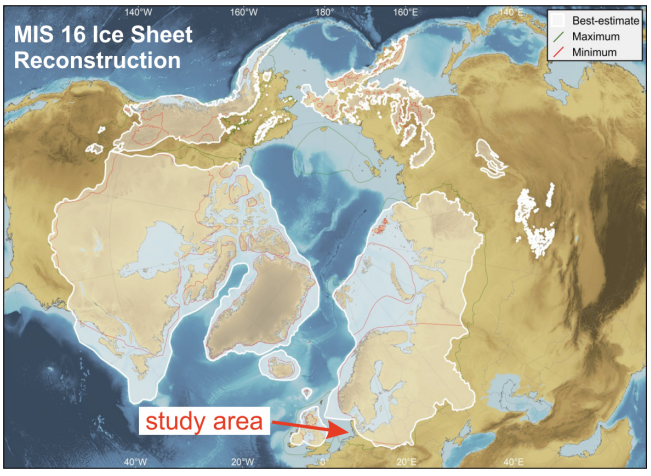

Figure 4. Reconstruction of MIS 16 ice sheets for the Northern Hemisphere (adapted from Batchelor et al., 2019).

It is relevant to understand the mechanisms of erosion and filling of TVs to understand their impact on the subsurface during future glaciations. In particular, the maximum incision depth of TVs is the most important number for radioactive waste repositories, as a potential storage location needs to be protected from erosion during climate extremes in the upcoming 1 Myr. To find this number, as many TVs as possible have to be examined for their incision depth. Our examples are representative of a large area of the North Sea where TVs have incised Neogene sands and clays, thereby providing an estimate of the maximum incision depth in Cenozoic sediments.

Equally important is the distribution of TVs as their fill may act as aquifers and thus lead to hydraulic connections between otherwise isolated aquifers in greater depths (BURVAL Working Group, 2009). Our results show that a very dense profile spacing and high resolution of reflection seismic data are essential to decipher the complexity and distribution of TVs for a specific region. In this regard, the

possibility of acquiring such data in the marine realm is unmatched by land-based measurements. Therefore, marine seismic surveys offer a unique opportunity to increase our understanding of the formation, filling and distribution pattern of TVs. This opportunity should be further exploited to answer open questions, such as a potential spatial correlation of TVs with widespread salt tectonics, and to improve our understanding of these highly erosive features to ensure the long-term protection of radioactive waste repositories.

Data availability. The data that support the findings of this study are available from the corresponding author upon request. The data will also be made publicly available through the PANGAEA data repository.

Author contributions. AL wrote the article, guided data acquisition and processed the data used for the article. JSvD and SK led the data acquisition, which was carried out by AL, HG and KFL. HG and SK provided valuable input for the streamlining of the article. The project administration was handled by JSvD and SK. All authors contributed valuable comments, discussions and guidance for the improvement of this article.

Competing interests. The contact author has declared that none of the authors has any competing interests.

Disclaimer. Publisher's note: Copernicus Publications remains neutral with regard to jurisdictional claims in published maps and institutional affiliations.

Special issue statement. This article is part of the special issue "Subglacial erosional landforms and their relevance for the long-term safety of a radioactive waste repository". It is the result of a virtual workshop held in December 2021.

Acknowledgements. We would like to thank the Schleswig-Holstein Agency for Coastal Defence, National Park and Marine Conservation (LKN.SH) and the State Agency for Agriculture, Environment and Rural Areas of Schleswig-Holstein (LLUR) for funding this work as part of the project "Nordfriesland Süd – the geological/sedimentological architecture and habitat distribution in the Wadden Sea – Shelf between the Amrum Bank and the Eider Channel (North Sea)". IHS Markit (Kingdom) and Schlumberger (Vista Desktop Seismic Data Processing) provided free academic licenses at Kiel University.

Additionally, we would like to thank the crew of R/V *Maria S. Merian* during expedition MSM98/2 and the technicians as well as the students who helped with the data acquisition.

We would also like to thank Daniel Hepp, Lukas Gegg and the anonymous reviewer for helpful suggestions that substantially improved the manuscript.

Financial support. This research has been supported by the state Schleswig-Holstein (funding programme Open Access Publikationsfonds).

Review statement. This paper was edited by Jörg Lang and reviewed by Daniel Hepp, Lukas Gegg and one anonymous referee.

References

Andersen, T. R., Huuse, M., Jørgensen, F., and Christensen, S.: Seismic investigations of buried tunnel valleys on- and offshore Denmark, Geol. Soc. Spec. Publ., 368, 129–144, https://doi.org/10.1144/SP368.14, 2012.

Batchelor, C. L., Margold, M., Krapp, M., Murton, D. K., Dalton, A. S., Gibbard, P. L., Stokes, C. R., Murton, J. B., and Manica, A.: The configuration of Northern Hemisphere ice sheets through the Quaternary, Nat. Commun., 10, 1–10, https://doi.org/10.1038/s41467-019-11601-2, 2019.

BURVAL Working Group: Buried Quaternary valleys – a geophysical approach, Z. Dtsch. Ges. Geowiss., 160, 237–247, https://doi.org/10.1127/1860-1804/2009/0160-0237, 2009.

Donovan, D. T.: The geology and origin of the Silver Pit and other closed basins in the North Sea, Proc. Yorksh. Geol. Soc., 39, 267–293, 1972.

Ehlers, J.: Reconstructing the Dynamics of the North-West European Pleistocene Ice Sheets, Quat. Sci. Rev., 9, 71–83, 1990.

Ehlers, J., Grube, A., Stephan, H. J., and Wansa, S.: Pleistocene glaciations of North Germany-New results, Dev. Quat. Sci., 15, 149–162, https://doi.org/10.1016/B978-0-444-53447-7.00013-1, 2011.

Hepp, D. A., Hebbeln, D., Kreiter, S., Keil, H., Bathmann, C., Ehlers, J., and Mörz, T.: An east-west-trending Quaternary tunnel valley in the south-eastern North Sea and its seismic-sedimentological interpretation, J. Quat. Sci., 27, 844–853, https://doi.org/10.1002/jqs.2599, 2012.

Huuse, M. and Lykke-Andersen, H.: Overdeepened Quaternary valleys in the eastern Danish North Sea: Morphology and origin, Quat. Sci. Rev., 19, 1233–1253, https://doi.org/10.1016/S0277-3791(99)00103-1, 2000.

Jentzsch, A.: Über die Bildung der preussischen Seeen., Zeitschrift der Dtsch. Geol. Gesellschaft, 36, 699–702, 1884.

Kehew, A. E., Nicks, L. P., and Straw, W. T.: Palimpsest tunnel valleys: Evidence for relative timing of advances in an interlobate area of the Laurentide ice sheet, Ann. Glaciol., 28, 47–52, https://doi.org/10.3189/172756499781821940, 1999.

Kirkham, J. D., Hogan, K. A., Larter, R. D., Self, E., Games, K., Huuse, M., Stewart, M. A., Ottesen, D., Arnold, N. S., and Dowdeswell, J. A.: Tunnel valley infill and genesis revealed by high-resolution 3-D seismic data, Geology, 49, 1516–1520, https://doi.org/10.1130/G49048.1, 2021.

Kristensen, T. B., Huuse, M., Piotrowski, J. A., and Clausen, O. R.: A morphometric analysis of tunnel valleys in the eastern North Sea based on 3D seismic data, J. Quat. Sci., 22, 801–815, https://doi.org/10.1002/jqs.1123, 2007.

Kristensen, T. B., Piotrowski, J. A., Huuse, M., Clausen, O. R., and Hamberg, L.: Time-transgressive tunnel valley formation indicated by infill sediment structure, North Sea – the role of glacio-

hydraulic supercooling, Earth Surf. Proc. Land., 33, 546–559, https://doi.org/10.1002/esp.1668, 2008.

Kuster, H. and Meyer, K.-D.: Glaziäre Rinnen im mittleren und nördlichen Niedersachsen, E&G Quaternary Sci. J., 29, 135–156, https://doi.org/10.3285/eg.29.1.12, 1979.

Lohrberg, A., Schwarzer, K., Unverricht, D., Omlin, A., and Krastel, S.: Architecture of tunnel valleys in the southeastern North Sea: new insights from high-resolution seismic imaging, J. Quat. Sci., 35, 892–906, https://doi.org/10.1002/jqs.3244, 2020.

Lohrberg, A., Krastel, S., Unverricht, D., and Schwarzer, K.: The Heligoland Glacitectonic Complex in the southeastern North Sea: indicators of a pre- or early-Elsterian ice margin, Boreas, 51, 10000117, https://doi.org/10.1111/bor.12551, 2022.

Lonergan, L., Maidment, S. C. R., and Collier, J. S.: Pleistocene subglacial tunnel valleys in the central North Sea basin: 3-D morphology and evolution, J. Quat. Sci., 21, 891–903, https://doi.org/10.1002/jqs.1015, 2006.

Loutre, M. F. and Berger, A.: Future climatic changes: Are we entering an exceptionally long interglacial?, Clim. Change, 46, 61–90, https://doi.org/10.1023/a:1005559827189, 2000.

Lutz, R., Kalka, S., Gaedicke, C., Reinhardt, L., and Winsemann, J.: Pleistocene tunnel valleys in the German North Sea: spatial distribution and morphology, Z. Dtsch. Ges. Geowiss., 160, 225–235, https://doi.org/10.1127/1860-1804/2009/0160-0225, 2009.

Ó Cofaigh, C.: Tunnel Valley Genesis, Encycl. Environ. Chang., 20, 1–19, https://doi.org/10.4135/9781446247501.n4006, 1996.

Ottesen, D., Stewart, M., Brönner, M., and Batchelor, C. L.: Tunnel valleys of the central and northern North Sea (56° N to 62° N): Distribution and characteristics, Mar. Geol., 425, 106199, https://doi.org/10.1016/j.margeo.2020.106199, 2020.

Piotrowski, J. A.: Tunnel-valley formation in northwest Germany-geology, mechanisms of formation and subglacial bed conditions for the Bornhöved tunnel valley, Sediment. Geol., 89, 107–141, https://doi.org/10.1016/0037-0738(94)90086-8, 1994.

Praeg, D.: Morphology, stratigraphy and genesis of buried Mid-Pleistocene tunnel-valleys in the Southern North Sea Basin, doctoral thesis, University of Edinburgh, United Kingdom, 1996.

Salomonsen, I.: Origin of a deep buried valley system in Pleistocene deposits of the eastern central North Sea, in: Proceedings of the 2nd Symposium on: Marine Geology – Geology of the North Sea and Skagerrak, 7–8 October 1993, Aarhus, Denmark, 7–19, https://doi.org/10.34194/seriec.v12.7106, 1995.

Sørensen, J. C. and Michelsen, O.: Upper Cenozoic sequences in the southeastern North Sea Basin, Bull. Geol. Soc. Denmark, 42, 74–95, https://doi.org/10.37570/bgsd-1995-42-08, 1995.

Stewart, M., Lonergan, L., and Hampson, G.: 3D seismic analysis of buried tunnel valleys in the Central North Sea: tunnel valley fill sedimentary architecture, Geol. Soc. London, Spec. Publ., 368, 173–184, https://doi.org/10.1144/SP368.9, 2012.

Stewart, M. A. and Lonergan, L.: Seven glacial cycles in the middle-late Pleistocene of northwest Europe: Geomorphic evidence from buried tunnel valleys, Geology, 39, 283–286, https://doi.org/10.1130/G31631.1, 2011.

Stewart, M. A., Lonergan, L., and Hampson, G.: 3D seismic analysis of buried tunnel valleys in the central North Sea: Morphology, cross-cutting generations and glacial history, Quat. Sci. Rev., 72, 1–17, https://doi.org/10.1016/j.quascirev.2013.03.016, 2013.

van der Vegt, P., Janszen, A., and Moscariello, A.: Tunnel valleys: current knowledge and future perspectives, Geol. Soc. London, Spec. Publ., 368, 75–97, https://doi.org/10.1144/SP368.13, 2012.

Winsemann, J., Koopmann, H., Tanner, D. C., Lutz, R., Lang, J., Brandes, C., and Gaedicke, C.: Seismic interpretation and structural restoration of the Heligoland glaciotectonic thrust-fault complex: Implications for multiple deformation during (pre-)Elsterian to Warthian ice advances into the southern North Sea Basin, Quat. Sci. Rev., 227, 1–15, https://doi.org/10.1016/j.quascirev.2019.106068, 2020.

continued from back cover

ISSN 0424-7116

CONTENTS

continued on the inside cover

ISSN 0424-7116